VISUALIZATION OF MOLECULAR DYNAMICS IN LIVE CELLS BY FLUORESCENT PROTEIN-BASED BIOSENSORS

EDITED BY: Jihye Seong and Yingxiao Wang
PUBLISHED IN: Frontiers in Cell and Developmental Biology

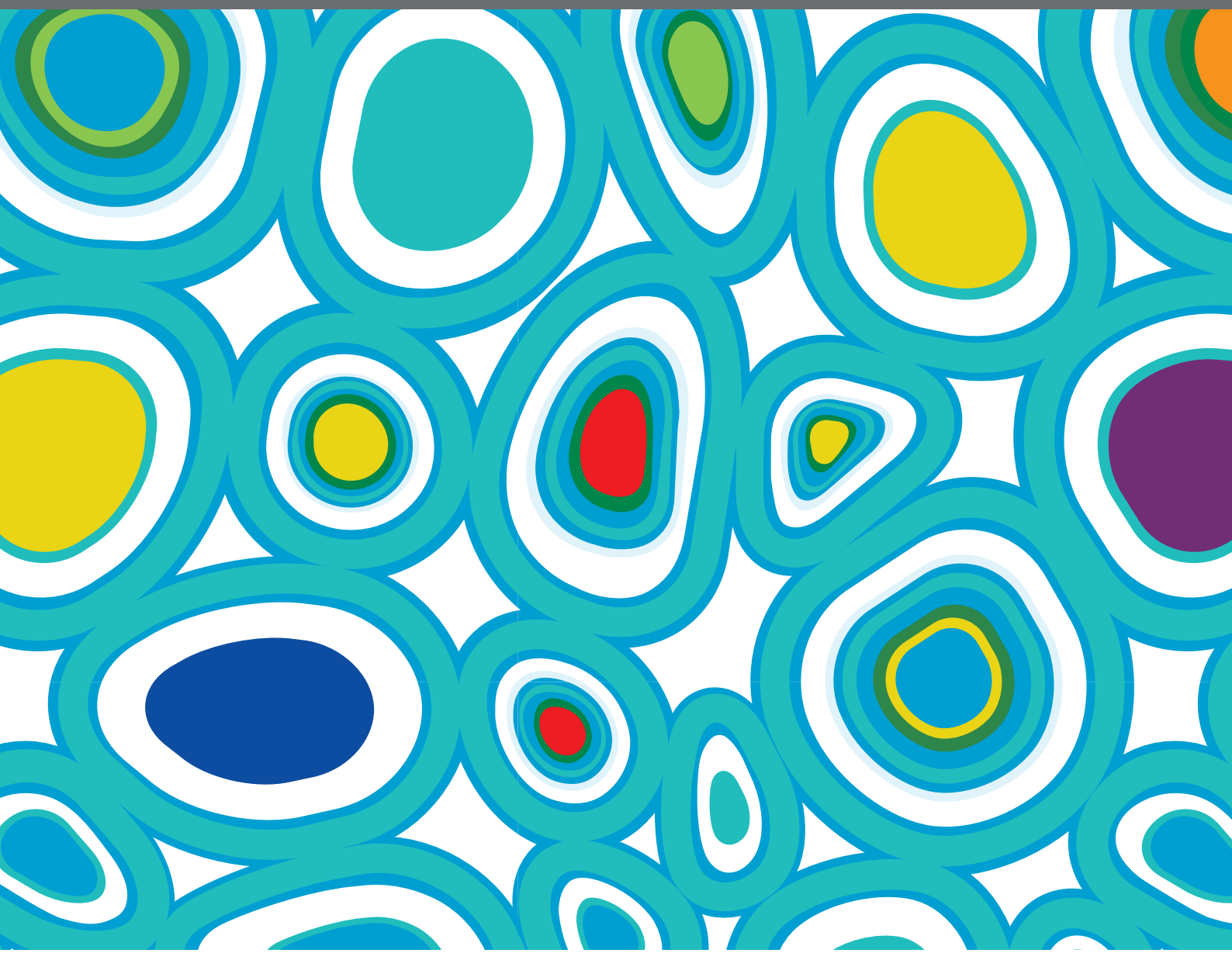

frontiers Research Topics

frontiers

ISSN 1664-8714
ISBN 978-2-83250-623-3
DOI 10.3389/978-2-83250-623-3

About Frontiers

Frontiers is more than just an open-access publisher of scholarly articles: it is a pioneering approach to the world of academia, radically improving the way scholarly research is managed. The grand vision of Frontiers is a world where all people have an equal opportunity to seek, share and generate knowledge. Frontiers provides immediate and permanent online open access to all its publications, but this alone is not enough to realize our grand goals.

Frontiers Journal Series

The Frontiers Journal Series is a multi-tier and interdisciplinary set of open-access, online journals, promising a paradigm shift from the current review, selection and dissemination processes in academic publishing. All Frontiers journals are driven by researchers for researchers; therefore, they constitute a service to the scholarly community. At the same time, the Frontiers Journal Series operates on a revolutionary invention, the tiered publishing system, initially addressing specific communities of scholars, and gradually climbing up to broader public understanding, thus serving the interests of the lay society, too.

Dedication to Quality

Each Frontiers article is a landmark of the highest quality, thanks to genuinely collaborative interactions between authors and review editors, who include some of the world's best academicians. Research must be certified by peers before entering a stream of knowledge that may eventually reach the public - and shape society; therefore, Frontiers only applies the most rigorous and unbiased reviews.
Frontiers revolutionizes research publishing by freely delivering the most outstanding research, evaluated with no bias from both the academic and social point of view. By applying the most advanced information technologies, Frontiers is catapulting scholarly publishing into a new generation.

What are Frontiers Research Topics?

Frontiers Research Topics are very popular trademarks of the Frontiers Journals Series: they are collections of at least ten articles, all centered on a particular subject. With their unique mix of varied contributions from Original Research to Review Articles, Frontiers Research Topics unify the most influential researchers, the latest key findings and historical advances in a hot research area! Find out more on how to host your own Frontiers Research Topic or contribute to one as an author by contacting the Frontiers Editorial Office: frontiersin.org/about/contact

VISUALIZATION OF MOLECULAR DYNAMICS IN LIVE CELLS BY FLUORESCENT PROTEIN-BASED BIOSENSORS

Topic Editors:
Jihye Seong, Korea Institute of Science and Technology (KIST), South Korea
Yingxiao Wang, University of California, San Diego, United States

Citation: Seong, J., Wang, Y., eds. (2022). Visualization of Molecular Dynamics in Live Cells by Fluorescent Protein-Based Biosensors.
Lausanne: Frontiers Media SA. doi: 10.3389/978-2-83250-623-3

Table of Contents

frontiers | Frontiers in Cell and Developmental Biology

TYPE Editorial
PUBLISHED 14 October 2022
DOI 10.3389/fcell.2022.1054774

OPEN ACCESS

EDITED AND REVIEWED BY
Akihiko Ito,
Kindai University, Japan

*CORRESPONDENCE
Jihye Seong,
jseong@kist.re.kr
Yingxiao Wang,
yiw015@eng.ucsd.edu

SPECIALTY SECTION
This article was submitted to Cell Adhesion and Migration, a section of the journal Frontiers in Cell and Developmental Biology

RECEIVED 27 September 2022
ACCEPTED 04 October 2022
PUBLISHED 14 October 2022

CITATION
Seong J and Wang Y (2022), Editorial: Visualization of molecular dynamics in live cells by fluorescent protein-based biosensors.
Front. Cell Dev. Biol. 10:1054774.
doi: 10.3389/fcell.2022.1054774

Editorial: Visualization of molecular dynamics in live cells by fluorescent protein-based biosensors

Jihye Seong[1,2,3]* and Yingxiao Wang[4]*

[1]Brain Science Institute, Korea Institute of Science and Technology (KIST), Seoul, South Korea, [2]Division of Bio-Medical Science and Technology, KIST School, Korea University of Science and Technology, Seoul, South Korea, [3]Department of Converging Science and Technology, Kyung Hee University, Seoul, South Korea, [4]Department of Bioengineering, Institute of Engineering in Medicine, University of California, San Diego, San Diego, CA, United States

KEYWORDS

fluorescent protein, fluorescent biosensor, live-cell imaging, FRET, molecular dynamics

Editorial on the Research Topic
Visualization of molecular dynamics in live cells by fluorescent protein-based biosensors

Cells continuously respond to a variety of stimulations, such as extracellular ligands, cell-cell interactions, and mechanical signals. These extracellular signals are received by membrane receptors, including ion channels, receptor tyrosine kinases (RTKs), G protein-coupled receptors (GPCRs), integrins, cadherins, and other adhesion molecules (Pierce et al., 2002; Kholodenko, 2006; Horwitz, 2012). They are translated and transferred into the cells through signaling pathways, for example, kinases and phosphatases, second messengers such as cAMP and Ca^{2+}, small GTPases, and transcription factors. The spatiotemporal interactions of these signaling molecules control complex cellular processes such as differentiation, cell migration, proliferation, and survival. Genetically encodable fluorescent protein (FP)-based biosensors have been developed for the real-time monitoring of molecular dynamics with the high spatiotemporal resolution, and applied to understand underlying mechanisms of complex cellular processes (Zacharias et al., 2000; Wang et al., 2008; Kim et al., 2021; Dong et al., 2022). Recent advances in the development and applications of the FP-based biosensors are introduced in the current topic entitled *Visualization of molecular dynamics in live cells by fluorescent protein-based biosensors*.

First, Zhou et al. revealed signaling dynamics in T cells after the activation of the chimeric antigen receptor (CAR) specific to the thyroid-stimulating hormone receptor (TSHR). Utilizing fluorescent resonance energy transfer (FRET)-based biosensors, they can observe rapid activation of ZAP70 kinase and ERK in TSHR CAR-T cells upon binding to target cancer cells, thus the efficacy of CAR-T cells can be investigated by FRET

imaging. Second, the FRET technology was also applied by Fang et al. to visualize the ERK activation upon cyclic mechanical stretch in airway smooth muscle cells *via* mechanosensitive Ca^{2+} channels. Furthermore, Kim et al. showed that the Piezo1-induced Ca^{2+} influx mediates membrane ruffling and cell survival through PKA, ERK, Rac1, and ROCK activity. Different fluorescent biosensors were applied to investigate various signaling dynamics in live cells, and membrane ruffling was analyzed by spatiotemporal image correlation spectroscopy (STICS). Finally, Kim et al. reviewed a variety of fluorescent biosensors with different sensing strategies such as bioluminescence resonance energy transfer (BRET), FRET, circular permuted FP (cpFP), and nanobody, for the real-time monitoring of each stage of GPCR activation. Thus, a broad range of dynamic signaling events in response to different extracellular stimuli can be monitored and tracked by live-cell imaging with advanced fluorescent biosensors.

The dynamic molecular interactions are tightly controlled in space and time. Thus, it is critical to monitor the real-time molecular events by fluorescent biosensors in subcellular regions. Ku et al. monitored the movement of chromatin in the nucleus by single-particle tracking of CRISPR/dCas9-tagged FP in live cells and reported the effects of transcription-dependent physical perturbations on the chromosome dynamics. In addition, Karasev et al. compared different nuclear localization signals (NLSs) with different importin specificities and identified uncommon NLSs optimized for neurons. They utilized these NLSs to develop an optogenetic tool for the nuclear export of proteins. Kim et al. reviewed the optimization processes for the development of FRET-based biosensors and discussed the available subcellular targeting sequences for fluorescent biosensors. These localization sequences include nuclear export signal (NES), NLS, mitochondrial targeting sequence, the signals for membrane microdomains and outside plasma membrane, and ER retention sequence. The correct subcellular localization of fluorescent biosensors is critical for the sensitive monitoring of subtle but essential physiological molecular events.

It has been significant efforts for the development of enhanced FPs and new fluorescent biosensors with diverse colors. Rad et al. explored the residues of a voltage-sensing domain to increase voltage sensitivity of the current genetically encoded voltage indicators (GEVIs) and developed Plos6-vs with improved dynamic range and faster response kinetics. Wu et al. reviewed fluorescent indicators for detecting monatomic ions such as Ca^{2+}, Zn^{2+}, K^{+}, Na^{+}, H^{+}, Cl^{-}, Cu^{+}, and toxic ions. They introduced various sensing strategies utilizing different colors of FPs, such as red, far-red, and near-infrared (NIR). Matlashov et al. developed a genetically encoded calcium indicator (GECI) based on FRET between miRFP670nano and miRFP720, iGECInano, which shows enhanced brightness and photostability and faster response kinetics. This NIR GECI allows spectral crosstalk-free combinations with green-colored biosensors. Finally, Ning et al. introduced Crimson, a bright, nontoxic, and non-aggregating red FP. The membrane-targeted Crimson-CAAX allows long-term labeling of thin neurites, dendritic spines, and filopodia in neurons and can be applied together with green-colored probes. The multicolor fluorescent biosensors will allow a deeper understanding of the complex molecular dynamics of multiple signaling events.

In summary, the current topic, composed of eight research articles and three review articles, introduces recent progresses in FP-based biosensors and their applications for the visualization of spatiotemporal molecular dynamics in live cells. The further development of advanced biosensor technologies and their applications in live-cell imaging will pave the way for the future discovery of the underlying mechanisms of complex molecular dynamics crucial for cell functions.

Author contributions

All authors listed have made a substantial, direct, and intellectual contribution to the work and approved it for publication.

Funding

The work is supported by KIST Institutional grant 2E31523, National Research Foundation of Korea grant 2021R1A2C1093429, and Samsung Research Funding and Incubation Center of Samsung Electronics under Project Number SRFC-TC2003-02 (JS) and NIH R35 GM140929, R01 CA262815, R01 EB029122, R01 HL121365, and R01 HD107206 (YW).

Conflict of interest

The authors declare that the research was conducted in the absence of any commercial or financial relationships that could be construed as a potential conflict of interest.

Publisher's note

References

Dong, C., Zheng, Y., Long-Iyer, K., Wright, E. C., Li, Y., and Tian, L. (2022). Fluorescence imaging of neural activity, neurochemical dynamics, and drug-specific receptor conformation with genetically encoded sensors. *Annu. Rev. Neurosci.* 45, 273–294. doi:10.1146/annurev-neuro-110520-031137

Horwitz, A. R. (2012). The origins of the molecular era of adhesion research. *Nat. Rev. Mol. Cell. Biol.* 13, 805–811. doi:10.1038/nrm3473

Kholodenko, B. N. (2006). Cell-signalling dynamics in time and space. *Nat. Rev. Mol. Cell. Biol.* 7, 165–176. doi:10.1038/nrm1838

Kim, H., Ju, J., Lee, H. N., Chun, H., and Seong, J. (2021). Genetically encoded biosensors based on fluorescent proteins. *Sensors (Basel)* 21, 795. doi:10.3390/s21030795

Pierce, K. L., Premont, R. T., and Lefkowitz, R. J. (2002). Seven-transmembrane receptors. *Nat. Rev. Mol. Cell. Biol.* 3, 639–650. doi:10.1038/nrm908

Wang, Y., Shyy, J. Y., and Chien, S. (2008). Fluorescence proteins, live-cell imaging, and mechanobiology: Seeing is believing. *Annu. Rev. Biomed. Eng.* 10, 1–38. doi:10.1146/annurev.bioeng.010308.161731

Zacharias, D. A., Baird, G. S., and Tsien, R. Y. (2000). Recent advances in technology for measuring and manipulating cell signals. *Curr. Opin. Neurobiol.* 10, 416–421. doi:10.1016/s0959-4388(00)00101-x

frontiers in Cell and Developmental Biology

ORIGINAL RESEARCH
published: 17 February 2022
doi: 10.3389/fcell.2022.845319

Signaling Dynamics of TSHR-Specific CAR-T Cells Revealed by FRET-Based Biosensors

Jing Zhou[1,2], Jiangqing Chen[3,4,5], Yanjie Huang[6], Xiaofei Gao[6], Chun Zhou[7], Xianhui Meng[3,4,5] and Jie Sun[3,4,5]**

[1]Department of Breast and Thyroid Surgery, Union Hospital, Tongji Medical College, Huazhong University of Science and Technology, Wuhan, China, [2]Department of Breast and Thyroid Surgery, People's Hospital of Dongxihu District Wuhan City and Union Dongxihu Hospital, Huazhong University of Science and Technology, Wuhan, China, [3]Liangzhu Laboratory, Zhejiang University Medical Center, Hangzhou, China, [4]Department of Cell Biology, Bone Marrow Transplantation Center of the First Affiliated Hospital, Zhejiang University School of Medicine, Hangzhou, China, [5]Institute of Hematology, Zhejiang University and Zhejiang Engineering Laboratory for Stem Cell and Immunotherapy, Hangzhou, China, [6]Key Laboratory of Structural Biology of Zhejiang Province, School of Life Sciences, Westlake University, Hangzhou, China, [7]School of Public Health, Sir Run Run Shaw Hospital, Zhejiang University School of Medicine, Hangzhou, China

OPEN ACCESS

Edited by:
Yingxiao Wang, University of California, San Diego, United States

Reviewed by:
Kazuhiro Aoki, Graduate University for Advanced Studies (Sokendai), Japan
Tian Chi, Yale University, United States

***Correspondence:**
Xianhui Meng
xianhm@zju.edu.cn
Jie Sun
sunj4@zju.edu.cn

Specialty section:
This article was submitted to Cell Adhesion and Migration, a section of the journal Frontiers in Cell and Developmental Biology

Received: *29 December 2021*
Accepted: *31 January 2022*
Published: *17 February 2022*

Citation:
Zhou J, Chen J, Huang Y, Gao X, Zhou C, Meng X and Sun J (2022) Signaling Dynamics of TSHR-Specific CAR-T Cells Revealed by FRET-Based Biosensors. Front. Cell Dev. Biol. 10:845319. doi: 10.3389/fcell.2022.845319

Although most patients with thyroid cancers have good prognosis and long-term survival, some patients are refractory to traditional therapeutic approaches and face a high risk of mortality. CAR-T therapy provides an attractive strategy to treat these patients. Considering the limited expression in thyroid tissues, thyroid-stimulating hormone receptor (TSHR) has been considered as a promising candidate as CAR-T target. However, it is still a challenge to find the optimal CAR design for the treatment of thyroid cancers. Dynamic signaling cascade is initiated by CAR molecules during CAR-T cell activation. The development of FRET-based biosensors enables us to detect the signaling dynamics of key kinases during CAR-T cell activation with high spatiotemporal resolution. Here using the ZAP70 and ERK biosensors, we visualized the dynamics of ZAP70 and ERK activities in TSHR-specific CAR-T cells upon antigen stimulation. We first constructed several TSHR-targeting CARs for the treatment of advanced thyroid cancers. The TSHR CAR-T cells with CD28 or 4-1BB co-stimulatory signaling domains exhibited potent cytotoxicity *in vitro*. By FRET imaging, we observed rapid increase of ZAP70 and ERK activities in TSHR CAR-T cells upon target cell binding. Even though CD28-based CAR-T cells had similar ZAP70 activation dynamics as 4-1BB-based CAR-T cells, they displayed slightly enhanced ERK activation, which may contribute to their faster anti-tumor kinetics *in vivo*. These results demonstrated the efficacy of TSHR CAR-T cells to treat advanced thyroid cancers. Our study indicated the potential of applying FRET biosensors to optimize the design of CAR for effective CAR-T therapy.

Keywords: FRET, ERK, ZAP70, CAR-T, TSHR, thyroid cancer

INTRODUCTION

Thyroid cancer is the most common endocrine cancer and accounts for 3% of the new cancer cases worldwide in 2020 (Sung et al., 2021). Majority of thyroid cancers are differentiated thyroid cancers (DTC, 94%), which mainly include papillary thyroid cancer (PTC, 80% of all cases), and follicular thyroid cancer (FTC, 15% of all cases). Although most patients with DTCs have excellent prognosis after radical surgery and radioactive iodine (RAI) treatment, a small fraction of them (about 20%)

may develop into advanced stage DTCs after tumor recurrence and metastasis, which may require reoperation. Large amount of fibrous and scar tissue in the surgical field will bring difficulties to the reoperation, which increases the incidence of permanent nerve injury and hypoparathyroidism, especially for patients who needs central lymph nodes dissection and/or cervical lymph nodes dissection again. It is reported that the incidence of permanent hypocalcemia and permanent vocal cord paralysis after re-dissection of cervical lymph nodes can be as high as 4.9 and 17.8% respectively, which may seriously affect the quality of patients' life. For such patients, exploring a new non-invasive treatment method is of great value. In addition, 5–10% of DTC cases with recurrence and metastasis are resistant to traditional therapy and suffer a high risk of mortality. It is reported that patients with refractory DTCs have less than 50% of 5-years survival rate (Laha et al., 2020). For these patients, it is urgent to explore new treatment methods.

Chimeric antigen receptor T (CAR-T) therapy represents a novel therapeutic approach and has achieved significant progress in treating hematological malignancies. The canonical CAR structure includes an scFv domain responsible for antigen recognition, a hinge and transmembrane domain, and a combined co-stimulatory and activation domain that initiates T cell activation. CAR molecules can reprogram T cell to recognize and eliminate tumor cells expressing specific antigens (van der Stegen et al., 2015). Although many challenges remain, experimental and clinical studies have shown some positive outcomes of CAR-T therapy for solid tumors (Newick et al., 2017). For advanced thyroid cancers, recent studies demonstrated that CAR-T therapy has potential therapeutic efficacy in treating anaplastic thyroid cancer (ATC) and medullary thyroid cancer (MTC) in preclinical models (Min et al., 2017; Bhoj et al., 2021).

Successful application of CAR-T therapy requires specific recognition of tumor cells. However, most solid tumors, including thyroid cancer, lack tumor-specific antigens that could be used to precisely distinguish tumor and normal tissue cells. Some tumor-associated antigens (TAA) have been used as CAR-T cell targets, while the risk of tumor relapse or severe on-target/off-tumor toxicity has to be evaluated carefully. As an alternative, lineage-specific antigens may be considered as targets of CAR-T cells in solid tumors as long as complete tissue eradiation is tolerant (Newick et al., 2017; Kosti et al., 2018). The thyroid-stimulating hormone receptor (TSHR) is a surface glycoprotein receptor whose expression is highly restricted to thyroid tissues. Evidence has shown continued high expression of TSHR in the majority of DTCs, including 90.8% in PTC, 89.2% in FTC, 78.2% in the cervical lymph node metastases, and 86.7% in the RAI-resistant metastases. These features suggest the potential of TSHR as CAR-T therapy targets for the treatment of advanced stage DTCs (Davies et al., 2002; Rowe et al., 2017).

Currently, the second-generation CARs that incorporate CD28 or 4-1BB signaling domains are the most prevalent CAR designs. Both CD28 and 4-1BB-based CAR-T cells can achieve complete tumor eradiation in clinical studies of refractory B cell malignancies. However, the different co-stimulatory domains have endowed CAR-T cells with distinct anti-tumor kinetics. CD28-based CAR-T cells often show rapid tumor eradiation with less persistence. In contrast, 4-1BB-based CAR-T cells often have less cytotoxic effect while persist longer *in vivo* (Feucht and Sadelain, 2020). Therefore, in the context of different solid tumors, the anti-tumor functions of CD28 and 4-1BB-based CARs may vary.

Nowadays, the development of genetically-encoded, FRET-based biosensors makes it possible to investigate kinetics of key signaling molecules in live cells with high spatiotemporal resolution. Recent studies have demonstrated that FRET-based biosensors can be used to monitor dynamics of some key molecules responsible for T cell activation (Xiang et al., 2011; Li et al., 2016; Wan et al., 2019). Particularly, CAR structures with modified CD3ζ domains were shown to induce different Zeta-chain-associated protein kinase 70 (ZAP70) activation kinetics in CAR-T cells upon antigen stimulation (Liu et al., 2021).

In this study, we designed CAR-T cells targeting TSHR and evaluated their efficacy for the treatment of metastatic thyroid cancers both *in vitro* and *in vivo*. Using FRET-based biosensors, we further quantified and compared the dynamics of ZAP70 and Extracellular signal-regulated kinase (ERK) signals in CD28 and 4-1BB-based CAR-T cells upon antigen stimulation. As a member of the Syk family of thrysine kinases, ZAP70 plays a crucial role in regulating T cells activation. After antigen engagement, ZAP70 is recruited to the phosphorylated CD3ζ subunits, where it is activated by LCK kinase and facilitates downstream signal amplification (Wang et al., 2010). Previous studies have suggested ZAP70 signal as a rate-limiting step in CAR-T cells activation. Insufficient activation of ZAP70 signal was thought to impair CAR-T cells functions (Gudipati et al., 2020). The ERK signal is considered as one of the main hubs to transduce proximal signals into nucleus during T cell activation. It is thought to exhibit a switch-like functions and the transient or persistent ERK dynamics could induce distinct gene expressions. The dynamics of ERK signal have been finely tuned by spatiotemporal networks to control cell fate decisions (Purvis and Lahav, 2013; Rohrs et al., 2020). Inside T cells, the ERK pathway is initiated by Rac-1 after the activation of Linker for activation of T cells (LAT), whose phosphorylation by ZAP70 makes it recruit multiple effector molecules for signal propagation. We found that TSHR binding elicits activation of ZAP70 and ERK in both CD28 and 4-1BB-based TSHR CAR-T cells. While two types of CAR-T cells had similar ZAP70 activity, different co-stimulatory signals resulted in distinctive ERK activation dynamics. This may be responsible for their different anti-tumor kinetics in mice.

MATERIALS AND METHODS

Cell Lines

293T cells, Jurkat T cells and K562 cells were obtained from ATCC. Thyroid cancer cell line 8505c cells was obtained from DSMZ (German Collection of Microorganisms and Cell Cultures). 293T cells and 8505c cells were cultured in high glucose DMEM medium with 10% fetal bovine serum (FBS)

and 1% penicillin/streptomycin (P/S). Jurkat T cells (clone E6-1) and K562 cells were cultured in IMDM medium with 10% FBS and 1% P/S. All cells were maintained in 5% CO_2 at 37°C.

Plasmids Construction

All plasmids were constructed using ClonExpress II One Step Cloning Kit (Vazyme, Nanjing, China) following manufacturer's instruction. Retrovirus plasmids encoding TSHR-specific CARs were constructed by inserting the CAR constructs into SFG γ-retroviral vector. For detection of CAR expression, a sequence encoding green fluorescence protein (GFP) was linked in the C-terminus of CAR by a P2A peptide. Plasmids used for cell line transduction were constructed in lentiviral vectors. To prepare the plasmid co-expressing TSHR and luciferase, the sequences encoding TSHR and luciferase reporter were linked by a P2A peptide. The ZAP70 and ERK biosensors were reported by previous studies. The ZAP70 biosensor used the peptide (SREYACISGEL) as ZAP70 substrate (Liu et al., 2021). The ERK biosensor used the peptide (PDVPRTPVDKAKLSFQFPF) as ERK substrate (Komatsu et al., 2011). For co-expression of ZAP70 biosensor or ERK biosensor and CARs in Jurkat T cells, the CAR construct was introduced in the C-terminus of biosensor sequence using a P2A peptide.

T Cell Isolation and Transduction

Human blood was obtained from healthy donors with written approval. PBMC was isolated using human lymphocyte isolation kit (Dakewe, Shenzhen, China). T cells were further purified using Pan T cell isolation kit (Miltenyi Biotec, Bergisch Gladbach, Germany) and cultured with X-VIVO 15 medium (Lonza) supplemented with 10% FBS, 1% P/S, 5 ng/ml IL-7 (Novoprotein, Shanghai, China) and 5 ng/ml IL-15 (Novoprotein). Immediately after T cell isolation, they were stimulated with CD3/CD28 T cell Activator Dynabeads (Invitrogen, Carlsbad, United States) at a ratio of 1:1. T cells transduction was performed after 48 h. Retrovirus was produced from 293T cell lines. T cells were transduced with retrovirus supernatants in retronectin (Takara, Otsu, Japan)-coated plates. To enhance transduction efficiency, the plates were centrifuged with 3000 rpm for 90 min.

In vitro Cytotoxic Assay

CAR-T cells were co-cultured with 5×10^4 target cells at different effector/target (E/T) ratio in target cell medium in black-walled 96 well plates. After 18 h, the cells were treated with D-luciferin (GoldBio, St. Louis, United States). Emitted light was detected by a luminescence plate reader (Thermo Varioskan Flash). Lysis percentage was calculated as [1-(luminescence intensity of each sample)/(luminescence intensity of target cells alone)] ×100.

Flow Cytometry

For cytokines and exhaustion markers analysis, CAR-T cells were stimulated with irradiated 8505c-TSHR cells for 24 h. The BD Cytometric Bead Array (CBA) kit were used to quantify the secretion level of IL-2, TNFα and IFN-γ of the supernatant of CAR-T cells following manufacturer's instruction. For intracellular cytokines staining, the Golgi plug protein transport inhibitor Brefeldin A (eBioscience, San Diego, United States) was added into the cultured medium 4 h before detection. T cells were then fixed and permeabilized with Fixation and Permeabilization kit (BD Biosciences, San Jose, United States) according to manufacturer's instruction. The following antibodies were used: FITC mouse anti-human TSHR (Santa Cruz Biotechnology, Santa Cruz, United States), Human IL-2 Flex Set (BD Biosciences), Human TNF Flex Set (BD Biosciences), Human IFN-γ Flex Set (BD Biosciences), BV421 rat anti-human IL-2 (BD Biosciences), PE-Cy7 mouse anti-human TNFα (BD Biosciences), PE-Cy7 anti-human CD279 (PD-1) (eBioscience), eFluor 450 anti-human CD223 (LAG-3) (eBioscience). Flow cytometry was performed on a CytoFLEX LX cytometer (Beckman Coulter, Brea, United States). A moflo Astrios EQ cell sorter (Beckman Coulter) was used for cell sorting. Data were analyzed with FlowJo software (FlowJo LLC, Ashland, United States).

Animal Experiments

Six- to 12-week-old NOD/SCID/IL-2Rγ^{null} (NSG) mice were obtained from Jihui Shanghai and housed in the Animal Core Facility at Westlake University. All procedures followed the Institutional Animal Care and Use Committee (IACUC) guideline. For the *in vivo* anti-tumor assay, mice were intravenously injected with 1×10^6 8505c-TSHR cells followed by 0.5×10^6 CAR-T cells the next day. To monitor tumor burden, mice were treated with 200 μL of 15 mg/ml D-luciferin by intraperitoneal injection. Bioluminescence imaging was performed using the Optima small animal imaging system (Biospace Lab, Paris, France).

Image Acquisition and Analysis

Time-lapse imaging was performed with a Nikon Eclipse Ti inverted microscope. A Tokai Hit ST Series Stage Top Incubator was used to maintain a 5% CO_2 at 37°C for cells during imaging. The W-VIEW GEMINI imaging splitting optics (Hamamatsu Photonics, Hamamatsu, Japan) with a 438/29 nm excitation filter, a 474/40 nm emission filter, a 535/25 nm emission filter, an iXon Ultra 897 EMCCD camera (Andor Technology, Belfast, United Kingdom) was used to acquire the ECFP and FRET fluorescent signals simultaneously. CAR-Jurkat T cells co-expressing ZAP70 or ERK biosensor were generated by lentivirus transduction. To monitor ZAP70 or ERK signal dynamics upon antigen stimulation, CAR-Jurkat T cells were dropped on the glass-bottom dishes coated with K562-TSHR cells. From that time on, images were acquired at an interval of 30 s for 40 min. The imaging data were analyzed by Fluocell software. The ECFP/FRET ratio of ZAP70 biosensor or the FRET/ECFP ratio of ERK biosensor for each cell was normalized before comparison.

Statistics

Statistical analysis was performed using GraphPad Prism 8 software. An unpaired, two-tailed student's *t*-test were used to

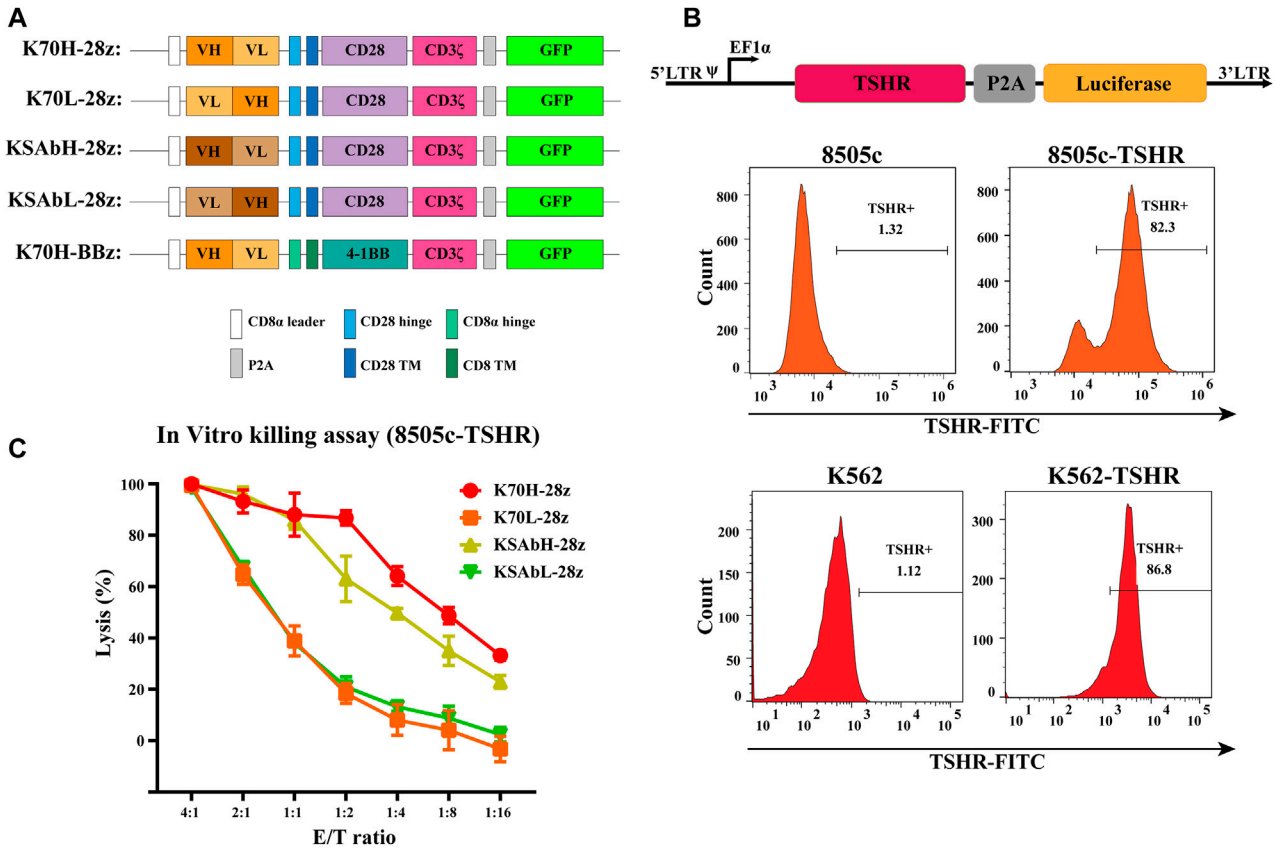

FIGURE 1 | Design of TSHR-specific CARs. **(A)** Construction of CARs with different scFvs and co-stimulatory domains. TM: transmembrane. **(B)** Generation of 8505c and K562 cell lines expressing TSHR antigen. **(C)** *In vitro* killing assay of primary CAR-T cells with different scFvs. Error bars: mean ± SD.

determine the statistical differences between two groups. A Kaplan-Meier curve and the log-rank test were used to compare the survival differences between the groups in animal experiments. A p value < 0.05 was considered to be statically significant.

RESULTS

Design of CAR Constructs Targeting TSHR

Based on a second-generation CAR construct we investigated the feasibility of CAR-T cells in treating TSHR-positive thyroid cancers. In our design, the ectodomain of CARs was a single chain variable fragment (scFv) that recognize TSHR, and the endodomain contained a CD28 or 4-1BB-derived costimulatory domains and CD3ζ-derived activation domain. To evaluate the expression level of CARs, a green fluorescence protein (GFP) was introduced downstream of CAR through a P2A self-cleavage peptide (**Figure 1A**). Although not strictly correlated, the expression of GFP could be used to estimate CAR expression level. To find the optimized scFvs, we constructed and compared scFvs from two anti-TSHR monoclonal antibodies (K1-70 and KSAb) that have been previously reported. As the arrangement of variable heavy chain (VH) and variable light chain (VL) fragment may largely affect the antigen recognition property, scFvs with different VH-VL arrangements were constructed for each antibody. Thus, four CD28-based CAR constructs with different scFvs (referred to K70H-28z, K70L-28z, KSAbH-28z and KSAbL-28z) were generated (**Figure 1A**).

Next, we produced CD28ζ CAR-T cells with different scFvs from primary T cells and compared their cytotoxic effect. Since most thyroid cell lines have lost their TSHR expression (Li et al., 2021), we established a TSHR-positive target cell line by transducing the full-length TSHR gene with a luciferase reporter into the thyroid cancer cell line 8505c (8505c-TSHR) (**Figure 1B**). Using 8505c-TSHR as the target cell, *in vitro* killing assay revealed the superior cytotoxic effect of K70H-28z CAR-T cells than its counterparts (**Figure 1C**). Therefore, the K1-70 derived VH-VL scFv was selected for subsequent studies.

In vitro Cytotoxicity of TSHR CAR-T Cells With CD28 or 4-1BB Co-Stimulatory Domain

Nowadays, the most widely used CARs in clinic contain either CD28 or 4-1BB as co-stimulatory domains. Both of them have achieved impressive results in clinical studies. However, CAR-T cells bearing CD28 or 4-1BB intracellular domains could have different cytotoxic functions and *in vivo* persistence (Feucht and

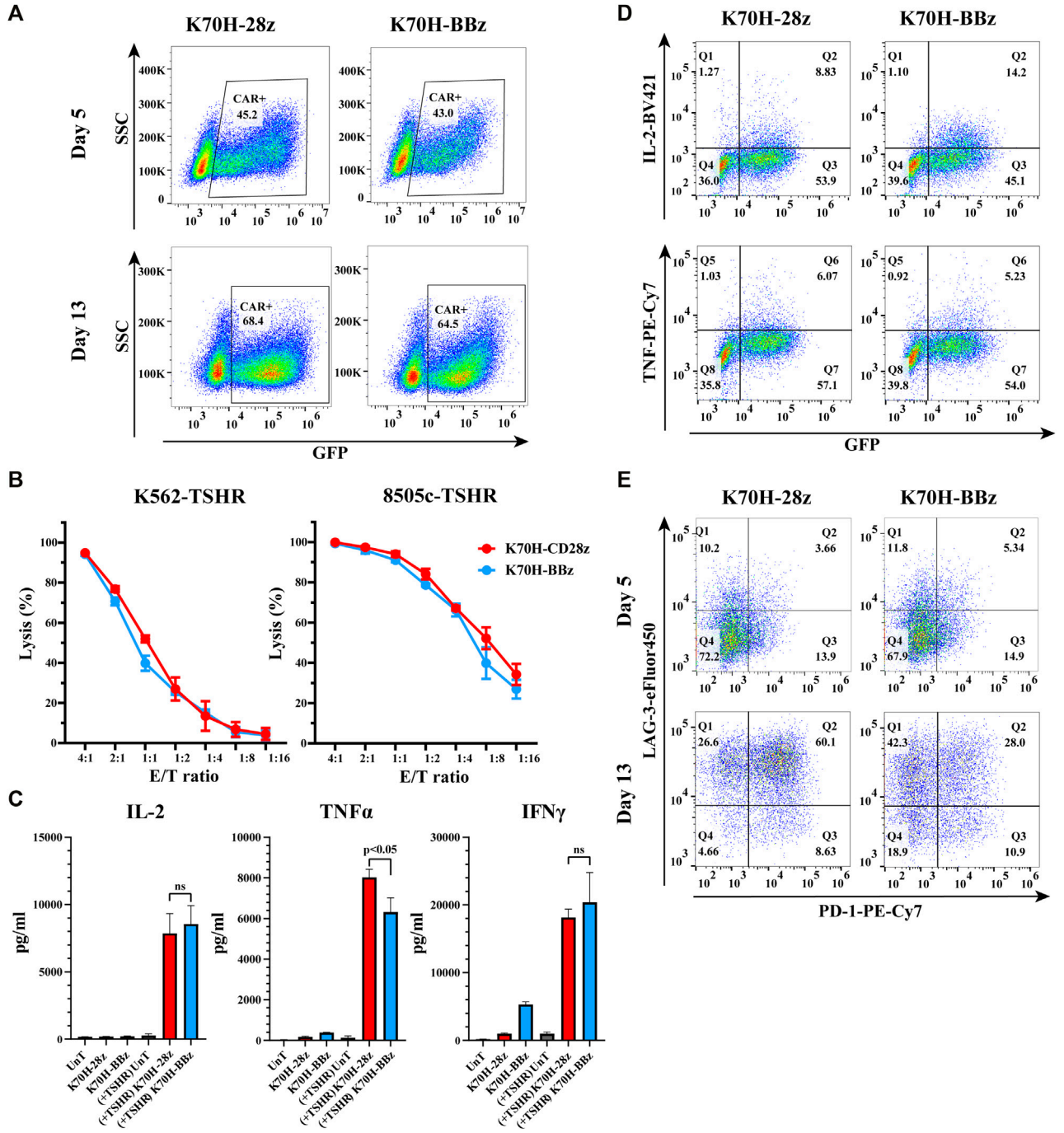

FIGURE 2 | *In vitro* characterization of CD28 and 4-1BB-based TSHR CAR-T cells. **(A)** CAR expression of primary T cells after retrovirus transduction. T cells were collected at day 5 and 13 after PBMC isolation and evaluated by FACS. CAR expression was indicated by GFP intensity of T cells. **(B)** *In vitro* killing assay of different CAR-T cells against indicated target cells. **(C–E)** CAR-T cells were co-cultured with irradiated 8505c-TSHR cells for 24 h. The cytokine secretion of the supernatant **(C)**, the intracellular cytokines expression **(D)** and the exhaustion genes expression **(E)** of CAR-T cells were evaluated by FACS. UnT: Untransduced T cells. Error bars: mean ± SD.

Sadelain, 2020). To find out the optimal co-stimulatory domain for thyroid cancer treatment, we compared the *in vitro* anti-tumor functions of CD28 and 4-1BB-based TSHR CAR-T cells. The CAR structures (K70H-28z & K70H-BBz) have the same scFv but different hinge and transmembrane domains (**Figure 1A**). Produced by retrovirus transduction, both CAR-

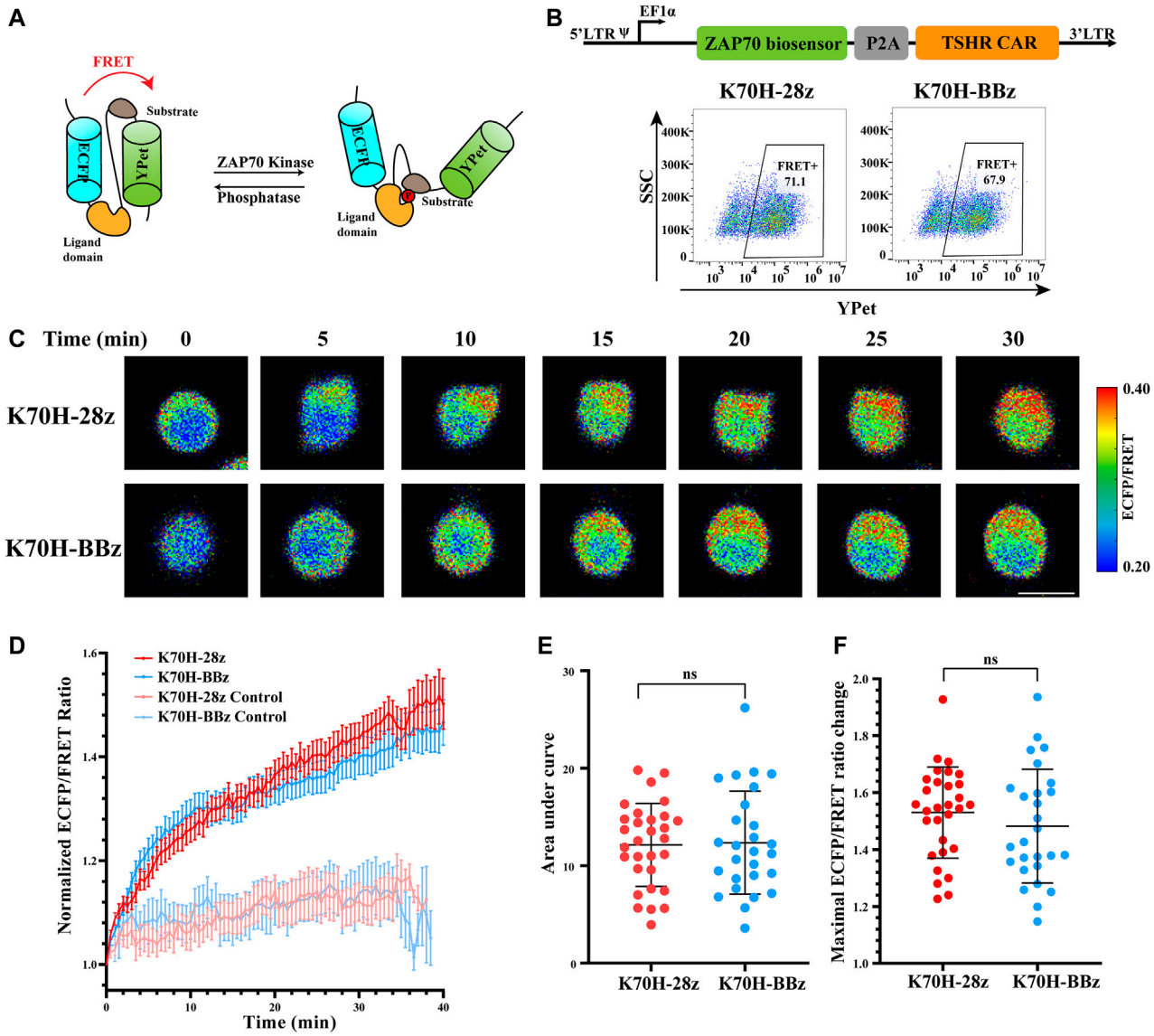

FIGURE 3 | Signaling dynamics of ZAP70 in CAR-T cells upon antigen stimulation. **(A)** Design of ZAP70 FRET biosensor. **(B)** Biosensor (CAR) expression of Jurkat T cells transduced with ZAP70 biosensor and TSHR CARs. **(C)** ZAP70 signal changes of CAR-Jurkat T cells over time after contacting with K562-TSHR cells. The activity of ZAP70 was visualized by ECFP/FRET ratio. Scale bar: 10 μm. **(D)** Time courses of ECFP/FRET ratio of ZAP70 biosensor in K70H-28z or K70H-BBz CAR-Jurkat T cells stimulated by K562-TSHR (n = 30 and 27 respectively) or K562 (Control, n = 10 and 10 respectively). Error bars: mean ± SEM. Accumulated signal intensity (area under curve) **(E)** and maximal ECFP/FRET ratio changes **(F)** of ZAP70 biosensor in CAR-Jurkat T cells. Error bars: mean ± SD.

T cells showed similar transduction efficiency (**Figure 2A**). Using either K562-TSHR (**Figure 1B**) or 8505c-TSHR as target cells, their cytotoxicity was compared by *in vitro* killing assay. We found comparable cytotoxic effect between K70H-28z and K70H-BBz CAR-T cells (**Figure 2B**). We then analyzed the cytokines release of CAR-T cells by FACS. Co-culture with 8505c-TSHR cells promoted K70H-28z and K70H-BBz CAR-T cells but not the untransduced T cells to secrete robust IL-2, TNFα and IFNγ (**Figure 2C**). The K70H-28z CAR-T cells secreted comparable levels of IL-2 and IFNγ, but higher levels of TNFα than K70H-BBz CAR-T cells (**Figure 2C**). Intracellular cytokines staining further confirmed that antigen stimulation notably induced GFP^+ CAR-T cells to secrete IL-2 and TNFα but not GFP^- T cells (**Figure 2D**).

After a period of *ex vivo* culture, which is often required for CAR-T cell expansion before infusion, we observed an increased GFP^+ ratio of the total populations, representing an enrichment of the CAR-T cells. To evaluate the exhaustion levels, we detected PD-1 and LAG-3 expression of CAR-T cells after antigen stimulation (**Figure 2E**). Compared to CAR-T cells at day 5,

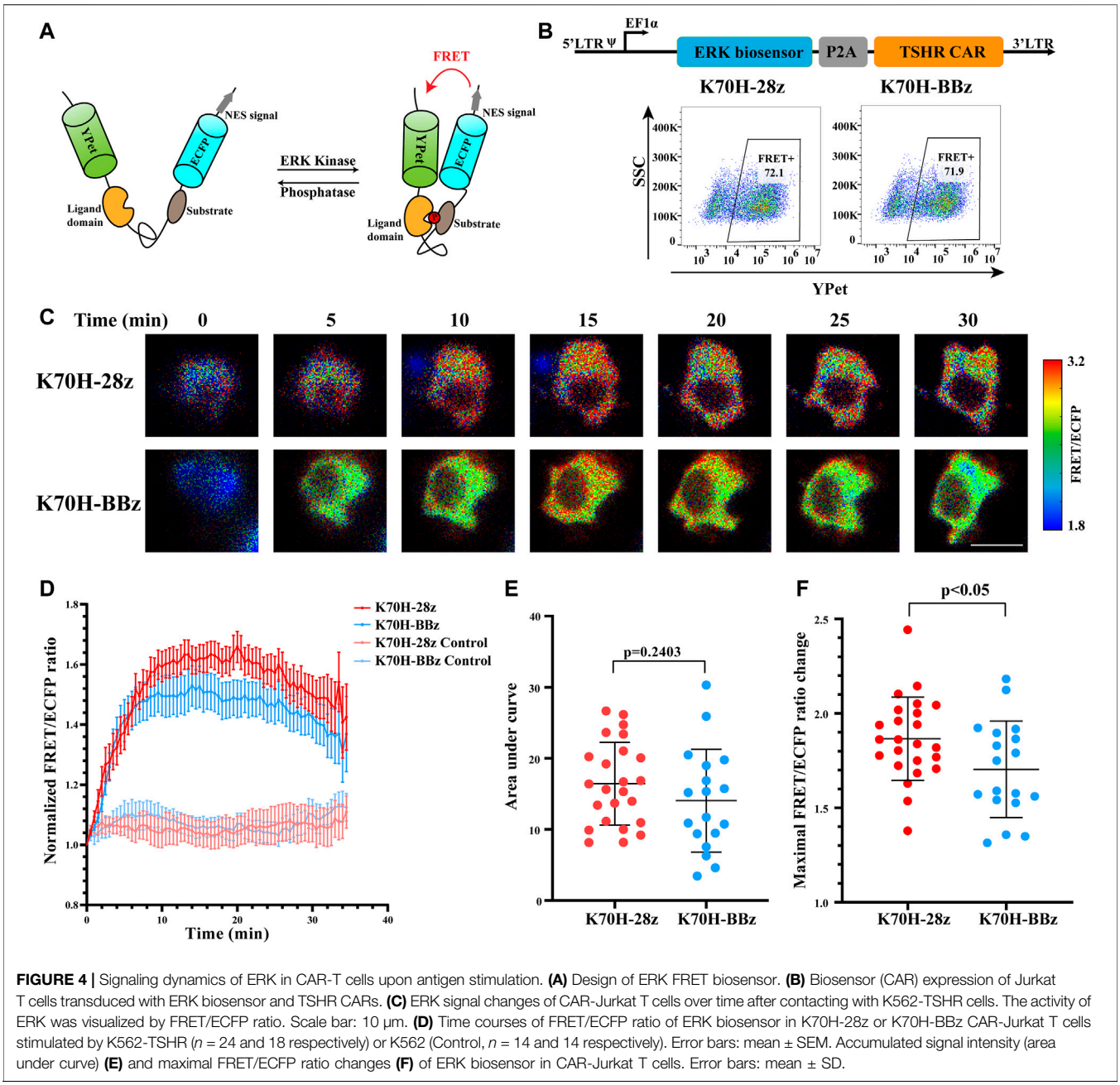

FIGURE 4 | Signaling dynamics of ERK in CAR-T cells upon antigen stimulation. **(A)** Design of ERK FRET biosensor. **(B)** Biosensor (CAR) expression of Jurkat T cells transduced with ERK biosensor and TSHR CARs. **(C)** ERK signal changes of CAR-Jurkat T cells over time after contacting with K562-TSHR cells. The activity of ERK was visualized by FRET/ECFP ratio. Scale bar: 10 μm. **(D)** Time courses of FRET/ECFP ratio of ERK biosensor in K70H-28z or K70H-BBz CAR-Jurkat T cells stimulated by K562-TSHR (n = 24 and 18 respectively) or K562 (Control, n = 14 and 14 respectively). Error bars: mean ± SEM. Accumulated signal intensity (area under curve) **(E)** and maximal FRET/ECFP ratio changes **(F)** of ERK biosensor in CAR-Jurkat T cells. Error bars: mean ± SD.

CAR-T cells at day 13 showed increased expression of both exhaustion markers (**Figure 2E**). Moreover, 60.1% of the K70H-28z CAR-T cells showed double positive of PD-1 and LAG-3, much higher than that of the K70H-BBz group (**Figure 2E**).

Similar ZAP70 Activation Downstream of CD28 or 4-1BB-Based TSHR CARs Revealed by FRET Imaging

Although previous studies have characterized different signal activities triggered by CD28 or 4-1BB-based CARs (Philipson et al., 2020), their signaling dynamics in the early stage of T cell activation are still elusive. To figure out how co-stimulatory molecules affect CAR-induced signal transductions, we first focused on the membrane-proximal signaling events that were activated at the earliest time after antigen stimulation. ZAP70 has been considered as one of the most important kinases to transduce CAR signals into downstream signaling cascades (Wang et al., 2010; Gudipati et al., 2020). We have applied FRET-based ZAP70 biosensor to monitor the activity changes of ZAP70 during TSHR CAR-T cells activation. The ZAP70 biosensor was designed to include a FRET pair of ECFP and YPet fluorescence proteins, a ZAP70 kinase-specific substrate

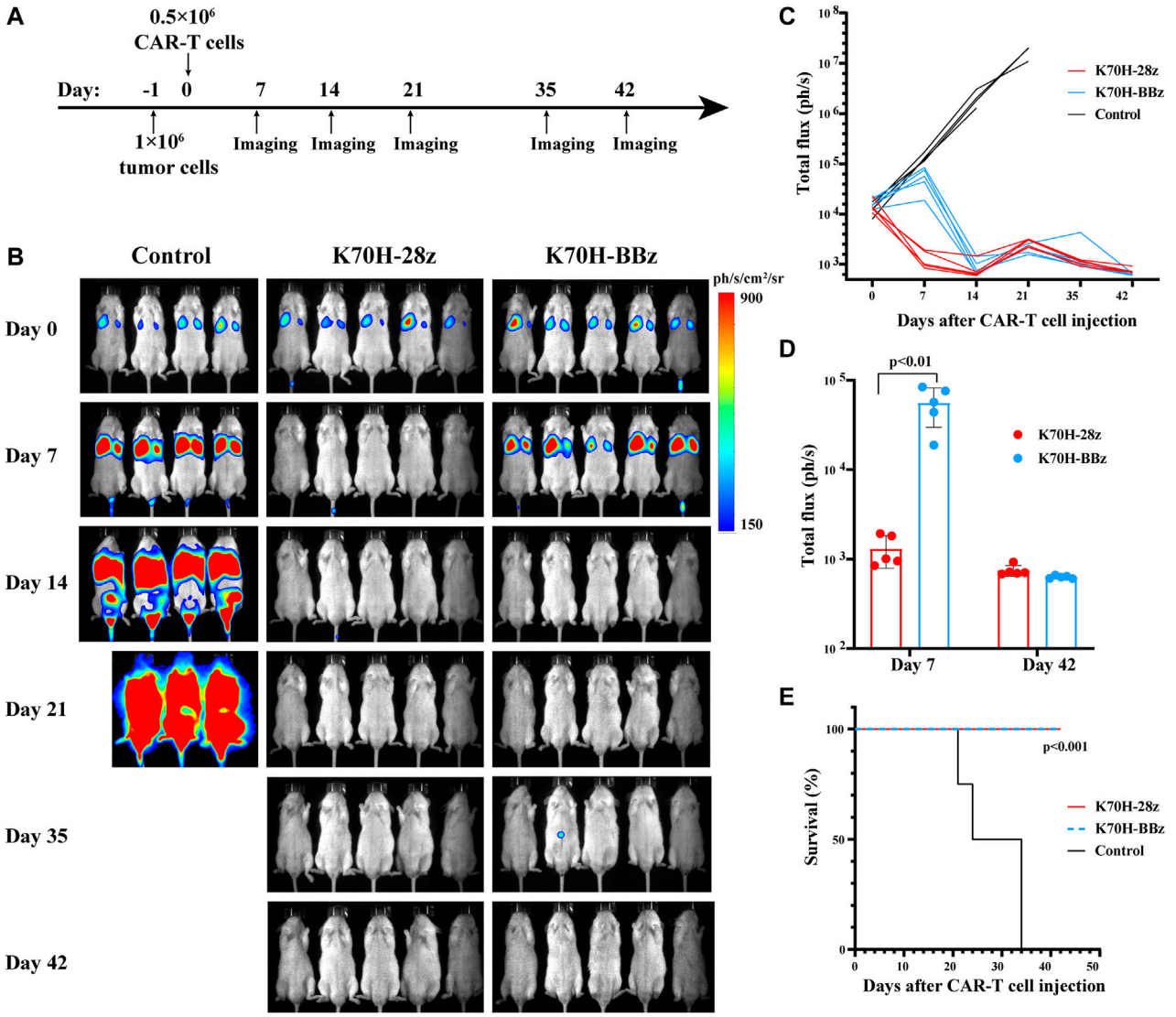

FIGURE 5 | *In vivo* anti-tumor functions of TSHR CAR-T cells. **(A)** Schematic timeline of the *in vivo* experimental design. NSG mice were intravenously injected with 1×10^6 8505c-TSHR cells. The next day, they were treated with 0.5×10^6 K70H-28z CAR-T cells (n = 5), K70H-BBz CAR-T cells (n = 5) or PBS (n = 4). **(B)** Bioluminescence imaging of mice at indicated days after treatment. **(C)** Quantification of tumor burden of mice. **(D)** Tumor burden of K70H-28z CAR and K70H-BBz CAR-T groups at day 7 and 42. Error bars: mean ± SD. **(E)** Kaplan-Meier analysis of survival of mice from different groups.

domain, and a ligand domain. Phosphorylation of the substrate by ZAP70 would cause conformational changes of the biosensor, resulting in reduction of FRET efficiency between ECFP and YPet (**Figure 3A**) (Liu et al., 2021). Therefore, the relative activity of ZAP70 could be evaluated by detecting the fluorescence ratio of ECFP and FRET (YPet). To assess the ZAP70 activity upon antigen stimulation, the Jurkat T cell line co-expressing ZAP70 biosensor and CARs (CAR-Jurkat T) were generated by lentivirus transduction. Both K70H-28z and K70H-BBz CAR-Jurkat T cells showed similar expression of biosensor (CAR) (**Figure 3B**). By FRET imaging, we observed remarkable changes of the ZAP70 activity in CAR-Jurkat T cells upon encountering with the K562-TSHR target cells (**Figure 3C**). The ZAP70 activity increased rapidly within 10 min after antigen stimulation. Thereafter, its signal continued to increase with slower speed (**Figure 3D**). We further quantified the accumulated signal intensity (area under curve) and maximal signal intensity (maximal ECFP/FRET ratio changes) of K70H-28z and K70H-BBz CARs. Neither the accumulated signal intensity nor the maximal signal intensity of ZAP70 between K70H-28z and K70H-BBz CARs showed significant difference (**Figures 3E,F**).

Different ERK Activation Dynamics in TSHR CAR-T Cells Revealed by FRET Imaging

To assess whether signals downstream of ZAP70 were affected by different co-stimulatory molecules, we investigated the signal dynamics of ERK during CAR-T cells activation by FRET-

based biosensor. The ERK biosensor used a flexible linker to connect the substrate, ligand domain and FRET pairs. It also included a nucleus exporting signal (NES) to increase detection sensitivity of cytosolic signal. The biosensor would increase its FRET efficiency when phosphorylated by ERK (**Figure 4A**) (Komatsu et al., 2011). The CAR-Jurkat T cells expressing ERK biosensor and K70H-28z or K70H-BBz CAR were generated by lentivirus transduction and showed similar expression of biosensor (CAR) between groups (**Figure 4B**). By FRET imaging we found that the ERK activity, as visualized by FRET/ECFP fluorescence ratio of CAR-Jurkat T cells increased upon K562-TSHR cells stimulation (**Figure 4C**). Statistical quantification suggested that the activity of ERK reached to a peak level in about 15 min and then underwent slow decrease (**Figure 4D**). The accumulated signal intensity of ERK in K70H-28z CAR was slightly higher than that of K70H-BBz CAR but without significant difference (**Figure 4E**). However, the maximal signal intensity of ERK in K70H-28z CAR was significantly higher than that of K70H-BBz CAR ($p < 0.05$) (**Figure 4F**). Collectively, compared with K70H-BBz CAR, K70H-28z CAR triggered similar ZAP70 signaling but significantly enhanced ERK signaling.

Different Anti-Tumor Kinetics of CD28 and 4-1BB-Based CAR-T Cells *in vivo*

Finally, we evaluated the anti-tumor functions of K70H-28z and K70H-BBz CAR-T cells by *in vivo* studies (**Figure 5A**). To mimic the distant metastasis of DTCs, of which lung and bone are the major sites, we established a xenograft animal model based on previous studies (Zhang et al., 2014). The 8505c-TSHR cells were intravenously injected into the immunodeficient NSG mice. We found the tumors cells accumulated in the lung at early stage. Bone and other tissue metastasis happened after 14 days and caused animal death in the control group (**Figures 5B,C,E**). By contrast, mice treated with either K70H-28z or K70H-BBz CAR-T cells successfully controlled tumor growth and survived without obvious side-effect (**Figures 5B,C,E**). Nevertheless, K70H-28z CAR-T cells were found to eradicate nearly all tumor cells within 7 days, while K70H-BBz CAR-T cells lagged behind (**Figures 5C,D**). This indicated faster anti-tumor kinetics of K70H-28z CAR-T cells than K70H-BBz CAR-T cells.

DISCUSSION

In this study, we developed a CAR-T therapy for TSHR-positive advanced thyroid cancers. The CAR constructs were designed to bear a monoclonal antibody-derived scFv targeting TSHR and a CD28 or 4-1BB co-stimulatory domain. Primary T cells equipped with the CD28 or 4-1BB-based CARs were demonstrated with potent anti-tumor efficacy both *in vitro* and *in vivo*. Moreover, we applied the FRET biosensors for ZAP70 and ERK to monitor the signaling dynamics of CAR-T cells in response to antigen stimulation. These results revealed different ERK activation properties of CD28 and 4-1BB-based CAR-T cells.

To recognize TSHR-positive tumor cells, we constructed scFvs from two monoclonal antibodies, K1-70 and KSAb. Both antibodies were derived from patients with Graves' disease. They have an estimated affinity of 25 and 22 pM for human TSHR, respectively (Sanders et al., 2010; Banga et al., 2013). The slightly higher affinity of K1-70 may contribute to the stronger cytotoxicity of K70H-28z CAR-T cells than KSAbH-28z CAR-T cells. Despite the potent anti-tumor effect of K70H-derived CAR-T cells, previous studies have suggested that the affinity of scFvs did not positively correlate with CAR-T cells functions (Ghorashian et al., 2019). The increased affinity of scFvs above threshold may not improve T cell activation but decrease selectivity. Fine-tuning of the scFv affinity may be required to maximize CAR-T cell functions as well as minimize possible on-target/off-tumor toxicity (Di Roberto et al., 2020).

To transduce the antigen stimulation into intracellular signals responsible for T cell activation, the cytoplasmic domains of CARs have been incorporated with a CD3ζ chain and a CD28 or 4-1BB derived co-stimulatory domain. Previous studies have suggested remarkable variations in functions of CAR-T cells equipped with various co-stimulatory domains. In CD19 CAR-T cells studies, 28z CAR-T cells exhibited higher effector functions with less persistence than BBz CAR-T cells (Shah and Fry, 2019; Ying et al., 2019). This functional discrepancy has been associated with different metabolic features. 28z CAR-T cells have shown enhanced aerobic glycolysis, while BBz CAR-T cells have exhibited greater mitochondrial oxidative phosphorylation (Kawalekar et al., 2016). Interestingly, phosphoproteomic analysis have indicated that 28z CAR and BBz CAR induce T cells activation through common signaling intermediates but with different kinetics and intensities (Salter et al., 2018).

We detected the ZAP70 and ERK signal activities in CAR-Jurkat T cells after antigen stimulation by FRET biosensors. Compared with methods like Western blot and mass spectrum, FRET biosensors could detect kinase activity in single live cells with high spatiotemporal resolution. This enables us to evaluate early signaling events of T cell activation. We observed the interaction with TSHR-positive tumor cells induced rapid increase of ZAP70 and ERK activities within minutes, indicating antigen-dependent activation of the CAR-Jurkat T cells. Different from previous studies, we did not observe significant difference of ZAP70 signal activities in K70H-28z and K70H-BBz CAR-T cells after activation (Salter et al., 2018; Philipson et al., 2020). One main reason responsible for these results may be the different detection methods. In previous studies, ZAP70 activity was evaluated by the phosphorylation level of some key phosphorylated sites like Y319. However, the phosphorylation state of the specific site did not precisely reflect the activity of kinase. In contrast, the FRET ratio change of FRET biosensors was determined by the phosphorylation of ZAP70-specific substrate, which could more accurately reflect the activation state of ZAP70. In addition, the previous comparison was done between CD19-targeting 28z and BBz CAR-T cells while in this study, TSHR-targeting CAR-T cells have different scFvs and CAR targets.

Nevertheless, ZAP70 activation mainly depends on CD3ζ instead of co-stimulatory molecules, which matched our results.

Consistent with previous studies, we observed an enhanced signal activity of ERK in 28z CAR-T cells when compared to BBz CAR-T cells (Salter et al., 2018). CD28 and 4-1BB as co-stimulatory molecules are thought to amplify ERK signaling with distinct mechanisms. CD28 may enhance ERK signaling by promoting the recruitment of Vav-1 to the plasma membrane, which is required for Rac-1 activation (Michel et al., 2000). 4-1BB may induce ERK activation via its downstream receptor TRAF2 to regulate Tpl2 activation (Xie et al., 2021). In CAR-T cells it is still elusive how CARs with different co-stimulatory molecules mediate the activation of ERK signal. Diverse signaling output derived from CD28 or 4-1BB may contribute to the amplification of ERK pathway. As observed in our studies, the different ERK activities of K70H-28z and K70H-BBz CAR-T cells may induce large distinction of downstream signals and contribute to different anti-tumor functions. Notably, we have observed that the ERK signal reached a peak value at about 15 min after antigen engagement, at which time ZAP70 signal also showed a short plateau. Thereafter, the increased ZAP70 activities did not promote further enhancement of ERK signals. The correlation of ZAP70 and ERK signals requires further investigation. In addition, single cell FRET imaging allowed us to observe heterogeneous activities of ZAP70 and ERK in individual CAR-T cells after antigen stimulation. This cell-to-cell heterogeneity obscured by traditional methods may be caused by distinct expression levels of CARs and related signaling molecules or different contacting strength with target cells. More importantly, this heterogeneity may lead to the diverse T cell differentiation and fates. However, with limited number of cells collected by FRET imaging, it is challenging to find possible links and correlations.

Although with comparable cytotoxic effects *in vitro*, we have shown that K70H-28z CAR-T cells had higher expression of the exhaustion genes than K70H-BBz CAR-T cells. This may suggest the shorter persistence of K70H-28z CAR-T cells. Meanwhile, the increased PD-1 and LAG-3 expression could be an indicator of T cell activation and the result of rapid effector functions of K70H-28z CAR-T cells (Wherry and Kurachi, 2015). Nevertheless, our *in vivo* experiments have observed potent anti-tumor functions of both designed CAR-T cells. Moreover, compared to K70H-BBz CAR-T cells, K70H-28z CAR-T cells have shown rapid elimination of tumor cells, which suggested higher effector functions. It should be noticed that although long-term persistence of CAR-T cells *in vivo* is essential to avoid tumor relapse, it may also enhance the risk of off-tumor toxicity (Kawalekar et al., 2016). In the context of thyroid cancer treatment, it requires further studies to balance the effector functions and long-term persistence of CAR-T cells.

Finally, our studies have shown the efficacy of TSHR CAR-T cells in the treatment of TSHR-positive thyroid cancers. We also showed that CD28 and 4-1BB-based CAR-T cells exhibited comparable anti-tumor functions with different kinetics. Live cell imaging using FRET biosensors revealed the dynamics of ZAP70 and ERK activities in both CAR-T cells during activation. These results promoted our understanding of CAR-T cells signaling and indicated potential applications of FRET biosensors in optimizing CAR designs. CAR-T cells therapy may overcome current obstacles for thyroid cancer treatment in the near future.

DATA AVAILABILITY STATEMENT

All data obtained and/or analyzed during the current study are available from the corresponding authors on reasonable request.

ETHICS STATEMENT

The studies involving human participants were reviewed and approved by Ethics Committee of Zhejiang University School of Medicine. The patients/participants provided their written informed consent to participate in this study. The animal study was reviewed and approved by Institutional Animal Care and Use Committee of Westlake University.

AUTHOR CONTRIBUTIONS

JZ, XM and JS designed the study. JZ, JC and XM performed the experiments. YH, XG and CZ provided experimental support and discussion. JZ, XM and JS wrote the manuscript. All authors read and approved the final manuscript.

FUNDING

This work was funded by the National Key R&D Program of China 2021YFA0909900 (JS), National Natural Science Foundation of China grants 31971324 (JS), 81702650 (JZ); 81973993 (XG) and 31971125 (CZ), Natural Science Foundation of Hubei Province 2020CFB839 (JZ), Foundation of the Scientific and Technological Bureau of Wuhan 2020020601012327 (JZ) and by Zhejiang Provincial Natural Science Foundation grant LR20H160003 (JS).

ACKNOWLEDGMENTS

We thank the support of Zhejiang Provincial Key Laboratory of Immunity and Inflammatory diseases.

REFERENCES

Banga, J.-P. S., Gilbert, J. A., Dunn-Walters, D., and Padoa, C. (2013). "Agonist Antibodies against TSHR," (Washington, DC: U.S. Patent and Trademark Office). U.S. Patent No 20100266493A1.

Bhoj, V. G., Li, L., Parvathaneni, K., Zhang, Z., Kacir, S., Arhontoulis, D., et al. (2021). Adoptive T Cell Immunotherapy for Medullary Thyroid Carcinoma Targeting GDNF Family Receptor Alpha 4. *Mol. Ther. - Oncolytics* 20, 387–398. doi:10.1016/j.omto.2021.01.012

Davies, T., Marians, R., and Latif, R. (2002). The TSH Receptor Reveals Itself. *J. Clin. Invest.* 110 (2), 161–164. doi:10.1172/jci0216234

Di Roberto, R. B., Castellanos-Rueda, R., Frey, S., Egli, D., Vazquez-Lombardi, R., Kapetanovic, E., et al. (2020). A Functional Screening Strategy for Engineering Chimeric Antigen Receptors with Reduced On-Target, Off-Tumor Activation. *Mol. Ther.* 28 (12), 2564–2576. doi:10.1016/j.ymthe.2020.08.003

Feucht, J., and Sadelain, M. (2020). Function and Evolution of the Prototypic CD28ζ and 4-1BBζ Chimeric Antigen Receptors. *Immuno-Oncology Technol.* 8, 2–11. doi:10.1016/j.iotech.2020.09.001

Ghorashian, S., Kramer, A. M., Onuoha, S., Wright, G., Bartram, J., Richardson, R., et al. (2019). Enhanced CAR T Cell Expansion and Prolonged Persistence in Pediatric Patients with ALL Treated with a Low-Affinity CD19 CAR. *Nat. Med.* 25 (9), 1408–1414. doi:10.1038/s41591-019-0549-5

Gudipati, V., Rydzek, J., Doel-Perez, I., Gonçalves, V. D. R., Scharf, L., Königsberger, S., et al. (2020). Inefficient CAR-Proximal Signaling Blunts Antigen Sensitivity. *Nat. Immunol.* 21 (8), 848–856. doi:10.1038/s41590-020-0719-0

Kawalekar, O. U., O'Connor, R. S., Fraietta, J. A., Guo, L., McGettigan, S. E., Posey, A. D., Jr., et al. (2016). Distinct Signaling of Coreceptors Regulates Specific Metabolism Pathways and Impacts Memory Development in CAR T Cells. *Immunity* 44 (2), 380–390. doi:10.1016/j.immuni.2016.01.021

Komatsu, N., Aoki, K., Yamada, M., Yukinaga, H., Fujita, Y., Kamioka, Y., et al. (2011). Development of an Optimized Backbone of FRET Biosensors for Kinases and GTPases. *MBoC* 22 (23), 4647–4656. doi:10.1091/mbc.E11-01-0072

Kosti, P., Maher, J., and Arnold, J. N. (2018). Perspectives on Chimeric Antigen Receptor T-Cell Immunotherapy for Solid Tumors. *Front. Immunol.* 9, 1104. doi:10.3389/fimmu.2018.01104

Laha, D., Nilubol, N., and Boufraqech, M. (2020). New Therapies for Advanced Thyroid Cancer. *Front. Endocrinol.* 11, 82. doi:10.3389/fendo.2020.00082

Li, H., Zhou, X., Wang, G., Hua, D., Li, S., Xu, T., et al. (2021). CAR-T Cells Targeting TSHR Demonstrate Safety and Potent Preclinical Activity against Differentiated Thyroid Cancer. *J. Clin. Endocrinol. Metab.* 9, dgab819. doi:10.1210/clinem/dgab819

Li, K., Xiang, X., Sun, J., He, H.-T., Wu, J., Wang, Y., et al. (2016). Imaging Spatiotemporal Activities of ZAP-70 in Live T Cells Using a FRET-Based Biosensor. *Ann. Biomed. Eng.* 44 (12), 3510–3521. doi:10.1007/s10439-016-1683-6

Liu, L., Limsakul, P., Meng, X., Huang, Y., Harrison, R. E. S., Huang, T.-S., et al. (2021). Integration of FRET and Sequencing to Engineer Kinase Biosensors from Mammalian Cell Libraries. *Nat. Commun.* 12 (1), 5031. doi:10.1038/s41467-021-25323-x

Michel, F., Mangino, G., Attal-Bonnefoy, G., Tuosto, L., Alcover, A., Roumier, A., et al. (2000). CD28 Utilizes Vav-1 to Enhance TCR-Proximal Signaling and NF-AT Activation. *J. Immunol.* 165 (7), 3820–3829. doi:10.4049/jimmunol.165.7.3820

Min, I. M., Shevlin, E., Vedvyas, Y., Zaman, M., Wyrwas, B., Scognamiglio, T., et al. (2017). CAR T Therapy Targeting ICAM-1 Eliminates Advanced Human Thyroid Tumors. *Clin. Cancer Res.* 23 (24), 7569–7583. doi:10.1158/1078-0432.CCR-17-2008

Newick, K., O'Brien, S., Moon, E., and Albelda, S. M. (2017). CAR T Cell Therapy for Solid Tumors. *Annu. Rev. Med.* 68, 139–152. doi:10.1146/annurev-med-062315-120245

Philipson, B. I., O'Connor, R. S., May, M. J., June, C. H., Albelda, S. M., and Milone, M. C. (2020). 4-1BB Costimulation Promotes CAR T Cell Survival through Noncanonical NF-Kb Signaling. *Sci. Signal.* 13 (625), eaay8248. doi:10.1126/scisignal.aay8248

Rowe, C. W., Paul, J. W., Gedye, C., Tolosa, J. M., Bendinelli, C., McGrath, S., et al. (2017). Targeting the TSH Receptor in Thyroid Cancer. *Endocr. Relat. Cancer* 24 (6), R191–R202. doi:10.1530/ERC-17-0010

Salter, A. I., Ivey, R. G., Kennedy, J. J., Voillet, V., Rajan, A., Alderman, E. J., et al. (2018). Phosphoproteomic Analysis of Chimeric Antigen Receptor Signaling Reveals Kinetic and Quantitative Differences that Affect Cell Function. *Sci. Signal.* 11 (544), eaat6753. doi:10.1126/scisignal.aat6753

Sanders, J., Núñez Miguel, R., Furmaniak, J., and Rees Smith, B. (2010). TSH Receptor Monoclonal Antibodies with Agonist, Antagonist, and Inverse Agonist Activities. *Methods Enzymol.* 485, 393–420. doi:10.1016/b978-0-12-381296-4.00022-1

Shah, N. N., and Fry, T. J. (2019). Mechanisms of Resistance to CAR T Cell Therapy. *Nat. Rev. Clin. Oncol.* 16 (6), 372–385. doi:10.1038/s41571-019-0184-6

Sung, H., Ferlay, J., Siegel, R. L., Laversanne, M., Soerjomataram, I., Jemal, A., et al. (2021). Global Cancer Statistics 2020: GLOBOCAN Estimates of Incidence and Mortality Worldwide for 36 Cancers in 185 Countries. *CA A. Cancer J. Clin.* 71 (3), 209–249. doi:10.3322/caac.21660

van der Stegen, S. J. C., Hamieh, M., and Sadelain, M. (2015). The Pharmacology of Second-Generation Chimeric Antigen Receptors. *Nat. Rev. Drug Discov.* 14 (7), 499–509. doi:10.1038/nrd4597

Wan, R., Wu, J., Ouyang, M., Lei, L., Wei, J., Peng, Q., et al. (2019). Biophysical Basis Underlying Dynamic Lck Activation Visualized by ZapLck FRET Biosensor. *Sci. Adv.* 5 (6), eaau2001. doi:10.1126/sciadv.aau2001

Wang, H., Kadlecek, T. A., Au-Yeung, B. B., Goodfellow, H. E. S., Hsu, L. Y., Freedman, T. S., et al. (2010). ZAP-70: an Essential Kinase in T-Cell Signaling. *Cold Spring Harbor Perspect. Biol.* 2 (5), a002279. doi:10.1101/cshperspect.a002279

Wherry, E. J., and Kurachi, M. (2015). Molecular and Cellular Insights into T Cell Exhaustion. *Nat. Rev. Immunol.* 15 (8), 486–499. doi:10.1038/nri3862

Xiang, X., Sun, J., Wu, J., He, H.-T., Wang, Y., and Zhu, C. (2011). A FRET-Based Biosensor for Imaging SYK Activities in Living Cells. *Cel. Mol. Bioeng.* 4 (4), 670–677. doi:10.1007/s12195-011-0211-x

Xie, X., Zhu, L., Jie, Z., Li, Y., Gu, M., Zhou, X., et al. (2021). TRAF2 Regulates T Cell Immunity by Maintaining a Tpl2-ERK Survival Signaling axis in Effector and Memory CD8 T Cells. *Cell Mol Immunol* 18 (9), 2262–2274. doi:10.1038/s41423-020-00583-7

Ying, Z., He, T., Wang, X., Zheng, W., Lin, N., Tu, M., et al. (2019). Parallel Comparison of 4-1BB or CD28 Co-stimulated CD19-Targeted CAR-T Cells for B Cell Non-hodgkin's Lymphoma. *Mol. Ther. - Oncolytics* 15, 60–68. doi:10.1016/j.omto.2019.08.002

Zhang, L., Gaskins, K., Yu, Z., Xiong, Y., Merino, M. J., and Kebebew, E. (2014). An *In Vivo* Mouse Model of Metastatic Human Thyroid Cancer. *Thyroid* 24 (4), 695–704. doi:10.1089/thy.2013.0149

Conflict of Interest: The authors declare that the research was conducted in the absence of any commercial or financial relationships that could be construed as a potential conflict of interest.

frontiers | Frontiers in Cell and Developmental Biology

REVIEW
published: 27 April 2022
doi: 10.3389/fcell.2022.885440

Fluorescent Indicators For Biological Imaging of Monatomic Ions

Sheng-Yi Wu[1], *Yi Shen*[1], *Irene Shkolnikov*[1,2] *and Robert E. Campbell*[1,3]*

[1]Department of Chemistry, University of Alberta, Edmonton, AB, Canada, [2]Department of Medical Sciences, University of Victoria, Victoria, BC, Canada, [3]Department of Chemistry, The University of Tokyo, Tokyo, Japan

Monatomic ions play critical biological roles including maintaining the cellular osmotic pressure, transmitting signals, and catalyzing redox reactions as cofactors in enzymes. The ability to visualize monatomic ion concentration, and dynamic changes in the concentration, is essential to understanding their many biological functions. A growing number of genetically encodable and synthetic indicators enable the visualization and detection of monatomic ions in biological systems. With this review, we aim to provide a survey of the current landscape of reported indicators. We hope this review will be a useful guide to researchers who are interested in using indicators for biological applications and to tool developers seeking opportunities to create new and improved indicators.

Keywords: monatomic ions, small molecule-based indicators, genetically encoded indicators, fluorescence imaging, protein engineering

OPEN ACCESS

Edited by:
Yingxiao Wang,
University of California, San Diego, United States

Reviewed by:
Tae-Jin Kim,
Pusan National University, South Korea
João Pessoa,
University of Coimbra, Portugal

***Correspondence:**
Robert E. Campbell
robert.e.campbell@ualberta.ca

Specialty section:
This article was submitted to Signaling, a section of the journal Frontiers in Cell and Developmental Biology

Received: *28 February 2022*
Accepted: *04 April 2022*
Published: *27 April 2022*

Citation:
Wu S-Y, Shen Y, Shkolnikov I and Campbell RE (2022) Fluorescent Indicators For Biological Imaging of Monatomic Ions. Front. Cell Dev. Biol. 10:885440. doi: 10.3389/fcell.2022.885440

1 INTRODUCTION

The interactions between biomolecules and inorganic ions are central to the chemistry of life. The most abundant monatomic inorganic ions in biology systems include sodium (Na^+), potassium (K^+), calcium (Ca^{2+}), iron (Fe^{2+}/Fe^{3+}) and chloride (Cl^-). Trace ions include zinc (Zn^{2+}), molybdenum (Mo^+), cobalt (Co^+), copper (Cu^{2+}/Cu^+), and manganese (Mn^{2+}) (Frieden, 1972). Together, these ions play important roles in physiology including serving as electrolytes, maintaining osmotic pressure and pH, and enabling neuronal activities. Likewise, some ions are incorporated into biologically relevant molecules such as cofactors that facilitate enzyme catalysis (Ainscough and Brodie, 1976). Important questions about the molecular basis of life rest on our understanding of ion dynamics in biological systems. Research into these questions relies on a diverse and highly optimized molecular toolkit for measuring ion concentration, mapping ion localization, and tracking ion flux with high spatiotemporal resolution.

There are a variety of non-imaging methods for measuring concentrations of metal ions. These methods include flame or graphite furnace atomic absorption spectroscopy (AAS) and inductively coupled plasma mass spectrometry (ICP-MS) (Ammann, 2007; Pröfrock and Prange, 2012; Cerchiaro et al., 2013). AAS analyzes only one element at a time, while the ICP-MS can quantitatively measure multiple elements simultaneously. While these methods can detect metal ions with very high sensitivity (parts per billion for AAS and parts per trillion for ICP-MS), they cannot distinguish between bound and free ions, or detect dynamic changes in ion concentrations

Abbreviations: BFP, blue fluorescent protein; CaM, calmodulin; CFP, cyan fluorescent protein; cp, circularly permuted; EC, extinction coefficient; FP, fluorescent protein; FRET, Förster resonance energy transfer; GECI, genetically encodable Ca^{2+} indicator; GEKI, genetically encodable K^+ indicator; GEMI, genetically encodable Mg^{2+} indicator; GEZI, genetically encodable Zn^{2+} indicator; GFP, green fluorescent protein; ncp, non-circularly permuted; QY, quantum yield; RFP, red fluorescent protein; YFP, yellow fluorescent protein.

with spatiotemporal resolution. Free ion concentration is of significant relevance to biologists because bound ions cannot be translocated across organelle or plasma membrane through ion channels or transporters. The adaptation of mass spectrometry with fixed biological samples has enabled elemental mapping at a cellular or subcellular level (Qin Z. et al., 2011). However, these techniques cannot provide dynamic information because they are destructive and are not suitable for use with living tissues. Ion-specific electrodes do provide real-time measurements at a single-cell level, but this technique is challenging and often impractical for measuring multiple cells simultaneously or at a subcellular level.

Imaging technology provides the spatiotemporal information of ion dynamics that eludes the aforementioned technologies. Dynamic changes of ion concentrations are the foundation of many important intra- and intercellular processes and reflect cellular responses to environmental perturbations (Leybaert and Sanderson, 2012; Yurinskaya et al., 2020). Measuring these ion concentrations enables inquiry into ion regulation and transportation, therefore tools for such measurements in tissue and whole organisms are of particular interest. Ion-sensitive indicators, coupled with light microscopy, are indispensable tools for the direct visualization of ion dynamics in multiple cells simultaneously with subcellular resolution.

Two categories of the fluorescent indicators are commonly used: small molecule-based synthetic indicators and genetically encodable protein-based indicators. Several properties are important for comparing the indicators: 1) brightness, the product of extinction coefficient (EC, the ability to absorb photons) and quantum yield (QY, the probability to emit a photon with every photon absorbed); 2) sensitivity, the amplitude of an indicator response to the ligand concentration in the detectable range, which is typically quantified as the maximum fluorescence change $\Delta F/F_0$ or ratio change $\Delta R/R_0$; 3) affinity, which is usually quantified by the dissociation constant (K_d); 4) specificity, the ability of the indicator to recognize the intended target rather than unintended targets; 5) photostability, the ability of a fluorophore to resist photobleaching; 6) pH sensitivity, which is characterized by the apparent pK_a (the acid dissociation constant), the pH at which the fluorescence is half of its maximum value; 7) kinetics, the rate at which the indicator responds to the ligand concentration change and is measured by the association rate constant k_{on} and the dissociation rate constant k_{off}; and finally, 8) targetability, the potential to be expressed in a specific cell type or a subcellular compartment.

Small molecule-based indicators and genetically encoded indicators are both associated with general advantages and disadvantages. Small molecule-based indicators are typically brighter and more photostable, but their use can be complicated by loading procedures and difficulties in subcellular or cell-specific targeting (Russell, 2011). Genetically encodable indicators can typically be expressed by the cellular machinery and trafficked to a specific location of the cell. However, applications can be limited by their relatively lower brightness and photostability. In this review, we aim to provide a detailed overview of the various types of indicators for monatomic ions, and compare them with respect to the properties listed above.

2 Ca^{2+} INDICATORS

2.1 The Role of Ca^{2+} in Cell Physiology

Ca^{2+} is involved in many central physiological activities (Clapham, 2007; Brini et al., 2014). As a universal second messenger, Ca^{2+} regulates cellular activities including cytoskeletal motility, phosphorylation and dephosphorylation-dependent enzymatic activity, and secretion of biomolecules such as neurotransmitters. During propagation of an action potential, voltage-sensitive Ca^{2+} channels on neurons open to allow an influx of Ca^{2+} (Brini et al., 2014). At a synapse, this influx of Ca^{2+} ions leads to neurotransmitter release and signal propagation. Because Ca^{2+} undergoes dramatic translocations during signaling events, being able to measure Ca^{2+} concentration dynamics is of particular importance.

The local concentration of Ca^{2+} varies from nanomolar level to millimolar level in cells. In the resting state, the intracellular concentration is typically maintained at approximately 100 nM in neurons (Khodorov et al., 1993; Bagur and Hajnóczky, 2017). Extracellular Ca^{2+} is typically maintained at 1 mM, 10,000-fold greater than the resting intracellular concentration. Ca^{2+} indicators with different affinities are developed to accommodate the wide span of Ca^{2+} concentrations in various biological contexts.

2.2 Small molecule-based Ca^{2+} indicators

Small molecule-based Ca^{2+} indicators (**Figure 1**) typically contain a fluorophore and a Ca^{2+} chelator and often exhibit an increase in fluorescence in response to Ca^{2+}. Ca^{2+} indicators are typically designed to operate through a photo-induced electron transfer (PeT) mechanism—a process in which an electron is transferred from the excited state electron donor, typically the Ca^{2+} chelator, to the electron acceptor, typically the fluorophore (**Figure 1A**) (Aigner et al., 2011). In absence of Ca^{2+}, the electron-rich Ca^{2+} chelator quenches the fluorophore *via* PeT as the electrons from the chelator are transferred to the low-energy molecular orbital of the fluorophore and prevent photo-excited electrons in the high-energy molecular orbital from returning to the low-energy molecule orbital. In presence of Ca^{2+}, this PeT mechanism is interrupted, allowing photo-excited electrons in the high-energy molecular orbital to return to the unoccupied low-energy molecular orbital by emitting fluorescence (Carter et al., 2014). The fluorescence of PeT-dependent small molecule-based Ca^{2+} indicators can be modulated by the presence of electron-rich or electron-withdrawing groups nearby.

2.2.1 BAPTA and BAPTA-Based Ca^{2+} Indicators

The development of BAPTA [1, 2-bis (*o*-aminophenoxy) ethane-*N*, *N*, *N*′, *N*′-tetraacetic acid], an EGTA [ethylene glycol-bis (β-aminoethyl ether)-*N*, *N*, *N*′, *N*′-tetraacetic acid] analogue, in 1980, was a milestone in the history of small molecule-based fluorescent Ca^{2+} indicator development (Tsien, 1980). BAPTA coordinates Ca^{2+} through the four

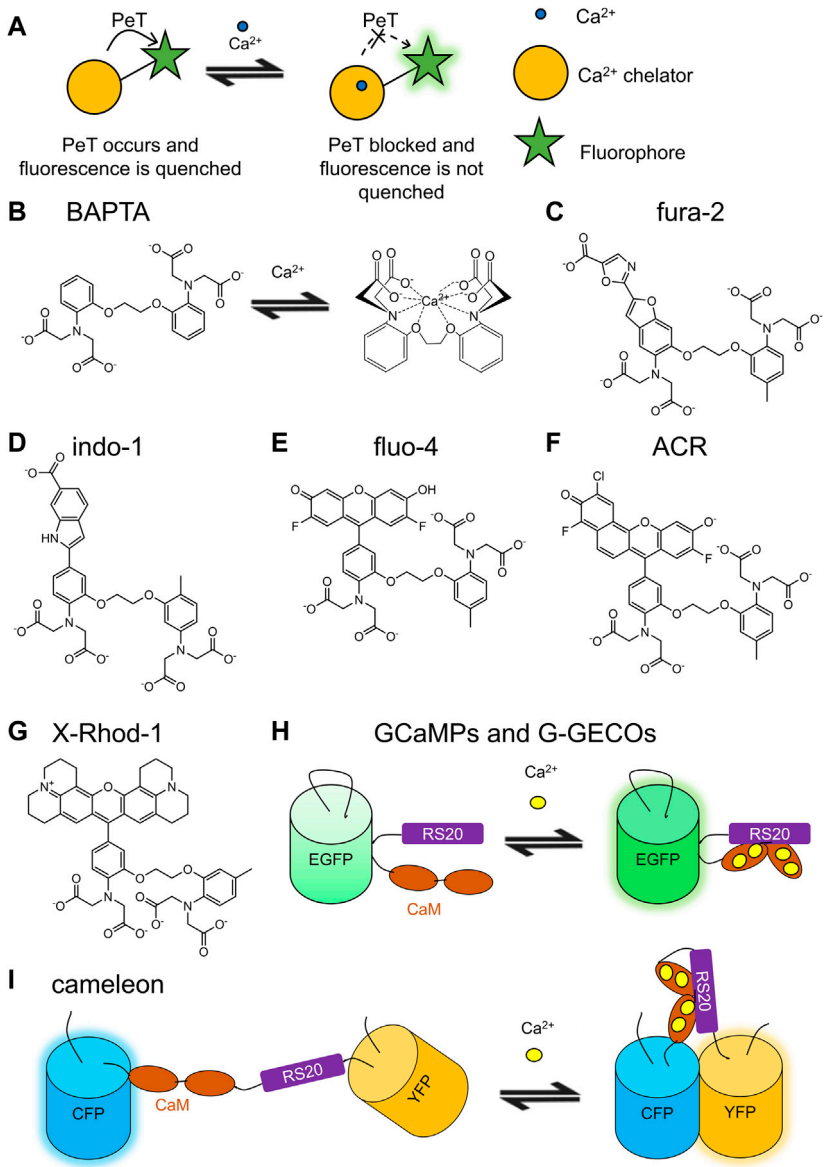

FIGURE 1 | Schematic representations and molecular structures of selected small molecule-based Ca^{2+} indicators and schematic representations of selected GECIs. **(A)** Photoinduced electron transfer (PeT) is the typical mechanism used by small molecule-based Ca^{2+} indicators (Aigner et al., 2011, 2). For indicators with positive responses, the fluorophore is quenched by the electron-rich Ca^{2+} chelator *via* PeT in the unbound state. The binding of Ca^{2+} reduces PeT-induced quenching, leading to brighter fluorophore. **(B)** BAPTA is the Ca^{2+}-binding motif for many small molecule-based Ca^{2+} indicators (Tsien, 1980). The binding of Ca^{2+} constrains the molecular structure of BAPTA, leading to a spectral change. **(C)** Fura-2 and **(D)** indo-1 are both derived from BAPTA and exhibit blue to green emission (Grynkiewicz et al., 1985). **(E)** Fluo-4 is based on a modified fluorescein fluorophore and exhibits bright green emission (Gee et al., 2000). **(F)** Rhodamine-based Asante Calcium Red (ACR) and **(G)** X-Rhod-1 exhibit red fluorescence (Tsien and Minta, 1991; Hyrc et al., 2013). **(H)** GCaMPs and G-GECOs are based on CaM/RS20 and cpEGFP (Nakai et al., 2001; Zhao et al., 2011). **(I)** Cameleon series is FRET-based GECIs, which show increased YFP fluorescence with Ca^{2+} binding (Miyawaki et al., 1997).

carbonyl oxygens, two ether oxygens, and the nitrogen of tertiary amine groups (**Figure 1B**). BAPTA binds Ca^{2+} with a K_d of 1.1×10^{-7} M, an affinity 10^5 fold greater than that for Mg^{2+}. Structurally, BAPTA differs from EGTA by replacing the methylenes between the nitrogen and the ether oxygen with a benzene ring, which renders the molecule fluorescent. Upon Ca^{2+} binding, the nitrogen atoms are twisted away from the same plane of the nearby benzene ring due to the structural constraint. This results in a major shift in the absorbance spectrum. The absorbance peaks at 254 nm (EC = $1.6 \times 10^4\ M^{-1}cm^{-1}$) and 287 nm (EC = $5.6 \times 10^3\ M^{-1}cm^{-1}$) in absence of Ca^{2+} and at 274 nm (EC = $4.2 \times 10^3\ M^{-1}cm^{-1}$) and 203 nm (EC = $4.1 \times 10^4\ M^{-1}cm^{-1}$) with 1 mM Ca^{2+}.

Derivatives of BAPTA were explored with the goal of creating improved Ca^{2+} indicators. Quin-2 is a green fluorescent indicator derived from BAPTA that exhibits a positive response upon Ca^{2+}

binding (Tsien and Pozzan, 1989). Its maximum excitation wavelength is at 339 nm and its maximum emission wavelength is at 492 nm. With a K_d of 115 nM for Ca^{2+}, quin-2 is suitable for cytosolic Ca^{2+} detection. Its K_d for Mg^{2+} is in millimolar range, making quin-2 specific for Ca^{2+}. Quin-2 has a EC < 5000 $M^{-1}cm^{-1}$ and QY of 0.03–0.14. Indo-1 (**Figure 1D**) and fura-2 (**Figure 1C**) are two bright and ratiometric Ca^{2+} indicators (Grynkiewicz et al., 1985). Both indicators have a K_d around 250 nM, slightly higher than that of quin-2. Indo-1 emits cyan light at 485 nm in a Ca^{2+} free environment and violet light at 410 nm in a Ca^{2+} rich environment, with excitation peaks at 349 and 331 nm, respectively. The ratiometric change in emission spectra upon Ca^{2+} binding allows emission ratiometric measurement. In contrast, fura-2 has a minor shift in emission peak from 512 to 505 nm with an increasing Ca^{2+} concentration. The excitation peak undergoes a larger blue shift from 362 to 335 nm, providing an opportunity for excitation ratiometric measurement. The QY increases from 0.23 to 0.49. Fura-2 enables applications using fluorescence microscopy with a single or dual-excitation setup. Fura-2 has a low affinity for Mg^{2+} (K_d = 1–2 mM) that allows intracellular Ca^{2+} imaging in various animal cells (Malgaroli et al., 1987).

BAPTA and BAPTA-based indicators were made cell-permeable by synthetic modification with acetoxymethyl (AM) ester groups to mask their carboxylate groups. These AM esters are readily hydrolyzed by cytosolic esterase as was originally demonstrated with human erythrocytes and rat mast cells (Tsien, 1981, 1983). This method is also used for other indicators with carboxylate groups including the ones for, Zn^{2+}, K^+, Mg^{2+}, Na^+, and H^+.

2.2.2 Fluorescein-Based Ca^{2+} Indicators

Fluorescein was used as the template to make various cell-compatible green indicators including fluo-1, fluo-2, fluo-3, fluo-4 (**Figure 1E**), fluo-8 series, Oregon green BAPTA-1 (OGB1), and Cal-520 (Minta et al., 1989; Gee et al., 2000; Lock et al., 2015). These green fluorescent indicators generally have higher sensitivity and faster kinetics than those of the BAPTA-based indicators mentioned above and bind Ca^{2+} with various affinities that allow detection in different cellular environments (Lock et al., 2015). For example, Cal-520 responds to Ca^{2+} faster than fluo-8H and provides a robust signal with a low signal-to-noise ratio (SNR) in subcellular regions of neurons. The fluo-8 series contains indicators with affinities ranging from 232 nM to 1.8 μM.

2.2.3 Rhodamine-Based Ca^{2+} Indicators

Red-shifted Ca^{2+} indicators provide unique advantages for live-cell imaging: red light penetrates deeper into tissues and allows simultaneous imaging with green indicators. The rhodamine-based rhod2 is maximally excited by light at 553 nm and maximally emits light at 576 nm (Minta et al., 1989). The QY ranges from 0.03 (Ca^{2+} free) to 0.10 (excess of Ca^{2+}) and the K_d value is 0.52 μM. Red-shifted and more sensitive variants such as rhod4 (Miranda et al., 2012; Lock et al., 2015)), rhod5N (Soibinet et al., 2008), Asante Calcium Red (ACR) (**Figure 1F**) (Hyrc et al., 2013), and X-Rhod-1 (**Figure 1G**) (Tsien and Minta, 1991) were further developed (Lock et al., 2015). Rhod5N has a maximum 150-fold change. ACR is excited at 537 nm and emits photons at 654 nm (Hyrc et al., 2013).

2.3 Genetically Encodable Ca^{2+} Indicators

Genetically encodable Ca^{2+} indicators (GECIs) share a general design that consists of a binding domain and a reporter domain. The reporter domain is typically a fluorescent protein (FP). Common choices for binding domains are the calmodulin (CaM)/CaM-binding peptide pair and troponin-C. Ca^{2+}-dependent conformational changes of the binding domain cause changes of the FP chromophore environment, which in turn alters the fluorescence profile, allowing the monitoring of the Ca^{2+} concentration dynamics. A large collection of GECIs is available with various colours and affinities.

2.3.1 FRET-Based Ca^{2+} Indicators

The development of fluorescent indicators has benefited from the expansion of the palette of FPs that have been discovered in nature or engineered from natural FPs. The currently available FP variants span the entire visible spectrum. A pair of FPs with different colours flanking at the ends of the Ca^{2+}-binding domain enables the development of Ca^{2+} indicators based on Förster resonance energy transfer (FRET) — a phenomenon where the excited donor chromophore of the FP pair transfers its energy directly to the acceptor chromophore without photons emitted (Broussard and Green, 2017). FRET efficiency is inversely proportional to the 6th power of the distance between two chromophores (Förster, 1948) and Ca^{2+} binding induced conformational change typically reduces the distance, leading to an increase in FRET efficiency, which is reflected as the emission ratio of the acceptor to the donor fluorescence.

The FRET-based cameleon series (**Figure 1I**) were the first genetically encodable fluorescent Ca^{2+} indicators developed. The binding domain, consisted of calmodulin (CaM) and CaM-binding peptide M13, was inserted between the flanking FPs, EBFP (enhanced blue FP) with EGFP (enhanced green FP) or ECFP (enhanced cyan FP) with EYFP (enhanced yellow FP) (Miyawaki et al., 1997). The cameleon with the ECFP/EYFP pair, named as YC (yellow cameleon), was further engineered. Noticeably, the YC series were the first genetically encodable indicators tested in a living organism. In 2000, Kerr and coworkers expressed recombinant YC2.1 and YC3.1 in *Caenorhabditis elegans* and recorded the FRET signal during pharynx muscle contractions (Kerr et al., 2000). Many further engineered YC indicators have been reported, including YC 3.6, YC 4.6, YC 6.1, and YC-nano series (Truong et al., 2001; Nagai et al., 2004; Horikawa et al., 2010). YC-nano variants exhibit remarkably high sensitivity ($\Delta R/R_0$ = 1,450%) and high Ca^{2+} affinities (K_d = 15–140 nM).

Troponin serves as the Ca^{2+}-binding domain in the TN series and Twitch series of FRET-based GECIs (Heim and Griesbeck, 2004; Mank et al., 2006; Mank and Griesbeck, 2008) For these GECIs, troponin C (TnC) is inserted between a pair of CFP and YFP (Citrine). CaM used in cameleons has many native binding partners that may cause interference and make

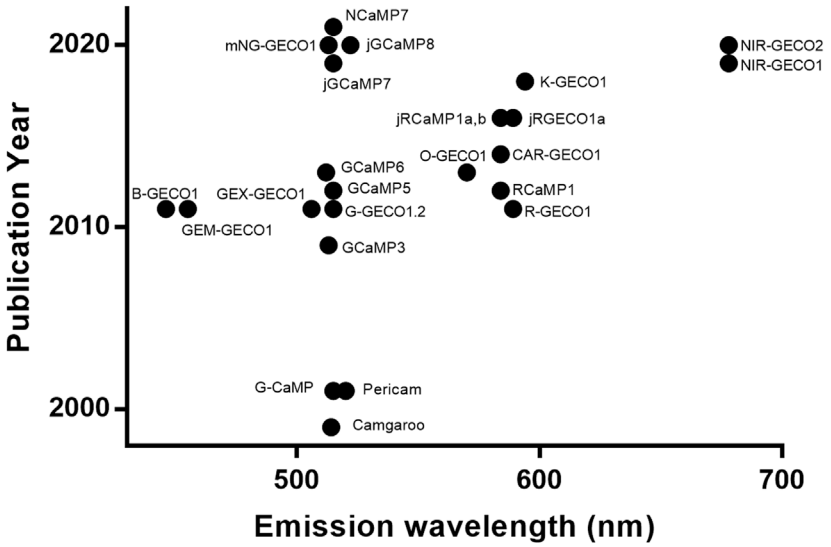

FIGURE 2 | Historical overview of GECI development. Selected GECIs are plotted with *y*-axis being the publication year and *x*-axis being the peak emission wavelength. The template FPs include ones based on BFP (Zhao et al., 2011), YFP (Baird et al., 1999), GFP (Nakai et al., 2001; Tian et al., 2009; Zhao et al., 2011; Akerboom et al., 2013; Dana et al., 2019; Zhang et al., 2021), mNeonGreen (Subach et al., 2020; Zarowny et al., 2020), mApple (Zhao et al., 2011; Dana et al., 2016), mRuby (Akerboom et al., 2013; Dana et al., 2016), FusionRed (Shen et al., 2018), and mIFP (Qian et al., 2019, 2020).

their in-cell response less substantial than their *in vitro* response. TnC, on the other hand, is only native to skeletal and cardiac muscles, and its Ca^{2+} binding can be affected by far fewer cellular binding partners. The TN series exhibit a wide range of affinities (K_d from 470 nM to 29 μM) and suitable $\Delta R/R_0$ values (e.g., ~160% for TN-L15 in HEK 293 cells) (Heim and Griesbeck, 2004; Mank et al., 2006; Mank and Griesbeck, 2008). TN-XXL was later engineered with the full-length TnC replaced by a minimal domain of TnC followed by directed evolution to obtain Twitch variants with varying maximum responses and affinities (Thestrup et al., 2014). With K_d values of ~100–200 nM, Twitch 1, Twitch 2, and Twitch 3 are suitable for lower Ca^{2+} concentration environments, such as the intracellular space. With K_d values of 280–925 μM, Twitch 4 and Twitch 5 are better-suited in higher Ca^{2+} concentration environments such as the endoplasmic reticulum.

In general, the vast majority of FRET-based GECIs use a pair of cyan (e.g., ECFP and mCerulean) and yellow (e.g., EYFP, cpVenus, and mCitrine) FPs to report FRET signal changes. The binding domains can be CaM- or TnC-based. They have been demonstrated as robust and effective tools in mammalian cells including dissociated neurons (Honarnejad et al., 2013; Thestrup et al., 2014).

2.3.2 Single FP-Based Ca^{2+} Indicators

Single FP-based Ca^{2+} indicators are, arguably, the crown jewels of the GECI field. Compared to FRET-based GECIs, their narrower excitation and emission spectra make them ideal for multiplexed imaging. With extensive engineering for more than 2 decades (**Figure 2**), they have achieved remarkably high sensitivity and colour variety. Selected single FP-based GECI are included in **Supplementary Table S1**.

2.3.2.1 Circularly Permuted and Non-Circularly Permuted FPs For Indicator Design

The two topologies for how an FP can be incorporated into an indicator are circularly permuted (cp) (**Figure 3B**) and non-circularly permuted (ncp) (**Figure 3A**) (Nasu et al., 2021). The cpFP topology involves rearrangement of the primary sequences of FPs by which the original N- and C-termini are connected *via* a new linker. New N- and C-termini are created on the β-barrel close to the phenolate group of the chromophore. An indicator based on a cpFP typically has the binding domain(s) fused to the new termini. The ncpFP-based indicators are based on the insertion of the binding domain into the primary sequence of the FP such that the binding domain is located close to the chromophore. The binding event changes the conformation of the binding domain, which subsequently influences the chromophore environment, leading to a fluorescence signal change. Here we summarize the collection of the single FP GECIs designed with cp and ncpFP topologies during the last 2 decades (**Figure 3**).

2.3.2.2 Camgaroos

Camgaroo was the first single FP-based GECI to be developed (Baird et al., 1999). It is based on a ncp design with a CaM inserted into the YFP sequence: EYFP (1–144)-GGT-CaM-EL-EYFP (146–238). The $\Delta F/F_0$ for this YFP-based GECI can be as large as 6-fold and the apparent K_d of camgaroo is 7 μM.

2.3.2.3 GCaMP

Green fluorescent GECIs are widely used and intensively optimized by indicator developers (**Figure 1H**). In 2001, Nakai and coworkers reported the first generation of GCaMP, which is a cpEGFP-based green GECI showing a positive response upon

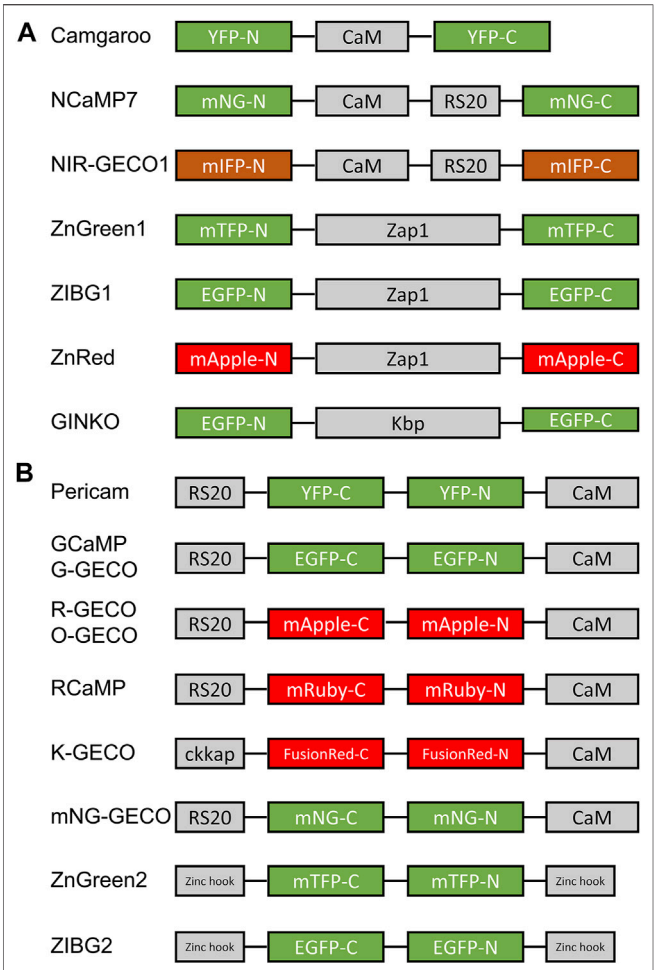

FIGURE 3 | Schematic illustrations of representative cp and ncp FP-based indicators. **(A)** An ncp FP-based indicator is constructed by inserting a binding domain into an FP. Examples of ncp FP-based indicators include camgaroo (Baird et al., 1999), NCaMP7 (Subach et al., 2020), NIR-GECO1 (Qian et al., 2019), ZnGreen1 (Chen and Ai, 2016), ZIBG1 (Chen et al., 2019), ZnRed (Chen and Ai, 2016), and GINKO (Shen et al., 2019). **(B)** A cp FP-based indicator is constructed by inserting a cp FP into a binding domain or by fusing two interacting motifs to the termini of the cp FP. The cpFP indicators include pericam (Nagai et al., 2001), GCaMP (Chen et al., 2013; Dana et al., 2019), G-GECO (Zhao et al., 2011), R-GECO (Zhao et al., 2011), O-GECO (Wu et al., 2013), RCaMP (Akerboom et al., 2013), K-GECO (Zhao et al., 2011), mNG-GECO (Zarowny et al., 2020), ZnGreen2 (Chen and Ai, 2016), and ZIBG2 (Chen et al., 2019).

Ca^{2+} binding ($\Delta F/F_0$ of 3.5), a Hill coefficient of 3.3, and a K_d of 235 nM (Nakai et al., 2001). The contemporaneous and similarly designed cpEYFP-based flash-pericam has a $\Delta F/F_0$ of 7 and a K_d of 700 nM (Nagai et al., 2001).

Initially, the first generation GECIs were not competitive to small molecule-based Ca^{2+} indicators in terms of brightness, photostability, and well-tuned affinities. This situation changed when GCaMP3 was introduced to the GECI toolbox. GCaMP3 was developed *via* structure-guided site-directed mutagenesis and semi-rational library screening. GCaMP3 is 4-fold brighter than GCaMP2, has a $\Delta F/F_0$ that is 3-fold that of GCaMP2, and a reduced Hill coefficient ($n_H = 2.1$) (Tallini et al., 2006; Tian et al., 2009, 3). GCaMP3 was able to provide a substantial response to a single action potential, enabling its broader utility in neuroscience. Because GECIs were prevalently applied in neuroscience, the GECI performance screening was done in dissociated neurons for the development of GCaMP6 (Chen et al., 2013), jGCaMP7 (Dana et al., 2019), and jGCaMP8 (Zhang et al., 2021). The letter "j" in the names denotes the Howard Hughes Medical Institute's Janelia campus, where they were developed.

jGCaMP7 variants were optimized for sensitivity, kinetics, Ca^{2+} affinity, and brightness (Dana et al., 2019). jGCaMP7s (sensitive) and jGCaMP7f (fast) have improved sensitivity and kinetics for single action potential imaging. jGCaMP7s provides the biggest response to a single action potential with a 65.6% increase in fluorescence. jGCaMP7f responds rapidly to 10 action potentials with a half-rise time of 75 ms and half-decay time of 520 ms, which is comparable to GCaMP6f (a half-rise time of 80 ms and half-decay time of 335 ms) (Chen et al., 2013; Dana et al., 2019). With a 50% increase in resting fluorescence compared to GCaMP6s, jGCaMP7b (bright) is suitable for use at lower protein expression levels. jGCaMP7c (contrast) has the largest fluorescent response ($\Delta F/F_0$ = 145) and the lowest brightness in the absence of Ca^{2+}.

The major improvement for the latest jGCaMP8 series is with respect to the kinetics (Zhang et al., 2021). Variants with various CaM-binding peptides were screened for high sensitivity and fast kinetics and resulted in jGCaMP8 variants that feature a CaM-binding peptide from endothelial nitric oxide synthase. Compared to jGCaMP7, all jGCaMP8 variants have shorter rise and decay times, making them more suitable for tracing fast-paced neuronal activities. The half-rise time in response to a single action potential is 7.0 ± 0.7 ms for jGCaMP8f, which is 3-fold shorter than that for jGCaMP7f.

2.3.2.4 mNeon Green-Based GECI

The brightness of GCaMPs is limited by the inherent brightness of EGFP. mNeonGreen is one of the brightest monomeric GFPs, which is 1.8-fold brighter than EGFP (Shaner et al., 2013). Zarowny *et al.* and Subach *et al.* independently developed ncp mNeonGreen-based GECIs named mNG-GECO1 and NCaMP7, respectively, (Subach et al., 2020; Zarowny et al., 2020). In the Ca^{2+}-bound state, brightness of mNG-GECO1 is 59% higher than that of GCaMP6s. Its $\Delta F/F_0$ of 45 is comparable to that of GCaMP6 (Chen et al., 2013), but the sensitivity of mNG-GECO1 is about half of that of GCaMP6s in neurons. The brightness of NCaMP7 is 70% higher than that of GCaMP6s and $\Delta F/F_0$ of NCaMP7 is 89. The sensitivity of NCaMP7 is comparable to that of GCaMP6s in neurons, but with slower kinetics. Although neither mNG-GECO nor NCaMP7 surpasses GCaMP6s as a tool for neuronal activity imaging, mNeon Green-based GECIs have an enormous potential to become state-of-art indicators for neuronal imaging with further optimization.

2.3.2.5 Red, Far-Red, and Near-Infrared GECI

Limited depth of imaging is one of the limitations associated with the green and blue GECIs, as biological samples absorb and scatter incoming light most strongly in this region of the

spectrum. Absorption and scattering are less severe with photons of longer wavelengths (Ash et al., 2017). Thus, the red-shifted GECIs are more suitable for deeper sample imaging. Another advantage of red-shifted GECIs is their spectral compatibility with blue light-activated optogenetics tools.

R-GECO was the first reported red-fluorescent GECI and was developed using cpRFP mApple (Zhao et al., 2011). R-GECO1 exhibits a 16-fold Ca^{2+} response. The brightness of R-GECO1 is 10.2 $mM^{-1}cm^{-1}$ at its brighter Ca^{2+}-bound state. Further engineering of R-GECO1 led to different variants: R-GECO1.2, O-GECO1, REX-GECO1, and CAR-GECO1 (Wu et al., 2013, 2014). R-GECO1.2 is twice as sensitive as R-GECO1 but has a larger K_d at 1,200 nM. O-GECO1 is a blue-shifted variant of R-GECO with excitation wavelengths at 543 nm (Ca^{2+} bound) and 545 nm (Ca^{2+} unbound), emission wavelengths at 564 nm (Ca^{2+} bound) and 570 nm (Ca^{2+} unbound), and an *in vitro* $\Delta F/F_0$ of 146. However, its weak affinity for Ca^{2+} (large K_d = 1,500 nM) made it not suitable for Ca^{2+} detection in low Ca^{2+} environments. Directed evolution on R-GECO1 led to a red-shifted variant CAR-GECO1 with peak excitation and emission wavelengths at 560 and 609 nm, respectively. CAR-GECO1 has a $\Delta F/F_0$ of 27 and a K_d of 490 nM *in vitro*. REX-GECO1 is a long Stokes shift red fluorescent indicator with a substantially blue-shifted excitation: the one-photon excitation is at 480 nm and the two-photon excitation is at 960 nm (Wu et al., 2014). REX-GECO1 has a $\Delta R/R_0$ (582–480 nm) of 100 *in vitro* and a K_d of 240 nM. Although effective, these mApple-based GECIs are all limited by photoactivation by blue light (Wu et al., 2013), preventing their utility with blue light-activated optogenetic tools.

In parallel to the development of R-GECO1, Akerboom and coworkers developed mRuby-based RCaMP series (Akerboom et al., 2013). RCaMP1f and RCaMP1h are sensitive to Ca^{2+} *in vitro* with $\Delta F/F_0$ values of 12.3 and 10.5, respectively. Their $\Delta F/F_0$ values in HEK cells are at 1.8 and 2.0, both smaller than that of R-GECO1 ($\Delta F/F_0$ = 2.5). RCaMP1f and 1 h also exhibit larger K_d values at 1,900 and 1,300 nM, respectively. On the other hand, RCaMP1f and 1 h are brighter than R-GECO1 with a one-photon brightness of 28 and 33 $mM^{-1}cm^{-1}$, respectively, and two-photon brightness of 9.2 and 8.1 $mM^{-1}cm^{-1}$, respectively, (one-photon brightness of R-GECO1 is 10.2 $mM^{-1}cm^{-1}$; two-photon brightness of R-GECO1 is 3.8 $mM^{-1}cm^{-1}$). The lack of photoactivation of RCaMP1 enables it to be used simultaneously with the blue light-activated channelrhodopsin-2 (ChR2).

Dana and coworkers optimized the RCaMP1h and R-GECOs for neuronal imaging (Dana et al., 2016). One of the resulting GECIs, jRGECO1a, has a $\Delta F/F_0$ of 11.6 and a K_d at 148 nM *in vitro*. Its performance in neurons is comparable to that of GCaMP6f. However, jRGECO1a inherited the photoactivatable property of R-GECO1, preventing it from being used with blue light-activated optogenetic tools. This effort also produced jRCaMP1a and 1b, which have K_d values at 214 and 712 nM (Akerboom et al., 2013). Although neither is more sensitive than jRGECO1a, they are both 2-fold brighter than jRGECO1a and allow simultaneous photo-stimulation of ChR2 and imaging of jRCaMP1a/b.

In other work, Shen and coworkers developed a FusionRed-based GECI called K-GECO1, with less blue-light photoactivation than that of R-GECOs and a higher Ca^{2+} affinity than those of RCaMPs (Shen et al., 2018). K-GECO1 was engineered with cpFusionRed as the fluorescent reporter domain and ckkap in place of RS20 in the Ca^{2+}-binding domain as previously described in RCaMP2 (Inoue et al., 2015). K-GECO1 has a K_d for Ca^{2+} at 165 nM and a brightness of 27 $mM^{-1}cm^{-1}$ (Shen et al., 2018). In neurons, K-GECO1 responds with action potentials with a better $\Delta F/F$ than most red GECIs except jRGECO1a. K-GECO1 has negligible blue-light photoactivation, enabling simultaneous imaging of K-GECO1 and photo-stimulation of optogenetic tools such as ChR2.

Despite the variety of β-barrel FPs, there are none that fluoresce well into the near-infrared region of the colour spectrum. Another class of FPs, biliverdin (BV)-binding FPs (BV-FPs), enable the development of more red-shifted GECIs by providing far-red to near-infrared fluorescence. NIR-GECO1, developed from the BV-FP mIFP, was the first reported NIR GECI. NIR-GECO1 is based on a ncp mIFP into which CaM and RS20 are inserted (Qian et al., 2019). NIR-GECO1 has an 8-fold inverse change and a K_d of 885 nM *in vitro*. The brightness of NIR-GECO1 is 3.9 $mM^{-1}cm^{-1}$ in the Ca^{2+}-unbound state and 0.4 $mM^{-1}cm^{-1}$ in the Ca^{2+}-bound state. The low brightness is due to the low QY inherited from its parent protein, mIFP (QY = 0.08) (Yu et al., 2015). The brightness of this BV-FP-based GECI is further limited by the amount of available BV in the tissue. When tested in the sensorimotor cortex of mice under paw stimuli, NIR-GECO1 revealed a response of only 0.3%, whereas the same stimuli could lead to a 10-fold greater fluorescence change with GCaMP6s.

Further development of NIR-GECO1 led to NIR-GECO2 and NIR-GECO2G (Qian et al., 2020). The most pronounced improvement is the higher affinities for Ca^{2+} with K_d values of 331 nM (NIR-GECO2) and 480 nM (NIR-GECO2G), in comparison to a K_d of 885 nM for NIR-GECO1. While sensitivity and brightness of the new variants remain similar to those of NIR-GECO1, the higher affinities alone are sufficient to substantially increase -$\Delta F/F$ to a single action potential (16, 17, and 4.5% for NIR-GECO2, NIR-GECO2G, and NIR-GECO1). The Ca^{2+} response levels of NIR-GECO2 and NIR-GECO2G are comparable to those of GCaMP6f (19%) and jRCaMP1a (15%). However, NIR-GECO2 and 2G have relatively slow kinetics (k_{off} values are 3.0 s^{-1} for NIR-GECO2 and 3.7 s^{-1} for NIR-GECO2G) and low brightness (4.0 $mM^{-1}cm^{-1}$ for NIR-GECO2 and 4.5 $mM^{-1}cm^{-1}$ for NIR-GECO2G). Development of a further improved variant may require further engineering of NIR-GECO or using a brighter BV-FP.

3 ZN^{2+} ION INDICATORS

3.1 The Roles of Zn^{2+} in Cell Physiology

Zinc (Zn^{2+}) is an essential trace metal element in biology. Zn^{2+} is incorporated in over 300 enzymes that have a broad range of biological functions including: regulation of smell, taste, and appetite; synthesis of DNA and RNA; hormonal regulation;

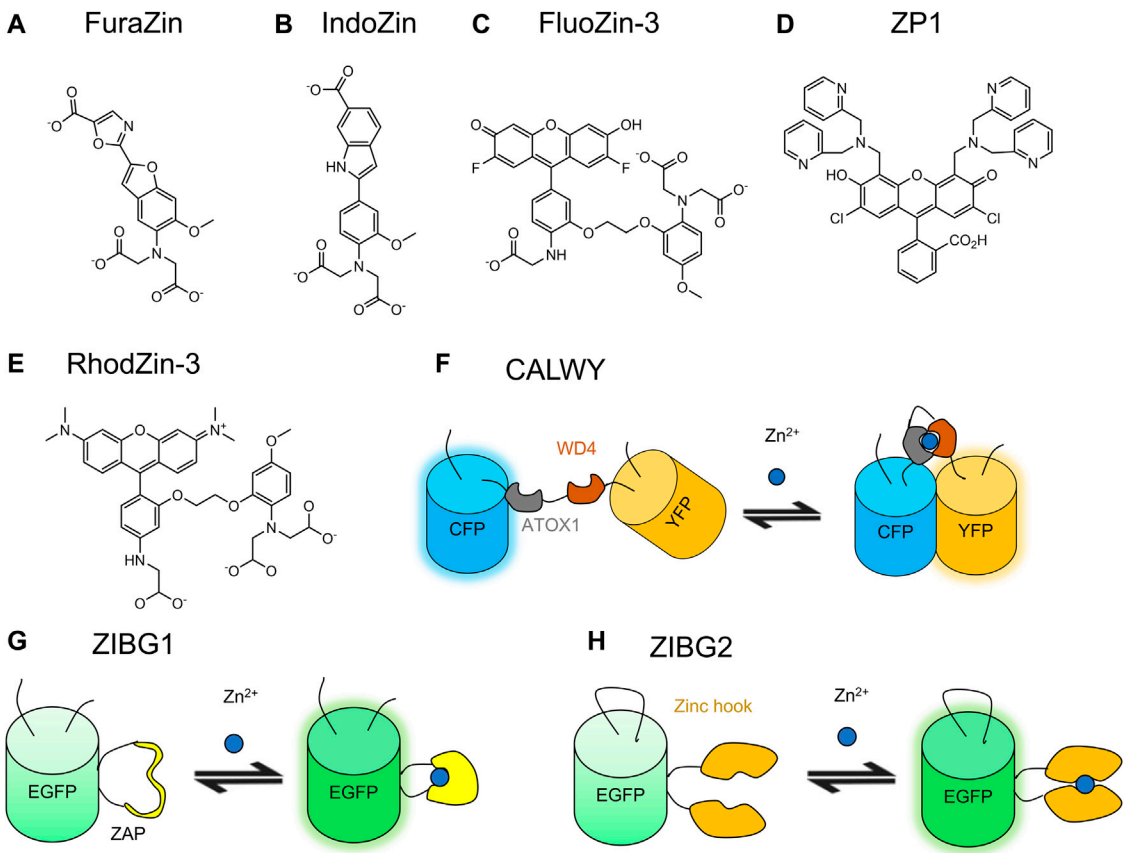

FIGURE 4 | Molecular structures of selected small molecule-based Zn^{2+} indicators and schematic representations of selected GEZIs. Many small molecule-based Zn^{2+} indicators are structurally similar to small molecule-based Ca^{2+} indicators. **(A)** FuraZin, **(B)** IndoZin, and **(C)** FluoZin-3 have fluorophore moieties that are identical to those of fura-2 and indo-1, and fluo-4, respectively, (Gee et al., 2002). **(D)** ZP1 is composed of a di-2-picolylamine (DPA) Zn^{2+} chelator and a green-fluorescent fluorescein moiety (Walkup et al., 2000). **(E)** RhodZin-3 is a rhodamine-based red fluorescent Zn^{2+} indicator (Gee et al., 2002). **(F)** CALWY (Vinkenborg et al., 2009) is a FRET-based GEZI with the Zn^{2+} binding moiety of ATOX1/WD4. **(G)** ZIBG1 (Chen et al., 2019) is based on the Zn^{2+} binding ZAP1 protein and ncpEGFP. **(H)** ZIBG2 (Chen et al., 2019) is based on Zinc hook and cpEGFP.

immune functions; and antioxidation (Frassinetti et al., 2006). Zn^{2+} is transported mainly by albumin in the blood and is maintained at a concentration of 1–10 μM in human serum or plasma (Frassinetti et al., 2006). Total cytosolic Zn^{2+} concentration is a few hundreds of micromolar, but most Zn^{2+} is tightly bound, leaving free Zn^{2+} at a picomolar level. Free Zn^{2+} is heterogeneously distributed in cell: 1 pM in the endoplasmic reticulum and the Golgi apparatus, 0.1 pM in the mitochondrial matrix, 180 pM in the cytosol, and 200 pM in the nucleus (Carter et al., 2014). Some important cellular activities are accompanied by Zn^{2+} dynamics. For example, Zn^{2+} secretion is associated with insulin secretion of human pancreatic β-cells (Chen et al., 2019). Zn^{2+} is also suggested to play important roles in the brain for its Ca^{2+}-dependent release from synaptic vesicles (Assaf and Chung, 1984).

3.2 Small Molecule-Based Zn^{2+} Indicators

Analogous to small molecule-based Ca^{2+} indicators, small molecule-based Zn^{2+} indicators also consist of a Zn^{2+} chelator and a fluorophore (**Figures 4A–E**), function using the principle of PeT, and are suitable for live-cell imaging. Common fluorophores include quinoline, fluorescein, 4-aminoapthalimide, and BODIPY (Carter et al., 2014). The small molecule-based Zn^{2+} indicators have been comprehensively reviewed previously by Carter and coworkers (Carter et al., 2014).

3.2.1 BAPTA-Based Zn^{2+} Indicators

As Zn^{2+} and Ca^{2+} are both divalent cations, existing Ca^{2+} indicators provided templates for the development of Zn^{2+} indicators. By removing one or more chelating moieties on the BAPTA-based Ca^{2+} indicators, Gee and coworkers created indicators that have a weaker affinity for Ca^{2+} and a much higher affinity for Zn^{2+} (Gee et al., 2002). These indicators include FluoZins, IndoZin, FuraZin, RhodZin, X-RhodZin, and NewPort Green PDX. Among these indicators, FuraZin (**Figure 4A**) and IndoZin (**Figure 4B**) are ratiometric indicators structurally similar to their templates fura-2 and indo-1, respectively. FuraZin exhibits ratiometric excitation at 378 and 330 nm; IndoZin exhibits ratiometric emission at 480 and 390 nm. FluoZin-1 and FluoZin-3 (**Figure 4C**) are extremely

sensitive to Zn^{2+} with a $\Delta F/F_0$ of 200. RhodZin (**Figure 4E**) and X-RhodZin also have large $\Delta F/F_0$ values of 150 and 100, respectively. FluoZin-3 and NewPort Green PDX are specific to Zn^{2+} with no response to Ca^{2+}. The affinities of these BAPTA-based Zn^{2+} indicators for Zn^{2+} are typically in the nanomolar (e.g., K_d = 15 nM for FluoZin-3) to micromolar (e.g., K_d = 40 μM for NewPort Green PDX) range, which are not ideal for physiological Zn^{2+} concentrations that are typically at the picomolar level.

3.2.2 Fluorescein-Based Zn^{2+} Indicator

Fluorescein-based Zn^{2+} indicators with other Zn^{2+}-binding moiety include Zinpyr (ZP), ZnAF, Zinspy (ZS), and QZ families. ZP indicators contain a di-2-picolylamine (DPA) Zn^{2+} chelator. ZP1 (**Figure 4D**) is cell-permeable and has no substantial response to Ca^{2+} or Mg^{2+} (Walkup et al., 2000). It binds $Zn^{2+}$with a $\Delta F/F_0$ of 3.1 and a K_d of 700 pM. The further improvement led to ZP3 with a brightness of 78 $mM^{-1}cm^{-1}$ in the Zn^{2+}-bound state, a $\Delta F/F_0$ of 6, and a K_d of 700 pM (Chang et al., 2004a). Instead of a symmetrical fluorescein platform with two DPA groups in ZP1—3, ZP4 employs an asymmetrical fluorescein platform with a Zn^{2+} chelator consisted of one DPA and an additional aniline group (Burdette et al., 2003). ZP4 is cell permeable and exhibits a $\Delta F/F_0$ of 5 and a K_d of 650 pM. More ZP variants were created with modification on the electron-withdrawing groups on either the fluorophore or the chelator. ZP8, for example, has a $\Delta F/F_0$ of 11 and a K_d of 600 pM (Chang et al., 2004b). ZP9 and ZP10 contain a pyrrole group and an *N*-methypyrrole group, respectively, in the asymmetrical Zn^{2+} chelator, weakening their affinities substantially (the K_d of ZP9 is 690 nM and that of ZP10 is 1.9 μM) (Zhang et al., 2008).

ZnAF probes were developed by attaching a DPA moiety to different positions on the benzoic acid moiety of fluorescein. ZnAF probes have lower background fluorescence than ZP probes. Among this family, ZnAF-2, ZnAF-1F, and ZnAF-2F are highly sensitive to Zn^{2+} with $\Delta F/F_0$ values of 51, 69, and 60, respectively, (Hirano et al., 2000, 2002).

By using one or two pyridyl amine thioether moieties as the Zn^{2+} chelator, ZS indicators help to address the lack of specificity of ZP indicators. While ZP indicators can also bind to Fe^{2+}, ZS2 and ZS4 show better specificity for Zn^{2+} over other divalent ions such as Fe^{2+}, Ca^{2+}, Mn^{2+}, and Mg^{2+} (Nolan and Lippard, 2004). ZS1, ZS2, and ZS3 exhibit $\Delta F/F_0$ values in the range of 1.5–4.5. Further improvement on ZS indicators lowered the background fluorescence and improved $\Delta F/F_0$ by replacing the thioether with a thiophene (Nolan et al., 2006). ZSF7 has a $\Delta F/F_0$ of 42 and a K_d of 33 μM.

The QZ family employs an 8-aminoquinoline to bind Zn^{2+}. These indicators show remarkably large $\Delta F/F_0$ values ($\Delta F/F_0$ = 150 for QZ1 and $\Delta F/F_0$ = 120 for QZ2). With an affinity in the micromolar range, they were only suitable for the detection of Zn^{2+} dynamics at relatively high concentrations of Zn^{2+}.

3.2.3 Other Fluorophore-Based Zn^{2+} Indicators

Fluorophores such as boron dipyrromethene (BODIPY) and rhodamine can provide some advantages when used for the construction of Zn^{2+} indicators. BDA (Wu et al., 2005), a BODIPY-based indicator, has a low pK_a of 2.1 and is less pH sensitive than fluorescein-based indicators. BDA is a sensitive green Zn^{2+} indicator with a $\Delta F/F_0$ of 10.5 and a K_d of 1 nM. These properties make BDA suitable for applications in which pH is not constant. Rhodamine is a photostable red fluorescent fluorophore that has been incorporated into Zn^{2+} indicators including ZRL1 (Du and Lippard, 2010), SiR-Zn (Koide et al., 2011), and ZIGIR (Ghazvini Zadeh et al., 2020). The peak excitation and emission wavelengths of ZRL1 are at 569 and 595 nm, respectively, (Du and Lippard, 2010). SiR-Zn incorporates a silicon atom in the chromophore and is more red-shifted than other rhodamine-based indicators with the peak excitation and emission wavelengths at 650 and 665 nm, respectively, (Koide et al., 2011). The indicator is useful for intracellular Zn^{2+} detection with a nanomolar affinity and a $\Delta F/F_0$ of 15. ZIGIR is a red Zn^{2+} indicator that is sensitive ($\Delta F/F_0$ > 100), cell-permeable, and granule-specific (Ghazvini Zadeh et al., 2020).

3.3 Genetically Encodable Zn^{2+} Indicators

The abundance of Zn^{2+}-binding proteins in nature provides a number of suitable candidates for engineering GEZIs. They include the CXXC-motif-containing metal-binding domains Atox1/WD4 used in the CALWY family, yeast transcription factor Zap1 in the Zap family, and yeast transcription factor Zif268 in the Zif family.

Most GEZIs are FRET-based. ECFP and mCitrine-based ZifCY2 exhibits a $\Delta R/R_0$ of 4.0 but is limited by its millimolar affinity (Dittmer et al., 2009). Benefiting from the higher Zn^{2+} affinities of the Atox1/WD4 Zn^{2+}-binding pair (**Figure 2B**), Cerulean and Citrine-based eCALWYs (**Figure 4F**) exhibit affinities ranging from picomolar to nanomolar (Vinkenborg et al., 2009). Zap indicators also exhibit high Zn^{2+} affinities: ECFP and mCitrine-based ZapCY1 exhibits a $\Delta R/R_0$ of 2.15 and a K_d of 2.5 pM; ZapCY2 exhibits a smaller $\Delta R/R_0$ of 1.5 and a larger K_d of 810 pM (Qin Y. et al., 2011).

The ZinCh and eZinCh indicators employ Zn^{2+}-binding pockets engineered into FPs. Cerulean and Citrine-based ZinCh-1 was engineered with double mutations of Y39H and S208C on both FPs, leading to two binding sites that each consist of a pair of H39 and C208 (Evers et al., 2007). Further optimization on the binding sites led to eZinCh-2 with a $\Delta R/R_0$ of 4 and a K_d of 1 nM (Hessels et al., 2015). Although it also binds Pb^{2+} and Cd^{2+}, eZinCh-2 is an effective intracellular GEZI for monitoring Zn^{2+} in the cytosol, the ER, the mitochondria, and vesicles.

Chen and coworkers developed single FP-based GEZIs with either Zap1 or a zinc hook as the binding domain (Chen and Ai, 2016; Chen et al., 2019). Zap1 contains two Zn^{2+} finger domains and undergoes a dramatic conformational change upon Zn^{2+} binding. The *Pyrococcus furiosus* Rad50 zinc hook peptide undergoes homodimerization upon Zn^{2+} binding. ZnGreen1, based on ncpmTFP1 and Zap1, shows superior performance relative to previous FRET-based GEZIs with a $\Delta F/F_0$ as large as 26.3 and a K_d of 633 pM (Chen and Ai, 2016). ZnGreen2, based on cpmTFP1 and zinc hooks, displays a $\Delta F/F_0$ of 8.7 and a K_d of 20 μM (Chen and Ai, 2016). One limitation of ZnGreen1 and ZnGreen2 is that they are inverse response indicators with poor

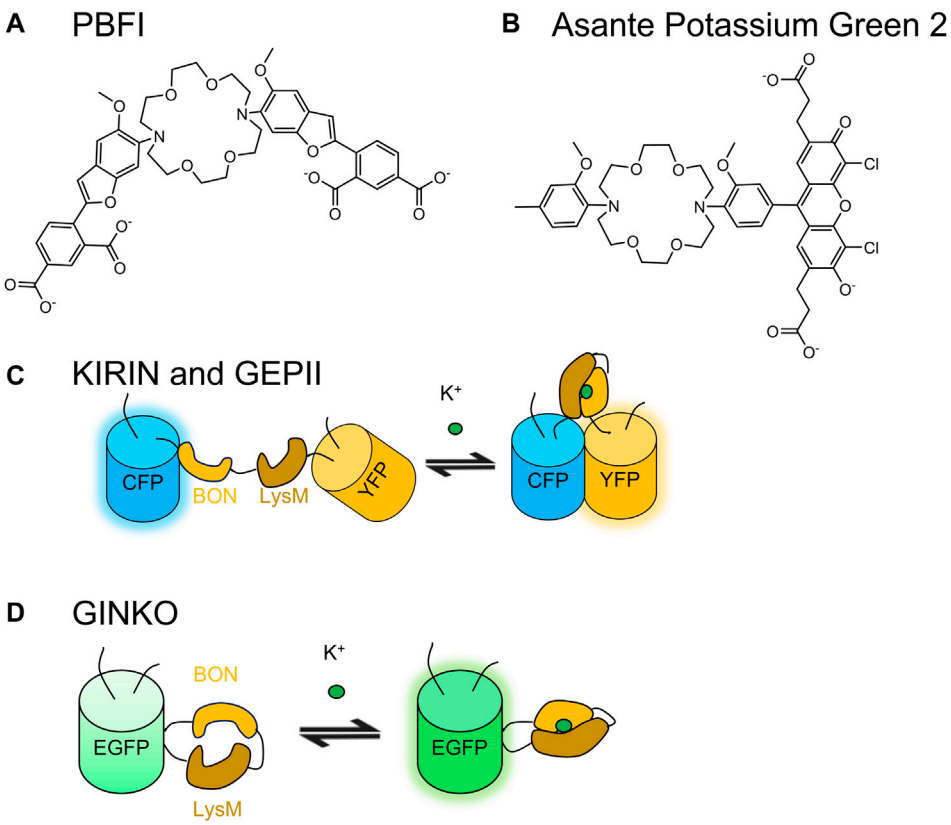

FIGURE 5 | Molecular structures of selected small molecule-based K^+ indicators (PBFI and Potassium Green 2) and schematic representations of selected GEKIs. Small molecule-based K^+ indicators **(A)** PBFI and **(B)** Asante Potassium Green 2 (APG-2) are based on 1, 10-diaza-4, 7, 13, 16-tetraoxacyclopentadecane (Minta and Tsien, 1989; Rimmele and Chatton, 2014). **(C)** FRET-based KIRIN and GEPII are based on Kbp that consists of a BON and a LysM domain (Ashraf et al., 2016; Shen et al., 2019). **(D)** GINKO1 and GINKO2 are based on Kbp and ncpEGFP (Shen et al., 2019; Wu et al., 2021).

photostability. To address this issue, Chen and coworkers replaced mTFP1 with EGFP to create ZIBG1 (**Figure 4G**) and ZIBG2 (**Figure 4H**) (Chen et al., 2019). ZIBG1 and ZIBG2 both respond positively to Zn^{2+} binding. ZIBG1 has a $\Delta F/F_0$ of 2.5 and a K_d of 2.81 μM; ZIBG2 has a $\Delta F/F_0$ of 7 and a K_d of 282 pM. A red fluorescent GEZI based on mApple and Zap1 was also created with a $\Delta F/F_0$ of 3.8 and two K_d values of 166 pM and 20 μM according to the biphasic titration curve.

GZnPs are a series of GEZIs also based on Zap1 and cpGFP (Qin et al., 2016; Fudge et al., 2018; Minckley et al., 2019). GZnP1 has a $\Delta F/F_0$ of 1.2 and a K_d of 34 pM. Engineering efforts on GZnP1 led to GZnP3 with a larger $\Delta F/F_0$ of 10 and a weaker affinity (K_d = 1.3 nM). The weakened affinity is more appropriate for Zn^{2+} released from granules.

4 K^+ INDICATORS

4.1 The Roles of K^+ in Cell Physiology

Potassium (K^+) is one of the most abundant ions in biology. Besides its role as an electrolyte for body fluid balance, K^+ also plays a pivotal role in excitable cells such as those in the heart and the nervous system (Humphries and Dart, 2015). In the resting state, K^+ is sequestered into cells by the Na^+/K^+ pump and other transporters to maintain a large concentration gradient with the intracellular K^+ concentration at around 150 mM and the extracellular K^+ concentration at around 5 mM. When cells are excited, K^+ effluxes through a variety of voltage-gated K^+ channels to repolarize cells after depolarization. The dynamics of K^+ fluxes reflect neuronal and cardiac signal propagation and therefore is an intriguing target for live-cell imaging applications.

4.2 Small Molecule-Based K^+ Indicator

Potassium binding benzofuran isophthalate (PBFI) is the earliest small molecule-based K^+ indicators (**Figure 5A**) (Minta and Tsien, 1989). It is excited by UV light at 350 nm in the K^+-unbound state and 344 nm in the K^+-bound state. Although the indicator is more specific for K^+ (K_d = 8 mM) than Na^+ (K_d = 21 mM), better specificity is required for cellular imaging to avoid signal interference by Na^+, which is typically at an intracellular concentration of 10–40 mM (Minta and Tsien, 1989). PBFI exhibits low brightness primarily due to its low QY of 0.024 in the K^+-unbound state and 0.072 in the K^+-bound state. Asante Potassium Green-1 (APG-1) is more red-shifted than PBFI with the peak excitation wavelength at 515 nm and the peak

emission wavelength at 540 nm (Rimmele and Chatton, 2014). APG-1 responds to K^+ with a maximum 4-fold change. Improved APG-2 (**Figure 5B**) and APG-4 were applied in permeabilized Jurkat and U937 cells to visualize changes in intracellular K^+ concentration (Rana et al., 2019). Recently, Ratiometric Potassium Sensor-1 (RPS-1) was developed with dual fluorophores: a K^+-responsive fluorophore Potassium Sensor 525 (PS525) and a non-responsive Coumarin 343 for internal calibration in living tissues (Wang et al., 2021). The dye displays a $\Delta F/F_0$ of 6 and an apparent K_d of 137 mM.

4.3 Genetically Encodable K^+ Indicators

The identification of K^+ binding protein (Kbp) enabled the development of GEKIs (Ashraf et al., 2016). Bischof *et al.* and Shen *et al.* developed FRET-based GEKIs named GEPII and KIRIN, respectively, (**Figure 5C**) (Ashraf et al., 2016; Shen et al., 2019; Bischof et al., 2019). The two indicators show comparable $\Delta R/R_0$ and affinity values: the mCerulean3 and cpVenus-based KIRIN has a $\Delta R/R_0$ of 1.5 and a K_d of 1.66 mM, and the mseCFP and cpVenus-based GEPII has a $\Delta R/R_0$ of 2.2 and a K_d of 0.42 mM. Both FRET indicators exhibit outstanding specificity for K^+, showing no response to Na^+ at physiologically relevant concentrations. In addition to the FRET-based GEKIs, Shen *et al.* also described ncpGFP-based GINKO1 (**Figure 5D**). GINKO1 exhibits a $\Delta F/F_0$ of 1.5 and higher specificity for K^+ (K_d = 0.42 mM) than Na^+ (K_d = 153 mM). Further engineering with site-directed mutagenesis and directed evolution led to GINKO2 with better sensitivity ($\Delta F/F_0$ = 14) and specificity (no response to Na^+ up to 150 mM) (Wu et al., 2021).

5 MG^{2+} INDICATORS

5.1 The Roles of Mg^{2+} in Cell Physiology

Mg^{2+} plays many pivotal roles in cellular processes and functions. Mg^{2+} serves as an important cofactor for almost every enzyme that needs ATP for catalysis; stabilizes nucleic acids through electrostatic interactions for DNA and RNA synthesis and repair; and regulates mitochondrial Ca^{2+} transport, voltage-gated Ca^{2+} channels, and voltage-gated K^+ channels as a Ca^{2+} antagonist (Pilchova et al., 2017). Most intracellular Mg^{2+} is bound to biomacromolecules, such that total intracellular concentration of total Mg^{2+} is 17–20 mM but only 0.25–1.5 mM is free Mg^{2+} (Grubbs, 2002; Romani, 2013). Cells maintain a steady-state Mg^{2+} concentration through transporters such as Mrs2p, which transports Mg^{2+} into mitochondria for Mg^{2+} sequestration (Kolisek et al., 2003).

5.2 Small Molecule-Based Mg^{2+} Indicators

Many small molecule-based Ca^{2+} indicators that exhibit an affinity for Mg^{2+} were modified into Mg^{2+} indicators with *o*-aminophenol-*N*, *N*, *O*-triacetic acid (APTRA) as the binding group. Some examples include Mag-fura-2 (**Figure 6A**), Mag-indo-1 (**Figure 6B**), and Magnesium Green (**Supplementary Table S2**) (Raju et al., 1989; Morelle et al., 1994; Zhao et al., 1996). Mag-fura-2 is excited at 369 nm and Mag-indo-1 is excited at 349 nm (Raju et al., 1989). Due to the phototoxicity associated with UV excitation, Mg^{2+} indicators with excitation at longer wavelengths were developed. The green indicators Magnesium Green and Mag-fluo-4 (**Figure 6C**) are excited at 506 and 490 nm, respectively, (Zhao et al., 1996; Shmigol et al., 2001). The above indicators are all subject to interference from Ca^{2+} in live-cell imaging due to their millimolar affinities for Mg^{2+} and micromolar affinities for Ca^{2+}.

Other binding motifs were sought to address the lack of Mg^{2+} specificity over Ca^{2+} observed with APTRA. One such motif is the charged β-diketone, which is used in KMG-103 (K_d = 1.8 mM for Mg^{2+}, K_d = 6.3 mM for Ca^{2+}) and KMG-104 (K_d = 2.1 for Mg^{2+}, K_d = 7.5 mM for Ca^{2+}) that bind Mg^{2+} preferentially (Komatsu et al., 2004). With an addition of a biarsenical structure to KMG-104, the FlAsH-based KMG-104-AsH (**Figure 6D**) exhibits an outstanding specificity with K_d values of 1.7 mM for Mg^{2+} and 100 mM for Ca^{2+} (Fujii et al., 2014). The FlAsH-based indicator remain quenched until it covalently links to a tetracysteine tagged protein through its biarsenical motif. This mechanism allows subcellular targeting and decreases background fluorescence. KMG-104-AsH is pH stable in the range of pH 5–6.5 and relatively photostable. The affinity, specificity and stability of KMG-104-AsH make it more suitable for live-cell Mg^{2+} imaging than APTRA-based indicators.

5.3 Genetically Encodable Mg^{2+} Indicators

As most Mg^{2+}-binding proteins also bind Ca^{2+} with a higher affinity, one of the main challenges for developing GEMIs was to first identify a Mg^{2+}-specific binding protein. The first reported GEMIs, the MagFRET series, were based on the Mg^{2+}-binding protein human centrin HsCen3 and FPs Cerulean and Citrine (**Figure 6E**) (Lindenburg et al., 2013). HsCen3 contains two binding sites that bind both Mg^{2+} and Ca^{2+}. MagFRET1 has a $\Delta R/R_0$ of 0.49 for Mg^{2+} and a $\Delta R/R_0$ of 0.19 for Ca^{2+}; MagFRET2 has a $\Delta R/R_0$ of 0.33 for Mg^{2+} and a $\Delta R/R_0$ of 0.031 for Ca^{2+}. MagFRET1, 2, 7, and 8 have suitable affinities for detecting Mg^{2+} (K_d = 0.15–0.89 mM) in the physiological concentration range of Mg^{2+}, but they all have high affinities for Ca^{2+} (K_d = 10–57 μM).

MagIC is a ratiometric GEMI based on mCherry and Mg^{2+}/Ca^{2+} sensitive cpVenus (Koldenkova et al., 2015). K_d values of MagIC are 5.1 mM for Mg^{2+} and 4.8 mM for Ca^{2+}. Its affinity for Mg^{2+} is too low for detection of intracellular Mg^{2+}. The indicator has an *in vitro* $\Delta R/R_0$ of 0.5 for Mg^{2+}, which is similar to that for Ca^{2+}. Just like MagFRETs, the sensitivity of MagIC to Ca^{2+} prevent it from being more widely applied. MARIO1 is another FRET-based GEMI based on a modified cytosolic Mg^{2+}-sensing domain of the *E. coli* Mg^{2+} transporter CorA (CorA-CD) (Maeshima et al., 2018). MARIO1 show improved sensitivity ($\Delta R/R_0$ = 1.53 for Mg^{2+}) but still lacks specificity (K_d = 6.2 mM for Ca^{2+} and K_d = 7.2 mM for Mg^{2+}).

6 NA^+ INDICATORS

6.1 The Role of Na^+ in Cell Physiology

As another one of the most abundant ions in biology, Na^+ has many important roles and functions. It regulates osmotic pressure and fluid balance (Reynolds et al., 2006). Na^+ also

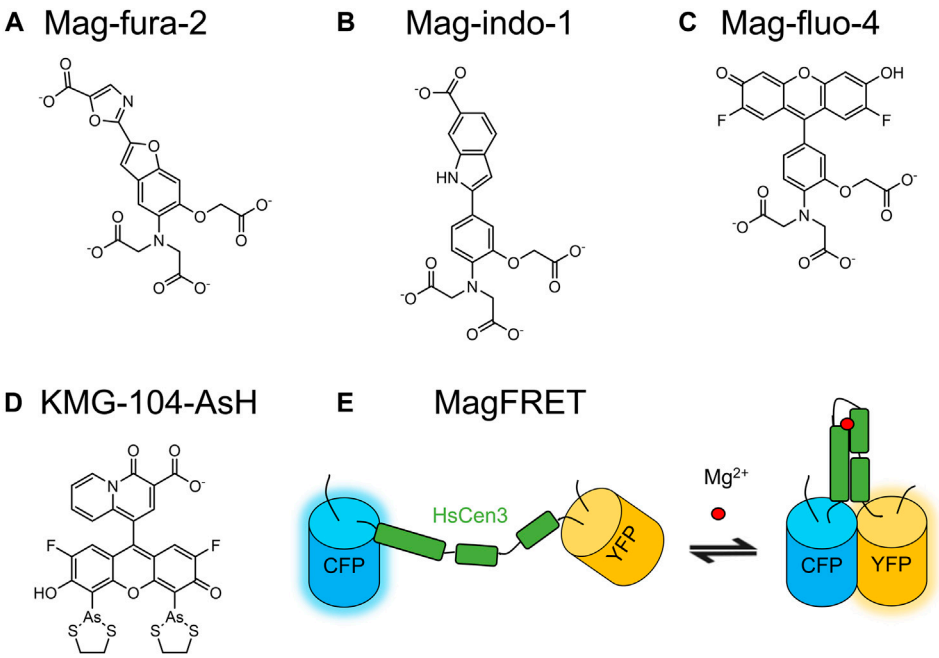

FIGURE 6 | Molecular structures of selected small molecule-based Mg^{2+} indicators and schematic representation of a selected GEMI. **(A)** Mag-fura-2 (Raju et al., 1989), **(B)** Mag-indo-1 (Morelle et al., 1994), and **(C)** Mag-fluo-4 (Shmigol et al., 2001) are based on fluorophore moieties that are identical to those of the BAPTA-based Ca^{2+} indicators fura-2, indo-1, and fluo-4, respectively. As a Mg^{2+}-binding moiety, they employ *o*-aminophenol-*N*, *N*, *O*-triacetic acid (APTRA) for Mg^{2+}-binding. **(D)** KMG-104-AsH is a FlAsH-type indicator based on a β-diketone Mg^{2+}-binding moiety (Fujii et al., 2014). KMG-104-AsH can be genetically targeted *via* covalent linking to tetracysteine-tagged proteins through its biarsenical groups. **(E)** MagFRET is a FRET-based genetically encodable Mg^{2+} indicator with the Mg^{2+} binding domain from human centrin HsCen3.

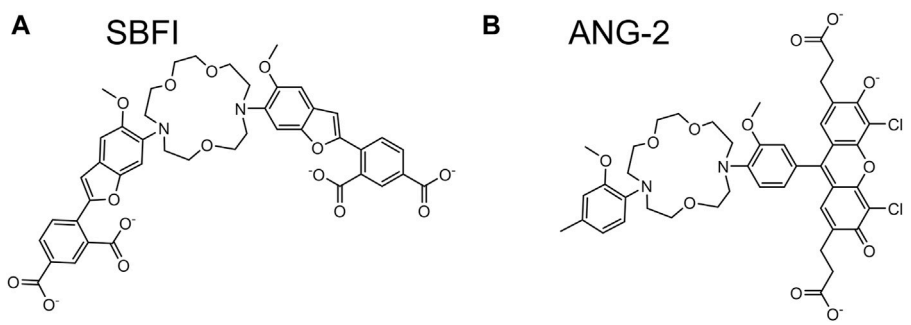

FIGURE 7 | Molecular structures of selected small molecule-based Na^+ indicators. Small molecule-based Na^+ indicators differ from K^+ indicators with respect to their crown ether moieties. Na^+ indicators are typically based on 1, 7-diaza-4, 10, 13-trioxacyclopentadecane as represented for **(A)** SBFI and **(B)** ANG-2 (Minta and Tsien, 1989; Roder and Hille, 2014).

plays roles in the immune system by enhancing immune responses for pathogen clearance and affecting the differentiation and functions of immune cells (Wilck et al., 2019). In the nervous system, Na^+ influxes during the depolarization phase of action potentials for signal propagation (Chahine and O'Leary, 2014). Na^+ concentration is around 10 mM intracellularly and over 100 mM extracellularly (Strazzullo and Leclercq, 2014). The large gradient across the membrane is maintained by the Na^+/K^+ pump, which provides energy for the translocation of Ca^{2+} and other neurotransmitters. There are several small molecule-based Na^+ indicators, but no genetically encodable indicators have been reported to date due to the lack of an appropriate Na^+-binding protein.

6.2 Small Molecule-Based Na^+ Indicators

Sodium binding benzofuran isophthalate (SBFI) (**Figure 7A**) was developed at the same time as PBFI (**Figure 6**). SBFI has a K_d of

7.4 mM for Na^+ and a K_d of 166 mM for K^+ (Minta and Tsien, 1989). The indicator provides a $\Delta F/F_0$ of 2. A drawback of SBFI is its low brightness attributed to its low QY of 0.045 in the Na^+-unbound state and 0.083 in the Na^+-bound state. Sodium Green has visible light excitation and brighter fluorescence that enable its usage in flow cytometry (Amorino and Fox, 1995). CoroNa Green has a peak excitation wavelength at 492 nm and a peak emission wavelength at 516 nm (Meier et al., 2006; Iamshanova et al., 2016). NaTRIUM Green 2 (ANG-2) (**Figure 7B**) is slightly red-shifted with peak excitation and emission wavelengths at 517 and 542 nm, respectively, (Roder and Hille, 2014; Iamshanova et al., 2016). The $\Delta F/F_0$ value of CoroNa Green is 4 and that of ANG-2 is 20 (Iamshanova et al., 2016). The K_d value of CoroNa Green for Na^+ is ~80 mM and that of ANG-2 is 34 mM in presence of K^+ and 20 mM in absence of K^+. SBFI, CoroNa Green and ANG-2 have been used to detect changes in intracellular Na^+ concentrations in prostate cancer cell lines (Iamshanova et al., 2016).

7 PH (H^+) INDICATORS

7.1 Importance of pH in Cell Physiology

Proton (H^+) concentration is measured as pH ($-\log[H^+]$). The pH values vary in different cellular compartments: 7.0–7.4 in the cytoplasm, 7.2 for ER, 6.4 in the Golgi apparatus, 5.0 in lysosomes, 5.4 in secretory granules, 6.2 in early endosomes, and 5.3 in late endosomes (Futai et al., 2000). The pH values of organelles are maintained mainly by vacuolar H^+-ATPase (V-ATPase), which actively pumps H^+ against its concentration gradient with the energy from ATP hydrolysis (Nelson et al., 2000). The pH environment is important for the functions of the organelles. For example, the lysosomal low pH is important for the optimal functions of lysosomal enzymes such as lysozyme. In other cases, proton gradients across organelle membrane or plasma membrane are used to provide energy for translocation of other molecules, such as neurotransmitters accumulated into synaptic vesicles (Farsi et al., 2017). In mitochondria, proton gradients provide energy for ATP synthesis (Reid et al., 1966). The capability provided by pH indicators (**Supplementary Table S3**), to measure pH in subcellular compartments of live cells, enables investigations of pH-related processes such as endocytosis and vesicle secretion.

7.2 Small Molecule-Based pH Indicators

Tsien and coworkers developed 2', 7'-bis (carboxyethyl)-5,6-carboxyfluorescein (BCECF), one of the first fluorescent small molecule-based pH indicators (Rink et al., 1982). BCECF has a pK_a at 6.98, ideal for intracellular pH measurement. The dye shows two peaks in the excitation spectrum at ~505 and ~470 nm. The emission intensity exhibits a 3-fold increase from pH 6.4 to pH 7.5. The isosbestic excitation wavelength of BCECF is at 440 nm, where the excitation would lead to a pH-independent emission. The seminaphtharhodafluor (SNARF) family is an alternative pH indicator series with dual excitation and dual emission. SNARF-1, for example, has two peak excitation wavelengths in an acidic environment at 515 and 544 nm, and a peak excitation wavelength of 573 nm in a basic environment (Whitaker et al., 1991). The peak emission wavelength shifts from 573 to 631 nm as pH increases. With yellow to orange fluorescence, SNARF series can be co-imaged in live cells with blue fluorescent dyes such as fura-2 (Martinez-Zaguilan et al., 1991). SNARF-1 and SNARF-2 both have pK_a values above 7 (7.6 for SNARF-1, 7.5 for SNARF-2). SNARF-4 has a lower pK_a of 6.4 to enable pH detection in slightly acidic environments (Marcotte and Brouwer, 2005). The pH indicators pHrodo green and red (Thermo-Fisher) are ideal indicators to image endocytosis because of their low fluorescence signal at neutral pH and increased fluorescence at acidic pH (Godfrey et al., 2008; Lindner et al., 2020).

7.3 Genetically Encodable pH Indicators

The development of many of the genetically encodable pH indicators was inspired and enabled by the intrinsic pH sensitivity of FPs themselves. The environmental pH can influence the protonated state of the chromophore, leading to fluorescence changes. EGFP shows dual excitation at approximately 390 and 480 nm and the ratio of the two peaks in the excitation spectra change in response to changes in pH (Kneen et al., 1998). When excited at 480 nm, EGFP shows an emission increases with increasing pH. EYFP (pK_a = 7.1) is more suitable for intracellular pH sensing than EGFP (pK_a = 6.15) due to its neutral pK_a (Llopis et al., 1998).

Fusing a pH-sensitive FP to a FRET donor or acceptor leads to a FRET-based pH indicator. For example, the FluBpH series is based on a fusion of EcFbFP, a flavin mononucleotide (FMN)-binding FP excited at 380 nm, and YFPs with different pK_a values, to generate FRET indicators covering different ranges of pH (Rupprecht et al., 2017). The YFPs include: Citrine (pK_a at 5.7), EYFP (pK_a at 6.1), and EYFP-H148G (pK_a at 7.5). The ratio of 570 nm (YFP fluorescence emission) to 495 nm (EcFbFP fluorescence emission) reflects the pH of the environment. Alternatively, a CFP and YFP-based pH indicator has a peak excitation wavelength at 410 nm and peak emission wavelengths at 476 nm (CFP) and 535 nm (YFP) (Hellwig et al., 2004). pHusion is a tandem concatenation of mRFP1 and the pH-sensitive EGFP (Gjetting et al., 2012). pH-Lemon, based on mTurquoise2 and EYFP, exhibits a highly sensitive ratio change in the range of pH 4.0–7.0 (Burgstaller et al., 2019).

Engineering of GFP for increased pH sensitivity has resulted in a variety of green pH indicators. One example is the ratiometric pH-sensitive variant E^2GFP (GFP with F64L/S65T/T203Y/L231H) with a pK_a around 7 (Bizzarri et al., 2006). E^2GFP shows ratiometric excitation and emission: the peak emission wavelength is at 510 nm at low pH and red shifts to 523 nm at high pH. In addition, the peak excitation wavelength is at 424 nm at low pH and becomes two peaks (401 and 515 nm) at high pH. Other engineering efforts resulted in the deGFPs that have a variety of pK_a values: deGFP1 variant (S65T/H148G/T203C, pK_a~8.0), deGFP2 (S65T/C48S/H148C, pK_a~7.2), deGFP3 (S65T/T203C, pK_a~6.9), and deGFP4 (S65T/C48S/H148C/T203C, pK_a~7.3) (Hanson et al., 2002).

Miesenböck and coworkers developed ratiometric pHluorin and ecliptic pHluorin by mutating key residues (Q94, R96, H148,

I167, T203, S205, and E222) that affect Y66 protonation or excitation spectrum (Miesenböck et al., 1998). With a fixed emission wavelength at 508 nm, ratiometric pHluorin exhibits an excitation ratio (395–475 nm) change greater than 3-fold in the pH range from 5.5 to 7.5. Ecliptic pHluorin has a ~5-fold fluorescence emission change in the pH range from 5.5 to 7.5. Superecliptic pHluorin introduced two mutations (F64L and S65T) on ecliptic pHluorin that led to better protein folding and improved sensitivity (~50-fold) required for imaging of neuronal synaptic vesicle fusion and neurotransmitter release (Sankaranarayanan et al., 2000).

In addition to EGFP, other FPs have been utilized to generate a palette of pH indicators with different colours. Introducing H148G to YFP led to pHVenus with a pK_a at 7.3 (Wachter et al., 1998). pHRed is a red pH indicator based on mKeima with a pK_a of 6.5 and a ratiometric change (585 nm *versus* 440 nm) over 10-fold (Tantama et al., 2011). pHTomato is another red pH indicator with peak excitation and emission wavelengths at 550 and 580 nm, respectively, (Li and Tsien, 2012). It has a higher pK_a at 7.8 and a $\Delta F/F_0$ over 1 in the range of pH 7.5–9.8. pHuji is an mApple-based pH indicator with a $\Delta F/F_0$ of 21 in the range of pH 5.5–7.5 (Shen et al., 2014). pHmScarlet, the latest addition to red pH indicators, is 6-fold brighter than pHuji (Liu et al., 2021). As described by Shen et al., a general limitation of red fluorescent pH indicators, with respect to their use for imaging of vesicle fusion, is their lower Hill coefficients (n_H) relative to green fluorescent pH indicators (Shen et al., 2014).

8 Cl^- INDICATORS

8.1 The Roles of Cl^- in Cell Physiology

Chloride (Cl^-) is an important anion in biology. It regulates proteins and genes including kinases (e.g., Cl^--dependent GTP-utilizing protein kinase, nucleoside diphosphate kinase (NDPK), and with-no-lysine kinase (WNK)), channels (e.g., Na^+-K^+-$2Cl^-$ cotransporter), and receptors (e.g., glutamate ionotropic receptor kainate (GRIK)) (Valdivieso and Santa-Coloma, 2019). Cl^- in mammalian cells is maintained at concentrations ranging from 5 to 100 mM by transporters such as potassium chloride cotransporter 2 (KCC2). The serum Cl^- concentration is maintained at 100 mM by the kidney. The gradient is used by chloride channels for cellular processes. For example, GABA type A receptor ($GABA_A$) conducts Cl^- upon GABA binding to allow signal propagations (Goetz et al., 2007).

8.2 Small Molecule-Based Cl^- Indicators

Small molecule-based Cl^- indicators include 6-methoxy-*N*-(3-sulfopropyl) quinolinium (SPQ), *N*-(ethoxycarbonylmethyl)-6-methoxyquinolinium bromide(MQAE),6-methoxy-*N*-ethylquinolinium iodide (MEQ), and lucigenin. These Cl^- indicators are quenched by Cl^- through collisional quenching. The rate of fluorescence quenching is accelerated by higher concentrations of Cl^-. All of them are long Stoke shift dyes that are excited by UV lights and emit photons at wavelengths approximately 100 nm longer than their peak excitation wavelengths (Verkman et al., 1989; Biwersi et al., 1994). When applied in cells, SPQ and MQAE show severe photobleaching (Krapf et al., 1988; Verkman et al., 1989). MEQ is much less prone to photobleaching than MQAE in Swiss 3T3 fibroblasts (Biwersi and Verkman, 1991). Lucigenin is incompatible with intracellular imaging because its electron-deficient acridine ring is prone to nucleophilic attack in biological samples (Biwersi et al., 1994).

8.2.1 Genetically Encodable Cl^- Indicators

YFP is intrinsically sensitive to Cl^- (**Supplementary Table S4**) (Wachter and James Remington, 1999). Its fluorescence is decreased by 40% with 150 mM Cl^- at pH 7.0. Cl^- binds near the chromophore and the binding destabilizes the deprotonated form of the chromophore due to charge repulsion. This also leads to elevated pK_a (5.2 without Cl^-, and 7.0 with Cl^-). T203Y is a key mutation for Cl^- binding presented in many YFP variants (Wachter and James Remington, 1999; Arosio et al., 2007). Further engineering led to better Cl^- indicator variants. For example, the H148Q mutation decreases the K_d from 777 to 100 mM and increases the fluorescence response to a 50% reduction in fluorescence in presence of Cl^- (Jayaraman et al., 2000). I152L was introduced to reduce the K_d to 85 mM for Cl^- (Galietta et al., 2001). A further engineered variant mCl-YFP, with eight mutations relative to EYFP, has a higher affinity and a reduced pH sensitivity (Zhong and Schleifenbaum, 2019). These Cl^- sensitive FPs also respond to other halides.

Kuner and Augustine developed the first ratiometric Cl^- indicator, Clomeleon, based on fusion of CFP to Cl^--sensitive YFP (Kuner and Augustine, 2000). Clomeleon undergoes a near 80% decrease of F_{527nm}/F_{485nm} ratio in presence of Cl^- *in vitro* and has a maximum 50% decrease in hippocampal neurons. Clomeleon has a K_d of 167 mM for Cl^-, leading to relatively small responses in physiologically relevant conditions. To decrease the K_d, H148Q, I152L, and V163S were introduced to Clomeleon and that reduced the K_d to ~30 mM (Markova et al., 2008). SuperClomeleon was engineered by changing in the linker between two FPs, replacing Cerulean with CFP, and introducing other beneficial mutations (S30R, Q69T and V163A) (Grimley et al., 2013). This improved indicator exhibits a dynamic range ($-\Delta R/R_0$) of 90% and a K_d of 8.1 mM.

ClopHensor is a dual indicator for pH and Cl^- that addresses complications arising from the pH sensitivity of YFP (Arosio et al., 2010). The indicator is a fusion of pH sensing E^2GFP and a DsRed monomer. E^2GFP can be excited at 488 nm for pH dependent Cl^- measurement or at 458 nm for pH-independent Cl^- measurement. The wavelength of 458 nm is an isosbestic point based on the pH titration profile of E^2GFP. DsRed is excited at 543 nm with no overlapping signal from E^2GFP. Its signal is affected by neither pH nor Cl^- concentrations. Hence, measurements with excitation at 458 nm, 488 nm, and 548 nm allow simultaneous measurement of pH and Cl^-.

Other FPs have been explored as alternative Cl^- indicators. The jellyfish *Phialidium sp* phiYFP was identified as a naturally occurring Cl^--sensitive ratiometric indicator (Tutol et al., 2019b). phiYFP has two peak excitation wavelengths at 400 and 480 nm and a peak emission wavelength at 540 nm. When excited at 480 nm, the fluorescence of phiYFP decreases modestly as Cl^-

concentration increases. When excited at 400 nm, phiYFP is a turn-on indicator with a $\Delta F/F_0$ of 2.5 in response to 400 mM Cl^-. Recently, mNeonGreen was identified as another turn-on Cl^- indicator with a $\Delta F/F_0$ of 20-fold, a K_d of 9.8 mM, but also a strong pH dependency that may limit its applications (Tutol et al., 2019a).

9 CU^+ INDICATORS

9.1 The Roles of Cu^+ in Cell Physiology

Copper is an essential nutrient to human health. It has implications in cardiovascular (Saari, 2000), immune (Percival, 1998), and nervous systems (Opazo et al., 2014). The element exists predominantly in two forms in biology: the monovalent Cu^+ and the divalent Cu^{2+}. The two different oxidation states of copper are exploited by enzymes that catalyze redox reactions (e.g., cytochrome c oxidase and NADH dehydrogenase) (Festa and Thiele, 2011). Many of these enzymes are located on the membranes of compartmented organelles in eukaryotic cells. Mitochondria, in particular, contain many copper-dependent enzymes for energy production (Baker et al., 2017). Most copper ions are in the cofactors of enzymes, leaving only 10^{-18}—10^{-13} M free Cu^+ (Tapiero et al., 2003). Excess copper is toxic because free Cu^+ can generate free radicals in cells and destabilize iron-sulfur clusters. Therefore, regulated trafficking is required to prevent cell damages (Stohs and Bagchi, 1995; Macomber and Imlay, 2009; Kaplan and Maryon, 2016). Fluorescent copper indicators enable monitoring of free Cu^+ concentration, thus leading to a better understanding of Cu^+ dynamics and localizations under stimuli or stress. To the best of our knowledge, there are no fluorescent indicators designed to be specific for Cu^{2+}.

9.2 Small Molecule-Based Cu^+ Indicators

CTAP-1 is the first small molecule-based fluorescent indicator for Cu^+ with a $\Delta F/F_0$ of 4.6 (Yang et al., 2005). The indicator consists of a tetrathiaza crown ether Cu^+-binding motif and a pyrazoline fluorophore. The tetrathiaza crown ether allows specific binding to Cu^+ (K_d = 40 nM) over other ions including Cu^{2+}, and monovalent ions K^+ and Na^+. The pyrazoline fluorophore has a peak emission wavelength at 480 nm with UV excitation. CTAP-1 is membrane permeable and allows monitoring of Cu^+ localization in NIH 3T3 cells grown in a medium supplemented with Cu^+. One drawback of CTAP-1 is that it aggregates in cells. This issue was largely addressed with CTAP-2, which also exhibits an improved $\Delta F/F_0$ of 65 (Morgan et al., 2011).

Coppersensor-1 (CS1) is another small molecule-based Cu^+ indicator based on BODIPY fluorophore and an azatetrathia binding domain (Zeng et al., 2006). The indicator displays a $\Delta F/F_0$ of 10 and peak excitation and emission wavelengths at 540 and 566 nm, respectively. CS3 is a more sensitive and brighter version with a $\Delta F/F_0$ of 75 (Dodani et al., 2011a, 20), enabling visualization of intracellular Cu^+ concentration at basal and depleted levels and identification of Ca^{2+}-dependent Cu^+ redistribution.

Some small molecule-based Cu^+ indicators were developed for more specific purposes. Mito-CS1 can be targeted to mitochondria *via* a triphenylphosphonium moiety and therefore enables Cu^+ imaging in mitochondria (Dodani et al., 2011b). RCS1, a ratiometric indicator, has a $\Delta R/R_0$ of 20 and peak emission wavelengths at 505 and 570 nm *in vitro* and is effective as demonstrated in live C6 rat glioma cells (Domaille et al., 2010). ACu1 can be excited by two-photon at 750 nm and was used to image Cu^+ in hippocampal slices at depths ranging from 90 to 220 μm (Su Lim et al., 2011). Cao Cu-3 is based on a tricarbocyanine scaffold and exhibits a $\Delta F/F_0$ of 9.6 with near-infrared fluorescence and was applied in live MG63 cells (Cao et al., 2012).

9.3 Genetically Encodable Cu^+ Indicators

The apparent Cu^+ affinities of the small molecule-based Cu^+ indicators range from 10^{-8} to 10^{-14} M, which is typically too weak for the basal concentration of Cu^+ in the cell. Genetically encodable Cu^+ indicators address this issue with improved Cu^+ affinities.

FRET-based genetically encodable Cu^+ indicators have been developed using several Cu^+-binding proteins. Wegner and coworkers reported Ace1-FRET, Mac1-FRET, and Amt1-FRET (Wegner et al., 2010, 2011). Amt1-FRET is based on a Cu^+-responsive transcriptional regulator Amt1 and the CFP/YFP FRET pair (Wegner et al., 2010). The indicator has a high affinity ($K_d = 2.5 \times 10^{-18}$ M) that enables visualization of the tightly regulated Cu^+. Ace1-FRET and Mac1-FRET are based on yeast copper regulators Ace1 and Mac1, respectively (Wegner et al., 2011). The two indicators show opposing responses to Cu^+: Mac1-FRET decreases in FRET efficiency upon Cu^+ binding and Ace1-FRET increases in FRET efficiency upon Cu^+ binding. Ace1-FRET has a K_d of $4.7 \times 10^{-18} \pm 8.8 \times 10^{-19}$ M and Mac1-FRET has a K_d of $9.7 \times 10^{-20} \pm 1.3 \times 10^{-20}$ M for Cu^+. The Zn^{2+} indicator eCALWY was also modified for Cu^+ binding (Vinkenborg et al., 2009; Koay et al., 2013). The Zn^{2+}-binding domains used in eCALWY are Cu^+ chaperones ATOX1 and WD4, which contains CXXC Zn^{2+}-binding motifs (Vinkenborg et al., 2009). Mutating several cysteines to methionines in the CXXC motifs abolished Zn^{2+} binding while retaining Cu^+ binding (Koay et al., 2013). The resulting eCALWY-C2M/C3M shows specific binding to Cu^+ ($K_d = 10^{-15}$–10^{-16} M) over Zn^{2+} ($K_d = 1.4 \times 10^{-6}$ M) and no binding to Co^{2+}, Cu^{2+}, or Ni^{2+}.

The single FP-based Cu^+ indicators include EGFP-145Amt1, YFP-Ace1 and YAGn series. EGFP-145Amt1is based on Amt1 and ncpEGFP (Liang et al., 2012). YFP-Ace1 is based on Ace1 and YFP (Liu et al., 2013). YFP-Ace1 was optimized by adding GGS linkers of different lengths before N146 of YFP. The resulting variants were named YAGn where n denotes the number of GGS repeats in the linker. YFP-Ace1 and YAG1 are excitation ratiometric at 440 and 496 nm. The longer linkers abolish the ratiometric change. The fluorescent response is 38, 35, 30, 25, and 25% for YFP-Ace1, YAG1, YAG2, YAG3, and YAG4, respectively. The Cu^+ affinity is increased with increasing linker lengths [K_d values for YFP-Ace1, YAG1, YAG2, YAG3, and YAG4 are

$(8.2 \pm 1.2) \times 10^{-18}$ M, $(2.0 \pm 0.8) \times 10^{-18}$ M, $(1.2 \pm 1.0) \times 10^{-18}$ M, $(4.6 \pm 1.2) \times 10^{-19}$ M, and $(3.3 \pm 0.9) \times 10^{-19}$ M].

10 INDICATORS FOR TOXIC IONS (PB^{2+}, CD^{2+}, AS^{3+} AND HG^{2+})

Indicators for toxic ions, Pb^{2+}, Cd^{2+}, As^{3+} and Hg^{2+} were developed for the general purpose of further investigating the mechanisms of their toxicities in cells. Many of these toxic ions can hijack the transporters for essential ions and thus disrupt their normal functions. Pd^{2+} can be imported through Ca^{2+} channels and N-methyl-D-aspartate (NMDA) receptor (Kerper and Hinkle, 1997; Mazzolini et al., 2001). It interferes with iron incorporation of hemoglobin and acts as a Ca^{2+} or Zn^{2+}analogue to disrupt Ca^{2+}-dependent signaling pathway and Zn^{2+}-dependent activities (Martinez-Finley et al., 2012). Similarly, Cd^{2+} mimics Ca^{2+} and Zn^{2+}, leading to detrimental effects on multiple organs (Bridges and Zalups, 2005). Mercury and mercury compounds are extremely toxic due to their reactivity with the thiol groups of cysteines and thus causes a detrimental effect on a variety of key enzymes (Clarkson and Magos, 2006). Arsenic can react with reduced thiol groups to disrupt protein metabolism in general; arsenic in the forms of arsenite and arsenate are particularly toxic to the nervous system and cardiovascular system by disrupting voltage-gated K^+ channels (Medda et al., 2020). Small molecule-based and genetically encodable fluorescent indicators are thus valuable tools to investigate the toxicity of these elements. Among these indicators, small molecule-based fluorescent indicators for Pb^{2+}, Cd^{2+}, and Hg^{2+} have been previously reviewed by Kim and coworkers (Ha et al., 2012).

Genetically encodable arsenic indicators include SenALiBs and GEARs. SenALiB is based on an *E. coli* arsenic sensing domain ArsR flanked by CFP and YFP (Soleja et al., 2019). Further optimized variant SenALiB-676n has a higher affinity for As^{3+} ($K_d = 0.676 \times 10^{-6}$ M) compared to SenALiB ($K_d = 2.6 \times 10^{-5}$ M). The indicator exhibits a maximum 10% increase in FRET ratio. GEAR-CV1 is based on a bacterial As^{3+} responsive transcriptional factor AfArsR from *Acidithiobacillus ferrooxidans* and exhibits a $\Delta R/R$ of 15.8 ± 0.2% and a K_d of 84.9 μM (Khan et al., 2021). After further improvement, GEAR-CV2 exhibits a larger FRET ratio change of 22 ± 3.5%. The single GFP-based GEAR-G1 exhibits a $\Delta F/F_0$ of 31.6% upon As^{3+} binding.

Pb^{2+} indicators include leadfluor-1 (LF1), leadglow, and the protein-based Met-lead 1.59 (Vijverberg and Westerink, 2012). LF1 combines a fluorescein-like scaffold and a dicarboxylate pseudocrown binding moiety (He et al., 2006). The indicator is sensitive with a $\Delta F/F_0$ of 18 and specific to Pb^{2+} over Li^+, Na^+, K^+, Mg^{2+}, Ca^{2+}, Mn^{2+}, Fe^{2+}, Co^{2+}, Ni^{2+}, Cu^{2+}, Zn^{2+}, Cd^{2+}, and Hg^{2+}. Leadglow is another sensitive and specific small molecule-based Pb^{2+} indicator (Marbella et al., 2009). The practicality of these two indicators is limited by their affinities for Pb^{2+} (LF1: $K_d = 23 \pm 4$ μM; Leadglow: $K_d = 217$ nM) that are too low for detecting typical Pb^{2+} concentration in the environment [a limit of 72 nM Pb^{2+} in drinking water has been set by the United States Environmental Protection Agency (Santucci and Scully, 2020)]. The genetically encodable Met-lead 1.59 provides an alternative for detection of low Pb^{2+} concentrations. It is based on *Cupriavidus metallidurans* CH34 Pb^{2+}-binding protein PbrR flanked by CFP and YFP, and exhibits an emission ratio (YFP/CFP) in the range of 3.3–5.7 and a biphasic response with K_d values of 69 nM and 22 μM (Chiu and Yang, 2012).

Cd^{2+} indicators include biologically compatible small molecule-based Liu Cd-1, Peng Cd-1, and Cheng Cd-1, as well as genetically encodable Cd-FRET. Liu Cd-1 consists of fluorescein and a thiosemicarbazide, and responds to Cd^{2+} with a $\Delta F/F_0$ of 1.5 (Liu et al., 2007). Peng Cd-1 is based on BODIPY fluorophore and presented ratiometric emission (655 nm in a Cd^{2+} free environment and 597 nm in a Cd^{2+} rich environment) (Peng et al., 2007). Cheng Cd-1 is another BODIPY-based Pb^{2+} indicator with superior sensitivity and affinity (Cheng et al., 2008). The fluorescence intensity of Cheng Cd-1 is enhanced by a maximum 195-fold with linear detection of Cd^{2+} in the nanomolar range. Cd-FRET was created by modifying Zn^{2+} indicator ZinCh-9 with a new $(Cys)_4$ metal-binding motif at the interface of the FPs (Vinkenborg et al., 2011). Met-cad 1.57 is another genetically encodable FRET-based Cd^{2+} indicator with a Cd^{2+}-binding protein CadR flanked by CFP and YFP (Chiu et al., 2013).

Various Hg^{2+} indicators have been developed to detect Hg^{2+}. Among these indicators, Zhao Hg-1 and Lin Hg-1 are biologically compatible and demonstrate remarkable dynamic ranges ($\Delta F/F_0$) of 1,200 and 1,000, respectively, (Lin et al., 2010; Zhao et al., 2010). Rhodamine spirolactam-based Zhao Hg-1 is nonfluorescent unless bound to Hg^{2+}, which converts the spirolactam to a ring-open amide form reversibly (Zhao et al., 2010). Lin Hg-1 is similarly based on thiolspirolactam to achieve high sensitivity (Lin et al., 2010). Zhao Hg-1 and Lin Hg-1 bind Hg^{2+} with K_d values of 4.6×10^{-7} M and 2.5×10^{-5} M, respectively. Compared to these indicators, BODIPY-based 8H-BDP and fluorescein-based Mercuryfluor-1 (MF1) bind Hg^{2+} with higher affinities (8H-BDP: $K_d = 6.3 \times 10^{-19}$ M; MF1: $K_d = 7.0 \times 10^{-11}$ M) but decreased fluorogenicity (8H-BDP: $\Delta F/F_0 = 27$; MF1: $\Delta F/F_0 = 170$) (Yoon et al., 2005; Lu et al., 2009). MF1 was used to detect Hg^{2+} levels in fish samples (Yoon et al., 2005). A Hg^{2+}-induced fluorescence change was detected in HeLa cells using 8H-BDP (Lu et al., 2009).

11 DISCUSSION

The decades of work on monatomic ion indicators have yielded many useful tools with diverse spectral properties, sensitivity, specificity, affinities, and brightness. In general, the most useful indicators have the following properties:

1) A large dynamic range that allows signal change to be easily detected.
2) High brightness to enable signal detection with a low concentration of the indicator.
3) A suitable affinity that is compatible with the ligand concentration in the target environment.
4) Fast kinetics to enable the detection of transient changes.

5) Specific targeting that allows measurement in specific cell types or subcellular compartments.
6) Colour variety that enables multiplexed and quantitative measurement.

Steps for making a successful indicator include **1)** finding an appropriate ligand-binding moiety and a fluorescent reporter, **2)** exploring different indicator designs, and finally **3)** extensive optimizations of spectral properties, response, affinity, kinetics, and other relevant properties. The properties of the ligand-binding moieties and the reporters can be assessed before initiating the development of an indicator, with the safe assumption that the resulting indicator will inherit some or all of these properties. That is, the binding moieties provide the ligand-binding properties, such as the affinity and specificity, and the fluorescent reporters provide the spectral properties.

Improving existing indicators can likewise involve choosing an alternative ligand binder or reporter. The green fluorescent mNeonGreen, for example, has been used to replace EGFP in Ca^{2+} indicators (Subach et al., 2020; Zarowny et al., 2020) and also used as a single FP Cl^- indicator (Tutol et al., 2019a). The brighter mNeonGreen allows an accordingly increased maximum brightness for mNeonGreen-based indicators. The availability of newly discovered or engineered binding moieties can inspire the development of novel indicators. For example, the discovery of Kbp enabled the development of genetically encodable potassium indicators with a superior specificity for K^+ over Na^+ (Ashraf et al., 2016; Bischof et al., 2017; Shen et al., 2019).

The initial development of indicators typically requires multiple designs. The pH indicators SNARFs, for example, were developed with multiple derivatives that exhibit different spectral properties and pK_a values (Whitaker et al., 1991). Creating a new single FP-based indicator typically involves attempts with cp and ncp designs to increase the probability of obtaining a ligand-sensitive design. NIR-GECO, for example, only responds to Ca^{2+} with the ncp mIFP (Qian et al., 2019). The initial construct of genetically encodable indicators rarely responds with optimal performance and thus requires further optimizations. The best example is the continuing optimization of the GCaMP series over the last 2 decades. The optimizations include site saturations on identified important sites and directed evolution. The screenings of variants were performed in *E. coli* and later hippocampal neurons, ultimately leading to the state-of-the-art GECIs (Chen et al., 2013; Dana et al., 2019; Zhang et al., 2021).

An important factor for the future development of genetically encodable monatomic ion indicators is the discovery and exploitation of new binding proteins. A new binding protein can potentially lead to a new monatomic ion indicator with a more favorable affinity, specificity, or kinetics. For example, the current Na^+ indicators are limited by both the lack of variety (there is not a genetically encodable Na^+ indicator available yet) and the lack of specificity for Na^+ over K^+. A new Na^+-binding motif could potentially fill the void and provide practical tools for Na^+ imaging. Such a development could be impactful, particularly if the resulting indicator could be used in combination with indicators for Ca^{2+} or K^+.

In this review, we discussed small molecule-based and genetically encodable indicators for monatomic ions of biological importance. Beyond the scope of this review, chemigenetic indicators are an emerging group of tools where the advantages of small molecule-based dyes and genetically encodable tags complement each other. For example, such indicators could benefit from both the superior brightness and photostability of synthetic small molecules as well as the genetically-targetable expression of proteins (Abdelfattah et al., 2019; Deo et al., 2021).

The diverse collection of monatomic ion indicators has enabled discoveries in biology and medicine. With an ever-expanding toolset, the future of biomedical research will benefit from a vast library of highly specific and reliable indicators. At the same time, new technologies and approaches for designs and optimizations emerge to benefit tool developers who are creating more robust and practical monatomic ion indicators at a faster-than-ever pace.

AUTHOR CONTRIBUTIONS

S-YW drafted the manuscript. All authors contributed to editing.

SUPPLEMENTARY MATERIAL

The Supplementary Material for this article can be found online at: https://www.frontiersin.org/articles/10.3389/fcell.2022.885440/full#supplementary-material

REFERENCES

Abdelfattah, A. S., Kawashima, T., Singh, A., Novak, O., Liu, H., Shuai, Y., et al. (2019). Bright and Photostable Chemigenetic Indicators for Extended *In Vivo* Voltage Imaging. *Science* 365, 699–704. doi:10.1126/science.aav6416

Aigner, D., Borisov, S. M., and Klimant, I. (2011). New Fluorescent Perylene Bisimide Indicators-A Platform for Broadband pH Optodes. *Anal. Bioanal. Chem.* 400, 2475–2485. doi:10.1007/s00216-010-4647-y

Ainscough, E. W., and Brodie, A. M. (1976). The Role of Metal Ions in Proteins and Other Biological Molecules. *J. Chem. Educ.* 53, 156. doi:10.1021/ed053p156

Akerboom, J., Carreras Calderón, N., Tian, L., Wabnig, S., Prigge, M., Tolö, J., et al. (2013). Genetically Encoded Calcium Indicators for Multi-Color Neural Activity Imaging and Combination with Optogenetics. *Front. Mol. Neurosci.* 6, 2. doi:10.3389/fnmol.2013.00002

Ammann, A. A. (2007). Inductively Coupled Plasma Mass Spectrometry (ICP MS): A Versatile Tool. *J. Mass. Spectrom.* 42, 419–427. doi:10.1002/jms.1206

Amorino, G. P., and Fox, M. H. (1995). Intracellular Na^+ Measurements Using Sodium Green Tetraacetate With Flow Cytometry. *Cytometry* 21, 248–256. doi:10.1002/cyto.990210305

Arosio, D., Garau, G., Ricci, F., Marchetti, L., Bizzarri, R., Nifosì, R., et al. (2007). Spectroscopic and Structural Study of Proton and Halide Ion Cooperative Binding to GFP. *Biophysical J.* 93, 232–244. doi:10.1529/biophysj.106.102319

Arosio, D., Ricci, F., Marchetti, L., Gualdani, R., Albertazzi, L., and Beltram, F. (2010). Simultaneous Intracellular Chloride and pH Measurements Using a GFP-Based Sensor. *Nat. Methods* 7, 516–518. doi:10.1038/nmeth.1471

Ash, C., Dubec, M., Donne, K., and Bashford, T. (2017). Effect of Wavelength and Beam Width on Penetration in Light-Tissue Interaction Using Computational Methods. *Lasers Med. Sci.* 32, 1909–1918. doi:10.1007/s10103-017-2317-4

Ashraf, K. U., Josts, I., Mosbahi, K., Kelly, S. M., Byron, O., Smith, B. O., et al. (2016). The Potassium Binding Protein Kbp Is a Cytoplasmic Potassium Sensor. *Structure* 24, 741–749. doi:10.1016/j.str.2016.03.017

Assaf, S. Y., and Chung, S.-H. (1984). Release of Endogenous Zn^{2+} From Brain Tissue During Activity. *Nature* 308, 734–736. doi:10.1038/308734a0

Bagur, R., and Hajnóczky, G. (2017). Intracellular Ca^{2+} Sensing: Its Role in Calcium Homeostasis and Signaling. *Mol. Cel* 66, 780–788. doi:10.1016/j.molcel.2017.05.028

Baird, G. S., Zacharias, D. A., and Tsien, R. Y. (1999). Circular Permutation and Receptor Insertion within Green Fluorescent Proteins. *Proc. Natl. Acad. Sci. U.S.A.* 96, 11241–11246. doi:10.1073/pnas.96.20.11241

Baker, Z. N., Cobine, P. A., and Leary, S. C. (2017). The Mitochondrion: A Central Architect of Copper Homeostasis. *Metallomics* 9, 1501–1512. doi:10.1039/c7mt00221a

Bischof, H., Burgstaller, S., Waldeck-Weiermair, M., Rauter, T., Schinagl, M., Ramadani-Muja, J., et al. (2019). Live-Cell Imaging of Physiologically Relevant Metal Ions Using Genetically Encoded FRET-Based Probes. *Cells* 8, 492. doi:10.3390/cells8050492

Bischof, H., Rehberg, M., Stryeck, S., Artinger, K., Eroglu, E., Waldeck-Weiermair, M., et al. (2017). Novel Genetically Encoded Fluorescent Probes Enable Real-Time Detection of Potassium *In Vitro* and *In Vivo*. *Nat. Commun.* 8, 1422. doi:10.1038/s41467-017-01615-z

Biwersi, J., Tulk, B., and Verkman, A. S. (1994). Long-Wavelength Chloride-Sensitive Fluorescent Indicators. *Anal. Biochem.* 219, 139–143. doi:10.1006/abio.1994.1242

Biwersi, J., and Verkman, A. S. (1991). Cell-Permeable Fluorescent Indicator for Cytosolic Chloride. *Biochemistry* 30, 7879–7883. doi:10.1021/bi00246a001

Bizzarri, R., Arcangeli, C., Arosio, D., Ricci, F., Faraci, P., Cardarelli, F., et al. (2006). Development of a Novel GFP-Based Ratiometric Excitation and Emission pH Indicator for Intracellular Studies. *Biophysical J.* 90, 3300–3314. doi:10.1529/biophysj.105.074708

Bridges, C. C., and Zalups, R. K. (2005). Molecular and Ionic Mimicry and the Transport of Toxic Metals. *Toxicol. Appl. Pharmacol.* 204, 274–308. doi:10.1016/j.taap.2004.09.007

Brini, M., Calì, T., Ottolini, D., and Carafoli, E. (2014). Neuronal Calcium Signaling: Function and Dysfunction. *Cell. Mol. Life Sci.* 71, 2787–2814. doi:10.1007/s00018-013-1550-7

Broussard, J. A., and Green, K. J. (2017). Research Techniques Made Simple: Methodology and Applications of Förster Resonance Energy Transfer (FRET) Microscopy. *J. Invest. Dermatol.* 137, e185–e191. doi:10.1016/j.jid.2017.09.006

Burdette, S. C., Frederickson, C. J., Bu, W., and Lippard, S. J. (2003). ZP4, an Improved Neuronal Zn^{2+} Sensor of the Zinpyr Family. *J. Am. Chem. Soc.* 125, 1778–1787. doi:10.1021/ja0287377

Burgstaller, S., Bischof, H., Gensch, T., Stryeck, S., Gottschalk, B., Ramadani-Muja, J., et al. (2019). pH-Lemon, a Fluorescent Protein-Based pH Reporter for Acidic Compartments. *ACS Sens.* 4, 883–891. doi:10.1021/acssensors.8b01599

Cao, X., Lin, W., and Wan, W. (2012). Development of a Near-Infrared Fluorescent Probe for Imaging of Endogenous Cu^{+} in Live Cells. *Chem. Commun.* 48, 6247–6249. doi:10.1039/c2cc32114a

Carter, K. P., Young, A. M., and Palmer, A. E. (2014). Fluorescent Sensors for Measuring Metal Ions in Living Systems. *Chem. Rev.* 114, 4564–4601. doi:10.1021/cr400546e

Cerchiaro, G., Manieri, T. M., and Bertuchi, F. R. (2013). Analytical Methods for Copper, Zinc and Iron Quantification in Mammalian Cells. *Metallomics* 5, 1336–1345. doi:10.1039/C3MT00136A

Chahine, M., and O'Leary, M. E. (2014). "Regulation/Modulation of Sensory Neuron Sodium Channels," in Voltage Gated Sodium Channels *Handbook of Experimental Pharmacology*. Editor P. C. Ruben (Berlin, Heidelberg: Springer), 111–135. doi:10.1007/978-3-642-41588-3_6

Chang, C. J., Nolan, E. M., Jaworski, J., Burdette, S. C., Sheng, M., and Lippard, S. J. (2004a). Bright Fluorescent Chemosensor Platforms for Imaging Endogenous Pools of Neuronal Zinc. *Chem. Biol.* 11, 203–210. doi:10.1016/j.chembiol.2004.01.017

Chang, C. J., Nolan, E. M., Jaworski, J., Okamoto, K.-I., Hayashi, Y., Sheng, M., et al. (2004b). ZP8, a Neuronal Zinc Sensor with Improved Dynamic Range; Imaging Zinc in Hippocampal Slices with Two-Photon Microscopy. *Inorg. Chem.* 43, 6774–6779. doi:10.1021/ic049293d

Chen, M., Zhang, S., Xing, Y., Li, X., He, Y., Wang, Y., et al. (2019). Genetically Encoded, Photostable Indicators to Image Dynamic Zn^{2+} Secretion of Pancreatic Islets. *Anal. Chem.* 91, 12212–12219. doi:10.1021/acs.analchem.9b01802

Chen, T.-W., Wardill, T. J., Sun, Y., Pulver, S. R., Renninger, S. L., Baohan, A., et al. (2013). Ultrasensitive Fluorescent Proteins for Imaging Neuronal Activity. *Nature* 499, 295–300. doi:10.1038/nature12354

Chen, Z., and Ai, H.-w. (2016). Single Fluorescent Protein-Based Indicators for Zinc Ion (Zn^{2+}). *Anal. Chem.* 88, 9029–9036. doi:10.1021/acs.analchem.6b01653

Cheng, T., Xu, Y., Zhang, S., Zhu, W., Qian, X., and Duan, L. (2008). A Highly Sensitive and Selective OFF-ON Fluorescent Sensor for Cadmium in Aqueous Solution and Living Cell. *J. Am. Chem. Soc.* 130, 16160–16161. doi:10.1021/ja806928n

Chiu, T.-Y., Chen, P.-H., Chang, C.-L., and Yang, D.-M. (2013). Live-Cell Dynamic Sensing of Cd^{2+} with a FRET-Based Indicator. *PLoS One* 8, e65853. doi:10.1371/journal.pone.0065853

Chiu, T.-Y., and Yang, D.-M. (2012). Intracellular Pb^{2+} Content Monitoring Using a Protein-Based Pb^{2+} Indicator. *Toxicol. Sci.* 126, 436–445. doi:10.1093/toxsci/kfs007

Clapham, D. E. (2007). Calcium Signaling. *Cell* 131, 1047–1058. doi:10.1016/j.cell.2007.11.028

Clarkson, T. W., and Magos, L. (2006). The Toxicology of Mercury and its Chemical Compounds. *Crit. Rev. Toxicol.* 36, 609–662. doi:10.1080/10408440600845619

Dana, H., Mohar, B., Sun, Y., Narayan, S., Gordus, A., Hasseman, J. P., et al. (2016). Sensitive Red Protein Calcium Indicators for Imaging Neural Activity. *Elife* 5, e12727. doi:10.7554/eLife.12727

Dana, H., Sun, Y., Mohar, B., Hulse, B. K., Kerlin, A. M., Hasseman, J. P., et al. (2019). High-performance Calcium Sensors for Imaging Activity in Neuronal Populations and Microcompartments. *Nat. Methods* 16, 649–657. doi:10.1038/s41592-019-0435-6

Deo, C., Abdelfattah, A. S., Bhargava, H. K., Berro, A. J., Falco, N., Farrants, H., et al. (2021). The HaloTag as a General Scaffold for Far-Red Tunable Chemigenetic Indicators. *Nat. Chem. Biol.* 17, 718–723. doi:10.1038/s41589-021-00775-w

Dittmer, P. J., Miranda, J. G., Gorski, J. A., and Palmer, A. E. (2009). Genetically Encoded Sensors to Elucidate Spatial Distribution of Cellular Zinc. *J. Biol. Chem.* 284, 16289–16297. doi:10.1074/jbc.M900501200

Dodani, S. C., Domaille, D. W., Nam, C. I., Miller, E. W., Finney, L. A., Vogt, S., et al. (2011a). Calcium-dependent Copper Redistributions in Neuronal Cells Revealed by a Fluorescent Copper Sensor and X-ray Fluorescence Microscopy. *Proc. Natl. Acad. Sci. U.S.A.* 108, 5980–5985. doi:10.1073/pnas.1009932108

Dodani, S. C., Leary, S. C., Cobine, P. A., Winge, D. R., and Chang, C. J. (2011b). A Targetable Fluorescent Sensor Reveals that Copper-Deficient SCO1 and SCO2 Patient Cells Prioritize Mitochondrial Copper Homeostasis. *J. Am. Chem. Soc.* 133, 8606–8616. doi:10.1021/ja2004158

Domaille, D. W., Zeng, L., and Chang, C. J. (2010). Visualizing Ascorbate-Triggered Release of Labile Copper within Living Cells Using a Ratiometric Fluorescent Sensor. *J. Am. Chem. Soc.* 132, 1194–1195. doi:10.1021/ja907778b

Du, P., and Lippard, S. J. (2010). A Highly Selective Turn-On Colorimetric, Red Fluorescent Sensor for Detecting Mobile Zinc in Living Cells. *Inorg. Chem.* 49, 10753–10755. doi:10.1021/ic101569a

Evers, T. H., Appelhof, M. A. M., de Graaf-Heuvelmans, P. T. H. M., Meijer, E. W., and Merkx, M. (2007). Ratiometric Detection of Zn(II) Using Chelating Fluorescent Protein Chimeras. *J. Mol. Biol.* 374, 411–425. doi:10.1016/j.jmb.2007.09.021

Farsi, Z., Jahn, R., and Woehler, A. (2017). Proton Electrochemical Gradient: Driving and Regulating Neurotransmitter Uptake. *Bioessays* 39, 1600240. doi:10.1002/bies.201600240

Festa, R. A., and Thiele, D. J. (2011). Copper: An Essential Metal in Biology. *Curr. Biol.* 21, R877–R883. doi:10.1016/j.cub.2011.09.040

Förster, T. (1948). Zwischenmolekulare Energiewanderung und Fluoreszenz. *Ann. Phys.* 437, 55–75. doi:10.1002/andp.19484370105

Frassinetti, S., Bronzetti, G. L., Caltavuturo, L., Cini, M., and Croce, C. D. (2006). The Role of Zinc in Life: A Review. *J. Environ. Pathol. Toxicol. Oncol.* 25, 597–610. doi:10.1615/jenvironpatholtoxicoloncol.v25.i3.40

Frieden, E. (1972). The Chemical Elements of Life. *Sci. Am.* 227, 52–60. doi:10.1038/scientificamerican0772-52

Fudge, D. H., Black, R., Son, L., LeJeune, K., and Qin, Y. (2018). Optical Recording of Zn^{2+} Dynamics in the Mitochondrial Matrix and Intermembrane Space with the GZnP2 Sensor. *ACS Chem. Biol.* 13, 1897–1905. doi:10.1021/acschembio.8b00319

Fujii, T., Shindo, Y., Hotta, K., Citterio, D., Nishiyama, S., Suzuki, K., et al. (2014). Design and Synthesis of a FlAsH-type Mg^{2+} Fluorescent Probe for Specific Protein Labeling. *J. Am. Chem. Soc.* 136, 2374–2381. doi:10.1021/ja410031n

Futai, M., Oka, T., Sun-Wada, G.-H., Moriyama, Y., Kanazawa, H., and Wada, Y. (2000). Luminal Acidification of Diverse Organelles by V-ATPase in Animal Cells. *J. Exp. Biol.* 203, 107–116. doi:10.1242/jeb.203.1.107

Galietta, L. J. V., Haggie, P. M., and Verkman, A. S. (2001). Green Fluorescent Protein-Based Halide Indicators with Improved Chloride and Iodide Affinities. *FEBS Lett.* 499, 220–224. doi:10.1016/S0014-5793(01)02561-3

Gee, K. R., Brown, K. A., Chen, W.-N. U., Bishop-Stewart, J., Gray, D., and Johnson, I. (2000). Chemical and Physiological Characterization of Fluo-4 Ca^{2+}-Indicator Dyes. *Cell Calcium* 27, 97–106. doi:10.1054/ceca.1999.0095

Gee, K. R., Zhou, Z.-L., Ton-That, D., Sensi, S. L., and Weiss, J. H. (2002). Measuring Zinc in Living Cells. *Cell Calcium* 31, 245–251. doi:10.1016/S0143-4160(02)00053-2

Ghazvini Zadeh, E. H., Huang, Z., Xia, J., Li, D., Davidson, H. W., and Li, W.-h. (2020). ZIGIR, a Granule-specific Zn^{2+} Indicator, Reveals Human Islet α Cell Heterogeneity. *Cel Rep.* 32, 107904. doi:10.1016/j.celrep.2020.107904

Gjetting, S. K., Ytting, C. K., Schulz, A., and Fuglsang, A. T. (2012). Live Imaging of Intra- and Extracellular pH in Plants Using pHusion, a Novel Genetically Encoded Biosensor. *J. Exp. Bot.* 63, 3207–3218. doi:10.1093/jxb/ers040

Godfrey, W. L., Gray, D., Beacham, D. W., Dzubay, J., Rukavishnikov, A., Martin, V., et al. (2008). Evaluation of Granulocyte Phagocytic Activity Using pHrodo Dye, a Novel Fluorogenic pH Indicator. *FASEB j.* 22, 569. doi:10.1096/fasebj.22.2_supplement.569

Goetz, T., Arslan, A., Wisden, W., and Wulff, P. (2007). GABAA Receptors: Structure and Function in the Basal Ganglia. *Prog. Brain Res.* 160, 21–41. doi:10.1016/S0079-6123(06)60003-4

Grimley, J. S., Li, L., Wang, W., Wen, L., Beese, L. S., Hellinga, H. W., et al. (2013). Visualization of Synaptic Inhibition with an Optogenetic Sensor Developed by Cell-free Protein Engineering Automation. *J. Neurosci.* 33, 16297–16309. doi:10.1523/JNEUROSCI.4616-11.2013

Grubbs, R. D. (2002). Intracellular Magnesium and Magnesium Buffering. *Biometals* 15, 251–259. doi:10.1023/A:1016026831789

Grynkiewicz, G., Poenie, M., and Tsien, R. Y. (1985). A New Generation of Ca^{2+} Indicators with Greatly Improved Fluorescence Properties. *J. Biol. Chem.* 260, 3440–3450. doi:10.1016/s0021-9258(19)83641-4

Hanson, G. T., McAnaney, T. B., Park, E. S., Rendell, M. E. P., Yarbrough, D. K., Chu, S., et al. (2002). Green Fluorescent Protein Variants as Ratiometric Dual Emission pH Sensors. 1. Structural Characterization and Preliminary Application. *Biochemistry* 41, 15477–15488. doi:10.1021/bi026609p

He, Q., Miller, E. W., Wong, A. P., and Chang, C. J. (2006). A Selective Fluorescent Sensor for Detecting Lead in Living Cells. *J. Am. Chem. Soc.* 128, 9316–9317. doi:10.1021/ja063029x

Heim, N., and Griesbeck, O. (2004). Genetically Encoded Indicators of Cellular Calcium Dynamics Based on Troponin C and Green Fluorescent Protein. *J. Biol. Chem.* 279, 14280–14286. doi:10.1074/jbc.M312751200

Hellwig, N., Plant, T. D., Janson, W., Schäfer, M., Schultz, G., and Schaefer, M. (2004). TRPV1 Acts as Proton Channel to Induce Acidification in Nociceptive Neurons. *J. Biol. Chem.* 279, 34553–34561. doi:10.1074/jbc.M402966200

Hessels, A. M., Chabosseau, P., Bakker, M. H., Engelen, W., Rutter, G. A., Taylor, K. M., et al. (2015). eZinCh-2: A Versatile, Genetically Encoded FRET Sensor for Cytosolic and Intraorganelle Zn^{2+} Imaging. *ACS Chem. Biol.* 10, 2126–2134. doi:10.1021/acschembio.5b00211

Hirano, T., Kikuchi, K., Urano, Y., Higuchi, T., and Nagano, T. (2000). Highly Zinc-Selective Fluorescent Sensor Molecules Suitable for Biological Applications. *J. Am. Chem. Soc.* 122, 12399–12400. doi:10.1021/ja002467f

Hirano, T., Kikuchi, K., Urano, Y., and Nagano, T. (2002). Improvement and Biological Applications of Fluorescent Probes for Zinc, ZnAFs. *J. Am. Chem. Soc.* 124, 6555–6562. doi:10.1021/ja025567p

Honarnejad, K., Kirsch, A. K., Daschner, A., Szybinska, A., Kuznicki, J., and Herms, J. (2013). FRET-based Calcium Imaging. *J. Biomol. Screen.* 18, 1309–1320. doi:10.1177/1087057113502672

Horikawa, K., Yamada, Y., Matsuda, T., Kobayashi, K., Hashimoto, M., Matsu-ura, T., et al. (2010). Spontaneous Network Activity Visualized by Ultrasensitive Ca^{2+} Indicators, Yellow Cameleon-Nano. *Nat. Methods* 7, 729–732. doi:10.1038/nmeth.1488

Humphries, E. S. A., and Dart, C. (2015). Neuronal and Cardiovascular Potassium Channels as Therapeutic Drug Targets. *J. Biomol. Screen.* 20, 1055–1073. doi:10.1177/1087057115601677

Hyrc, K. L., Minta, A., Escamilla, P. R., Chan, P. P. L., Meshik, X. A., and Goldberg, M. P. (2013). Synthesis and Properties of Asante Calcium Red-A Novel Family of Long Excitation Wavelength Calcium Indicators. *Cell Calcium* 54, 320–333. doi:10.1016/j.ceca.2013.08.001

Iamshanova, O., Mariot, P., Lehen'kyi, V. y., and Prevarskaya, N. (2016). Comparison of Fluorescence Probes for Intracellular Sodium Imaging in Prostate Cancer Cell Lines. *Eur. Biophys. J.* 45, 765–777. doi:10.1007/s00249-016-1173-7

Inoue, M., Takeuchi, A., Horigane, S.-i., Ohkura, M., Gengyo-Ando, K., Fujii, H., et al. (2015). Rational Design of a High-Affinity, Fast, Red Calcium Indicator R-CaMP2. *Nat. Methods* 12, 64–70. doi:10.1038/nmeth.3185

Jayaraman, S., Haggie, P., Wachter, R. M., Remington, S. J., and Verkman, A. S. (2000). Mechanism and Cellular Applications of a Green Fluorescent Protein-Based Halide Sensor. *J. Biol. Chem.* 275, 6047–6050. doi:10.1074/jbc.275.9.6047

Kaplan, J. H., and Maryon, E. B. (2016). How Mammalian Cells Acquire Copper: An Essential but Potentially Toxic Metal. *Biophysical J.* 110, 7–13. doi:10.1016/j.bpj.2015.11.025

Kerper, L. E., and Hinkle, P. M. (1997). Lead Uptake in Brain Capillary Endothelial Cells: Activation by Calcium Store Depletion. *Toxicol. Appl. Pharmacol.* 146, 127–133. doi:10.1006/taap.1997.8234

Kerr, R., Lev-Ram, V., Baird, G., Vincent, P., Tsien, R. Y., and Schafer, W. R. (2000). Optical Imaging of Calcium Transients in Neurons and Pharyngeal Muscle of *C. elegans*. *Neuron* 26, 583–594. doi:10.1016/S0896-6273(00)81196-4

Khan, S. S., Shen, Y., Fatmi, M. Q., Campbell, R. E., and Bokhari, H. (2021). Design and Prototyping of Genetically Encoded Arsenic Biosensors Based on Transcriptional Regulator AfArsR. *Biomolecules* 11, 1276. doi:10.3390/biom11091276

Khodorov, B., Pinelis, V., Golovina, V., Fajuk, D., Andreeva, N., Uvarova, T., et al. (1993). On the Origin of a Sustained Increase in Cytosolic Ca^{2+} Concentration after a Toxic Glutamate Treatment of the Nerve Cell Culture. *FEBS Lett.* 324, 271–273. doi:10.1016/0014-5793(93)80132-e

Kim, H. N., Ren, W. X., Kim, J. S., and Yoon, J. (2012). Fluorescent and Colorimetric Sensors for Detection of Lead, Cadmium, and Mercury Ions. *Chem. Soc. Rev.* 41, 3210–3244. doi:10.1039/C1CS15245A

Kneen, M., Farinas, J., Li, Y., and Verkman, A. S. (1998). Green Fluorescent Protein as a Noninvasive Intracellular pH Indicator. *Biophysical J.* 74, 1591–1599. doi:10.1016/s0006-3495(98)77870-1

Koay, M. S., Janssen, B. M. G., and Merkx, M. (2013). Tuning the Metal Binding Site Specificity of a Fluorescent Sensor Protein: From Copper to Zinc and Back. *Dalton Trans.* 42, 3230–3232. doi:10.1039/C2DT32082G

Koide, Y., Urano, Y., Hanaoka, K., Terai, T., and Nagano, T. (2011). Evolution of Group 14 Rhodamines as Platforms for Near-Infrared Fluorescence Probes Utilizing Photoinduced Electron Transfer. *ACS Chem. Biol.* 6, 600–608. doi:10.1021/cb1002416

Koldenkova, V. P., Matsuda, T., and Nagai, T. (2015). MagIC, a Genetically Encoded Fluorescent Indicator for Monitoring Cellular Mg^{2+} Using a Non-förster Resonance Energy Transfer Ratiometric Imaging Approach. *J. Biomed. Opt.* 20, 1. doi:10.1117/1.JBO.20.10.101203

Kolisek, M., Zsurka, G., Samaj, J., Weghuber, J., Schweyen, R. J., and Schweigel, M. (2003). Mrs2p Is an Essential Component of the Major Electrophoretic Mg^{2+} Influx System in Mitochondria. *EMBO J.* 22, 1235–1244. doi:10.1093/emboj/cdg122

Komatsu, H., Iwasawa, N., Citterio, D., Suzuki, Y., Kubota, T., Tokuno, K., et al. (2004). Design and Synthesis of Highly Sensitive and Selective Fluorescein-

Derived Magnesium Fluorescent Probes and Application to Intracellular 3D Mg^{2+} Imaging. *J. Am. Chem. Soc.* 126, 16353–16360. doi:10.1021/ja049624l

Krapf, R., Berry, C. A., and Verkman, A. S. (1988). Estimation of Intracellular Chloride Activity in Isolated Perfused Rabbit Proximal Convoluted Tubules Using a Fluorescent Indicator. *Biophysical J.* 53, 955–962. doi:10.1016/S0006-3495(88)83176-X

Kuner, T., and Augustine, G. J. (2000). A Genetically Encoded Ratiometric Indicator for Chloride. *Neuron* 27, 447–459. doi:10.1016/s0896-6273(00)00056-8

Leybaert, L., and Sanderson, M. J. (2012). Intercellular Ca^{2+} Waves: Mechanisms and Function. *Physiol. Rev.* 92, 1359–1392. doi:10.1152/physrev.00029.2011

Li, Y., and Tsien, R. W. (2012). pHTomato, a Red, Genetically Encoded Indicator that Enables Multiplex Interrogation of Synaptic Activity. *Nat. Neurosci.* 15, 1047–1053. doi:10.1038/nn.3126

Liang, J., Qin, M., Xu, R., Gao, X., Shen, Y., Xu, Q., et al. (2012). A Genetically Encoded Copper(I) Sensor Based on Engineered Structural Distortion of EGFP. *Chem. Commun.* 48, 3890–3892. doi:10.1039/C2CC30531C

Lim, C. S., Han, J. H., Kim, C. W., Kang, M. Y., Kang, D. W., and Cho, B. R. (2011). A Copper(I)-Ion Selective Two-Photon Fluorescent Probe for *In Vivo* Imaging. *Chem. Commun.* 47, 7146–7148. doi:10.1039/C1CC11568E

Lin, W., Cao, X., Ding, Y., Yuan, L., and Yu, Q. (2010). A Reversible Fluorescent Hg^{2+} Chemosensor Based on a Receptor Composed of a Thiol Atom and an Alkene Moiety for Living Cell Fluorescence Imaging. *Org. Biomol. Chem.* 8, 3618–3620. doi:10.1039/c0ob00081g

Lindenburg, L. H., Vinkenborg, J. L., Oortwijn, J., Aper, S. J. A., and Merkx, M. (2013). MagFRET: The First Genetically Encoded Fluorescent Mg^{2+} Sensor. *PLoS One* 8, e82009. doi:10.1371/journal.pone.0082009

Lindner, B., Burkard, T., and Schuler, M. (2020). Phagocytosis Assays with Different pH-Sensitive Fluorescent Particles and Various Readouts. *BioTechniques* 68, 245–250. doi:10.2144/btn-2020-0003

Liu, A., Huang, X., He, W., Xue, F., Yang, Y., Liu, J., et al. (2021). pHmScarlet Is a pH-Sensitive Red Fluorescent Protein to Monitor Exocytosis Docking and Fusion Steps. *Nat. Commun.* 12, 1413. doi:10.1038/s41467-021-21666-7

Liu, J., Karpus, J., Wegner, S. V., Chen, P. R., and He, C. (2013). Genetically Encoded Copper(I) Reporters with Improved Response for Use in Imaging. *J. Am. Chem. Soc.* 135, 3144–3149. doi:10.1021/ja3106779

Liu, W., Xu, L., Sheng, R., Wang, P., Li, H., and Wu, S. (2007). A Water-Soluble "Switching on" Fluorescent Chemosensor of Selectivity to Cd^{2+}. *Org. Lett.* 9, 3829–3832. doi:10.1021/ol701620h

Llopis, J., McCaffery, J. M., Miyawaki, A., Farquhar, M. G., and Tsien, R. Y. (1998). Measurement of Cytosolic, Mitochondrial, and Golgi pH in Single Living Cells with Green Fluorescent Proteins. *Proc. Natl. Acad. Sci. U.S.A.* 95, 6803–6808. doi:10.1073/pnas.95.12.6803

Lock, J. T., Parker, I., and Smith, I. F. (2015). A Comparison of Fluorescent Ca^{2+} Indicators for Imaging Local Ca^{2+} Signals in Cultured Cells. *Cell Calcium* 58, 638–648. doi:10.1016/j.ceca.2015.10.003

Lu, H., Xiong, L., Liu, H., Yu, M., Shen, Z., Li, F., et al. (2009). A Highly Selective and Sensitive Fluorescent Turn-On Sensor for Hg^{2+} and its Application in Live Cell Imaging. *Org. Biomol. Chem.* 7, 2554–2558. doi:10.1039/b902912e

Macomber, L., and Imlay, J. A. (2009). The Iron-Sulfur Clusters of Dehydratases Are Primary Intracellular Targets of Copper Toxicity. *Proc. Natl. Acad. Sci. U.S.A.* 106, 8344–8349. doi:10.1073/pnas.0812808106

Maeshima, K., Matsuda, T., Shindo, Y., Imamura, H., Tamura, S., Imai, R., et al. (2018). A Transient Rise in Free Mg^{2+} Ions Released from ATP-Mg Hydrolysis Contributes to Mitotic Chromosome Condensation. *Curr. Biol.* 28, 444–451. e6. doi:10.1016/j.cub.2017.12.035

Malgaroli, A., Milani, D., Meldolesi, J., and Pozzan, T. (1987). Fura-2 Measurement of Cytosolic Free Ca^{2+} in Monolayers and Suspensions of Various Types of Animal Cells. *J. Cel Biol* 105, 2145–2155. doi:10.1083/jcb.105.5.2145

Mank, M., and Griesbeck, O. (2008). Genetically Encoded Calcium Indicators. *Chem. Rev.* 108, 1550–1564. doi:10.1021/cr078213v

Mank, M., Reiff, D. F., Heim, N., Friedrich, M. W., Borst, A., and Griesbeck, O. (2006). A FRET-Based Calcium Biosensor with Fast Signal Kinetics and High Fluorescence Change. *Biophysical J.* 90, 1790–1796. doi:10.1529/biophysj.105.073536

Marbella, L., Serli-Mitasev, B., and Basu, P. (2009). Development of a Fluorescent Pb^{2+} Sensor. *Angew. Chem.* 121, 4056–4058. doi:10.1002/ange.200806297

Marcotte, N., and Brouwer, A. M. (2005). Carboxy SNARF-4F as a Fluorescent pH Probe for Ensemble and Fluorescence Correlation Spectroscopies. *J. Phys. Chem. B* 109, 11819–11828. doi:10.1021/jp0510138

Markova, O., Mukhtarov, M., Real, E., Jacob, Y., and Bregestovski, P. (2008). Genetically Encoded Chloride Indicator with Improved Sensitivity. *J. Neurosci. Methods* 170, 67–76. doi:10.1016/j.jneumeth.2007.12.016

Martinez-Finley, E. J., Chakraborty, S., Fretham, S. J. B., and Aschner, M. (2012). Cellular Transport and Homeostasis of Essential and Nonessential Metals. *Metallomics* 4, 593–605. doi:10.1039/c2mt00185c

Martinez-Zaguilan, R., Martinez, G. M., Lattanzio, F., and Gillies, R. J. (1991). Simultaneous Measurement of Intracellular pH and Ca^{2+} Using the Fluorescence of SNARF-1 and Fura-2. *Am. J. Physiology-Cell Physiol.* 260, C297–C307. doi:10.1152/ajpcell.1991.260.2.C297

Mazzolini, M., Traverso, S., and Marchetti, C. (2001). Multiple Pathways of Pb^{2+} Permeation in Rat Cerebellar Granule Neurones. *J. Neurochem.* 79, 407–416. doi:10.1046/j.1471-4159.2001.00557.x

Medda, N., Patra, R., Ghosh, T. K., and Maiti, S. (2020). Neurotoxic Mechanism of Arsenic: Synergistic Effect of Mitochondrial Instability, Oxidative Stress, and Hormonal-Neurotransmitter Impairment. *Biol. Trace Elem. Res.* 198, 8–15. doi:10.1007/s12011-020-02044-8

Meier, S. D., Kovalchuk, Y., and Rose, C. R. (2006). Properties of the New Fluorescent Na^+ Indicator CoroNa Green: Comparison with SBFI and Confocal Na^+ Imaging. *J. Neurosci. Methods* 155, 251–259. doi:10.1016/j.jneumeth.2006.01.009

Miesenböck, G., De Angelis, D. A., and Rothman, J. E. (1998). Visualizing Secretion and Synaptic Transmission with pH-Sensitive Green Fluorescent Proteins. *Nature* 394, 192–195. doi:10.1038/28190

Minckley, T. F., Zhang, C., Fudge, D. H., Dischler, A. M., LeJeune, K. D., Xu, H., et al. (2019). Sub-nanomolar Sensitive GZnP3 Reveals TRPML1-Mediated Neuronal Zn^{2+} Signals. *Nat. Commun.* 10, 4806. doi:10.1038/s41467-019-12761-x

Minta, A., Kao, J. P. Y., and Tsien, R. Y. (1989). Fluorescent Indicators for Cytosolic Calcium Based on Rhodamine and Fluorescein Chromophores. *J. Biol. Chem.* 264, 8171–8178. doi:10.1016/s0021-9258(18)83165-9

Minta, A., and Tsien, R. Y. (1989). Fluorescent Indicators for Cytosolic Sodium. *J. Biol. Chem.* 264, 19449–19457. doi:10.1016/s0021-9258(19)47321-3

Miranda, J. G., Weaver, A. L., Qin, Y., Park, J. G., Stoddard, C. I., Lin, M. Z., et al. (2012). New Alternately Colored FRET Sensors for Simultaneous Monitoring of Zn^{2+} in Multiple Cellular Locations. *PLOS ONE* 7, e49371. doi:10.1371/journal.pone.0049371

Miyawaki, A., Llopis, J., Heim, R., McCaffery, J. M., Adams, J. A., Ikura, M., et al. (1997). Fluorescent Indicators for Ca^{2+} Based on Green Fluorescent Proteins and Calmodulin. *Nature* 388, 882–887. doi:10.1038/42264

Morelle, B., Salmon, J. M., Vigo, J., and Viallet, P. (1994). Measurement of Intracellular Magnesium Concentration in 3T3 Fibroblasts with the Fluorescent Indicator Mag-Indo-1. *Anal. Biochem.* 218, 170–176. doi:10.1006/abio.1994.1156

Morgan, M. T., Bagchi, P., and Fahrni, C. J. (2011). Designed to Dissolve: Suppression of Colloidal Aggregation of Cu(I)-Selective Fluorescent Probes in Aqueous Buffer and In-Gel Detection of a Metallochaperone. *J. Am. Chem. Soc.* 133, 15906–15909. doi:10.1021/ja207004v

Nagai, T., Sawano, A., Park, E. S., and Miyawaki, A. (2001). Circularly Permuted green Fluorescent Proteins Engineered to Sense Ca^{2+}. *Proc. Natl. Acad. Sci. U.S.A.* 98, 3197–3202. doi:10.1073/pnas.051636098

Nagai, T., Yamada, S., Tominaga, T., Ichikawa, M., and Miyawaki, A. (2004). Expanded Dynamic Range of Fluorescent Indicators for Ca^{2+} by Circularly Permuted Yellow Fluorescent Proteins. *Proc. Natl. Acad. Sci. U.S.A.* 101, 10554–10559. doi:10.1073/pnas.0400417101

Nakai, J., Ohkura, M., and Imoto, K. (2001). A High Signal-To-Noise Ca^{2+} Probe Composed of a Single green Fluorescent Protein. *Nat. Biotechnol.* 19, 137–141. doi:10.1038/84397

Nasu, Y., Shen, Y., Kramer, L., and Campbell, R. E. (2021). Structure- and Mechanism-Guided Design of Single Fluorescent Protein-Based Biosensors. *Nat. Chem. Biol.* 17, 509–518. doi:10.1038/s41589-020-00718-x

Nelson, N., Perzov, N., Cohen, A., Hagai, K., Padler, V., and Nelson, H. (2000). The Cellular Biology of Proton-Motive Force Generation by V-ATPases. *J. Exp. Biol.* 203, 89–95. doi:10.1242/jeb.203.1.89

Nolan, E. M., and Lippard, S. J. (2004). The Zinspy Family of Fluorescent Zinc Sensors: Syntheses and Spectroscopic Investigations. *Inorg. Chem.* 43, 8310–8317. doi:10.1021/ic048778z

Nolan, E. M., Ryu, J. W., Jaworski, J., Feazell, R. P., Sheng, M., and Lippard, S. J. (2006). Zinspy Sensors with Enhanced Dynamic Range for Imaging Neuronal Cell Zinc Uptake and Mobilization. *J. Am. Chem. Soc.* 128, 15517–15528. doi:10.1021/ja065759a

Opazo, C. M., Greenough, M. A., and Bush, A. I. (2014). Copper: From Neurotransmission to Neuroproteostasis. *Front. Aging Neurosci.* 6, 143. doi:10.3389/fnagi.2014.00143

Peng, X., Du, J., Fan, J., Wang, J., Wu, Y., Zhao, J., et al. (2007). A Selective Fluorescent Sensor for Imaging Cd^{2+} in Living Cells. *J. Am. Chem. Soc.* 129, 1500–1501. doi:10.1021/ja0643319

Percival, S. S. (1998). Copper and Immunity. *Am. J. Clin. Nutr.* 67, 1064S–1068S. doi:10.1093/ajcn/67.5.1064S

Pilchova, I., Klacanova, K., Tatarkova, Z., Kaplan, P., and Racay, P. (2017). The Involvement of Mg^{2+} in Regulation of Cellular and Mitochondrial Functions. *Oxidative Med. Cell Longevity* 2017, 6797460. doi:10.1155/2017/6797460

Pröfrock, D., and Prange, A. (2012). Inductively Coupled Plasma-Mass Spectrometry (ICP-MS) for Quantitative Analysis in Environmental and Life Sciences: A Review of Challenges, Solutions, and Trends. *Appl. Spectrosc.* 66, 843–868. doi:10.1366/12-06681

Qian, Y., Cosio, D. M. O., Piatkevich, K. D., Aufmkolk, S., Su, W.-C., Celiker, O. T., et al. (2020). Improved Genetically Encoded Near-Infrared Fluorescent Calcium Ion Indicators for *In Vivo* Imaging. *Plos Biol.* 18, e3000965. doi:10.1371/journal.pbio.3000965

Qian, Y., Piatkevich, K. D., Mc Larney, B., Abdelfattah, A. S., Mehta, S., Murdock, M. H., et al. (2019). A Genetically Encoded Near-Infrared Fluorescent Calcium Ion Indicator. *Nat. Methods* 16, 171–174. doi:10.1038/s41592-018-0294-6

Qin, Y., Dittmer, P. J., Park, J. G., Jansen, K. B., and Palmer, A. E. (2011a). Measuring Steady-State and Dynamic Endoplasmic Reticulum and Golgi Zn^{2+} with Genetically Encoded Sensors. *Proc. Natl. Acad. Sci. U.S.A.* 108, 7351–7356. doi:10.1073/pnas.1015686108

Qin, Y., Sammond, D. W., Braselmann, E., Carpenter, M. C., and Palmer, A. E. (2016). Development of an Optical Zn^{2+} Probe Based on a Single Fluorescent Protein. *ACS Chem. Biol.* 11, 2744–2751. doi:10.1021/acschembio.6b00442

Qin, Z., Caruso, J. A. J., Lai, B., Matusch, A., and Becker, J. S. (2011b). Trace Metal Imaging with High Spatial Resolution: Applications in Biomedicine. *Metallomics* 3, 28–37. doi:10.1039/C0MT00048E

Raju, B., Murphy, E., Levy, L. A., Hall, R. D., and London, R. E. (1989). A Fluorescent Indicator for Measuring Cytosolic Free Magnesium. *Am. J. Physiology-Cell Physiol.* 256, C540–C548. doi:10.1152/ajpcell.1989.256.3.C540

Rana, P. S., Gibbons, B. A., Vereninov, A. A., Yurinskaya, V. E., Clements, R. J., Model, T. A., et al. (2019). Calibration and Characterization of Intracellular Asante Potassium Green Probes, APG-2 and APG-4. *Anal. Biochem.* 567, 8–13. doi:10.1016/j.ab.2018.11.024

Reid, R. A., Moyle, J., and Mitchell, P. (1966). Synthesis of Adenosine Triphosphate by a Protonmotive Force in Rat Liver Mitochondria. *Nature* 212, 257–258. doi:10.1038/212257a0

Reynolds, R. M., Padfield, P. L., and Seckl, J. R. (2006). Disorders of Sodium Balance. *BMJ* 332, 702–705. doi:10.1136/bmj.332.7543.702

Rimmele, T. S., and Chatton, J.-Y. (2014). A Novel Optical Intracellular Imaging Approach for Potassium Dynamics in Astrocytes. *PLoS One* 9, e109243. doi:10.1371/journal.pone.0109243

Rink, T. J., Tsien, R. Y., and Pozzan, T. (1982). Cytoplasmic pH and Free Mg^{2+} in Lymphocytes. *J. Cel Biol.* 95, 189–196. doi:10.1083/jcb.95.1.189

Roder, P., and Hille, C. (2014). ANG-2 for Quantitative Na^{+} Determination in Living Cells by Time-Resolved Fluorescence Microscopy. *Photochem. Photobiol. Sci.* 13, 1699–1710. doi:10.1039/c4pp00061g

Romani, A. M. P. (2013). "Magnesium Homeostasis in Mammalian Cells," in Metallomics And the Cell *Metal Ions in Life Sciences*. Editor L. Banci (Dordrecht: Springer Netherlands), 69–118. doi:10.1007/978-94-007-5561-1_4

Rupprecht, C., Wingen, M., Potzkei, J., Gensch, T., Jaeger, K.-E., and Drepper, T. (2017). A Novel FbFP-Based Biosensor Toolbox for Sensitive *In Vivo* Determination of Intracellular pH. *J. Biotechnol.* 258, 25–32. doi:10.1016/j.jbiotec.2017.05.006

Russell, J. T. (2011). Imaging Calcium Signalsin Vivo: a Powerful Tool in Physiology and Pharmacology. *Br. J. Pharmacol.* 163, 1605–1625. doi:10.1111/j.1476-5381.2010.00988.x

Saari, J. T. (2000). Copper Deficiency and Cardiovascular Disease: Role of Peroxidation, Glycation, and Nitration. *Can. J. Physiol. Pharmacol.* 78, 848–855. doi:10.1139/y00-054

Sankaranarayanan, S., De Angelis, D., Rothman, J. E., and Ryan, T. A. (2000). The Use of pHluorins for Optical Measurements of Presynaptic Activity. *Biophysical J.* 79, 2199–2208. doi:10.1016/S0006-3495(00)76468-X

Santucci, R. J., and Scully, J. R. (2020). The Pervasive Threat of lead (Pb) in Drinking Water: Unmasking and Pursuing Scientific Factors that Govern lead Release. *Proc. Natl. Acad. Sci. U.S.A.* 117, 23211–23218. doi:10.1073/pnas.1913749117

Shaner, N. C., Lambert, G. G., Chammas, A., Ni, Y., Cranfill, P. J., Baird, M. A., et al. (2013). A Bright Monomeric Green Fluorescent Protein Derived from *Branchiostoma lanceolatum*. *Nat. Methods* 10, 407–409. doi:10.1038/nmeth.2413

Shen, Y., Dana, H., Abdelfattah, A. S., Patel, R., Shea, J., Molina, R. S., et al. (2018). A Genetically Encoded Ca^{2+} Indicator Based on Circularly Permutated Sea Anemone Red Fluorescent Protein eqFP578. *BMC Biol.* 16, 9. doi:10.1186/s12915-018-0480-0

Shen, Y., Rosendale, M., Campbell, R. E., and Perrais, D. (2014). pHuji, a PH-Sensitive Red Fluorescent Protein for Imaging of Exo- and Endocytosis. *J. Cel Biol.* 207, 419–432. doi:10.1083/jcb.201404107

Shen, Y., Wu, S.-Y., Rancic, V., Aggarwal, A., Qian, Y., Miyashita, S.-I., et al. (2019). Genetically Encoded Fluorescent Indicators for Imaging Intracellular Potassium Ion Concentration. *Commun. Biol.* 2, 18. doi:10.1038/s42003-018-0269-2

Shmigol, A. V., Eisner, D. A., and Wray, S. (2001). Simultaneous Measurements of Changes in Sarcoplasmic Reticulum and Cytosolic $[Ca^{2+}]$ in Rat Uterine Smooth Muscle Cells. *J. Physiol.* 531, 707–713. doi:10.1111/j.1469-7793.2001.0707h.x

Soibinet, M., Souchon, V., Leray, I., and Valeur, B. (2008). Rhod-5N as a Fluorescent Molecular Sensor of Cadmium(II) Ion. *J. Fluoresc.* 18, 1077–1082. doi:10.1007/s10895-008-0352-z

Soleja, N., Manzoor, O., Khan, P., and Mohsin, M. (2019). Engineering Genetically Encoded FRET-Based Nanosensors for Real Time Display of Arsenic (As^{3+}) Dynamics in Living Cells. *Sci. Rep.* 9, 11240. doi:10.1038/s41598-019-47682-8

Stohs, S., and Bagchi, D. (1995). Oxidative Mechanisms in the Toxicity of Metal Ions. *Free Radic. Biol. Med.* 18, 321–336. doi:10.1016/0891-5849(94)00159-H

Strazzullo, P., and Leclercq, C. (2014). Sodium. *Adv. Nutr.* 5, 188–190. doi:10.3945/an.113.005215

Subach, O. M., Sotskov, V. P., Plusnin, V. V., Gruzdeva, A. M., Barykina, N. V., Ivashkina, O. I., et al. (2020). Novel Genetically Encoded Bright Positive Calcium Indicator NCaMP7 Based on the mNeonGreen Fluorescent Protein. *Ijms* 21, 1644. doi:10.3390/ijms21051644

Tallini, Y. N., Ohkura, M., Choi, B.-R., Ji, G., Imoto, K., Doran, R., et al. (2006). Imaging Cellular Signals in the Heart *In Vivo* : Cardiac Expression of the High-Signal Ca^{2+} Indicator GCaMP2. *Proc. Natl. Acad. Sci. U.S.A.* 103, 4753–4758. doi:10.1073/pnas.0509378103

Tantama, M., Hung, Y. P., and Yellen, G. (2011). Imaging Intracellular pH in Live Cells with a Genetically Encoded Red Fluorescent Protein Sensor. *J. Am. Chem. Soc.* 133, 10034–10037. doi:10.1021/ja202902d

Tapiero, H., Townsend, D. M., and Tew, K. D. (2003). Trace Elements in Human Physiology and Pathology. Copper. *Biomed. Pharmacother.* 57, 386–398. doi:10.1016/s0753-3322(03)00012-x

Thestrup, T., Litzlbauer, J., Bartholomäus, I., Mues, M., Russo, L., Dana, H., et al. (2014). Optimized Ratiometric Calcium Sensors for Functional *In Vivo* Imaging of Neurons and T Lymphocytes. *Nat. Methods* 11, 175–182. doi:10.1038/nmeth.2773

Tian, L., Hires, S. A., Mao, T., Huber, D., Chiappe, M. E., Chalasani, S. H., et al. (2009). Imaging Neural Activity in Worms, Flies and Mice with Improved GCaMP Calcium Indicators. *Nat. Methods* 6, 875–881. doi:10.1038/nmeth.1398

Truong, K., Sawano, A., Mizuno, H., Hama, H., Tong, K. I., Mal, T. K., et al. (2001). FRET-based *In Vivo* Ca^{2+} Imaging by a New Calmodulin-GFP Fusion Molecule. *Nat. Struct. Biol.* 8, 1069–1073. doi:10.1038/nsb728

Tsien, R., and Pozzan, T. (1989). "[14] Measurement of Cytosolic Free Ca^{2+} with Quin2," in Methods In Enzymology *Biomembranes Part S* (Academic Press), 230–262. doi:10.1016/S0076-6879(89)72017-6

Tsien, R. Y. (1981). A Non-disruptive Technique for Loading Calcium Buffers and Indicators into Cells. *Nature* 290, 527–528. doi:10.1038/290527a0

Tsien, R. Y. (1983). Intracellular Measurements of Ion Activities. *Annu. Rev. Biophys. Bioeng.* 12, 91–116. doi:10.1146/annurev.bb.12.060183.000515

Tsien, R. Y., and Minta, A. (1991). *Fluorescent Indicator Dyes for Calcium Working at Long Wavelengths*. Available at: https://patents.google.com/patent/US5049673A/en (Accessed February 9, 2021).

Tsien, R. Y. (1980). New Calcium Indicators and Buffers with High Selectivity against Magnesium and Protons: Design, Synthesis, and Properties of Prototype Structures. *Biochemistry* 19, 2396–2404. doi:10.1021/bi00552a018

Tutol, J. N., Kam, H. C., and Dodani, S. C. (2019a). Identification of mNeonGreen as a pH-Dependent, Turn-On Fluorescent Protein Sensor for Chloride. *ChemBioChem* 20, 1759–1765. doi:10.1002/cbic.201900147

Tutol, J. N., Peng, W., and Dodani, S. C. (2019b). Discovery and Characterization of a Naturally Occurring, Turn-On Yellow Fluorescent Protein Sensor for Chloride. *Biochemistry* 58, 31–35. doi:10.1021/acs.biochem.8b00928

Valdivieso, Á. G., and Santa-Coloma, T. A. (2019). The Chloride Anion as a Signalling Effector. *Biol. Rev.* 94, 1839–1856. doi:10.1111/brv.12536

Verkman, A. S., Sellers, M. C., Chao, A. C., Leung, T., and Ketcham, R. (1989). Synthesis and Characterization of Improved Chloride-Sensitive Fluorescent Indicators for Biological Applications. *Anal. Biochem.* 178, 355–361. doi:10.1016/0003-2697(89)90652-0

Vijverberg, H. P. M., and Westerink, R. H. S. (2012). Sense in Pb^{2+} Sensing. *Toxicol. Sci.* 130, 1–3. doi:10.1093/toxsci/kfs221

Vinkenborg, J. L., Nicolson, T. J., Bellomo, E. A., Koay, M. S., Rutter, G. A., and Merkx, M. (2009). Genetically Encoded FRET Sensors to Monitor Intracellular Zn^{2+} Homeostasis. *Nat. Methods* 6, 737–740. doi:10.1038/nmeth.1368

Vinkenborg, J. L., van Duijnhoven, S. M. J., and Merkx, M. (2011). Reengineering of a Fluorescent Zinc Sensor Protein Yields the First Genetically Encoded Cadmium Probe. *Chem. Commun.* 47, 11879–11881. doi:10.1039/C1CC14944J

Wachter, R. M., Elsliger, M.-A., Kallio, K., Hanson, G. T., and Remington, S. J. (1998). Structural Basis of Spectral Shifts in the Yellow-Emission Variants of green Fluorescent Protein. *Structure* 6, 1267–1277. doi:10.1016/S0969-2126(98)00127-0

Wachter, R. M., and James Remington, S. (1999). Sensitivity of the Yellow Variant of Green Fluorescent Protein to Halides and Nitrate. *Curr. Biol.* 9, R628–R629. doi:10.1016/S0960-9822(99)80408-4

Walkup, G. K., Burdette, S. C., Lippard, S. J., and Tsien, R. Y. (2000). A New Cell-Permeable Fluorescent Probe for Zn^{2+}. *J. Am. Chem. Soc.* 122, 5644–5645. doi:10.1021/ja000868p

Wang, Z., Detomasi, T. C., and Chang, C. J. (2021). A Dual-Fluorophore Sensor Approach for Ratiometric Fluorescence Imaging of Potassium in Living Cells. *Chem. Sci.* 12, 1720–1729. doi:10.1039/d0sc03844j

Wegner, S. V., Arslan, H., Sunbul, M., Yin, J., and He, C. (2010). Dynamic Copper(I) Imaging in Mammalian Cells with a Genetically Encoded Fluorescent Copper(I) Sensor. *J. Am. Chem. Soc.* 132, 2567–2569. doi:10.1021/ja9097324

Wegner, S. V., Sun, F., Hernandez, N., and He, C. (2011). The Tightly Regulated Copper Window in Yeast. *Chem. Commun.* 47, 2571–2573. doi:10.1039/C0CC04292G

Whitaker, J. E., Haugland, R. P., and Prendergast, F. G. (1991). Spectral and Photophysical Studies of Benzo[c]xanthene Dyes: Dual Emission pH Sensors. *Anal. Biochem.* 194, 330–344. doi:10.1016/0003-2697(91)90237-n

Wilck, N., Balogh, A., Markó, L., Bartolomaeus, H., and Müller, D. N. (2019). The Role of Sodium in Modulating Immune Cell Function. *Nat. Rev. Nephrol.* 15, 546–558. doi:10.1038/s41581-019-0167-y

Wu, J., Abdelfattah, A. S., Miraucourt, L. S., Kutsarova, E., Ruangkittisakul, A., Zhou, H., et al. (2014). A Long Stokes Shift Red Fluorescent Ca^{2+} Indicator Protein for Two-Photon and Ratiometric Imaging. *Nat. Commun.* 5, 5262. doi:10.1038/ncomms6262

Wu, J., Liu, L., Matsuda, T., Zhao, Y., Rebane, A., Drobizhev, M., et al. (2013). Improved Orange and Red Ca^{2+} Indicators and Photophysical Considerations for Optogenetic Applications. *ACS Chem. Neurosci.* 4, 963–972. doi:10.1021/cn400012b

Wu, S.-Y., Wen, Y., Serre, N. B. C., Laursen, C. C. H., Dietz, A. G., Taylor, B. R., et al. (2021). *A Sensitive and Specific Genetically Encodable Biosensor for Potassium Ions*. Laurel Hollow, NY: bioRxiv. doi:10.07.46341010.1101/2021.10.07.463410

Wu, Y., Peng, X., Guo, B., Fan, J., Zhang, Z., Wang, J., et al. (2005). Boron Dipyrromethene Fluorophore Based Fluorescence Sensor for the Selective Imaging of Zn(II) in Living Cells. *Org. Biomol. Chem.* 3, 1387–1392. doi:10.1039/b501795e

Yang, L., McRae, R., Henary, M. M., Patel, R., Lai, B., Vogt, S., et al. (2005). Imaging of the Intracellular Topography of Copper with a Fluorescent Sensor and by Synchrotron X-Ray Fluorescence Microscopy. *Proc. Natl. Acad. Sci. U.S.A.* 102, 11179–11184. doi:10.1073/pnas.0406547102

Yoon, S., Albers, A. E., Wong, A. P., and Chang, C. J. (2005). Screening Mercury Levels in Fish with a Selective Fluorescent Chemosensor. *J. Am. Chem. Soc.* 127, 16030–16031. doi:10.1021/ja0557987

Yu, D., Baird, M. A., Allen, J. R., Howe, E. S., Klassen, M. P., Reade, A., et al. (2015). A Naturally Monomeric Infrared Fluorescent Protein for Protein Labeling *In Vivo*. *Nat. Methods* 12, 763–765. doi:10.1038/nmeth.3447

Yurinskaya, V. E., Vereninov, I. A., and Vereninov, A. A. (2020). Balance of Na^+, K^+, and Cl^- Unidirectional Fluxes in Normal and Apoptotic U937 Cells Computed with All Main Types of Cotransporters. *Front. Cel Developmental Biol.* 8, 591872. (Accessed January 16, 2022). doi:10.3389/fcell.2020.591872

Zarowny, L., Aggarwal, A., Rutten, V. M. S., Kolb, I., Patel, R., Huang, H.-Y., et al. (2020). Bright and High-Performance Genetically Encoded Ca^{2+} Indicator Based on mNeonGreen Fluorescent Protein. *ACS Sens.* 5, 1959–1968. doi:10.1021/acssensors.0c00279

Zeng, L., Miller, E. W., Pralle, A., Isacoff, E. Y., and Chang, C. J. (2006). A Selective Turn-On Fluorescent Sensor for Imaging Copper in Living Cells. *J. Am. Chem. Soc.* 128, 10–11. doi:10.1021/ja055064u

Zhang, X.-a., Hayes, D., Smith, S. J., Friedle, S., and Lippard, S. J. (2008). New Strategy for Quantifying Biological Zinc by a Modified Zinpyr Fluorescence Sensor. *J. Am. Chem. Soc.* 130, 15788–15789. doi:10.1021/ja807156b

Zhang, Y., Rózsa, M., Liang, Y., Bushey, D., Wei, Z., Zheng, J., et al. (2021). Fast and Sensitive GCaMP Calcium Indicators for Imaging Neural Populations. *Neurophotonics* 1, 025008. doi:10.1101/2021.11.08.467793

Zhao, M., Hollingworth, S., and Baylor, S. M. (1996). Properties of Tri- and Tetracarboxylate Ca^{2+} Indicators in Frog Skeletal Muscle Fibers. *Biophysical J.* 70, 896–916. doi:10.1016/S0006-3495(96)79633-9

Zhao, Y., Araki, S., Wu, J., Teramoto, T., Chang, Y.-F., Nakano, M., et al. (2011). An Expanded Palette of Genetically Encoded Ca^{2+} Indicators. *Science* 333, 1888–1891. doi:10.1126/science.1208592

Zhao, Y., Sun, Y., Lv, X., Liu, Y., Chen, M., and Guo, W. (2010). Rhodamine-based Chemosensor for Hg^{2+} in Aqueous Solution with a Broad pH Range and its Application in Live Cell Imaging. *Org. Biomol. Chem.* 8, 4143–4147. doi:10.1039/c0ob00013b

Zhong, C., and Schleifenbaum, J. (2019). Genetically Encoded Calcium Indicators: A New Tool in Renal Hypertension Research. *Front. Med.* 6, 128. doi:10.3389/fmed.2019.00128

Conflict of Interest: The authors declare that the research was conducted in the absence of any commercial or financial relationships that could be construed as a potential conflict of interest.

Publisher's Note: All claims expressed in this article are solely those of the authors and do not necessarily represent those of their affiliated organizations, or those of the publisher, the editors and the reviewers. Any product that may be evaluated in this article, or claim that may be made by its manufacturer, is not guaranteed or endorsed by the publisher.

frontiers | Frontiers in Cell and Developmental Biology

ORIGINAL RESEARCH
published: 13 May 2022
doi: 10.3389/fcell.2022.865056

Förster Resonance Energy Transfer-Based Single-Cell Imaging Reveals Piezo1-Induced Ca^{2+} Flux Mediates Membrane Ruffling and Cell Survival

*Heon-Su Kim[1,2], Jung-Soo Suh[1], Yoon-Kwan Jang[1], Sang-Hyun Ahn[1], Gyu-Ho Choi[1], Jin-Young Yang[1], Gah-Hyun Lim[1], Youngmi Jung[1], Jie Jiang[3], Jie Sun[3], Myungeun Suk[4], Yingxiao Wang[5] and Tae-Jin Kim[1,2,6]**

[1]Department of Integrated Biological Science, Pusan National University, Pusan, South Korea, [2]Institute of Systems Biology, Pusan National University, Pusan, South Korea, [3]Department of Cell Biology, School of Medicine, Zhejiang University, Hangzhou, China, [4]Department of Mechanical Engineering, Dong-Eui University, Pusan, South Korea, [5]Department of Bioengineering, Institute of Engineering in Medicine, University of California, San Diego, La Jolla, CA, United States, [6]Department of Biological Sciences, Pusan National University, Pusan, South Korea

OPEN ACCESS

Edited by:
Fen Wang,
Texas A&M University, United States

Reviewed by:
Charles David Cox,
Victor Chang Cardiac Research Institute, Australia
Mingzhi Luo,
Changzhou University, China

***Correspondence:**
Tae-Jin Kim
tjkim77@pusan.ac.kr

Specialty section:
This article was submitted to Signaling, a section of the journal Frontiers in Cell and Developmental Biology

Received: 29 January 2022
Accepted: 25 April 2022
Published: 13 May 2022

Citation:
Kim H-S, Suh J-S, Jang Y-K, Ahn S-H, Choi G-H, Yang J-Y, Lim G-H, Jung Y, Jiang J, Sun J, Suk M, Wang Y and Kim T-J (2022) Förster Resonance Energy Transfer-Based Single-Cell Imaging Reveals Piezo1-Induced Ca^{2+} Flux Mediates Membrane Ruffling and Cell Survival. Front. Cell Dev. Biol. 10:865056. doi: 10.3389/fcell.2022.865056

A mechanosensitive ion channel, Piezo1 induces non-selective cation flux in response to various mechanical stresses. However, the biological interpretation and underlying mechanisms of cells resulting from Piezo1 activation remain elusive. This study elucidates Piezo1-mediated Ca^{2+} influx driven by channel activation and cellular behavior using novel Förster Resonance Energy Transfer (FRET)-based biosensors and single-cell imaging analysis. Results reveal that extracellular Ca^{2+} influx *via* Piezo1 requires intact caveolin, cholesterol, and cytoskeletal support. Increased cytoplasmic Ca^{2+} levels enhance PKA, ERK, Rac1, and ROCK activity, which have the potential to promote cancer cell survival and migration. Furthermore, we demonstrate that Piezo1-mediated Ca^{2+} influx upregulates membrane ruffling, a characteristic feature of cancer cell metastasis, using spatiotemporal image correlation spectroscopy. Thus, our findings provide new insights into the function of Piezo1, suggesting that Piezo1 plays a significant role in the behavior of cancer cells.

Keywords: FRET, biosensors, Piezo1, calcium, membrane ruffling

INTRODUCTION

Piezo1, a mechanosensitive channel, has been continuously investigated since its first cloning in 2010 (Coste et al., 2010). Piezo1 translates mechanical stimulation from the peripheral microenvironment into an electrical signal, and is a non-selective cation channel that is permeable to Na^+, K^+, Mg^{2+}, and Ca^{2+}, with a slight preference for Ca^{2+}(Coste et al., 2010; Coste et al., 2012; Lin et al., 2019). Mechanosensitivity of the Piezo1 channel is involved in various physiological functions, such as red blood cell volume, epithelial homeostasis, blood pressure regulation, vascular and lymphatic development, and bone formation (Ranade et al., 2014; Cahalan et al., 2015; Wang et al., 2016; Gudipaty et al., 2017; Nonomura et al., 2018; Sun et al., 2019). Impairment of Piezo1 activity resulting from inherited mutations and genetic manipulations has been associated with hereditary xerocytosis, lymphatic dysplasia, and hemolytic anemia (Zarychanski et al., 2012; Andolfo et al., 2013; Lukacs et al., 2015; Alper, 2017).

Two models have been suggested to understand the gating mechanism by which Piezo1 opens a central pore in response to mechanical force. The first model is the force-from-lipid model (Kung et al., 2010; Anishkin et al., 2014), where the tension of the cell membrane changes and the membrane flattens and contracts due to external stimuli; the interaction between 24 transmembrane helices consisting of the arm of Piezo1 and membrane lipids is altered and the arm is transformed into a flat shape. Eventually, the dome-shaped Piezo1 flattens, fulfilling the free energy required for channel gating and leading to the passage of ions (Lewis and Grandl, 2015; Cox et al., 2017; Lin et al., 2019). In other words, the channel reacts to a very local stimulus, such as a change in membrane tension, and carries out mechanotransduction (Cox et al., 2016; Syeda et al., 2016). The second model is the force-from-filament model, which suggests that Piezo1 physically binds to ambient non-compliant structures such as the extracellular matrix and cytoskeleton structures, and mechanogating occurs in response to mechanical stimuli from the structures or movement of the membrane-bound channels relative to the stationary structures (Markin and Hudspeth, 1995; Gillespie and Walker, 2001; Liang et al., 2013; Jin et al., 2017). In a study by Wang et al. (2020) endogenous Piezo1 was found to be bound to a mechanotransduction complex composed of E-cadherin, β-catenin, vinculin, and actin cytoskeleton, suggesting that this interaction could sense remote mechanical perturbation across a cell and regulate Piezo1-induced ion gating. Both the aforementioned models cannot be dismissed as it continues to be reported that Piezo1 could be regulated by both mechanisms.

The plasma membrane and the Piezo1 channel itself have been stimulated in various ways, such as poking, stretching, shear stress, and osmotic stress induction, in previous studies (Coste et al., 2010; Ranade et al., 2014; Syeda et al., 2016; Wang et al., 2018). Additionally, Piezo1 was found to be activated by Yoda1 and Jedi1, both of which are Piezo1-specific agonists (Syeda et al., 2015; Wang et al., 2018), although both agonists may not reflect the physiological role of Piezo1 where mechanical force is the native stimuli. Yoda1 can enter the hydrophobic-binding pocket of Piezo1 from the intracellular leaflet of the membrane, which is near the residues 1961–2063 of Piezo1, and effectively lower the mechanical threshold of the channel required for the conformational change of the Piezo1 arm and channel flattening (Botello-Smith et al., 2019). It has been hypothesized that Jedi1 binds to the extracellular side of transmembrane helical units THU1-THU3, and this stimulation passes through two extracellular loops of the blade and beam structure, which opens the Piezo1 channel (Wang et al., 2018). Interestingly, it has been assumed that the Piezo1 activation mechanisms, whether via physical stimulation or chemical treatment, have independent mechanotransduction pathways (Wang et al., 2018; Zhao et al., 2018; Botello-Smith et al., 2019). The Piezo1 R2135A mutant form, which abrogated mechanical opening mediated by membrane stretch, could lead to Ca^{2+} influx in response to Yoda1, and the A2094W mutant form, which severely reduced Yoda1-sensitivity, could trigger inward currents upon pressure (Botello-Smith et al., 2019). Additionally, it was observed in a study that Jedi1 failed to potentiate poking-induced currents in ΔL15-16 or ΔL19-20 Piezo1-expressing cells, whereas Yoda1 successfully induced (Wang et al., 2018; Zhao et al., 2018). Therefore, the Piezo1 channel is opened by a variety of mechanisms, but these mechanisms are not always interrelated.

Various cancer cells change the expression of proteins that are related to calcium ions, such as calcium channels, pumps, exchangers, and binding proteins, to remodel calcium signaling for tumor progression (Stewart et al., 2015; Monteith et al., 2017). Moreover, it has been reported that experimental or pharmacological inhibition of such calcium ion-related proteins influences cancer cell development (Monteith et al., 2017). The elevated levels of Ca^{2+} ions in the cytoplasm can activate cancer cell proliferation *via* cell cycle progression and various cellular signaling pathways. Indeed, calcium plays a significant role in the expression of immediate-early genes, such as *FOS*, *JUN*, and *MYC*, as well as in the phosphorylation of retinoblastoma-associated protein in the G1/S transition, and the activity of various Ca^{2+}-dependent transcription factors, including the nuclear factor of activated T-cells, nuclear factor kappa-light-chain-enhancer of activated B cells, and cAMP response element-binding protein (CREB) (Sée et al., 2004; Roderick and Cook, 2008; Prevarskaya et al., 2014). Ca^{2+}/calmodulin-dependent protein kinases (CaMKs) and calcineurin are also activated by Ca^{2+}, and can facilitate the progression of the cell cycle by regulating cyclin D1 expression and the activity of cyclin-dependent kinases (CDKs) and CREB, a transcription factor that is involved in the G1/S transition, by binding to the cyclin D1 promoter (Tombes et al., 1995; Morris et al., 1998; Khanna and Hosenpud, 1999; Schneider et al., 2002; Kahl and Means, 2004). Calcium and CaMK2 control centrosome duplication and the separation of the duplicated chromosomes to the daughter cells (Roderick and Cook, 2008). There are several cellular pathways that are regulated by calcium which activate cell proliferation; for example, the extracellular signal-regulated kinase 1/2 (ERK 1/2) pathway, which is a downstream effector of Ras, activates activator protein-1 (AP-1) and E26 transformation-specific factor and drives cyclin D1 expression and CDK4 activation (Roderick and Cook, 2008). The Ca^{2+}-cAMP-protein kinase A (PKA) pathway also activates CREB (Zhang et al., 2020).

Calcium also promotes cell migration through interactions with various compounds. Calpain, a calcium-dependent protease, cleaves focal adhesion proteins such as integrin, talin, and vinculin, and focal adhesion turnover is upregulated by the phosphorylation of focal adhesion kinase (FAK) *via* CaMK2 and calcineurin (Ridley et al., 2003; Su et al., 2006; Prevarskaya et al., 2011). Myosin light-chain kinase (MLCK) activation by Ca^{2+} phosphorylates myosin light chain (MLC), which results in cell rear-end retraction and allows the cell to migrate toward the front (Yang and Huang, 2005). A conformational change occurs when S100A4, a member of the S100 family of EF-hand calcium-binding proteins, binds to calcium to cause the exposure of its interaction domain, which allows the protein to interact with various cytoskeletal proteins such as actin, non-muscle myosin IIA, non-muscle myosin IIB, myosin heavy chain IIA, and tropomyosin (Kim and Helfman, 2003; Tarabykina et al., 2007). Furthermore, RasGRF1 is activated in a calcium-dependent manner through interaction between its isoleucine-glutamine

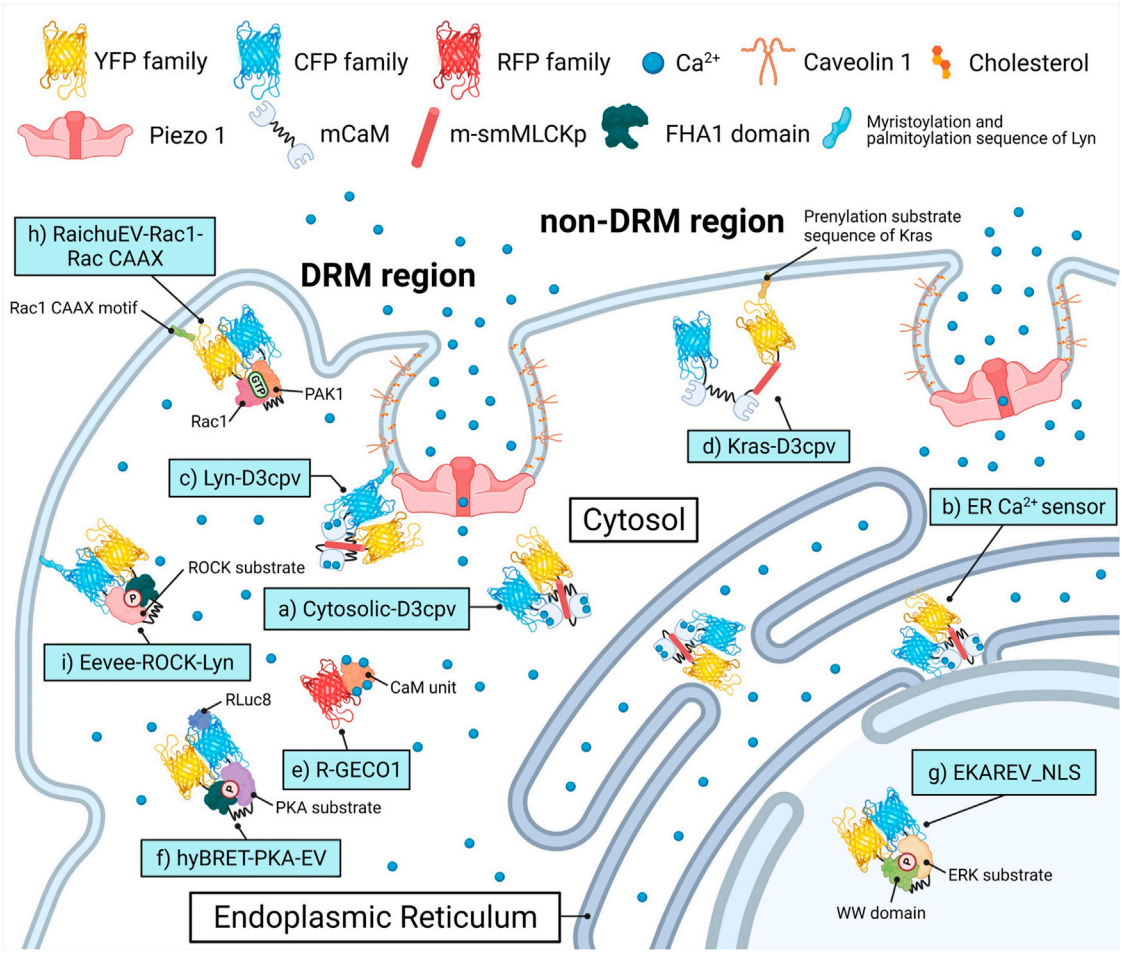

FIGURE 1 | Biosensors and targeting strategies employed in this study. Each of the biosensors visualized the target's activity in a specific microenvironment and was expressed solely to avoid crosstalk between optical signals of fluorescence proteins. **(A)** Cytosol Ca^{2+} indicator, Cytosolic-D3cpv used in **Figures 2**, **5**. **(B)** Endoplasmic reticulum (ER) Ca^{2+} indicator, ER Ca^{2+} sensor used in **Figure 3**. **(C)** DRM region Ca^{2+} indicator, Lyn-D3cpv used in **Figure 4**. **(D)** non-DRM region Ca^{2+} indicator, Kras-D3cpv used in **Figure 4**. **(E)** Cytosolic Ca^{2+} indicator, R-GECO1 used in **Figure 4**. **(F)** PKA activity indicator, hyBRET-PKA-EV used in **Figure 6**. **(G)** ERK activity indicator, EKAREV_NLS used in **Figure 6**. **(H)** Rac1 activity indicator, RaichuEV-Rac1-Rac CAAX used in **Figure 7**. **(I)** ROCK activity indicator, Eevee-ROCK-Lyn used in **Figure 7**. DRM, detergent-resistant membrane. YFP, yellow fluorescent protein. CFP, cyan fluorescent protein. RFP, red fluorescent protein. (m) CaM, (mutated) calmodulin. m-smMLCKp, mutated smooth muscle myosin light chain kinase peptide. FHA1, forkhead-associate 1. PAK1, p21 activated kinase 1. PKA, protein kinase A. ERK, extracellular signal-regulated kinase. Rac1, Rac-GTP complex bound to the P21. ROCK, Rho-associated protein kinase. RLuc8, Renilla luciferase 8.

domain and calmodulin and acts as RacGEF, which activates Rac1 by exchanging Rac1-bound GDP for GTP (Buchsbaum et al., 1996; Zippel et al., 2000; Umeda et al., 2018). The activated Rac1 leads to lamellipodium extension and membrane ruffling by inducing branched actin filament polymerization (Ridley et al., 1992; Connolly et al., 2005). Consequently, calcium and the related signals upregulate cancer cell migration by enhancing focal adhesion turnover, cell rear-end retraction, interaction with cytoskeletal proteins, and branched actin filament polymerization.

Although the biological pathways and phenomena that are triggered by Ca^{2+} influx through various channels have been widely studied, the effects of Piezo1 on these phenomena remain unclear. In this study, a variety of biosensors were adopted to visualize various cellular-physiological activities triggered by Piezo1-induced Ca^{2+} flux in the single-cell microenvironment level (**Figure 1**). We evaluated calcium signal dynamics in the cytoplasm and the endoplasmic reticulum (ER) lumen in response to Yoda1, the plasma membrane microdomain and cytoskeletal structure required for the normal function of Piezo1, and the cellular pathways and membrane ruffling induced by extracellular calcium influx. We found that Piezo1-induced calcium flux upregulated membrane ruffling and cancer cell survival.

MATERIALS AND METHODS

DNA Plasmids and Gene Construction

The detailed information of all plasmids and primer sequences used are listed in **Supplementary Tables S1, S2**, respectively. Restriction enzyme cloning was performed to construct new

plasmids, and the procedure is described in **Supplementary Table S3**. All PCR products were directly sequenced for genetic confirmation by Macrogen (Republic of Korea).

Cell Culture and Transfection

The MCF-7, SiHa, and BeWo cell lines were purchased from the Korean Cell Line Bank (KCLB; Seoul, Republic of Korea), and HEK293A and HeLa cell lines were provided by Dr. Jihye Seong (Korea Institute of Science and Technology, Seoul, South Korea). The MCF-7 cells were cultured in RPMI-1640 medium (CM058; GenDEPOT, Barker, TX, United States) supplemented with 10% (v/v) fetal bovine serum (FBS; WB0015; HyClone), 100 U/mL penicillin, 100 μg/ml streptomycin (CA005, GenDEPOT), and 0.01 mg/ml insulin solution from bovine pancreas (I0516, Sigma). The HEK293A, HeLa, and SiHa cells were cultured in Dulbecco's modified Eagle's medium (DMEM; CM002, GenDEPOT) containing 10% (v/v) FBS, 100 U/ml penicillin, and 100 μg/ml streptomycin. The BeWo cells were cultured in DMEM/F-12 medium (LM002-08, Welgene) supplemented with 10% (v/v) FBS, 100 U/ml penicillin, and 100 μg/ml streptomycin. The cells were cultured in a humidified incubator with 95% air and 5% CO_2 at 37°C. The DNA plasmids were transfected into the cells using Lipofectamine 3000 (L3000, Invitrogen) following the manufacturer's protocol.

Solutions and Chemicals

To prepare the Ca^{2+}-free medium, Hank's balanced salt solution (HBSS; 14175-095, Gibco) was supplemented with 20 mM hydroxyethylpiperazine ethane sulfonic acid (HEPES; Dojindo), 0.5 mM ethylene glycol-bis(2-aminoethylether)-N,N,N',N'-tetraacetic acid (EGTA; E3889, Sigma), 1 mM magnesium chloride ($MgCl_2$; M8266, Sigma), and 1 mM magnesium sulfate ($MgSO_4$; 746452, Sigma) (Kim et al., 2015). To prepare the Ca^{2+} medium, HBSS was supplemented with 20 mM HEPES, 1 mM $MgSO_4$, and 1 mM calcium chloride ($CaCl_2$; 18230S0301, JUNSEI). The Ca^{2+} medium did not include EGTA, a calcium chelator, or $MgCl_2$, a supplemented ion. To represent normal conditions, CO_2-independent culture medium (18045088, Gibco) containing 0.5% (v/v) FBS, 4 mM L-glutamine (LS002-1, Welgene), 100 U/ml penicillin, and 100 μg/ml streptomycin was used. Yoda1 (SML1558), methyl-β-cyclodextrin (MβCD; 332615), ML-7 (I2764), gadolinium (III) chloride hexahydrate (G7535), and thapsigargin (T9033) were purchased from Sigma-Aldrich. Nocodazole (S2775) was purchased from Selleckchem. Cytochalasin D (ab143484) was obtained from Abcam.

Viability Assay

The WST-8 assay was used to determine the cell viability. The MCF-7 cells were seeded at 8×10^3 cells/well in 96-well plates and incubated for 24 h at 37°C before being treated with an RPMI-containing control (0.5% DMSO) or Yoda1 (0.1–25 μM) for 24 h. After washing, the cells were treated with Cellrix Viability Assay kit (B1007-500, MediFab) in DMEM without phenol red (31053028, Gibco) for 2 h at 37°C. The optical density of the solubilized formazan product was measured using a Glomax Multi + Microplate Multi Reader (9,301–010, Promega, United States) at a wavelength of 450 nm.

Reverse Transcription-Polymerase Chain Reaction

Total RNA was extracted from MCF-7 cells with TRIsure (BIO-38033, Bioline), and 300 ng of total RNA was used for cDNA synthesis using the Compact cDNA Synthesis kit (SG-CDNAC100, SmartGene) according to the manufacturer's instructions. To evaluate gene expression levels, RT-PCR was performed with 2× Dye Mixed Hot Start Taq (SG-2XDM-HTaq, SmartGene) following the manufacturer's protocol. The bands of PCR products were measured densitometrically using ImageJ software version 1.53c (National Institutes of Health; https://imagej.nih.gov/ij). Glyceraldehyde-3- phosphate dehydrogenase (GAPDH) expression was used as a loading control.

Western Blotting

After washing with cold phosphate-buffered saline (PBS; LB004-02, WELGENE), cells were lysed with the CETi lysis buffer with inhibitors (TLP-121CETi, TransLab) and centrifuged at 13,000 rpm for 15 min at 4°C. Protein concentration was determined using a Pierce BCA Protein Assay Kit (23227, Thermo Scientific) following the manufacturer's protocol. Each lysate was added to 5× SDS-PAGE Sample Buffer (TLP-102.1, TransLab) and heated at 100°C for 5 min. Proteins (50 μg/lane) were loaded onto 8% SDS-polyacrylamide gel, subjected to electrophoresis, and then transferred to an Immobilon-P PVDF Membrane (IPNH00010, Merck Millipore). The membranes were blocked in 5% (w/v) skim milk in Tris-buffered saline with Tween 20 at pH 7.4 (TBST; TLP-118.1, TransLab) for 1 h 30 min at 20°C. Membranes were incubated with the following primary antibodies in 5% (w/v) skim milk in TBST: anti-PIEZO1 (MBS435119, MyBioSource) diluted 1:500 and anti-GAPDH (HC301, TransGen Biotech) diluted to 1:2000; at 4°C overnight. The membranes were then washed three times with TBST and incubated with horseradish peroxidase-conjugated anti-mouse IgG secondary antibodies (1:2,000; sc-516102, Santa Cruz) in 1% (w/v) skim milk and TBST at 20°C for 60 min. Immunoreactive protein bands were detected using ECL Ottimo (TLP-112.1, TransLab) and measured densitometrically using an iBright FL1500 Imaging System (A44241, Invitrogen) and ImageJ software. GAPDH was used as the loading control.

Microscopy and Image Acquisition and Analysis

Cells expressing several exogenous proteins were cultured in a confocal dish (100350, SPL Life Sciences) and starved in RPMI-1640 or DMEM containing 0.5% (v/v) FBS for 6 h before imaging. Shortly before the experiment, the cells were washed, and the medium was replaced appropriately according to the experimental conditions. Images were obtained using a Leica DMi8 THUNDER microscope equipped with a scientific complementary metal-oxide-semiconductor (sCMOS) camera (K5, Leica), HC PL APO 40x/1.30 OIL objective lens (11506329, Leica), HC PL APO 100x/1.40–0.70 OIL objective lens (11506220, Leica), CYR71010 filter cube (11525416, Leica), and DFT51010 filter cube (11525418, Leica). Throughout the live

imaging, the temperature was maintained at 37°C by an HX Controller (DHC2-0N1C03N, LCI). The detailed filter sets for the fluorescence channels are listed in **Supplementary Table S4**. The LASX software version 3.6.0. (Leica, https://www.leica-microsystems.com/products/microscope-software/p/leica-las-x-ls/). was used to acquire images and compute the fluorescence emission intensity. A specific region was selected as a region of interest (ROI) to observe the signals and perform quantification. The fluorescence intensity in the background region was selected and quantified to remove the signal from the ROI of the fluorescence channels. The ratio images were displayed in the intensity-modified display mode, where the color of the pixel was determined by the FRET/CFP ratio and red fluorescence protein (RFP) intensity. Quantified values were analyzed using the GraphPad Prism (version 7.0.0) software for Windows (GraphPad Software; https://www.graphpad.com/). The control groups showed that the imaging environments, including temperature, pH, and drug treatment process, did not disturb the cell physiology.

Spatiotemporal Image Correlation Spectroscopy Analysis

Spatiotemporal Image Correlation Spectroscopy (STICS) analysis was used to determine the direction and velocity of the GFP-cortactin localized in the lamellipodia of cells using the ImageJ plugin STICS map jru v2 (Stowers Institute for Medical Research in Kansas City; https://research.stowers.org/imagejplugins/), which actualizes a method developed by Hebert et al. After visualizing the membrane ruffling by live-cell imaging, the LASX software corrected the background of the fluorescence images and exported successive images in the AVI format. The ImageJ software converted the video files to grayscale and 32-bit images and executed the STICS map jru v2. For one experimental group, we analyzed 12 independent cells and selected one ROI per cell. The ROI consisted of 9 (3 × 3) particles. The obtained flow mapping images were overlaid with gray-scaled GFP-cortactin images, and the velocity values were analyzed statistically.

Statistical Analysis

All results are expressed as mean ± standard error of the mean (SEM) with GraphPad Prism 7.0.0. Statistical analyses were performed using unpaired two-tailed *t*-test to determine the statistical significance of the differences between two groups. We considered the *p*-values at *<0.05, **<0.01, ***<0.001, and ****<0.0001 to be statistically significant.

RESULTS

Piezo1-Mediated Extracellular Ca^{2+} Influx and Endoplasmic Reticulum-Stored Ca^{2+} Release by Yoda1

Yoda1 was used to activate the Piezo1 channel in order to visualize Ca^{2+} influx through the channel and the associated cell biological activity. We performed a viability assay before the live-cell imaging to determine the appropriate treatment concentration and the cytotoxicity of Yoda1 (**Figure 2A**). All experimental groups that were administered Yoda1 did not show cell death and survived to a higher extent compared to the control group; 0.1–10 μM Yoda1 increased cell viability in a dose-dependent manner, and the increase in viability was relatively low but still higher than that of the control at 25 μM (**Figure 2A**). Thus, treatment with Yoda1 enhanced cell viability, and a concentration range of 1–5 μM Yoda1 was applied to the cells in this study. Next, reverse transcription-polymerase chain reaction (RT-PCR) and Western blotting were performed to confirm the function of Piezo1 shRNA used in this study (**Figures 2B–E**). Piezo1 shRNA lowered the mRNA level of Piezo1 to 54% and the protein level to 31%, whereas the cells transfected with the control shRNA did not show a decrease in the mRNA and protein levels, revealing that the introduction of Piezo1 shRNA silenced the channel specifically (**Figures 2B–E**).

We transfected cytosolic-D3cpv, a FRET-based cytosolic Ca^{2+} indicator, into MCF-7 cells which express Piezo1 endogenously (**Figures 2F,G**) to detect Yoda1-induced extracellular Ca^{2+} influx. The biosensor had been designed to report an increased FRET/CFP ratio when the calcium level in the cytoplasm increases. We observed an increase in cytosolic Ca^{2+} levels when Yoda1 was added to the cells expressing cytosolic-D3cpv that were incubated in a CO_2-independent culture medium (Yoda1 group). Next, Yoda1 was administered to cells co-transfected with cytosolic D3cpv and Piezo1 shRNA to verify that calcium influx was dependent on Piezo1, but not other calcium-permeable channels, evidenced by a significant decrease in the FRET/CFP ratio (Yoda1 + Piezo1 KD group). To confirm that the increase in the FRET/CFP ratio was specifically caused by extracellular Ca^{2+} influx, we utilized a Ca^{2+}-free medium (Yoda1 + w/o Ca^{2+} group) to create a Ca^{2+}-free environment outside the cell. A significant reduction in the ratio was also observed. We reaffirmed that the decrease in the FRET/CFP ratio was specifically due to calcium, and not due to any other ions unintentionally excluded, using cells incubated in the Ca^{2+} medium (Yoda1 + w/Ca^{2+} group), and observed a higher FRET/CFP ratio in these cells compared to that the Yoda1 group. Collectively, our results showed that Yoda1 induced extracellular Ca^{2+} influx by specifically stimulating Piezo1, and the FRET/CFP ratio obtained by cytosolic-D3cpv was influenced specifically by calcium and represented the change in Ca^{2+} levels in the cytoplasm (**Figures 2F,G**).

We next visualized the cytoplasmic calcium levels of various cell lines treated with Yoda1 to study whether the Yoda1-induced dynamics of extracellular Ca^{2+} influx are different in different cell lines. We co-transfected the biosensor and Piezo1-tdTomato into these cell lines and observed FRET/CFP ratio change after Yoda1 treatment (**Figures 2H–J**), while both the native HEK293A and HeLa cell lines transfected with cytosolic D3cpv did not show FRET/CFP ratio change. Although HEK293 and Hela cells endogenously express functional Piezo1 (McHugh et al., 2010; Dubin et al., 2017), the expression levels may not be sufficient to respond to 1 μM Yoda1. The results obtained confirmed that Yoda1 specifically activated Piezo1. In contrast to the MCF-7 cells, both the HEK293A and HeLa cell lines transfected with

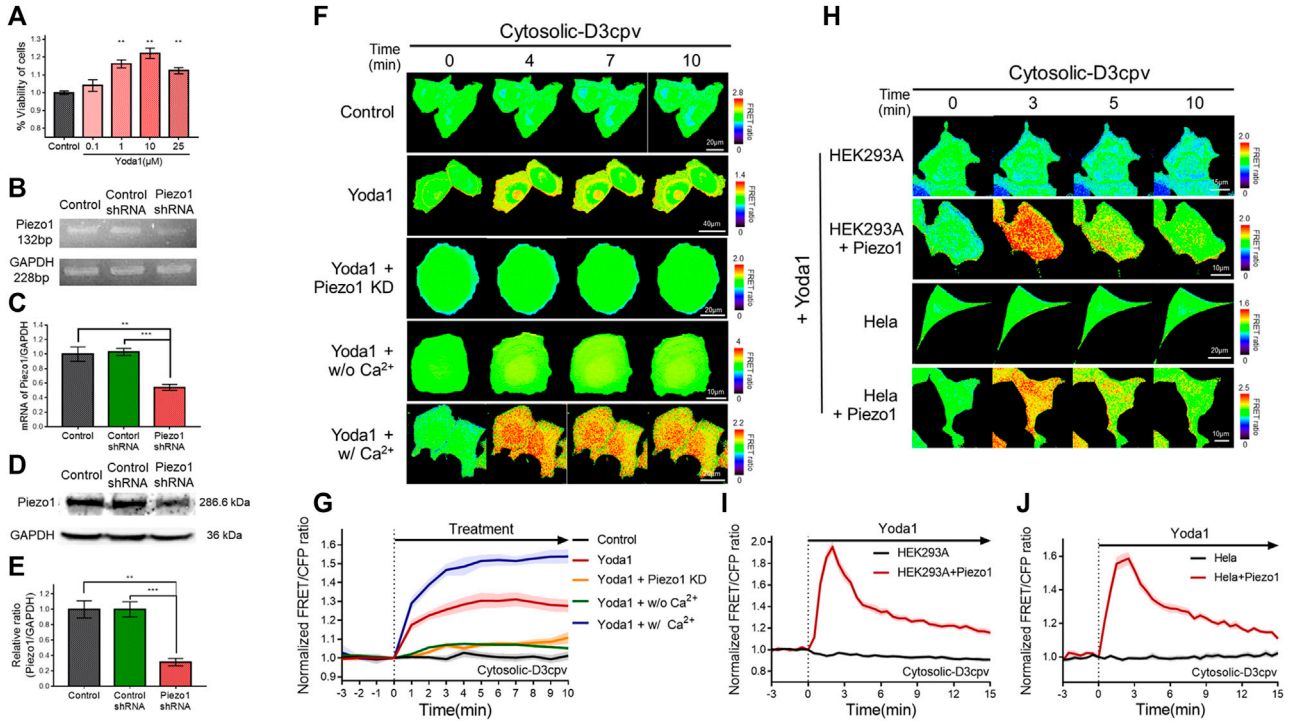

FIGURE 2 | Piezo1-mediated extracellular Ca^{2+} influx induced by Yoda1 in various cell lines. **(A)** Viability of MCF-7 cells exposed to control [0.2% (v/v) DMSO] and Yoda1 (0.1–25 μM) for 24 h, measured using the WST-8 assay. The bar graphs describe mean values of cell viability with error bars indicating the standard error of the mean (S.E.M) (n = 4, $^{**}p < 0.01$, student t-test). **(B,D)** Piezo1 expression in MCF-7 cells with or without control/Piezo1 shRNA as analysed by **(B)** RT-PCR and **(D)** western blotting. GAPDH was used as an internal control. **(C,E)** The bar graphs describe the cumulative densitometric analysis of **(C)** RT-PCR and **(E)** western blot bands normalized to the GAPDH. Data are presented as the means ± S.E.M (n = 4, $^{**}p < 0.01$ and $^{***}p < 0.001$, student t-test). **(F,H)** Time-lapse FRET images of the Cytosolic-D3cpv in **(F)** MCF-7 cells, **(H)** HEK293A and HeLa cells introduced with or without exogenous Piezo1. MCF-7 cells were exposed to control [0.2% (v/v) DMSO] and Yoda1 (1 μM) dissolved in CO_2-independent culture medium (Yoda1 group), Ca^{2+}-free medium (Yoda1 + w/o Ca^{2+} group), and Ca^{2+} medium (Yoda1 + w/Ca^{2+} group), respectively. **(F)** Yoda1 + Piezo1 KD group and **(H)** HEK293A and HeLa cells were incubated in CO_2-independent culture medium. The color scale bars represent the range of the FRET/CFP emission ratio determined using the biosensor. Hot and cold colors indicate high and low Ca^{2+} concentration, respectively. **(G,I,J)** The time courses represent the average of the normalized FRET/CFP emission ratio changes of cytosolic-D3cpv in **(G)** MCF-7, **(I)** HEK293A, and **(J)** HeLa cells. The lines are mean values of normalized emission ratios, with diluted colors indicating the S.E.M (n = 7).

Piezo1 revealed a relatively short duration of FRET/CFP ratio peak and faster recovery of the ratio to the baseline (**Figures 2I,J**). We administrated Yoda1 to SiHa and BeWo cell lines, which express Piezo1 endogenously, and observed that the SiHa cells showed relatively slow recovery of the calcium level to the baseline, similar to the observation with the MCF-7 cells. However, the calcium signal dynamics in the BeWo cells were similar to those of the HEK293A and HeLa cells transfected with exogenous Piezo1 (**Supplementary Figure S2**). Thus, these results suggested that the calcium influx caused by Yoda1-treated Piezo1 and its dynamics differed depending on the cell line.

We determined whether the calcium concentration in the ER changed when cells were treated with Yoda1 since a slight increase in cytosolic calcium levels was observed when the cells were exposed to Yoda1 under Ca^{2+}-free conditions (**Figure 2G**). The ER Ca^{2+} sensor, which has a calreticulin signal sequence (CRsig) and ER retention sequence (KDEL) at the N terminus and C terminus of cytosolic-D4cpv, respectively (Kim et al., 2017), was expressed in the MCF-7 cells, and live imaging was conducted, which revealed that ER calcium levels decreased when the cells were exposed to Yoda1 (**Figures 3A–C**). Interestingly, the Yoda1 + w/o Ca^{2+} group, which was in an extracellular calcium-free environment, released more calcium than the Yoda1 and Yoda1 + w/Ca2+ groups in extracellular calcium. Therefore, we assumed that calcium restoration in the ER does not occur properly if cells were not supplied with calcium from the extracellular region. Additionally, the results suggest that Yoda1-induced ER-stored calcium release did not require extracellular calcium. In addition, we administrated Yoda1 after gadolinium (Gd^{3+}) pre-treatment, which reduces the extracellular calcium influx mediated by Piezo1 (Deivasikamani et al., 2019). We hypothesized that cells exposed to Gd^{3+} release more ER stored Ca^{2+}, which is mediated by ER membrane-located Piezo1, in response to Yoda1 than "Yoda1" experimental group, although there is calcium in the extracellular region. In groups administrated with Gd^{3+}, 1 μM Yoda1 led to a higher FRET ratio decrease than the Yoda1 group (**Supplementary Figure S3**). To confirm the Piezo1-indeced ER-stored Ca^{2+} dynamics, we treated thapsigargin (TG), which depletes Ca^{2+} in ER, before Yoda1 treatment. Interestingly, Yoda1 resulted in immediate calcium influx into ER in the presence of extracellular calcium

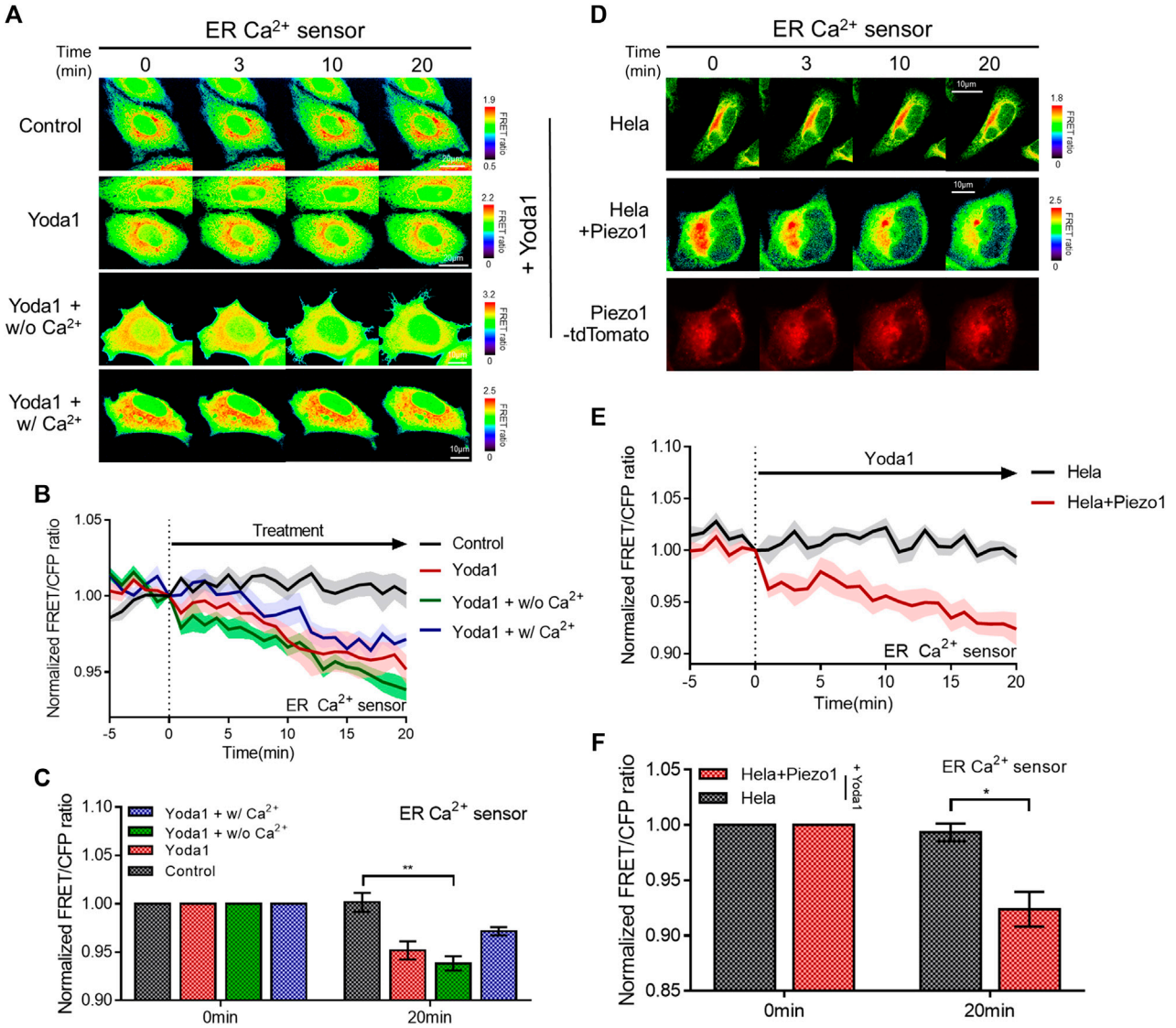

FIGURE 3 | Piezo1-dependent ER-stored Ca^{2+} release in response to Yoda1. **(A,D)** Time-lapse FRET images of the ER Ca^{2+} sensor in **(A)** MCF-7 and **(D)** HeLa cells. The cells were exposed to control [0.2% (v/v) DMSO] and Yoda1 (1 μM) dissolved in CO_2-independent culture medium (Yoda1 group), Ca^{2+}-free medium (Yoda1 + w/o Ca^{2+} group), and Ca^{2+} medium (Yoda1 + w/Ca^{2+} group), respectively. The color scale bars represent the range of the FRET/CFP emission ratio determined using the biosensor. Hot and cold colors indicate high and low Ca^{2+} concentration, respectively. **(D)** The red fluorescence protein images confirmed the expression of Piezo1-tdTomato. **(B,E)** The time courses represent the average of the normalized FRET/CFP emission ratio changes of the ER Ca^{2+} sensor. The lines are mean values of the normalized emission ratios, with diluted colors indicating the S.E.M (n = 7). **(C,F)** The bar graph describes the mean values of the normalized FRET/CFP emission ratios of the ER Ca^{2+} sensor at the described time with error bars indicating the S.E.M (n = 7, $^*p < 0.05$ and $^{**}p < 0.01$, Student's t-test).

(**Supplementary Figure S4**). We assume that Piezo1-mediated extracellular Ca^{2+} influx increases cytosolic calcium concentration and the ion flow into ER via routes except for Piezo1. However, Piezo1-mediated ER calcium influx occurred slowly in the absence of extracellular calcium (**Supplementary Figure S4**). Recently, it was reported that Piezo1 is at various subcellular organelles, in particular mitochondria, and the channel activation increases cytosolic Ca^{2+} concentration (Liao et al., 2021). Mitochondria have a relatively higher Ca^{2+} concentration than the cytoplasm (Arnaudeau et al., 2001). Therefore, these results could suggest that Yoda1 activates Piezo1 located at mitochondria and leads to mitochondria-stored Ca^{2+} efflux, and the ion was slowly introduced into ER deficient in calcium through other pathways except Piezo1. Next, we monitored the ER-stored Ca^{2+} level of the HeLa cell line to examine whether ER-stored calcium release depended on Piezo1 expression and found that extracellular Ca^{2+} influx was not observed in response to Yoda1 (**Figures 3D–F**). HeLa cells expressing the ER Ca^{2+} sensor alone did not trigger a decrease in the FRET/CFP ratio. However, the cells co-transfected with the

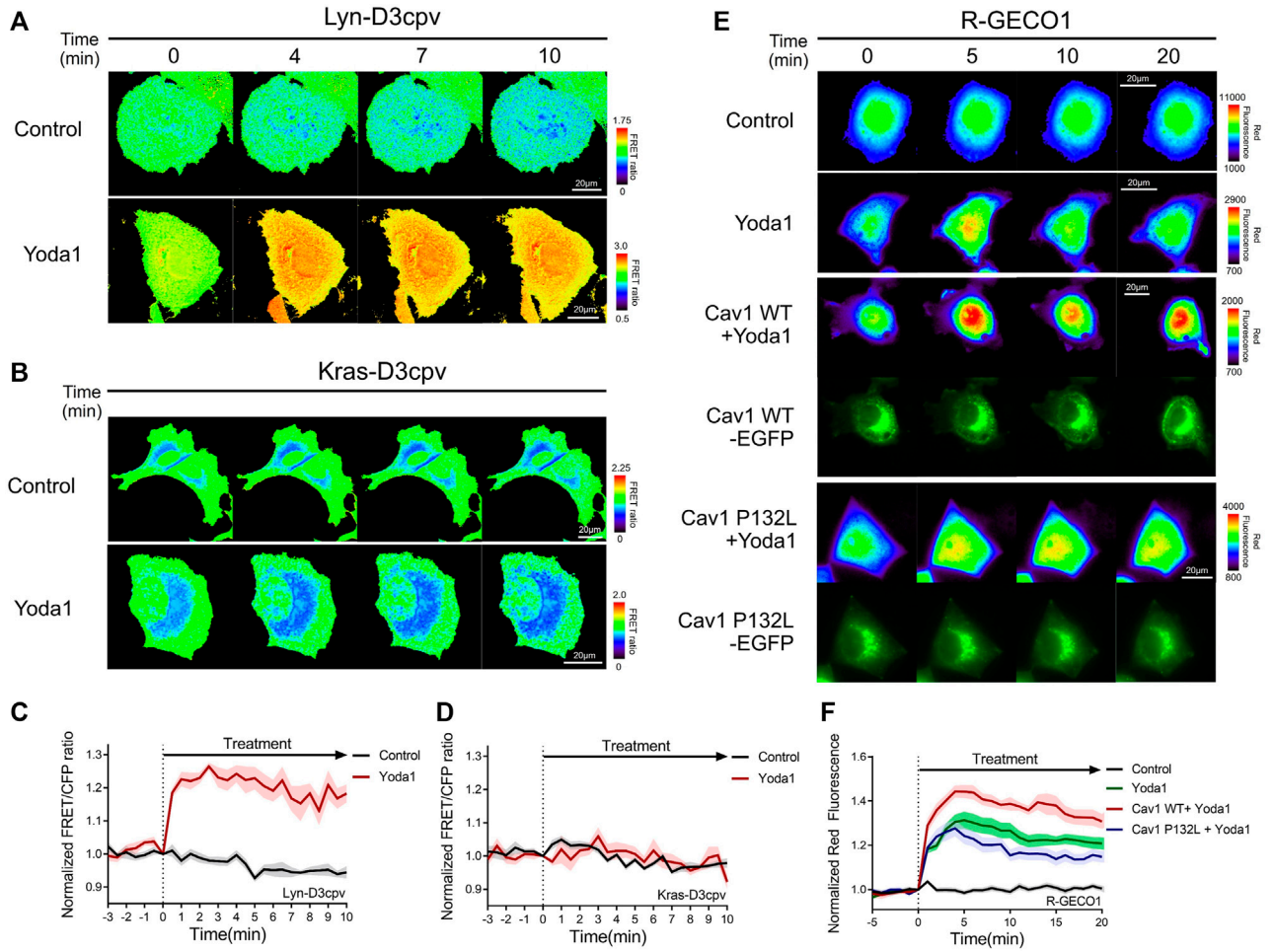

FIGURE 4 | Detergent-resistant membrane (DRM) and caveolin were required for normal Piezo1 function. **(A,B)** Time-lapse FRET images of the **(A)** Lyn-D3cpv and **(B)** Kras-D3cpv in MCF-7 cells. **(E)** Time-lapse red fluorescence protein (RFP) emission ratio images of the R-GECO1 in MCF-7 cells transfected with Cav1 WT and Cav1 P132L. The cells were exposed to the control [0.2% (v/v) DMSO] and Yoda1 (1 μM) dissolved in CO_2-independent culture medium. The color scale bars represent the range of the **(A,B)** FRET/CFP or **(E)** RFP emission ratios determined using the biosensor. Hot and cold colors indicate high and low Ca^{2+} concentrations, respectively. The images of green fluorescence channel confirmed the expression of the intended caveolin-1 constructs **(C,D,F)** The time courses represent the average of the normalized **(C,D)** FRET/CFP emission ratio changes of **(C)** Lyn-D3cpv and **(D)** Kras-D3cpv, and **(F)** RFP emission ratio changes of R-GECO1. The lines are mean values of the normalized emission ratios, with diluted colors indicating the S.E.M [**(C,D)** $n = 7$, **(F)** $n = 20$ for control and Cav1 P132L + Yoda 1, and $n = 14$ for Yoda1 and Cav1 WT + Yoda1].

biosensor and exogenous Piezo1 showed ER-stored calcium release (**Figures 3D–F**). Therefore, Yoda1 induced ER calcium release by activating Piezo1, and the degree of ER calcium release was affected by extracellular Ca^{2+} levels.

Intact Caveolin, Cholesterol, and Various Cytoskeletal Structures Are Required for the Normal Function of Piezo1

The detergent-resistant membrane (DRM), known as a lipid raft, is a membrane microdomain that contains an amount of sphingolipid and cholesterol and acts as a scaffold for many different signaling pathways because a variety of integral membrane proteins are embedded in it, such as insulin-like growth factor-I receptor and phosphoinositide 3-kinases (Huo et al., 2003; Mollinedo and Gajate, 2015). Caveolae, a subset of DRM characterized by omega-or cup-shaped membrane microdomains, contains caveolins that line the membrane and stabilize the caveolae structure (Pelkmans et al., 2004; Schlörmann et al., 2010). Lipid rafts and caveolar microdomains play essential roles in modulating calcium signals because these structures contain various key proteins, which are associated with Ca^{2+}, such as STIM1, CaMK2, PKC, and PLC (Pani and Singh, 2009). In particular, cholesterol and multiple signaling molecules in the microdomain interact with diverse ion channels and regulate the function and membrane localization of channels (Levitan et al., 2010). It has been reported that methyl-β-cyclodextrin (MβCD), a cholesterol-depletion agent, completely reduced the β2-adrenergic stimulation of Cav1.2 channels (Balijepalli et al., 2006; Tsujikawa et al., 2008)

and suppressed the activity of mechanosensitive channels in human leukemia K562 cells (Morachevskaya et al., 2007). TRPM7 was reported to localize in fractions associated with caveolae in bradykinin-stimulated cells, suggesting that TRPM7-caveolae-lipid raft association may facilitate the localization of TRPM7 to cell membrane receptors (Yogi et al., 2009). Components of membrane microdomain also play a role in Piezo1 activation and inactivation; margaric acid inhibits Piezo1 activation, and polyunsaturated fatty acids modulate channel inactivation (Romero et al., 2019). In addition, cholesterol depletion with MβCD caused a shift in the midpoint activation pressure of Piezo1, increased channel latency, and slowed channel inactivation (Ridone et al., 2020).

Live-cell imaging was performed to study the location and functions of Piezo1, and whether this channel requires lipids and membrane microdomain structures/for its normal function. We employed two distinct types of FRET-based Ca^{2+} biosensors tethered at DRM and non-DRM microdomains (Kim et al., 2018) (**Figures 4A–D**) to assess the variation of Piezo1-induced calcium influx with the type of membrane microdomains. Lyn-D3cpv is used to visualize the calcium signal of the DRM region by using the myristoylation and palmitoylation sequence of Lyn kinase at the N-terminal sequence of cytosolic D3cpv. Kras-D3cpv, which has a prenylation substrate sequence of Kras at the C-terminus of cytosolic D3cpv, was utilized to observe the change in calcium concentration in the non-DRM region. We observed a change in the FRET/CFP ratio when the cells transfected with Lyn-D3cpv were exposed to Yoda1, indicating the occurrence of Ca^{2+} influx at the DRM region. However, the FRET/CFP ratio did not change in the group transfected with Kras-D3cpv (**Figures 4A–D**). Next, we investigated whether mutated caveolin-1 influences Yoda1-induced Piezo1 Ca^{2+} gating function. MCF-7 cells were co-transfected with R-GECO1, a red fluorescent genetically encoded Ca indicator (Zhao et al., 2011), and caveolin-1 wild-type (Cav1 WT) or caveolin 1 P132L (Cav1 P132L), a mutant that has oligomerization defects and accumulates in the ER or Golgi apparatus and does not support caveolae formation (Hayer et al., 2010) (**Figures 4E,F**). In response to Yoda1, the expression of wild-type caveolin 1 in the plasma membrane (Cav1 WT + Yoda1 group) induced a relatively higher Piezo1-mediated Ca^{2+} influx than the Yoda1 group, which only expresses R-GECO1 (**Figures 4E,F**). The cells expressing Cav1 P132L showed a relatively lower calcium influx than that in the Cav1 WT group post-treatment with Yoda1 (**Figures 4E,F**).

Live cell imaging was then performed to verify whether the integrity of cholesterol in the lipid raft is required for the normal function of Piezo1. We administered Yoda1 after the cholesterol of cells expressing cytosolic D3cpv was depleted by using 5 mM MβCD for 1 h. No cytosolic calcium influx (**Figures 5A,B**) was observed. In previous work, which used relatively low concentrations of MβCD, the cholesterol depletion interfered with the dynamics of 5 μM Yoda1-induced calcium signaling (Chong et al., 2021). Our results showed that Piezo1-mediated Ca^{2+} influx dynamics by 1 μM Yoda1 could absolutely be destroyed by 5 mM MβCD pretreatment. These results are consistent with earlier reports that the compressive stress-induced calcium influx via Piezo1 is reduced following the reduction of Cav1 expression and MβCD treatment (Mingzhi et al., 2019). Collectively, our results show that Piezo1 mainly induced calcium influx in the DRM region, and the integrity of the caveolin and the cholesterol constituting the lipid raft is required for the normal function of Piezo1.

There are three major cytoskeleton structures connected to the cell plasma membrane: Actin filaments, microtubules, and actomyosin (Sitarska and Diz-Muñoz, 2020). These structures support the membrane and play an essential role in mechanotransduction (Gittes et al., 1993; Ananthakrishnan and Ehrlicher, 2007; Clark et al., 2007; Salbreux et al., 2012; Murrell et al., 2015; Morley et al., 2016; Pandya et al., 2017; Yan et al., 2018). We hypothesized that changes in the cytoskeletal support affect the function of Piezo1, which detects mechanical stress from the membrane and extracellular microenvironments. Cells expressing cytosolic D3cpv were pretreated with cytochalasin D (CytoD), which disrupts actin microfilaments (Brenner and Korn, 1980); nocodazole (Noco), which binds to β-tubulin and interferes with the polymerization of microtubules (Mejillano et al., 1996); and ML-7, an MLCK inhibitor (Saitoh et al., 1987) for 30 min, 1 h, and 1 h respectively, and exposed to Yoda1 (**Figures 5C–E**) to examine Piezo1-mediated calcium signals in cells where specific single cytoskeleton structure was compromised. We observed that CytoD pretreatment had a negligible effect on calcium influx dynamics. However, cells with microtubule disruption induced by Noco (Noco group) and ML-7 group having abnormal actomyosin activity took a longer time to reach the maximum FRET/CFP ratio value compared to that in the control and CytoD groups (**Figures 5C–E**). Collectively, our results suggest that the integrity of the microtubules and actomyosin is required for the calcium signal dynamics caused by Yoda1-induced Piezo1 activation to function properly. Cells implicates the cytoskeleton in the dynamics of the Ca^{2+} signaling not the magnitude, thus they are for all intents and purposes dispensable for the Yoda-1 mediated activation of Piezo1.

Yoda1 Promoted PKA, ERK, Rac1, and ROCK Activity in an Extracellular Ca^{2+}-And Piezo1-Dependent Manner

We investigated the biological pathways that are activated by Piezo1-mediated extracellular calcium influx, since increased cytosolic calcium has an effect on various cell signaling pathways. We used the hyBRET-PKA-EV and EKAREV_NLS biosensors, which are designed to show increased FRET/CFP ratios by the activation of PKA and ERK, respectively, to examine whether increased cytosolic calcium promotes the PKA and ERK signaling pathways that enhance cell survival and proliferation (**Figures 6A–F**) (Komatsu et al., 2011; Komatsu et al., 2018). Yoda1-induced activation of PKA and ERK was observed in the cells of the Yoda1 group incubated in a CO_2-independent culture medium, but this increase was significantly reduced in the Piezo1 KD group. We observed a decrease in the FRET/CFP ratio in the absence of extracellular calcium. We then reaffirmed whether the decrease in the FRET/CFP ratio resulted only from calcium by using a medium containing Ca^{2+} (Yoda1 + w/Ca^{2+}

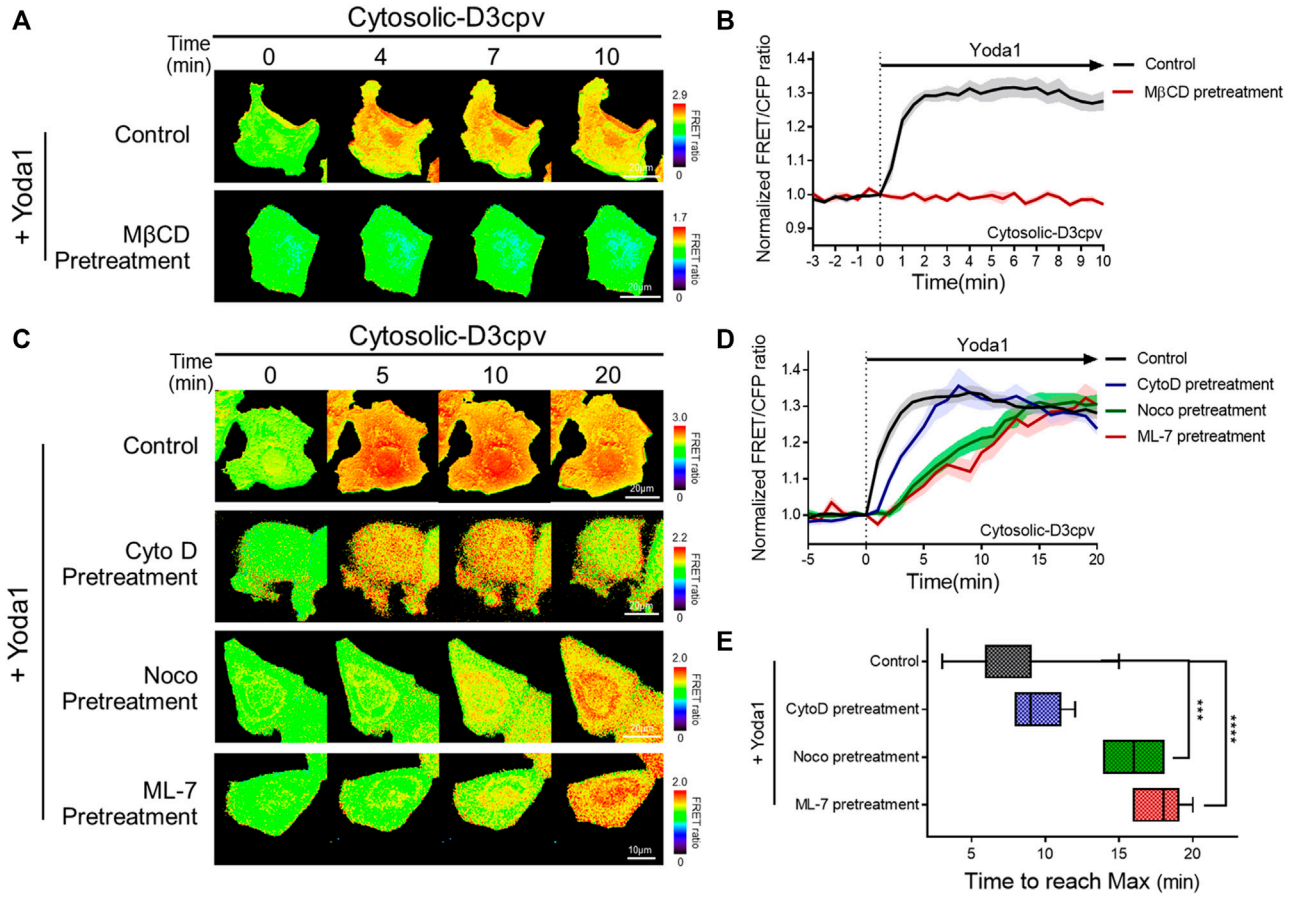

FIGURE 5 | Intactness of cholesterol, microtubules, and actomyosin structures plays an important role in the normal function of Piezo1. **(A,C)** Time-lapse FRET images of the cytosolic-D3cpv in untreated MCF-7 cells and cells pretreated with **(A)** MβCD, **(C)** cytochalasin D (CytoD), nocodazole (Noco), and ML-7. All cells were exposed to Yoda1 (1 μM) dissolved in CO_2-independent culture medium. The color scale bars represent the range of the FRET/CFP emission ratio detected using the biosensor. Hot and cold colors indicate high and low Ca^{2+} concentrations, respectively. **(B,D)** The time courses represent the average of the normalized FRET/CFP emission ratio changes of the cytosolic-D3cpv in **(B)** MβCD, **(D)** CytoD, Noco, and ML-7 pretreatment groups. The lines are mean values of normalized emission ratios, with diluted colors indicating the S.E.M ($n = 7$). **(E)** The box plots describe the time taken to reach the maximum value of the FRET/CFP ratio in the control, CytoD, Noco, and ML-7 pretreatment groups with whiskers representing minimum and maximum values, respectively. ($n = 7$, $^{***}p < 0.001$ and $^{****}p < 0.0001$, Student *t*-test).

group), and observed a higher FRET/CFP ratio compared to that observed in the Yoda1 group (**Figures 6A–F**).

Subsequently, the RaichuEV-Rac1-Rac CAAX and Eevee-ROCK-Lyn biosensors were employed to visualize the activity of Rac1 and ROCK, which is a downstream effector of RhoA. The forementioned biosensors detect an increased FRET/CFP ratio in response to Rac1 and ROCK activation, respectively (Komatsu et al., 2011; Li et al., 2017) (**Figures 7A–F**). We observed that Yoda1 promoted the activity of Rac1 and ROCK, and decreased the expression of Piezo1 by shRNA reduced the response of these two effectors to Yoda1. The FRET/CFP ratio reduced in the Yoda1 + w/o Ca^{2+} group when extracellular calcium was absent; however, the cells incubated in the Ca^{2+} medium showed the highest Rac1 and ROCK activation (**Figures 7A–F**). Intriguingly, we observed that Yoda1 slightly activated the ERK, Rac1, and ROCK in Yoda1 + Piezo1 KD group (**Figures 6D,F** and **Figures 7C–F**). It has been previously reported that Yoda1 slightly induced the activation of ERK and Akt independent of Piezo1 (Dela Paz and Frangos, 2018), which is consistent with our results. Nevertheless, Piezo1 and calcium play a significant role in the activation of ERK, Rac1 and ROCK because the presence of extracellular calcium and the integrity of Piezo1 expression caused greater activation of cellular signals in all the Yoda1 treatments. Therefore, extracellular calcium influx through Piezo1 upregulates PKA, ERK, Rac1, and ROCK activities which have the potential to promote cancer cell survival, proliferation, and migration.

Extracellular Ca^{2+} Influx *via* Piezo1 and Downstream Effectors Regulates Membrane Ruffling

Cells extend protrusions toward desired spaces and form new focal adhesions for migration (Mayor and Etienne-Manneville, 2016). Specifically, lamellipodia, a sheet-like membrane protrusion, is mainly found at the leading edge and results

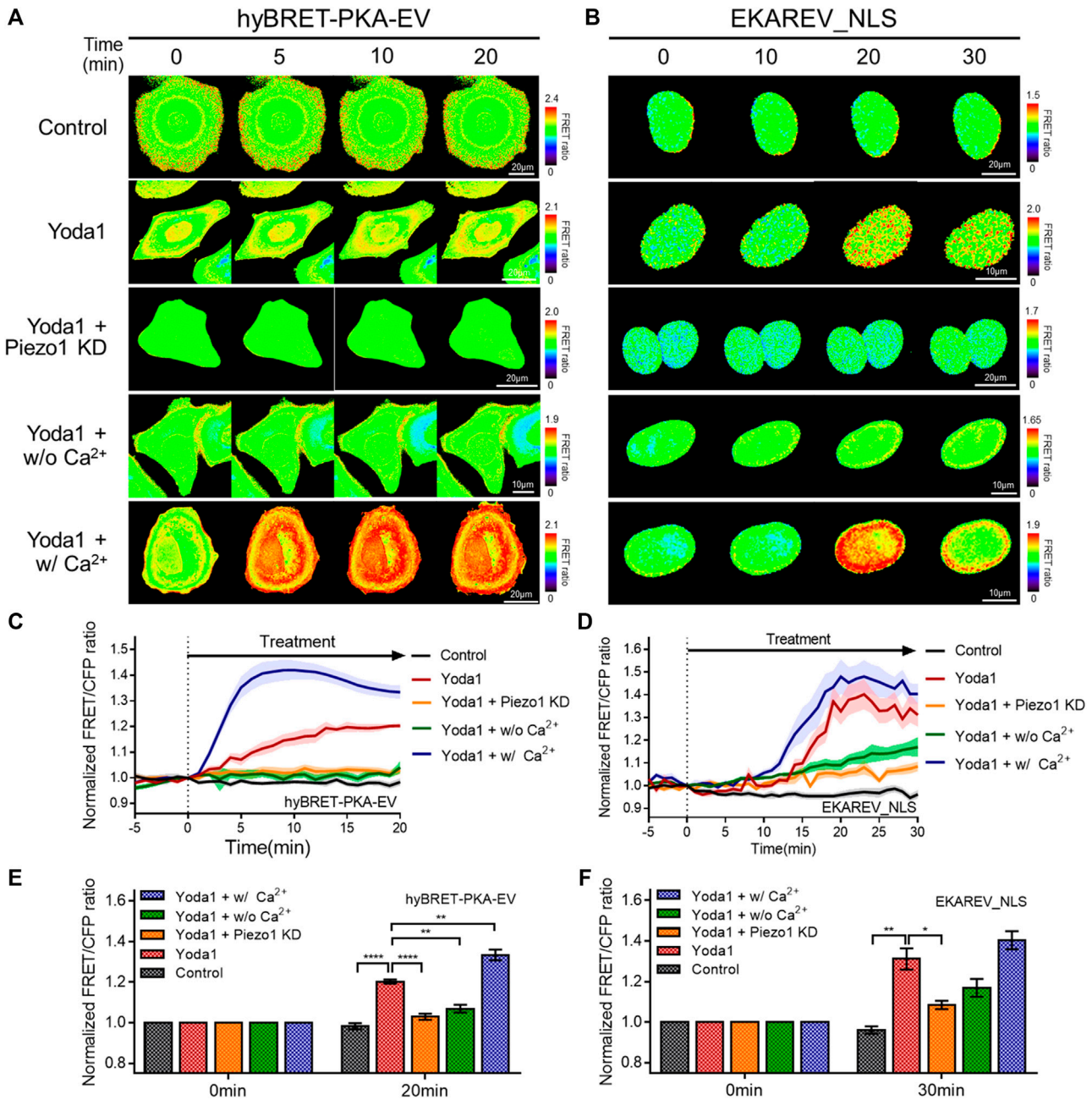

FIGURE 6 | Effects of Piezo1-induced cytosolic calcium increase on PKA and ERK activity. **(A,B)** Time-lapse FRET images of the **(A)** hyBRET-PKA-EV and **(B)** EKAREV_NLS in MCF-7 cells. The cells were exposed to the control [0.2% (v/v) DMSO] and Yoda1 (5 μM for hyBRET-PKA-EV and 1 μM for EKAREV_NLS) dissolved in CO_2-independent culture medium (Yoda1 group), Ca^{2+}-free medium (Yoda1 + w/o Ca^{2+} group) and Ca^{2+} medium (Yoda1 + w/Ca^{2+} group), respectively. The Yoda1 + Piezo1 KD group was incubated in CO_2-independent culture medium. The color scale bars represent the range of the FRET/CFP emission ratio determined using the biosensor. Hot and cold colors indicate high and low **(A)** PKA and **(B)** ERK activity, respectively. **(C,D)** The time courses represent the average of the normalized FRET/CFP emission ratio changes of **(C)** hyBRET-PKA-EV and **(D)** EKAREV_NLS. The lines are mean values of normalized emission ratios, with diluted colors indicating the S.E.M (n = 7). **(E,F)** The bar graph describes the mean values of the normalized FRET/CFP emission ratios of **(E)** hyBRET-PKA-EV and **(F)** EKAREV_NLS at the indicated times with error bars indicating the S.E.M (n = 7, $^{*}p < 0.05$, $^{**}p < 0.01$ and $^{****}p < 0.0001$, Student's t-test).

from branched actin filament polymerization (Krause and Gautreau, 2014; Mayor and Etienne-Manneville, 2016). Migrating cells generate lamellipodia by activating the Rac-WAVE/SCAR-Arp2/3 signaling axis. The actin-rich dendritic network appears to look like the cell membrane is forming hair-like ruffles when viewed from the extracellular regions, which is called membrane ruffling (Krause and Gautreau, 2014; Isogai et al., 2015). It has been reported that the store-

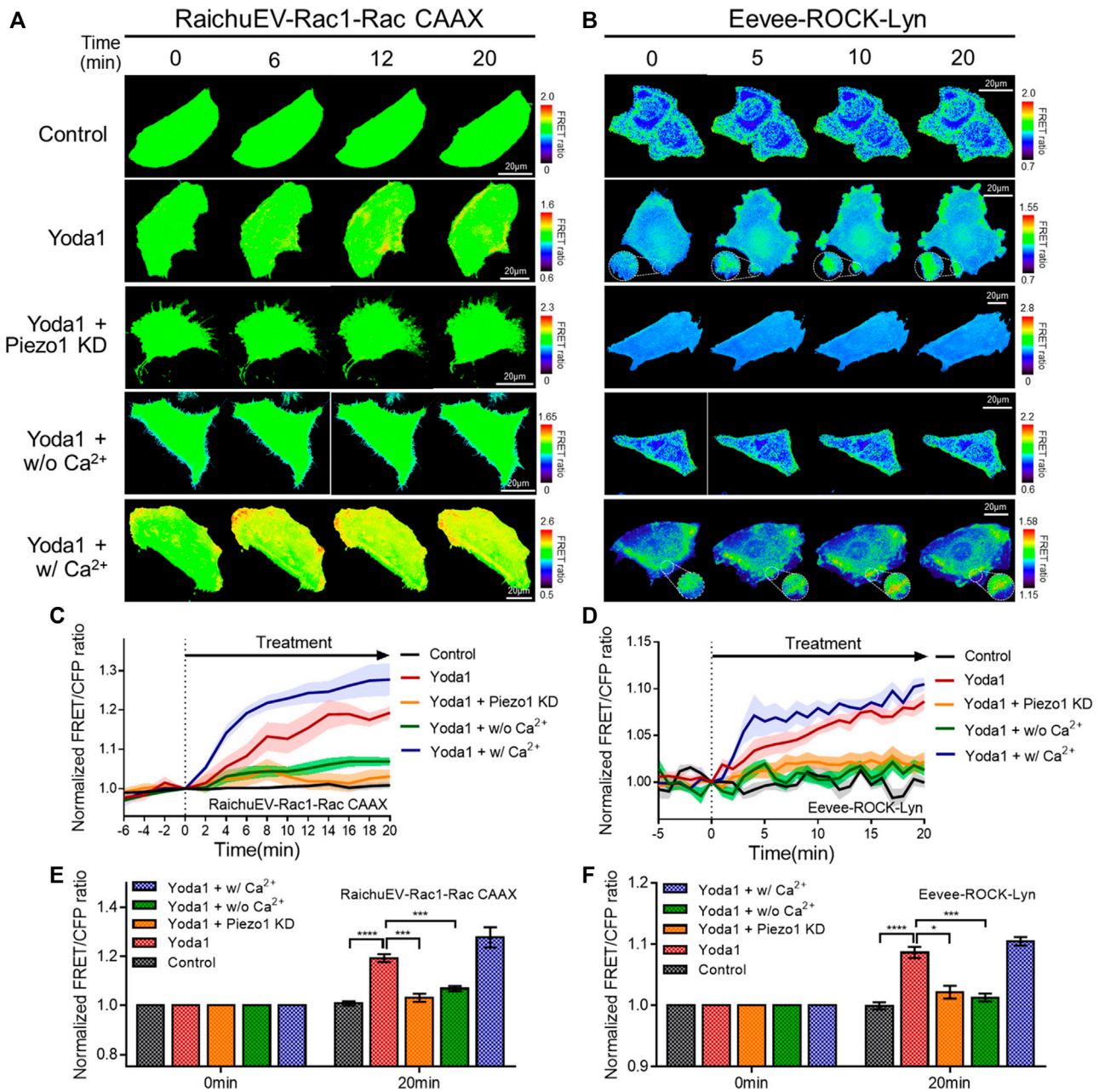

FIGURE 7 | Extracellular calcium influx through Piezo1 increases Rac1 and ROCK activity. **(A,B)** Time-lapse FRET images of the **(A)** RaichuEV-Rac1-Rac CAAX and **(B)** Eevee-ROCK-Lyn in MCF-7 cells. The cells were exposed to control [0.2% (v/v) DMSO] and Yoda1 (1 μM for RaichuEV-Rac1-Rac CAAX and 5 μM for Eevee-ROCK-Lyn) dissolved in CO_2-independent culture medium (Yoda1 group), Ca^{2+}-free medium (Yoda1 + w/o Ca^{2+} group), and Ca^{2+} medium (Yoda1 + w/Ca^{2+} group), respectively. The Yoda1 + Piezo1 KD group was incubated in a CO_2-independent culture medium. The color scale bars represent the range of the FRET/CFP emission ratio determined using the biosensor. Hot and cold colors indicate high and low **(A)** Rac1 and **(B)** ROCK activity, respectively. **(C,D)** The time courses represent the average of the normalized FRET/CFP emission ratio changes of **(C)** RaichuEV-Rac1-Rac CAAX and **(D)** Eevee-ROCK-Lyn. The lines are mean values of normalized emission ratios, with diluted colors indicating the S.E.M (n = 7). **(E,F)** The bar graph describes the mean values of the normalized FRET/CFP emission ratios of **(E)** RaichuEV-Rac1-Rac CAAX and **(F)** Eevee-ROCK-Lyn at the indicated times with the error bars indicating the S.E.M (n = 7, $^{*}p < 0.05$, $^{***}p < 0.001$ and $^{****}p < 0.0001$, Student's t-test).

operated Ca^{2+} entry (SOCE) complex composed of STIM1 and ORAI1 plays an important role in membrane ruffling (Lopez-Guerrero et al., 2017). As shown in **Figure 7**, Piezo1-induced extracellular calcium influx upregulated the activity of Rac1, which promotes branched actin filament polymerization, and ROCK, which plays a role in ROCK-mediated actin cytoskeleton rearrangement, and rear-end retraction. Since Piezo1 activation-induced membrane ruffling remains poorly understood, we

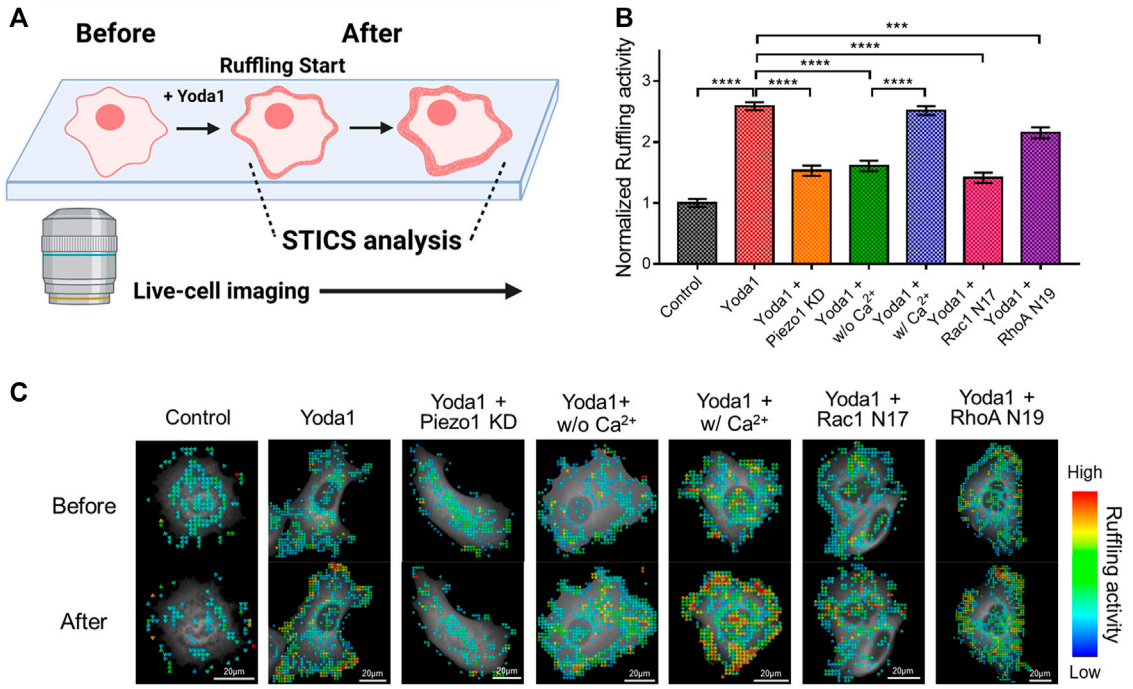

FIGURE 8 | Effects of Piezo1-induced extracellular calcium influx on membrane ruffling. **(A)** A schematic illustration explaining the procedure for analyzing the membrane ruffling with STICS. Live-cell imaging was used to visualize membrane ruffling, which occurs briefly after Yoda1 treatment, and STICS analyzed the videos, or a series of images, showing the movement. The illustration was created using BioRender (https://biorenders.com/) **(B)** The bar graph describes the mean values of the normalized ruffling activity with error bars indicating the S.E.M (the number of analyzed particles = 108, $^{***}p < 0.001$ and $^{****}p < 0.0001$, Student's *t*-test). The cells were treated with the control [0.2% (v/v) DMSO] and Yoda1 (1 μM) dissolved in CO_2-independent culture medium (Yoda1 group), Ca^{2+}-free medium (Yoda1 + w/o Ca^{2+} group), and Ca^{2+} medium (Yoda1 + w/Ca^{2+} group), respectively. The Yoda1 + Piezo1 KD, Rac1 N17, and RhoA N19 groups were incubated in a CO_2-independent culture medium. **(C)** The flow mapping images represent the velocity of the GFP-cortactin particles expressed in MCF-7 cells. The color scale bars represent the range of the ruffling activity calculated by STICS. Hot and cold colors indicate high and low ruffling activity, respectively.

explored this phenomenon using spatiotemporal image correlation spectroscopy (STICS), which analyses the velocity of particles in live imaging data (Hebert et al., 2005; Yi et al., 2011; Hartzell et al., 2016) (**Figure 8**). We transfected MCF-7 cells with GFP-tagged cortactin, a membrane ruffling marker, to observe membrane ruffling activity. Cortactin, a substrate of Src, mediates cell shaping, membrane protrusion, membrane ruffling, and lamellipodia by contributing to actin cytoskeleton rearrangement (Wu and Parsons, 1993; Weed and Parsons, 2001; Ammer and Weed, 2008). We visualized real-time cell membrane ruffling after Yoda1 treatment, and the velocity values of the fluorescence particles in the ruffling region were derived with STICS; these values were named "ruffling activity" (**Figure 8A**). We observed active membrane ruffling in the Yoda1 group (**Supplementary Video S2**) following Yoda1 administration to the cells incubated in the CO_2-independent culture medium, but the ruffling was significantly reduced in the Piezo1 KD group (**Figures 8B,C**) (**Supplementary Video S3**). The cells incubated in calcium-free conditions showed decreased cell membrane ruffling; however, ruffling activity in the Yoda1 + w/Ca^{2+} group was the same as that in the Yoda1 group (**Supplementary Videos S4, S5**). We then introduced Rac1 N17 and RhoA N19, a dominant-negative construct of Rac1 and RhoA, respectively, into each group to identify the downstream effectors that regulate the membrane ruffling induced by Piezo1-mediated extracellular calcium influx. As expected, the cells introduced with dominant-negative RhoA exhibited more active membrane ruffling than the Rac1 N17-introduced cells (**Figures 8B,C**) (**Supplementary Videos S6, S7**) post-Yoda1 treatment. We conjectured that continuous and active membrane ruffling in the Yoda1 and Yoda1 + w/Ca^{2+} groups required the presence of extracellular calcium and the intactness of Piezo1 and the downstream effectors (**Supplementary Videos S1–7**). Collectively, these results show that Piezo1-induced extracellular calcium influx results in membrane ruffling, a precursor of cell migration, and this ruffling is regulated to a greater extent by Rac1 compared to that by RhoA.

4 DISCUSSION

Various aspects of Piezo1 have been studied over the years, including the structure of the channel, mechanogating mechanism, activation dynamics, its interaction with surrounding proteins and agonists, physiological functions, and associated diseases (Coste et al., 2010; Coste et al., 2012; Lukacs et al., 2015; Gudipaty et al., 2017; Jin et al., 2017; Wang

et al., 2018; Botello-Smith et al., 2019; Wang et al., 2020). In this study, we investigated Yoda1-treated MCF-7 cells, which express Piezo1 endogenously, and explored Piezo1-induced Ca^{2+} flux, cellular signaling, and cellular requirements for the normal function of the channel. Additionally, membrane ruffling mediated by Ca^{2+} influx and Piezo1 was also examined.

Yoda1 administration triggered the decrease in the ER calcium sensor FRET/CFP ratio, indicating the release of ER-stored calcium (**Figure 3**). Since Yoda1-induced ER-stored calcium release remains poorly understood, we suggest two potential theories to explain this phenomenon. First, Piezo1 located in the ER is activated by Yoda1, resulting in calcium efflux. During the synthesis of most membrane proteins in the ER that are located in the plasma membrane, some parts of the proteins are inside the ER or vesicles and then the proteins turn towards the extracellular region in the plasma membrane. In other word, the parts always face the exoplasmic space (i.e., the lumen of the ER, vesicles and cell exterior) (Harvey et al., 2008). It has been demonstrated that a variety of calcium-permeable ion channels, which are mainly in the plasma membrane and induce extracellular calcium influx, are also located in the ER membrane and mediate ER-stored calcium release (Takeshima et al., 2015). Previous studies showed that Piezo1 is also present in the ER (Satoh et al., 2006; McHugh et al., 2010). Recently, it has been reported that Piezo1 located in ER membrane triggers ER-stored Ca^{2+} release (Liao et al., 2021). In addition, the patch of negatively charged residues 2393-DEEED-2397 of Piezo1, placed above the extracellular fenestration sites, has an important role in the selection of cations over anions, suggesting that cations might enter the ion-conducting pathway through the "extracellular" fenestration sites (Zhao et al., 2018). Therefore, we could also conclude that cations go into the central pore through the "exoplasmic space," the lumen of the ER. Accordingly, we suggest a model that Piezo1 is located in the ER-lipid bilayer, and the top part of the channel which usually faces the extracellular region in the plasma membrane might face the inside of ER, and Piezo1 could trigger ER-stored Ca^{2+} release. Since Yoda1 binds to the Piezo1-hydrophobic binding pocket near the membrane's intracellular leaflet (Botello-Smith et al., 2019), the agonist can effectively approach the binding site, which is exposed to the cytosol and is found in both the plasma membrane and ER. Therefore, we hypothesized that Yoda1 treatment activated Piezo1 and induced calcium release in the ER. In this work, we mainly examined and validated this hypothesis. Second, the Ca^{2+} influx mediated by Piezo1 activates ER-located calcium efflux channels and receptors. As illustrated in **Figure 6**, PKA was upregulated in a Piezo1-induced calcium-dependent manner. Ca^{2+}-calmodulin signaling promotes cAMP levels by upregulating adenylyl cyclase, and PKA, its downstream effector, activates ryanodine receptors (RYRs) and inositol 1,4,5-trisphosphate receptors (IP_3Rs), which mediate ER-stored calcium release (Reiken et al., 2003; Taylor, 2017). Hence, Piezo1-induced calcium influx in itself creates an environment that can cause ER-stored calcium release.

As shown in **Figures 5C–E**, the cells pretreated with Noco and ML-7 showed different dynamics of Yoda1-induced calcium signaling than those observed in the control group. Intriguingly, the maximum values of the FRET/CFP ratio were similar among all groups; Noco and ML-7 delayed the time to reach the maximum ratio value (**Figures 5D,E**). The plasma membrane, where various transmembrane and membrane-bound proteins are embedded in the lipid bilayer, is supported by the cytoskeleton complex (Sitarska and Diz-Muñoz, 2020). Components of the cytoskeleton, including microtubules and actomyosin, are key intracellular structures that support membrane mechanics and play an essential role in mechanotransduction (Gittes et al., 1993; Ananthakrishnan and Ehrlicher, 2007; Murrell et al., 2015; Morley et al., 2016; Yan et al., 2018). The microtubules, whose polymerization was interrupted by nocodazole, are rigid structures in cells and play a significant role in maintaining cell shape and polarized pseudopodial activity (Rodionov et al., 1993). Upon the acetylation of α-tubulin, which is a component of the microtubule, the stiffness of the plasma membrane is increased, and cells require more force to trigger mechanosensitive channels (Morley et al., 2016; Yan et al., 2018). In addition, TRPV1, a non-selective cation channel, binds to a network of subcortical microtubules *via* cytoplasmic tubulin-binding motifs in mammalian osmo-sensory neurons (Prager-Khoutorsky et al., 2014). Therefore, microtubules play an important role in maintaining cellular elasticity and mechanotransduction. It was reported that the microtubule stabilizer paclitaxel increased Piezo2-mediated mechanically activated currents, but these currents were reduced by vincristine, a microtubule destabilizer, suggesting that microtubules are involved in Piezo2 mechanotransduction (Chang and Gu, 2020). Thus, the results of the previous study showed similar trends to our results, showing that microtubule disruption by nocodazole results in altered Piezo1 function. The cell cortex contains membrane-bound actomyosin, which is composed of myosin II and its substrate, F-actin (Sitarska and Diz-Muñoz, 2020). The interaction between myosin II and actin filaments generates a contractile force that controls the cell shape and plays a role in mechanotransduction (Clark et al., 2007; Murrell et al., 2015; Pandya et al., 2017). ML-7 is a selective inhibitor of MLCK, which phosphorylates MLC and potentiates contractility in actomyosin (Saitoh et al., 1987). Therefore, we assume that pre-treatment with ML-7 reduces the contractile force of actomyosin, alters intracellular tension and plasma membrane elasticity, and changes the activity of Piezo1, which senses mechanical stimulus from the local membrane or ambient cellular microenvironment.

5 CONCLUSION

In conclusion, we found that Yoda1-induced Piezo1 activation increased cytosolic calcium levels *via* extracellular calcium influx and release of ER-stored calcium. The intactness of the caveolin, cholesterol and cytoskeletal structures are required for Piezo1 to function normally. Furthermore, Yoda1 treatment induced the activation of PKA, ERK, Rac1, and ROCK, and membrane ruffling in a Ca^{2+}-and Piezo1-dependent manner. Taken together, our results indicate that Piezo1 induces calcium flux-upregulated cell survival and membrane ruffling (**Figure 9**). These data provide a novel insight that cancer cells expressing Piezo1 might use the channel to promote cell survival and migration; therefore, Piezo1 could be an important target for treating such cancer cells.

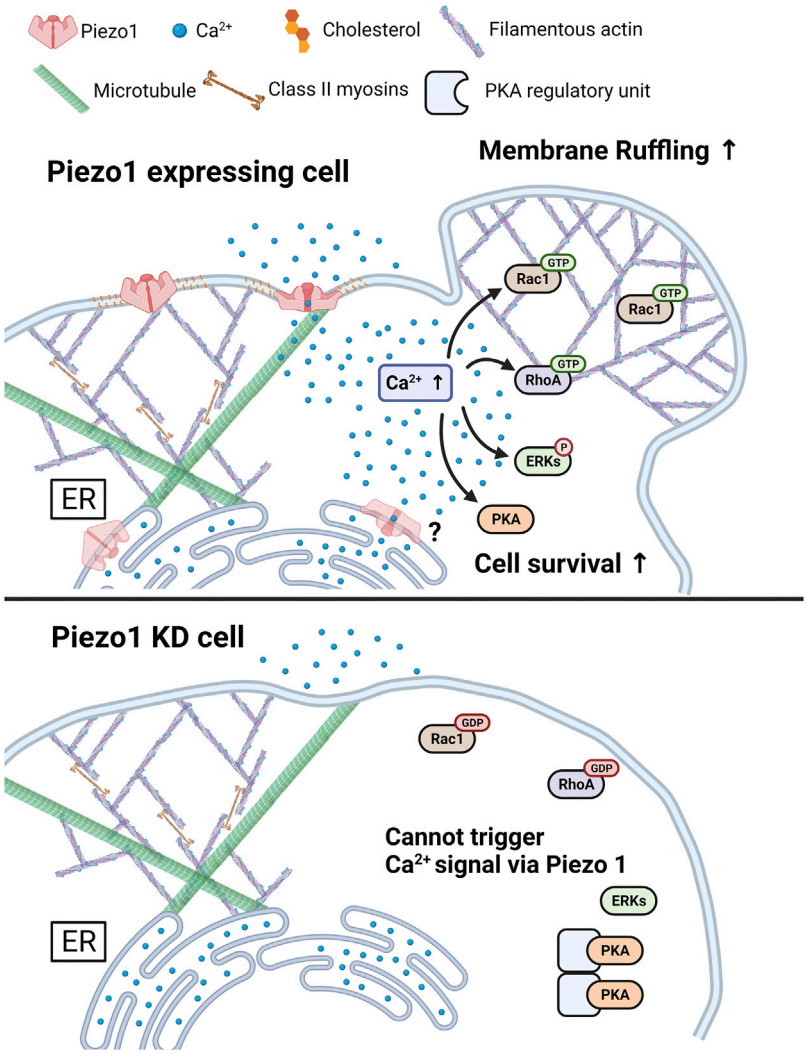

FIGURE 9 | A graphical summary describes the effects of Piezo1-mediated Ca^{2+} flux. The increase in cytosolic Ca^{2+} levels induced by Piezo1 activates PKA, ERK, RhoA, and Rac1, and promotes cell survival and membrane ruffling. For the normal functioning of Piezo1, the integrity of caveolin, cholesterol, and cytoskeletal structure such as microtubules and actomyosin structures was required. The Piezo1 KD cell inhibits the triggering of activation of Ca^{2+} signal, following cell survival and membrane ruffling induced by Piezo1. The figure was created using BioRender.

DATA AVAILABILITY STATEMENT

The raw data supporting the conclusion of this article will be made available by the authors, without undue reservation.

AUTHOR CONTRIBUTIONS

H-SK and T-JK contributed to conception and design of the study. H-SK, J-SS, Y-KJ, and S-HA conducted the data curation. H-SK, S-HA, G-HC, and MS performed the statistical analysis. MS, JJ, JS, and YW validated the data. HK wrote the first draft of the manuscript. J-YY, G-HL, YJ, YW, and T-JK reviewed and edited the manuscript. T-JK supervised this project.

FUNDING

This work was supported by a National Research Foundation of Korea (NRF) grant funded by the Korean government (MSIT) (No. 2020R1C1C1010107).

SUPPLEMENTARY MATERIAL

The Supplementary Material for this article can be found online at: https://www.frontiersin.org/articles/10.3389/fcell.2022.865056/full#supplementary-material

REFERENCES

Alper, S. L. (2017). Genetic Diseases of PIEZO1 and PIEZO2 Dysfunction. *Curr. Top. Membr.* 79, 97–134. doi:10.1016/bs.ctm.2017.01.001

Ammer, A. G., and Weed, S. A. (2008). Cortactin Branches Out: Roles in Regulating Protrusive Actin Dynamics. *Cell Motil. Cytoskelet.* 65, 687–707. doi:10.1002/cm.20296

Ananthakrishnan, R., and Ehrlicher, A. (2007). The Forces behind Cell Movement. *Int. J. Biol. Sci.* 3, 303–317. doi:10.7150/ijbs.3.303

Andolfo, I., Alper, S. L., De Franceschi, L., Auriemma, C., Russo, R., De Falco, L., et al. (2013). Multiple Clinical Forms of Dehydrated Hereditary Stomatocytosis Arise from Mutations in PIEZO1. *Blood* 121, 3925. doi:10.1182/blood-2013-02-482489

Anishkin, A., Loukin, S. H., Teng, J., and Kung, C. (2014). Feeling the Hidden Mechanical Forces in Lipid Bilayer Is an Original Sense. *Proc. Natl. Acad. Sci. U. S. A.* 111, 7898–7905. doi:10.1073/pnas.1313364111

Arnaudeau, S., Kelley, W. L., Walsh, J. V., and Demaurex, N. (2001). Mitochondria Recycle Ca2+ to the Endoplasmic Reticulum and Prevent the Depletion of Neighboring Endoplasmic Reticulum Regions. *J. Biol. Chem.* 276, 29430–29439. doi:10.1074/jbc.m103274200

Balijepalli, R. C., Foell, J. D., Hall, D. D., Hell, J. W., and Kamp, T. J. (2006). Localization of Cardiac L-type Ca(2+) Channels to a Caveolar Macromolecular Signaling Complex Is Required for Beta(2)-Adrenergic Regulation. *Proc. Natl. Acad. Sci. U. S. A.* 103, 7500–7505. doi:10.1073/pnas.0503465103

Botello-Smith, W. M., Jiang, W., Zhang, H., Ozkan, A. D., Lin, Y. C., Pham, C. N., et al. (2019). A Mechanism for the Activation of the Mechanosensitive Piezo1 Channel by the Small Molecule Yoda1. *Nat. Commun.* 10, 4503. doi:10.1038/s41467-019-12501-1

Brenner, S. L., and Korn, E. D. (1980). The Effects of Cytochalasins on Actin Polymerization and Actin ATPase Provide Insights into the Mechanism of Polymerization. *J. Biol. Chem.* 255, 841. doi:10.1016/s0021-9258(19)86107-0

Buchsbaum, R., Telliez, J. B., Goonesekera, S., and Feig, L. A. (1996). The N-Terminal Pleckstrin, Coiled-Coil, and IQ Domains of the Exchange Factor Ras-GRF Act Cooperatively to Facilitate Activation by Calcium. *Mol. Cell Biol.* 16, 4888–4896. doi:10.1128/mcb.16.9.4888

Cahalan, S. M., Lukacs, V., Ranade, S. S., Chien, S., Bandell, M., and Patapoutian, A. (2015). Piezo1 Links Mechanical Forces to Red Blood Cell Volume. *Elife* 4, e07370. doi:10.7554/eLife.07370

Chang, W., and Gu, J. (2020). Role of Microtubules in Piezo2 Mechanotransduction of Mouse Merkel Cells. *J. Neurophysiol.* 124, 1824. doi:10.1152/jn.00502.2020

Chong, J., De Vecchis, D., Hyman, A. J., Povstyan, O. V., Ludlow, M. J., Shi, J., et al. (2021). Modeling of Full-Length Piezo1 Suggests Importance of the Proximal N-Terminus for Dome Structure. *Biophysical J.* 120, 1343–1356. doi:10.1016/j.bpj.2021.02.003

Clark, K., Langeslag, M., Figdor, C. G., and Van Leeuwen, F. N. (2007). Myosin II and Mechanotransduction: a Balancing Act. *Trends Cell Biol.* 17, 178–186. doi:10.1016/j.tcb.2007.02.002

Connolly, B. A., Rice, J., Feig, L. A., and Buchsbaum, R. J. (2005). Tiam1-IRSp53 Complex Formation Directs Specificity of Rac-Mediated Actin Cytoskeleton Regulation. *Mol. Cell Biol.* 25, 4602–4614. doi:10.1128/MCB.25.11.4602-4614.2005

Coste, B., Mathur, J., Schmidt, M., Earley, T. J., Ranade, S., Petrus, M. J., et al. (2010). Piezo1 and Piezo2 Are Essential Components of Distinct Mechanically Activated Cation Channels. *Science* 330, 55–60. doi:10.1126/science.1193270

Coste, B., Xiao, B., Santos, J. S., Syeda, R., Grandl, J., Spencer, K. S., et al. (2012). Piezo Proteins Are Pore-Forming Subunits of Mechanically Activated Channels. *Nature* 483, 176–181. doi:10.1038/nature10812

Cox, C. D., Bae, C., Ziegler, L., Hartley, S., Nikolova-Krstevski, V., Rohde, P. R., et al. (2016). Removal of the Mechanoprotective Influence of the Cytoskeleton Reveals PIEZO1 Is Gated by Bilayer Tension. *Nat. Commun.* 7, 10366. doi:10.1038/ncomms10366

Cox, C. D., Bavi, N., and Martinac, B. (2017). Origin of the Force: The Force-From-Lipids Principle Applied to Piezo Channels. *Curr. Top. Membr.* 79, 59–96. doi:10.1016/bs.ctm.2016.09.001

Deivasikamani, V., Dhayalan, S., Abudushalamu, Y., Mughal, R., Visnagri, A., Cuthbertson, K., et al. (2019). Piezo1 Channel Activation Mimics High Glucose as a Stimulator of Insulin Release. *Sci. Rep.* 9, 16876. doi:10.1038/s41598-019-51518-w

Dela Paz, N. G., and Frangos, J. A. (2018). Yoda1-induced Phosphorylation of Akt and ERK1/2 Does Not Require Piezo1 Activation. *Biochem. Biophys. Res. Commun.* 497, 220–225. doi:10.1016/j.bbrc.2018.02.058

Dubin, A. E., Murthy, S., Lewis, A. H., Brosse, L., Cahalan, S. M., Grandl, J., et al. (2017). Endogenous Piezo1 Can Confound Mechanically Activated Channel Identification and Characterization. *Neuron* 94, 266–270. doi:10.1016/j.neuron.2017.03.039

Gillespie, P. G., and Walker, R. G. (2001). Molecular Basis of Mechanosensory Transduction. *Nature* 413, 194–202. doi:10.1038/35093011

Gittes, F., Mickey, B., Nettleton, J., and Howard, J. (1993). Flexural Rigidity of Microtubules and Actin Filaments Measured from Thermal Fluctuations in Shape. *J. Cell Biol.* 120, 923–934. doi:10.1083/jcb.120.4.923

Gudipaty, S. A., Lindblom, J., Loftus, P. D., Redd, M. J., Edes, K., Davey, C. F., et al. (2017). Mechanical Stretch Triggers Rapid Epithelial Cell Division through Piezo1. *Nature* 543, 118–121. doi:10.1038/nature21407

Hartzell, C. A., Jankowska, K. I., Burkhardt, J. K., and Lewis, R. S. (2016). Calcium Influx through CRAC Channels Controls Actin Organization and Dynamics at the Immune Synapse. *eLife* 5, e14850. doi:10.7554/eLife.14850

Harvey, L., Arnold, B., Paul, M., Chris, A. K., Monty, K., Matthew, P. S., et al. (2008). "Moving Protiens into Membranes and Organelles,", in *Molecular Cell Biology Fifth edition*. New York: W.H. Freeman, 653–695.

Hayer, A., Stoeber, M., Bissig, C., and Helenius, A. (2010). Biogenesis of Caveolae: Stepwise Assembly of Large Caveolin and Cavin Complexes. *Traffic* 11, 361. (Copenhagen, Denmark). doi:10.1111/j.1600-0854.2009.01023.x

Hebert, B., Costantino, S., and Wiseman, P. W. (2005). Spatiotemporal Image Correlation Spectroscopy (STICS) Theory, Verification, and Application to Protein Velocity Mapping in Living CHO Cells. *Biophys. J.* 88, 3601–3614. doi:10.1529/biophysj.104.054874

Huo, H., Guo, X., Hong, S., Jiang, M., Liu, X., and Liao, K. (2003). Lipid Rafts/caveolae Are Essential for Insulin-like Growth Factor-1 Receptor Signaling during 3T3-L1 Preadipocyte Differentiation Induction. *J. Biol. Chem.* 278, 11561–11569. doi:10.1074/jbc.M211785200

Isogai, T., Van Der Kammen, R., Leyton-Puig, D., Kedziora, K. M., Jalink, K., and Innocenti, M. (2015). Initiation of Lamellipodia and Ruffles Involves Cooperation between mDia1 and the Arp2/3 Complex. *J. Cell Sci.* 128, 3796–3810. doi:10.1242/jcs.176768

Jin, P., Bulkley, D., Guo, Y., Zhang, W., Guo, Z., Huynh, W., et al. (2017). Electron Cryo-Microscopy Structure of the Mechanotransduction Channel NOMPC. *Nature* 547, 118–122. doi:10.1038/nature22981

Kahl, C. R., and Means, A. R. (2004). Regulation of Cyclin D1/Cdk4 Complexes by Calcium/calmodulin-dependent Protein Kinase I. *J. Biol. Chem.* 279, 15411–15419. doi:10.1074/jbc.M312543200

Khanna, A. K., and Hosenpud, J. D. (1999). Cyclosporine Induces the Expression of the Cyclin Inhibitor P21. *Transplantation* 67, 1262. doi:10.1097/00007890-199905150-00011

Kim, E. J., and Helfman, D. M. (2003). Characterization of the Metastasis-Associated Protein, S100A4. Roles of Calcium Binding and Dimerization in Cellular Localization and Interaction with Myosin. *J. Biol. Chem.* 278, 30063–30073. doi:10.1074/jbc.M304909200

Kim, T.-J., Kim, K.-A., and Jung, S. H. (2017). Development of an Endoplasmic Reticulum Calcium Sensor Based on Fluorescence Resonance Energy Transfer. *Sensors Actuators B Chem.* 247, 520–525. doi:10.1016/j.snb.2017.03.083

Kim, T. J., Joo, C., Seong, J., Vafabakhsh, R., Botvinick, E. L., Berns, M. W., et al. (2015). Distinct Mechanisms Regulating Mechanical Force-Induced Ca^{2+} Signals at the Plasma Membrane and the ER in Human MSCs. *eLife* 4, e04876. doi:10.7554/eLife.04876

Kim, T. J., Lei, L., Seong, J., Suh, J. S., Jang, Y. K., Jung, S. H., et al. (2018). Matrix Rigidity-dependent Regulation of Ca 2+ at Plasma Membrane Microdomains by FAK Visualized by Fluorescence Resonance Energy Transfer. *Adv. Sci.* 6, 1801290. (Weinheim, Baden-Wurttemberg, Germany). doi:10.1002/advs.201801290

Komatsu, N., Aoki, K., Yamada, M., Yukinaga, H., Fujita, Y., Kamioka, Y., et al. (2011). Development of an Optimized Backbone of FRET Biosensors for Kinases and GTPases. *Mol. Biol. Cell* 22, 4647–4656. doi:10.1091/mbc.E11-01-0072

Komatsu, N., Terai, K., Imanishi, A., Kamioka, Y., Sumiyama, K., Jin, T., et al. (2018). A Platform of BRET-FRET Hybrid Biosensors for Optogenetics, Chemical Screening, and *In Vivo* Imaging. *Sci. Rep.* 8, 8984. doi:10.1038/s41598-018-27174-x

Krause, M., and Gautreau, A. (2014). Steering Cell Migration: Lamellipodium Dynamics and the Regulation of Directional Persistence. *Nat. Rev. Mol. Cell Biol.* 15, 577–590. doi:10.1038/nrm3861

Kung, C., Martinac, B., and Sukharev, S. (2010). Mechanosensitive Channels in Microbes. *Annu. Rev. Microbiol.* 64, 313–329. doi:10.1146/annurev.micro.112408.134106

Levitan, I., Fang, Y., Rosenhouse-Dantsker, A., and Romanenko, V. (2010). Cholesterol and Ion Channels. *Sub-cellular Biochem.* 51, 509. doi:10.1007/978-90-481-8622-8_19

Lewis, A. H., and Grandl, J. (2015). Mechanical Sensitivity of Piezo1 Ion Channels Can Be Tuned by Cellular Membrane Tension. *eLife* 4, e12088. doi:10.7554/eLife.12088

Li, C., Imanishi, A., Komatsu, N., Terai, K., Amano, M., Kaibuchi, K., et al. (2017). A FRET Biosensor for ROCK Based on a Consensus Substrate Sequence Identified by KISS Technology. *Cell Struct. Funct.* 42, 1–13. doi:10.1247/csf.16016

Liang, X., Madrid, J., Gärtner, R., Verbavatz, J. M., Schiklenk, C., Wilsch-Bräuninger, M., et al. (2013). A NOMPC-dependent Membrane-Microtubule Connector Is a Candidate for the Gating Spring in Fly Mechanoreceptors. *Curr. Biol.* 23, 755–763. doi:10.1016/j.cub.2013.03.065

Liao, J., Lu, W., Chen, Y., Duan, X., Zhang, C., Luo, X., et al. (2021). Upregulation of Piezo1 (Piezo Type Mechanosensitive Ion Channel Component 1) Enhances the Intracellular Free Calcium in Pulmonary Arterial Smooth Muscle Cells from Idiopathic Pulmonary Arterial Hypertension Patients. *Hypertension* 77, 1974–1989. doi:10.1161/hypertensionaha.120.16629

Lin, Y.-C., Guo, Y. R., Miyagi, A., Levring, J., Mackinnon, R., and Scheuring, S. (2019). Force-induced Conformational Changes in PIEZO1. *Nature* 573, 230–234. doi:10.1038/s41586-019-1499-2

Lopez-Guerrero, A. M., Tomas-Martin, P., Pascual-Caro, C., Macartney, T., Ball, G., Rojas-Fernandez, A., et al. (2017). Regulation of Membrane Ruffling by Polarized STIM1 and ORAI1 in Cortactin-Rich Domains. *Sci. Rep.* 7, 383. doi:10.1038/s41598-017-00331-4

Lukacs, V., Mathur, J., Mao, R., Bayrak-Toydemir, P., Procter, M., Cahalan, S. M., et al. (2015). Impaired PIEZO1 Function in Patients with a Novel Autosomal Recessive Congenital Lymphatic Dysplasia. *Nat. Commun.* 6, 8329. doi:10.1038/ncomms9329

Markin, V. S., and Hudspeth, A. J. (1995). Gating-spring Models of Mechanoelectrical Transduction by Hair Cells of the Internal Ear. *Annu. Rev. biophysics Biomol. Struct.* 24, 59. doi:10.1146/annurev.bb.24.060195.000423

Mayor, R., and Etienne-Manneville, S. (2016). The Front and Rear of Collective Cell Migration. *Nat. Rev. Mol. Cell Biol.* 17, 97–109. doi:10.1038/nrm.2015.14

McHugh, B. J., Buttery, R., Lad, Y., Banks, S., Haslett, C., and Sethi, T. (2010). Integrin Activation by Fam38A Uses a Novel Mechanism of R-Ras Targeting to the Endoplasmic Reticulum. *J. Cell Sci.* 123, 51–61. doi:10.1242/jcs.056424

Mejillano, M. R., Shivanna, B. D., and Himes, R. H. (1996). Studies on the Nocodazole-Induced GTPase Activity of Tubulin. *Arch. Biochem. Biophys.* 336, 130–138. doi:10.1006/abbi.1996.0540

Mingzhi, L., Kenneth, K. Y. H., Zhaowen, T., Linhong, D., and Allen, P. L. (2019). Compressive Stress Enhances Invasive Phenotype of Cancer Cells via Piezo1 Activation. Available at: https://bmcmolcellbiol.biomedcentral.com/articles/10.1186/s12860-021-00401-6. (Accessed date: February 5, 2022).

Mollinedo, F., and Gajate, C. (2015). Lipid Rafts as Major Platforms for Signaling Regulation in Cancer. *Adv. Biol. Regul.* 57, 130. doi:10.1016/j.jbior.2014.10.003

Monteith, G. R., Prevarskaya, N., and Roberts-Thomson, S. J. (2017). The Calcium-Cancer Signalling Nexus. *Nat. Rev. Cancer* 17, 367–380. doi:10.1038/nrc.2017.18

Morachevskaya, E., Sudarikova, A., and Negulyaev, Y. (2007). Mechanosensitive Channel Activity and F-Actin Organization in Cholesterol-Depleted Human Leukaemia Cells. *Cell Biol. Int.* 31, 374–381. doi:10.1016/j.cellbi.2007.01.024

Morley, S. J., Qi, Y., Iovino, L., Andolfi, L., Guo, D., Kalebic, N., et al. (2016). Acetylated Tubulin Is Essential for Touch Sensation in Mice. *eLife* 5, e20813. doi:10.7554/eLife.20813

Morris, T. A., Delorenzo, R. J., and Tombes, R. M. (1998). CaMK-II Inhibition Reduces Cyclin D1 Levels and Enhances the Association of P27kip1 with Cdk2 to Cause G1 Arrest in NIH 3T3 Cells. *Exp. Cell Res.* 240, 218–227. doi:10.1006/excr.1997.3925

Murrell, M., Oakes, P. W., Lenz, M., and Gardel, M. L. (2015). Forcing Cells into Shape: the Mechanics of Actomyosin Contractility. *Nat. Rev. Mol. Cell Biol.* 16, 486–498. doi:10.1038/nrm4012

Nonomura, K., Lukacs, V., Sweet, D. T., Goddard, L. M., Kanie, A., Whitwam, T., et al. (2018). Mechanically Activated Ion Channel PIEZO1 Is Required for Lymphatic Valve Formation. *Proc. Natl. Acad. Sci. U. S. A.* 115, 12817–12822. doi:10.1073/pnas.1817070115

Pandya, P., Orgaz, J. L., and Sanz-Moreno, V. (2017). Actomyosin Contractility and Collective Migration: May the Force Be with You. *Curr. Opin. Cell Biol.* 48, 87–96. doi:10.1016/j.ceb.2017.06.006

Pani, B., and Singh, B. B. (2009). Lipid Rafts/caveolae as Microdomains of Calcium Signaling. *Cell calcium* 45, 625–633. doi:10.1016/j.ceca.2009.02.009

Pelkmans, L., Bürli, T., Zerial, M., and Helenius, A. (2004). Caveolin-stabilized Membrane Domains as Multifunctional Transport and Sorting Devices in Endocytic Membrane Traffic. *Cell* 118, 767–780. doi:10.1016/j.cell.2004.09.003

Prager-Khoutorsky, M., Khoutorsky, A., and Bourque, C. W. (2014). Unique Interweaved Microtubule Scaffold Mediates Osmosensory Transduction via Physical Interaction with TRPV1. *Neuron* 83, 866–878. doi:10.1016/j.neuron.2014.07.023

Prevarskaya, N., Ouadid-Ahidouch, H., Skryma, R., and Shuba, Y. (2014). Remodelling of Ca2+ Transport in Cancer: How it Contributes to Cancer Hallmarks? *Philos. Trans. R. Soc. Lond B Biol. Sci.* 369, 20130097. doi:10.1098/rstb.2013.0097

Prevarskaya, N., Skryma, R., and Shuba, Y. (2011). Calcium in Tumour Metastasis: New Roles for Known Actors. *Nat. Rev. Cancer* 11, 609–618. doi:10.1038/nrc3105

Ranade, S. S., Qiu, Z., Woo, S. H., Hur, S. S., Murthy, S. E., Cahalan, S. M., et al. (2014). Piezo1, a Mechanically Activated Ion Channel, Is Required for Vascular Development in Mice. *Proc. Natl. Acad. Sci. U. S. A.* 111, 10347–10352. doi:10.1073/pnas.1409233111

Reiken, S., Lacampagne, A., Zhou, H., Kherani, A., Lehnart, S. E., Ward, C., et al. (2003). PKA Phosphorylation Activates the Calcium Release Channel (Ryanodine Receptor) in Skeletal Muscle: Defective Regulation in Heart Failure. *J. Cell Biol.* 160, 919–928. doi:10.1083/jcb.200211012

Ridley, A. J., Paterson, H. F., Johnston, C. L., Diekmann, D., and Hall, A. (1992). The Small GTP-Binding Protein Rac Regulates Growth Factor-Induced Membrane Ruffling. *Cell* 70, 401–410. doi:10.1016/0092-8674(92)90164-8

Ridley, A. J., Schwartz, M. A., Burridge, K., Firtel, R. A., Ginsberg, M. H., Borisy, G., et al. (2003). Cell Migration: Integrating Signals from Front to Back. *Science* 302, 1704. (New York, N.Y.). doi:10.1126/science.1092053

Ridone, P., Pandzic, E., Vassalli, M., Cox, C. D., Macmillan, A., Gottlieb, P. A., et al. (2020). Disruption of Membrane Cholesterol Organization Impairs the Activity of PIEZO1 Channel Clusters. *J. Gen. Physiol.* 152, e201912515. doi:10.1085/jgp.201912515

Roderick, H. L., and Cook, S. J. (2008). Ca2+ Signalling Checkpoints in Cancer: Remodelling Ca2+ for Cancer Cell Proliferation and Survival. *Nat. Rev. Cancer* 8, 361–375. doi:10.1038/nrc2374

Rodionov, V. I., Gyoeva, F. K., Tanaka, E., Bershadsky, A. D., Vasiliev, J. M., and Gelfand, V. I. (1993). Microtubule-dependent Control of Cell Shape and Pseudopodial Activity Is Inhibited by the Antibody to Kinesin Motor Domain. *J. Cell Biol.* 123, 1811–1820. doi:10.1083/jcb.123.6.1811

Romero, L. O., Massey, A. E., Mata-Daboin, A. D., Sierra-Valdez, F. J., Chauhan, S. C., Cordero-Morales, J. F., et al. (2019). Dietary Fatty Acids Fine-Tune Piezo1 Mechanical Response. *Nat. Commun.* 10, 1200–1214. doi:10.1038/s41467-019-09055-7

Saitoh, M., Ishikawa, T., Matsushima, S., Naka, M., and Hidaka, H. (1987). Selective Inhibition of Catalytic Activity of Smooth Muscle Myosin Light Chain Kinase. *J. Biol. Chem.* 262, 7796–7801. doi:10.1016/s0021-9258(18)47638-7

Salbreux, G., Charras, G., and Paluch, E. (2012). Actin Cortex Mechanics and Cellular Morphogenesis. *Trends Cell Biol.* 22, 536–545. doi:10.1016/j.tcb.2012.07.001

Satoh, K., Hata, M., Takahara, S., Tsuzaki, H., Yokota, H., Akatsu, H., et al. (2006). A Novel Membrane Protein, Encoded by the Gene Covering KIAA0233, Is Transcriptionally Induced in Senile Plaque-Associated Astrocytes. *Brain Res.* 1108, 19–27. doi:10.1016/j.brainres.2006.06.050

Schlörmann, W., Steiniger, F., Richter, W., Kaufmann, R., Hause, G., Lemke, C., et al. (2010). The Shape of Caveolae Is Omega-like after Glutaraldehyde Fixation and Cup-like after Cryofixation. *Histochem Cell Biol.* 133, 223–228. doi:10.1007/s00418-009-0651-8

Schneider, G., Oswald, F., Wahl, C., Greten, F. R., Adler, G., and Schmid, R. M. (2002). Cyclosporine Inhibits Growth through the Activating Transcription factor/cAMP-Responsive Element-Binding Protein Binding Site in the Cyclin D1 Promoter. *J. Biol. Chem.* 277, 43599–43607. doi:10.1074/jbc.M204787200

Sée, V., Rajala, N. K., Spiller, D. G., and White, M. R. (2004). Calcium-dependent Regulation of the Cell Cycle via a Novel MAPK--NF-kappaB Pathway in Swiss 3T3 Cells. *J. Cell Biol.* 166, 661–672. doi:10.1083/jcb.200402136

Sitarska, E., and Diz-Muñoz, A. (2020). Pay Attention to Membrane Tension: Mechanobiology of the Cell Surface. *Curr. Opin. Cell Biol.* 66, 11–18. doi:10.1016/j.ceb.2020.04.001

Stewart, T. A., Yapa, K. T., and Monteith, G. R. (2015). Altered Calcium Signaling in Cancer Cells. *Biochimica biophysica acta* 1848, 2502. doi:10.1016/j.bbamem.2014.08.016

Su, L. T., Agapito, M. A., Li, M., Simonson, W. T., Huttenlocher, A., Habas, R., et al. (2006). TRPM7 Regulates Cell Adhesion by Controlling the Calcium-dependent Protease Calpain. *J. Biol. Chem.* 281, 11260–11270. doi:10.1074/jbc.M512885200

Sun, W., Chi, S., Li, Y., Ling, S., Tan, Y., Xu, Y., et al. (2019). The Mechanosensitive Piezo1 Channel Is Required for Bone Formation. *eLife* 8, e47454. doi:10.7554/eLife.47454

Syeda, R., Xu, J., Dubin, A. E., Coste, B., Mathur, J., Huynh, T., et al. (2015). Chemical Activation of the Mechanotransduction Channel Piezo1. *Elife* 4, e07369. doi:10.7554/eLife.07369

Syeda, R., Florendo, M. N., Cox, C. D., Kefauver, J. M., Santos, J. S., Martinac, B., et al. (2016). Piezo1 Channels Are Inherently Mechanosensitive. *Cell Rep.* 17, 1739–1746. doi:10.1016/j.celrep.2016.10.033

Takeshima, H., Venturi, E., and Sitsapesan, R. (2015). New and Notable Ion-Channels in the Sarcoplasmic/endoplasmic Reticulum: Do They Support the Process of Intracellular Ca^{2+} Release? *J. Physiol.* 593, 3241–3251. doi:10.1113/jphysiol.2014.281881

Tarabykina, S., Griffiths, T. R., Tulchinsky, E., Mellon, J. K., Bronstein, I. B., and Kriajevska, M. (2007). Metastasis-associated Protein S100A4: Spotlight on its Role in Cell Migration. *Curr. Cancer Drug Targets* 7, 217–228. doi:10.2174/156800907780618329

Taylor, C. W. (2017). Regulation of IP3 Receptors by Cyclic AMP. *Cell calcium* 63, 48–52. doi:10.1016/j.ceca.2016.10.005

Tombes, R. M., Grant, S., Westin, E. H., and Krystal, G. (1995). G1 Cell Cycle Arrest and Apoptosis Are Induced in NIH 3T3 Cells by KN-93, an Inhibitor of CaMK-II (The Multifunctional Ca2+/CaM Kinase). *Cell Growth Differ.* 6, 1063–1070.

Tsujikawa, H., Song, Y., Watanabe, M., Masumiya, H., Gupte, S. A., Ochi, R., et al. (2008). Cholesterol Depletion Modulates Basal L-type Ca2+ Current and Abolishes its -adrenergic Enhancement in Ventricular Myocytes. *Am. J. Physiol. Heart Circ. Physiol.* 294, H285–H292. doi:10.1152/ajpheart.00824.2007

Umeda, K., Negishi, M., and Katoh, H. (2018). RasGRF1 Mediates Brain-Derived Neurotrophic Factor-Induced Axonal Growth in Primary Cultured Cortical Neurons. *Biochem. Biophys. Rep.* 17, 56–64. doi:10.1016/j.bbrep.2018.11.011

Wang, J., Jiang, J., Yang, X., Wang, L., and Xiao, B. (2020). Tethering Piezo Channels to the Actin Cytoskeleton for Mechanogating via the E-Cadherin-β-Catenin Mechanotransduction Complex. Available at: https://www.sciencedirect.com/science/article/pii/S2211124722000584?via%3Dihub#fig4. (Accessed date: February 5, 2022).

Wang, S., Chennupati, R., Kaur, H., Iring, A., Wettschureck, N., and Offermanns, S. (2016). Endothelial Cation Channel PIEZO1 Controls Blood Pressure by Mediating Flow-Induced ATP Release. *J. Clin. Invest.* 126, 4527–4536. doi:10.1172/jci87343

Wang, Y., Chi, S., Guo, H., Li, G., Wang, L., Zhao, Q., et al. (2018). A Lever-like Transduction Pathway for Long-Distance Chemical- and Mechano-Gating of the Mechanosensitive Piezo1 Channel. *Nat. Commun.* 9, 1300. doi:10.1038/s41467-018-03570-9

Weed, S. A., and Parsons, J. T. (2001). Cortactin: Coupling Membrane Dynamics to Cortical Actin Assembly. *Oncogene* 20, 6418–6434. doi:10.1038/sj.onc.1204783

Wu, H., and Parsons, J. T. (1993). Cortactin, an 80/85-kilodalton Pp60src Substrate, Is a Filamentous Actin-Binding Protein Enriched in the Cell Cortex. *J. Cell Biol.* 120, 1417–1426. doi:10.1083/jcb.120.6.1417

Yan, C., Wang, F., Peng, Y., Williams, C. R., Jenkins, B., Wildonger, J., et al. (2018). Microtubule Acetylation Is Required for Mechanosensation in Drosophila. *Cell Rep.* 25, 1051. doi:10.1016/j.celrep.2018.09.075

Yang, S., and Huang, X. Y. (2005). Ca2+ Influx through L-type Ca2+ Channels Controls the Trailing Tail Contraction in Growth Factor-Induced Fibroblast Cell Migration. *J. Biol. Chem.* 280, 27130–27137. doi:10.1074/jbc.M501625200

Yi, K., Unruh, J. R., Deng, M., Slaughter, B. D., Rubinstein, B., and Li, R. (2011). Dynamic Maintenance of Asymmetric Meiotic Spindle Position through Arp2/3-Complex-Driven Cytoplasmic Streaming in Mouse Oocytes. *Nat. Cell Biol.* 13, 1252–1258. doi:10.1038/ncb2320

Yogi, A., Callera, G. E., Tostes, R., and Touyz, R. M. (2009). Bradykinin Regulates Calpain and Proinflammatory Signaling through TRPM7-Sensitive Pathways in Vascular Smooth Muscle Cells. *Am. J. physiology. Regul. Integr. Comp. physiology* 296, R201. doi:10.1152/ajpregu.90602.2008

Zarychanski, R., Schulz, V. P., Houston, B. L., Maksimova, Y., Houston, D. S., Smith, B., et al. (2012). Mutations in the Mechanotransduction Protein PIEZO1 Are Associated with Hereditary Xerocytosis. *Blood* 120, 1908–1915. doi:10.1182/blood-2012-04-422253

Zhang, H., Kong, Q., Wang, J., Jiang, Y., and Hua, H. (2020). Complex Roles of cAMP-PKA-CREB Signaling in Cancer. *Exp. Hematol. Oncol.* 9, 32. doi:10.1186/s40164-020-00191-1

Zhao, Q., Zhou, H., Chi, S., Wang, Y., Wang, J., Geng, J., et al. (2018). Structure and Mechanogating Mechanism of the Piezo1 Channel. *Nature* 554, 487–492. doi:10.1038/nature25743

Zhao, Y., Araki, S., Wu, J., Teramoto, T., Chang, Y. F., Nakano, M., et al. (2011). An Expanded Palette of Genetically Encoded Ca^{2+} Indicators. *Science* 333, 1888. (New York, N.Y.). doi:10.1126/science.1208592

Zippel, R., Balestrini, M., Lomazzi, M., and Sturani, E. (2000). Calcium and Calmodulin Are Essential for Ras-GRF1-Mediated Activation of the Ras Pathway by Lysophosphatidic Acid. *Exp. Cell Res.* 258, 403–408. doi:10.1006/excr.2000.4937

Conflict of Interest: The authors declare that the research was conducted in the absence of any commercial or financial relationships that could be construed as a potential conflict of interest.

Publisher's Note: All claims expressed in this article are solely those of the authors and do not necessarily represent those of their affiliated organizations, or those of the publisher, the editors and the reviewers. Any product that may be evaluated in this article, or claim that may be made by its manufacturer, is not guaranteed or endorsed by the publisher.

frontiers | Frontiers in Cell and Developmental Biology

ORIGINAL RESEARCH
published: 19 May 2022
doi: 10.3389/fcell.2022.847852

FRET Visualization of Cyclic Stretch-Activated ERK *via* Calcium Channels Mechanosensation While Not Integrin β1 in Airway Smooth Muscle Cells

Xin Fang, Kai Ni, Jia Guo, Yaqin Li, Ying Zhou, Hui Sheng, Bing Bu, Mingzhi Luo, Mingxing Ouyang and Linhong Deng**

Institute of Biomedical Engineering and Health Sciences, School of Pharmacy & School of Medicine, Changzhou University, Changzhou, China

OPEN ACCESS

Edited by:
Jihye Seong,
Korea Institute of Science and Technology, South Korea

Reviewed by:
Tae-Jin Kim,
Pusan National University, South Korea
Dian Jing,
Shanghai Jiao Tong University, China

***Correspondence:**
Mingxing Ouyang
mxouyang@cczu.edu.cn
Linhong Deng
dlh@cczu.edu.cn

Specialty section:
This article was submitted to Signaling, a section of the journal Frontiers in Cell and Developmental Biology

Received: *03 January 2022*
Accepted: *05 April 2022*
Published: *19 May 2022*

Citation:
Fang X, Ni K, Guo J, Li Y, Zhou Y, Sheng H, Bu B, Luo M, Ouyang M and Deng L (2022) FRET Visualization of Cyclic Stretch-Activated ERK via Calcium Channels Mechanosensation While Not Integrin β1 in Airway Smooth Muscle Cells. Front. Cell Dev. Biol. 10:847852. doi: 10.3389/fcell.2022.847852

Mechanical stretch is one type of common physiological activities such as during heart beating, lung breathing, blood flow through the vessels, and physical exercise. The mechanical stimulations regulate cellular functions and maintain body homeostasis. It still remains to further characterize the mechanical-biomechanical coupling mechanism. Here we applied fluorescence resonance energy transfer (FRET) technology to visualize ERK activity in airway smooth muscle (ASM) cells under cyclic stretch stimulation in airway smooth muscle (ASM) cells, and studied the mechanosensing pathway. FRET measurements showed apparent ERK activation by mechanical stretch, which was abolished by ERK inhibitor PD98059 pretreatment. Inhibition of extracellular Ca^{2+} influx reduced ERK activation, and selective inhibition of inositol 1,4,5-trisphosphate receptor (IP_3R) Ca^{2+} channel or SERCA Ca^{2+} pump on endoplasmic reticulum (ER) blocked the activation. Chemical inhibition of the L-type or store-operated Ca^{2+} channels on plasma membrane, or inhibition of integrin β1 with siRNA had little effect on ERK activation. Disruption of actin cytoskeleton but not microtubule one inhibited the stretch-induced ERK activation. Furthermore, the ER IP_3R-dependent ERK activation was not dependent on phospholipase C-IP_3 signal, indicating possibly more mechanical mechanism for IP_3R activation. It is concluded from our study that the mechanical stretch activated intracellular ERK signal in ASM cells through membrane Ca^{2+} channels mechanosensation but not integrin β1, which was mediated by actin cytoskeleton.

Keywords: cyclic stretch, mechanosensation, ERK, calcium channel, fluorescence resonance energy transfer

INTRODUCTION

Mechanical forces associated with cyclic stretch play important roles in the control of vascular functions and pulmonary circulation homeostasis, and stretch exercise in ordinary life shows benefits in improving physical and mental health (Geneen et al., 2017; Fang et al., 2019). In medical emergency, however, mechanical ventilation with repetitive cyclic stretch can result in inflammation and lung tissue injury (Slutsky and Ranieri, 2014; Horie et al., 2016). In the past decades, mechanical stretch in regulating physiological functions and cellular signaling has attracted wide research

interests (Sadoshima and Izumo, 1993; Loperena et al., 2018; Chu et al., 2019; Ren et al., 2021). The mechanotransduction mechanism of mechanical stimulation to cellular biochemical signals has been a topic that is yet to be fully understood.

Physiologically, mechanical stimulations show fundamental roles in cell behaviors, tissue and organ developments, and disease-associated processes (Ingber, 2003; Mammoto et al., 2013; Qi et al., 2016). Several mechanisms have been discovered for the mechanical stimulations to biochemical signal transformations including cellular mechanosensitive components and extracellular matrix (Swaminathan and Gloerich, 2021). For instance, Polycystin-1, a large-size molecule with eleven transmembrane domains, has been shown to act as the mechanosensing component to modulate mechanical stretch-induced bone-cell differentiation (Dalagiorgou et al., 2013; Dalagiorgou et al., 2017). Membrane-localized ion channels TRPV4 and Piezo2 played central roles in calcium oscillation induced by physiological (8%) and injurious (18% of strain) levels of mechanical strains in chondrocytes, respectively (Du et al., 2020). Kim et al. investigated the mechanism of cellular Ca^{2+} signaling induced by pulling force using optical laser tweezers, and found that the endoplasmic reticulum (ER) Ca^{2+} release is mediated by both actin cytoskeleton and mechanosensitive Ca^{2+} channels on the plasma membrane (Kim et al., 2015).

Cellular biochemical activities are regulated by mechanical stretch at multiple levels. It has been observed for long that cells reorient themselves nearly perpendicular to the direction of cyclic stretch, and so does the actin cytoskeleton (Hayakawa et al., 2001; Wang et al., 2001; Jungbauer et al., 2008; Liu et al., 2008). Except for morphological changes, ATP release is visualized by induction of mechanical stretch in human airway smooth muscle (ASM) cells (Takahara et al., 2014), and the ATP release is regulated by Ca^{2+} signaling via caveolae-mechanosensitive pathway in alveolar epithelium (Diem et al., 2020). The level of total reactive oxygen species by mitochondrial and NADPH oxidases is increased under mechanical stretch in retinal pigment epithelial cells (Liang et al., 2019). Cyclic mechanical stretch also increases β_{1D}-integrin protein level and activates the downstream signaling proteins focal adhesion kinase (FAK) and RhoA (Zhang et al., 2007). The abundance of CD40 in endothelial cells is upregulated through transforming growth factor β1 signaling when co-cultured with smooth muscle cells under cyclic stretch stimulation (Korff et al., 2007). A recent study identified mechanical stretch-mediated transcriptome profile changes during skin regeneration including nine robust hub genes and six transcriptional factors–mRNA regulatory network (Liu W. et al., 2021). Cyclic stretch also regulates extracellular secretions of vascular smooth muscle cells including microvesicles and growth factors, leading to functional modulations of surrounding cells and tissues (Wang et al., 2017; Liu J.-T. et al., 2021).

Mechanical stretch has been shown to stimulate the MAPK family ERK1/2 and c-Jun NH2-terminal kinase (JNK), depending on the stress fiber strain but not FAK in endothelial cells (Correa-Meyer et al., 2002; Hsu et al., 2010; Schmidt et al., 2016). Alexander et al. reported stretch-induced ERK1/2 activation mediated by phospholipase A_2 (PLA_2)-dependent release of arachidonic acid in renal epithelial cells (Alexander et al., 2004). Myosin II-regulated tension on the stress fibers shows positive correlation with ERK activation in fibroblasts (Hirata et al., 2015). Kim et al. reported that in mechanical stretch-induced loss of myelin proteins, the release of Ca^{2+} from endoplasmic reticulum (ER) resulted in ERK activation in oligodendrocytes (Kim et al., 2020). Although ERK activation by mechanical stretch has been well documented, it still remains to further characterize the mechanosensitive pathway for the mechanical-biomechanical coupling to activate ERK kinase.

Airway smooth muscle (ASM) cells, one major component of bronchial tissue underneath the epithelia, provide mechanical support and contraction force in the bronchial during breathing, and excessive ASM mass is related to airway hyper-responsiveness under asthmatic condition, which has been a treatment target (Zuyderduyn et al., 2008; Balestrini et al., 2021). As a chronical disease impacting a large population in the world, asthma can be characterized with airway inflammation, increased ASM mass and prolonged contraction in the bronchial (Zuyderduyn et al., 2008; Doeing and Solway, 2013). ERK also shows crucial roles in regulating ASM cell proliferation and interleukin expression in lymphocytes in asthma-related conditions (Burgess et al., 2008; Li et al., 2010). Here we applied fluorescence resonance energy transfer (FRET) biosensor to directly visualize cellular ERK activity induced by cyclic stretch in ASM cells which are under physiological stretch during breathing. The FRET biosensor allows to visualize the dynamic ERK activity in live cells along with subcellular resolution (Komatsu et al., 2011; Ponsioen et al., 2021), which provided the fine measurement of ERK activation during the cyclic stretch stimulation. Our work demonstrated in ASM cells that Ca^{2+} channels via actin cytoskeleton, particularly those channels on ER membrane, acted as the mechanosensing pathway to the downstream activation of ERK. Interestingly, the ER IP_3R-dependent ERK activation by cyclic stretch was independent of upstream PLC-IP_3 signal, indicating possibly more mechanical mechanism for the IP_3R activation.

MATERIALS AND METHODS

Chemical Reagents

2-Amino-ethoxydiphenyl borate (2-APB, 100 μM), Nifedipine (10 μM), $LaCl_3$ (100 μM), Cytochalasin D (1 μM), Blebbistatin (20 μM), Nocodazole (1 μM), ML-7 (20 μM), the ROCK inhibitor Y27632 (20 μM), and phalloidin-TRITC were purchased from Sigma-Aldrich. Thapsigargin (TG, 10 μM) was purchased from Abcam, U73122 (10 μM) from MedChemExpress, and fibronectin from Corning. ITGB1 (Beta1) siRNA (Integrin siRNA, 30 nM) was purchased from Thermo Fisher Scientific.

Cell Culture

Primary ASM cells were isolated from the tracheas of 6-8-week-old Sprague Dawley rats as described previously (approved by the Ethics Committee of Changzhou University on Studies Ethics, Grant No. NSFC 11532003) (Wang et al., 2016). The cells were maintained in low-glucose Dulbecco's modified Eagle's medium (DMEM, Sigma-Aldrich) supplemented with 10% fetal bovine

serum (FBS, Thermo), 100 μg/ml penicillin, and 100 unit/ml streptomycin at 37°C with 5% CO_2 in a humidified incubator.

Construction of Nuclear Localized ERK FRET Biosensor (Nuc-ERK FRET)

To make nuclear localized ERK biosensor, the nuclear-exporting signal (NES) peptide in the construct was replaced with double nuclear-localized signal (NLS) peptide (2x Pro-Lys-Lys-Lys-Arg-Lys-Val). Briefly, ECFP DNA fragment with 2xNLS sequence at the C-terminal was amplified by PCR. Both the original construct and amplified ECFP fragment were digested by NotI and SalI restriction enzymes, followed by ligation of the two digested products together to generate Nuc-ERK FRET construct.

Plasmid and siRNA Transfections

DNA plasmid and siRNA were transfected into ASM cells by using Lipofectamine3000 according to the manual protocol (Invitrogen). Briefly, cells were passaged in medium without antibiotics into 6-well plates the day before transfection. By following the protocol, 2.5 μg biosensor DNA, 4 μl P3000, and 4 μl Lipofectamine3000 were mixed to assemble Lipid-DNA particles for each well before adding it into the cell culture. The medium was changed in 8 h and cell imaging experiments were performed 40–64 h later.

For siRNA co-transfection, when cells reached 60%–80% confluency, siRNA (30 nM) was transfected into the cells with 4 μl Lipofectamine3000 reagent. The medium was changed in 8 h, and after siRNA transfection for 24 h, the ERK FRET biosensor DNA was further transfected into the cells.

Verification of ITGB1 siRNA Transfection Efficiency by qPCR

The efficiency of ITGB1 siRNA transfection was assessed with mRNA expression using Real-Time Quantitative PCR (qPCR) assay. Total RNA from cultured ASM cells was extracted using the TRI Reagent RNA Isolation Reagent (#T9424, Sigma). Total RNA weighing 500 ng was applied to generate 1st strand cDNA by using the Revert Aid First Strand cDNA Synthesis Kit (#K1622, Thermo, MA). The sequences of associated qPCR primers for rat ITGB1 were derived from the previous report including GAATGGAGTGAATGGGACAGGAG (ITGB1 forward), CAGATGAACTGAAGGACCACCTC (ITGB1 reverse), and the control GAPDH primers AGGTCGGTGTGA ACGGATTTG (forward) and GGGGTCGTTGATGGCAACA (reverse) (Luo et al., 2018). The primers were synthesized from General Biosystems (Anhui, China), and PowerUp SYBR Green Master Mix (#A25742, Applied Biosystems, CA) was used for PCR amplification. The reaction was run in the qRT-PCR system (StepOnePlus, Applied Biosystems) with 1 μL of the cDNA in a 10 μL reaction according to the manufacturer's instructions. Calibration and normalization were done using the $2^{-\Delta\Delta CT}$ method, where ΔΔCT = CT (target gene) -CT (reference gene), and CT referred to the PCR cycle number by reaching the defined fluorescence intensity. Fold changes in mRNA expression were calculated based on the resulting CT values from three independent experiments.

Mechanical Stretch

After DNA transfection for 24 h, cells were detached using Accutase solution (Sigma), and transferred to collagen I and fibronectin (40 μg/ml) double-coated 6-well BioFlex plates (Flexcell International Corporation, Hillsborough, NC, United States). After which the cells were cultured in the medium containing 1% FBS for 12–16 h and reached 60–80% confluence before the mechanical stretch. Cyclic stretch was applied with a 0.5-Hz sinusoidal curve at 12% elongation by using a Flexcell® FX-5000™ Tension System (Flexcell® International Corporation). The computer program-controlled bioreactor used vacuum and positive air pressure to apply cyclic strain to cells cultured on flexible-bottomed BioFlex plates. After

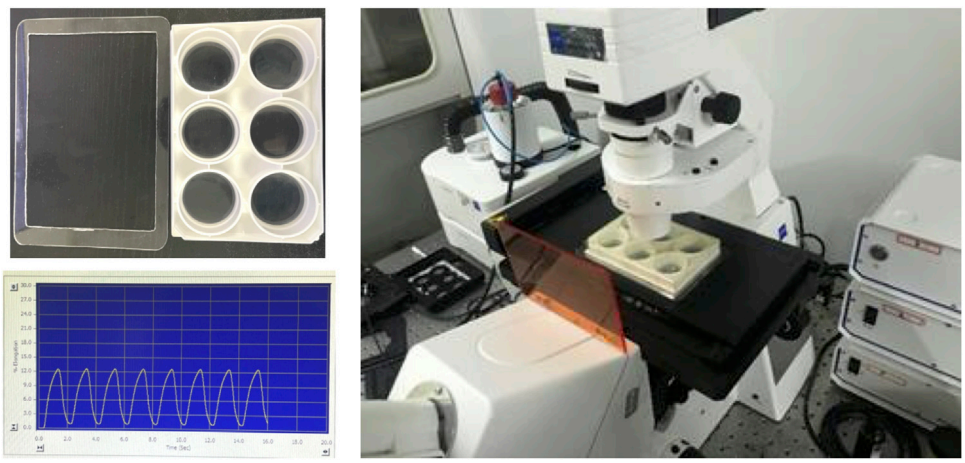

FIGURE 1 | The setup to load the BioFlex plate on the microscope stage for FRET imaging, and the sample of 0.5-Hz sinusoidal curve from cyclic stretch by using the Flexcell® System.

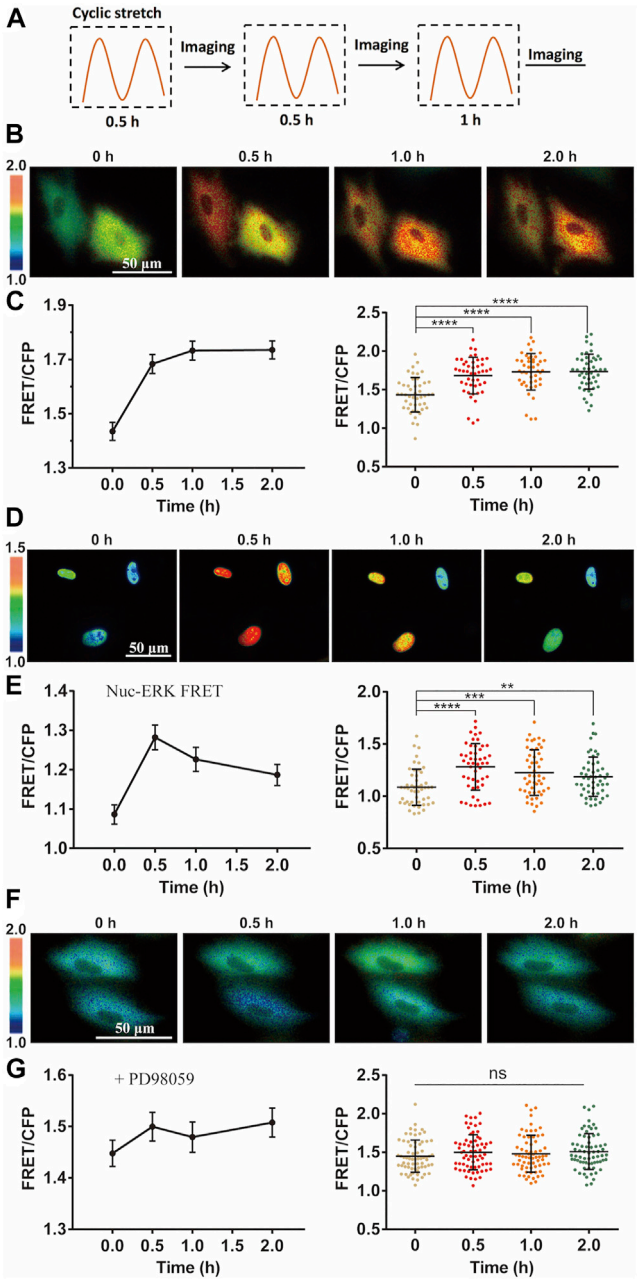

FIGURE 2 | Cyclic stretch-induced ERK activation by FRET measurements. FRET/ECFP emission ratiometric images show the activation of ERK by cyclic stretch in ASM cells pre-incubated in 1% FBS culture medium. Scale bar = 50 μm. **(A)** Illustrated experimental procedures of cyclic stretch stimulation (with a 0.5-Hz sinusoidal curve at 12% elongation deformation) followed by FRET imaging in multiple cycles. **(B,C)** ERK FRET ratio (YPet/ECFP) images **(B)**, and quantifications of the FRET changes in curves (Mean ± S.E.M.) and scattering dots (Mean ± S.D. $n = 46$) **(C)** after cells were stimulated with cyclic stretch for the indicated time. **(D,E)** FRET images with Nuc-ERK FRET biosensor in cells **(D)**, and their statistical quantifications ($n = 50$) **(E)** after cyclic stretch at the indicated time points. **(F,G)** ERK FRET images **(E)** and FRET statistical quantifications ($n = 67$) **(G)** in cells pre-treated with 10 μM PD98059 inhibitor for 1 h. Student's t-test was performed between the control and one experimental group, and multiple rounds of t-test were done for the variable experimental conditions. *, **, ***, and **** indicate $p < 0.05$, 0.01, 0.001, and 0.0001 from Student's t-test analysis while 'ns' for no significant difference, and so on through the paper.

the durations of cyclic stretch, the BioFlex plates with cells were moved from the Flexcell incubator to Zeiss microscopy for FRET imaging. The images of a group of cells were acquired within 10 min for each well.

FRET Microscopy Imaging

The processes of FRET imaging and quantification were similar to our recent descriptions (Ouyang et al., 2019; Yao et al., 2020). Briefly, the Zeiss microscopy system (Zeiss Cell Observer) was equipped with the functions of multi-positions, fine auto-focusing, and automatic-switchable dichroic rotator. The scope stage was supplemented with an incubator box (Zeiss) to maintain temperature at 37°C and 5% CO_2 for live cell samples. During FRET image acquisitions through ECFP and FRET (YPet) channels, the parameters for excitation filter and dichroic mirror were 436 ± 10 and 455 nm, respectively, and the emission filters of ECFP and FRET (YPet) channels were 480 ± 20 nm and 535 ± 15 nm, respectively.

To take the FRET images before and after the cyclic stretch, we made an accessory holder with acrylic plate to load the BioFlex plate on the microscopy stage, as shown in **Figure 1**. Before starting the stretch, 15–20 positions of fluorescent cells were selected per well, and FRET images were acquired as the pre-stretch condition. After the duration (0.5–1 h) of cyclic stretch, the same positions of cells were reloaded with minor adjustments, and the FRET images were taken within 10 min for each well before the next cycle.

FRET Quantification and Statistical Analysis

FRET quantifications were processed using the Wang Lab (UCSD)-developed software package FluoCell in MATLAB (available on http://github.com/lu6007/fluocell) (Qin et al., 2019). Fluorescence signals from ECFP and FRET (YPet) images were measured after background subtractions, and the ratio of the two channels was calibrated in the pixel-to-pixel manner. Data procession and statistical analysis were done by the software of Graphpad Prism 6, and Excel. The quantified FRET data from a group of cells was expressed in curves (Mean ± S.E.M.), and scattering dots (Mean ± S.D.). *, **, *** and **** indicate $p < 0.05$, 0.01, 0.001, and 0.0001 from Student's t-test, which was applied for significant difference analysis. Multiple times of t-test analysis done between the control and one experimental group were carried for variable experimental conditions using Graphpad Prism 6. All described FRET experiments have been repeated independently on different days with similar conclusions, and statistical quantifications were performed based on the data acquired from different time.

RESULTS

Cyclic Mechanical Stretch-Induced ERK Activation Measured by FRET Biosensor

To understand how mechanical stimulation from cyclic stretch activates biochemical signals in live cells, we applied FRET

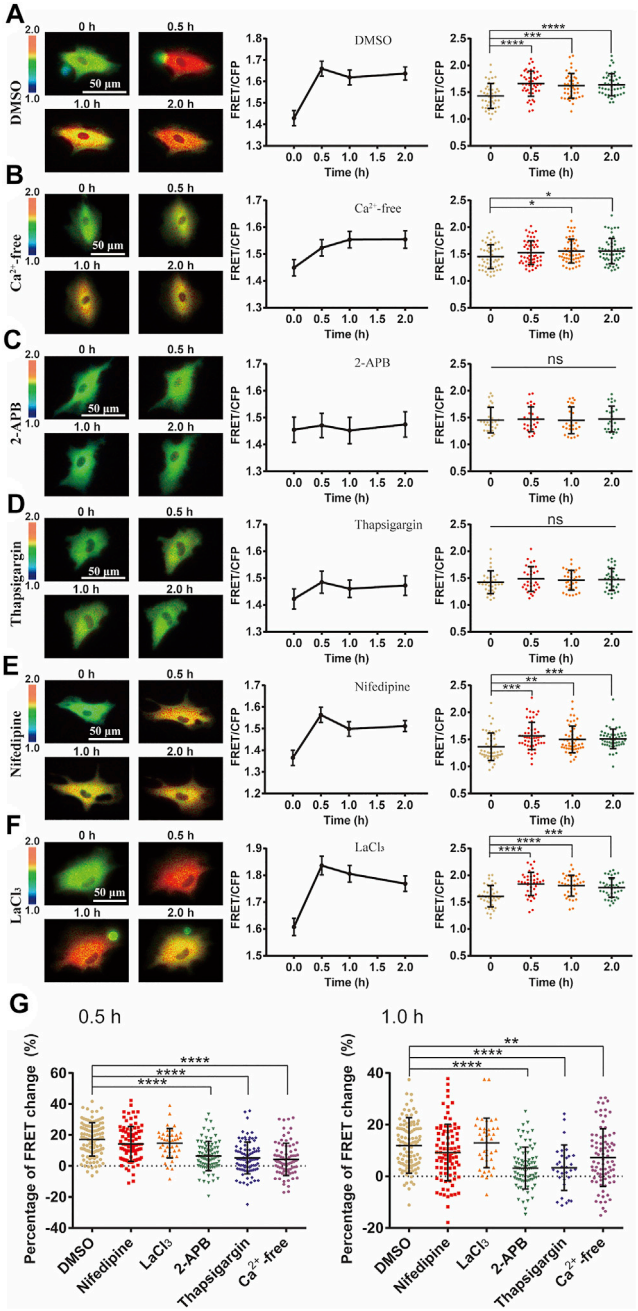

FIGURE 3 | Ca^{2+} channel-dependent ERK activation by cyclic stretch. ASM cells were pretreated with inhibitors of variable Ca^{2+} channels followed by cyclic stretch and imaging. FRET ratiometric images along with FRET change quantifications are shown for each condition before and after cyclic stretch. **(A–F)** FRET changes of ERK biosensor in cells under control (0.1% (v/v) DMSO) condition (N = 42) **(A)**; in Ca^{2+}-free culture medium (n = 53) **(B)**; pre-treated with 100 μM 2-APB, an IP_3R blocker (n = 26) **(C)**; 10 μM Thapsigargin, a SERCA pump blocker (n = 32) **(D)**; 10 μM Nifedipine, a L-type Ca^{2+} channel blocker (n = 52) **(E)**; 100 μM $LaCl_3$, store-operated Ca^{2+} channel (SOC) blocker (n = 39) **(F)**. **(G)** Statistical quantifications for the percentage changes of FRET ratio (YPet/ECFP) in ASM cells before and after 0.5 h cyclic (left graph) and total 1 h stretch (right graph). The conditions from **(A–F)** were pre-treated with DMSO (control), Nifedipine, $LaCl_3$, 2-APB, Thapsigargin or in calcium-free medium, respectively. (*Continued*)

FIGURE 3 | n = *108, 87, 39, 84, 90/32, 83 in the indicated order. Student's t-test was performed between the control and one experimental group, and multiple rounds of t-test were done for the variable experimental conditions.*

biosensor to measure ERK kinase activity in ASM cells. According to the previous study (Takahara et al., 2014), 12% strain deformation with a 0.5-Hz sinusoidal curve was within the physiological scale and was applied on the cells seeding on the elastic membrane by the Flexcell® Tension System, which could induce alignment of cells perpendicularly to the stretch direction in 7.5 h (**Supplementary Figure S1**). In regarding the inapplicability of visualizing the FRET signals on the microscope simultaneously during the cyclic stretch, the procedures were carried out in the following process: the FRET images were taken after 0.5 h-stretch followed by another 0.5 h-stretch and imaging, and then continued with one more 1 h-stretch and imaging (depicted in **Figure 2A**). The imaging was usually done within 10–30 min between the three times of stretch, and images of similar cell positions were acquired each time.

Intracellular ERK in the cytoplasm was activated by the mechanical stretch, as seen by the FRET changes (**Figure 2B**). FRET quantification from a group of cells showed apparent activity increase with statistical significance (**Figure 2C**). As control, no apparent FRET change was observed in the similar imaging procedure without stretch stimulation (**Supplementary Figure S2**). The platelet-derived growth factor (PDGF) regulates ERK activity in ASM cell proliferation and also inflammation in asthmatic condition (Lee et al., 2001; Kardas et al., 2020). The magnitude of ERK FRET change (~15–20%) from the mechanical stretch was comparable to PDGF-stimulated FRET change in ASM cells (**Supplementary Figure S3**). In consideration of ERK shuttling between the cell cytoplasm and nucleus, we modified the ERK biosensor to generate nuclear localized version Nuc-ERK FRET. As shown in **Figures 2D,E**, nuclear ERK was also activated by the mechanical stretch, which indicates the cytoplasmic increase is not due to nuclear ERK transportation. Hence, we used cytoplasmic FRET measurement to represent the whole cells in the following study. The ERK activation reported by FRET signals was verified by increased phosphorylation level of ERK with phospho-ERK antibody immunoblotting under the cyclic stretch (**Supplementary Figure S4**). The 12% strain deformation of ASM cells is within the physiological range of stretch magnitude (Takahara et al., 2014), which is also seen by the maintained cell shape (**Figure 2B**) and actin stress fibers (**Supplementary Figure S5**) after stretch. We further pretreated the cells with ERK inhibitor PD98059, which abolished stretch-induced FRET signals (**Figures 2F,G**), hence the FRET changes truly reported ERK activity.

Ca^{2+} Channel-Dependent ERK Activation by Cyclic Stretch

We then investigated the mechanosensitive components in transducing the mechanical stimulation into biochemical signals in cells. Ca^{2+} channels located on plasma membrane or endoplasmic reticulum (ER) are sensitive to

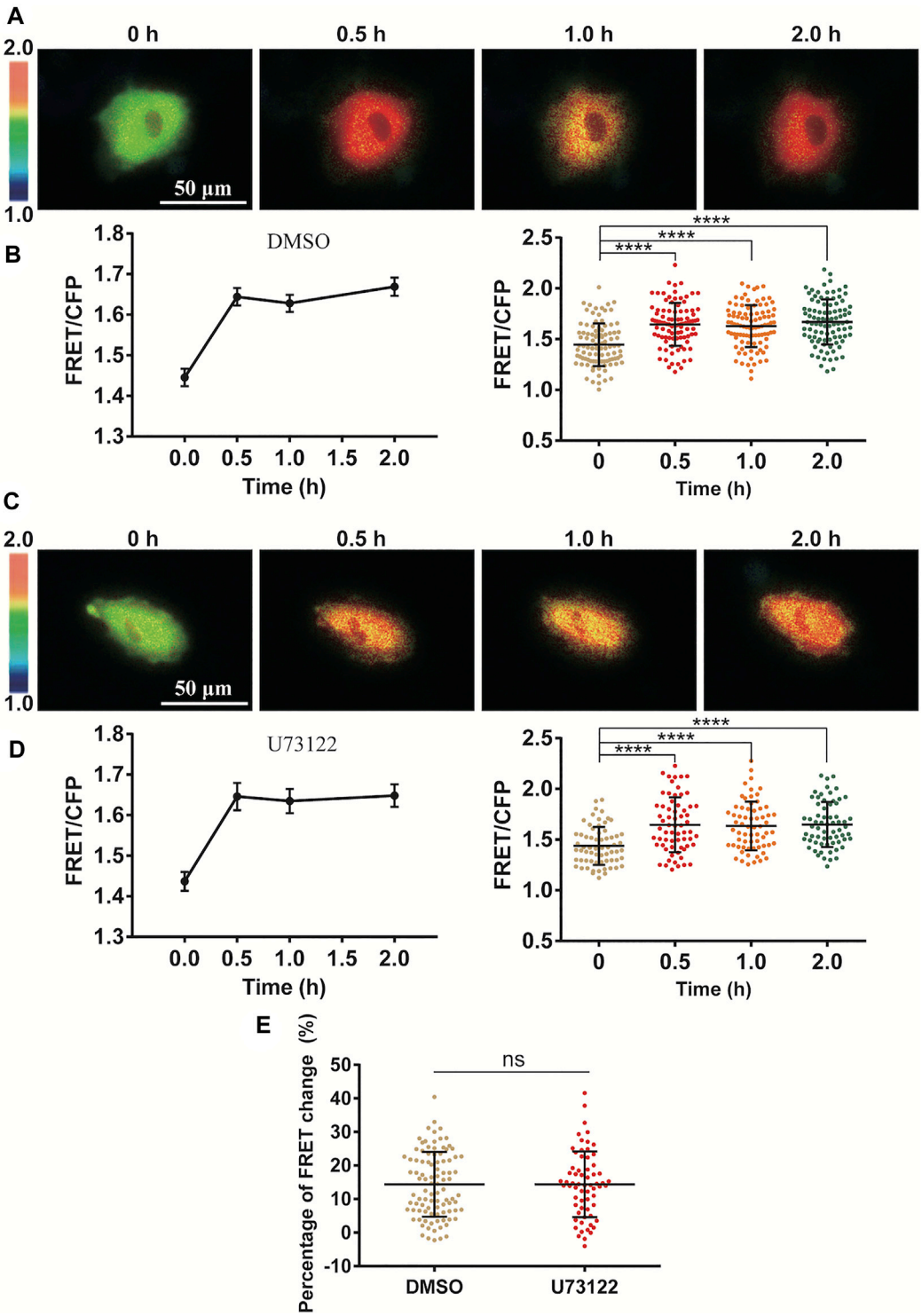

FIGURE 4 | Independence of PLC-IP_3 signal for cyclic stretch-induced ERK activation. ASM cells were pretreated with PLC inhibitor U73122 (10 μM) for 1.5 h followed by cyclic stretch. **(A–D)** FRET ratiometric images and quantification of FRET changes before and after cyclic stretch under the conditions of control (DMSO) **(A,B)** and U73122 treatment **(C,D)**. **(E)** Statistical comparison of FRET changes between the control (n = 96) and U73122 (n = 65) treatment after 0.5 h cyclic stretch, which is based on FRET data from three independent experiments. Student's t-test was performed between the control and one experimental group.

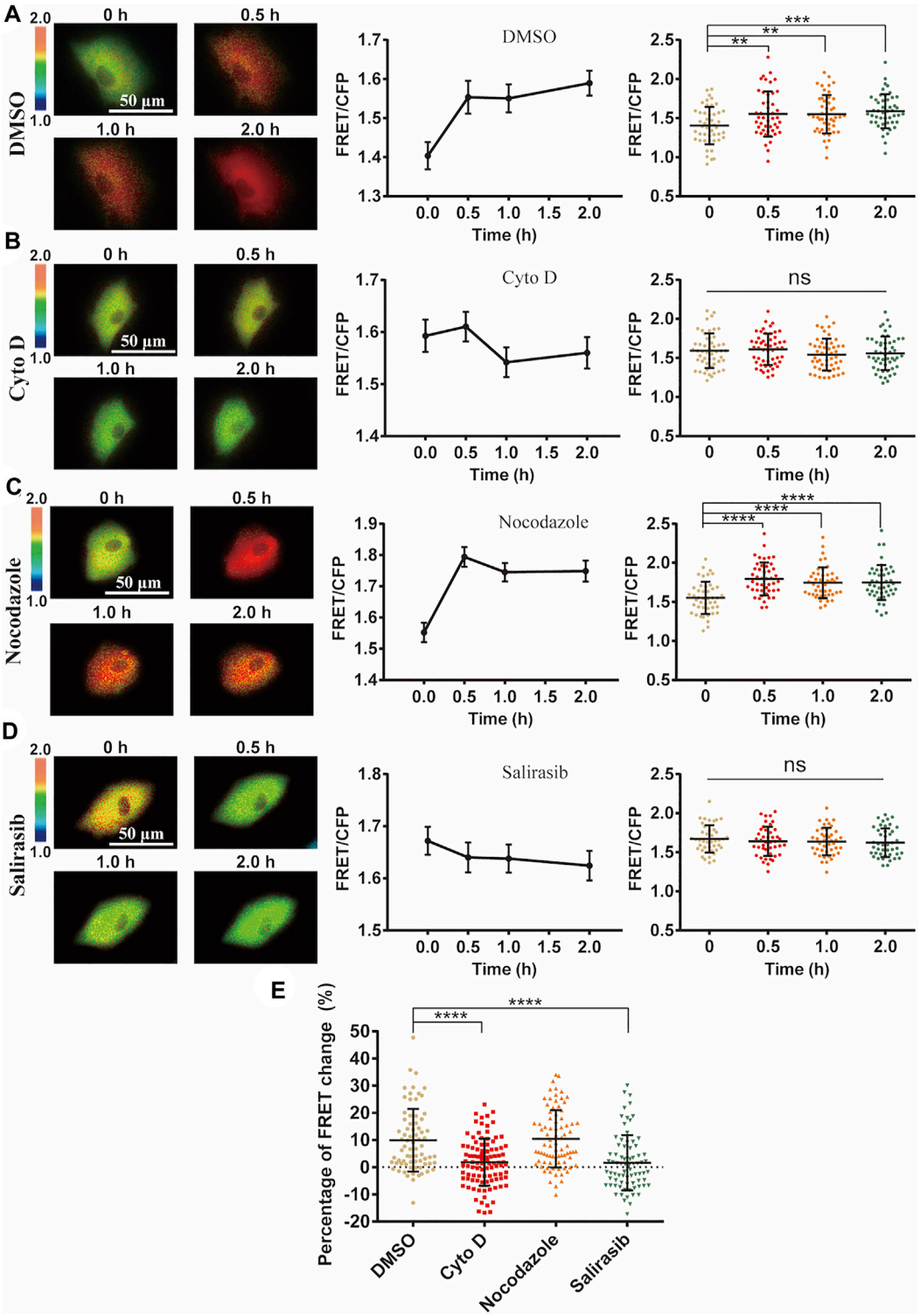

FIGURE 5 | Role of cell cytoskeleton on cyclic stretch-induced ERK activation. ASM cells were pretreated with cytoskeleton or Ras inhibitors, followed by cyclic stretch and imaging. FRET ratiometric images along with change quantifications are shown for each condition before and after cyclic stretch. **(A–D)** ERK FRET ratiometric images and statistical quantifications of FRET changes in ASM cells pretreated with DMSO (n = 47) **(A)**, 1 μM Cyto D (N = 51) **(B)**, 1 μM Nocodazole (n = 45) **(C)**, and 75 μM Ras inhibitor Salirasib (n = 43) **(D)**. **(E)** Statistical comparisons of FRET percentage changes in ASM cells pre-treated with DMSO, Cyto D, Nocodazole, and Salirasib (n = 73, 99, 82, 77) **(A–D)** before and after 0.5 h cyclic stretch, based on image data from two independent experiments. Student's t-test was performed between the control and one experimental group.

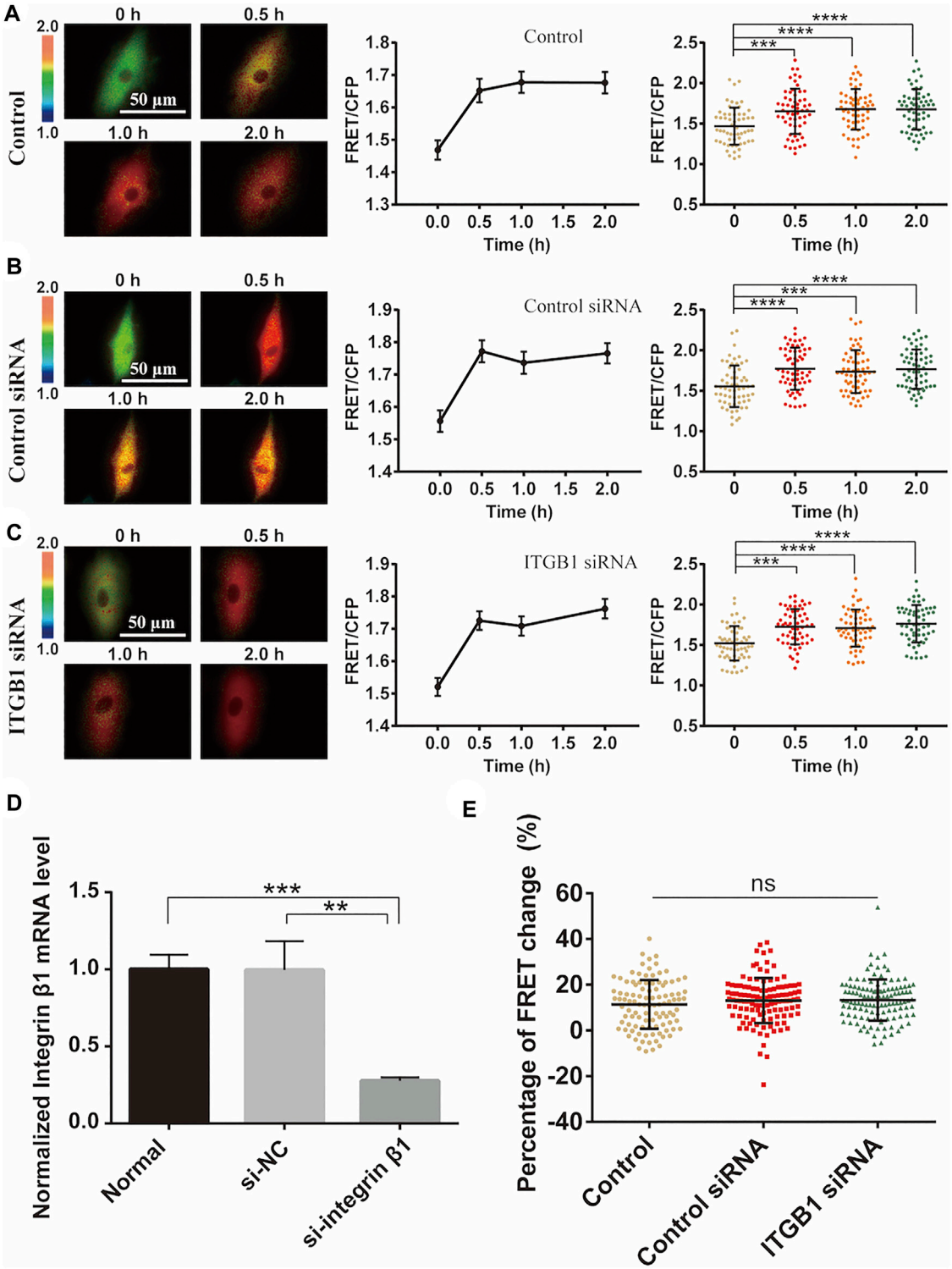

FIGURE 6 | Integrin β1 (ITGB1) signal in cyclic stretch-induced ERK activation. ASM cells were transfected with ITGB1 inhibitory siRNA, followed by cyclic stretch and imaging. **(A–C)** FRET ratiometric images along with FRET change quantifications are shown before and after cyclic stretch in ASM cells without transfection **(A)**, or transfected with control scramble siRNA **(B)** and ITGB1 siRNA **(C)** (n = 58, 60, 58), respectively. **(D)** qPCR quantification from three experimental data confirmed the reduced level of ITGB1 mRNA expression after siRNA transfection. **(E)** Statistical comparisons of FRET percentage changes in cells without transfection, or transfected with control or ITGB1 siRNA (n = 103, 116, 121) **(E)** before and after 0.5 h stretch. Student's t-test was performed between the control and one experimental group.

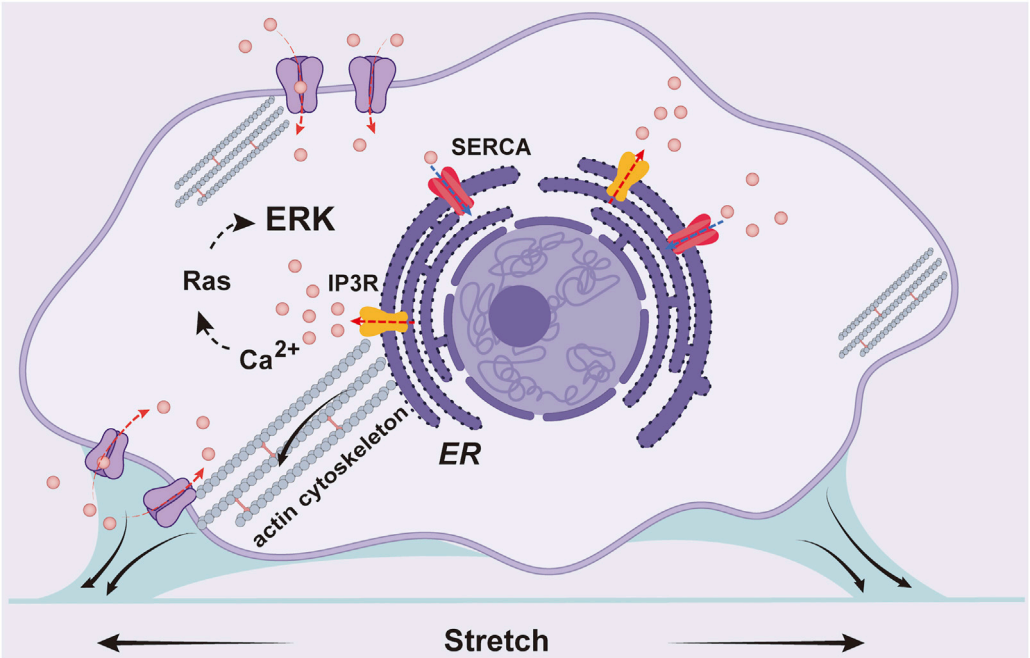

FIGURE 7 | A schematic illustration for the mechanical activation of ERK in ASM cells. The cyclic stretch applied on the cells activates Ca^{2+} channels on the plasma and ER membranes including IP_3R and SERCA pump, likely mediated by force transmission through actin cytoskeleton, and Ca^{2+} signals further trigger downstream pathway to activate ERK.

mechanical stimulations (Kim et al., 2015). By switching the culture medium to Ca^{2+}-free one before cyclic stretch, ERK activation was inhibited with a delayed response (**Figures 3A,B**). This suggests that Ca^{2+} channels on the plasma membrane had significant contributive role while not essential to the mechanical activation of ERK. However, by selective chemical inhibition of IP_3R Ca^{2+} channel with 2-APB, or SERCA pump with Thapsigargin on ER membrane (Wang et al., 2021), the mechanical activation of ERK was almost blocked (**Figures 3C,D**), indicating that Ca^{2+} release from the ER store had an essential role. In contrast, there was little effect on the ERK activation by inhibition of L-type Ca^{2+} channel with nifedipine, or store-operated Ca^{2+} channel (SOC) with $LaCl_3$ on plasma membrane (Parekh and Putney, 2005; Wang et al., 2021) (**Figures 3E,F**). From statistical comparison of the FRET changes (in percentage) after 0.5 h stretch and total 1 h stretch (**Figure 3G**), inhibition of IP_3R or SERCA pump on ER membrane had the most significant impact on the mechanical activation of ERK, followed by inhibiting extracellular Ca^{2+} uptakes with reduced delayed response, while L-type Ca^{2+} channel and SOC on the plasma membrane were not actively involved into the ERK activation.

Cyclic Stretch-Induced ERK Activation Not Dependent on PLC-IP_3 Signal

Since Ca^{2+} release through IP_3R channel on ER membrane was essential in the stretch activation of ERK (**Figure 3**), we further looked at whether inositol 1,4,5-triphosphate (IP_3) production was necessary in turning on the IP_3R channel. As a classic pathway, phospholipase C (PLC) is an enzyme that hydrolyzes PIP2 on the plasma membrane to generate IP_3, which results in opening the IP_3R Ca^{2+} channel (Bartlett et al., 2020). In our experiments, inhibition of PLC activity with specific inhibitor U73122 had little effect on the cyclic stretch-induced ERK activation in comparison to the control group (**Figures 4A–E**). This indicates that the PLC-IP_3 signaling pathway was not essential in mechanical stimulation of IP_3R Ca^{2+} channel for ERK activation.

The Regulatory Role of Actin Cytoskeleton on the Mechanical Activation of ERK

Actin cytoskeleton often serves for mechanical transmission within cells (Wei et al., 2020). We hence checked the role of cytoskeleton in the mechanical activation of ERK by FRET measurements. After loss of actin cytoskeleton integrity with Cytochalasin D (Cyto D) treatment which inhibited actin filament polymerization (**Supplementary Figure S5**), cyclic stretch-induced ERK activation was almost completely inhibited (**Figures 5A,B**). Contrarily, inhibition of microtubule cytoskeleton with Nocodazole treatment did not show much effect (**Figure 5C**). The small GTPase Ras acts upstream of ERK through Ras-Raf-MEK-ERK signaling (Rudzka et al., 2021). The stretch-induced ERK activation was suppressed by pretreatment with Ras inhibitor Salirasib

(**Figure 5D**), supporting that mechanically induced Ca^{2+} signal activated ERK through Ras pathway.

Cyclic Stretch-Induced ERK Activation Independent of Integrin β1

Integrins are mechanosensitive molecules on plasma membrane (Sun et al., 2016; Potla et al., 2020). Integrin β1 (ITGB1) is a predominant subunit in forming functional heterodimers with integrin α1, α2. . .α11, and α_v subunits (Cai et al., 2021), so we tried to regulate the representative β1 to check its role in the cyclic stretch-induced activation of ERK. After knockdown of ITGB1 expression with siRNA in cells, there was no obvious impact on the cyclic stretch-induced ERK activation in comparison to the control groups (**Figures 6A–C**). The reduced mRNA expression of ITGB1 was confirmed by qPCR measurements (**Figure 6D**). Statistical quantifications confirmed no significant change in the mechanical stretch-activated ERK by ITGB1 knockdown (**Figure 6E**). These data indicate that integrin $\alpha_{(x)}\beta1$ was not the primary mechanosensor in the mechanical activation of ERK.

DISCUSSION

The physical stretches seem critical for body health and organ homeostasis, whereas extreme stretch can be hurting as seen in sports and clinical applications (Crawford et al., 2021; Kaczka, 2021). By applying the Flexcell® tension system, we investigated cyclic stretch-induced ERK activation in ASM cells, particularly paying attention to the mechanosensitive pathway for the mechanical stimulation to biochemical signal transduction.

FRET measurements showed that ERK was efficiently activated by the mechanical stretch (**Figures 2A–F**). Previous studies have shown that Ca^{2+} signals in stem cells are sensitive to mechanical stimulations (Horie et al., 2016), so we checked whether Ca^{2+} channels are among the mechanosensing components for the ERK activation. Inhibition of extracellular Ca^{2+} uptakes partially reduced the mechanical activation of ERK while blocked Ca^{2+} release from the ER store had complete inhibition (**Figures 3A–D**). L-type Ca^{2+} channel or SOC channel on the plasma membrane was not actively engaged into the induced ERK activation (**Figures 3E,F**). Therefore, the mechanical stretch-induced activation of Ca^{2+} channels was essential for downstream ERK activation, which is within the mechanosensing pathway.

The Ca^{2+} channels on the ER membrane are essential for the mechanical activation of ERK (**Figures 3C,D**), and this observation is consistent with the previous report that Ca^{2+} signal from the ER store is induced by pulling force on the cell surface by optical laser tweezers (Kim et al., 2015). In considering that inhibition of IP_3R channel on ER blocked the ERK activation (**Figure 3C**), and IP_3 is the ligand to turn on IP_3R channel, however, inhibition of PLC-IP_3 pathway had little effect (**Figures 4A–E**). Therefore, PLC-dependent IP_3 production was not essential in the ERK activation, indicating possibly more mechanical mechanism for ER IP_3R channel activation from cyclic stretch stimulation.

Actin cytoskeleton can pass the stretch force within the cells. Loss of actin cytoskeleton resulted in abolishing the mechanical activation of ERK, but not by loss of microtubule cytoskeleton (**Figure 5**), indicating that actin cytoskeleton has the crucial role on ERK activation. Possibly actin cytoskeleton passed the force to trigger the ER Ca^{2+} signals (Kim et al., 2015), which is also suggested from our data (**Figures 5A–E**). Ca^{2+} signals can further activate PKC to induce Ras-Raf-MEK-ERK pathway (Liao et al., 2020; Yan et al., 2020), and our data showed that inhibition of Ras truly blocked the mechanical activation of ERK (**Figures 5D,E**). These data indicate that actin cytoskeleton belongs to the mechanosensing component for ERK activation.

Integrins are mechanosensitive molecules and regulate focal adhesions to transmit the force inside cells (Michael et al., 2009). Integrin subunit β1 forms functional heterodimers with variable integrin subunits $\alpha_{(x)}$, so we regulated β1 to check its role in the stretch-induced ERK activation. Interestingly, by reduction of β1 expression with siRNA, there was no apparent change in the ERK activation level (**Figure 6**). Since cells were attached well under the siRNA transfection, the stretch force may be still transmitted efficiently to activate ERK. Previous studies reported that mechanical stretch up-regulates integrin β_{1D} expression to result in FAK and RhoA activations (Zhang et al., 2007), while ERK activation by mechanical stretch is independent of FAK (Hsu et al., 2010). Hence, our observation seems consistent with that. Therefore, integrin $\alpha_{(x)}\beta1$ did not act essentially as the primary mechanosensing component in this stretch activation of ERK in ASM cells.

CONCLUSION

In summary, we visualized cyclic stretch-induced ERK activation by FRET biosensor in ASM cells, and provided molecular insights for the mechanosensitive pathway from mechanical stimulation to ERK biochemical activity. Data shows that Ca^{2+} channels and actin cytoskeleton are essential mechanosensing components, while integrin β1 is not essential in the mechanotransduction. Together with previous work, our experimental results support the following hypothesis for the mechanical activation of ERK in ASM cells (**Figure 7**): the cyclic stretch applied on the cells activates Ca^{2+} channels mechanically on the plasma and ER membranes, likely mediated by force transmission through actin cytoskeleton, and Ca^{2+} signals further trigger downstream signaling pathways including ERK activity in the cells.

The contributions of this work to the cyclic stretch study may be described as follows: 1) methodologically, directly visualized ERK activation by cyclic stretch in live cells at different time points with FRET biosensor, whereas previous studies were mostly done in cell lysis by using antibody detections; 2) identified that calcium channels, particularly IP_3R channel and SERCA pump on ER membrane, but not integrin $\alpha_{(x)}\beta1$ signals, are the primary mechanosensitive components for ERK activation, which is likely mediated *via* force transmission through actin cytoskeleton; 3) the ER IP_3R channel-dependent ERK activation does not rely on the classic upstream phospholipase C-IP_3 signal, indicating possibly a more mechanical

mechanism for IP_3R activation by cyclic stretch. Therefore, this work provides progress in understanding this mechanical-biomechanical coupling process.

DATA AVAILABILITY STATEMENT

The original contributions presented in the study are included in the article/**Supplementary Material**, further inquiries can be directed to the corresponding authors.

AUTHOR CONTRIBUTIONS

MO and LD conceived the project and designed the research; XF performed the majority of experiments; XF and MO did the major data analysis and organization; YL made the nuclear ERK FRET construct; KN, YZ, and HS helped some experiments and data analysis; JG, BB, and ML provided discussion and technique support; LD provided the setup of equipment; MO, LD, and XF wrote the manuscript.

FUNDING

This work was supported financially by the National Natural Science Foundation of China (NSFC 11872129, 11532003, 1902051) and partially by the Natural Science Foundation of Jiangsu Province (BK20181416), and the Jiangsu Provincial Department of Education.

ACKNOWLEDGMENTS

We appreciate Lei Liu, Jingjing Li, and Yan Pan at Changzhou University for experimental assistances.

SUPPLEMENTARY MATERIAL

The Supplementary Material for this article can be found online at: https://www.frontiersin.org/articles/10.3389/fcell.2022.847852/full#supplementary-material

REFERENCES

Alexander, L. D., Alagarsamy, S., and Douglas, J. G. (2004). Cyclic Stretch-Induced cPLA2 Mediates ERK 1/2 Signaling in Rabbit Proximal Tubule Cells. *Kidney Int.* 65, 551–563. doi:10.1111/j.1523-1755.2004.00405.x

Balestrini, A., Joseph, V., Dourado, M., Reese, R. M., Shields, S. D., Rouge, L., et al. (2021). A TRPA1 Inhibitor Suppresses Neurogenic Inflammation and Airway Contraction for Asthma Treatment. *J. Exp. Med.* 218 (4), e20201637. doi:10.1084/jem.20201637

Bartlett, P. J., Cloete, I., Sneyd, J., and Thomas, A. P. (2020). IP3-Dependent Ca(2+) Oscillations Switch into a Dual Oscillator Mechanism in the Presence of PLC-Linked Hormones. *iScience* 23, 101062. doi:10.1016/j.isci.2020.101062

Burgess, J. K., Lee, J. H., Ge, Q., Ramsay, E. E., Poniris, M. H., Parmentier, J., et al. (2008). Dual ERK and Phosphatidylinositol 3-kinase Pathways Control Airway Smooth Muscle Proliferation: Differences in Asthma. *J. Cel. Physiol.* 216, 673–679. doi:10.1002/jcp.21450

Cai, C., Sun, H., Hu, L., and Fan, Z. (2021). Visualization of Integrin Molecules by Fluorescence Imaging and Techniques. *Biocell* 45, 229–257. doi:10.32604/biocell.2021.014338

Chu, S.-Y., Chou, C.-H., Huang, H.-D., Yen, M.-H., Hong, H.-C., Chao, P.-H., et al. (2019). Mechanical Stretch Induces Hair Regeneration through the Alternative Activation of Macrophages. *Nat. Commun.* 10, 1524. doi:10.1038/s41467-019-09402-8

Correa-Meyer, E., Pesce, L., Guerrero, C., and Sznajder, J. I. (2002). Cyclic Stretch Activates ERK1/2 via G Proteins and EGFR in Alveolar Epithelial Cells. *Am. J. Physiol. Lung Cel Mol Physiol* 282, L883–L891. doi:10.1152/ajplung.00203.2001

Crawford, S. K., Wille, C. M., Stiffler-Joachim, M. R., Lee, K. S., Bashford, G. R., and Heiderscheit, B. C. (2021). Spatial Frequency Analysis Detects Altered Tissue Organization Following Hamstring Strain Injury at Time of Injury but Not Return to Sport. *BMC Med. Imaging* 21, 190. doi:10.1186/s12880-021-00721-1

Dalagiorgou, G., Piperi, C., Adamopoulos, C., Georgopoulou, U., Gargalionis, A. N., Spyropoulou, A., et al. (2017). Mechanosensor Polycystin-1 Potentiates Differentiation of Human Osteoblastic Cells by Upregulating Runx2 Expression via Induction of JAK2/STAT3 Signaling Axis. *Cell. Mol. Life Sci.* 74, 921–936. doi:10.1007/s00018-016-2394-8

Dalagiorgou, G., Piperi, C., Georgopoulou, U., Adamopoulos, C., Basdra, E. K., and Papavassiliou, A. G. (2013). Mechanical Stimulation of Polycystin-1 Induces Human Osteoblastic Gene Expression via Potentiation of the Calcineurin/NFAT Signaling axis. *Cel. Mol. Life Sci.* 70, 167–180. doi:10.1007/s00018-012-1164-5

Diem, K., Fauler, M., Fois, G., Hellmann, A., Winokurow, N., Schumacher, S., et al. (2020). Mechanical Stretch Activates Piezo1 in Caveolae of Alveolar Type I Cells to Trigger ATP Release and Paracrine Stimulation of Surfactant Secretion from Alveolar Type II Cells. *FASEB J.* 34, 12785–12804. doi:10.1096/fj.202000613rrr

Doeing, D. C., and Solway, J. (2013). Airway Smooth Muscle in the Pathophysiology and Treatment of Asthma. *J. Appl. Physiol. (1985)* 114, 834–843. doi:10.1152/japplphysiol.00950.2012

Du, G., Li, L., Zhang, X., Liu, J., Hao, J., Zhu, J., et al. (2020). Roles of TRPV4 and Piezo Channels in Stretch-Evoked Ca(2+) Response in Chondrocytes. *Exp. Biol. Med. (Maywood)* 245, 180–189. doi:10.1177/1535370219892601

Fang, Y., Wu, D., and Birukov, K. G. (2019). Mechanosensing and Mechanoregulation of Endothelial Cell Functions. *Compr. Physiol.* 9 (2), 873–904. doi:10.1002/cphy.c180020

Geneen, L. J., Moore, R. A., Clarke, C., Martin, D., Colvin, L. A., and Smith, B. H. (2017). Physical Activity and Exercise for Chronic Pain in Adults: An Overview of Cochrane Reviews. *Cochrane Database Syst. Rev.* 4, CD011279. doi:10.1002/14651858.CD011279.pub3

Hayakawa, K., Sato, N., and Obinata, T. (2001). Dynamic Reorientation of Cultured Cells and Stress Fibers under Mechanical Stress from Periodic Stretching. *Exp. Cel Res.* 268, 104–114. doi:10.1006/excr.2001.5270

Hirata, H., Gupta, M., Vedula, S. R. K., Lim, C. T., Ladoux, B., and Sokabe, M. (2015). Actomyosin Bundles Serve as a Tension Sensor and a Platform for ERK Activation. *EMBO Rep.* 16, 250–257. doi:10.15252/embr.201439140

Horie, S., Ansari, B., Masterson, C., Devaney, J., Scully, M., O'Toole, D., et al. (2016). Hypercapnic Acidosis Attenuates Pulmonary Epithelial Stretch-Induced Injury via Inhibition of the Canonical NF-κB Pathway. *Intensive Care Med. Exp.* 4, 8. doi:10.1186/s40635-016-0081-6

Hsu, H.-J., Lee, C.-F., Locke, A., Vanderzyl, S. Q., and Kaunas, R. (2010). Stretch-Induced Stress Fiber Remodeling and the Activations of JNK and ERK Depend on Mechanical Strain Rate, but Not FAK. *PLoS One* 5, e12470. doi:10.1371/journal.pone.0012470

Ingber, D. (2003). Mechanobiology and Diseases of Mechanotransduction. *Ann. Med.* 35, 564–577. doi:10.1080/07853890310016333

Jungbauer, S., Gao, H., Spatz, J. P., and Kemkemer, R. (2008). Two Characteristic Regimes in Frequency-Dependent Dynamic Reorientation of Fibroblasts on Cyclically Stretched Substrates. *Biophysical J.* 95, 3470–3478. doi:10.1529/biophysj.107.128611

Kaczka, D. W. (2021). Oscillatory Ventilation Redux: Alternative Perspectives on Ventilator-Induced Lung Injury in the Acute Respiratory Distress Syndrome. *Curr. Opin. Physiol.* 21, 36–43. doi:10.1016/j.cophys.2021.03.006

Kardas, G., Daszyńska-Kardas, A., Marynowski, M., Brząkalska, O., Kuna, P., and Panek, M. (2020). Role of Platelet-Derived Growth Factor (PDGF) in Asthma as an Immunoregulatory Factor Mediating Airway Remodeling and Possible Pharmacological Target. *Front. Pharmacol.* 11, 47. doi:10.3389/fphar.2020.00047

Kim, J., Adams, A. A., Gokina, P., Zambrano, B., Jayakumaran, J., Dobrowolski, R., et al. (2020). Mechanical Stretch Induces Myelin Protein Loss in Oligodendrocytes by Activating Erk1/2 in a Calcium-Dependent Manner. *Glia* 68, 2070–2085. doi:10.1002/glia.23827

Kim, T. J., Joo, C., Seong, J., Vafabakhsh, R., Botvinick, E. L., Berns, M. W., et al. (2015). Distinct Mechanisms Regulating Mechanical Force-Induced Ca^{2+} Signals at the Plasma Membrane and the ER in Human MSCs. *Elife* 4, e04876. doi:10.7554/eLife.04876

Komatsu, N., Aoki, K., Yamada, M., Yukinaga, H., Fujita, Y., Kamioka, Y., et al. (2011). Development of an Optimized Backbone of FRET Biosensors for Kinases and GTPases. *Mol. Biol. Cel* 22, 4647–4656. doi:10.1091/mbc.e11-01-0072

Korff, T., Aufgebauer, K., and Hecker, M. (2007). Cyclic Stretch Controls the Expression of CD40 in Endothelial Cells by Changing Their Transforming Growth Factor-β1 Response. *Circulation* 116, 2288–2297. doi:10.1161/circulationaha.107.730309

Lee, J.-H., Johnson, P. R. A., Roth, M., Hunt, N. H., and Black, J. L. (2001). ERK Activation and Mitogenesis in Human Airway Smooth Muscle Cells. *Am. J. Physiol. Lung Cel Mol Physiol* 280, L1019–L1029. doi:10.1152/ajplung.2001.280.5.l1019

Li, Y. Y., Liu, X. S., Liu, C., Xu, Y. J., and Xiong, W. N. (2010). Role of Extracellular Signal-Regulated Kinase in Regulating Expression of Interleukin 13 in Lymphocytes from an Asthmatic Rat Model. *Chin. Med. J. (Engl)* 123, 1715–1719.

Liang, X., Wang, Z., Gao, M., Wu, S., Zhang, J., Liu, Q., et al. (2019). Cyclic Stretch Induced Oxidative Stress by Mitochondrial and NADPH Oxidase in Retinal Pigment Epithelial Cells. *BMC Ophthalmol.* 19, 79. doi:10.1186/s12886-019-1087-0

Liao, W.-H., Hsiao, M.-Y., Kung, Y., Liu, H.-L., Béra, J.-C., Inserra, C., et al. (2020). TRPV4 Promotes Acoustic Wave-Mediated BBB Opening via Ca(2+)/PKC-delta Pathway. *J. Adv. Res.* 26, 15–28. doi:10.1016/j.jare.2020.06.012

Liu, B., Qu, M.-J., Qin, K.-R., Li, H., Li, Z.-K., Shen, B.-R., et al. (2008). Role of Cyclic Strain Frequency in Regulating the Alignment of Vascular Smooth Muscle Cells *In Vitro*. *Biophysical J.* 94, 1497–1507. doi:10.1529/biophysj.106.098574

Liu, J.-T., Bao, H., Fan, Y.-J., Li, Z.-T., Yao, Q.-P., Han, Y., et al. (2021). Platelet-Derived Microvesicles Promote VSMC Dedifferentiation after Intimal Injury via Src/Lamtor1/mTORC1 Signaling. *Front. Cel Dev. Biol.* 9, 744320. doi:10.3389/fcell.2021.744320

Liu, W., Xiong, S., Zhang, Y., Du, J., Dong, C., Yu, Z., et al. (2021). Transcriptome Profiling Reveals Important Transcription Factors and Biological Processes in Skin Regeneration Mediated by Mechanical Stretch. *Front. Genet.* 12, 757350. doi:10.3389/fgene.2021.757350

Loperena, R., Van Beusecum, J. P., Itani, H. A., Engel, N., Laroumanie, F., Xiao, L., et al. (2018). Hypertension and Increased Endothelial Mechanical Stretch Promote Monocyte Differentiation and Activation: Roles of STAT3, Interleukin 6 and Hydrogen Peroxide. *Cardiovasc. Res.* 114, 1547–1563. doi:10.1093/cvr/cvy112

Luo, L., Li, E., Zhao, S., Wang, J., Zhu, Z., Liu, Y., et al. (2018). Gasoline Exhaust Damages Spermatogenesis through Downregulating α6-Integrin and β1-Integrin in the Rat Model. *Andrologia* 50, e13045. doi:10.1111/and.13045

Mammoto, T., Mammoto, A., and Ingber, D. E. (2013). Mechanobiology and Developmental Control. *Annu. Rev. Cel Dev. Biol.* 29, 27–61. doi:10.1146/annurev-cellbio-101512-122340

Michael, K. E., Dumbauld, D. W., Burns, K. L., Hanks, S. K., and García, A. J. (2009). Focal Adhesion Kinase Modulates Cell Adhesion Strengthening via Integrin Activation. *Mol. Biol. Cel* 20, 2508–2519. doi:10.1091/mbc.e08-01-0076

Ouyang, M., Wan, R., Qin, Q., Peng, Q., Wang, P., Wu, J., et al. (2019). Sensitive FRET Biosensor Reveals Fyn Kinase Regulation by Submembrane Localization. *ACS Sens.* 4, 76–86. doi:10.1021/acssensors.8b00896

Parekh, A. B., and Putney, J. W., Jr. (2005). Store-Operated Calcium Channels. *Physiol. Rev.* 85, 757–810. doi:10.1152/physrev.00057.2003

Ponsioen, B., Post, J. B., Buissant des Amorie, J. R., Laskaris, D., van Ineveld, R. L., Kersten, S., et al. (2021). Quantifying Single-Cell ERK Dynamics in Colorectal Cancer Organoids Reveals EGFR as an Amplifier of Oncogenic MAPK Pathway Signalling. *Nat. Cel Biol* 23, 377–390. doi:10.1038/s41556-021-00654-5

Potla, R., Hirano-Kobayashi, M., Wu, H., Chen, H., Mammoto, A., Matthews, B. D., et al. (2020). Molecular Mapping of Transmembrane Mechanotransduction through the β1 Integrin-CD98hc-TRPV4 Axis. *J. Cel Sci* 133. doi:10.1242/jcs.248823

Qi, Y.-X., Yao, Q.-P., Huang, K., Shi, Q., Zhang, P., Wang, G.-L., et al. (2016). Nuclear Envelope Proteins Modulate Proliferation of Vascular Smooth Muscle Cells during Cyclic Stretch Application. *Proc. Natl. Acad. Sci. U.S.A.* 113, 5293–5298. doi:10.1073/pnas.1604569113

Qin, Q., Laub, S., Shi, Y., Ouyang, M., Peng, Q., Zhang, J., et al. (2019). Fluocell for Ratiometric and High-Throughput Live-Cell Image Visualization and Quantitation. *Front. Phys.* 7, 154. doi:10.3389/fphy.2019.00154

Ren, D., Song, J., Liu, R., Zeng, X., Yan, X., Zhang, Q., et al. (2021). Molecular and Biomechanical Adaptations to Mechanical Stretch in Cultured Myotubes. *Front. Physiol.* 12, 689492. doi:10.3389/fphys.2021.689492

Rudzka, D. A., Mason, S., Neilson, M., McGarry, L., Kalna, G., Hedley, A., et al. (2021). Selection of Established Tumour Cells through Narrow Diameter Micropores Enriches for Elevated Ras/Raf/MEK/ERK MAPK Signalling and Enhanced Tumour Growth. *Small GTPases* 12, 294–310. doi:10.1080/21541248.2020.1780108

Sadoshima, J., and Izumo, S. (1993). Mechanical Stretch Rapidly Activates Multiple Signal Transduction Pathways in Cardiac Myocytes: Potential Involvement of an Autocrine/Paracrine Mechanism. *EMBO J.* 12, 1681–1692. doi:10.1002/j.1460-2075.1993.tb05813.x

Schmidt, J. B., Chen, K., and Tranquillo, R. T. (2016). Effects of Intermittent and Incremental Cyclic Stretch on ERK Signaling and Collagen Production in Engineered Tissue. *Cel. Mol. Bioeng.* 9, 55–64. doi:10.1007/s12195-015-0415-6

Slutsky, A. S., and Ranieri, V. M. (2014). Ventilator-Induced Lung Injury. *N. Engl. J. Med.* 370, 980. doi:10.1056/NEJMc1400293

Sun, Z., Guo, S. S., and Fässler, R. (2016). Integrin-Mediated Mechanotransduction. *J. Cel. Biol.* 215, 445–456. doi:10.1083/jcb.201609037

Swaminathan, V., and Gloerich, M. (2021). Decoding Mechanical Cues by Molecular Mechanotransduction. *Curr. Opin. Cel Biol.* 72, 72–80. doi:10.1016/j.ceb.2021.05.006

Takahara, N., Ito, S., Furuya, K., Naruse, K., Aso, H., Kondo, M., et al. (2014). Real-Time Imaging of ATP Release Induced by Mechanical Stretch in Human Airway Smooth Muscle Cells. *Am. J. Respir. Cel Mol Biol* 51, 772–782. doi:10.1165/rcmb.2014-0008oc

Wang, J. H.-C., Goldschmidt-Clermont, P., Wille, J., and Yin, F. C.-P. (2001). Specificity of Endothelial Cell Reorientation in Response to Cyclic Mechanical Stretching. *J. Biomech.* 34, 1563–1572. doi:10.1016/s0021-9290(01)00150-6

Wang, L., Bao, H., Wang, K.-X., Zhang, P., Yao, Q.-P., Chen, X.-H., et al. (2017). Secreted miR-27a Induced by Cyclic Stretch Modulates the Proliferation of Endothelial Cells in Hypertension via GRK6. *Sci. Rep.* 7, 41058. doi:10.1038/srep41058

Wang, M., Sun, Y., Li, L., Wu, P., Dkw, O., and Shi, H. (2021). Calcium Channels: Noteworthy Regulators and Therapeutic Targets in Dermatological Diseases. *Front. Pharmacol.* 12, 702264. doi:10.3389/fphar.2021.702264

Wang, Y., Lu, Y., Luo, M., Shi, X., Pan, Y., Zeng, H., et al. (2016). Evaluation of Pharmacological Relaxation Effect of the Natural Product Naringin on *In Vitro* Cultured Airway Smooth Muscle Cells and *In Vivo* Ovalbumin-Induced Asthma Balb/c Mice. *Biomed. Rep.* 5, 715–722. doi:10.3892/br.2016.797

Wei, F., Xu, X., Zhang, C., Liao, Y., Ji, B., and Wang, N. (2020). Stress Fiber Anisotropy Contributes to Force-Mode Dependent Chromatin Stretching and Gene Upregulation in Living Cells. *Nat. Commun.* 11, 4902. doi:10.1038/s41467-020-18584-5

Yan, A., Song, L., Zhang, Y., Wang, X., and Liu, Z. (2020). Systemic Inflammation Increases the Susceptibility to Levodopa-Induced Dyskinesia in 6-OHDA Lesioned Rats by Targeting the NR2B-Medicated PKC/MEK/ERK Pathway. *Front. Aging Neurosci.* 12, 625166. doi:10.3389/fnagi.2020.625166

Yao, H., Wang, L., Guo, J., Liu, W., Li, J., Wang, Y., et al. (2020). Genetically Encoded FRET Biosensor Detects the Enzymatic Activity of Prostate-

Specific Antigen. *Mol. Cell Biomech.* 17, 101–111. doi:10.32604/mcb.2020.09595

Zhang, S. J., Truskey, G. A., and Kraus, W. E. (2007). Effect of Cyclic Stretch on β1D-Integrin Expression and Activation of FAK and RhoA. *Am. J. Physiology-Cell Physiol.* 292, C2057–C2069. doi:10.1152/ajpcell.00493.2006

Zuyderduyn, S., Sukkar, M. B., Fust, A., Dhaliwal, S., and Burgess, J. K. (2008). Treating Asthma Means Treating Airway Smooth Muscle Cells. *Eur. Respir. J.* 32, 265–274. doi:10.1183/09031936.00051407

Conflict of Interest: The authors declare that the research was conducted in the absence of any commercial or financial relationships that could be construed as a potential conflict of interest.

Publisher's Note: All claims expressed in this article are solely those of the authors and do not necessarily represent those of their affiliated organizations, or those of the publisher, the editors, and the reviewers. Any product that may be evaluated in this article, or claim that may be made by its manufacturer, is not guaranteed or endorsed by the publisher.

frontiers | Frontiers in Cell and Developmental Biology

ORIGINAL RESEARCH
published: 16 June 2022
doi: 10.3389/fcell.2022.868143

Conserved Amino Acids Residing Outside the Voltage Field Can Shift the Voltage Sensitivity and Increase the Signal Speed and Size of *Ciona* Based GEVIs

Masoud Sepehri Rad[1,2], *Lawrence B. Cohen*[1,3]* *and Bradley J. Baker*[1,4]*

[1]Brain Science Institute, Korea Institute of Science and Technology (KIST), Seoul, South Korea, [2]Department of Neuroscience, University of Wisconsin, Madison, WI, United States, [3]Cellular and Molecular Physiology, Yale University School of Medicine, New Haven, CT, United States, [4]Division of Bio-Medical Science and Technology, KIST School, Korea University of Science and Technology (UST), Seoul, South Korea

OPEN ACCESS

Edited by:
Yingxiao Wang,
University of California, San Diego,
United States

Reviewed by:
Kiryl Piatkevich,
Westlake University, China
Ludovic Tricoire,
Sorbonne Universités, France

***Correspondence:**
Lawrence B. Cohen
Lawrence.b.cohen@hotmail.com
Bradley J. Baker
Bradley.baker19@gmail.com

Specialty section:
This article was submitted to Signaling, a section of the journal Frontiers in Cell and Developmental Biology

Received: *02 February 2022*
Accepted: *13 May 2022*
Published: *16 June 2022*

Citation:
Sepehri Rad M, Cohen LB and Baker BJ (2022) Conserved Amino Acids Residing Outside the Voltage Field Can Shift the Voltage Sensitivity and Increase the Signal Speed and Size of Ciona Based GEVIs. Front. Cell Dev. Biol. 10:868143. doi: 10.3389/fcell.2022.868143

To identify potential regions of the voltage-sensing domain that could shift the voltage sensitivity of *Ciona intestinalis* based Genetically Encoded Voltage Indicators (GEVIs), we aligned the amino acid sequences of voltage-gated sodium channels from different organisms. Conserved polar residues were identified at multiple transmembrane/loop junctions in the voltage sensing domain. Similar conservation of polar amino acids was found in the voltage-sensing domain of the voltage-sensing phosphatase gene family. These conserved residues were mutated to nonpolar or oppositely charged amino acids in a GEVI that utilizes the voltage sensing domain of the voltage sensing phosphatase from *Ciona* fused to the fluorescent protein, super ecliptic pHluorin (A227D). Different mutations shifted the voltage sensitivity to more positive or more negative membrane potentials. Double mutants were then created by selecting constructs that shifted the optical signal to a more physiologically relevant voltage range. Introduction of these mutations into previously developed GEVIs resulted in Plos6-v2 which improved the dynamic range to 40% ΔF/F/100 mV, a 25% increase over the parent, ArcLight. The onset time constant of Plos6-v2 is also 50% faster than ArcLight. Thus, Plos6-v2 appears to be the GEVI of choice.

Keywords: voltage, voltage imaging, GEVI, fluorescence, voltage sensing domain

INTRODUCTION

Genetically encoded voltage indicators (GEVIs) are potentially powerful tools for monitoring electrical activity in the brain. Kinetics, brightness and the signal size are some of the important properties of a GEVI (Bando et al., 2019; Rhee et al., 2020). Optimizing the properties of the GEVIs is important for improving the utility of GEVIs for imaging fast electrical activities in neural tissue and *in vivo* (Storace et al., 2015; Inagaki et al., 2017). GEVIs with fast kinetics and large dynamic signals are needed to follow the voltage transients of neurons. In recent years, several attempts have been reported to improve GEVI's properties (Gong et al., 2015; Piao et al., 2015; Lou et al., 2016; Storace et al., 2016; Jung et al., 2017; Lee et al., 2017; Sepehri Rad et al., 2017; Piatkevich et al., 2018; Adam et al., 2019; Lee et al., 2019).

The first GEVI to consistently yield voltage-dependent optical signals in mammalian cells was VSFP2 which consisted of two FPs fused in tandem to the carboxy terminus of the voltage sensing domain (VSD) from the *Ciona* voltage sensing phosphatase (Dimitrov et al., 2007). The two FPs were the Fluorescence Resonance Energy Transfer (FRET) donor/acceptor pair of Cerulean and Citruline enabling voltage induced conformational changes of the protein to alter the FRET efficiency thereby producing an optical signal. Given that FRET efficiency is dependent upon the distance and orientation of the FRET pair chromophores, the tandem fusion of the FPs limited the dynamic range of the GEVI's response. Several approaches were employed to improve VSFP2. One approach was to separate the FRET pair with the VSD resulting in Nabi (Sung et al., 2015) and VSFP Butterfly (Akemann et al., 2012) having one FP near the N-terminus while the other was at the C-terminus. VSFP Butterfly has had some success in reporting neuronal activity *in vivo* (Akemann et al., 2012; Carandini et al., 2015; Empson et al., 2015).

Another approach was to systematically replace the FRET pair at the C-terminus with single FPs including the pH-sensitive Super Ecliptic pHluorin (Miesenbock et al., 1998; Ng et al., 2002) and screen for voltage sensitivity. In an effort to reduce the variable expression of these GEVIs during screening, stable cell lines were created which was to have a profound effect of GEVI development (Jin et al., 2012). All of the stable cell lines expressing the GEVI with Super Ecliptic pHluorin yielded a very small signal of around 1% ΔF/F/100 mV except for one. That one exception gave a 15% ΔF/F/100 mV due to a spontaneous mutation converting the alanine at position 227 in Super Ecliptic pHluorin to aspartic acid. Optimization of the linker length between the VSD and the FP domain resulted in the GEVI, ArcLight, which remains one of the best GEVIs available to date (Bando et al., 2019).

ArcLight yields a large change in fluorescence in response to changes in membrane potentials (Jin et al., 2012). ArcLight can give up to a 40% ΔF/F for a 100 mV depolarization of the plasma membrane in HEK 293 cells (Han et al., 2013). However, its fast time constant is ~10 ms comprising 65% of the optical signal. Since action potentials are 1–2 ms, ArcLight will only reach ~10% of its maximal signal by the time the spike has subsided. To improve ArcLight, mutagenesis on the *Ciona* phosphataseVSD was performed. Using the architecture of ArcLight with the wildtype *Ciona* VSD fused to Super Ecliptic pHluorin yielded the GEVI, CC1 (Piao et al., 2015). CC1 required strong depolarization of the plasma membrane (~150 mV depolarization step) to observe a fluorescence change providing an excellent control for monitoring shifts in the voltage response to more negative potentials. Introducing mutations to conserved polar resides in the transmembrane segments of the VSD altered the voltage range, the speed of optical response, and the signal size of the GEVI (Piao et al., 2015). The resulting probe, Bongwoori, exhibited faster kinetics enabling the resolution of action potentials in a hippocampal neuron firing at 60 Hz. Altering the composition of the amino acid linker between the VSD and the FP domain of Bongwoori further improved the dynamic response resulting in two novel GEVIs, Bongwoori-Pos6 and Bongwoori-R3 that differ in their voltage sensitivities (Lee et al., 2017). The plasma membrane potential at which 50% of the total fluorescence change occurs ($V_{1/2}$) was near -30 mV for Bongwoori-Pos6 while Bongwoori-R3 is near 0 mV. Bongwoori-Pos6 is potentially more suited for measuring subthreshold potentials while Bongwoori-R3 is more suited for action potentials.

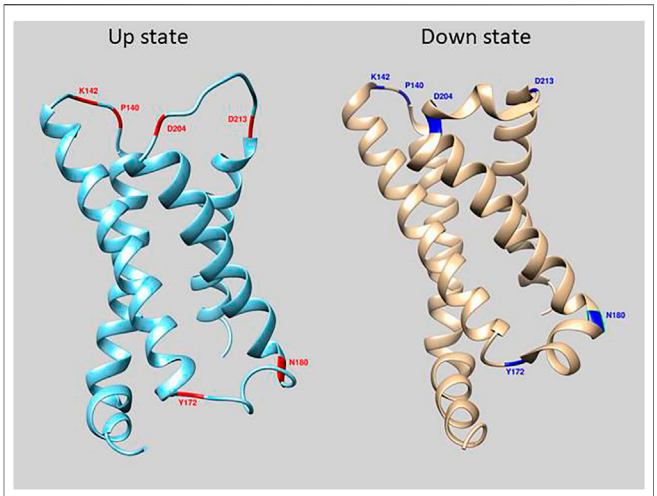

FIGURE 1 | Location of mutations in loop regions of the VSD of Ciona Voltage Sensing Phosphatase. The crystal structure of the down state is in cyan and up state is in beige (Li et al., 2014). Red and Blue regions depict amino acid positions that were mutated in this study.

In this report, we investigate the effect on the voltage-dependent optical signal that amino acids in the cytosolic and extracellular loops in the voltage sensing domain (VSD) have for GEVIs based on the voltage sensing phosphatase gene from *Ciona* (Murata et al., 2005). Previously, we have shown that introducing mutations near the external transmembrane/loop junction of the first transmembrane segment (S1) of the VSD in ArcLight (**Figure 1**) altered the cellular expression pattern enabling the optical reporting of voltage changes in internal membranes (Sepehri Rad et al., 2018). However, this only occurred in about 20% of the cells expressing this mutated GEVI, Aahn. The other 80% expressing Aahn yielded optical signals dominated by the plasma membrane signals.

Here we expand the mutagenesis to other loop regions in the VSD and report the effect on the size and voltage range of the voltage dependent optical signal. Aligning the VSD from the *Ciona* VSP to different subtypes of voltage-gated sodium channels from several different organisms identified conserved polar amino acids near the transmembrane/loop junctions in the VSD. Mutagenesis of these conserved polar amino acids in intra/extracellular loops in the VSD affected the voltage range of the *Ciona* based GEVIs even though they reside outside of the voltage field. Making double mutant constructs, we have successfully shifted the voltage sensitivity of CC1 to more negative potentials and improved its signal size for physiologically relevant voltage ranges.

MATERIALS AND METHODS

Plasmid DNA Designs and Construction

The CC1(WT) construct was described in Piao et al., 2015. Double mutant probes [CC1(WT)-D204K-Y172A and CC1(WT)-D204K-Y172S] were made by a two-step PCR process using CC1(WT)-Y172A and CC1(WT)-Y172S as template DNA respectively. Primers used for amplification of the S1, S2, and S3 transmembrane domains with a single mutation (D204K) in first step PCR reaction were: LC226: 5-ATA CGA CTC ACT ATA GGG-3 and LC230: 5- accGTATTC CTTTAACACAGT -3. Primers used for amplification of S4 transmembrane domain and florescence protein in first step PCR reaction were: LC229: 5- ACT GTG TTA AAG GAA TAC ggt -3 and LC193: 5- GCGATATCTTCTTTTGTTaaaa -3. In the second step PCR, we used primers LC226 and LC193 and combined the first step PCR products. The second step PCR product then was digested with restriction enzymes Nhe1 and Kpn1 and inserted into the corresponding sites of the CC1(WT) construct. Similarly, we used CC1(WT)-Y172A and CC1(WT)-Y172S as template DNA respectively to generate the double mutant probes [CC1(WT)-D204A-Y172A and CC1(WT)-D204A-Y172S]. For amplification of the S1, S2, and S3 transmembrane domains with a single mutation (D204A) in first step PCR reaction these primers were used: LC226: 5-ATA CGA CTC ACT ATA GGG-3 and LC232: 5- accGTATTCGGC TAACACAGT -3. Primers used for amplification of S4 transmembrane domain and florescence protein in first step PCR reaction were: LC231: 5- ACT GTG TTA GCC GAA TAC ggt -3 and LC193: 5- GCGATATCTTCTTTTGTTaaaa -3. We then used primers LC226 and LC193 to combine the first step PCR products. Using enzymes Nhe1 and Kpn1, the second step PCR product then was digested and inserted into the corresponding sites of the CC1(WT) construct. All DNA constructs were confirmed by DNA sequencing (Cosmogenetech, Republic of Korea).

Cell Culture

HEK293 cells were maintained in DMEM (High Glucose DMEM; Gibco) supplemented with 10% (v/v) fetal bovine serum (FBS; Invitrogen). HEK293 cells were seeded on to #0 coverslips coated with poly-L-lysine (Ted Pella, Inc.) in a 24-well culture dish and kept in an incubator at 37°C under air with 5% CO_2. Transfection was performed by using Lipofectamine 2000 (Invitrogen) following the manufacturer's instructions. Cells were roughly 20% confluent when transfected and were imaged 24 to hours after transfection.

Patch Clamp

Electrophysiology recordings were performed at 33°C and the chamber was perfused with a bath solution containing 150 mM NaCl, 4 mM KCl, 2 mM CaCl2, 1 mM MgCl2, 5 mM D-Glucose, and 5 mM HEPES (pH 7.4). Glass patch pipettes (capillary tubing with 1.5/0.84 mm; World Precision Instruments) were pulled by a P-97 micropipette puller (Sutter Instruments, United States) to make patch pipettes with 3–5 MΩ resistance when filled with internal solution containing (in mM) 120 K-aspartate, four NaCl, four $MgCl_2$, one $CaCl_2$, 10 EGTA, three Na2ATP, and five HEPES, pH 7.2. Using a Patch Clamp EPC10 amplifier (HEKA) with a holding potential of −70 mV, whole-cell voltage clamp was done in transfected HEK293 cells. The osmolality of the bath solution was 318 mOsm/kg and that of the pipette solution was 291 mOsm/kg H_2O.

Wide-Field Imaging

We used an inverted microscope (IX71; Olympus, Japan) equipped with a 60X oil-immersion lens with 1.35-numerical aperture (NA) for imaging the whole-cell patch clamped cells. Illumination light was provided by a 75 W Xenon arc lamp (Cairn Research). The excitation filter for all constructs was 472/30 nm, the emission filter was 496/LP and the dichroic was 495 nm (Semrock, NY). The fluorescence image was demagnified by an Optem zoom system, A45699 (Qioptiq LINOS) and the sample imaged onto a NeuroCCD-SM camera with 80 × 80 pixels controlled by NeuroPlex software (RedShirtImaging, GA). The images were recorded at a frame rate of 500 fps.

Optical Signal Analysis

Acquired images from patch clamp fluorometry were analyzed using NeuroPlex software (RedShirtImaging, United States), Excel (Microsoft, United States), and Origin8.6 (Origin Labs, United States). The resulting traces from whole cell voltage clamp experiments of HEK 293 cells were averaged for 16 trials. To calculate the % ΔF/F, we first subtracted the dark image from all frames, then the average of a region of interest in each frame during a voltage step (F) was subtracted from the average of the region taken from ten frames prior to the event of interest (F0), and finally this value was divided by F0 by the following formula: %ΔF/F=[(F-F_0)/F_0]100. ΔF/F values for all of the tested constructs were plotted in OriginPro 2019 (OriginLab, United States) and fitted to a Boltzmann function (signal size was normalized from zero, minimum, to one, maximum) to acquire voltage sensitivities as previously described (Piao et al., 2015). Frame subtraction images were achieved by subtracting the average of light intensities of 20 frames during the 200 mV depolarization step from average of 20 frames at the beginning of the recording.

RESULTS

The GEVI, CC1, contains the wild type VSD sequences of the *Ciona intestinalis* voltage sensing phosphatase gene with the FP, Super Ecliptic pHlorin A227D, fused to the carboxy-terminus of the protein. Introduction of mutations in the α-helix/loop junctions in the VSD of CC1 yielded probes with shifted voltage sensitivity in a more positive or a more negative direction. To identify other regions of the VSD which contribute to determining the voltage sensitivity, 148 voltage-gated sodium channels (Nav) from different organisms were aligned with the VSD from Ciona VSP. Nav channels were chosen since they have four VSDs in each protein. The four VSDs from each sodium channel were separated into distinct sequences. The resulting alignment

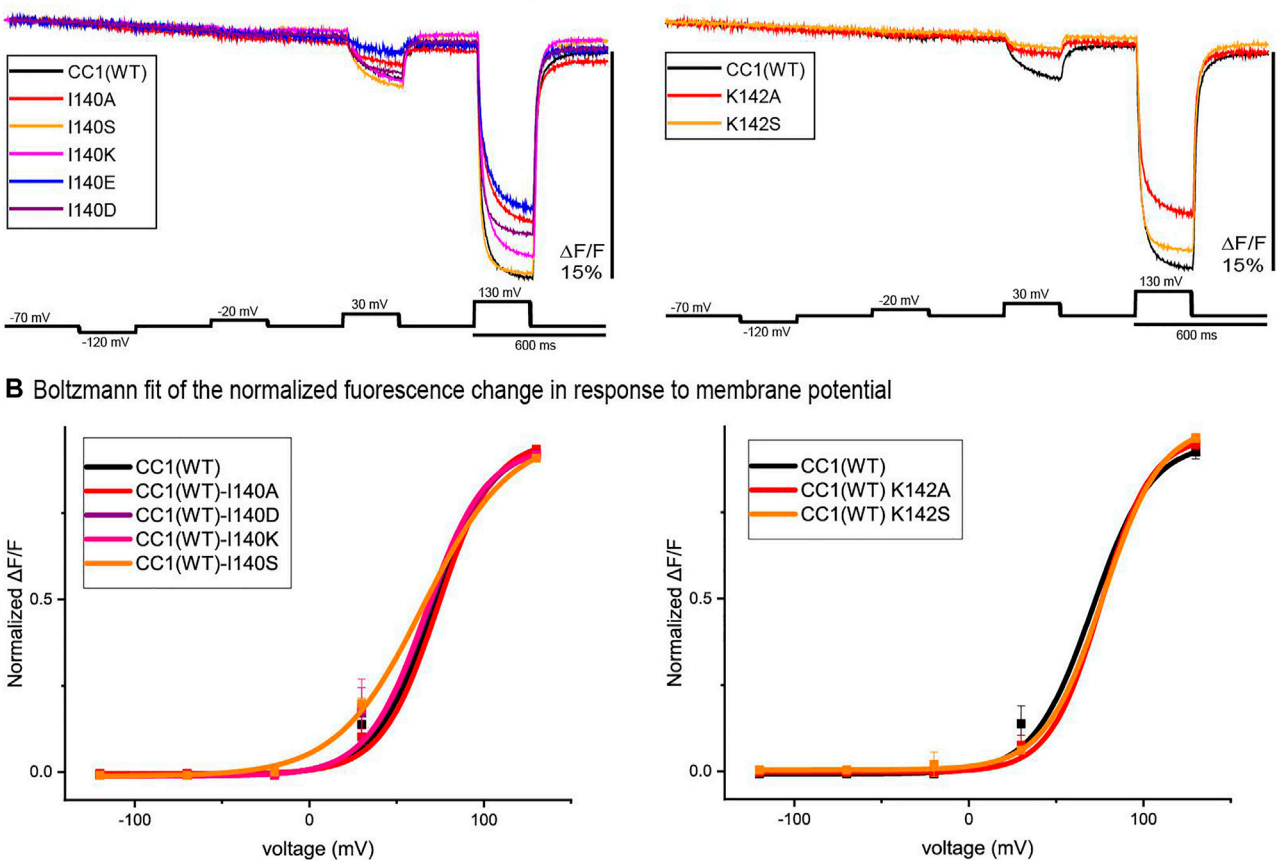

FIGURE 2 | S1-S2 loop mutations in the CC1 starting construct. **(A)**. The traces are representative fluorescent signals from voltage-clamped HEK293 cells (average of 16 trials for each cell) expressing CC1(WT) or CC1 with an S1-S2 loop mutant. Each trace is the average of three cells. The holding potential was –70mV. The pulse protocol is given in the black trace and was identical for all constructs. No temporal filtering was used for the traces. Images were recorded at a frame rate of 500 fps. **(B)**. Boltzmann fit of the normalized fluorescence change in response to membrane potential (n = 3 for all constructs).

consisted of 593 VSDs (**Supplementary Figure S1**). Conserved polar residues were detected at multiple transmembrane/loop junctions (**Figure 1**), two sites in the S1-S2 loop (I140 and K142), two sites in the S2-S3 loop (Y172 and N180), and another two sites in the S3-S4 loop of the VSD (D204 and D213). These conserved residues were mutated to nonpolar or oppositely charged amino acids.

S1-S2 Loop Mutants

Two potential sites of interest were identified in the S1-S2 loop, I140 and K142. **Figure 2** compares the traces of the S1-S2 loop mutations at those locations with that of the original CC1 construct. Except for I140S, none of the S1-S2 loop mutations shifted the voltage sensitivity significantly. While the I140A, I140E, K142A, and K142S mutations decreased the signal size for a 100 mV depolarization, I140S increased the signal size from 2.5 to 3.5% (**Figure 2A**). The I140S mutation shifted the $V_{1/2}$ voltage at half-maximum signal from +70 mV to +48 mV (**Figure 2B**).

S2-S3 Loop Mutants

Figure 3 illustrates the optical signal traces of the intracellular S2-S3 loop mutants in comparison to the CC1 starting construct. While Y172D did not change the signal size for a 100 mV depolarization, Y172A, Y172S, Y172K, and Y172R did increase the signal size compared to the CC1. Y172R and Y172K increased the signal size from 2.5 to 4.8% and 5% respectively. In contrast, the N180D mutation had a deleterious effect decreasing the signal size from 2.5 to 0.8% for a 100 mV step (**Figure 3A**). The Y172 mutations tested slightly shifted the voltage response to more negative potentials, with Y172A having the largest effect. This single mutation shifted the voltage at half maximum from +70 mV to +45 mV. The mutations in the S2-S3 loop junction (N180) did not change the voltage sensitivity significantly (**Figure 3B**).

S3-S4 Loop Mutants

Figure 4 represents the optical signal traces from the extracellular S3-S4 loop mutants. D204S, D204K, D204E, D204R, D204T, and

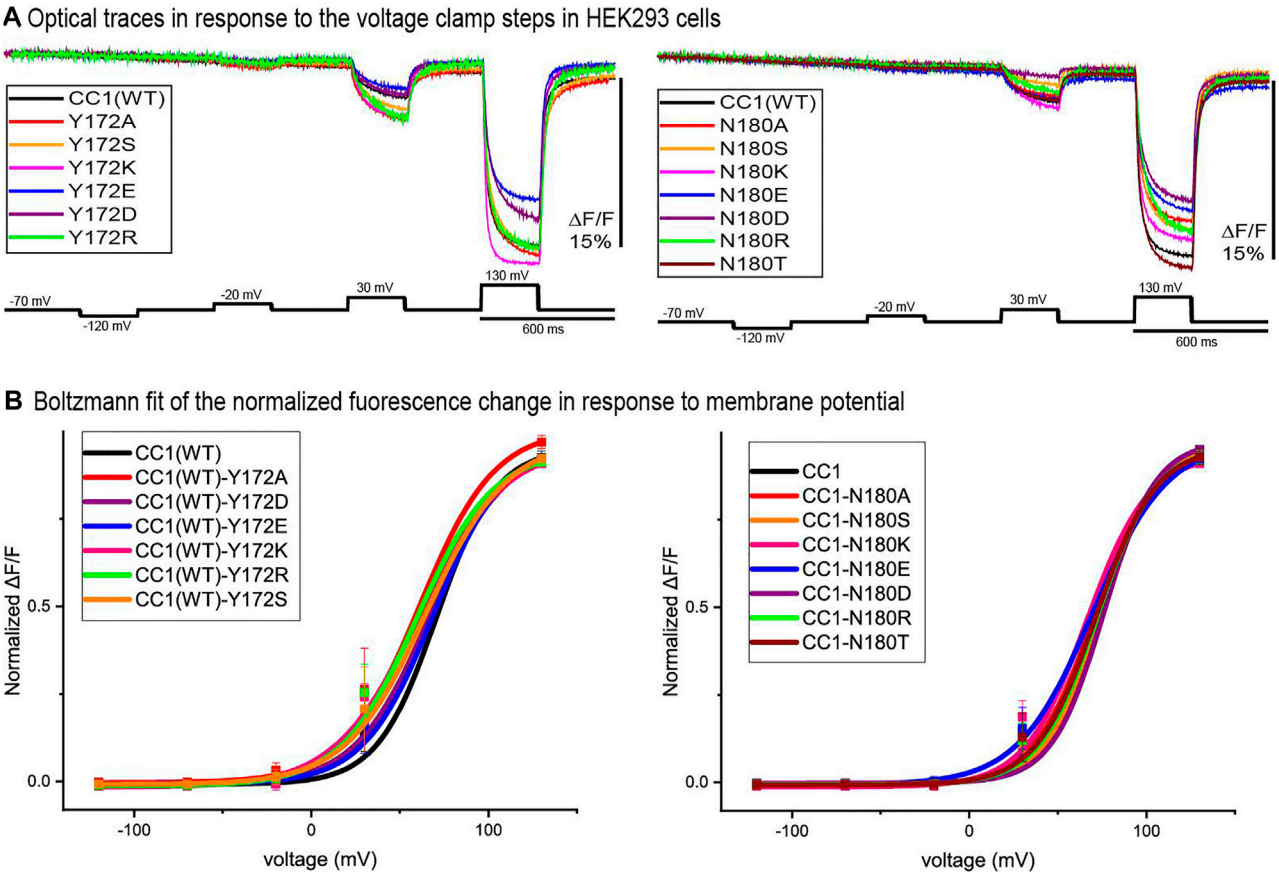

FIGURE 3 | S2-S3 loop mutations in the CC1 starting construct. **(A)**. Representative fluorescent traces of HEK cells expressing the CC1(WT) or CC1(WT) with an S2-S3 loop mutant in the whole cell patch clamp configuration. The cells were subjected to the voltage command pulses in black. Each trace is from average of three cells and the results from each cell is the average of 16 trials. The traces are fluorescent optical signals from plasma membrane without temporal filtering. Images were recorded at a frame rate of 500 fps. **(B)**. Boltzmann fit of the normalized fluorescence change for the CC1 construct and its derivative probes with single mutation in the S2-S3 loop (n = 3 for all constructs).

D204Y have a larger signal size for 100 mV depolarizations compared to the parent CC1 signal; D204K has the largest effect increasing the signal size from 2.5 to 8.1% for a 100 mV depolarization to +30 mV. D213A, D213S, D213K, D213T, D213Y, and D204A have a smaller signal size for 100 mV depolarizations (**Figure 4A**). While the D204A mutation did not shift the voltage versus fluorescence trace, all of the other mutations tested at this location shifted the voltage response of the CC1 probe to more negative potentials. D204K had the most pronounced effect shifting the $V_{1/2}$ from +70 mV to +17 mV. Mutations at the D213 position were mostly deleterious with none of the new constructs yielding a signal larger than the original CC1 version (**Figure 4B**).

Double Mutants

The CC1 starting construct has a voltage response shifted to more positive potentials compared to the physiological voltage range (-100 mV to +30 mV). We tried to further increase the signal size for a 100 mv depolarization by shifting the voltage sensitivity to even more negative potentials using double mutations. Comparing optical traces of the loop mutants with that of the starting CC1 construct we selected constructs that showed relatively large voltage shifts to more negative potentials and made four new probes. The voltage response of these double mutant constructs are shifted to even more negative potentials and as a result they give a larger signal compared to CC1 for a 100 mv depolarization (**Figure 5A**). Y172A/D204K had the largest effect (**Figure 5B**). This construct increased the signal size for 100 mv depolarizations compared to the CC1 optical signal from 2.5 to 13.8% for a 100 mv depolarization.

A Triple Mutant

Bongwoori-Pos6 is an ArcLight derived-GEVI with a modified linker region connecting the VSD to the FP domains of the GEVI (Lee et al., 2017). The $V_{1/2}$ for Bongwoori-Pos6 is

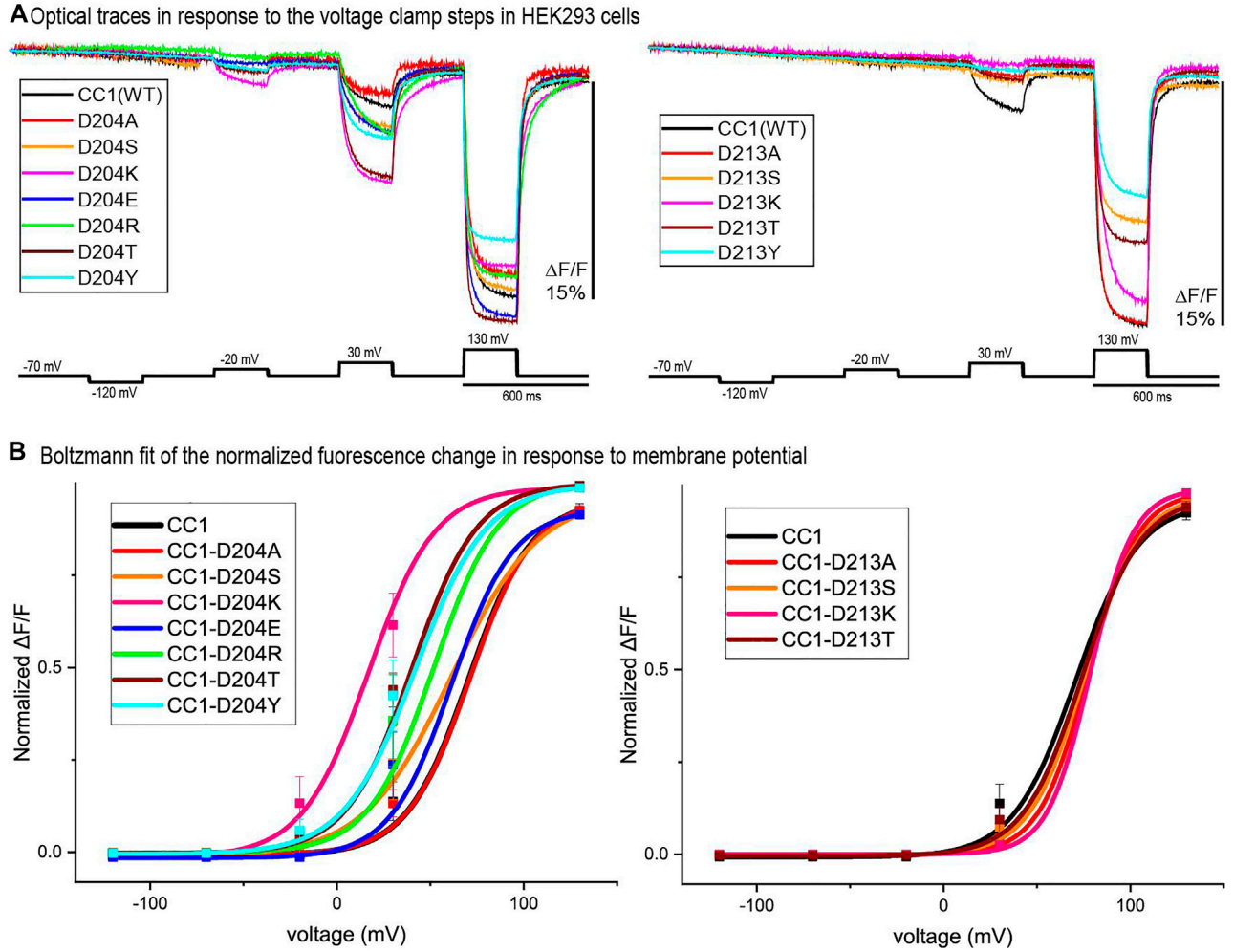

FIGURE 4 | S3-S4 loop mutations in the CC1 starting construct. **(A)**. HEK 293 cells expressing the CC1(WT) or CC1(WT) with an S3-S4 loop mutant were voltage-clamped. The traces are fluorescent optical signals (average of three cells) from plasma membrane without temporal filtering. Each cell is the average of 16 trials. Images were recorded at a frame rate of 500 fps. **(B)**. The voltage-fluorescence curve of the normalized optical signal for the CC1 construct and its derivative probes with single mutation at S3-S4 loop (n = 3 for all constructs).

-28 mV and exhibits an 18% ΔF/F/100 mV depolarization step of the plasma membrane. Bongwoori-Pos6 also exhibits faster kinetics with a t on of 6 ± 1 msec and a τ off of 8 ± 1 msec. Introducing the combination of the loop mutations that shifted the voltage response of CC1 (Y172A and D204K) with another mutation in the transmembrane segment S2 of the VSD (D164N) that has also been shown to affect the voltage range (Piao et al., 2015) with the Bongwoori-Pos6 linker resulted in a much improved signal size (**Figure 6A**). This new GEVI is designated Plos6-v2 and has a ~40% for 100 mV depolarization step compared to the 18% signal for a 100 mV depolarization for Bongwoori-Pos6 (Lee et al., 2017). Plos6-v2 is also larger than the CC1 loop mutants in **Figure 5**. D204K-Y172A is 34.1%; D204K-Y172K is 33.2%; D204K-Y172R is 29.0%; and D204K-Y172S is 35.8%.

The onset of the voltage-dependent signal for Plos6-v2 was best fitted by a double exponential decay yielding a fast time constant (τ on) of 5.8 ± 0.3 msec (N = 3) for the 50 mV depolarization step. However, the fast component only accounted for 25 ± 0.8% of the amplitude. The slow component was 24.8 ± 1.4 msec. The speed of the onset signal for the 100 mV depolarization step again exhibited a fast component near 6 msec (5.5 ± 0.1 msec), but the fast component improved to 63 ± 2.5% of the amplitude. The slow component for the 100 mV onset of the signal was 22.2 ± 0.1 msec. At 200 mV, the fast component of the onset signal was 4 ± 0.8 msec and constituted 69 ± 1.6% of the signal. The slow component for the 200 mV onset signal was 20.6 ± 1.6 msec. The speed of the off signal was best fitted by a single exponential decay function yielding a τ off of 15.4 ± 0.5 msec for the 50 mV

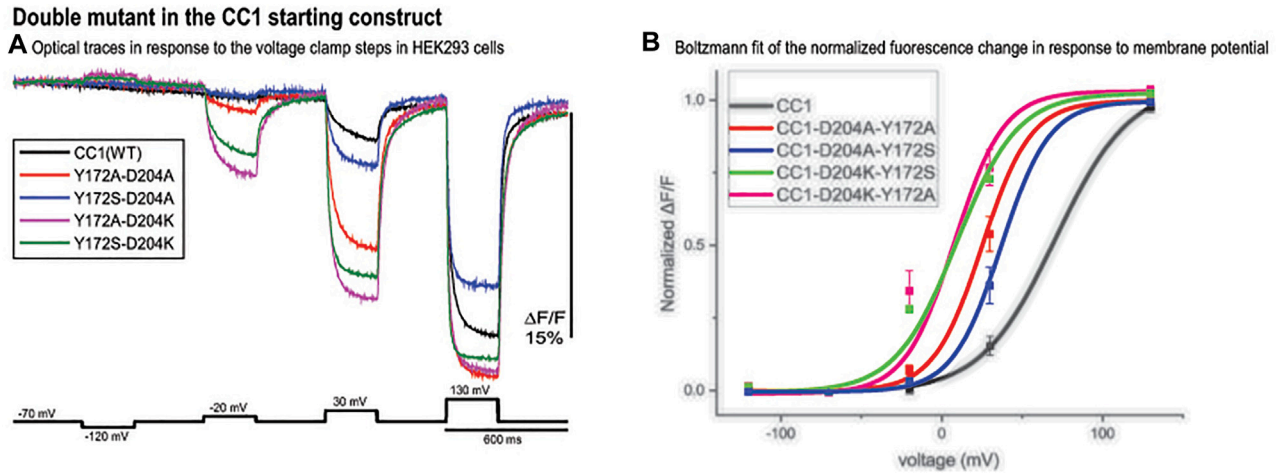

FIGURE 5 | Double mutant in the CC1 starting construct. **(A)**. Fluorescence response of HEK293 cells expressing CC1(WT) or CC1(WT) with double mutations in the loops to depolarizing and hyperpolarizing voltage steps. The traces are the average of three cells (each cell is the average of 16 trials) without temporal filtering. Images were recorded at a frame rate of 500 fps. **(B)**. The optical signal was normalized and fitted to a Boltzmann equation. All double mutant combinations shifted the voltage response to more negative potentials (n = 3 for all constructs).

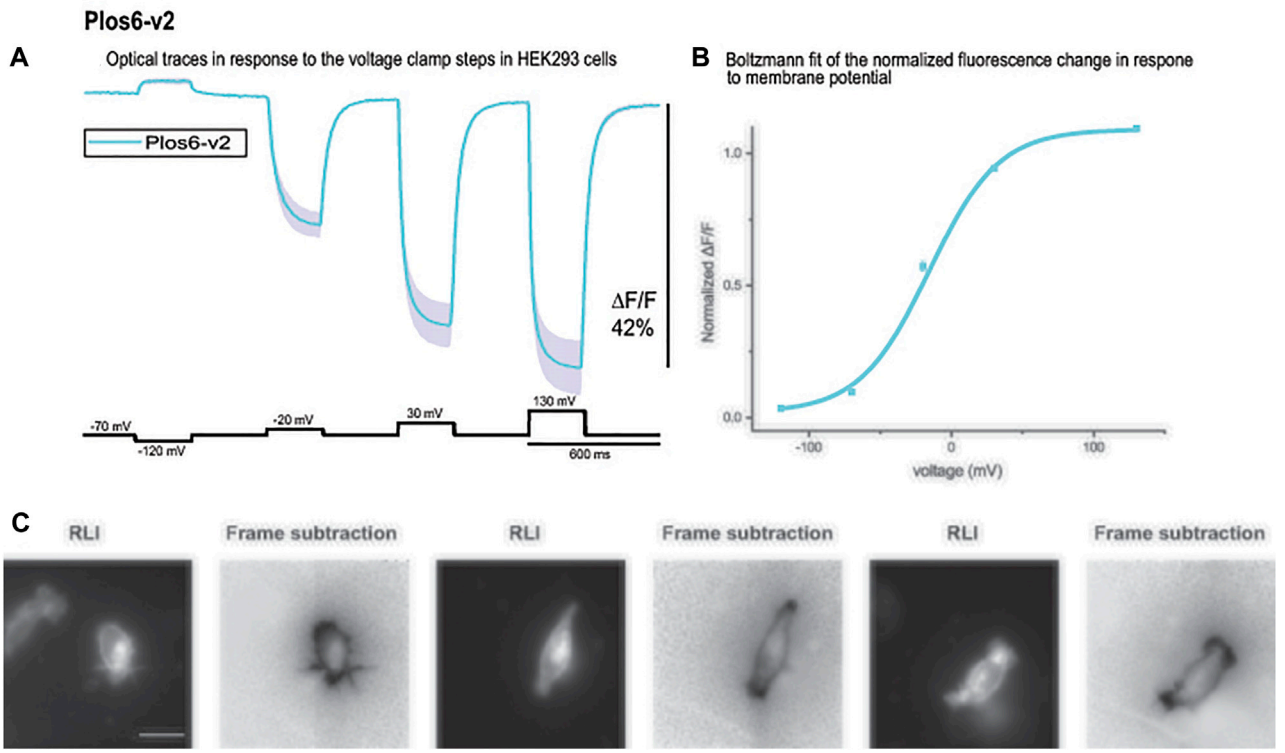

FIGURE 6 | The large fluorescence response of Plos6-v2. **(A)**. Plos6-v2 was expressed in HEK-293 cells and subjected to whole cell voltage clamp. The dark line represents the average of three cells. The shaded region is the standard error of the mean. **(B)**. Plos6-v2 Blotzmann fit of the fluorescence change as a function of voltage. **(C)**. Resting light images (RLI) and corresponding frame subtraction images of three cells expressing Plos6-v2. The fluorescence average for each pixel from 20 frames during the 200 mV depolarization step were subtracted from the fluorescence average of 20 frames at the beginning of the recording when the cells were held at a holding potential of −70 mV. The scale bar represents 20 μm.

depolarization step, 14.7 ± 0.6 msec for the 100 mV depolarization step, and 13.9 ± 0.5 msec for the 200 mV step.

As can be seen from the Boltzmann fit in **Figure 6B**, the voltage response of Plos6-v2 was more attuned to the physiological range of neuronal activities. Plos6-v2 exhibited good membrane expression with some discernable internal fluorescence. Plotting the frame subtraction difference of the light levels during the 200 mV depolarization step from the initial fluorescence observed at the holding nicely reveals the population of probe at the plasma membrane (**Figure 6C**). Regions of interest were then determined by the frame subtraction image.

DISCUSSION

The challenges of *in vivo* voltage imaging can be reduced by increasing the fluorescence change in response to voltage transients of a GEVI. Classical approaches to achieve a larger optical signal involve improving the trafficking of the protein and the speed of the optical response. The improved trafficking of a GEVI increases the population of probe that can respond to voltage transients as well as reduces the non-responding internal fluorescence thereby improving the signal-to-noise ratio (Rhee et al., 2020). Improving the speed of the GEVI can also improve the signal-to-noise ratio. For example, ArcLight exhibits a maximal 40% ΔF/F/100 mV depolarization step of the plasma membrane. The kinetics of that fluorescence change is best fit by a double exponential decay with a fast component (τ on ~10 msec) accounting for 65% of the amplitude (Jin et al., 2012). As a result, a neuron expressing ArcLight would exhibit a nearly 5% change in fluorescence during the firing of a 2 msec action potential. Increasing the fast component of the voltage-induced optical signal to a τ on ~ 2 msec would improve the change in fluorescence to 16% (Yi et al., 2018).

Another approach is to optimize the voltage-dependent optical signal of a GEVI by manipulating the voltage range of the GEVI (Jung et al., 2017). CC1-Pos6 gave a voltage-dependent optical signal of over 50% ΔF/F for a 200 mV depolarization of the plasma membrane (Lee et al., 2017). However, the signal size was below 10% ΔF/F/100 mV limiting the usefulness for imaging neurological activities. Mutagenesis of conserved polar amino acids in the transmembrane segments of the VSD affected the voltage sensitivity of Ciona based GEVIs (Piao et al., 2015) prompting several approaches to shift the voltage response of CC1-Pos6 while trying to maintain the large signal size Partial success was achieved with Bongwoori-Pos6 which had nearly a 20% ΔF/F/100 mV signal, improved kinetics, and a $V_{1/2}$ near -30 mV.

Guided by the sequences of voltage-gated sodium channels, we demonstrate in this report that polar residues in the transmembrane loop junctions of the VSD can also affect the characteristics of the voltage-dependent optical signal. We identified several mutations in the helix/loop junctions in the VSD that shift the voltage sensitivity of the GEVI. In the S1-S2 loop region I140A, E and K142A, S mutations shifted the voltage sensitivity to more positive voltages while the I140S, K and D resulted in little change in the voltage range of the optical response. In the intracellular S2-S3 loop, Y172A, S, K and R mutations shifted the voltage response to more negative potentials and N180S, R, T shifted the voltage response to more positive potentials. Mutagenesis of D204S, K, E, R, T, and Y in S3-S4 loop shifted the voltage response to more negative potentials, while D204A and D213A, S, K, T, and Y mutations shifted the voltage response of the optical signal to more positive potentials.

Selecting mutations that showed the largest voltage shift to more negative potentials, we made four double mutant probes. The voltage response of these new GEVIs are shifted to even more negative potentials and as a result they gave a larger signal compared to CC1 for a 100 mv depolarization step (**Figure 5A**). Y172A/D204K showed the biggest effect, it increased the signal size from 2.5 to 13.8%. Combining the D164N/Y172A/D204K mutations with Bongwoori-Pos6 increased its optical signal size even further. The resulting construct, Plos6-v2, gives a 40% ΔF/F optical signal for a 100 mV depolarization (**Figure 6A**) which is a 10-fold improvement over the original CC1 GEVI (Piao et al., 2015) and a ~2-fold improvement over Bongwoori-Pos6 (Lee et al., 2017). The speed of Plos6-v2 is comparable to the improved speed of Bongwoori-Pos6, an important result given the slow kinetics of previous GEVIs utilizing the D164N mutation in the S2 domain of the VSD (Piao et al., 2015). The $V_{1/2}$ of Plos6-v2 is -22 mV (**Figure 6B**) which is well positioned for detecting action potentials as well as subthreshold synaptic activity.

ArcLight-derived GEVIs convert a voltage-induced conformational change of the protein into an optical signal allowing the visualization of neuronal circuit activity (Borden et al., 2017; Platisa et al., 2022). This mechanism involves the movement of the VSD (Siegel and Isacoff, 1997; Dimitrov et al., 2007; Villalba-Galea et al., 2009), the photophysical properties of the FP domain (Kang and Baker, 2016; Kang et al., 2021), the linker region connecting the VSD to the FP (Jung et al., 2015; Lee et al., 2017) as well as potential interactions between neighboring GEVIs via the dimerization of the VSD (Rayaprolu et al., 2018; Leong et al., 2021). By exploring the ability to alter the voltage range of a protein by mutating amino acids in the loop regions of the VSD, we have developed a novel GEVI with ~40% ΔF/F/100 mV. While ArcLight has been reported to yield a 40% ΔF/F/100 mV, in our hands we consistently observe a 30% signal (Piao et al., 2015). The 40% signal of Plos6-v2 is a substantial improvement in the dynamic range and exbits faster kinetics than ArcLight. Plos6-v2 should therefore be a useful tool for optically monitoring neuronal activity.

DATA AVAILABILITY STATEMENT

The raw data supporting the conclusion of this article will be made available by the authors, without undue reservation.

AUTHOR CONTRIBUTIONS

MS designed and performed the experiments, analysed data, and assisted in the writing of the manuscript. LC analysed data and assisted in writing the manuscript. BB designed experiments, analysed data and assisted in writing the manuscript.

FUNDING

LC was supported by U.S. NIDCD grant DC005259. BB was funded by the Korea Institute of Science and Technology grant 2E31523.

ACKNOWLEDGMENTS

We thank Lee Min Leong for assistance during the revision of this manuscript.

SUPPLEMENTARY MATERIAL

The Supplementary Material for this article can be found online at: https://www.frontiersin.org/articles/10.3389/fcell.2022.868143/full#supplementary-material

REFERENCES

Adam, Y., Kim, J. J., Lou, S., Zhao, Y., Xie, M. E., Brinks, D., et al. (2019). Voltage Imaging and Optogenetics Reveal Behaviour-dependent Changes in Hippocampal Dynamics. *Nature* 569, 413–417. doi:10.1038/s41586-019-1166-7

Akemann, W., Mutoh, H., Perron, A., Park, Y. K., Iwamoto, Y., and Knöpfel, T. (2012). Imaging Neural Circuit Dynamics with a Voltage-Sensitive Fluorescent Protein. *J. Neurophysiology* 108, 2323–2337. doi:10.1152/jn.00452.2012

Bando, Y., Sakamoto, M., Kim, S., Ayzenshtat, I., and Yuste, R. (2019). Comparative Evaluation of Genetically Encoded Voltage Indicators. *Cell. Rep.* 26, 802–813. doi:10.1016/j.celrep.2018.12.088

Borden, P. Y., Ortiz, A. D., Waiblinger, C., Sederberg, A. J., Morrissette, A. E., Forest, C. R., et al. (2017). Genetically Expressed Voltage Sensor ArcLight for Imaging Large Scale Cortical Activity in the Anesthetized and Awake Mouse. *Neurophoton* 4, 031212. doi:10.1117/1.nph.4.3.031212

Carandini, M., Shimaoka, D., Rossi, L. F., Sato, T. K., Benucci, A., and Knopfel, T. (2015). Imaging the Awake Visual Cortex with a Genetically Encoded Voltage Indicator. *J. Neurosci.* 35, 53–63. doi:10.1523/jneurosci.0594-14.2015

Dimitrov, D., He, Y., Mutoh, H., Baker, B. J., Cohen, L., Akemann, W., et al. (2007). Engineering and Characterization of an Enhanced Fluorescent Protein Voltage Sensor. *PLoS One* 2, e440. doi:10.1371/journal.pone.0000440

Empson, R. M., Goulton, C., Scholtz, D., Gallero-Salas, Y., Zeng, H., and Knöpfel, T. (2015). Validation of Optical Voltage Reporting by the Genetically Encoded Voltage Indicator VSFP-Butterfly from Cortical Layer 2/3 Pyramidal Neurons in Mouse Brain Slices. *Physiol. Rep.* 3, e12468. doi:10.14814/phy2.12468

Gong, Y., Huang, C., Li, J. Z., Grewe, B. F., Zhang, Y., Eismann, S., et al. (2015). High-speed Recording of Neural Spikes in Awake Mice and Flies with a Fluorescent Voltage Sensor. *Science* 350, 1361–1366. doi:10.1126/science.aab0810

Han, Z., Jin, L., Platisa, J., Cohen, L. B., Baker, B. J., and Pieribone, V. A. (2013). Fluorescent Protein Voltage Probes Derived from ArcLight that Respond to Membrane Voltage Changes with Fast Kinetics. *PLoS One* 8, e81295. doi:10.1371/journal.pone.0081295

Inagaki, S., Tsutsui, H., Suzuki, K., Agetsuma, M., Arai, Y., Jinno, Y., et al. (2017). Genetically Encoded Bioluminescent Voltage Indicator for Multi-Purpose Use in Wide Range of Bioimaging. *Sci. Rep.* 7, 42398. doi:10.1038/srep42398

Jin, L., Han, Z., Platisa, J., Wooltorton, J. R. A., Cohen, L. B., and Pieribone, V. A. (2012). Single Action Potentials and Subthreshold Electrical Events Imaged in Neurons with a Fluorescent Protein Voltage Probe. *Neuron* 75, 779–785. doi:10.1016/j.neuron.2012.06.040

Jung, A., Garcia, J. E., Kim, E., Yoon, B.-J., and Baker, B. J. (2015). Linker Length and Fusion Site Composition Improve the Optical Signal of Genetically Encoded Fluorescent Voltage Sensors. *Neurophoton* 2, 021012. doi:10.1117/1.nph.2.2.021012

Jung, A., Rajakumar, D., Yoon, B.-J., and Baker, B. J. (2017). Modulating the Voltage-Sensitivity of a Genetically Encoded Voltage Indicator. *Exp. Neurobiol.* 26, 241–251. doi:10.5607/en.2017.26.5.241

Kang, B. E., and Baker, B. J. (2016). Pado, a Fluorescent Protein with Proton Channel Activity Can Optically Monitor Membrane Potential, Intracellular pH, and Map Gap Junctions. *Sci. Rep.* 6, 23865. doi:10.1038/srep23865

Kang, B. E., Leong, L. M., Kim, Y., Miyazaki, K., Ross, W. N., and Baker, B. J. (2021). Mechanism of ArcLight Derived GEVIs Involves Electrostatic Interactions that Can Affect Proton Wires. *Biophys. J.* 120, 1916–1926. doi:10.1016/j.bpj.2021.03.009

Lee, S., Geiller, T., Jung, A., Nakajima, R., Song, Y.-K., and Baker, B. J. (2017). Improving a Genetically Encoded Voltage Indicator by Modifying the Cytoplasmic Charge Composition. *Sci. Rep.* 7, 8286. doi:10.1038/s41598-017-08731-2

Lee, S., Song, Y.-K., and Baker, B. J. (2019). Engineering Photoactivatability in Genetically Encoded Voltage and pH Indicators. *Front. Cell. Neurosci.* 13, 482. doi:10.3389/fncel.2019.00482

Leong, L. M., Kang, B. E., and Baker, B. J. (2021). Improving the Flexibility of Genetically Encoded Voltage Indicators via Intermolecular FRET. *Biophys. J.* 120, 1927–1941. doi:10.1016/j.bpj.2021.03.010

Li, Q., Wanderling, S., Paduch, M., Medovoy, D., Singharoy, A., Mcgreevy, R., et al. (2014). Structural Mechanism of Voltage-dependent Gating in an Isolated Voltage-Sensing Domain. *Nat. Struct. Mol. Biol.* 21, 244–252. doi:10.1038/nsmb.2768

Lou, S., Adam, Y., Weinstein, E. N., Williams, E., Williams, K., Parot, V., et al. (2016). Genetically Targeted All-Optical Electrophysiology with a Transgenic Cre-dependent Optopatch Mouse. *J. Neurosci.* 36, 11059–11073. doi:10.1523/jneurosci.1582-16.2016

Miesenböck, G., De Angelis, D. A., and Rothman, J. E. (1998). Visualizing Secretion and Synaptic Transmission with pH-Sensitive Green Fluorescent Proteins. *Nature* 394, 192–195. doi:10.1038/28190

Murata, Y., Iwasaki, H., Sasaki, M., Inaba, K., and Okamura, Y. (2005). Phosphoinositide Phosphatase Activity Coupled to an Intrinsic Voltage Sensor. *Nature* 435, 1239–1243. doi:10.1038/nature03650

Ng, M., Roorda, R. D., Lima, S. Q., Zemelman, B. V., Morcillo, P., and Miesenböck, G. (2002). Transmission of Olfactory Information between Three Populations of Neurons in the Antennal Lobe of the Fly. *Neuron* 36, 463–474. doi:10.1016/s0896-6273(02)00975-3

Piao, H. H., Rajakumar, D., Kang, B. E., Kim, E. H., and Baker, B. J. (2015). Combinatorial Mutagenesis of the Voltage-Sensing Domain Enables the Optical Resolution of Action Potentials Firing at 60 Hz by a Genetically Encoded Fluorescent Sensor of Membrane Potential. *J. Neurosci.* 35, 372–385. doi:10.1523/jneurosci.3008-14.2015

Piatkevich, K. D., Jung, E. E., Straub, C., Linghu, C., Park, D., Suk, H.-J., et al. (2018). A Robotic Multidimensional Directed Evolution Approach Applied to Fluorescent Voltage Reporters. *Nat. Chem. Biol.* 14, 352–360. doi:10.1038/s41589-018-0004-9

Platisa, J., Zeng, H., Madisen, L., Cohen, L. B., Pieribone, V. A., and Storace, D. A. (2022). Voltage Imaging in the Olfactory Bulb Using Transgenic Mouse Lines Expressing the Genetically Encoded Voltage Indicator ArcLight. *Sci. Rep.* 12, 1875. doi:10.1038/s41598-021-04482-3

Rayaprolu, V., Royal, P., Stengel, K., Sandoz, G., and Kohout, S. C. (2018). Dimerization of the Voltage-Sensing Phosphatase Controls its Voltage-Sensing and Catalytic Activity. *J. Gen. Physiol.* 150, 683–696. doi:10.1085/jgp.201812064

Rhee, J. K., Leong, L. M., Mukim, M. S. I., Kang, B. E., Lee, S., Bilbao-Broch, L., et al. (2020). Biophysical Parameters of GEVIs: Considerations for Imaging Voltage. *Biophys. J.* 119, 1–8. doi:10.1016/j.bpj.2020.05.019

Sepehri Rad, M., Choi, Y., Cohen, L. B., Baker, B. J., Zhong, S., Storace, D. A., et al. (2017). Voltage and Calcium Imaging of Brain Activity. *Biophysical J.* 113, 2160–2167. doi:10.1016/j.bpj.2017.09.040

Sepehri Rad, M., Cohen, L. B., Braubach, O., and Baker, B. J. (2018). Monitoring Voltage Fluctuations of Intracellular Membranes. *Sci. Rep.* 8, 6911. doi:10.1038/s41598-018-25083-7

Siegel, M. S., and Isacoff, E. Y. (1997). A Genetically Encoded Optical Probe of Membrane Voltage. *Neuron* 19, 735–741. doi:10.1016/s0896-6273(00)80955-1

Storace, D. A., Braubach, O. R., Jin, L., Cohen, L. B., and Sung, U. (2015). Monitoring Brain Activity with Protein Voltage and Calcium Sensors. *Sci. Rep.* 5, 10212. doi:10.1038/srep10212

Storace, D., Sepehri Rad, M., Kang, B., Cohen, L. B., Hughes, T., and Baker, B. J. (2016). Toward Better Genetically Encoded Sensors of Membrane Potential. *Trends Neurosci.* 39, 277–289. doi:10.1016/j.tins.2016.02.005

Sung, U., Sepehri-Rad, M., Piao, H. H., Jin, L., Hughes, T., Cohen, L. B., et al. (2015). Developing Fast Fluorescent Protein Voltage Sensors by Optimizing FRET Interactions. *PLoS One* 10, e0141585. doi:10.1371/journal.pone.0141585

Villalba-Galea, C. A., Sandtner, W., Dimitrov, D., Mutoh, H., Knöpfel, T., and Bezanilla, F. (2009). Charge Movement of a Voltage-Sensitive Fluorescent Protein. *Biophysical J.* 96, L19–L21. doi:10.1016/j.bpj.2008.11.003

Yi, B., Kang, B. E., Lee, S., Braubach, S., and Baker, B. J. (2018). A Dimeric Fluorescent Protein Yields a Bright, Red-Shifted GEVI Capable of Population Signals in Brain Slice. *Sci. Rep.* 8, 15199. doi:10.1038/s41598-018-33297-y

Conflict of Interest: The authors declare that the research was conducted in the absence of any commercial or financial relationships that could be construed as a potential conflict of interest.

Publisher's Note: All claims expressed in this article are solely those of the authors and do not necessarily represent those of their affiliated organizations, or those of the publisher, the editors and the reviewers. Any product that may be evaluated in this article, or claim that may be made by its manufacturer, is not guaranteed or endorsed by the publisher.

frontiers | Frontiers in Cell and Developmental Biology

REVIEW
published: 20 June 2022
doi: 10.3389/fcell.2022.885394

Resource for FRET-Based Biosensor Optimization

Heonsu Kim[1†], *Gyuho Choi*[2†], *Myung Eun Suk*[3*] *and Tae-Jin Kim*[1,2,4*]

[1]Institute of Systems Biology, Pusan National University, Busan, South Korea, [2]Department of Integrated Biological Science, Pusan National University, Busan, South Korea, [3]Department of Mechanical Engineering, IT Convergence College of Materials and Components Engineering, Dong-Eui University, Busan, South Korea, [4]Department of Biological Sciences, Pusan National University, Busan, South Korea

After the development of Cameleon, the first fluorescence resonance energy transfer (FRET)-based calcium indicator, a variety of FRET-based genetically encoded biosensors (GEBs) have visualized numerous target players to monitor their cell physiological dynamics spatiotemporally. Many attempts have been made to optimize GEBs, which require labor-intensive effort, novel approaches, and precedents to develop more sensitive and versatile biosensors. However, researchers face considerable trial and error in upgrading biosensors because examples and methods of improving FRET-based GEBs are not well documented. In this review, we organize various optimization strategies after assembling the existing cases in which the non-fluorescent components of biosensors are upgraded. In addition, promising areas to which optimized biosensors can be applied are briefly discussed. Therefore, this review could serve as a resource for researchers attempting FRET-based GEB optimization.

Keywords: genetically encoded biosensor, optimization, FRET, sensor domain, ligand domain, linker, localization signal

OPEN ACCESS

Edited by:
Jihye Seong,
Korea Institute of Science and Technology, South Korea

Reviewed by:
João Pessoa,
University of Coimbra, Portugal
Kazuhiro Aoki,
Graduate University for Advanced Studies (Sokendai), Japan

***Correspondence:**
Myung Eun Suk
msuk@deu.ac.kr
Tae-Jin Kim
tjkim77@pusan.ac.kr

[†]*These authors contributed equally to this work and share the first authorship*

Specialty section:
This article was submitted to Signaling, a section of the journal Frontiers in Cell and Developmental Biology

Received: *28 February 2022*
Accepted: *17 May 2022*
Published: *20 June 2022*

Citation:
Kim H, Choi G, Suk ME and Kim T-J (2022) Resource for FRET-Based Biosensor Optimization. Front. Cell Dev. Biol. 10:885394. doi: 10.3389/fcell.2022.885394

1 INTRODUCTION

After successful cloning of green fluorescent protein (GFP) originating from *Aequorea victoria* and having it exogenously expressed in cells (Morin and Hastings, 1971; Prasher et al., 1992), researchers have developed genetically encoded biosensors (GEBs) using fluorescent proteins (FPs). These GEBs allow visualization of various cellular biochemical parameters, such as ion concentration, cellular properties, and enzymatic activity (Miyawaki et al., 1997; Zhang et al., 2001; Wang et al., 2005). GEB is a chimeric protein expressed by transduction of an expression vector into cells and consists of organic fluorescent materials such as FPs or bioluminescent proteins and various components that induce the function of the biosensor (Sanford and Palmer, 2017; Greenwald et al., 2018; Terai et al., 2019). The advantage of GEB is that it directly interacts with endogenous players in cells and spatiotemporally visualizes intra- and extra-cellular properties. In addition, because it contains fluorescent proteins, chemical dyes inducing cytotoxicity are not required, and GEBs are observed and analyzed using microscopic imaging modalities or microplate readers. To date, researchers have developed biosensors in various categories based on circularly permuted FP, dimerization-dependent FP, reconstitution of split FP, bioluminescence resonance energy transfer (BRET), and fluorescence resonance energy transfer (FRET) (Sanford and Palmer, 2017; Kim et al., 2021). In this review, we mainly deal with FRET-based GEBs in particular.

FRET is a physical phenomenon of non-radiative energy transfer between two close chromophores with spectral overlap; an emission spectrum of donor fluorophore overlaps an

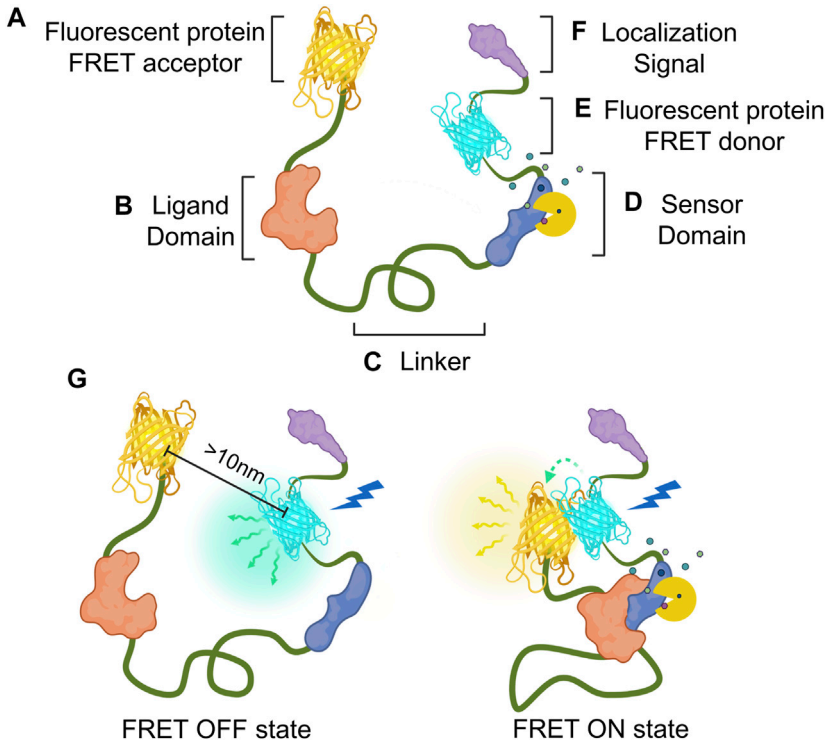

FIGURE 1 | Composition and mechanism of FRET-based GEB. Genetically encoded biosensor (GEB) consists of the following components. **(A,E)** Fluorescent proteins for acting as acceptor and donor, respectively; **(B)** ligand domain for recognizing the conformational change of the sensor domain; **(C)** linker for connecting the components of the GEB, which can affect the structure and performance of GEB; **(D)** sensor domain for detecting researcher's target of interest such as enzyme activity (yellow Pacman shape) or target molecule (small polygons); and **(F)** localization signal for placing GEBs in specific microdomains in a cell. **(G)** Mechanism of FRET-based GEB on FRET OFF state and FRET ON state. In the FRET OFF state, because ligand and sensor domain are not interacting with each other, donor and acceptor fluorescent protein generally keep a distance longer than 10 nm. Therefore, donor emission (green winding arrow and blue-green emanating glow) can be mainly detected by donor excitation (blue thunder shape). But In the FRET ON state, since GEB is activated by a specific target signal, The interaction between ligand and sensor domain makes two fluorescent proteins close. Due to this FRET phenomenon (green dashed-fading arrow), acceptor emission (yellow winding arrow and yellow emanating glow) can be mainly detected by donor excitation.

excitation spectrum of acceptor fluorophore (Förster, 1948; Jares-Erijman and Jovin, 2003). When a donor fluorophore absorbs excitation light, the donor transfers its energy to a neighboring acceptor fluorophore no farther than 10 nm, which results in the emission of the acceptor fluorophore and FRET ON state (**Figure 1G**). As FRET is a precise phenomenon that occurs between close molecules, it has now been widely used in biology as a tool to detect the interaction and proximity of two proteins. Since the development of the first genetically encoded calcium indicator (GECI) based on the FRET phenomenon (Miyawaki et al., 1997), many researchers have developed FRET-based GEB to monitor various target molecules and optimized biosensors to measure the activities of the targets of interest more accurately and sensitively.

Researchers have mainly optimized their biosensors using the following strategies. The first tactic is to adapt the improved FPs to their GEBs. The early FPs constituting the FRET pair, mainly cyan fluorescent protein (CFP) and yellow fluorescent protein (YFP), have many disadvantages. The acceptor YFP has poor resistance to low pH and photostability (Griesbeck et al., 2001; Nagai et al., 2002). In the case of CFP, the quantum yield, which is the degree to efficiently emit photons in response to excitation, had to be improved for better FRET efficiency (Rizzo et al., 2004; Goedhart et al., 2010; Goedhart et al., 2012). Many researchers have reported refined FPs, and FRET-exclusive FPs that allow the FRET pair to form dimers have been developed to stabilize the basal FRET signal (Nguyen and Daugherty, 2005). Applying these upgraded FPs to GEBs improved the FRET efficiency radiated by the biosensors (Allen and Zhang, 2006; Komatsu et al., 2011). Because there are several excellent review papers on FP development (Tsien, 1998; Zimmer, 2002; Chudakov et al., 2010), we do not focus on this topic in this article. The second upgrade strategy involves rearranging the order of the components constituting the GEBs. Two FPs of Mermaid 1, a voltage sensor, were located at the C-terminal of the amino acid sequence in a row (Tsutsui et al., 2008). However, Mermaid 2, developed by Tsutsui et al., showed an enhanced FRET ratio change by placing each FP in the N- and C-termini of the sensor domain, respectively (Tsutsui et al., 2013). The last strategy is to structurally analyze that, except for fluorescent proteins, the remaining components constituting the biosensor interact with the target molecules or other components; thereafter, each component is manipulated based on previous studies (Palmer et al., 2006). This process requires knowledge of other researchers'

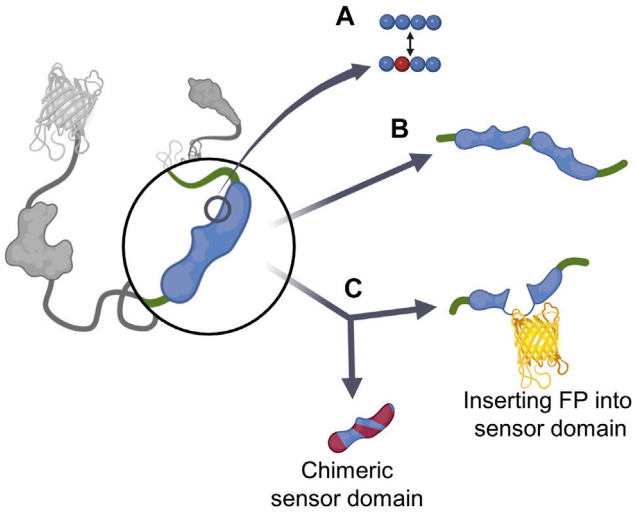

FIGURE 2 | Existing cases of sensor domain optimization strategies **(A)** Mutagenesis. **(B)** Additional sensor domain. **(C)** Reconstituting sensor domain, which is divided into chimeric sensor domain and inserting FP into sensor domain.

ideas, peptide domains that have been previously used and improved, and numerous examples of biosensor optimizations. However, discussions on strategies and cases in which researchers have optimized the components of GEBs are still lacking.

Here, we introduce several optimization strategies based on how the non-fluorescent components of FRET-based GEBs were refined by many researchers. At the end of this review, there is a brief introduction to fields where biosensors were newly applied as GEBs have been improved. Before starting this review, we define the components that compose a biosensor and have been optimized as follows (**Figures 1A–F**). The sensor domain plays a role in translating the property of the observer's interest into the appropriate conformational change of the biosensor (**Figure 1D**). The ligand domain recognizes conformational changes in the sensor domain (**Figure 1B**). The linker is the connection between components that affect the structure and performance of the GEBs (**Figure 1C**). Localization signals are peptides that can place the GEBs in specific subcellular locations (**Figure 1F**).

2 SENSOR DOMAIN

The sensor domain, which directly interacts with cellular players to induce the conformational change of GEBs, plays a key role in the biosensor's target sensing ability (Terai et al., 2019). To optimize biosensors, researchers have analyzed the interaction between the sensor domain and target player or ligand domain

TABLE 1 | Summary of sensor domain optimization strategies.

Sensor Domain					
Method	**Aim**	**Sensor Name**	**Target**	**Original Form**	**Optimized Form**
Mutagenesis	Increasing affinity to target player	Epac-S H187	cAMP	Klarenbeek et al. (2011)	Klarenbeek et al. (2015)
		ZAP70 kinase saFRET biosensor	ZAP70	Li et al. (2016)	Liu et al. (2021)
	Decreasing affinity to target player	Cameleon 3	Ca2+	-	Miyawaki et al. (1997)
		FLIPmal-Y Series	Maltose	-	Fehr et al. (2002)
		ZapCY2	Zn^{2+}	Qiao et al. (2006)	Qin et al. (2011)
	Decreasing affinity to non-target player	TN-XL	Ca^{2+}	Heim and Griesbeck, (2004)	Mank et al. (2006)
	Increasing affinity to ligand domain	EKAREV	ERK	Harvey et al. (2008)	Komatsu et al. (2011)
		AKAR3EV	PKA	Allen and Zhang, (2006)	Komatsu et al. (2011)
	Imaging at 25°C	ATeam1.03NL	ATP	Imamura et al. (2009)	Tsuyama et al. (2013)
Additional sensor domain	Increasing affinity to target player	TN-XXL	Ca^{2+}	Mank et al. (2006)	Mank et al. (2008)
	Monitoring two targets simultaneously	ICUPID	PKA, cAMP	Dipilato and Zhang, (2009)	Ni et al. (2011)
		KCAP-1	PKC, PKA	Schleifenbaum et al. (2004)	Brumbaugh et al. (2006)
Reconstituting sensor domain	Creating chimeric sensor domain	Chimera Cx	V^{+}	Lundby et al. (2010)	Mishina et al. (2012)
	Inserting FP into sensor domain	$FLII^{X}Pglu$-Y Series	Glucose	Fehr et al. (2003)	Deuschle et al. (2005)

and devised various strategies around this (**Figure 2**; **Table 1**). The first strategy involved mutagenesis (**Figure 2A**). By mutating one or several residues that play an important role in binding between the sensor domain and its counterpart, the affinity of the sensor domain to target players was regulated. Researchers mainly mutate several residues, but in some cases, the mutation of only one residue had a significant effect on the function of the GEB (Klarenbeek et al., 2015). Moreover, the addition of the same or different sensor domains improves the ability of the biosensor to measure the activities of multiple players simultaneously (**Figure 2B**). The last method we introduce creates a new sensor domain by combining parts originating from different proteins or inserting another component of the biosensor in the middle of the sensor domain (**Figure 2C**). Thus, the sensor domain can be reconstructed.

2.1 Mutagenesis

2.1.1 Increasing Affinity to Target Player

Biosensors can be optimized by increasing the affinity of the sensor domain to the target molecule. To produce an optimized FRET GEB detecting cyclic adenosine monophosphate (cAMP) with exchange protein directly activated by cAMP1 (EPAC1), Klarenbeek et al. examined several fluorescent protein pairs and residues in the sensor domain (Klarenbeek et al., 2015). In particular, EPAC-S H107 using EPAC1 with Q270E mutation, which causes the sensor domain to have a high affinity for cAMP, showed a 1.6-fold larger FRET ratio change than that of the forerunner having the same FP pair and wild type (WT) EPAC1.

Biosensors that measure kinase activity mainly use truncated peptide sequences, including phosphorylatable residues as the sensor domain. Recently, a case using a platform that combines FRET-seq, a method coupling FRET signals to next-generation sequencing (NGS), and mammalian cell libraries to increase the affinity of a consensus peptide to target kinase was reported (Liu et al., 2021). The first step of this platform was to create a self-activating FRET (saFRET) biosensor by inserting an active kinase domain into the C-terminus of the template biosensor. This process enabled the biosensor to emit an enhanced FRET ratio change in response to external stimuli and reduce the noise signal caused by endogenous cellular kinases. Next, libraries of substrate peptides using the saFRET biosensor were generated. Using degenerate primers, a mix of oligonucleotide sequences covering all possible nucleotide combinations, researchers created two peptide libraries by randomizing neighboring residues of the phosphorylated tyrosine residue: Library 1 (−1, −2, −3, and Y) and Library 2 (Y, +1, +2, and +3). Additionally, the possibility of false-positive selection was reduced by using control libraries of the kinase-dead version of the saFRET biosensor; the control libraries enabled researchers to select substrate peptides that only respond to the target kinase. The saFRET biosensor libraries were then transduced into mammalian cells using viral libraries, and the FRET ratios of individual cells expressing biosensor variants were analyzed and sorted using fluorescence-activated cell sorting (FACS). As a result, with NGS using RNA of the cell emitting a high-FRET ratio, the authors successfully optimized the biosensors that monitor the activity of Fyn and zeta-chain-associated protein kinase 70 (ZAP70) by identifying refined substrate sequences that responded highly to the active kinase domain and lowly to the dead kinase substrates. In this process, substrate peptides with a high affinity to the Src homology 2 (SH2) domain, a ligand domain of the biosensors, were naturally selected. Because this platform screened for improved biosensors using mammalian cells, not bacterial or yeast cells, there was no need to consider differences in translation and post-translational modification depending on the host, and no additional selection steps were required.

2.1.2 Decreasing Affinity to Target Player

Increasing the affinity to the target is not the only way to upgrade the performance of GEBs; researchers have also optimized the sensor domain by reducing the affinity to target molecules. Cameleon3, a genetically encoded calcium indicator (GECI), contains a calmodulin (CaM) in which one component reacting to Ca^{2+} with high affinity was removed via the E104Q mutation (Miyawaki et al., 1997). As a result, the biosensor showed a consistent and simplified sigmoidal curve according to the Ca^{2+} concentration.

The FLIPmal biosensor family detects cellular maltose using maltose-binding protein (MBP) as the sensor domain (Fehr et al., 2002). The primary FLIPmal involving WT MBP had a dissociation constant (K_d) of 2 μM for maltose. To expand the range of the biosensor for maltose measurements, tryptophan residues of MBP were mutagenized to alanine to decrease substrate affinity (Fehr et al., 2002). FLIPmal-25μ, which has W230A-mutated MBP, showed a K_d of 25 μM, and FLIPmal-225μ using W62A MBP had a K_d of 226 μM. With these biosensors, researchers have successfully measured various maltose concentration ranges.

The Zap1-based Zn^{2+} probe family uses two Zap1 zinc fingers as the sensor domain. One WT zinc finger detects Zn^{2+} using two cysteines and two histidines (Qiao et al., 2006). The K_d of ZapCY1 using two WT zinc fingers for the ion is 2.5 pM (Qin et al., 2011). To measure Zn^{2+} at a higher concentration range, researchers sequentially mutated the cysteines to histidines, and two types of mutation forms were adapted to the biosensor; Cys2His2 mutation was C581H and C618H, and His4 had C581H, C586H, C618H, and C623H mutations. ZapCY2, a Cys2His2 form biosensor, had K_d of 811 pM in cell and the K_ds of ZapCV2 with Cys2His2 mutation and ZapCV5 with His4 mutation for Zn^{2+} were 2.3 nM and 0.3 μM, respectively (Qin et al., 2011). The conversion of more residues to histidine decreased the affinity of the biosensor to Zn^{2+}, allowing researchers to measure Zn^{2+} at a high concentration range.

2.1.3 Decreasing Affinity to Non-Target Player

The sensor domain is able to interact with other molecules with properties similar to those of the target players. Therefore, to increase the specificity of the biosensor target, researchers carried out mutations that lower the affinity of the sensor domain to target player analogs. TN-L15, which uses the EF-hand III and IV of chicken skeletal muscle troponin C (csTnC) to detect Ca^{2+}, displayed conformational changes and FRET ratio changes in response to Mg^{2+} (Heim and Griesbeck, 2004). Mank et al.

improved the specificity of the sensor domain by mutating the D111 and D147 residues of csTnC capable of binding with magnesium into asparagine, leading to increased FRET ratio change and increased sensitive visualization of intracellular Ca^{2+} dynamics (Mank et al., 2006).

2.1.4 Increasing Affinity to Ligand Domain and Altering Reaction Conditions

Depending on which ligand domain is included in the biosensor that measures kinase activity, amino acids around the phosphorylatable residue can be substituted to increase the affinity between the sensor and ligand domains. EKAREV, an extracellular signal-regulated kinase (ERK) activity biosensor, uses the WW domain as a ligand domain to detect phosphothreonine (pThr) (Komatsu et al., 2011). To increase the affinity between the WW domain and substrate peptide, the researcher mutated the pThr +1 position into proline. AKAR3EV, a protein kinase A (PKA) activity biosensor, involves the forkhead-associated 1 (FHA1) domain as a ligand domain for detecting pThr. Consequently, the pThr +3 position was changed to aspartic acid to enhance its affinity to FHA1 (Komatsu et al., 2011).

There is a case of sensor modification using mutagenesis to increase the affinity between the sensor domain and target molecule in a unique experimental environment. AT1.03, which measures intracellular adenosine triphosphate (ATP) status, uses ε subunit of *Bacillus subtilis* FoF1-ATP synthase as sensor domain (Imamura et al., 2009). However, AT1.03 expressed in *Drosophila* S2 cells had poor sensitivity to ATP because of the unique imaging environment with a temperature of 25°C (Tsuyama et al., 2013). In 2013, Tsuyama et al. developed AT1.03NL biosensor by conducting a mutation of M60 in N-terminal domain (NTD) to N and K132 in C-terminal domain (CTD) to L and observed that the biosensor successfully monitored intracellular ATP status in *Drosophila melanogaster* and *Caenorhabditis elegans* at a temperature range is of 20–25°C (Tsuyama et al., 2013).

2.2 Additional Sensor Domain

It was reported that a biosensor had two identical sensor domains to increase the affinity to the target molecule and FRET ratio change. In the case of TN-XL, which uses EF-hand III and IV of csTnC as the sensor domain to detect Ca^{2+}, the efficiency of the biosensor was improved by adding one more sensor domain, and the advanced biosensor was called TN-XXL (Mank et al., 2008).

There are several cases in which the activity of two targets can be measured simultaneously by including two different sensor domains in one biosensor sequence. ICUPID, a biosensor detecting PKA, and cAMP dynamics, contains three FPs: CFP, red fluorescent protein (RFP), and YFP. (Ni et al., 2011). Between the CFP-RFP pair, there is a PKA substrate peptide and FHA1 domain pair, which can sense PKA activity, and the EPAC1 detecting cAMP was concatenated between the RFP-YFP pair. Therefore, by analyzing the RFP/CFP and YFP/RFP values emitted simultaneously by one biosensor in response to a specific stimulus, the status of intracellular PKA activity and cAMP can be visualized simultaneously. KCAP-1, which was generated by inserting a seven-amino acid PKA consensus sequence (Kemptide) into KCP-1, which measures the activity of protein kinase C (PKC), was designed to monitor the activity of PKC and PKA at the same time (Brumbaugh et al., 2006). In the intermediate FRET ratio state, the ratio increased when PKC was activated, and the FRET efficiency decreased if PKA activity was upregulated. The introduction of additional negative charges by PKA phosphorylation at Kemptide resulted in a disturbance of ionic interaction, inducing reduced FRET efficiency.

2.3 Reconstituting the Sensor Domain

In addition to changing specific residues of the sensor domain, there are cases in which a new chimeric sensor domain is created by combining several parts derived from different proteins to enhance the performance of the biosensor. VSFP2.3 is a genetically encodable voltage-sensing fluorescent probe that uses monomeric voltage-sensitive phosphatase (Ci-VSP) originating from *Ciona intestinalis* as the sensor domain (Lundby et al., 2010). In 2012, Mishina et al. transplanted homologous amino acid motifs of mKv3.1, a tetrameric voltage-activated potassium channel, into VSFP2.3 to create a novel chimeric biosensor, the chimeric Cx family (Mishina et al., 2012). Researchers developed Chimera C5 by replacing the Ci-VSP 227–236 amino acid with a counterpart of mKv3.1. Strikingly, Chimera C5 responded faster to activation and deactivation and displayed a higher total response than VSFP2.3.

The performance of the GEB can be improved by inserting an FP in the middle of the sensor domain sequence. The FLIPglu biosensor family, which monitors intracellular glucose, uses the mature glucose/galactose-binding protein MglB from *Escherichia coli* as its sensor domain (Fehr et al., 2003). To optimize the biosensor, Deuschle et al. searched for a site to insert the FP in the MglB sequence (Deuschle et al., 2005). The desired insertion site was required to satisfy the following conditions: it is solvent-exposed, located between regions of well-formed secondary structure, and capable of sterically accommodating the FP. Among the candidates, $FLII^{12}Pglu\text{-}600\mu$, in which ECFP was inserted after the 12th amino acid of MglB, showed the most improved FRET ratio change.

3 LIGAND DOMAIN

The primary form of GEB consists of only the FRET pair and sensor domain, and the emitted FRET ratio changes only due to conformational changes in the sensor domain (Terai et al., 2019). However, for a more dynamic conformational change of the biosensor, researchers have begun to incorporate a ligand domain, which detects the change in the sensor domain, into the biosensor structure. Therefore, the introduction of the ligand domain itself is an optimization of the GEBs (Terai et al., 2019). There are various types of ligand domains depending on the target players, but this review focuses on cases in which the ligand domain has been upgraded (**Figure 3**; **Table 2**).

3.1 Detecting Phosphorylated Residue

AKAR, which measures the activity of PKA, uses 14-3-3 protein as a ligand domain to capture pThr (Zhang et al., 2001). However, the binding affinity of 14-3-3 to pThr was too strong, preventing dephosphorylation of phosphorylated residues, which made it difficult for AKAR to monitor the effect of intracellular

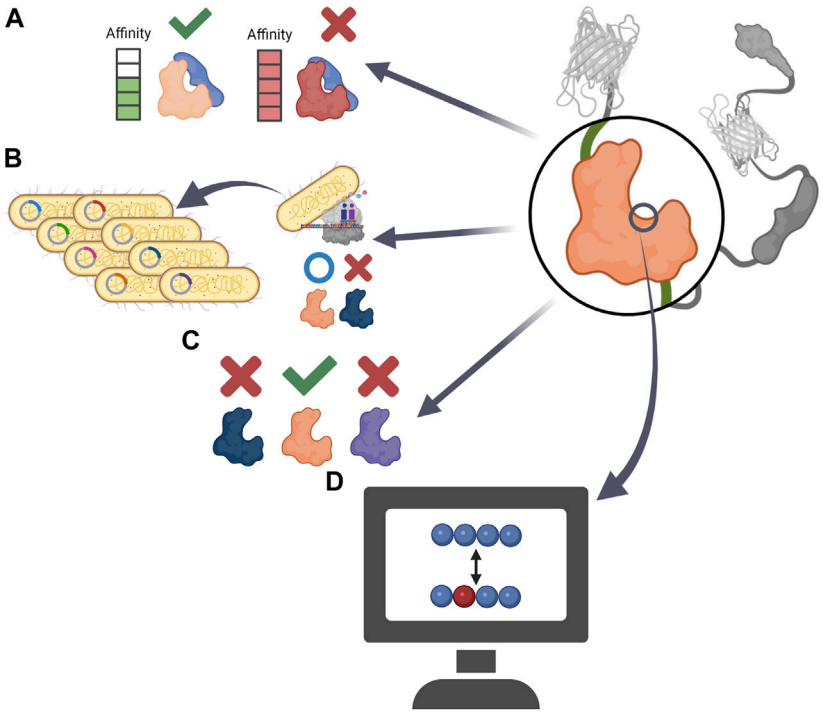

FIGURE 3 | Schematic precedents of ligand domain optimization **(A)** Constructing a GEB that can reversibly respond to external stimuli by using ligand domain with adequate affinity to sensor domain. **(B)** By replacing the ligand domain that *Escherichia coli* could not express, the GEB could be applied to a high-throughput bacterial colony screen **(C)** Developing target specific GEB by comparing the performance of ligand domains derived from various proteins. **(D)** Creating new ligand domain having low affinity to endogenous player via computational analysis.

TABLE 2 | Summary of ligand domain optimization strategies.

Ligand Domain

Method	Aim	Sensor Name	Target	Original Form	Optimized Form
Changing to ligand domain having appropriate affinity	Making biosensor reversible for detecting bi-directional PKA related signal	AKAR2	PKA	Zhang et al. (2001)	Zhang et al. (2005)
Changing to the ligand domain that *Escherichia coli* can translate	To apply the GEB to high-throughput bacterial colony screen	CyclinB1-Cdk1 activity sensor V2	Cdk1	Gavet and Pines, (2010)	Belal et al. (2014)
Comparing ligand domain homologies	Finding PDGFR activity-specific ligand domain	PDGFR biosensor	PDGFR	-	Seong et al. (2017)
Mutagenesis based on computational analysis	Decreasing affinity with endogenous players	Design X	Ca^{2+}	Griesbeck et al. (2001)	Palmer et al. (2004), Palmer et al. (2006)

phosphatase on PKA substrate peptide. Four years later, AKAR2, the successor to AKAR, used FHA1 as its ligand domain (Zhang et al., 2005). FHA1, a modular phosphothreonine binding domain with relatively low binding affinity, did not interfere with the dephosphorylation of pThr and made AKAR2 a reversible reporter detecting the bi-directional state of PKA substrate (**Figure 3A**).

There is a case in which the ligand domain was replaced with another protein for a transfected host to express the biosensor well. For GEB optimization using high-throughput bacterial colony screening, Belal et al. attempted to express the cyclin B1-Cdk1 activity sensor in *Escherichia coli* (Belal et al., 2014). However, the biosensor was not translated well in *E. coli* because of the polo box domain of Plk1, a ligand domain of the biosensor. Therefore, the ligand domain was replaced with FHA2, and the improved biosensor was well expressed in bacteria and could be applied to the screening platform (**Figure 3B**).

The FHA family is not the only family used to detect phosphothreonine. In the case of the EKAR family measuring the activity of ERK, the WW domain has been used as a ligand domain since 2008, which continues to be utilized, and EKAREN4/5, which has high specificity for ERK but low for CDK1, was developed in 2021 (Harvey et al., 2008; Ponsioen et al.,

2021). Therefore, an appropriate ligand domain should be examined according to the substrate peptide of the target player.

The SH2 domain, which detects phosphotyrosine (pTyr), can be derived from various proteins (Nair et al., 1995; Songyang and Cantley, 1995). Each SH2 domain has a different preferred environment and affinity for pTyr, which may affect the performance of the GEB. To develop a FRET-based platelet-derived growth factor receptor (PDGFR) biosensor measuring PDGFR phosphorylation, Seong et al. examined the SH2 domains derived from Src, Nck2, and Shp2 (Seong et al., 2017). The biosensor using the SH2 domain of Src showed conformational change and FRET ratio change not only by activated PDGFRs but also by other kinases, meaning that the SH2 domain originating from Src did not have specificity for PDGFR activity. However, the biosensor containing the SH2 domain of Nck2 and Shp2 displayed a PDGFR activity-specific FRET ratio change, and the SH2 domain derived from Nck2 efficiently improved the performance of the PDGFR biosensor located in the plasma membrane. Therefore, when developing or optimizing a biosensor to monitor the activity of protein tyrosine kinases, it is important to examine various types of SH2 ligands (**Figure 3C**).

3.2 Reducing Affinity With an Endogenous Player: For Precise Ca^{2+} Monitoring

Biosensors can be optimized by preventing the sensor and ligand domains from interacting with their endogenous cellular partners (**Figure 3D**). Because the WT ligand domain, a skeletal muscle myosin light chain kinase (skMLCK), of primary cameleons, a GECI using CaM as the sensor domain, could interact with endogenous CaM, cameleons failed to accurately respond to the Ca^{2+} concentration in the CaM-rich regions such as the plasma membrane of neurons (Griesbeck et al., 2001; Heim and Griesbeck, 2004). To create an improved Cameleon that does not bind to endogenous CaM, Palmer et al. structurally analyzed and mutated the sensor and ligand domains in the GEB and called the optimized CaM-skMLCK pairs 'Design X'. In 2004, the salt-bridge interaction between WT CaM and WT skMLCK peptides was investigated to develop Design 1 (D1) (Palmer et al., 2004). To break the salt-bridge between skMLCK of cameleon and WT CaM, the basic target residues of skMLCK peptide and acidic residues of CaM were reversed, thus preventing the biosensor components from binding with their WT counterparts. As a result, the researchers successfully developed D1, which has a relatively low affinity for Ca^{2+} (K_d = 60 μM) and was not significantly affected by large concentrations of excess CaM. In 2006, Designs 2, 3, and 4 were released (Palmer et al., 2006). To destabilize the binding between WT CaM and skMLCK peptide in the Cameleon in other ways, the researchers analyzed steric bumps in WT skMLCK and complementary holes in WT CaM. Based on this study, a small but important residue that plays a key role in WT CaM-WT skMLCK interaction was replaced with bulkier or charged residues, resulting in the development of mutated versions of skMLCK (mskMLCK), which sterically clashed with WT CaM. Thereafter, by mutating the CaM residues that interacted with WT skMLCK, the researchers created mutated versions of CaM (mCaM) that bound well to mskMLCK peptide but not to WT skMLCK. In this way, three combinations of mCaM-mskMLCK, which bound weakly to WT CaM but interacted much more strongly than the WT CaM-WT skMLCK pair, were created and named D2, D3, and D4. The new Designs could sensitively measure various ranges of Ca^{2+} concentrations that had not been monitored before and successfully visualize calcium in cellular microenvironments with unique Ca^{2+} concentrations, such as in the lipid rafts and mitochondria.

4 LINKER

GEBs are chimeric proteins in which peptide sequences derived from various proteins are collected in one amino acid chain. Therefore, a connection inevitably exists between each component, which is called a linker. Because these linkers have a significant influence on the physical structure of GEBs, there have been various attempts at their optimization thereof (**Figure 4**; **Table 3**).

Initially, the linker optimization process improved the FRET ratio by changing the direction of the fluorescent protein through various amino acid changes between FPs and the Ca^{2+}-sensing domains, while Miyawaki et al. developed the Cameleon1 biosensor (Miyawaki et al., 1997). Because of these studies, various attempts have been made on linker optimization.

There are various types of linkers depending on the purpose of the linker, but they can be broadly divided into flexible and rigid linkers (Gräwe and Stein, 2021).

The flexible linker has the feature of free movement between proteins linked by a linker that does not have a specific structure. A typical example is glycine-rich linkers. Because glycine has a small side chain, it was considered optimal for folding, structure, and function of the GEB linker (Chen et al., 2013). If the linker is flexible, the relative orientation between the donor and acceptor proteins changes. Therefore, the orientation factor, k^2, which is related to the FRET ratio, was set to ⅔. Therefore, the FRET efficiency can be calculated using the distance between the donor and acceptor without considering the variation in the orientation factor between fluorescent proteins (Terai et al., 2019).

The rigid linker is a linker with a specific structure and usually has an α-helical structure, which can be adjusted to prevent free interactions between the two connected proteins (Swanson and Sivaramakrishnan, 2014). A typical example is the $(EAAAK)_N$-motif. The α-helical structure has been applied in FRET protein sensors to monitor glycine (Zhang et al., 2018), redox potential (Kolossov et al., 2011), and ionic strength (Liu et al., 2017). If the linker is rigid, because of the fixed distance, during folding or shape changes in the linker due to sensor activation or environmental conditions such as ionic interactions (Liu et al., 2017) or the oxidation status of disulfide bridges (Kolossov et al., 2011), a high FRET ratio change can be obtained.

The linker affects the three-dimensional physical structure of the biosensor, and it is possible to manage the binding between the sensor and ligand domains. Here we introduce cases that affect the efficiency of the FRET sensor by optimizing the linker.

4.1 Optimize Linker Length

There was a case in which various combinations of linkers were optimized through a vector library (**Figure 4A**). Twitch, a calcium indicator, has a sensor domain, and TnC is concatenated between

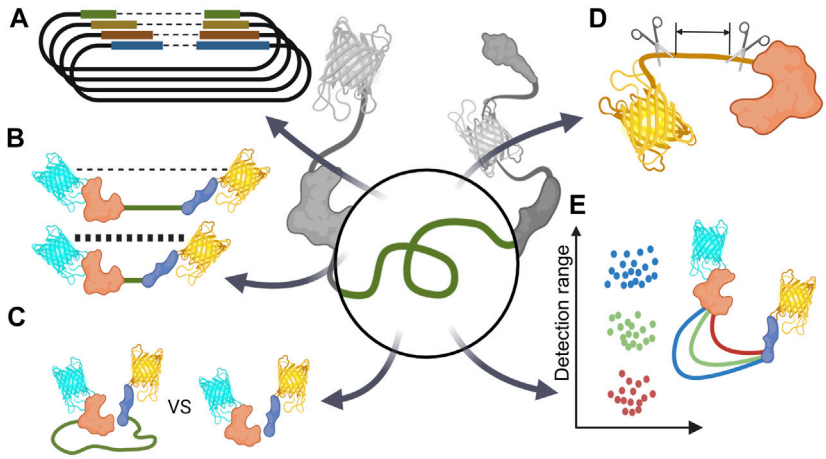

FIGURE 4 | Schematic diagram of linker optimization strategy **(A)** Optimize linker length via vector library. **(B)** Minimize basal FRET signal by extend linker **(C)** Comparing unimolecular and bimolecular biosensors. **(D)** Reducing unintentional linker-like peptides such as protein terminal parts or short peptide originated from restriction enzyme DNA sequence. **(E)** Changing sensor detection range via linker optimization.

TABLE 3 | Summary of linker optimization strategies.

Linker					
Method	**Aim**	**Sensor Name**	**Target**	**Original Form**	**Optimized Form**
Testing 49 combinations of proline linkers via vector library	Optimize linker length	Twitch	Ca^{2+}	Mank et al. (2008)	Thestrup et al. (2014)
Add rigid linker	Linker optimization for reducing basal FRET signal	CY-RL7	redox status	Kolossov et al. (2008)	Kolossov et al. (2011)
Insert EV linker		AKAR3EV	PKA	Allen and Zhang, (2006)	Komatsu et al. (2011)
		AMPKAREV	AMPK	Tsou et al. (2011)	Konagaya et al. (2017)
Add GSGGPPGSGGSG Linker, 58a.a linker and 10a.a Linker		NIR Rac1	Rac1	Miskolci et al. (2016); Moshfegh et al. (2014)	Shcherbakova et al. (2018)
Extend EV linker from 116a.a to 244a.a		Booster-PKA	PKA	Komatsu et al. (2011)	Watabe et al. (2020)
Insert flexible linker	Unimolecular biosensor VS. bimolecular biosensor	FLAME/PTB-EYFP, EGFR-ECFP	EGFR	-	Offterdinger et al. (2004)
Add (GGSGGS) repeat sequence		CA-L2-WY	Zn^{2+}	Van Dongen et al. (2006)	Van Dongen et al. (2007)
Add or remove EV linker		KARs/bimKARs	ERK	-	Depry et al. (2015)
Delete a.a sequence of FPs N/C terminus and sensor domain C terminus	Optimization for reducing unintentional linker-like peptides	FLIPglu-600u Δ13	Glucose	Fehr et al. (2003)	Deuschle et al. (2005)
Delete a.a sequence of restriction enzyme site		$FLII^{12}Pglu$-δ6		Deuschle et al. (2005)	Takanaga et al. (2008)
Add glycine or serine	Changing sensor detection range	YC-Nano	Ca^{2+}	Nagai et al. (2004)	Horikawa et al. (2010)
Adjust repeats from $(GPGGA)_8$ to $(GPGGA)_5$		TSMod F25	Mechanical strain	Grashoff et al. (2010)	Brenner et al. (2016)
Replace $(GPGGA)_8$ linker with HP35 linker		HP35-TS		Grashoff et al. (2010)	Austen et al. (2015)
SDM at N68A, K70M of HP35-TS		HP35st-TS		-	Austen et al. (2015)

the donor and acceptor. Thestrup et al. used a vector library to determine the optimal number of proline residues that connect the sensor domain N/C terminal and each fluorescent protein. They revealed the linker combination with the highest FRET efficiency by comparing a total of 49 linker combinations, from 1 to 7 prolines, and the front and back of the sensor domain (Thestrup et al., 2014).

4.2 Linker Optimization for Reducing Basal FRET Signal

In most cases of FRET-based biosensors, they are mainly used as ratio metrics through fractional calculations of donor and FRET signals. Therefore, if the difference between the basal FRET ratio before the reaction and the FRET ratio after the reaction is significant, it can be said that the FRET biosensor has high sensitivity. To increase this difference, the linker can be optimized to increase the FRET signal after reaction; on the contrary, the linker can be optimized to have a low basal FRET signal when the reaction does not occur to increase the difference between the basal FRET signal and the activated FRET signal (**Figure 4B**).

The use of a rigid linker to reduce the basal FRET signal is the CY-RL7 redox sensor (Kolossov et al., 2011). In the CY-RL5 biosensor structure (Kolossov et al., 2008), the RL5 linker, which is sensitive to redox status, is located between the CFP-YFP pair; when the linker is reduced (OFF state), the α-helix structure of the linker is changed, and the distance between the CFP-YFPs is increased, which leads to a decrease in the FRET signal. Conversely, when the linker is oxidized (ON state), the distance between the two fluorescent proteins decreases, resulting in an increase in the FRET signal. To improve the FRET ratio change, Kolossov et al. added the EAAAK rigid linker at the RL5 linker to reduce the distance between the donor and acceptor. They observed a six-fold change in FRET efficiency (Kolossov et al., 2008) and named this newly optimized sensor CY-RL7.

The cases of using a flexible linker to reduce basal level FRET signal are the AKAR3EV (Komatsu et al., 2011) and AMPKAREV (Konagaya et al., 2017) biosensors that use EV linker. The EV linker is a flexible linker consisting of repetitive SAGG peptides developed by Matsuda Lab. AKAR3 (Allen and Zhang, 2006) and AMPKAR (Tsou et al., 2011) biosensors have donor and acceptor at both ends, and ligand domains and sensor domains are attached between them. In Matsuda Lab, EV linkers were added between domains to increase the distance between the donor and acceptor. As a result, the basal FRET signal was reduced, thereby improving the FRET efficiency of the biosensor. They named the newly optimized sensors AKAR3EV and AMPKAREV, respectively.

Because the linker optimization process is closely related to the three-dimensional structure of the biosensor, if each part of the sensor is shuffled or replaced with another protein in the existing sensor, the basal FRET ratio will change owing to the change in the physical structure. Therefore, it is necessary to optimize the linker accordingly.

In the case of the NIR-Rac1 (Shcherbakova et al., 2018) biosensor using the miRFP670-miRFP720 FRET pair, the Forster radius (R_0) value of the fluorescent protein pair was 8.3 nm, 1.5–1.7 times longer than that of the normal CFP-YFP pair. Therefore, a relatively longer linker was used to separate fluorescent proteins.

In the case of the Booster-PKA (Watabe et al., 2020) biosensor, Watabe et al. arranged the PKA substrate at the C-terminus while designing the biosensor, so that the distance between the donor and the acceptor is closest when the sensor responds. However, this structure allowed the distance between the donor and acceptor to be close in the basal state. Therefore, to increase the sensitivity of the sensor, the length of the previously constructed EV linker was extended from 116 a. a to 244 a. a and the distance between fluorescent proteins was increased to lower the basal FRET signal.

4.3 Unimolecular Biosensor VS. Bimolecular Biosensor

In the case of a linker-connected type, unimolecular biosensor (UnimB), because the ligand and sensor domains move together at a relatively constant distance, the sensor response is more constant than that in the separated type, bimolecular biosensor (BimB), in which the distance between domains is not constant and the possibility of interaction with endogenous proteins induces the noise in the FRET signal. In addition, because the unimolecular Biosensor is expressed from single vector, accurate measurement of FRET is possible because all compartments show the same expression level and are located in the same region (Kim et al., 2021) (**Figure 4C**).

There are cases where the optimization was performed as UnimB using a linker because BimB did not react. An increase in the emission intensity of the acceptor by EGF treatment was observed when the PTB-EYFP/EGFR-ECFP bimolecular (Offterdinger et al., 2004) biosensors were used to measure EGFR autophosphorylation; however, there was no change in the FRET ratio observed. However, FLAME (Offterdinger et al., 2004), in which the two constructs were combined through a linker, successfully changed the FRET ratio via EGF stimulation.

To optimize the BimB Zn^{2+} indicator, CFP-Atox1 and WD4-YFP, Van Dongen et al. compared the FRET ratio in each case by inserting two to nine GGSGGS repeat sequences between Atox1 and WD4, the metal-binding domains. Each biosensor had a unique K_d value and FRET ratio change range. In particular, CA-L2-WY containing $(GGSGGS)_2$ showed the most remarkable FRET ratio change upon Zn^{2+} stimulation (Van Dongen et al., 2007).

However, UnimBs were not advantageous in all cases. Depending on the characteristics of the ligand domain and the sensor domain or the location of the sensor, BimB showed a better FRET ratio in some cases than in others.

The efficiencies of UnimB and BimB types of kinase activity reporters that measure various kinase activities were compared, and the change in efficiency was found to be different for each biosensor. There were even cases where it did not change (Depry et al., 2015). These differences depended on the target location and the location of the sensor. In particular, the biosensor placed on the plasma membrane showed improved FRET ratio values in BimB (Depry et al., 2015).

4.4 Linker Optimization for Reducing Unintentional Linker-like Peptides

When constructing a sensor for the first time, WT proteins are usually used. WT proteins have the advantage of reliability in the

operation of the sensor by showing a physiologically similar reaction to that of the proteins present in the living body. However, most WT proteins have several peptide sequences, each possessing a terminal region. These peptide sequences unintentionally affect the operation of the biosensor, or even though these sequences have no function, they act as linkers. Therefore, these peptide sequences could also be optimized (**Figure 4D**).

It may be necessary to consider the sequence between the sensor components for sensor optimization. To optimize the FLIPglu-600u (Fehr et al., 2003) biosensor, which is one of the FLIPglu biosensor family that measures the intracellular glucose concentration, the amino acid sequence of the N/C-terminus part of the fluorescent protein (Li et al., 1997), and the C-terminus part of the sensor domain was removed. The authors named the cloned sensor FLIPglu-600u Δ13 (Deuschle et al., 2005). This sensor showed a FRET ratio change of approximately threefold. In addition, the authors cloned the FLII^{12}Pglu (Deuschle et al., 2005) biosensor in which a fluorescent protein was inserted between the sensor domains to optimize FLIPglu-600u Δ13. In the optimization process of this sensor, a restriction enzyme sequence occurred during the cloning process, and the FLII^{12}Pglu-δ6 (Takanaga et al., 2008), which removed this sequence, showed the highest efficiency. However, the FRET ratio was more influenced by the composition of the removed amino acid than by the length of the linker removed (Takanaga et al., 2008).

4.5 Linker Optimization for Changing Sensor Detection Range

Linker optimization sometimes improved the detection range of the biosensor rather than improving the FRET ratio (**Figure 4E**).

There is a case where the detection range was changed by changing the sequence of several amino acids in the linker. The genetically encoded calcium indicator (GECI), YC2.60, and YC3.60 (Nagai et al., 2004), had a structure in which the CaM and M13 domains were connected through two glycines. Horikawa et al. added glycine or serine to the linker to diversify the saturation concentration of calcium by changing the sensitivity of the sensor to calcium. This helped develop the YC-Nano family, a collection of sensors that can measure various calcium concentration ranges (Horikawa et al., 2010).

Tension-sensing FRET biosensors are biosensors developed to measure various tensions within cells. To measure the physical force, these types of sensors use elastic linkers. Therefore, the linker itself acts as a force-sensing sensor domain. By modifying these linkers, researchers have diversified the range of force measurements.

In the case of TSMod F40 (Grashoff et al., 2010), mechanical strain in the range of 1–6 pN in the cell could be measured using the flagelliform linker sequence $(GPGGA)_8$, which is an elastic linker derived from spider silk protein. To adjust the force measurement range, Brenner et al. developed TSMod F25 and TSMod F50 (Brenner et al., 2016), in which the repeat number of the GPGGA sequence was adjusted to 5 and 10, respectively, and the measurable range was compared with that of TSMod F40. As a result, the TSMod F25 containing a $(GPGGA)_5$ linker could have an improved force measurement range of 2–11 pN compared to that of the TSMod F40.

To adjust the force measurement range, the linker was substituted with other protein types. Austen et al. produced HP35-TS (Austen et al., 2015) by replacing the linker of the TSMod F40 biosensor with villin headpiece peptide (HP35), an ultrafast folding peptide. The HP35-TS was able to measure the force range of 6–8 pN, which is stronger than the TSMod F40 with a measuring range of 1–6 pN. In addition, HP35st-TS (Austen et al., 2015) containing a more stable folding peptide was produced through N68A and K70M mutations in HP35-TS, which can measure a stronger force range of 9–11pN.

5 LOCALIZATION SIGNAL

Most target players in cells exist naturally in specific subcellular locations, depending on their role. For example, during the cell adhesion process of human mesenchymal stem cells, Ca^{2+} and focal adhesion kinase (FAK) activities depend on the plasma membrane microdomain (Kim et al., 2019). Additionally, the same player exists at different concentrations depending on where they are. The concentration of local endogenous CaM near the mouth of the channels was higher than that of cytoplasmic CaM (Mori et al., 2004). In addition, calcium is present at 100 nM–2 μM concentrations in the cytosol, 100–800 μM in the endoplasmic reticulum, and 100 nM–500 μM in the mitochondria (Arnaudeau et al., 2001; Samtleben et al., 2013). Therefore, to accurately monitor the physiology of a target molecule in a specific region, researchers need to anchor their GEB to the site where the biosensor can adequately interact with the cellular player by using a localization signal (LS). With this strategy, researchers were able to successfully visualize the activity of a target player, which was difficult to detect using a biosensor located at an inappropriate site (Kim et al., 2019). We will introduce examples of successful monitoring of site-specific target player activity or increased FRET ratio change using various LSs. Representative LSs for locating biosensors in subcellular regions are summarized in **Figure 5** and **Table 4**.

Some LSs can place biosensors on specific histone proteins (**Figure 5C**). By positioning the H3K9me3 biosensor precisely at the H3 position of histone with histone H3 sequence in the C-terminus of the GEB, the biosensor successfully monitored the interaction between H3 and players regarding K9H3 methylation and showed an improved FRET ratio change compared to the K9 reporter, a previous version without Histone H3 LS (Lin et al., 2004; Peng et al., 2018).

Several LSs are located in biosensors at specific mitochondrial regions. Park et al. developed mito-ZifCY1.173, which can monitor the Zn^{2+} concentration in the mitochondrial matrix by inserting a mitochondrial targeting sequence (MTS) into the N-terminal of ZifCY1 (Park et al., 2012) (**Figure 5D**). In addition, Sato et al. successfully analyzed diacylglycerol (DAG) dynamics in the outer mitochondrial membrane by attaching the C-terminal sequence of Bcl-xl to Daglas, a GBE sensing DAG (Sato et al., 2006) (**Figure 5E**).

A variety of LSs can position GEBs in specific plasma membrane microdomains. To visualize Src kinase activity

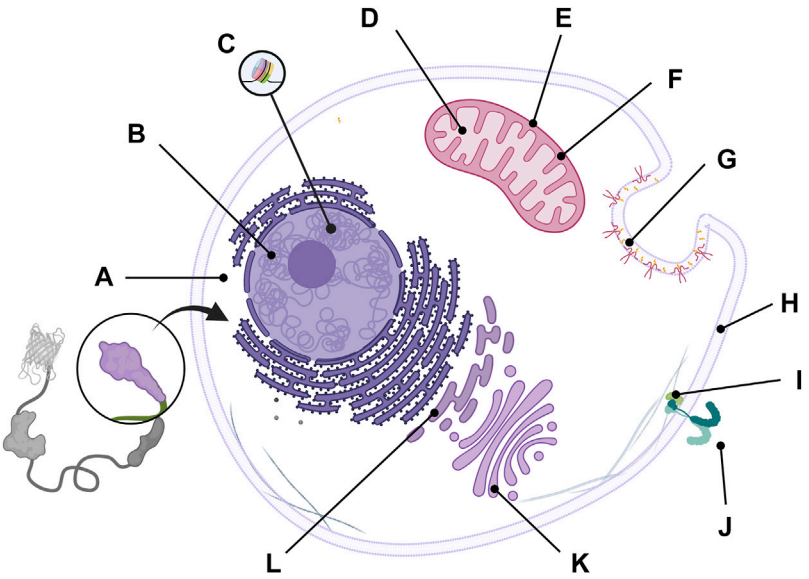

FIGURE 5 | Representative localization signal to guide GEBs at specific cellular microdomain. The biosensors can be placed at **(A)** cytosol by attaching nuclear export signal (NES), **(B)** nucleus by including nuclear localization signal (NLS), **(C)** a nucleosome subunit by using Histone H3, **(D)** mitochondrial matrix by attaching mitochondrial targeting sequence (MTS), **(E)** mitochondrial outer membrane by containing C-terminal sequence of Bcl-xl, **(F)** mitochondrial intermembrane region by including leader sequence from the second mitochondria derived activator of caspases (SMAC), **(G)** lipid raft by using Lyn acylation substrate sequences, **(H)** nonraft by attaching K-Ras prenylation sequences, **(I)** IRS-1 working site by using PH and PTB domain of IRS-1, **(J)** Extracellular region by including Igκ-chain leader sequence and PDGFR transmembrane domain, **(K)** Golgi apparatus by attaching eNOS targeting domain, and **(L)** endoplasmic reticulum (ER) by containing calreticulin signal sequence (CRsig) and ER retention sequence (KDEL).

TABLE 4 | Summary of representative localization signals.

Localization Signal			
Localization Signal	**Location**	**Sensor Name**	**References**
Nuclear export signal (NES)	Cytosol	EKAREV	Komatsu et al. (2011)
Nuclear localization signal (NLS)	Nuclear	JNKAR1EV-NLS	Kim et al. (2020)
Histone H3	Histone H3	H3K9me3 Biosensor	Peng et al. (2018)
Mitochondrial targeting sequence (MTS)	Mitochondrial matrix	mito-ZifCY1.173	Park et al. (2012)
C-terminal sequence of Bcl-xl	Mitochondrial outer membrane	Daglas-mit1	Sato et al. (2006)
Leader sequence from the second mitochondria derived activator of caspases (SMAC)	Mitochondrial intermembrane region	SMAC-mCherry-GZnP2	Fudge et al. (2018)
Lyn acylation substrate sequences	Lipid raft	Lyn-Src biosensor	Seong et al. (2009)
K-Ras prenylation sequences	Nonraft	Kras-Src biosensor	Seong et al. (2009)
PH and PTB domain of IRS-1	IRS-1	Phocus-2ppnes	Sato et al. (2002)
Igκ-chain leader sequence and PDGFR transmembrane domain	Extracellular region	MT1-MMP biosensor	Ouyang et al. (2008)
eNOS targeting domain	Golgi apparatus	eNOS-Aktus	Sasaki et al. (2003)
Calreticulin signal sequence (CRsig) and ER retention sequence (KDEL)	Endoplasmic reticulum (ER)	ER Ca^{2+} sensor	Kim et al. (2017)

according to the plasma membrane compartment, a FRET-based Src biosensor was located in the lipid raft or non-raft region by using Lyn acylation substrate sequences and K-Ras prenylation sequences, respectively (Seong et al., 2009) (**Figures 5G,H**). Interestingly, researchers observed that Src in the lipid raft region responded much more slowly and weakly to growth factors or pervanadate than non-raft domains. With visualization of drugs breaking the cytoskeletal structure, it

was revealed that Src in the non-raft region is at rest and is activated immediately, but another Src population in the lipid raft domain responds relatively slowly to external stimuli because it is in an endosome-like structure near the nucleus. In addition, GEBs can radiate increased FRET ratio changes by using a player's endogenous LS. Phocus, a biosensor that can measure insulin receptor activity in response to insulin treatment, could be situated near the insulin receptor by including a pleckstrin-homology (PH) domain and a phosphotyrosine-binding (PTB) domain, both of which are derived from insulin receptor substrate-1 (IRS-1) in the N-terminal and nuclear export signal (NES) in the C-terminal (Sato et al., 2002) (**Figure 5I**). Consequently, the Phocus behaved similar to an IRS-1 and was located next to the insulin receptor, inducing more phosphorylation opportunities in the biosensor. As a result, the GEB showed a larger FRET ratio change than the same biosensor in the cytoplasm.

To visualize the activity of the target molecule in the extracellular region, researchers have inserted the Igκ-chain leader sequence in the N-terminus and PDGFR transmembrane domain in the C-terminus of biosensors (**Figure 5J**). Ouyang et al. successfully analyzed the extracellular activity of membrane type 1 matrix metalloproteinase (MT1-MMP), which remodels the extracellular matrix (Ouyang et al., 2008), and Hires et al. detected glutamate on the surface of cultured dissociated hippocampal neurons (Hires et al., 2008).

Unintentionally embedded LS in GEB components can negatively affect the performance of biosensors. The ICUE biosensor contained the full sequence of EPAC1 to detect cAMP, inducing the biosensor to be situated in the mitochondria or membrane because of the N-terminal region and DEP domain of EPAC1 (DiPilato et al., 2004). Therefore, ICUE is perturbed by endogenous cellular functions and cannot detect the target signal well. ICUE2, a successor to ICUE, used truncated EPAC1 as its sensor domain to exclude the endogenous LSs and to improve the shortcomings, and the biosensor could be evenly distributed in the cytoplasm (Violin et al., 2008). Therefore, when designing a biosensor, it is necessary to check whether the unintentionally included LS lies within the GEB amino acid sequence.

There are more types of LS than we have introduced in this review. To measure the activity of a target player in a cellular region that has not been investigated before, the LS of a protein in the area can be applied to the biosensor.

6 DISCUSSION

The biosensors improved by these optimization tactics can not only visualize the dynamics of target players more precisely and sensitively but also be applied to several prospective fields. For example, an optimized FRET-based biosensor can be applied to high-throughput drug screening (HTDS) (Liu et al., 2021). Drug screening using biosensors makes it easy for researchers to obtain high-dimensional experimental results and real-time measurements of the drug's effect on target molecules in living cells. The previously introduced ZAP70 kinase saFRET biosensor showed increased FRET ratio change in response to drug stimulation by including an active kinase domain and met the conditions to be applied to HTDS, and the dynamic range of the FRET-based GEB must exceed at least 20% (Inglese et al., 2007). Using the optimized FRET-based biosensor, the 96-member kinase inhibitor library was screened, and three potential ZAP70 inhibitors were identified.

By adding the function of the "activator" to the FRET-based GEB, it is possible to visualize the activity of the target player and manipulate the physiology of cells simultaneously. Sun et al. created the Shp2-integrated sensing and activating protein (Shp2-iSNAP), which not only detects the phosphorylation of SIRPα, a receptor of CD47 transmitting "don't eat me" signal but also inhibits the SIRPα downstream signal with protein tyrosine phosphatase included in biosensor sequence (Sun et al., 2017). When bone marrow-derived macrophages (BMDMs) expressing the biosensor were stimulated by tumor cells that highly express CD47, researchers observed the phosphorylation of SIRPα. However, the macrophage cells engineered by protein tyrosine phosphatase in the biosensor engulfed the cancer cells despite the interaction between BMDMs and CD47. In this way, the biosensor combined with an activator can be used for therapeutic purposes by reprogramming the cells.

In this review, we introduced examples where researchers have optimized biosensor components independently of FPs, and these are summarized in **Tables 1–4**. To upgrade GEBs, researchers adopted various optimization strategies depending on the target players and experimentally confirmed the tactics. As reported in this paper, researchers not only increased the affinity between the sensor and ligand domains, but paradoxically decreased the affinity to enhance the function and activity of GEB. Meanwhile, it should be taken into account that optimization strategies belonging to one category can upgrade other GEB compartments. For example, a method meliorating sensor domain could be utilized to improve the ligand domain. In addition, to optimize GEBs, the physical structure of GEB's compartments and experimental temperature were even considered. In this paper, we have presented methods to optimize GEB through various examples, but variables still exist, so it may be necessary to try optimization through various approaches depending on the situation of each researcher. Nevertheless, we hope that the various GEB optimization factors presented in this paper will inspire researchers who want to develop new types of optimized GEBs or improve the performance of existing biosensors.

AUTHOR CONTRIBUTIONS

HK and GC contributed to the conception and design of the study. HK and GC wrote the first draft of the manuscript. MS and T-JK reviewed and edited the manuscript. MS and T-JK supervised the project.

FUNDING

This work was funded by the National Research Foundation of Korea (NRF) grant 2020R1C1C1010107 (T-JK), 2022M3E5F2017929 (T-JK), 2019R1G1A1099074 (MS) and 2021R1F1A1060910 (MS).

ACKNOWLEDGMENTS

In this study, the fluorescent biosensor database (https://biosensordb.ucsd.edu/index.php) was used to collect information on the FRET-based biosensor. All figures were created with BioRender (https://biorender.com/).

REFERENCES

Allen, M. D., and Zhang, J. (2006). Subcellular Dynamics of Protein Kinase A Activity Visualized by FRET-Based Reporters. *Biochem. Biophysical Res. Commun.* 348, 716–721. doi:10.1016/j.bbrc.2006.07.136

Arnaudeau, S., Kelley, W. L., Walsh, J. V., and Demaurex, N. (2001). Mitochondria Recycle Ca^{2+} to the Endoplasmic Reticulum and Prevent the Depletion of Neighboring Endoplasmic Reticulum Regions. *J. Biol. Chem.* 276, 29430–29439. doi:10.1074/jbc.M103274200

Austen, K., Ringer, P., Mehlich, A., Chrostek-Grashoff, A., Kluger, C., Klingner, C., et al. (2015). Extracellular Rigidity Sensing by Talin Isoform-Specific Mechanical Linkages. *Nat. Cell. Biol.* 17, 1597–1606. doi:10.1038/ncb3268

Belal, A. S. F., Sell, B. R., Hoi, H., Davidson, M. W., and Campbell, R. E. (2014). Optimization of a Genetically Encoded Biosensor for Cyclin B1-Cyclin Dependent Kinase 1. *Mol. Biosyst.* 10, 191–195. doi:10.1039/c3mb70402e

Brenner, M. D., Zhou, R., Conway, D. E., Lanzano, L., Gratton, E., Schwartz, M. A., et al. (2016). Spider Silk Peptide Is a Compact, Linear Nanospring Ideal for Intracellular Tension Sensing. *Nano Lett.* 16, 2096–2102. doi:10.1021/acs.nanolett.6b00305

Brumbaugh, J., Schleifenbaum, A., Gasch, A., Sattler, M., and Schultz, C. (2006). A Dual Parameter FRET Probe for Measuring PKC and PKA Activity in Living Cells. *J. Am. Chem. Soc.* 128, 24–25. doi:10.1021/ja0562200

Chen, X., Zaro, J. L., and Shen, W.-C. (2013). Fusion Protein Linkers: Property, Design and Functionality. *Adv. Drug Deliv. Rev.* 65, 1357–1369. doi:10.1016/j.addr.2012.09.039

Chudakov, D. M., Matz, M. V., Lukyanov, S., and Lukyanov, K. A. (2010). Fluorescent Proteins and Their Applications in Imaging Living Cells and Tissues. *Physiol. Rev.* 90, 1103–1163. doi:10.1152/physrev.00038.2009

Depry, C., Mehta, S., Li, R., and Zhang, J. (2015). Visualization of Compartmentalized Kinase Activity Dynamics Using Adaptable BimKARs. *Chem. Biol.* 22, 1470–1479. doi:10.1016/j.chembiol.2015.10.004

Deuschle, K., Okumoto, S., Fehr, M., Looger, L. L., Kozhukh, L., and Frommer, W. B. (2005). Construction and Optimization of a Family of Genetically Encoded Metabolite Sensors by Semirational Protein Engineering. *Protein Sci.* 14, 2304–2314. doi:10.1110/ps.051508105

Dipilato, L. M., and Zhang, J. (2009). The Role of Membrane Microdomains in Shaping β2-adrenergic Receptor-Mediated cAMP Dynamics. *Mol. Biosyst.* 5, 832. doi:10.1039/b823243a

DiPilato, L. M., Cheng, X., and Zhang, J. (2004). Fluorescent Indicators of cAMP and Epac Activation Reveal Differential Dynamics of cAMP Signaling within Discrete Subcellular Compartments. *Proc. Natl. Acad. Sci. U.S.A.* 101, 16513–16518. doi:10.1073/pnas.0405973101

Fehr, M., Frommer, W. B., and Lalonde, S. (2002). Visualization of Maltose Uptake in Living Yeast Cells by Fluorescent Nanosensors. *Proc. Natl. Acad. Sci. U.S.A.* 99, 9846–9851. doi:10.1073/pnas.142089199

Fehr, M., Lalonde, S., Lager, I., Wolff, M. W., and Frommer, W. B. (2003). Imaging of the Dynamics of Glucose Uptake in the Cytosol of COS-7 Cells by Fluorescent Nanosensors. *J. Biol. Chem.* 278, 19127–19133. doi:10.1074/jbc.M301333200

Förster, T. (1948). Zwischenmolekulare Energiewanderung und Fluoreszenz. *Ann. Phys.* 437, 55–75. doi:10.1002/andp.19484370105

Fudge, D. H., Black, R., Son, L., Lejeune, K., and Qin, Y. (2018). Optical Recording of Zn^{2+} Dynamics in the Mitochondrial Matrix and Intermembrane Space with the GZnP2 Sensor. *ACS Chem. Biol.* 13, 1897–1905. doi:10.1021/acschembio.8b00319

Gavet, O., and Pines, J. (2010). Activation of Cyclin B1-Cdk1 Synchronizes Events in the Nucleus and the Cytoplasm at Mitosis. *J. Cell. Biol.* 189, 247–259. doi:10.1083/jcb.200909144

Goedhart, J., Van Weeren, L., Hink, M. A., Vischer, N. O. E., Jalink, K., and Gadella, T. W. J. (2010). Bright Cyan Fluorescent Protein Variants Identified by Fluorescence Lifetime Screening. *Nat. Methods* 7, 137–139. doi:10.1038/nmeth.1415

Goedhart, J., Von Stetten, D., Noirclerc-Savoye, M., Lelimousin, M., Joosen, L., Hink, M. A., et al. (2012). Structure-Guided Evolution of Cyan Fluorescent Proteins towards a Quantum Yield of 93%. *Nat. Commun.* 3, 751. doi:10.1038/ncomms1738

Gräwe, A., and Stein, V. (2021). Linker Engineering in the Context of Synthetic Protein Switches and Sensors. *Trends Biotechnol.* 39, 731–744. doi:10.1016/j.tibtech.2020.11.007

Grashoff, C., Hoffman, B. D., Brenner, M. D., Zhou, R., Parsons, M., Yang, M. T., et al. (2010). Measuring Mechanical Tension across Vinculin Reveals Regulation of Focal Adhesion Dynamics. *Nature* 466, 263–266. doi:10.1038/nature09198

Greenwald, E. C., Mehta, S., and Zhang, J. (2018). Genetically Encoded Fluorescent Biosensors Illuminate the Spatiotemporal Regulation of Signaling Networks. *Chem. Rev.* 118, 11707–11794. doi:10.1021/acs.chemrev.8b00333

Griesbeck, O., Baird, G. S., Campbell, R. E., Zacharias, D. A., and Tsien, R. Y. (2001). Reducing the Environmental Sensitivity of Yellow Fluorescent Protein. Mechanism and Applications. *J. Biol. Chem.* 276, 29188–29194. doi:10.1074/jbc.M102815200

Harvey, C. D., Ehrhardt, A. G., Cellurale, C., Zhong, H., Yasuda, R., Davis, R. J., et al. (2008). A Genetically Encoded Fluorescent Sensor of ERK Activity. *Proc. Natl. Acad. Sci. U.S.A.* 105, 19264–19269. doi:10.1073/pnas.0804598105

Heim, N., and Griesbeck, O. (2004). Genetically Encoded Indicators of Cellular Calcium Dynamics Based on Troponin C and Green Fluorescent Protein. *J. Biol. Chem.* 279, 14280–14286. doi:10.1074/jbc.M312751200

Hires, S. A., Zhu, Y., and Tsien, R. Y. (2008). Optical Measurement of Synaptic Glutamate Spillover and Reuptake by Linker Optimized Glutamate-Sensitive Fluorescent Reporters. *Proc. Natl. Acad. Sci. U.S.A.* 105, 4411–4416. doi:10.1073/pnas.0712008105

Horikawa, K., Yamada, Y., Matsuda, T., Kobayashi, K., Hashimoto, M., Matsu-Ura, T., et al. (2010). Spontaneous Network Activity Visualized by Ultrasensitive Ca^{2+} Indicators, Yellow Cameleon-Nano. *Nat. Methods* 7, 729–732. doi:10.1038/nmeth.1488

Imamura, H., Huynh Nhat, K. P., Togawa, H., Saito, K., Iino, R., Kato-Yamada, Y., et al. (2009). Visualization of ATP Levels inside Single Living Cells with Fluorescence Resonance Energy Transfer-Based Genetically Encoded Indicators. *Proc. Natl. Acad. Sci. U.S.A.* 106, 15651–15656. doi:10.1073/pnas.0904764106

Inglese, J., Johnson, R. L., Simeonov, A., Xia, M., Zheng, W., Austin, C. P., et al. (2007). High-Throughput Screening Assays for the Identification of Chemical Probes. *Nat. Chem. Biol.* 3, 466–479. doi:10.1038/nchembio.2007.17

Jares-Erijman, E. A., and Jovin, T. M. (2003). FRET Imaging. *Nat. Biotechnol.* 21, 1387–1395. doi:10.1038/nbt896

Kim, T.-J., Kim, K.-A., and Jung, S. H. (2017). Development of an Endoplasmic Reticulum Calcium Sensor Based on Fluorescence Resonance Energy Transfer. *Sensors Actuators B Chem.* 247, 520–525. doi:10.1016/j.snb.2017.03.083

Kim, T.-J., Lei, L., Seong, J., Suh, J.-S., Jang, Y.-K., Jung, S. H., et al. (2019). Matrix Rigidity-Dependent Regulation of Ca^{2+} at Plasma Membrane Microdomains by FAK Visualized by Fluorescence Resonance Energy Transfer. *Adv. Sci.* 6, 1801290. doi:10.1002/advs.201801290

Kim, H.-S., Suh, J.-S., Jang, Y.-K., Ahn, S.-H., Raja, G., Kim, J.-C., et al. (2020). Anti-cancer Potential of Persimmon (Diospyros Kaki) Leaves via the PDGFR-Rac-JNK Pathway. *Sci. Rep.* 10, 18119. doi:10.1038/s41598-020-75140-3

Kim, H., Ju, J., Lee, H. N., Chun, H., and Seong, J. (2021). Genetically Encoded Biosensors Based on Fluorescent Proteins. *Sensors* 21, 795. doi:10.3390/s21030795

Klarenbeek, J. B., Goedhart, J., Hink, M. A., Gadella, T. W. J., and Jalink, K. (2011). A mTurquoise-Based cAMP Sensor for Both FLIM and Ratiometric Read-Out Has Improved Dynamic Range. *PLoS One* 6, e19170. doi:10.1371/journal.pone.0019170

Klarenbeek, J., Goedhart, J., Van Batenburg, A., Groenewald, D., and Jalink, K. (2015). Fourth-Generation Epac-Based FRET Sensors for cAMP Feature Exceptional Brightness, Photostability and Dynamic Range: Characterization of Dedicated Sensors for FLIM, for Ratiometry and with High Affinity. *Plos One* 10, e0122513. doi:10.1371/journal.pone.0122513

Kolossov, V. L., Spring, B. Q., Sokolowski, A., Conour, J. E., Clegg, R. M., Kenis, P. J. A., et al. (2008). Engineering Redox-Sensitive Linkers for Genetically Encoded FRET-Based Biosensors. *Exp. Biol. Med. (Maywood)* 233, 238–248. doi:10.3181/0707-RM-192

Kolossov, V. L., Spring, B. Q., Clegg, R. M., Henry, J. J., Sokolowski, A., Kenis, P. J. A., et al. (2011). Development of a High-Dynamic Range, GFP-Based FRET Probe Sensitive to Oxidative Microenvironments. *Exp. Biol. Med. (Maywood)* 236, 681–691. doi:10.1258/ebm.2011.011009

Komatsu, N., Aoki, K., Yamada, M., Yukinaga, H., Fujita, Y., Kamioka, Y., et al. (2011). Development of an Optimized Backbone of FRET Biosensors for Kinases and GTPases. *MBoC* 22, 4647–4656. doi:10.1091/mbc.E11-01-0072

Konagaya, Y., Terai, K., Hirao, Y., Takakura, K., Imajo, M., Kamioka, Y., et al. (2017). A Highly Sensitive FRET Biosensor for AMPK Exhibits Heterogeneous AMPK Responses Among Cells and Organs. *Cell. Rep.* 21, 2628–2638. doi:10.1016/j.celrep.2017.10.113

Li, X., Zhang, G., Ngo, N., Zhao, X., Kain, S. R., and Huang, C.-C. (1997). Deletions of the Aequorea Victoria Green Fluorescent Protein Define the Minimal Domain Required for Fluorescence. *J. Biol. Chem.* 272, 28545–28549. doi:10.1074/jbc.272.45.28545

Li, K., Xiang, X., Sun, J., He, H.-T., Wu, J., Wang, Y., et al. (2016). Imaging Spatiotemporal Activities of ZAP-70 in Live T Cells Using a FRET-Based Biosensor. *Ann. Biomed. Eng.* 44, 3510–3521. doi:10.1007/s10439-016-1683-6

Lin, C.-W., Jao, C. Y., and Ting, A. Y. (2004). Genetically Encoded Fluorescent Reporters of Histone Methylation in Living Cells. *J. Am. Chem. Soc.* 126, 5982–5983. doi:10.1021/ja038854h

Liu, B., Poolman, B., and Boersma, A. J. (2017). Ionic Strength Sensing in Living Cells. *ACS Chem. Biol.* 12, 2510–2514. doi:10.1021/acschembio.7b00348

Liu, L., Limsakul, P., Meng, X., Huang, Y., Harrison, R. E. S., Huang, T.-S., et al. (2021). Integration of FRET and Sequencing to Engineer Kinase Biosensors from Mammalian Cell Libraries. *Nat. Commun.* 12, 5031. doi:10.1038/s41467-021-25323-x

Lundby, A., Akemann, W., and Knöpfel, T. (2010). Biophysical Characterization of the Fluorescent Protein Voltage Probe VSFP2.3 Based on the Voltage-Sensing Domain of Ci-VSP. *Eur. Biophys. J.* 39, 1625–1635. doi:10.1007/s00249-010-0620-0

Mank, M., Reiff, D. F., Heim, N., Friedrich, M. W., Borst, A., and Griesbeck, O. (2006). A FRET-Based Calcium Biosensor with Fast Signal Kinetics and High Fluorescence Change. *Biophysical J.* 90, 1790–1796. doi:10.1529/biophysj.105.073536

Mank, M., Santos, A. F., Direnberger, S., Mrsic-Flogel, T. D., Hofer, S. B., Stein, V., et al. (2008). A Genetically Encoded Calcium Indicator for Chronic *In Vivo* Two-Photon Imaging. *Nat. Methods* 5, 805–811. doi:10.1038/nmeth.1243

Mishina, Y., Mutoh, H., and Knöpfel, T. (2012). Transfer of Kv3.1 Voltage Sensor Features to the Isolated Ci-VSP Voltage-Sensing Domain. *Biophysical J.* 103, 669–676. doi:10.1016/j.bpj.2012.07.031

Miskolci, V., Wu, B., Moshfegh, Y., Cox, D., and Hodgson, L. (2016). Optical Tools to Study the Isoform-specific Roles of Small GTPases in Immune Cells. *J. Immunol.* 196, 3479–3493. doi:10.4049/jimmunol.1501655

Miyawaki, A., Llopis, J., Heim, R., McCaffery, J. M., Adams, J. A., Ikura, M., et al. (1997). Fluorescent Indicators for Ca^{2+} based on Green Fluorescent Proteins and Calmodulin. *Nature* 388, 882–887. doi:10.1038/42264

Mori, M. X., Erickson, M. G., and Yue, D. T. (2004). Functional Stoichiometry and Local Enrichment of Calmodulin Interacting with Ca^{2+} Channels. *Science* 304, 432–435. doi:10.1126/science.1093490

Morin, J. G., and Hastings, J. W. (1971). Energy Transfer in a Bioluminescent System. *J. Cell. Physiol.* 77, 313–318. doi:10.1002/jcp.1040770305

Moshfegh, Y., Bravo-Cordero, J. J., Miskolci, V., Condeelis, J., and Hodgson, L. (2014). A Trio-Rac1-Pak1 Signalling axis Drives Invadopodia Disassembly. *Nat. Cell. Biol.* 16, 571–583. doi:10.1038/ncb2972

Nagai, T., Ibata, K., Park, E. S., Kubota, M., Mikoshiba, K., and Miyawaki, A. (2002). A Variant of Yellow Fluorescent Protein with Fast and Efficient Maturation for Cell-Biological Applications. *Nat. Biotechnol.* 20, 87–90. doi:10.1038/nbt0102-87

Nagai, T., Yamada, S., Tominaga, T., Ichikawa, M., and Miyawaki, A. (2004). Expanded Dynamic Range of Fluorescent Indicators for Ca(2+) by Circularly Permuted Yellow Fluorescent Proteins. *Proc. Natl. Acad. Sci. U. S. A.* 101, 10554–10559. doi:10.1073/pnas.0400417101

Nair, S. A., Kim, M. H., Warren, S. D., Choi, S., Songyang, Z., Cantley, L. C., et al. (1995). Identification of Efficient Pentapeptide Substrates for the Tyrosine Kinase Pp60c-Src. *J. Med. Chem.* 38, 4276–4283. doi:10.1021/jm00021a017

Nguyen, A. W., and Daugherty, P. S. (2005). Evolutionary Optimization of Fluorescent Proteins for Intracellular FRET. *Nat. Biotechnol.* 23, 355–360. doi:10.1038/nbt1066

Ni, Q., Ganesan, A., Aye-Han, N.-N., Gao, X., Allen, M. D., Levchenko, A., et al. (2011). Signaling Diversity of PKA Achieved via a Ca^{2+}-cAMP-PKA Oscillatory Circuit. *Nat. Chem. Biol.* 7, 34–40. doi:10.1038/nchembio.478

Offterdinger, M., Georget, V., Girod, A., and Bastiaens, P. I. H. (2004). Imaging Phosphorylation Dynamics of the Epidermal Growth Factor Receptor. *J. Biol. Chem.* 279, 36972–36981. doi:10.1074/jbc.M405830200

Ouyang, M., Lu, S., Li, X.-Y., Xu, J., Seong, J., Giepmans, B. N. G., et al. (2008). Visualization of Polarized Membrane Type 1 Matrix Metalloproteinase Activity in Live Cells by Fluorescence Resonance Energy Transfer Imaging. *J. Biol. Chem.* 283, 17740–17748. doi:10.1074/jbc.M709872200

Park, J. G., Qin, Y., Galati, D. F., and Palmer, A. E. (2012). New Sensors for Quantitative Measurement of Mitochondrial Zn^{2+}. *ACS Chem. Biol.* 7, 1636–1640. doi:10.1021/cb300171p

Palmer, A. E., Jin, C., Reed, J. C., and Tsien, R. Y. (2004). Bcl-2-mediated Alterations in Endoplasmic Reticulum Ca^{2+} Analyzed with an Improved Genetically Encoded Fluorescent Sensor. *Proc. Natl. Acad. Sci. U.S.A.* 101, 17404–17409. doi:10.1073/pnas.0408030101

Palmer, A. E., Giacomello, M., Kortemme, T., Hires, S. A., Lev-Ram, V., Baker, D., et al. (2006). Ca^{2+} Indicators Based on Computationally Redesigned Calmodulin-Peptide Pairs. *Chem. Biol.* 13, 521–530. doi:10.1016/j.chembiol.2006.03.007

Peng, Q., Lu, S., Shi, Y., Pan, Y., Limsakul, P., Chernov, A. V., et al. (2018). Coordinated Histone Modifications and Chromatin Reorganization in a Single Cell Revealed by FRET Biosensors. *Proc. Natl. Acad. Sci. U.S.A.* 115. doi:10.1073/pnas.1811818115

Ponsioen, B., Post, J. B., Buissant des Amorie, J. R., Laskaris, D., van Ineveld, R. L., Kersten, S., et al. (2021). Quantifying Single-Cell ERK Dynamics in Colorectal Cancer Organoids Reveals EGFR as an Amplifier of Oncogenic MAPK Pathway Signalling. *Nat. Cell. Biol.* 23, 377–390. doi:10.1038/s41556-021-00654-5

Prasher, D. C., Eckenrode, V. K., Ward, W. W., Prendergast, F. G., and Cormier, M. J. (1992). Primary Structure of the Aequorea Victoria Green-Fluorescent Protein. *Gene* 111, 229–233. doi:10.1016/0378-1119(92)90691-H

Qiao, W., Mooney, M., Bird, A. J., Winge, D. R., and Eide, D. J. (2006). Zinc Binding to a Regulatory Zinc-Sensing Domain Monitored *In Vivo* by Using FRET. *Proc. Natl. Acad. Sci. U.S.A.* 103, 8674–8679. doi:10.1073/pnas.0600928103

Qin, Y., Dittmer, P. J., Park, J. G., Jansen, K. B., and Palmer, A. E. (2011). Measuring Steady-State and Dynamic Endoplasmic Reticulum and Golgi Zn^{2+} with Genetically Encoded Sensors. *Proc. Natl. Acad. Sci. U.S.A.* 108, 7351–7356. doi:10.1073/pnas.1015686108

Rizzo, M. A., Springer, G. H., Granada, B., and Piston, D. W. (2004). An Improved Cyan Fluorescent Protein Variant Useful for FRET. *Nat. Biotechnol.* 22, 445–449. doi:10.1038/nbt945

Samtleben, S., Jaepel, J., Fecher, C., Andreska, T., Rehberg, M., and Blum, R. (2013). Direct Imaging of ER Calcium with Targeted-Esterase Induced Dye Loading (TED). *JoVE* 75, e50317. doi:10.3791/50317

Sanford, L., and Palmer, A. (2017). Recent Advances in Development of Genetically Encoded Fluorescent Sensors. *Methods Enzym.* 589, 1–49. doi:10.1016/bs.mie.2017.01.019

Sasaki, K., Sato, M., and Umezawa, Y. (2003). Fluorescent Indicators for Akt/protein Kinase B and Dynamics of Akt Activity Visualized in Living Cells. *J. Biol. Chem.* 278, 30945–30951. doi:10.1074/jbc.M212167200

Sato, M., Ozawa, T., Inukai, K., Asano, T., and Umezawa, Y. (2002). Fluorescent Indicators for Imaging Protein Phosphorylation in Single Living Cells. *Nat. Biotechnol.* 20, 287–294. doi:10.1038/nbt0302-287

Sato, M., Ueda, Y., and Umezawa, Y. (2006). Imaging Diacylglycerol Dynamics at Organelle Membranes. *Nat. Methods* 3, 797–799. doi:10.1038/nmeth930

Schleifenbaum, A., Stier, G., Gasch, A., Sattler, M., and Schultz, C. (2004). Genetically Encoded FRET Probe for PKC Activity Based on Pleckstrin. *J. Am. Chem. Soc.* 126, 11786–11787. doi:10.1021/ja0460155

Seong, J., Lu, S., Ouyang, M., Huang, H., Zhang, J., Frame, M. C., et al. (2009). Visualization of Src Activity at Different Compartments of the Plasma Membrane by FRET Imaging. *Chem. Biol.* 16, 48–57. doi:10.1016/j.chembiol.2008.11.007

Seong, J., Huang, M., Sim, K. M., Kim, H., and Wang, Y. (2017). FRET-Based Visualization of PDGF Receptor Activation at Membrane Microdomains. *Sci. Rep.* 7, 1593. doi:10.1038/s41598-017-01789-y

Shcherbakova, D. M., Cox Cammer, N., Huisman, T. M., Verkhusha, V. V., and Hodgson, L. (2018). Direct Multiplex Imaging and Optogenetics of Rho GTPases Enabled by Near-Infrared FRET. *Nat. Chem. Biol.* 14, 591–600. doi:10.1038/s41589-018-0044-1

Songyang, Z., and Cantley, L. C. (1995). SH2 Domain Specificity Determination Using Oriented Phosphopeptide Library. *Methods Enzymol.* 254, 523–535. doi:10.1016/0076-6879(95)54037-7

Sun, J., Lei, L., Tsai, C.-M., Wang, Y., Shi, Y., Ouyang, M., et al. (2017). Engineered Proteins with Sensing and Activating Modules for Automated Reprogramming of Cellular Functions. *Nat. Commun.* 8, 477. doi:10.1038/s41467-017-00569-6

Swanson, C. J., and Sivaramakrishnan, S. (2014). Harnessing the Unique Structural Properties of Isolated α-Helices. *J. Biol. Chem.* 289, 25460–25467. doi:10.1074/jbc.R114.583906

Takanaga, H., Chaudhuri, B., and Frommer, W. B. (2008). GLUT1 and GLUT9 as Major Contributors to Glucose Influx in HepG2 Cells Identified by a High Sensitivity Intramolecular FRET Glucose Sensor. *Biochimica Biophysica Acta (BBA) - Biomembr.* 1778, 1091–1099. doi:10.1016/j.bbamem.2007.11.015

Terai, K., Imanishi, A., Li, C., and Matsuda, M. (2019). Two Decades of Genetically Encoded Biosensors Based on Förster Resonance Energy Transfer. *Cell. Struct. Funct.* 44, 153–169. doi:10.1247/csf.18035

Thestrup, T., Litzlbauer, J., Bartholomäus, I., Mues, M., Russo, L., Dana, H., et al. (2014). Optimized Ratiometric Calcium Sensors for Functional *In Vivo* Imaging of Neurons and T Lymphocytes. *Nat. Methods* 11, 175–182. doi:10.1038/nmeth.2773

Tsien, R. Y. (1998). The Green Fluorescent Protein. *Annu. Rev. Biochem.* 67, 509–544. doi:10.1146/annurev.biochem.67.1.509

Tsou, P., Zheng, B., Hsu, C.-H., Sasaki, A. T., and Cantley, L. C. (2011). A Fluorescent Reporter of AMPK Activity and Cellular Energy Stress. *Cell. Metab.* 13, 476–486. doi:10.1016/j.cmet.2011.03.006

Tsutsui, H., Karasawa, S., Okamura, Y., and Miyawaki, A. (2008). Improving Membrane Voltage Measurements Using FRET with New Fluorescent Proteins. *Nat. Methods* 5, 683–685. doi:10.1038/nmeth.1235

Tsutsui, H., Jinno, Y., Tomita, A., Niino, Y., Yamada, Y., Mikoshiba, K., et al. (2013). Improved Detection of Electrical Activity with a Voltage Probe Based on a Voltage-Sensing Phosphatase. *J. Physiol.* 591, 4427–4437. doi:10.1113/jphysiol.2013.257048

Tsuyama, T., Kishikawa, J.-i., Han, Y.-W., Harada, Y., Tsubouchi, A., Noji, H., et al. (2013). *In Vivo* Fluorescent Adenosine 5'-Triphosphate (Atp) Imaging of Drosophila Melanogaster and Caenorhabditis Elegans by Using a Genetically Encoded Fluorescent Atp Biosensor Optimized for Low Temperatures. *Anal. Chem.* 85, 7889–7896. doi:10.1021/ac4015325

Van Dongen, E. M. W. M., Dekkers, L. M., Spijker, K., Meijer, E. W., Klomp, L. W. J., and Merkx, M. (2006). Ratiometric Fluorescent Sensor Proteins with Subnanomolar Affinity for Zn(II) Based on Copper Chaperone Domains. *J. Am. Chem. Soc.* 128, 10754–10762. doi:10.1021/ja0610030

Van Dongen, E. M. W. M., Evers, T. H., Dekkers, L. M., Meijer, E. W., Klomp, L. W. J., and Merkx, M. (2007). Variation of Linker Length in Ratiometric Fluorescent Sensor Proteins Allows Rational Tuning of Zn(II) Affinity in the Picomolar to Femtomolar Range. *J. Am. Chem. Soc.* 129, 3494–3495. doi:10.1021/ja069105d

Violin, J. D., DiPilato, L. M., Yildirim, N., Elston, T. C., Zhang, J., and Lefkowitz, R. J. (2008). β2-Adrenergic Receptor Signaling and Desensitization Elucidated by Quantitative Modeling of Real Time cAMP Dynamics. *J. Biol. Chem.* 283, 2949–2961. doi:10.1074/jbc.M707009200

Wang, Y., Botvinick, E. L., Zhao, Y., Berns, M. W., Usami, S., Tsien, R. Y., et al. (2005). Visualizing the Mechanical Activation of Src. *Nature* 434, 1040–1045. doi:10.1038/nature03469

Watabe, T., Terai, K., Sumiyama, K., and Matsuda, M. (2020). Booster, a Red-Shifted Genetically Encoded Förster Resonance Energy Transfer (FRET) Biosensor Compatible with Cyan Fluorescent Protein/Yellow Fluorescent Protein-Based FRET Biosensors and Blue Light-Responsive Optogenetic Tools. *ACS Sens.* 5, 719–730. doi:10.1021/acssensors.9b01941

Zhang, J., Ma, Y., Taylor, S. S., and Tsien, R. Y. (2001). Genetically Encoded Reporters of Protein Kinase A Activity Reveal Impact of Substrate Tethering. *Proc. Natl. Acad. Sci. U.S.A.* 98, 14997–15002. doi:10.1073/pnas.211566798

Zhang, J., Hupfeld, C. J., Taylor, S. S., Olefsky, J. M., and Tsien, R. Y. (2005). Insulin Disrupts β-adrenergic Signalling to Protein Kinase A in Adipocytes. *Nature* 437, 569–573. doi:10.1038/nature04140

Zhang, W. H., Herde, M. K., Mitchell, J. A., Whitfield, J. H., Wulff, A. B., Vongsouthi, V., et al. (2018). Monitoring Hippocampal glycine with the Computationally Designed Optical Sensor GlyFS. *Nat. Chem. Biol.* 14, 861–869. doi:10.1038/s41589-018-0108-2

Zimmer, M. (2002). Green Fluorescent Protein (GFP): Applications, Structure, and Related Photophysical Behavior. *Chem. Rev.* 102, 759–782. doi:10.1021/cr010142r

Conflict of Interest: The authors declare that the research was conducted in the absence of any commercial or financial relationships that could be construed as a potential conflict of interest.

GLOSSARY

GEB genetically encoded biosensor
FP fluorescent protein
WT wild type
saFRET self-activating FRET
ZAP70 zeta-chain-associatedproteinkinase70
SH2 Src homology 2
GECI genetically encoded calcium indicator
MBP maltose binding protein
csTnC chicken skeletal muscle troponinC
pThr Phosphothreonine
FHA1 forkhead-associated
NTD N-terminal domain
CTD C-terminal domain
Ci-VSP monomeric voltage-sensitive phosphatase
pTyr phosphotyrosine
skMLCK skeletal muscle myosin light chain kinase
mskMLCK mutated versions of skMLCK
mCaM mutated versions of CaM
BimB bimolecular biosensor
UnimB unimolecular biosensor
a.a amino acid
bimKARs bimolecular kinase activity reporters
KARs kinase activity reporters
SDM site-directed mutagenesis
MTS mitochondrial targeting sequence
LS localization signal
NES nuclear export signal
HTDS high throughput drug screening
Shp2-iSNAP Shp2-integrated sensing and activating protein
BMDMs bone marrow-derived macrophages
PTB phosphotyrosine-binding
PH pleckstrin-homology

frontiers | Frontiers in Cell and Developmental Biology

BRIEF RESEARCH REPORT
published: 29 June 2022
doi: 10.3389/fcell.2022.880107

Design and Initial Characterization of a Small Near-Infrared Fluorescent Calcium Indicator

Mikhail E. Matlashov[1], *Jorge Vera*[2], *Ludmila A. Kasatkina*[1], *Kamran Khodakhah*[2] *and Vladislav V. Verkhusha*[1,3]*

[1]Department of Genetics and Gruss-Lipper Biophotonics Center, Albert Einstein College of Medicine, Bronx, NY, United States, [2]Department of Neuroscience, Albert Einstein College of Medicine, Bronx, NY, United States, [3]Medicum, Faculty of Medicine, University of Helsinki, Helsinki, Finland

Near-infrared (NIR) genetically encoded calcium indicators (GECIs) are becoming powerful tools for neuroscience. Because of their spectral characteristics, the use of NIR GECIs helps to avoid signal loss from the absorption by body pigments, light-scattering, and autofluorescence in mammalian tissues. In addition, NIR GECIs do not suffer from cross-excitation artifacts when used with common fluorescent indicators and optogenetics actuators. Although several NIR GECIs have been developed, there is no NIR GECI currently available that would combine the high brightness in cells and photostability with small size and fast response kinetics. Here, we report a small FRET-based NIR fluorescent calcium indicator iGECInano. We characterize iGECInano *in vitro*, in non-neuronal mammalian cells, and primary mouse neurons. iGECInano demonstrates the improvement in the signal-to-noise ratio and response kinetics compared to other NIR GECIs.

Keywords: GECI, iRFP, FRET, calcium imaging, far-red, biosensor

OPEN ACCESS

Edited by:
Yingxiao Wang,
University of California, San Diego, United States

Reviewed by:
Srdjan D. Antic,
University of Connecticut Health Center, United States
Xavier Morató Arus,
ACE Alzheimer Research Center Barcelona, Spain

***Correspondence:**
Vladislav V. Verkhusha
vladislav.verkhusha@einsteinmed.edu

Specialty section:
This article was submitted to Signaling, a section of the journal Frontiers in Cell and Developmental Biology

Received: *21 February 2022*
Accepted: *27 May 2022*
Published: *29 June 2022*

Citation:
Matlashov ME, Vera J, Kasatkina LA, Khodakhah K and Verkhusha VV (2022) Design and Initial Characterization of a Small Near-Infrared Fluorescent Calcium Indicator. Front. Cell Dev. Biol. 10:880107. doi: 10.3389/fcell.2022.880107

INTRODUCTION

Genetically encoded fluorescent calcium indicators (GECIs) engineered from fluorescent proteins (FPs) have long been used in neuroscience for imaging neuronal activities. GECIs allow the optical monitoring of neuronal firing in multiple individual cells and can be genetically targeted to specific subsets of neurons. GECIs based on green fluorescent protein (GFP), including indicators of the GCaMP (Chen et al., 2013; Dana et al., 2019) or Twitch (Thestrup et al., 2014) families are now widely used for studies of brain circuits (Broussard et al., 2014; Lin and Schnitzer, 2016; Luo et al., 2018). However, GFP-based GECIs have several drawbacks that limit their use. They require illumination with blue–green light (480–520 nm), which is strongly absorbed by body pigments and highly scattered in brain tissues. Therefore, neural imaging in deep layers requires invasive surgical procedures, such as implanting optical fibers or prisms (Jennings et al., 2015; Gaffield et al., 2016). In addition, the excitation spectrum of such indicators overlaps with the activation spectrum of the most widely used genetically encoded channelrhodopsin actuators, such as channelrhodopsin ChR2 (Boyden et al., 2005). To overcome these drawbacks, several red-shifted GECIs have been developed using red FPs, such as RGECO (Zhao et al., 2011) or RCaMP (Akerboom et al., 2013; Inoue et al., 2015). However, these indicators have not completely solved the problem of high light absorption by brain tissues and require the careful adjustment of light intensities to be combined with channelrhodopsins.

The development of near-infrared (NIR) FPs of the IFP (Shu et al., 2009; Yu et al., 2015) and iRFP (Shcherbakova et al., 2016; Matlashov et al., 2020) families allowed to shift fluorescence excitation and emission to a near-infrared tissue transparency optical window (650–900 nm). Although these FPs require the binding of biliverdin IXa (BV) linear tetrapyrrole as a chromophore, they are suitable for imaging in mammalian tissues where BV is produced as a result of heme catabolism. So far, only a very few NIR GECIs have been developed (Shcherbakova, 2021), with current state-of-the-art indicators being iGECI (Shemetov et al., 2021) and NIR-GECO2G (Qian et al., 2020). iGECI is a Förster resonance energy transfer (FRET)-based NIR indicator. It has relatively high effective brightness and photostability in mammalian cells and allows imaging in deep layers of the mouse cortex. However, iGECI suffers from slow signal decay (t_{off}) and has a large molecular weight of 86 kDa, which may affect protein targeting and packaging efficiency in adeno-associated virus (AAV). NIR-GECO2G is an intensiometric indicator composed of a single modified mIFP protein. It is characterized by fast on and off kinetics and a high magnitude of response per single action potential (up to 17%) in cultured neurons (Qian et al., 2020). This indicator, however, suffers from relatively low brightness in mammalian cells and fast photobleaching.

Both iGECI and NIR-GECO2G can be used in a spectral crosstalk-free combination with popular GFP-based indicators and channelrhodopsin actuators, allowing the simultaneous monitoring of several cellular parameters or optical modulation and monitoring of neuronal activities. While both indicators have their advantages, they are still far from an ideal NIR GECI, which would combine the high brightness in cells and photostability with fast kinetics and low molecular weight.

Here, we develop a small NIR GECI of 58 kDa based on a FRET pair consisting of miRFP670nano (Oliinyk et al., 2019) and miRFP720 (Shcherbakova et al., 2018), NIR FPs, and a minimal troponin C (TnC)-based Ca-sensitive domain. We describe the molecular evolution and high throughput screening of calcium indicators in bacterial and mammalian cells. We characterize the obtained NIR GECI *in vitro*, in human HeLa cells and mouse primary neurons and compare its performance with iGECI and NIR-GECO2G. We demonstrate that the resultant NIR GECI combines the advantages of all current NIR GECI indicators.

RESULTS

Engineering and Molecular Evolution of Small Near-Infrared Genetically Encoded Calcium Indicator Variants

To design iGECInano, we used a Ca^{2+}-sensing domain from Twitch-2B (Thestrup et al., 2014) developed from a minimal Ca^{2+}-binding domain of troponin C (TnC_m). Unlike Ca^{2+}-sensing domains in iGECI and NIR-GECO2G that are based on calmodulin, TnC_m does not require a binding partner peptide and only has two Ca^{2+}-binding motifs, called EF-hands. Therefore, indicators with TnC_m should have simpler and likely faster conformational changes associated with Ca^{2+}-binding and lower calcium buffering in cells. To build a FRET pair, we chose miRFP720 FP as the FRET-acceptor and miRFP670nano FP (Oliinyk et al., 2019) as the FRET-donor. miRFP670nano is a single domain NIR FP characterized by fast maturation time and a twice smaller size compared to all other currently available NIR FPs. To generate an initial library of NIR GECI variants, we fused miRFP670nano and miRFP720 to TnC_m directly or *via* randomized linkers of 1–4 amino acid residues in length.

An initial screening of NIR GECI variants was performed similarly to the process previously described (Shemetov et al., 2021) (**Figure 1A**). In short, we transformed the library of NIR iGECI variants into BL21 (DE3) bacterial strain expressing heme oxygenase, collected the brightest cells using a fluorescence-activated cell sorter (FACS), plated them on Petri dishes, and then transferred the mature colonies onto a nitrocellulose membrane. The colonies were further screened for functional response by measuring the baseline FRET in the presence of 1 mM EGTA and 50 μg/ml ionomycin, then, they were sprayed with a solution containing 100 mM $CaCl_2$ to measure the FRET change in response to Ca^{2+}. The NIR GECI variants that had miRFP670nano at the N-terminus and miRFP720 at the C-terminus demonstrated a higher Ca^{2+}-response compared to those with the reversed orientation of the NIR FPs. We selected the NIR GECI clones demonstrating the highest Ca^{2+}-response for further characterization in bacterial lysates using multiwell plates.

In bacterial lysates, we recorded the fluorescence spectra in the presence of 1 mM Ca^{2+} or 1 mM EGTA. We identified several NIR GECI variants demonstrating an approximately 60% drop of the donor/FRET ratio in response to 1 mM Ca^{2+} (or an approximately 2.5-fold higher donor/FRET ratio in the Ca^{2+}-free state compared to Ca^{2+}-loaded states). Bacterial lysates of these variants had about 4–6 times brighter fluorescence in the donor channel compared to the lysates expressing iGECI control (**Figure 1B**), likely due to a higher protein expression level due to smaller size.

NIR GECI variants exhibiting the highest brightness and largest Ca^{2+} response were further tested in lysates of mammalian cells. We transfected HeLa with plasmid-encoding NIR GECI variants under the CMV promoter. 24 h after transfection, 5 μM BV was added, and 48 h after transfection, cells were lysed and their fluorescence spectra were recorded in the presence of 1 mM Ca^{2+} or 1 mM EGTA. The brightest variant with the largest Ca^{2+} response had a linker between miRFP670nano and TnC_m consisting of two Pro amino acid residues (L1) and a linker between TnC_m and miRFP720 consisting of a single Pro residue (L2) (**Figures 1C,D**). We named this variant iGECInano. We concluded that, short rigid linkers between NIR FPs and the Ca^{2+}-sensing domain were essential for advanced iGECInano properties.

In Vitro Characterization of iGECInano

The absorption spectrum of iGECInano had two major absorption maxima at 640 and 700 nm corresponding to the absorption of miRFP670nano donor and miRFP720 acceptor

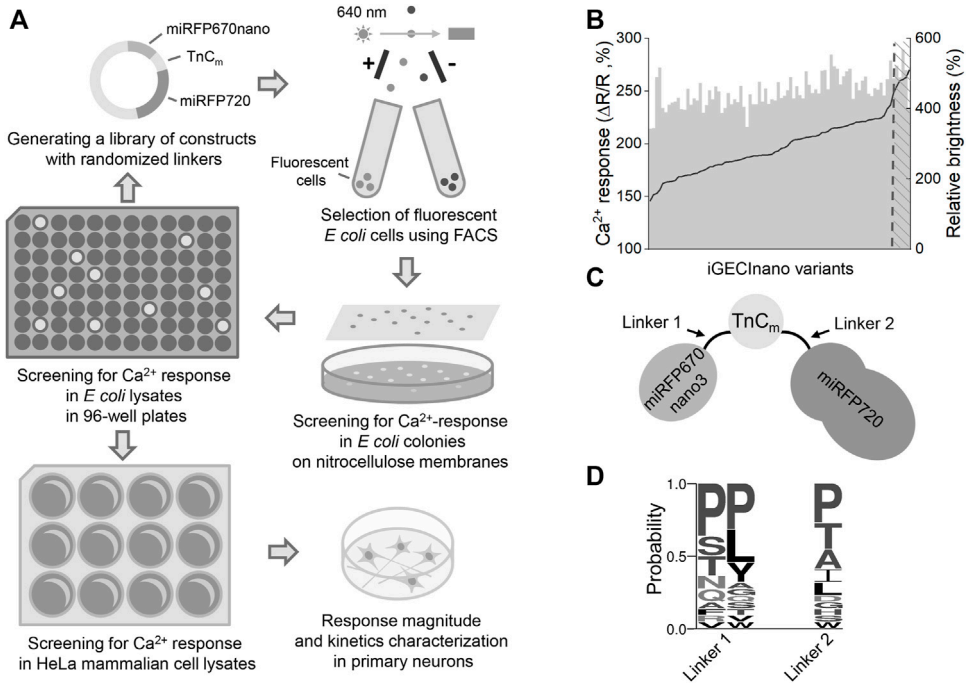

FIGURE 1 | The indicator design and screening strategy. **(A)** The library of the NIR GECI variants with randomized linkers was pre-sorted for positive fluorescence of miRFP670nano and miRFP720. Collected cells were plated on Petri dishes, mature colonies transferred to nitrocellulose membranes and screened for the calcium response by spraying with ionomycin/EGTA solution, then with the Ca^{2+} solution and comparing with the miRFP670nano/FRET ratio. The colonies demonstrating the highest response were further used for screening in bacterial lysates, then in mammalian lysates. The final indicator variant was tested in cultured neurons. **(B)** Evolution of iGECInano variants in bacteria. The amplitude of the FRET/donor ratio change in response to 1 mM Ca^{2+} (black) and relative brightness (gray) of the tested indicator variants. The brightness of the iGECInano variants was normalized on the brightness of iGECI. Variants with a response above the 250% threshold were sequenced and tested in HeLa cells. **(C)** Schematic of the iGECInano structural design. A minimal TnC-based Ca^{2+}-sensing domain TnC_m derived from Twitch-2B indicator is sandwiched between a FRET pair of miRFP670nano (FRET donor) and miRFP720 (FRET acceptor). **(D)** The frequency of amino acid residues in randomized linkers of iGECInano variants, having a Ca^{2+} response above 250% threshold.

(**Figure 2A**; **Table 1**). iGECInano also had a smaller absorption peak at 390 nm corresponding to the Soret band of BV in NIR FPs, attributed to the absorbance of individual pyrrole rings, and a peak at 280 nm attributed to a sum of absorbances of BV and aromatic residues of the apoprotein. The indicator had very low absorption at 450–500 nm, allowing it to combine with GFP-based indicators and opsin-based optogenetic actuators.

Next, we measured the fluorescence emission of iGECInano in the presence of 1 mM $CaCl_2$ (Ca^{2+}-loaded state) or 1 mM EGTA (Ca^{2+}-free state) in the lysates of HeLa cells. iGECInano fluorescence spectrum had two peaks at 670 and 718 nm, corresponding to miRFP670nano and miRFP720, respectively (**Figure 2B**). iGECInano exhibited an approximately 400% change in the FRET-acceptor to FRET-donor fluorescence ratio between the Ca^{2+}-free and Ca^{2+}-loaded states, mainly attributed to the decrease in miRFP670nano3 fluorescence. A small increase of FRET acceptor fluorescence in response to Ca^{2+} likely resulted from the compensation of the decrease of the donor and increase of the acceptor fluorescence signals.

We then measured the Ca^{2+} affinity of iGECInano (**Figure 2C**). The obtained Kd was 530 ± 20 nM, with a Hill coefficient of 1.53 ± 0.08. As expected, since TnC_m has only two EF-hands, it demonstrated the relatively simple dependency of the signal on Ca^{2+} concentration compared to iGECI (Shemetov et al., 2021). Interestingly, the Ca^{2+} affinity of iGECInano was somewhat lower than reported for Twitch-2B (200 nM), which contained the same TnC_m domain.

We also studied the pH stability of iGECInano in the presence of 1 mM $CaCl_2$ or 1 mM EGTA (**Figure 2D**). We observed minimal fluorescence changes between pH 6.0–10.0 and a decrease of fluorescence in the acidic range with pK_a 4.6 ± 0.1 for Ca^{2+}-loaded and 4.8 ± 0.2 for Ca^{2+}-free states. This pH dependence was similar to iGECI (Shemetov et al., 2021) and substantially broader than observed for the NIR–GECO series of indicators (Qian et al., 2019).

Performance of iGECInano in Non-Neuronal Mammalian Cells

Next, we compared the effective (cellular) brightness of iGECInano, iGECI, and NIR-GECO2G expressed in transiently transfected HeLa cells under the same CMV promoter. In the absence of an externally added BV, iGECInano was approximately 3-folds dimmer compared to iGECI (**Figure 3A**). However, in the presence of 5 μM external BV, iGECInano demonstrated about 40% higher brightness

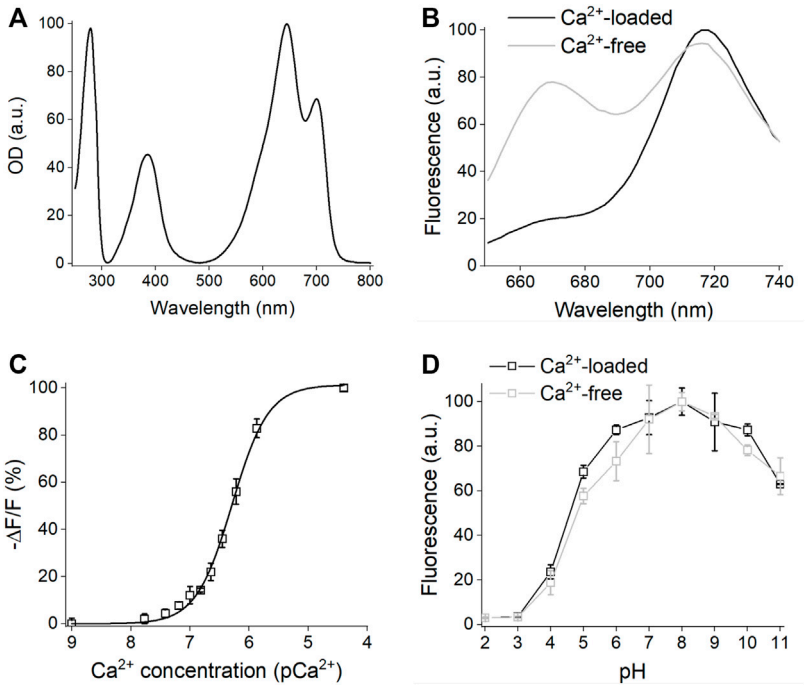

FIGURE 2 | *In vitro* characterization of iGECInano. **(A)** Absorbance spectrum of purified iGECInano. **(B)** Fluorescence spectra of iGECInano in HeLa cells lysate in the presence of 1 mM Ca^{2+} (black line) or 1 mM EGTA (gray line). **(C)** Dependence of purified iGECInano fluorescence on Ca^{2+} concentration. **(D)** Dependence of purified iGECI fluorescence on the pH value in the presence of 1 mM EGTA (gray), or 1 mM Ca^{2+} (black). Error bars are SEM, n = 4 experiments.

compared to iGECI (although not statistically significant, $p > 0.05$) and about 100% higher brightness compared to NIR-GECO2G (**Figure 3B**). iGECInano had lower than iGECI effective brightness in the absence of exogenous BV, even though neither miRFP670nano nor miRFP720 required BV supply to brightly fluoresce in mammalian cells.

miRFP670nano (Oliinyk et al., 2019) was reported to be more photostable compared to miRFP670 used in iGECI. However, iGECInano appeared to be somewhat less photostable (photobleaching $t_{0.5}$ = 780 ± 60 s) compared to iGECI ($t_{0.5}$ = 1750 ± 150 s). Still, it was significantly more photostable than NIR-GECO2G ($t_{0.5}$ = 75 ± 15 s) (**Figure 3C**).

Finally, iGECInano allowed reliable recording of histamine-induced Ca^{2+}-oscillations in HeLa cells (**Figure 3D**). Overall, although iGECInano had a relatively low cellular brightness without exogenous BV, its higher photostability and pH dependence allows it to be competitive with NIR-GECO2G. In experiments on cultured cells or tissues, external BV can be easily supplied to increase the iGECInano signal.

Characterization of iGECInano in Primary Mouse Neurons

Next, we compared the performance of NES-iGECInano and NES-iGECI (versions of the indicators fused with a nuclear export signal, therefore localized primarily in the cytoplasm and not in the nucleus), as well as NIR-GECO2G, in mouse primary neurons isolated from the cortex. On seventh DIV, the cultured neurons were transduced with AAVs encoding iGECInano, iGECI, or NIR-GECO2G under the CAG promoter and incubated for 7–9 days in the presence of 5 μM BV. All three indicators demonstrated a uniformly distributed fluorescence in the cytoplasm of neurons (**Figure 4A**). We then stimulated neuronal activity using 1-ms single pulse electric field stimulation while imaging the fluorescence of cell bodies (**Figure 4B**). The changes in fluorescence induced after electric stimulation showed a peak between −21.7% and −44.9% among cells expressing different sensors, without a significant difference between groups [mean −ΔF/F of 21.7% (11.8%–33.5%), 17.8% (14.3%–21.1%), and 44.9% (27.1%–67.5%) for iGECInano, iGECI, and NIR-GECO2G; $p > 0.05$ for all paired comparison] (**Figure 4C**). Values are the mean and (25%–75%) quartiles. To assess the kinetics of the evoked signals in cortical neurons, we first measured the onset of the fluorescence responses. Cells expressing iGECInano and iGECI showed similar time-to-peak values [0.7 s (0.4–0.85 s) vs. 0.6 s (0.35–0.65 s) for iGECInano and iGECI, respectively; p = 0.327], while cells expressing NIR-GECO2G presented a response onset of 1.8 s ([1.4–2.2 s), showing a slower kinetics compared to both, iGECInano (p = 0.029) and iGECI (p = 0.018) (**Figure 4D**). We then measured the decay of the evoked changes in fluorescence, finding that cells expressing iGECInano showed the fastest kinetics, being ~2.3 times faster than cells expressing iGECI [2.4 s (1.3–3.1 s) vs. 5.7 s (5.4–7.4 s) for iGECInano and iGECI, respectively; p = 0.002], and ~2 times faster than cells expressing NIR-GECO2G [2.4 s (1.3–3.1 s) vs. 4.9 s (4.0–6.1 s) for iGECInano and NIR-

TABLE 1 | Comparison of iGECInano with other NIR GECIs and widely used GCaMP6s.

GECI name	Ex/Em (nm)	Molecular brightness vs. EGFP, %[a]		pK_a $_{apo}$, pK_a $_{sat}$,	Photostability $t_{0.5}$, s[b]		Effective brightness, %[c]		Dynamic range (ΔF/F), fold	Hill coefficients n_1 and n_2	K_{d1} and K_{d2}, nM	Rise time, s[d]	Decay time, s[d]	ΔF/F, % per 1 AP		References
		w/o Ca^{2+}	with Ca^{2+}		HeLa cells	Mouse neurons	w/o BV	with BV						In neurons	*In vivo*	
iGECInano	donor 645/670 acceptor 702/720	n.a.	n.a.	4.6, 4.8	780	n.a.	16	140	4×	1.53	530	0.7	2.4	–21.7	n.a.	This work
iGECI	donor 640/670 acceptor 702/720	37	6.0	4.5, 4.5	1795	1735	46	100	6×	2.5 and 0.90	15 and 890	0.7 0.6	14 5.7	–5.7 (–12.9 with BV) –17.8	~–5 to 20 n.a.	Shemetov et al. (2021) This work
NIR-GECO1	678/704	12	1.0	5.1, 4.9	100[b]	134[b]	2.4[f]	20[f]	8×	0.99	215 and 885	1.5[f]	4.0[f]	~–4.5 (~–10 with BV[f])	n.a.	Qian et al. (2019)
NIR-GECO2G	678/704	13	1.3	5.3, 4.8	n.a.	~130[e]	~5[e]	n.a.	n.a.	0.78	480	~1.2	~3	~–16	n.a.	Qian et al. (2020)
							22 (this work)	75 (this work)				1.8	4.9	–44.9	n.a.	This work
NIR-GECO2	678/704	12	0.75	5.3, 4.8	n.a.	~130[e]	~2[e]	n.a.	n.a.	0.94	331	~1.3	~3.5	~–17	n.a.	Qian et al. (2020)
GCaMP6s	497/515	~5	123	9.8, 6.0	n.a.	n.a.	n.a.	n.a.	60×	2.9	144	0.48	1.8	28	23	Chen et al. (2013)

[a]*Molecular brightness is determined by extinction coefficient multiplied by quantum yield.*

[b]*Determined in (Shemetov et al., 2021), using 605/30 nm excitation and 647 nm long-pass emission filters at 14 mW/cm2 light power density at the back aperture of the lens, and normalized to absorption efficiency of the biosensors at 605 nm.*

[c]*Determined in transiently transfected live HeLa cells. Effective (a.k.a. cellular) brightness of iGECI with 25 μM of exogenous BV was assumed to be 100%.*

[d]*Determined for 1–10 electrical pulses in cultured neurons, without adding exogenous BV.*

[e]*Estimated based on data in (Shemetov et al., 2021) and (Qian et al., 2020).*

[f]*Measured in (Shemetov et al., 2021). Other NIR-GECO1 data are from (Qian et al., 2019). n.a., not available.*

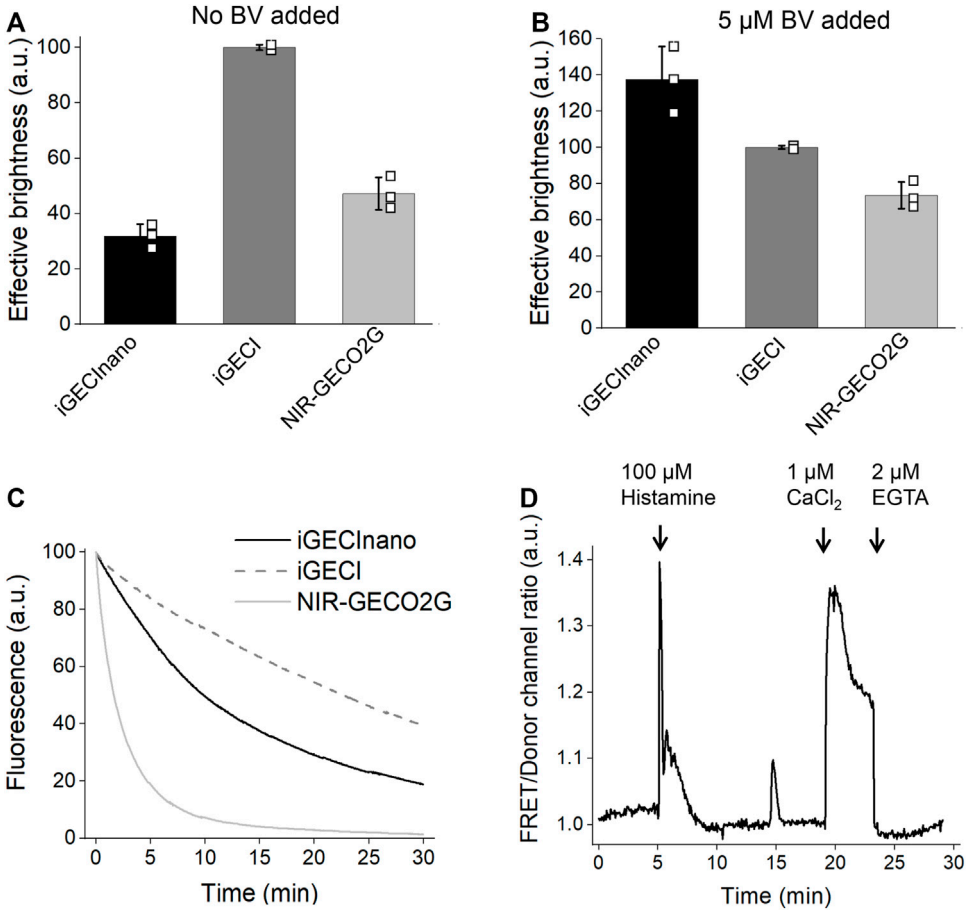

FIGURE 3 | Characterization of iGECInano in live human HeLa cells. **(A,B)** Comparison of iGECInano, iGECI, and NIR-GECO2G brightness in live HeLa cells in the absence of BV **(A)** and in the presence of 5 μM BV **(B)** measured using flow cytometry and normalized on iGECI fluorescence. The 640 nm laser was used for excitation, and a 647 nm long-pass edge filter to detect fluorescence. Fluorescence intensities were normalized to the absorption efficiencies of the indicators at 640 nm. In **(A,B)**, $n = 3$ individual experiments. **(C)** Photobleaching curves of iGECInano, iGECI, and NIR-GECO2G in live HeLa cells excited using a 605/30 nm bandpass and imaged using a 647 nm long-pass filter. Photobleaching data were normalized to the absorption efficiencies of indicators at 605 nm. 5 μM exogenous BV was supplied 24 h before the experiment. $n = 5$ cells. **(D)** Typical Ca^{2+} transients reported by iGECInano in live HeLa cells. Ratio changes of the FRET acceptor (ex. 605 nm, em. 725/40 nm) to the donor (ex. 605 nm, em. 680/20 nm) fluorescence intensities upon treatment with 100 μM of histamine, followed by changing the media to one containing 10 μM ionomycin and 1 mM Ca^{2+} and then 2 mM EGTA.

GECO2G, respectively; $p = 0.035$] (**Figure 4E**). Taken together, these data show that iGECInano displays faster kinetics when compared to iGECI and NIR-GECO2G.

The observed faster kinetics probably resulted from a smaller and simpler Ca^{2+}-sensing domain of iGECInano, which did not require interdomain interactions like the binding of M13 or RS20 peptides in calmodulin-based indicators. Therefore, iGECInano combines fast response kinetics with favorable photochemical characteristics (**Table 1**).

DISCUSSION

Using a rational design followed by random mutagenesis and screening in both bacteria and mammalian cells, we have developed the smallest NIR FRET-based indicator for Ca^{2+} ions, iGECInano. The iGECInano indicator is based on a pair of monomeric NIR FPs engineered from the bacterial phytochromes such as miRFP670nano and miRFP720 and is characterized by high cellular brightness in the presence of BV and fast Ca^{2+}-response kinetics (**Figures 3**, **4**). In addition, iGECInano is approximately 1.5 times smaller compared to iGECI (1,563 bp for iGECInano versus 2,394 bp for iGECI) making it suitable for packaging into AAV vectors, which have a strict 4.5–4.9 kbp limit for inserts, including a promoter and other regulatory elements (Dong et al., 1996).

In the presence of exogenous BV, iGECInano was substantially brighter in cells compared to iGECI and NIR-GECO2G. Also, compared to NIR-GECO2G, both iGECI and iGECInano exhibited a broader pH stability and photostability. Surprisingly, iGECInano seems to have a lower affinity to BV as compared to iGECI. Since the miRFP670nano and miRFP720 proteins themselves show bright fluorescence in the absence of external BV when individually expressed in mammalian cells, we

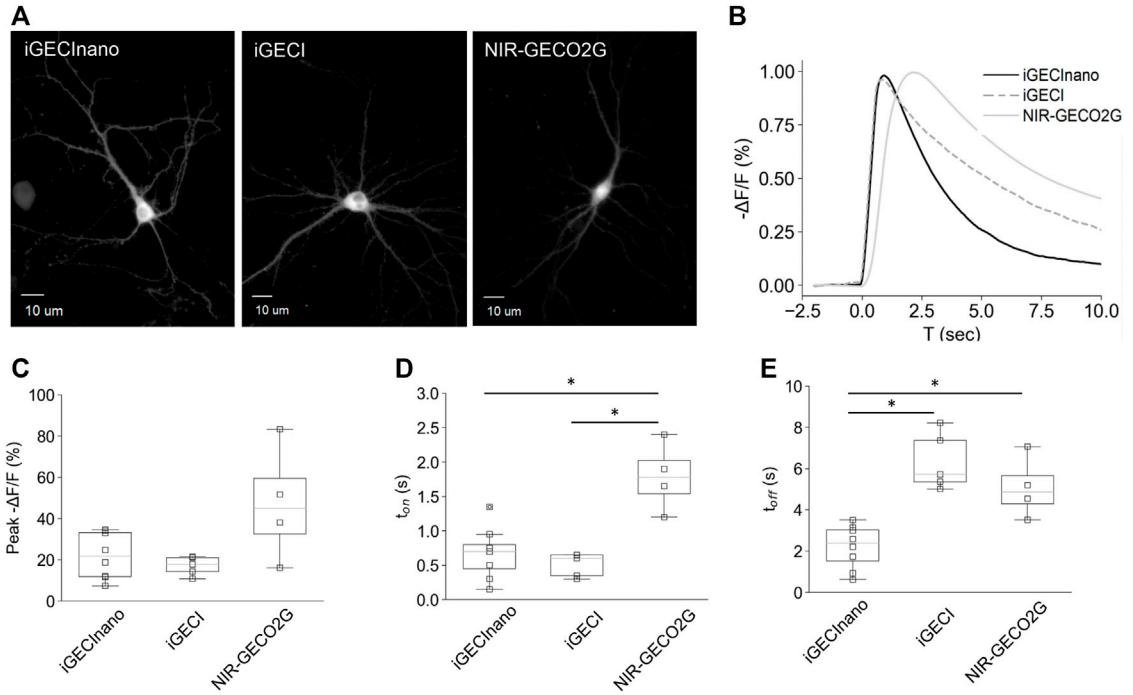

FIGURE 4 | Performance of iGECInano in cultured primary mouse neurons. **(A)** Images of neurons expressing NES-iGECInano, NES-iGECI, and NIR-GECO2G. **(B)** Normalized fluorescence change recorded from cells expressing iGECInano, iGECI, and NIR-GECO2G evoked with a single pulse of electric stimulation (traces represent the mean value). **(C–E)** Box plots showing peak fluorescent **(C)**, time to peak (t_{on}) **(D)**, and decay time (t_{off}) of the evoked responses **(B)**. Box plots show median, 25 and 75 quartiles, and max and min values. Statistical significance ($p < 0.05$, Kruskal–Wallis and Dunn's multiple comparison test) is shown with an asterisk (*). Cells per condition: iGECInano ($n = 8$), iGECI ($n = 5$), NIR-GECO2G ($n = 4$).

think that the current configuration of the indicator may somehow affect BV binding by the NIR FP pair. An additional cycle of evolution of iGECInano in mammalian cells may resolve the problem in the future. For *in vitro* experiments, the fluorescent signal of iGECInano can be enhanced with exogenous BV. At the same time, iGECInano may become a template for further evolution and generation of the first NIR GECI transgenic mouse enabling an efficient incorporation of endogenous BV during protein maturation.

Both iGECI and iGECInano possessed two emission peaks at 670 and 718 nm (**Figure 2**); however, Ca^{2+}-response was mostly characterized by a drop of fluorescence in the donor channel, while the fluorescence in the FRET channel stayed at the same level. It can be partly explained by the overlaying fluorescence spectra for donor and acceptor, therefore the rise of acceptor fluorescence was partly compensated by the drop of donor fluorescence. This also means that for some applications, the indicator can be used as intensiometric, with only the donor channel used for Ca^{2+} imaging.

Although we have not directly compared a signal-to-noise ratio of iGECInano and indicators of GCaMPs series, we assume that in cell cultures, iGECInano or any of the currently available NIR GECIs would have a lower signal-to-noise ratio compared to GCaMP6, as the latter has a higher molecular brightness (123 for GCaMP6 vs. 12–37 for NIR GECIs) and a much higher dynamic range (60x for GCaMP6 vs. 4-8x for NIR GECIs) (**Table 1**). However, deep-tissue imaging GFP-based indicators, such as GCaMP6, will suffer from signal loss from absorbance by body pigments and light-scattering and higher background from autofluorescence. Emerging NIR GECIs can help overcome this problem and, as they evolve, have the potential to compete with golden standard GFP-based indicators in the future.

CONCLUSION

iGECInano, developed in this article, has sufficient brightness and photostability in cells, fast response kinetics, and low molecular size, therefore, combining the advantages of the current state-of-the-art ratiometric iGECI and intensiometric NIR-GECO2G.

Further improvement of iGECI could consist of additional reduction of its size by using a smaller FRET-acceptor, such as red-shifted NIR FP designed from cyanobacteriochrome, which is not currently available yet. Also, a small, single-domain miRFP670nano is amenable to circular permutations as its N- and C-termini are located closely. The circularly permuted miRFP670nano as a FRET-donor could further improve the FRET changes between calcium-free and calcium-loaded states.

iGECInano could be further used in spectral crosstalk-free combinations with popular GFP-based biosensors, allowing the monitoring of several cellular parameters, and with optogenetic

actuators for simultaneous optical modulation and monitoring of calcium dynamics in all-optical setups. Moreover, appending a soma-targeting sequence to iGECInano and creating a transgenic mouse stably expressing iGECInano for efficient incorporation of available endogenous biliverdin, as well as the combination of this genotype with biliverdin reductase-A knock-out, should increase the signal-to-noise ratio, allowing advanced *in vivo* applications.

MATERIALS AND METHODS

Design of Bacterial and Mammalian Plasmids

miRFP670nano and a truncated version of miRFP720 (deletion of 17 N-terminal amino acids, miRFP720Δ17N) were PCR-amplified from pmiRFP670nano and pmiRFP720-N1 plasmids. A minimal TnC (TnC_m) sensing module was PCR-amplified from Twitch-2B-pcDNA3 (Addgene #49531). A NIR-GECO2G gene was PCR-amplified from pAAV-CAG-NIR-GECO2G (Addgene #159605). A plasmid pUCmini-iCAP-PHP.eB encoding-modified AAV2/9 capsid was kindly provided by Prof. V. Gradinaru (California Institute of Technology, Addgene #103005). A pHelper plasmid was from the AAV-Helper Free System kit (Agilent #240071). Plasmids encoding iGECI were previously constructed in our lab. For the cytoplasm-restricted localization, nuclear export (NES) signal peptide NELALKLAGLDINK was appended to the N-terminus of iGECInano *via* a short GGGS linker using a primer-extension PCR.

For the bacterial expression of GECI variants, pBAD/HisD vector (Life Technologies/Invitrogen) was used. Mammalian expression plasmids were based on a pEGFP-N1 vector (Clontech) with a standard CMV promoter. For the expression in dissociated neurons, iGECInano or NIR-GECO2G genes were cloned into pAAV-CAG-mRuby (Addgene #99123) in place of mRuby.

Molecular Evolution of iGECInano

DNA fragments encoding miRFP670nano, TnC_m, and miRFP720Δ17N were PCR amplified and ligated into the pEGFP-N1 vector. A set of constructs was created with miRFP670nano3 at the N-terminus and miRFP720 at the C-terminus and vice versa connected directly or with 1–4 a.a. randomized linkers. All variants were cloned into the pBAD/His-D vector and transformed into BL21 AI *E. coli* host (ThermoFisher Scientific) containing a pWA23h plasmid encoding heme oxygenase (HO) for BV synthesis. Cells were grown overnight in an LB medium containing 0.02% rhamnose and 0.05% arabinose for induction of HO and iGECI syntheses, respectively.

The library of clones was sorted with FACS, using double-positive gating for eliminating non-fluorescent clones resulting from stop-codons and frameshifts. The pre-sorted library was plated on Petri dishes containing 0.02% rhamnose and 0.05% arabinose so that approximately 100 colonies were growing on each dish. Dishes were incubated overnight at 37°C, then for 24 h at 18°C. Colonies were transferred to nitrocellulose membranes and permeabilized by spraying with Ca^{2+}-free solution (30 mM MOPS, pH 7.5, 100 mM KCl, 50 μg/ml poly-L-lysine, 50 μg/ml ionomycin). Membranes were incubated for 5 min, and basal fluorescence in the donor (ex. 605 nm, em. 680 nm) and FRET (ex. 605 nm, em. 720 nm) channels were acquired using an IVIS instrument (Perkin Elmer/Caliper Life Sciences). Then, membranes were treated by spraying with high Ca^{2+} solution (30 mM MOPS, pH 7.5, 100 mM KCl, 50 μg/ml poly-L-lysine, 50 μg/ml ionomycin, 100 mM $CaCl_2$), incubated for 5 min, and the Ca^{2+}-loaded state of fluorescence was recorded using the same filter sets. Data were analyzed using ImageJ software. 12–16 dishes or approximately 1,200–1,600 colonies were screened on membranes for each library per a round of screening.

Clones with the best Ca^{2+}-loaded/basal fluorescence ratio (typically 50–100 colonies per a round of screening) were transferred to 5 ml LB liquid culture in 24 deep-well plates containing 0.02% rhamnose and incubated for 2 h at 37°C on a rotating shaker. Then, arabinose was added to 0.05%, the culture was incubated for 3 h at 37°C, then for 24 h at 25°C. The bacterial pellets were lysed with B-PER (ThermoFisher Scientific). The cleared lysates were transferred to 96-well plates and divided. One part was loaded with 1 mM $CaCl_2$ and another one with 2 mM EGTA. Fluorescences of the donor (ex. 605 nm, em. 670 nm) and FRET (ex. 605 nm, em. 720 nm) were acquired using the SpectraMax M2 plate reader (Molecular Devices).

The best performing constructs were subcloned into a mammalian expression vector and evaluated in HeLa cell lysates. HeLa cells were transiently transfected using FuGENE HD (Promega); 24 h after transfection, 5 μM BV was added. 48 h after transfection, the cells were harvested and lysed with M-PER (ThermoFisher Scientific). Lysates were cleared by centrifugation and divided in two samples; one part was loaded with 1 mM $CaCl_2$ and another one with 2 mM EGTA. Fluorescence spectra were recorded with the FluoroMax-3 spectrofluorometer (Horiba). The best performing clones were subjected to a new round of L1 and L2 evolutions in *E. coli* and HeLa cells. Three rounds of evolution and screening were performed to identify the final indicator variants.

Protein Purification and *In Vitro* Characterization

The iGECI constructs with polyhistidine tags at the N-terminus were expressed in the BL21-AI host (Life Technologies/Invitrogen) containing a pWA23h plasmid. Bacteria were grown in an LB medium supplemented with ampicillin, kanamycin, and 0.02% rhamnose for 2 h at 37°C, followed by the induction of protein expression with 0.05% arabinose for 3 h at 37°C, then 24 h at 25°C on a rotating shaker. The proteins were purified using Ni-NTA agarose (Qiagen).

For absorbance measurements, a Hitachi U-2000 spectrophotometer was used. Fluorescence spectra in the range of 650–740 nm were recorded with the FluoroMax-3 spectrofluorometer.

Ca^{2+} titrations were carried out using EGTA-buffered Ca^{2+} solutions (Calcium Calibration Buffer Kit, Life Technologies). We

prepared buffers by mixing a Ca^{2+}-EGTA buffer and an EGTA buffer to give free Ca^{2+} concentrations ranging from 0 to 39 μM at 25°C. Fluorescence intensities were plotted against Ca^{2+} concentrations and fitted by a sigmoidal binding function to determine Kd.

Using a series of Hydrion buffers (Micro Essential Laboratory), pH stability was studied in the presence of either 2 mM EGTA or 1 mM $CaCl_2$. Fluorescence was excited at 620 nm, and the emission was recorded at 640–760 nm. The area under the spectra at different pH values was quantified.

A comparison of the brightness of iGECInano, iGECI, and NIR-GECO2G was performed in HeLa cells transiently transfected with FuGENE HD. For a BV-saturated condition, 5 μM BV was added 24 h after transfection. 48 h after transfection, cells were analyzed with a BD LSRII flow cytometer using a 640 nm excitation laser and a 647 nm long-pass edge emission filter. The NIR fluorescence intensity was normalized to the efficiency of absorption at 640 nm for each indicator. Flow cytometry gating was performed using intact, single cells.

Photobleaching measurements of the indicators in live HeLa cells and dissociated mouse neurons were performed with the ×100, 1.4 NA oil-immersion objective lens (UPlanSApo, Olympus) and a 605/30-nm excitation and a 647 nm long-pass emission filters at a light power density of 14 mW cm^{-2} measured at the back aperture of the objective lens (~8.3 W cm^{-2} at the specimen plane) and normalized to the efficiency of absorption at 605 nm for each indicator.

Histamine Oscillations

To measure Ca^{2+} transitions evoked by histamine, HeLa cells were transiently transfected with iGECI using FuGENE HD (Promega) and cultured for 48 h. Then, the medium was changed to Live Cell Imaging Solution (Life Technologies, Invitrogen), supplemented with 1 mM $CaCl_2$, 100 mM KCl and 1 mM D-glucose, and basal fluorescence in the donor (excitation, 605 nm; emission, 667/30 nm) and FRET (excitation, 605 nm; emission, 725/40 nm) channels was recorded. Time-lapse imaging was performed with an Olympus IX81 inverted epifluorescence microscope, equipped with a 200 W xenon lamp (Sutter Instruments) and a ×60, 1.35 NA oil-immersion objective lens (UPlanSApo, Olympus). The microscope was operated with SlideBook v. 6.0.8 software (Intelligent Imaging Innovations). A histamine solution was added to the cells to a final concentration of 100 μM, and the fluorescence was recorded for 10 min. After that, the imaging solution with Ca^{2+} and histamine was replaced by a Ca^{2+}-free imaging solution, and the cells were incubated for 5 min to equilibrate Ca^{2+}. Then, an imaging solution containing 2 mM EGTA was added to the cells, and fluorescence was recorded for another 5 min. The images were analyzed using ImageJ software.

Preparation of High-Titer AAVs

AAV particles were obtained as described (Challis et al., 2019). Briefly, plasmid DNA for AAV production was purified with the NucleoBond Xtra Maxi EF kit (Macherey-Nagel), and AAV-293T cells (Agilent) were co-transfected with pAAV-CAG-NIR-GECO2G or pAAV-CAG-iGECInano plasmid, AAV capsid plasmid pUCmini-iCAP-PHP.eB, and pHelper using polyethyleneimine (PEI; Santa Cruz). Cell medium was collected 72 h after transfection. The cells and the medium were collected 120 h after transfection and combined with the medium collected at 72 h. The cells were harvested by centrifugation and then lysed with a salt-active nuclease (HL-SAN, ArcticZymes). Polyethylene glycol (PEG, 8%) was added to the medium, and the mixture was incubated for 2 h on ice and then pelleted. The PEG pellet was treated with HL-SAN and combined with the lysed cells. The cell suspension was clarified by centrifugation. The supernatant was applied on an iodixanol gradient and subjected to ultracentrifugation for 2 h and 25 min at 350,000 g. The virus fraction was collected, washed, and enriched at an Amicon Ultra-15 100,000 MWCO centrifuge device. The virus titer was determined by qPCR. An aliquot of the virus was treated with DNase I and proteinase K and then used as a template for qPCR. A pAAV-CaMKII–iGECInano plasmid of known concentration that was digested with EcoRI was used as a reference.

Imaging of Primary Dissociated Neurons

Neurons were isolated from the hippocampi of P0–P1 Swiss Webster mice using a published protocol (Beaudoin et al., 2012) and cultured in a Neurobasal Plus medium with B-27 Plus Supplement (Gibco), additional GlutaMAX (1 mM; Gibco), 100 U ml^{-1} penicillin, and 100 μg ml^{-1} streptomycin, on poly (D-lysine) (EMD Millipore)-coated glass coverslips (thickness, 0.13–0.17 mm; diameter, 12 mm; ThermoFisher Scientific) at a density of ~70,000 cells per coverslip. Half of the medium was exchanged twice per week. For experiments with AAVs, neurons were transduced at DIV7 with 10^9 viral genomes (vg) per well (in 24-well plates) and recorded at DIV16–DIV18 at 37°C. The Grass S48 stimulator (Grass Instruments) and custom platinum electrodes (0.5-mm diameter) were used for field stimulation (1 ms single pulses, 50 V). The following synaptic transmission inhibitors were applied: 10 μM CNQX (R&D Systems), 10 μM gabazine (Santa Cruz Biotechnology), 10 μM (R)-CPP (Enzo Life Sciences), and 1 μM (S)-MCPG (Cayman Chemicals). A field stimulation using 1 ms single pulses, 50 V, in the presence of synaptic transmission inhibitors was previously described to generate single APs in cultured neurons (Wardill et al., 2013). A 617 nm light-emitting diode (LED) (Mightex Systems) was used for fluorescence excitation. The excitation filter was 620/15 nm, with a 640LP dichroic mirror, and the emission filter was 667/30 nm for iGECI and iGECInano and 720/40 nm for NIR-GECO2G. The frame rate was 10 Hz for NIR-GECO2G and 5 Hz for iGECI and iGECInano. Fluorescence was recorded using an Orca-Flash4.0 LT camera (Hamamatsu), an Olympus IX81 microscope, and a LUCPlanFLN ×20, 0.45 NA air objective lens (Olympus). Light power density at the specimen plane was 1.4 W cm^{-2} (six-folds lower than in the photobleaching experiments), and the total duration of imaging was less than 0.5 h. The bath solution contained (in mM) 125 NaCl, 2.5 KCl, 1 $MgCl_2$, 10 HEPES, 3 $CaCl_2$, and 30 D-glucose at pH

7.3, 305–307 mOsm. The stimulator, camera, and LEDs were controlled by Master-8 (AMPI) and MatLab R2018b (MathWorks). Each neuronal recording was performed from an individual coverslip. Stimulation evoked changes in the fluorescence were quantified relative to the 10 s baseline before stimulation. Time to the peak was measured as the time between stimulus onset and the peak of the evoked response. Decay time was quantified as the time constant of a fitted single exponential curve. Data analysis was performed using Igor Pro 9 software. A statistical analysis was performed using the Kruskal–Wallis test correcting for the False Discovery Rate. We inform *p* values (q) corrected for multiple comparisons. We used GraphPad Prism v. 9.3.1 software.

DATA AVAILABILITY STATEMENT

The original contributions presented in the study are included in the article; further inquiries can be directed to the corresponding author.

ETHICS STATEMENT

The animal study was reviewed and approved by the Animal Usage Committee of Albert Einstein College of Medicine.

AUTHOR CONTRIBUTIONS

MM developed and characterized the iGECInano *in vitro* and in non-neuronal mammalian cells. JV and KK performed the iGECInano characterization in neurons. LK prepared the neuronal cultures. VV conceived and directed the whole project and, together with MM, designed the experiments, analyzed the data, and wrote the manuscript. All authors reviewed the manuscript.

FUNDING

This work was supported by the grants R35 GM122567 and RF1 NS115581 from the U.S. National Institutes of Health, 226178 from the Chan Zuckerberg Initiative, and 322226 from the Academy of Finland.

ACKNOWLEDGMENTS

We thank Julian Guarque-Chabrera (Albert Einstein College of Medicine, United States) for the assistance with the statistical analysis, Olena Oliinyk (University of Helsinki, Finland) and Daria Shcherbakova (Albert Einstein College of Medicine, United States) for the discussions of the results and manuscript.

REFERENCES

Akerboom, J., Carreras Calderón, N., Tian, L., Wabnig, S., Prigge, M., Tolö, J., et al. (2013). Genetically Encoded Calcium Indicators for Multi-Color Neural Activity Imaging and Combination with Optogenetics. *Front. Mol. Neurosci.* 6, 2. doi:10.3389/fnmol.2013.00002

Beaudoin, G. M. J., 3rd, Lee, S.-H., Singh, D., Yuan, Y., Ng, Y.-G., Reichardt, L. F., et al. (2012). Culturing Pyramidal Neurons from the Early Postnatal Mouse hippocampus and Cortex. *Nat. Protoc.* 7 (9), 1741–1754. doi:10.1038/nprot.2012.099

Boyden, E. S., Zhang, F., Bamberg, E., Nagel, G., and Deisseroth, K. (2005). Millisecond-timescale, Genetically Targeted Optical Control of Neural Activity. *Nat. Neurosci.* 8 (9), 1263–1268. doi:10.1038/nn1525

Broussard, G. J., Liang, R., and Tian, L. (2014). Monitoring Activity in Neural Circuits with Genetically Encoded Indicators. *Front. Mol. Neurosci.* 7, 97. doi:10.3389/fnmol.2014.00097

Challis, R. C., Kumar, S. R., Chan, K. Y., Challis, C., Beadle, K., Jang, M. J., et al. (2019). Publisher Correction: Systemic AAV Vectors for Widespread and Targeted Gene Delivery in Rodents. *Nat. Protoc.* 14 (8), 2597. doi:10.1038/s41596-019-0155-5

Chen, T.-W., Wardill, T. J., Sun, Y., Pulver, S. R., Renninger, S. L., Baohan, A., et al. (2013). Ultrasensitive Fluorescent Proteins for Imaging Neuronal Activity. *Nature* 499 (7458), 295–300. doi:10.1038/nature12354

Dana, H., Sun, Y., Mohar, B., Hulse, B. K., Kerlin, A. M., Hasseman, J. P., et al. (2019). High-performance Calcium Sensors for Imaging Activity in Neuronal Populations and Microcompartments. *Nat. Methods* 16 (7), 649–657. doi:10.1038/s41592-019-0435-6

Dong, J.-Y., Fan, P.-D., and Frizzell, R. A. (1996). Quantitative Analysis of the Packaging Capacity of Recombinant Adeno-Associated Virus. *Hum. Gene Ther.* 7 (17), 2101–2112. doi:10.1089/hum.1996.7.17-2101

Gaffield, M. A., Amat, S. B., Bito, H., and Christie, J. M. (2016). Chronic Imaging of Movement-Related Purkinje Cell Calcium Activity in Awake Behaving Mice. *J. Neurophysiology* 115 (1), 413–422. doi:10.1152/jn.00834.2015

Inoue, M., Takeuchi, A., Horigane, S.-i., Ohkura, M., Gengyo-Ando, K., Fujii, H., et al. (2015). Rational Design of a High-Affinity, Fast, Red Calcium Indicator R-CaMP2. *Nat. Methods* 12 (1), 64–70. doi:10.1038/nmeth.3185

Jennings, J. H., Ung, R. L., Resendez, S. L., Stamatakis, A. M., Taylor, J. G., Huang, J., et al. (2015). Visualizing Hypothalamic Network Dynamics for Appetitive and Consummatory Behaviors. *Cell* 160 (3), 516–527. doi:10.1016/j.cell.2014.12.026

Lin, M. Z., and Schnitzer, M. J. (2016). Genetically Encoded Indicators of Neuronal Activity. *Nat. Neurosci.* 19 (9), 1142–1153. doi:10.1038/nn.4359

Luo, L., Callaway, E. M., and Svoboda, K. (2018). Genetic Dissection of Neural Circuits: A Decade of Progress. *Neuron* 98 (4), 865. doi:10.1016/j.neuron.2018.05.004

Matlashov, M. E., Shcherbakova, D. M., Alvelid, J., Baloban, M., Pennacchietti, F., Shemetov, A. A., et al. (2020). A Set of Monomeric Near-Infrared Fluorescent Proteins for Multicolor Imaging across Scales. *Nat. Commun.* 11 (1), 239. doi:10.1038/s41467-019-13897-6

Oliinyk, O. S., Shemetov, A. A., Pletnev, S., Shcherbakova, D. M., and Verkhusha, V. V. (2019). Smallest Near-Infrared Fluorescent Protein Evolved from Cyanobacteriochrome as Versatile Tag for Spectral Multiplexing. *Nat. Commun.* 10 (1), 279. doi:10.1038/s41467-018-08050-8

Qian, Y., Cosio, D. M. O., Piatkevich, K. D., Aufmkolk, S., Su, W.-C., Celiker, O. T., et al. (2020). Improved Genetically Encoded Near-Infrared Fluorescent Calcium Ion Indicators for *In Vivo* Imaging. *PLoS Biol.* 18 (11), e3000965. doi:10.1371/journal.pbio.3000965

Qian, Y., Piatkevich, K. D., Mc Larney, B., Abdelfattah, A. S., Mehta, S., Murdock, M. H., et al. (2019). A Genetically Encoded Near-Infrared Fluorescent Calcium Ion Indicator. *Nat. Methods* 16 (2), 171–174. doi:10.1038/s41592-018-0294-6

Shcherbakova, D. M., Baloban, M., Emelyanov, A. V., Brenowitz, M., Guo, P., and Verkhusha, V. V. (2016). Bright Monomeric Near-Infrared Fluorescent Proteins as Tags and Biosensors for Multiscale Imaging. *Nat. Commun.* 7, 12405. doi:10.1038/ncomms12405

Shcherbakova, D. M., Cox Cammer, N., Huisman, T. M., Verkhusha, V. V., and Hodgson, L. (2018). Direct Multiplex Imaging and Optogenetics of Rho GTPases Enabled by Near-Infrared FRET. *Nat. Chem. Biol.* 14 (6), 591–600. doi:10.1038/s41589-018-0044-1

Shcherbakova, D. M. (2021). Near-infrared and Far-Red Genetically Encoded Indicators of Neuronal Activity. *J. Neurosci. Methods* 362, 109314. doi:10.1016/j.jneumeth.2021.109314

Shemetov, A. A., Monakhov, M. V., Zhang, Q., Canton-Josh, J. E., Kumar, M., Chen, M., et al. (2021). A Near-Infrared Genetically Encoded Calcium Indicator for *In Vivo* Imaging. *Nat. Biotechnol.* 39 (3), 368–377. doi:10.1038/s41587-020-0710-1

Shu, X., Royant, A., Lin, M. Z., Aguilera, T. A., Lev-Ram, V., Steinbach, P. A., et al. (2009). Mammalian Expression of Infrared Fluorescent Proteins Engineered from a Bacterial Phytochrome. *Science* 324 (5928), 804–807. doi:10.1126/science.1168683

Thestrup, T., Litzlbauer, J., Bartholomäus, I., Mues, M., Russo, L., Dana, H., et al. (2014). Optimized Ratiometric Calcium Sensors for Functional *In Vivo* Imaging of Neurons and T Lymphocytes. *Nat. Methods* 11 (2), 175–182. doi:10.1038/nmeth.2773

Wardill, T. J., Chen, T.-W., Schreiter, E. R., Hasseman, J. P., Tsegaye, G., Fosque, B. F., et al. (2013). A Neuron-Based Screening Platform for Optimizing Genetically-Encoded Calcium Indicators. *PLoS One* 8 (10), e77728. doi:10.1371/journal.pone.0077728

Yu, D., Baird, M. A., Allen, J. R., Howe, E. S., Klassen, M. P., Reade, A., et al. (2015). A Naturally Monomeric Infrared Fluorescent Protein for Protein Labeling *In Vivo*. *Nat. Methods* 12 (8), 763–765. doi:10.1038/nmeth.3447

Zhao, Y., Araki, S., Wu, J., Teramoto, T., Chang, Y.-F., Nakano, M., et al. (2011). An Expanded Palette of Genetically Encoded Ca 2+ Indicators. *Science* 333 (6051), 1888–1891. doi:10.1126/science.1208592

Conflict of Interest: The authors declare that the research was conducted in the absence of any commercial or financial relationships that could be construed as a potential conflict of interest.

Publisher's Note: All claims expressed in this article are solely those of the authors and do not necessarily represent those of their affiliated organizations, or those of the publisher, the editors, and the reviewers. Any product that may be evaluated in this article, or claim that may be made by its manufacturer, is not guaranteed or endorsed by the publisher.

frontiers | Frontiers in Cell and Developmental Biology

ORIGINAL RESEARCH
published: 29 June 2022
doi: 10.3389/fcell.2022.893468

A Bright, Nontoxic, and Non-aggregating red Fluorescent Protein for Long-Term Labeling of Fine Structures in Neurons

Lin Ning[1†], Yang Geng[1,2†], Matthew Lovett-Barron[3‡], Xiaoman Niu[2], Mengying Deng[4], Liang Wang[4], Niloufar Ataie[5], Alex Sens[5], Ho-Leung Ng[5], Shoudeng Chen[6], Karl Deisseroth[3], Michael Z. Lin[1,3] and Jun Chu[4]**

[1]Department of Neurobiology, Stanford University, Stanford, CA, United States, [2]Interdisciplinary Research Center on Biology and Chemistry, Shanghai Institute of Organic Chemistry, Chinese Academy of Sciences, China University of Chinese Academy of Sciences, Beijing, China, [3]Department of Bioengineering, Stanford University, Stanford, CA, United States, [4]Guangdong Provincial Key Laboratory of Biomedical Optical Imaging Technology and Center for Biomedical Optics and Molecular Imaging, and CAS Key Laboratory of Health Informatics, Shenzhen Institute of Advanced Technology, Chinese Academy of Sciences, Shenzhen, China, [5]Department of Biochemistry and Molecular Biophysics, Kansas State University, Manhattan, KS, United States, [6]Guangdong Provincial Key Laboratory of Biomedical Imaging, The Fifth Affiliated Hospital, Sun Yat-sen University, Zhuhai, China

Red fluorescent proteins are useful as morphological markers in neurons, often complementing green fluorescent protein-based probes of neuronal activity. However, commonly used red fluorescent proteins show aggregation and toxicity in neurons or are dim. We report the engineering of a bright red fluorescent protein, Crimson, that enables long-term morphological labeling of neurons without aggregation or toxicity. Crimson is similar to mCherry and mKate2 in fluorescence spectra but is 100 and 28% greater in molecular brightness, respectively. We used a membrane-localized Crimson-CAAX to label thin neurites, dendritic spines and filopodia, enhancing detection of these small structures compared to cytosolic markers.

Keywords: red fluorescent protein, RFP, crimson, non-aggregating, long-term, label, neuron

OPEN ACCESS

Edited by:
Yingxiao Wang, University of California, San Diego, United States

Reviewed by:
Tae-Jin Kim, Pusan National University, South Korea
Benjamin S. Glick, The University of Chicago, United States

****Correspondence:***
Michael Z. Lin
mzlin@stanford.edu
Jun Chu
jun.chu@siat.ac.cn

†These authors have contributed equally to this work

*‡**Present Address:***
Matthew Lovett-Barron, University of California San Diego, La Jolla, CA, United States

Specialty section:
This article was submitted to Signaling, a section of the journal Frontiers in Cell and Developmental Biology

Received: *10 March 2022*
Accepted: *25 April 2022*
Published: *29 June 2022*

Citation:
Ning L, Geng Y, Lovett-Barron M, Niu X, Deng M, Wang L, Ataie N, Sens A, Ng H-L, Chen S, Deisseroth K, Lin MZ and Chu J (2022) A Bright, Nontoxic, and Non-aggregating red Fluorescent Protein for Long-Term Labeling of Fine Structures in Neurons. Front. Cell Dev. Biol. 10:893468. doi: 10.3389/fcell.2022.893468

INTRODUCTION

Fluorescent proteins (FPs) are valuable tools for visualizing cellular processes in living cells. After the cloning of *Aequoria victoria* green fluorescent protein (GFP), a variety of FPs with different wavelengths have been discovered in marine organisms (Day and Davidson, 2009). Red fluorescent proteins (RFPs) (emission peak in the 585–620 nm range) (Cranfill et al., 2016), including commonly used mCherry (Shaner et al., 2004), are particularly useful for 2-color imaging in conjunction with GFP or GFP-based indicators. Even for single-wavelength experiments, RFPs have advantages over GFPs in that their longer excitation wavelengths generate less phototoxicity and autofluorescence, and their longer emission wavelengths are scattered less severely *in vivo*. A variety of RFPs have been developed to improve brightness, maturation, and monomericity, while covering emission wavelengths from the red to the far-red (Shen et al., 2015; Ng and Lin, 2016). Some of these RFPs are even brighter than GFP and perform well when expressed alone or fused to subcellular tags in standard proliferating cell types (Cranfill et al., 2016).

One surprisingly uncommon use of RFPs, however, is in membrane labeling of mammalian neurons. In neurons, synapses are located on dendritic spines, mushroom-shaped membrane

protrusions less than 1 μm^3 in volume on which synapses form. Spines evolve from filopodia during neuronal differentiation, undergo morphological changes in response to neurotransmitter activation and during learning (Holtmaat et al., 2009; Xu et al., 2009), and exhibit abnormalities in number or morphology in several neurological diseases, such as the retention of filopodia-like morphology in Fragile X syndrome (Govek et al., 2004; Woolfrey et al., 2009; Sala and Segal, 2014). Thus, accurate visualization of filopodia spine number and morphology in living neurons over long experimental time-courses would be highly beneficial to the study of synaptic differentiation or pathogenesis. Membrane-targeting of GFP has been shown to improve detection of small neuronal structures (Craske et al., 2005; Han et al., 2011; Zhou et al., 2012; De Rubeis et al., 2013; Michaelsen-Preusse et al., 2016). However, due to the lower phototoxicity and autofluorescence at their excitation wavelengths, membrane-targeted RFPs would be useful as well. We and others have used mCherry-CAAX to label the neuronal membrane in transient transfection experiments (St-Pierre et al., 2014; Feng et al., 2019), but whether alternative RFPs may be brighter or exhibit less toxicity has not been explored.

In this study, we develop a bright, non-toxic RFP named Crimson with excitation and emission spectra similar to mCherry (Shaner et al., 2004). Crimson shows comparable maturation speed and higher molecular brightness compared to mCherry. Comparing the brightness and toxicity of Crimson to two RFPs [FusionRed (Shemiakina et al., 2012) and mCherry] and one far-red FP [mKate2 (Pletnev et al., 2008)] with excitation peak ranging from 580 to 590 nm, we found Crimson was both brightest and least toxic in both cytosolic and membrane-targeted forms. Moreover, Crimson did not exhibit lysosomal accumulations, as was observed in mCherry (Laviv et al., 2016) and mCherry-derived mScarlet (Fenno et al., 2020). Finally, we found that Crimson-CAAX enhanced detection of filopodia and spines compared to cytosolic fluorescent proteins.

MATERIALS AND METHODS

Mutagenesis and screening of libraries. Crimson is engineered from mNeptune2 by rational mutagenesis. Mutations at specific residues were introduced by overlap-extension PCR. All PCR products were cut and ligated into a constitutive bacterial expression vector pNCS (Allele Biotech). To easily screen bright Crimson variants, Clover-Crimson tandem fusions with high intramolecular FRET efficiency were constructed. Chemically competent *Escherichia coli* strain XL-10 Gold (Invitrogen) were transformed and grown overnight on LB/agar at 34°C and maintained thereafter at room temperature for ~6 h. For each round of mutagenesis, a number of colonies approximately tenfold higher than the expected library diversity were screened to ensure full coverage. Agar plates were screened for transmitted color by eye and for fluorescence in a BlueView Transilluminator (Vernier) with 400- to 500-nm excitation light and a yellow acrylic long-pass filter. Bacterial colonies of interest were patched on LB/agar plates and incubated overnight at 34°C. Bacteria were resuspended in PBS or lysates were extracted with B-PER II (Pierce), and FRET spectra were obtained on a Safire II plate reader (Tecan). DNA sequences of all constructs are available upon request.

Characterization of Crimson *in vitro*. Fluorescent proteins with polyhistidine tags were expressed from pNCS vectors in XL-10 gold bacterial cells, purified with cobalt-chelating affinity chromatography (Pierce) and desalted into phosphate-buffered saline (PBS) pH 7.2 using gel filtration columns (Bio-Rad). Excitation spectra and emission spectra were measured with an Infinite M1000 fluorometer (Tecan). Extinction coefficients were calculated using the base-denaturation method (Shaner et al., 2004). Quantum yields were determined using mKate2 as a standard (QY = 0.40). pH titrations were performed using a series of pH buffers ranging from 2 to 10.5 (Citrate-Tris-Glycine buffer, 50 mM each. The desired pH was achieved by adding 2 M sodium hydroxide or 2 M hydrochloric acid). *In vitro* photobleaching measurements were performed in PBS droplets under mineral oil on an IX83 inverted microscope with a 40 × /1.25-numerical aperture (NA) oil-immersion objective, a 100-W metal halide lamp (Olympus) at 100% neutral density, a 580/15-nm excitation filter (Omega), and an optiMOS Scientific CMOS camera (Qimaging) controlled by Micro-Manager software. Images were acquired every 1 s under continuous illumination. Times were scaled to produce photon output rates of 1,000 per molecule per s as previously described (Shaner et al., 2004). Maturation experiments were performed by measuring change in fluorescence following exposure of Crimson-expressing *E. coli* grown in deoxygenated media to normal atmosphere. Size exclusion chromatography (SEC) was performed on a LC-20A (SHIMADZU) high-pressure liquid chromatography (HPLC) system with a Superdex 200 10/300 GL column (GE Bioscience). 200 µL of each fluorescent protein at concentration 10 µM or 333 µM (~10 mg/mL) were loaded. The column was operated at the flow rate of 0.5 mL/min with 50 mM PBS (pH 7) as the mobile phase. *In vitro* photobleaching measurements were performed in aqueous droplets of purified proteins in mineral oil using an Olympus IX83 inverted microscope with a 40 × /1.25-numerical aperture (NA) silicone oil-immersion objective (Olympus), an X-cite 120-W metal halide lamp (Lumen Dynamics) and a 568/20 nm excitation filter (Omega). The illumination power at the objective was 20 mW. Images were taken every 1 s under continuous illumination. Times were adjusted to produce photon output rates of 1,000 per molecule per second as described previously.

Characterization of RhoA FRET sensors with green/red FRET pairs. To construct RhoA-GR, three PCR fragments encoding truncated dClover2 (aa 1–217, Clover-N149Y/G160S), RhoA sensing domains from Raichu-RhoA FRET sensors and full-length RFP (mRuby3 or Crimson) were ligated into modified pcDNA3.1 vector using In-Fusion kit. HeLa cells were maintained in high glucose Dulbecco's Modified Eagle Medium (DMEMClone) supplemented with 10% FBS (Invitrogen) and 1% penicillin-streptomycin (HyClone) at 37°C in air with 5% CO_2. Cells were transfected at 80–90% confluency with Lipofectamine 2000 (Invitrogen) in 35 mm

dishes. Transfections were carried out according to manufacturer's instructions.

To determine the green/red emission ratio change of RhoA-GR with dClover2-mRuby3 or dClover2-Crismon, transfected cells expressing RhoA-GR were trypsinized and transferred to 96-well glass-bottom microplate (Cellvis) after 48 h transfection. Cells were allowed to settle down to the bottom of a microplate for 10 min at room temperature. Fluorescence spectra on transfected cells were obtained on an Infinite M1000 PRO (TECAN) fluorometer using 450-nm excitation light with 10-nm bandwidth. Emission was collected from 470 to 750 nm in 2-nm steps with 10-nm bandwidth. The red/green emission ratio was calculated from integrated red emission (mRuby3: 560–750 nm, Crimson: 580–750 nm) divided by integrated green emission (500–550 nm).

Constructs for neuron imaging. For pcDNA3.1-RFP cyto plasmids, each RFP expression cassette was amplified by PCR from parent template, and then cloned into pcDNA3.1 empty vector by infusion cloning method. For pcDNA3.1-RFP-CAAX plasmids, CAAX sequence was synthesized as part of In-Fusion cloning primer and subsequent cloning steps were performed as described in In-Fusion kit (Takara Bio, # 639650). In order to have the expression of two-color FPs in neurons at 1:1 ratio, we utilized a bi-directional plasmid, which was created in the lab earlier. In this special expression construct, A CMV enhancer region is flanked bi-directionally by a miniCMV promoter and a CAGGs promoter; either direction can drive the expression of one target protein independently. Crimson-CAAX and mTurquoise2 were then cloned into this plasmid by In-Fusion cloning method with mTurquoise2 driven by the β-actin promoter and RFP-CAAX driven by the mini-β-actin promoter. For zebrafish expression, we fused mTurquoise2 with Crimson-CAAX with a P2A peptide in between, and then subcloned the fused sequence into a Tol2 plasmid.

Neuron cell culture. All cell culture reagents were obtained from Life Technologies unless otherwise specified. 24-well glass-bottom cell culture plates were pre-coated with poly-D-lysine (0.2 mg/ml, Sigma) for 2 h at 37°C and washed with PBS. Hippocampal neurons were dissected from embryonic day 18 (E18) rats, dissociated with papain and DNaseI, and then plated at a density of 30,000 per cm^2 in Neurobasal medium supplemented with B27, 2 mM GlutaMAX, 1% FBS. Cultures were maintained at 37°C in 5% carbon dioxide (CO_2) and 100% humidity. Entire medium was replaced on 1DIV and refreshed 50% once on 8DIV. Neurons were transfected on 9DIV using Lipofectamine 2000 transfection kit (Clontech) following the manufacture's instruction. 0.5 μg DNA was used for each well of neurons in a 24-well plate. All animal procedures were approved by the Institutional Animal Care and Use Committee at Stanford University and Chinese Academy of Sciences, Shanghai.

Characterization of Crimson in neurons. Live cell photobleaching was performed on neurons using an inverted wide-field microscope (Zeiss, Axiovert 200). Prior to the experiment, culture medium was replaced with imaging solution (HBSS + Hepes + L-glutamate). Cells were placed in a temperature chamber heated up to 37 C with 5% CO_2, and continuously excited using Xenon Arc lamp filtered at 568/20 nm with a 20 ×0.75 NA objective lens, and images were detected with an emission filter at 620/60 nm. Time-series images were acquired every 10 s for each variant until the initial intensity was decreased by at least 40%.

Hippocampal neurons were transfected on 9 DIV and imaged on 12 DIV for brightness and aggregation measurements, and 18 DIV (cytosolic RFP-transfected neurons) or 15 DIV (membrane-bound RFP-transfected neurons) for viability measurements.

For brightness measurements, RFPs were imaged with a confocal scanning microscope (Leica, SP8), with a 585-nm laser whose power was set to a fixed level that captured all signals without saturation. At multiple positions, stacks of 40 sections with 0.5-μm spacing were acquired and then z-projected to create maximal intensity images. For cytosolic RFPs, 6 to 10 fields were imaged as technical replicates and a single mean intensity per cell area was calculated, and the experiment was repeated 3 times. For RFP-CAAX fusions, 5 to 8 fields were imaged as technical replicates and a single mean intensity per cell area was calculated, and the experiment was repeated 3 times. For viability measurements, a 10 × 10 grid of images was captured with a 10× lens to cover the inscribed square area of one well on a 24-well glass-bottom cell culture plate, and the experiment was repeated 3 times.

Image analysis. For brightness analysis, background was subtracted from each image. To quantify the brightness of RFPs in the whole cell, ImageJ was used to create a mask representing the contour of neurons with a threshold showing the majority of neurites, and the region of interest (ROI) was generated from the mask. The same criteria were applied to all images. The mean grey value within the ROI was then measured and divided by the ROI area to calculate brightness per cell area. For viability counting, neurons were assessed in a blinded manner.

Toxicity counting. The percentage of healthy neurons versus the total amount of transfected neurons was quantified to evaluate toxicity. Healthy neurons were defined as those with normal neuronal morphology lacking broken neurites or blebbing. Unhealthy neurons were defined as those with round cell bodies but broken neurites or blebbing. Dead neurons were defined as those with irregular or fragmented cell bodies and extensively fragmented neurites (Keskitalo et al., 2014; Zhang et al., 2014). Only transfected neurons were quantified to minimize the bias of transfection efficiency between different constructs.

Statistical analysis. Each biological replicate produced one data point per condition. The normality of data was confirmed using the Wilk-Shapiro test, then a single-factor ANOVA test was performed, with pairwise differences between Crimson and each other RFP assessed using the Dunnett post-hoc test.

Comparison of Crimson-CAAX and cytosolic mTurquoise2. For 1-photon imaging, cultured rat hippocampal neurons were transfected with a bi-directional vector co-expressing Crimson-CAAX and mTurquoise2 at 9DIV and imaged at 14–15DIV using either an epifluorescence microscope (Zeiss, Axiovert 200) with excitation at 440/10 nm and 568/20 nm and emission at 472/30 nm and 620/60 nm or using a confocal microscope (Leica,

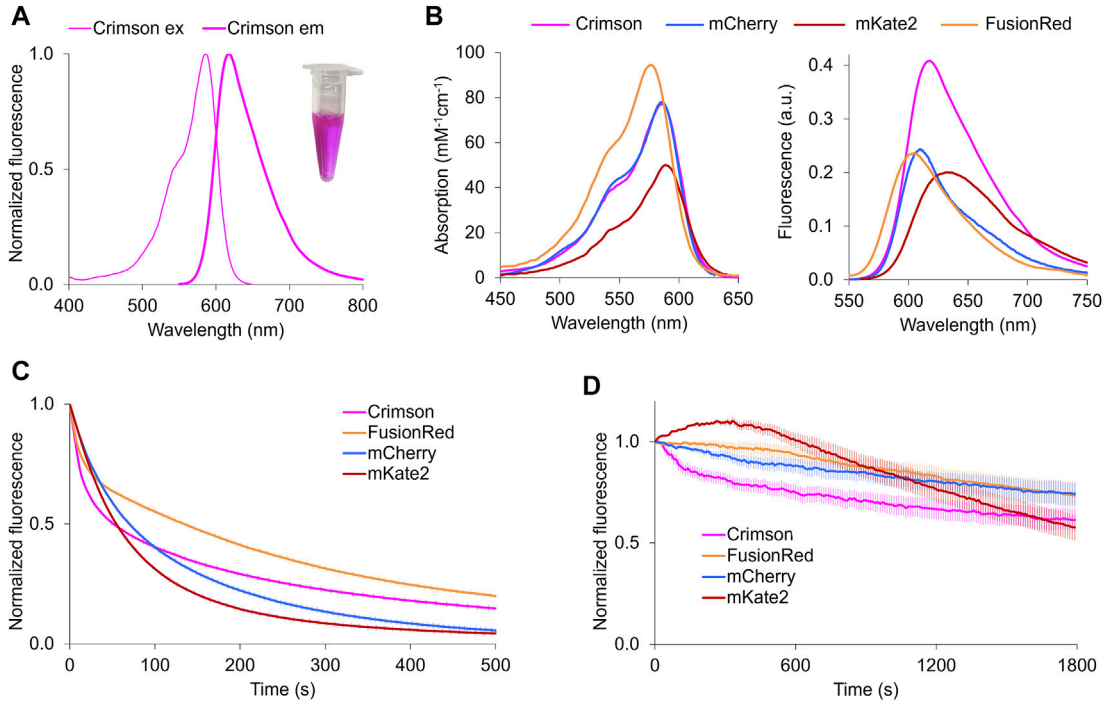

FIGURE 1 | Characterization of Crimson *in vitro* and neurons. **(A)** Fluorescence spectra of Crimson. Inset, purified Crimson in visible light. **(B)** Absorption (left) and emission (right) of RFPs with excitation maxima at 580–590 nm. Absorbance spectra are scaled to peak extinction coefficient. Emission spectra are scaled so that areas under the curves are proportional to peak brightness (product of peak extinction coefficient and quantum yield). **(C)** Photobleaching kinetics of purified RFPs under arc lamp illumination with a 568/20-nm excitation filter. Time is scaled so that emission is normalized to 1000 photons per s. Imaging interval = 1 s. Each curve is the mean of two independent experiments with the error bars denoting SD (standard deviation, $n \geq 6$). **(D)** Photobleaching of RFPs in transfected neurons under 585-nm laser illumination. Fluorescent intensity of each time frame is subtracted against the background and normalized to time point 0. Imaging interval = 10 s. Each curve is the mean with the error bars denoting SD ($n = 3$).

SP8) with excitation at 440 and 585 nm and emission at 450–510 nm and 595–675 nm. For 2-photon imaging, a Tol2 vector co-expressing mTurquoise2 and Crimson-CAAX was injected into the zebrafish embryos at 1-cell stage. Larval zebrafish with identifiable fluorescence at 7 days post-fertilization were paralyzed in 1 µm/µL α-bungarotoxin (Tocris) and mounted on their side in 2% low-melting-point agarose (Sigma). Two-photon fluorescence images (1024 × 1024 pixels) were obtained with an Olympus FVMPE multiphoton laser scanning microscope (Olympus), and a 25× objective (1.05 NA; Olympus) at 3×-18× optical zoom, 8–12.5 µs/pixel dwell times, and 3-5 frame averages. Fluorophores were excited at 1030 nm and emission was detected simultaneously with red and green channels.

Crystallization and structure solution of Crimson0.9. Prior to crystallization, hexahistidine-Crimson0.9 was purified using size-exclusion chromatography to remove aggregation. Thereafter, Crimson0.9 was buffer-exchanged with 50 mM Tris (hydroxymethyl) aminomethane, 25 mM NaCl, 4.0 mM TCEP at pH 7.4, and concentrated to 10 mg/ml for crystallization. Crimson0.9 was crystallized at 12°C in a dark chamber by sitting-drop vapor diffusion using 1 µL of 10 mg/ml Crimson0.9 in 50 mM Tris Base, 25 mM NaCl, 4.0 mM TCEP pH 7.4 mixed with 1 µL of 0.2 M $MgCl_2$, 0.1 M Bis-Tris HCl pH 6.5, and 25% PEG 3350 and 1 µL of 1 M glycerol. Crimson0.9 crystals were cryoprotected in paratone oil and flash-frozen in liquid nitrogen. X-ray diffraction data were collected at the Stanford Synchrotron Radiation Laboratory on Beamline 12–2. The crystal structure was solved by molecular replacement using Phaser as part of the CCP4 suite55. Models of Crimson0.9 and the fluorophore were built with the Coot program. Refinement to 2.04 Å was performed in the REFMAC5 program with model rebuilding in Coot. Water molecules were manually added by inspection throughout the refinement process. The final model is composed of xx water molecules and all residues except residues 1–4 and 233–244 of chain A, 1–6 and 233–244 of chain B, 1–6 and 232–244 of chain C, 1–7 and 232–244 of chain D, as these did not show interpretable electron density. The quality of the model was then analyzed using the programs MolProbity and PROCHECK. The coordinates and reflections are deposited in the PDB with accession code 6MKP.

RESULTS

Development of a Bright red Fluorescent Protein

To obtain a bright RFP with similar excitation and emission spectra with mCherry, we performed structure-directed mutagenesis of mNeptune2, a bright and fast-maturing far-red

TABLE 1 | Key characteristics of red fluorescent proteins with excitation peak at 580–590 nm.

	Crimson	mCherry	mKate2	FusionRed
Ex peak (nm)	588	587	588	580
Em peak (nm)	617	610	633	608
EC ($mM^{-1}cm^{-1}$)	77	72	63	95
QY	0.42	0.22	0.4	0.19
Brightness[a]	32	16	25	18
Photostability (s)[b]	49	68	58	131
Maturation half-time (min)[c]	14	15	< 20	130
Maturation efficiency[d]	50%	44%	49%	24%
pKa	4.2	< 4.5	5.4	4.6
Oligomerization	dimer	monomer	dimer	monomer

[a]*Calculated as the product of QY at peak excitation and EC in units of mM^{-1} cm^{-1}.*
[b]*Predicted time for fluorescence to photobleach by 50% under arc-lamp illumination with excitation intensity adjusted to produce 1,000 emission photons per molecule per second.*
[c]*Time for fluorescence to obtain half-maximal value after exposure to oxygen.*
[d]*Functional chromophore concentration divided by total protein concentration. Functional chromophore is determined using the base-denaturation method as EC measurement. This excludes unfolded and broken-chromophore (backbone cleavage before the first residue of chromophore) components. Total protein is determined by absorbance at 280 nm.*

fluorescent protein (Chu et al., 2014). We first performed mutagenesis on positions 11, 13, 28, and 41 to optimize the hydrogen bond interaction with the chromophore acylimine oxygen. After screening, a blue-shifted variant was obtained with best performance which carried three-point mutations at position 11, 28, and 41 (mNeptune2-M11S/S28H/G41N), while position 13 remained the same as the parent. We then introduced mutations into the outer barrel, the inner barrel and the loop respectively, in order to further blue-shift fluorescence spectra and optimize folding, maturation, photostability and brightness (**Supplementary Figure S1** and **Supplementary Table S1**). After several rounds of screening, we obtained a bright RFP with peak excitation/emission at 588/617 nm (**Figure 1A**). This protein, named Crimson, differs from mNeptune2 by 33 mutations (13 inside the barrel) and 3 deletions (**Supplementary Figure S1**). Of these, 9 mutations mainly account for the spectral characteristics of Crimson (**Supplementary Figure S2**).

Crimson's extinction coefficient (EC) of 77 $mM^{-1}cm^{-1}$ and quantum yield (QY) of 0.42 makes it ~100% brighter than mCherry and FusionRed and 28% brighter than mKate2 per mature molecule (**Table 1**). Crimson's absorption spectrum is similar to that of mCherry and mKate2, while its emission peak lies between those of mCherry and mKate2 (**Figure 1B**). Both absorption and emission spectra are redder for Crimson than for FusionRed (**Figure 1B**). Crimson exhibits reduced formation of a green fluorescent side-product common to eqFP578-derived RFPs (**Supplementary Figure S3A**), and is more pH-resistant than mKate2 (**Supplementary Figure S3B**, **Table 1**). Crimson exhibited bi-exponential fluorescence decay under one-photon widefield microscopy *in vitro*, with a faster initial drop to 50% brightness but slower subsequent photobleaching compared to mCherry, mKate2, and FusionRed (**Figure 1C**). Under laser illumination of cells expressing each RFP, Crimson again exhibited a fast initial drop, followed by photobleaching at a rate similar to mCherry and slower than mKate2 and FusionRed (**Figure 1D**). Similar to mKate2, Crimson is dimeric at 10 μM (**Supplementary Figure S3C**), consistent with minimal change to the dimeric interface during the evolution of these proteins from TagRFP. Crimson exhibited maturation speed and efficiency at 37°C comparable to mCherry and mKate2 and superior to FusionRed (**Table 1**).

Crimson's high EC, high QY, and large emission separation from GFPs may make it a good Förster resonance energy transfer (FRET) acceptor for GFPs, especially when detecting FRET using sensitized emission (Bajar et al., 2016b). We thus assessed the performance of Crimson as a FRET acceptor compared to other RFPs including mRuby3 (Bajar et al., 2016a) and mScarlet-I (Bindels et al., 2017), two bright and blue-shifted monomeric RFPs. Indeed when fused to the bright GFP dClover2 (Bajar et al., 2016a), Crimson produced more efficient FRET than all tested RFPs and a higher RFP/GFP peak emission ratio than mCherry, mKate2, or FusionRed (**Supplementary Figure S4**). Incidentally, dClover2-mRuby3, dClover2-mScarlet-I, and dClover2-FusionRed would be predicted to exhibit more efficient FRET based on their longer Förster radii (r_0) calculated from spectral characteristics of mature proteins, so the higher FRET efficiency of dClover2-Crimson also suggests superior maturation of Crimson. In mammalian cells, a Raichu RhoA reporter using dClover2-Crimson as the FRET pair demonstrated a larger emission ratio change upon activation than the one using dClover2-mRuby3 (**Supplementary Figure S4**). These results indicate that Crimson functions well as a FRET acceptor for GFPs. However, since Crimson is dimeric, it is not suitable for FRET applications involving fusion of Crimson to a cellular protein, such as protein-protein interaction and protein conformational changes, because this forced dimer may interfere with function or location of protein of interest.

Structural Basis of Spectral Tuning in Crimson

To understand the mechanism of spectral tuning in Crimson, we determined the atomic structure of a spectrally identical evolutionary predecessor, Crimson0.9, at a resolution of 2.0 Å at pH 6.7–6.8 (**Supplementary Table S2**). The crystallographic unit of Crimson0.9 contains four monomers with two parallel and two cross-dimerization interfaces. The positions of the chromophore and nearby amino acid side chains were similar in the four monomers (**Supplementary Figure S5**). As expected, each monomer has a typical eleven-stranded β-barrel structure with a central α-helix containing the covalently attached chromophore in the *cis* conformation (**Figure 2**, **Supplementary Figure S5**).

The Crimson0.9 structure reveals both similarities to and differences from the parental protein Neptune. Crimson0.9 retains the more planar chromophore conformation of Neptune relative to mKate, which may contribute to its higher extinction coefficient and quantum yield relative to mKate (**Figure 2A**). The primary structural change from the parental Neptune to Crimson0.9 is the loss of a hydrogen bond to the chromophore acylimine oxygen. In Neptune, this

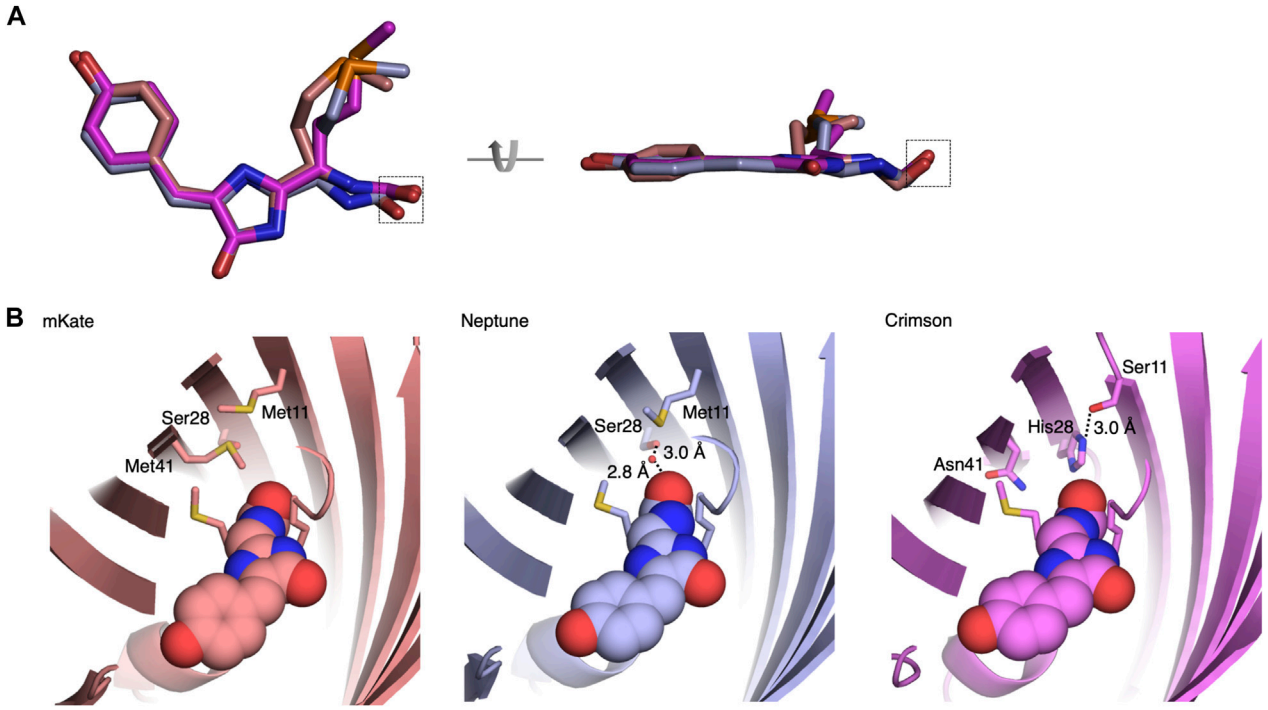

FIGURE 2 | Structural basis of blue-shifting for Asn41, His28, and Ser11 in Crimson. **(A)** Alignment of Crimson (magenta), Neptune (PDB entry 3IP2, light blue) and mKate (PDB entry 3BXC, pink) chromophores. The chromophore rings are more coplanar in Crimson or Neptune than in mKate. The chromophore acylimine oxygen is indicated by the dashed box. **(B)** Hydrogen-bond interactions between the chromophore acylimine oxygen and its surrounding residues in Crimson, mKate and Neptune. In mKate, the acylimine oxygen does not engage in any hydrogen bond interactions. In Neptune, a water molecule donates a hydrogen bond to the acylimine oxygen and accepts a hydrogen bond from Ser-28. In Crimson, a hydrogen bond between Ser-11 and His-28 precludes one between His-28 and the acylimine oxygen. In addition, the side chain of Asn-41 is too short to hydrogen bond to the acylimine oxygen.

hydrogen bond is responsible for the excitation and emission red-shift relative to its predecessor mKate (Lin et al., 2009). Gly-41 of Neptune, whose lack of a side chain allows room for the water molecule, is mutated in Crimson0.9 to Asn-41. In mCardinal (Chu et al., 2014), a redder Neptune variant, Gln-41 serves as a hydrogen bond donor for the acylimine oxygen, but the side chain of Asn-41 of Crimson0.9 is too short to perform a similar function (**Figure 2B**). In addition, Ser-28, which assists in holding the water molecule in place in Neptune, is replaced with the larger His-28 in Crimson0.9, occluding water from the chromophore acylimine vicinity (**Figure 2B**). The electron density of His-28 in the Crimson0.9 crystal is consistent with two rotamers with different and mutually exclusive hydrogen-bonding patterns: in one, the Nε atom donates a hydrogen bond to the chromophore and the Nδ atom lacks hydrogen bond partners, while in the other, the Nε is hydrogen-bonded to Ser-11 and Nδ lacks hydrogen bond partners (**Figure 2B**). However, the electron density of Ser-11 indicates that its hydroxyl group is oriented toward His-28 despite not being hindered from adopting alternative conformations; this suggests that His-28 indeed is engaged in a hydrogen bond with only Ser-11.

Finally, His-28 is unlikely to exert any electrostatic influence on chromophore electronic distributions, as it is predicted to be uncharged at physiological pH by the PROPKA3.0 program. Thus, the acylimine group of Crimson both lacks hydrogen bonding and exists within a neutral environment. These features are shared between Crimson and mKate (**Figure 2**), and would be consistent with the similarity of their spectra (**Figure 1**). Thus, the M11S, S28H, and G41N mutations acquired in the evolution of Crimson from Neptune essentially undo the red-shifting effect of the M41G mutation acquired in the evolution of Neptune from mKate, while allowing for higher molecular brightness.

Comparison of Cytosolic Red Fluorescent Proteins for Brightness, Aggregation, and Toxicity in Neurons

As improved RFPs are especially needed in neuronal applications, we compared the performance of Crimson and other RFPs in cultured primary hippocampal neurons. While measurements of extinction coefficient and quantum yield on purified proteins *in vitro* allow an objective measurement of per-molecule brightness of mature fluorescent protein, apparent brightness of fluorescent protein constructs in cells is also influenced by the

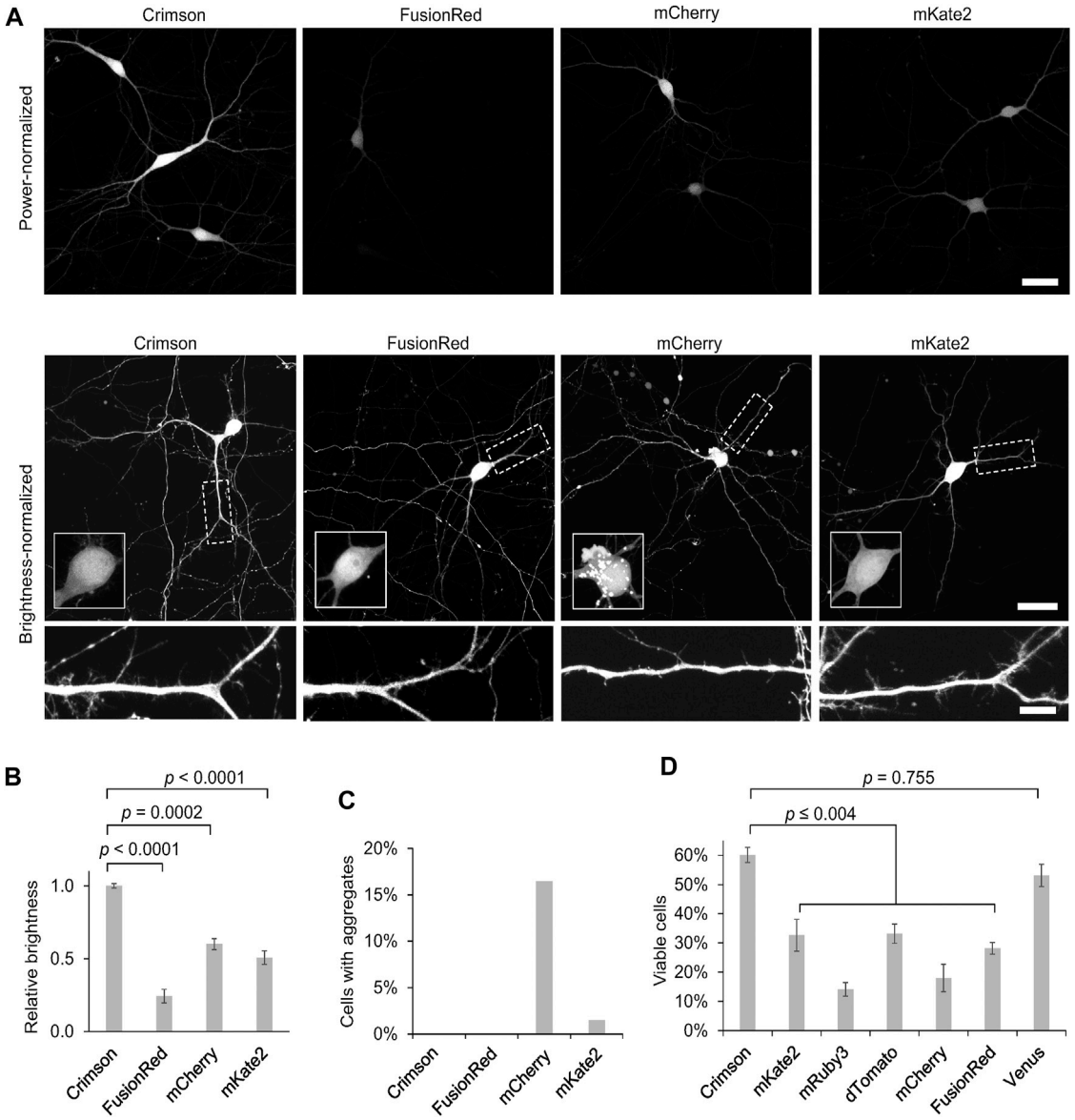

FIGURE 3 | Cytosolic Crimson is brighter and less cytotoxic than other RFPs in neurons. **(A)** Comparison of RFPs in rat hippocampal neurons imaged with confocal microscopy 3 days post-transfection at 12 DIV. Top, representative images of transfected neurons acquired and displayed with identical settings are shown. Scale bar = 20 μm. Bottom, representative images with brightness adjusted to similar levels for display. Cell bodies are enlarged in the insets within the upper panels. Dendritic segments indicated by the dashed rectangle are enlarged in the lower panels. Scale bar = 5 μm. **(B)** Quantification of RFP brightness 3 days post-transfection at 12 DIV. Error bars = SEM (Standard Error of the Mean). Overall $p < 0.0001$ by one-factor ANOVA. **(C)** Quantification of the percentage of neurons with aggregates among total transfected neurons 3 days post-transfection at 12 DIV. **(D)** Quantification of the percentage of healthy neurons among total transfected neurons 9 days post-transfection at 18 DIV. Error bars = SEM. Overall $p < 0.0001$ by one-factor ANOVA.

efficiency of protein maturation and folding, the half-life of the protein and even cell types may cause variations; thus such characteristics should be empirically tested. We thus expressed Crimson, FusionRed, mCherry, and mKate2 in 9 days *in vitro* (DIV) cultured rat hippocampal neurons. After 3 days of expression (12 DIV), Crimson was significantly brighter than the other RFPs when imaged under the same conditions (**Figure 3A**), with a whole-cell-brightness 4.3-, 1.6-, and 2-fold of that of FusionRed, mCherry, and mKate2, respectively (**Figure 3B**).

We noticed large aggregates in the cell bodies of mCherry-transfected neurons (**Figure 3A**, **Figure 3C**). As protein aggregates could lead to neuronal death after long-term expression, we next measured the ability of neurons to survive over time when expressing various fluorescent proteins. In addition to the above RFPs, we also tested the

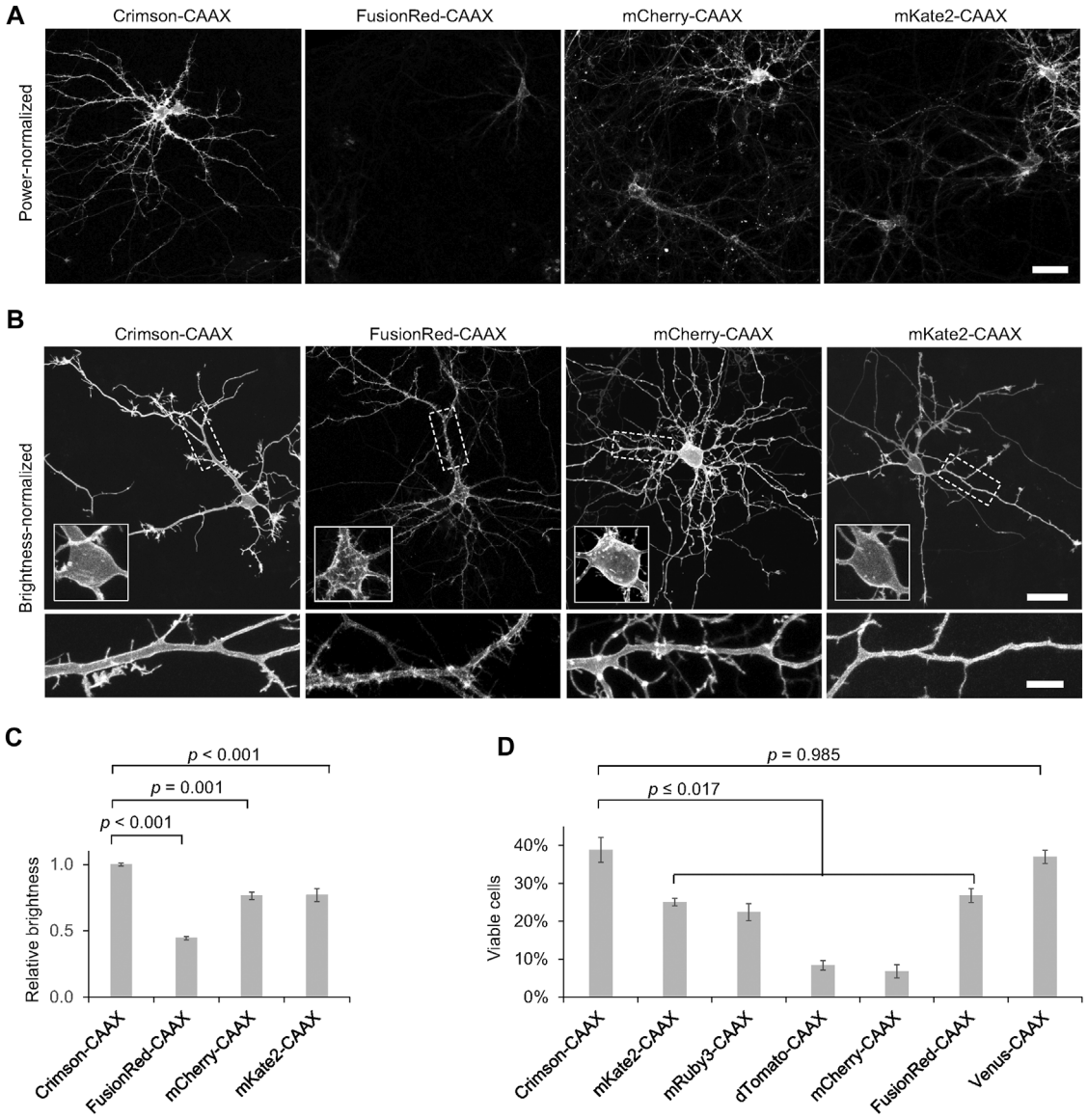

FIGURE 4 | Crimson-CAAX labels the cytoplasmic membrane well in neurons. **(A)** Brightness comparison of RFP-CAAX fusions in rat hippocampal neurons 3 days post-transfection at 12 DIV. Representative confocal images of transfected neurons acquired and displayed with identical settings are shown. Scale bar = 20 μm. **(B)** RFP-CAAX fusions visualized with confocal microscopy 3 days post-transfection at 12 DIV, with image brightness adjusted to similar levels for display. Cell bodies are enlarged in the insets within the upper panels. Dendritic segments indicated by the dashed rectangle are enlarged in the lower panels. Scale bar = 20 μm (upper panels) or 5 μm (lower panels). **(C)** Quantification of brightness of RFP-CAAX constructs 3 days post-transfection at 12 DIV. Error bars = SEM. Overall $p < 0.001$ by one-factor ANOVA. **(D)** Quantification of the percentage of healthy neurons among total transfected neurons 6 days post-transfection at 15 DIV. Crimson-CAAX-expressing neurons demonstrated the highest viability. Error bars = SEM. Overall $p < 0.0001$ by one-factor ANOVA.

effects of chronic expression of mRuby3, dTomato, and the YFP Venus. We added mRuby3 to test a monomeric RFP with higher brightness than mCherry, dTomato to determine if expression of a strongly dimeric RFP might actually be the least toxic by reducing the concentration of free monomers with an unbound dimerization interface, and Venus as a widely used derivative of *Aequoria victoria* GFP. After 9 days of expression (at 18 DIV), Crimson-expressing neurons demonstrated significantly higher survival rates than neurons expressing the other RFPs, and similar survival rates as neurons expressing low-toxicity Venus (**Figure 3D**). Interestingly, dTomato was as toxic as mKate2 and more toxic than Crimson, suggesting that strong dimer affinity is not the main mechanism for the reduced toxicity of Crimson. On the other hand, the strong monomers mCherry and FusionRed also were more toxic than Crimson, suggesting that monomerization alone is also not correlated with survival. Regardless, Crimson performs better than the spectrally

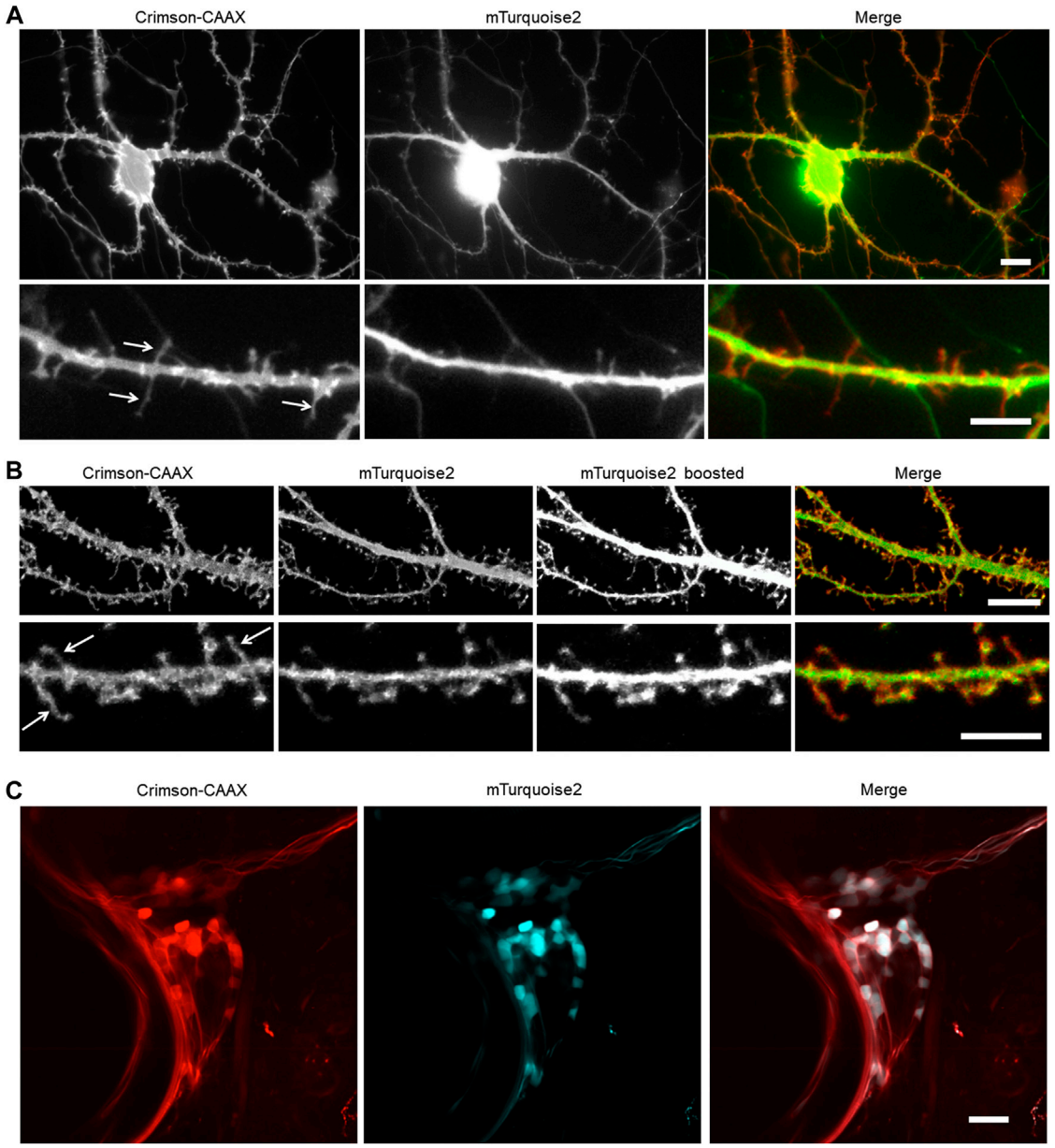

FIGURE 5 | Membrane-bound Crimson improves the detection of small processes. **(A,B)** Visualization of cultured rat hippocampal neurons with an epifluorescent microscope **(A)** and a confocal microscope **(B)**. Neurons were co-transfected with cytosolic mTurquoise2 and Crimson-CAAX at 9 DIV and imaged at 14 DIV. Lower panels show dendrites from the same culture at higher magnification. Arrows indicate thin spines and filopodia visible with Crimson-CAAX but not with cytosolic mTurquoise2. Scale bars = 10 μm (upper panels) and 5 μm (lower panels). **(C)** Visualization of zebrafish trigeminal ganglion by two-photon microscopy *in vivo*. Zebrafish was injected with DNA at one-cell stage and imaged at 7-day post-fertilization. Scale bar = 20 μm.

similar mCherry, mKate2, and FusionRed fully visualizing the dendritic processes of neurons with improved brightness and reduced toxicity.

Comparison of Membrane-Tethered Red Fluorescent Proteins in Neurons

To determine the utility of RFPs for labeling the neuronal plasma membrane, we transfected neurons with a series of RFP fusions to the CAAX farnesylation motif and quantified the brightness of each RFP-CAAX reporter. We observed that Crimson-CAAX was significantly brighter than mKate2-CAAX, mCherry-CAAX, or FusionRed-CAAX (**Figures 4A,C**). We then adjusted excitation power to equalize brightness across RFPs to visualize fluorescence distributions within neurons. While mKate2-CAAX, FusionRed-CAAX and Crimson-CAAX distributed along the plasma membrane and evenly labelled neurites and dendritic spines, mCherry-CAAX accumulated in aggregates within dendritic shafts (**Figure 4B**).

We then assessed the viability of neurons expressing the same set of RFPs previously tested for toxicity, but now fused to the CAAX motif. Crimson-CAAX exhibited significantly higher survival rates than neurons expressing the other RFP-CAAX fusions, and similar survival rates as neurons expressing a Venus-CAAX fusion (**Figure 4D**). Neurons expressing dTomato-CAAX and mCherry-CAAX showed the least viability. Strikingly, dTomato-CAAX created dramatic rod-like structures in neurons (**Supplementary Figure S6**). This suggests that dTomato may contain an interface capable of polymerization once dTomato is concentrated and oriented at the membrane by farnesylation.

Crimson-CAAX in Imaging Dendritic Spines *Ex Vivo* and *in vivo*

We hypothesized that Crimson-CAAX would allow more sensitive detection of small membrane structures such as filopodia and spines than a cytosolic fluorescent protein, due to the low amount of cytosol in these small structures. To compare Crimson-CAAX with a cytosolic fill FP, we co-expressed Crimson-CAAX with cytosolic mTurquoise2 in primary hippocampal neurons. In standard wide-field epifluorescence microscopy, Crimson-CAAX distributed evenly in soma and the neuronal processes, and clearly labeled thin dendritic processes (**Figure 5A**). In contrast, cytosolic mTurquoise2 was mostly detected in the soma and the proximal portions of the dendrites and did not label the thinner dendritic processes as clearly (**Figure 5A**, upper panels). At high magnification, Crimson-CAAX could be seen along the membrane of spines and filopodia, with similar brightness per membrane length compared to nearby dendritic membranes. In contrast, cytosolic mTurqouise2 produced signals that were orders of magnitude dimmer in spines than in adjacent dendritic shafts, causing scatter from dendritic shafts to reduce the signal-to-background ratio for detection of spines and filopodia (**Figure 5A**, lower panels).

Crimson-CAAX also performed better than mTurquoise2 in labeling thin structures in optical-sectioning microscopy. In confocal microscopy, filopodia and spines became visible in the cytosolic mTurquoise2 channel only when the brightness was boosted and part of the dendrite shafts became overexposed, whereas filopodia, spines, and dendritic shafts could be visualized with similar intensities in the Crimson-CAAX channel (**Figure 5B**). We also tested Crimson-CAAX versus cytosolic mTurquoise2 in the neurons of living zebrafish under two-photon illumination. Zebrafish dendrites are small in diameter, measuring <3 μm at their widest point, compared to 5–10 μm of mammalian neurons. In the trigeminal ganglion and developing spinal cord, cytosolic mTurquoise2 was only visible in a small fraction of Crimson-positive neurites, even when using laser and detector settings that produced more mTurquoise2 than Crimson-CAAX signal intensity in cell bodies (**Figure 5C**). Thus, in one-photon widefield, one-photon confocal, and two-photon microscopy, Crimson-CAAX improved the detection of filopodia and spines.

DISCUSSION

In this study, we developed a new bright RFP, Crimson, with similar excitation and emission spectra as the widely used mCherry and mKate2. In neurons, Crimson is brighter and less toxic than mKate2, mCherry, or FusionRed, either when expressed in the cytosol or targeted to the membrane. A membrane-targeted form of Crimson improves the visualization of spines and filopodia, which contain minuscule amounts of cytoplasm, compared to a cytosolic fluorescent protein. In one-photon microscopy, Crimson-CAAX reliably visualizes filopodia and thin spine necks, which are only clearly visible with cytosolic FPs when the dendritic shafts are overexposed. In two-photon microscopy, Crimson-CAAX outperforms the cytosolic FP in labeling thin neurites. Thus, Crimson-CAAX may be useful for studying synaptic morphology in development (Yoshihara et al., 2009) or for sparse labeling and circuit tracing *in vivo* (Xu and Sudhof, 2013). It may be especially useful for testing interventions in models of neurodevelopmental disorders characterized by abnormal filopodia or spines (De Rubeis et al., 2013; Michaelsen-Preusse et al., 2016).

The fact that the weakly dimeric Crimson is less toxic to neurons than the more monomeric mCherry or FusionRed in both cytosolic and membrane-bound forms is surprising. This observation suggests that the presence of a dimeric interface is not necessarily deleterious to the cell. Crimson is also less toxic than the similarly dimeric mKate2 and the more dimeric dTomato, which suggests that dimerization is not necessarily protective either. Indeed, dTomato when targeted to the membrane creates dramatic rod-like structures in neurons and is highly toxic. Thus factors other than homodimerization affinity alone influence toxicity. One explanation could be that mutation of Crimson at 23 exterior-facing locations (**Supplementary Figure S1**) alters its interactions with endogenous neuronal proteins in a manner that reduces toxicity.

Certain tetrameric RFPs have previously been shown to be suitable for whole cell labeling (Strack et al., 2008; Strack et al., 2009). For example, DsRed-Express2 is reportedly bright, nontoxic and reasonably photostable (Strack et al., 2008). While it is possible for DsRed-Express2 to work with a CAAX signal to the extent that it can be targeted to the membrane, it may form aggregates at the cell membrane, as was observed in DsRed.T3-CAAX, the precursor of DsRed-Express2 (Schwirz et al., 2020). We have also observed that tdTomato-CAAX forms large rod-like structures (**Supplementary Figure S6**), presumably due to interaction between tdTomato-CAAX chains at the parallel dimerization interface (the two Tomato domains in tdTomato form a cross-dimer, leaving the parallel dimerization interface unoccupied). Therefore, tetrameric RFP-CAAX fusions would not be a preferred choice for membrane labelling.

In summary, Crimson is a bright RFPs that is uniquely useful for long-term imaging in neurons, either as a cytosolic protein or as a membrane-targeted fusion. It is brighter than mCherry, mKate2, and FusionRed, commonly used RFPs or far-red FPs in its spectral class, and it is also uniquely non-toxic to neurons after long-term expression. With these

favorable characteristics, Crimson may be a favorable starting point for further engineering to create a fully monomeric version that is compatible with fusion to a variety of neuronal proteins.

DATA AVAILABILITY STATEMENT

The original contributions presented in the study are included in the article/Supplementary Material, further inquiries can be directed to the corresponding authors.

AUTHOR CONTRIBUTIONS

JC and ML conceived and designed the experiments. LN and YG performed Crimson and Crimson-CAAX imaging in neurons, LN, YG, and XN finished data analysis. ML and KD designed and performed the two-photon imaging in zebrafish. NA, AS, HN, and SC resolved the crystal structure of Crimson0.9 and analyzed structural data. JC, MD, and LW performed protein mutagenesis and characterization of Crimson *in vitro* and in non-neuronal cells. LN, YG, ML, ML, and JC wrote the paper.

FUNDING

This work was supported by National Key Research and Development Program of China (2021YFF0502904, 2020YFA0908802, 2017YFA0700403), National Natural Science Foundation of China (Grant 81927803, 31670872, 21874145, 31671044, 91849204, 31671044, 32171192, 32000732, 32000731), the National Program on Key Basic Research Project of China to Y.G. (2016YFA0501901), Natural Science Foundation of Shanghai (19ZR1468600, 201409003800), Shenzhen Science and Technology Innovation Committee (Grant KQJSCX20170331161420421, JCYJ20170818163925063, JCYJ20170818164040422), Guangdong Basic and Applied Basic Research Foundation (2020B121201010), Natural Science Foundation of Shenzhen (JCYJ20200109115633343). NIH BRAIN Initiative grant 1RF1MH11410 (ML and LN.). MD was supported by China Postdoctoral Science Foundation (Grant 2018M633180) and Natural Science Foundation of Guangdong (Grant 2020A151501675). HN is funded by NSF CAREER Award 1833181. KD is funded by NIH and HHMI. ML is funded by NIH grant (K99MH112840).

ACKNOWLEDGMENTS

We thank Charu Ramakrishnan for advice on zebrafish construct design.

SUPPLEMENTARY MATERIAL

The Supplementary Material for this article can be found online at: https://www.frontiersin.org/articles/10.3389/fcell.2022.893468/full#supplementary-material

REFERENCES

Bajar, B. T., Wang, E. S., Zhang, S., Lin, M. Z., and Chu, J. (2016a). A Guide to Fluorescent Protein FRET Pairs. *Sensors (Basel)* 16. doi:10.3390/s16091488

Bajar, B. T., Wang, E. S., Lam, A. J., Kim, B. B., Jacobs, C. L., Howe, E. S., et al. (2016b). Improving Brightness and Photostability of Green and Red Fluorescent Proteins for Live Cell Imaging and FRET Reporting. *Sci. Rep.* 6, 20889. doi:10.1038/srep20889

Bindels, D. S., Haarbosch, L., Van Weeren, L., Postma, M., Wiese, K. E., Mastop, M., et al. (2017). mScarlet: a Bright Monomeric Red Fluorescent Protein for Cellular Imaging. *Nat. Methods* 14, 53–56. doi:10.1038/nmeth.4074

Chu, J., Haynes, R. D., Corbel, S. Y., Li, P., González-González, E., Burg, J. S., et al. (2014). Non-invasive Intravital Imaging of Cellular Differentiation with a Bright Red-Excitable Fluorescent Protein. *Nat. Methods* 11, 572–578. doi:10.1038/nmeth.2888

Cranfill, P. J., Sell, B. R., Baird, M. A., Allen, J. R., Lavagnino, Z., De Gruiter, H. M., et al. (2016). Quantitative Assessment of Fluorescent Proteins. *Nat. Methods* 13, 557–562. doi:10.1038/nmeth.3891

Craske, M. L., Fivaz, M., Batada, N. N., and Meyer, T. (2005). Spines and Neurite Branches Function as Geometric Attractors that Enhance Protein Kinase C Action. *J. Cell Biol.* 170, 1147–1158. doi:10.1083/jcb.200503118

Day, R. N., and Davidson, M. W. (2009). The Fluorescent Protein Palette: Tools for Cellular Imaging. *Chem. Soc. Rev.* 38, 2887–2921. doi:10.1039/b901966a

De Rubeis, S., Pasciuto, E., Li, K. W., Fernández, E., Di Marino, D., Buzzi, A., et al. (2013). CYFIP1 Coordinates mRNA Translation and Cytoskeleton Remodeling to Ensure Proper Dendritic Spine Formation. *Neuron* 79, 1169–1182. doi:10.1016/j.neuron.2013.06.039

Feng, J., Zhang, C., Lischinsky, J. E., Jing, M., Zhou, J., Wang, H., et al. (2019). A Genetically Encoded Fluorescent Sensor for Rapid and Specific *In Vivo* Detection of Norepinephrine. *Neuron* 102, 745–761. doi:10.1016/j.neuron.2019.02.037

Fenno, L. E., Ramakrishnan, C., Kim, Y. S., Evans, K. E., Lo, M., Vesuna, S., et al. (2020). Comprehensive Dual- and Triple-Feature Intersectional Single-Vector Delivery of Diverse Functional Payloads to Cells of Behaving Mammals. *Neuron* 107, 836–853. doi:10.1016/j.neuron.2020.06.003

Govek, E.-E., Newey, S. E., Akerman, C. J., Cross, J. R., Van Der Veken, L., and Van Aelst, L. (2004). The X-Linked Mental Retardation Protein Oligophrenin-1 Is Required for Dendritic Spine Morphogenesis. *Nat. Neurosci.* 7, 364–372. doi:10.1038/nn1210

Han, C., Jan, L. Y., and Jan, Y.-N. (2011). Enhancer-driven Membrane Markers for Analysis of Nonautonomous Mechanisms Reveal Neuron-Glia Interactions in Drosophila. *Proc. Natl. Acad. Sci. U.S.A.* 108, 9673–9678. doi:10.1073/pnas.1106386108

Holtmaat, A., Bonhoeffer, T., Chow, D. K., Chuckowree, J., De Paola, V., Hofer, S. B., et al. (2009). Long-term, High-Resolution Imaging in the Mouse Neocortex through a Chronic Cranial Window. *Nat. Protoc.* 4, 1128–1144. doi:10.1038/nprot.2009.89

Keskitalo, S., Farkas, M., Hanenberg, M., Szodorai, A., Kulic, L., Semmler, A., et al. (2014). Reciprocal Modulation of AÎ²42 Aggregation by Copper and Homocysteine. *Front. Aging Neurosci.* 6, 237. doi:10.3389/fnagi.2014.00237

Laviv, T., Kim, B. B., Chu, J., Lam, A. J., Lin, M. Z., and Yasuda, R. (2016). Simultaneous Dual-Color Fluorescence Lifetime Imaging with Novel Red-Shifted Fluorescent Proteins. *Nat. Methods* 13, 989–992. doi:10.1038/nmeth.4046

Lin, M. Z., Mckeown, M. R., Ng, H.-L., Aguilera, T. A., Shaner, N. C., Campbell, R. E., et al. (2009). Autofluorescent Proteins with Excitation in the Optical Window for Intravital Imaging in Mammals. *Chem. Biol.* 16, 1169–1179. doi:10.1016/j.chembiol.2009.10.009

Michaelsen-Preusse, K., Zessin, S., Grigoryan, G., Scharkowski, F., Feuge, J., Remus, A., et al. (2016). Neuronal Profilins in Health and Disease:

Relevance for Spine Plasticity and Fragile X Syndrome. *Proc. Natl. Acad. Sci. U.S.A.* 113, 3365–3370. doi:10.1073/pnas.1516697113

Ng, H.-L., and Lin, M. Z. (2016). Structure-guided Wavelength Tuning in Far-Red Fluorescent Proteins. *Curr. Opin. Struct. Biol.* 39, 124–133. doi:10.1016/j.sbi.2016.07.010

Pletnev, S., Shcherbo, D., Chudakov, D. M., Pletneva, N., Merzlyak, E. M., Wlodawer, A., et al. (2008). A Crystallographic Study of Bright Far-Red Fluorescent Protein mKate Reveals pH-Induced Cis-Trans Isomerization of the Chromophore. *J. Biol. Chem.* 283, 28980–28987. doi:10.1074/jbc.m800599200

Sala, C., and Segal, M. (2014). Dendritic Spines: the Locus of Structural and Functional Plasticity. *Physiol. Rev.* 94, 141–188. doi:10.1152/physrev.00012.2013

Schwirz, J., Yan, Y., Franta, Z., and Schetelig, M. F. (2020). Bicistronic Expression and Differential Localization of Proteins in Insect Cells and Drosophila Suzukii Using Picornaviral 2A Peptides. *Insect Biochem. Mol. Biol.* 119, 103324. doi:10.1016/j.ibmb.2020.103324

Shaner, N. C., Campbell, R. E., Steinbach, P. A., Giepmans, B. N. G., Palmer, A. E., and Tsien, R. Y. (2004). Improved Monomeric Red, Orange and Yellow Fluorescent Proteins Derived from Discosoma Sp. Red Fluorescent Protein. *Nat. Biotechnol.* 22, 1567–1572. doi:10.1038/nbt1037

ShemiakinaII, Ermakova, G. V., Cranfill, P. J., Baird, M. A., Evans, R. A., Souslova, E. A., et al. (2012). A Monomeric Red Fluorescent Protein with Low Cytotoxicity. *Nat. Commun.* 3, 1204. doi:10.1038/ncomms2208

Shen, Y., Lai, T., and Campbell, R. E. (2015). Red Fluorescent Proteins (RFPs) and RFP-Based Biosensors for Neuronal Imaging Applications. *Neurophoton* 2, 031203. doi:10.1117/1.nph.2.3.031203

St-Pierre, F., Marshall, J. D., Yang, Y., Gong, Y., Schnitzer, M. J., and Lin, M. Z. (2014). High-fidelity Optical Reporting of Neuronal Electrical Activity with an Ultrafast Fluorescent Voltage Sensor. *Nat. Neurosci.* 17, 884–889. doi:10.1038/nn.3709

Strack, R. L., Hein, B., Bhattacharyya, D., Hell, S. W., Keenan, R. J., and Glick, B. S. (2009). A Rapidly Maturing Far-Red Derivative of DsRed-Express2 for Whole-Cell Labeling. *Biochemistry* 48, 8279–8281. doi:10.1021/bi900870u

Strack, R. L., Strongin, D. E., Bhattacharyya, D., Tao, W., Berman, A., Broxmeyer, H. E., et al. (2008). A Noncytotoxic DsRed Variant for Whole-Cell Labeling. *Nat. Methods* 5, 955–957. doi:10.1038/nmeth.1264

Woolfrey, K. M., Srivastava, D. P., Photowala, H., Yamashita, M., Barbolina, M. V., Cahill, M. E., et al. (2009). Epac2 Induces Synapse Remodeling and Depression and its Disease-Associated Forms Alter Spines. *Nat. Neurosci.* 12, 1275–1284. doi:10.1038/nn.2386

Xu, T., Yu, X., Perlik, A. J., Tobin, W. F., Zweig, J. A., Tennant, K., et al. (2009). Rapid Formation and Selective Stabilization of Synapses for Enduring Motor Memories. *Nature* 462, 915–919. doi:10.1038/nature08389

Xu, W., and Südhof, T. C. (2013). A Neural Circuit for Memory Specificity and Generalization. *Science* 339, 1290–1295. doi:10.1126/science.1229534

Yoshihara, Y., De Roo, M., and Muller, D. (2009). Dendritic Spine Formation and Stabilization. *Curr. Opin. Neurobiol.* 19, 146–153. doi:10.1016/j.conb.2009.05.013

Zhang, J., Sun, X., Zheng, S., Liu, X., Jin, J., Ren, Y., et al. (2014). Myelin Basic Protein Induces Neuron-specific Toxicity by Directly Damaging the Neuronal Plasma Membrane. *PLoS One* 9, e108646. doi:10.1371/journal.pone.0108646

Zhou, L., Jones, E. V., and Murai, K. K. (2012). EphA Signaling Promotes Actin-Based Dendritic Spine Remodeling through Slingshot Phosphatase. *J. Biol. Chem.* 287, 9346–9359. doi:10.1074/jbc.m111.302802

Conflict of Interest: The authors declare that the research was conducted in the absence of any commercial or financial relationships that could be construed as a potential conflict of interest.

Publisher's Note: All claims expressed in this article are solely those of the authors and do not necessarily represent those of their affiliated organizations, or those of the publisher, the editors and the reviewers. Any product that may be evaluated in this article, or claim that may be made by its manufacturer, is not guaranteed or endorsed by the publisher.

frontiers | Frontiers in Cell and Developmental Biology

ORIGINAL RESEARCH
published: 07 July 2022
doi: 10.3389/fcell.2022.822026

Effects of Transcription-Dependent Physical Perturbations on the Chromosome Dynamics in Living Cells

Hyeyeong Ku[1,2†], Gunhee Park[3†], Jiyoung Goo[1,2], Jeongmin Lee[1,4], Tae Lim Park[3], Hwanyong Shim[3], Jeong Hee Kim[2,5], Won-Ki Cho[3,6]* and Cherlhyun Jeong[1,2]**

[1]Chemical and Biological Integrative Research Center, Korea Institute of Science and Technology (KIST), Seoul, South Korea, [2]KHU-KIST Department of Converging Science and Technology, Kyung Hee University, Seoul, South Korea, [3]Department of Biological Sciences, Korea Advanced Institute of Science and Technology (KAIST), Daejeon, South Korea, [4]Division of Life Sciences, Korea University, Seoul, South Korea, [5]Department of Oral Biochemistry and Molecular Biology, Kyung Hee University, Seoul, South Korea, [6]KI for Health Science and Technology (KIHST), Korea Advanced Institute of Science and Technology (KAIST), Daejeon, South Korea

OPEN ACCESS

Edited by:
Yingxiao Wang,
University of California, San Diego,
United States

Reviewed by:
Myong-Hee Sung,
National Institutes of Health (NIH),
United States
Hodaka Fujii,
Hirosaki University, Japan

***Correspondence:**
Jeong Hee Kim
jhkimh@khu.ac.kr
Won-Ki Cho
wonkicho@kaist.ac.kr
Cherlhyun Jeong
che.jeong@kist.re.kr

†These authors have contributed equally to this work

Specialty section:
This article was submitted to Signaling, a section of the journal Frontiers in Cell and Developmental Biology

Received: 25 November 2021
Accepted: 23 May 2022
Published: 07 July 2022

Citation:
Ku H, Park G, Goo J, Lee J, Park TL, Shim H, Kim JH, Cho W-K and Jeong C (2022) Effects of Transcription-Dependent Physical Perturbations on the Chromosome Dynamics in Living Cells. Front. Cell Dev. Biol. 10:822026. doi: 10.3389/fcell.2022.822026

Recent studies with single-particle tracking in live cells have revealed that chromatin dynamics are directly affected by transcription. However, how transcription alters the chromatin movements followed by changes in the physical properties of chromatin has not been elucidated. Here, we measured diffusion characteristics of chromatin by targeting telomeric DNA repeats with CRISPR-labeling. We found that transcription inhibitors that directly block transcription factors globally increased the movements of chromatin, while the other inhibitor that blocks transcription by DNA intercalating showed an opposite effect. We hypothesized that the increased mobility of chromatin by transcription inhibition and the decreased chromatin movement by a DNA intercalating inhibitor is due to alterations in chromatin rigidity. We also tested how volume confinement of nuclear space affects chromatin movements. We observed decreased chromatin movements under osmotic pressure and with overexpressed chromatin architectural proteins that compact chromatin.

Keywords: chromatin dynamics, CRISPR labeling, telomere, single-particle tracking, transcription, gene expression regulation, epigenetic modulation, fluorescence microscopy

INTRODUCTION

The molecular genetic material, DNA, exists in a form of chromatin in eukaryotes throughout most of the cell cycle. Chromatin is a higher-order fiber structure of DNA formed by nucleosomes composed of histones. It is located inside a nucleus separated from cytoplasm by a physical barrier, known as a nuclear membrane. Transcription and many other gene regulatory processes occur within the chromatin context in the compartmentalized nuclear space.

Recently established chromatin conformation capture (3C)-based sequencing and advanced live-cell imaging techniques have suggested that cell-type specific intrinsic structures and dynamics of chromatin are responsible for regulating gene expression (Rowley and Corces, 2018; Oudelaar and Higgs, 2021). A series of studies using 3C-based sequencing have shown that chromatin sub-organization reflects different gene expression patterns across cell types (Dekker and Mirny, 2016). Moreover, chromatin is folded into unique loop structures, so-called topologically associated domains (TADs), by chromatin architectural proteins including CTCF and Cohesin complex. These TADs provide spatial constraints that promote physical contacts among gene regulatory elements within a single TAD (Dixon et al., 2012; Nora et al., 2012; Rao et al., 2014; Chang et al., 2020).

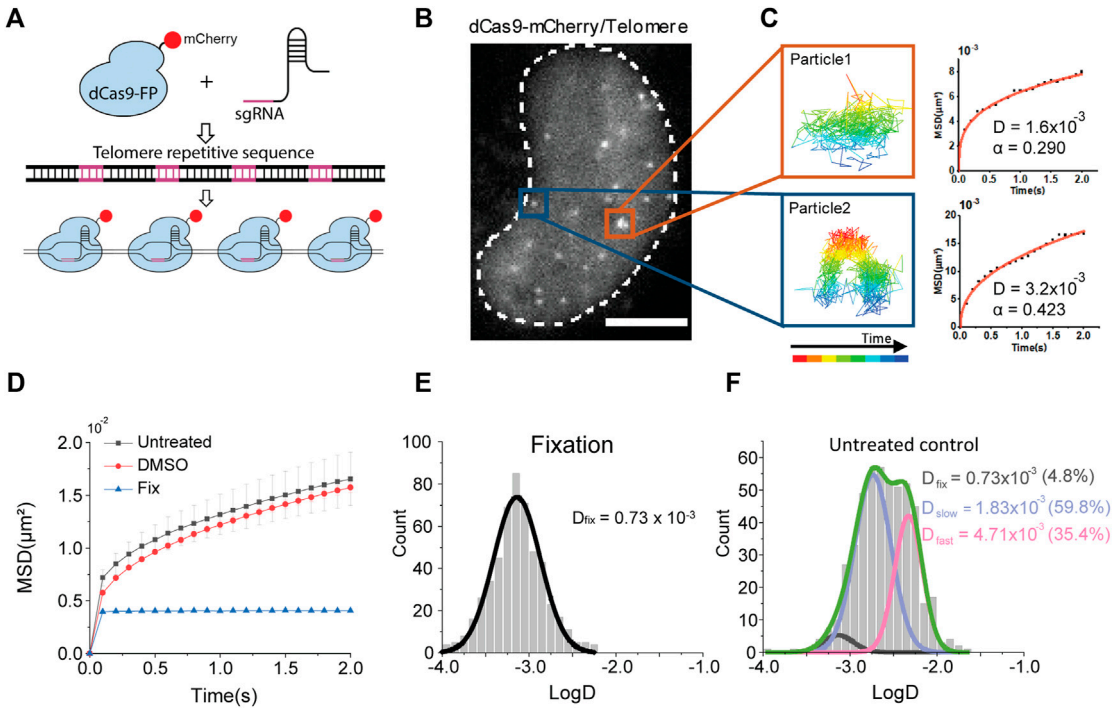

FIGURE 1 | Single chromatin locus tracking and diffusion analysis. **(A)** A schematic representation of CRISPR/dCas9-labeling on telomere sequences. **(B)** A representative image of fluorescently labeled chromatin loci in a living cell nucleus. The scale bar represents 5 μm. **(C)** Examples of single locus tracking for diffusion analysis. **(D)** Averaged MSD-t plots for each time interval in live cells under normal culture media (N = 34 cells, *n* = 520 trajectories), DMSO treatment (N = 32 cells, *n* = 653 trajectories), and fixed cells (N = 32 cells, *n* = 575 trajectories). **(E,F)** Distributions of diffusion constants for individual trajectories in **(E)** fixed cells and **(F)** normally cultured cells.

Accumulated evidence with real-time tracking of chromatin loci in live cells indicates that dynamics of chromatin are related to gene expression regulation, rather than mere thermal motions in the cell nucleus (Babokhov et al., 2020). Given the fact that molecular components for transcription, such as RNA polymerases, transcription factors, and the chromatin architectural proteins along with chromatin fibers, are physical entities with masses and volumes, the mobility of chromatin should be altered by their interactions for transcriptional controls.

Here, we investigated how alterations in physical properties of chromatin, rigidity, and volume confinement, influence chromosome dynamics in human cells. We found chromosome movements are directly affected by changes in physical properties of chromatin by calculating diffusion constants with single locus tracking in live-cell nuclei. Because the movement of chromosomes is heterogenous in the living cell nucleus, we statistically measured the motions of each chromosome by labeling telomere loci with a CRISPR/dCas9-based labeling system (Hilbert et al., 2021).

RESULTS

Fluorescently Labeling Chromosome *via* Telomeres for Single Locus Tracking

To label specific chromatin loci within a single cell nucleus, we adopted CRISPR/dCas9-based labeling system which allows us to stably label specific DNA sequences by using nuclease-deactivated Cas9 (dCas9) with a small guide (sg) RNA (Chen et al., 2013; Gu et al., 2018). To visualize DNA regions, dCas9 fused with fluorescent protein is guided to the specific sites by sgRNAs which often target multiple nearby sequences to achieve a signal-to-noise ratio above a background fluorescence intensity. However, there is a limitation that a robust way to express multiple sgRNAs in the cell has not been established. Although a method to insert multiple sgRNAs in a single expression vector has recently been introduced, it requires a thorough optimization process to validate functional sgRNAs in the vector (Gu et al., 2018). Hence, one convenient way to label chromatin is by targeting telomere sequences which consist of repeated sequences conserved across different chromosomes (Moyzis et al., 1988). By targeting telomeres, we could label multiple genomic sites with a single sgRNA in the cell nucleus (**Figure 1A**).

We expressed the sgRNA targeting human telomere regions along with a fluorescent protein, mCherry, fused dCas9 in HeLa cells (**Figure 1B**). Fluorescence imaging with highly inclined and laminated optical (HILO) sheet illumination could capture telomere loci in the nucleus. We continuously imaged the telomere loci for 2 minutes and analyzed each trajectory of the locus to calculate diffusion constants (**Figure 1C**). We found most of the chromatin movements show confined diffusions.

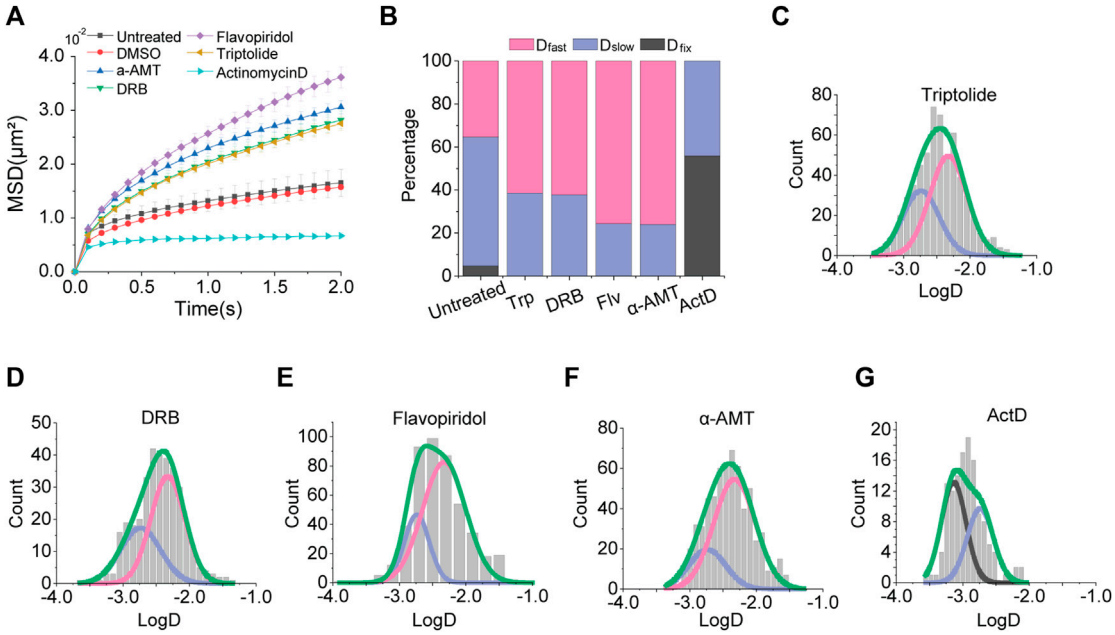

FIGURE 2 | Effects of transcription inhibitors. **(A)** Averaged MSD-t plots for each time interval is normally cultured cells and transcription inhibitor treated cells. (triptolide, N = 27 cells, *n* = 633 trajectories; DRB, N = 22 cells, *n* = 370 trajectories; flavopiridol, N = 30 cells, *n* = 501 trajectories; a-amanitin, N = 33 cells, *n* = 671 trajectories; actinomycin D, N = 33 cells, *n* = 633 trajectories) **(B)** Percentages of diffusion constant components from multimodal Gaussian fittings for each condition. **(C–G)** Distributions of diffusion constants for individual trajectories in cells treated with triptolide, DRB, flavopiridol, a-amanitin, and actinomycin D, respectively. Green lines represent fitting with triple Gaussian peaks for the entire distribution. Pink, blue, and black lines represent single Gaussian portions for fast, slow, and fixed diffusions, respectively.

Diffusion Analysis of Chromosome Movement

We plotted averaged mean square displacement (MSD) over time from trajectories for diffusion analysis -is normally cultured Hela cells (**Figure 1D**). We note that we collected more than 200 trajectories from at least 20 cells for each experimental condition throughout this study to secure statistical significance.

Since chromatin is a relatively long polymer within a confined space, we fitted the MSD-t plot with the anomalous diffusion equation, $4Dt^{\alpha}$, for two-dimensional motions. We found an apparent diffusion constant from all over the trajectories, D_{app} was 3.33 (±0.001, s. e.) x 10^{-3} μm^2/s with an anomalous coefficient α = 0.292 (±0.004, s. e.) (**Supplementary Figure S1, Table S1**). We could not observe any significant changes under dimethyl sulfoxide (DMSO), a solvent for reagents in the following experiments. We next analyzed fluctuations of the chromatin loci in fixed cells to check the thermal diffusion constant, which is measured as 0.101 (N.S.) × 10^{-3} μm^2/s. We performed fixed cell imaging under the same condition used for live cell imaging.

A distribution of D_{app} from individual trajectories under the normal condition, however, showed a multimodal distribution compared to a distribution from fixed cells (**Figures 1E,F**; Table S2). We fitted the distribution with triple Gaussian peaks, assuming that the multimodal distribution of D_{app} is due to mixed trajectories from 1) a global long-range movement of chromatin (D_{fast}), 2) a local movement of chromatin loci (D_{slow}), and 3) an immobilized portion with thermal fluctuation under the imaging condition (D_{fixed}). (Chen et al., 2013; Gu et al., 2018). For fitting with triple Gaussian peaks, we fixed the diffusion constant of thermal fluctuation as D_{fix} = 0.73 (±0.06, s. e.) × 10^{-3} μm^2/s obtained from fixed cells, since we performed all imaging under the same condition (**Figure 1F**).

Effects of Transcriptional Perturbations on Chromosome Movement

We next sought to test the effects of transcription activity on chromatin dynamics with known transcription inhibitors; triptolide, 5,6-Dichloro-1-β-d-ribofuranosyl-benzimidazole (DRB), flavopiridol, alpha-amanitin, and actinomycin D, which act at different steps during transcription. Triptolide is an inhibitor for blocking transcription initiation, which covalently binds to X-box binding protein 1 (XBP1), one of the two helicase subunits of an initiation transcription factor Transcription factor II Human (TFIIH) (Titov et al., 2011). Flavopiridol and DRB inhibit transcription at the elongation step by inhibition of positive-transcription elongation factor b (P-TEFb) (Chao and Price, 2001; Peterlin and Price, 2006). Alpha-amanitin and actinomycin D are global transcription inhibitors by specifically binding to a catalytic active site of RNA polymerase II and intercalating into DNA at GpC sites, respectively (Kirk, 1960; Jacob et al., 1970).

Under treatment of each transcription inhibitor, we measured the apparent diffusion constant (**Figure 2A**). Interestingly, we

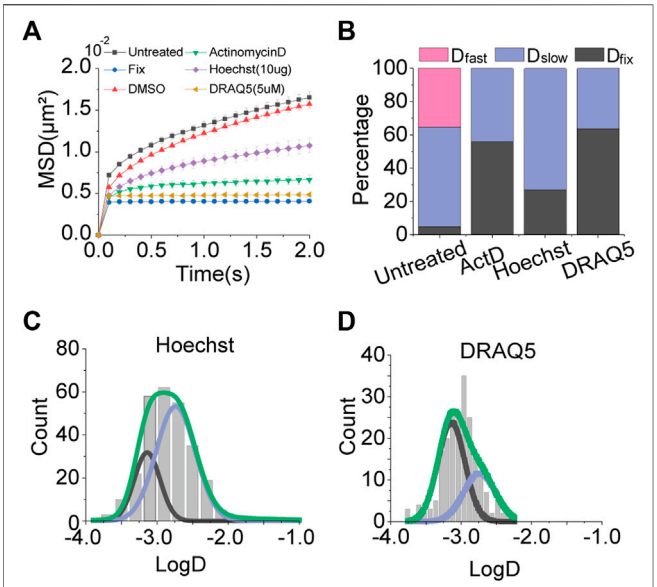

FIGURE 3 | Effects of DNA intercalators. **(A)** Averaged MSD-t plots for each time interval is normally cultured cells and DNA intercalator treated cells. (Hoechst, N = 20 cells, n = 293 trajectories; DRAQ5, N = 20 cells, *n* = 262 trajectories) **(B)** Percentages of diffusion constant components from multimodal Gaussian fittings for each condition. **(C,D)** Distributions of diffusion constants for individual trajectories in cells treated with Hoechst and DRAQ5, respectively. Green lines represent fitting with triple Gaussian peaks for the entire distribution. Blue and black lines represent single Gaussian portions for slow and fixed diffusions, respectively.

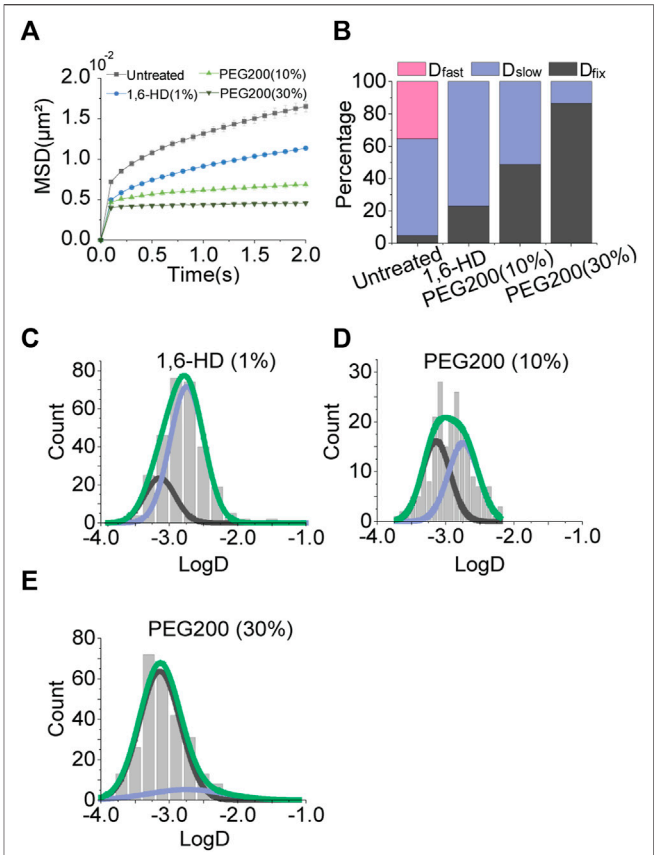

FIGURE 4 | Effects of osmotic pressure. **(A)** Averaged MSD-t plots for each time interval under the normal condition and osmotic pressures (1% 1,6-hexanediol, N = 31 cells, *n* = 314 trajectories; 10% PEG200, N = 20 cells, *n* = 231 trajectories; 30% PEG200, N = 20 cells, *n* = 302 trajectories). **(B)** Percentages of diffusion constant components from multimodal Gaussian fittings for each condition. **(C–E)** Distributions of diffusion constants for individual trajectories in cells treated with 1% 1,6-hexanediol, 10% PEG200, and 30% PEG200, respectively. Green lines represent fitting with triple Gaussian peaks for the entire distribution. Blue and black lines represent single Gaussian portions for slow and fixed diffusions, respectively.

observed a consistent increase in chromatin mobility for most transcription inhibitors we used, except for actinomycin D. We confirmed that the effect of a transcription inhibitor is general in another cell line, HEK293 (**Supplementary Figure S2**). The MSD-t plot for actinomycin D treatment showed a drastic decrease in the chromatin movements. These results imply that transcription restrains the mobility of chromatin. However, the inconsistent results from actinomycin D treatment may be due to the difference mechanisms for transcription inhibition because actinomycin D intercalates into DNA all over the chromatin, unlike other transcription inhibitors which merely target specific transcription factors.

We further checked multimodal distributions of diffusion constants for each inhibitor and represented the results of multiple Gaussian fitting as bar graphs for comparison (**Figure 2B**). We fitted the distributions with a triple Gaussian. However, if triple Gaussian fitting is failed, we fitted with double Gaussian without a peak failed for triple Gaussian peaks (**Figures 2D–G**). For example, a fitting with triple Gaussian peaks for DRB treatment failed for D_{fixed}, then we fitted the distribution with double Gaussian peaks without the D_{fixed} peak (**Supplementary Figure S3**).

We found a consistent increase in a portion of D_{fast} and a decrease in a portion of D_{slow} for inhibitors that target transcription factors (**Figures 2B–G**). These results indicate that the inhibition of transcription promotes global movements of chromatin by removing domestic constraints, such as the disassociation of transcription factors from chromatin so that it gives more flexibility to chromatin. Under these conditions, the D_{fixed} portion disappeared.

On the other hand, the treatment of actinomycin D showed a completely different distribution (**Figures 2B,G**). Under actinomycin D treatment, the D_{fast} portion disappeared, while D_{fixed} was dominantly increased. We speculate this result may be due to an increase in chromatin rigidity induced by the effect of DNA intercalation.

Effects of DNA Intercalators on Chromosome Movement

Based on the result of actinomycin D treatment, we tested other DNA intercalators; Hoechst and DRAQ5, which are fluorescent DNA staining dyes usable for live cell imaging. Consistent with the result of actinomycin D treatment, MSD-t plots for Hoechst and DRAQ5 showed a decrease in chromatin motions (**Figure 3A**).

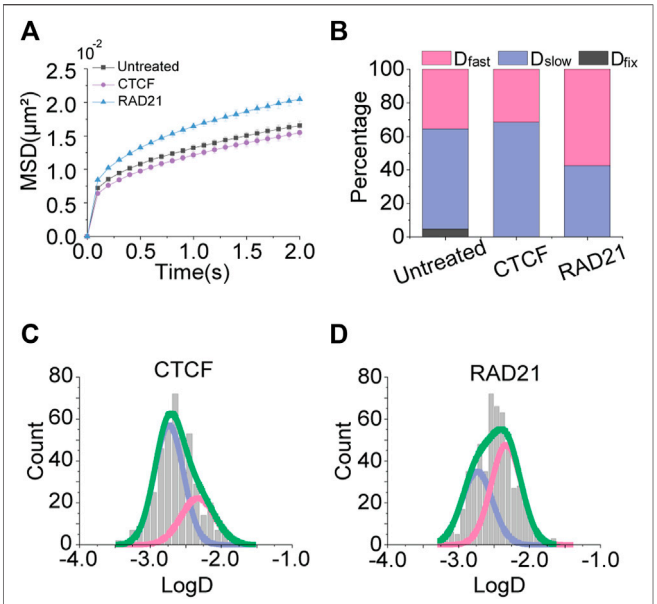

FIGURE 5 | Effects of chromatin architectural protein overexpression. **(A)** Averaged MSD-t plots for each time interval under the normal condition and with overexpression of CTCF and RAD21. (CTCF, N = 32 cells, *n* = 449 trajectories; RAD21, N = 45 cells, *n* = 566 trajectories) **(B)** Percentages of diffusion constant components from multimodal Gaussian fittings for each condition. **(C,D)** Distributions of diffusion constants for individual trajectories in cells treated with CTCF and RAD21 overexpression, respectively. Green lines represent fitting with triple Gaussian peaks for the entire distribution. Pink and blue lines represent single Gaussian portions for fast and slow diffusions, respectively.

Results of multiple Gaussian fitting for the distributions of diffusion constants for the intercalators were also in agreement with the result of actinomycin D treatment (**Figures 2B,G**; **Figures 3B–D**). D_{fast} disappeared, while D_{fixed} was drastically increased. Taken together, these results imply that DNA intercalators may increase the rigidity of chromatin so which causes a reduction in the global mobility of chromosomes. Slight differences in portions of D_{fixed} and D_{slow} for each intercalator may be due to differences in intercalating mechanisms for different intercalators (Almaqwashi et al., 2016a; Almaqwashi et al., 2016b).

Effects of Cellular Osmotic Pressures on Chromatin Motions

Recent microscopy techniques that interrogate liquid properties of biomolecular condensates have captured subnuclear membraneless organelles that undergo liquid-liquid phase-separation (LLPS) for their formations (Hyman et al., 2014; Banani et al., 2017; Sabari et al., 2020). RNA Polymerase II and essential transcription factors also have been verified to form a cluster with liquid properties, which is so-called a transcriptional condensate (Cho et al., 2018; Sabari et al., 2018).

Especially, the transcriptional condensates and nuclear speckles, which are comparably abundant subnuclear organelles, are known to be functional for gene expression regulation on active genes in the processes of transcription and splicing, respectively. Given that chromatin is where genes are located, those organelles also could be physical constrains for chromatin mobility. The condensates are thought to be formed by cooperative interactions of nucleic acids and proteins that contain intrinsically disordered regions (IDRs). Hydrophobic interaction is considered one of the key driving forces for condensation (Hyman et al., 2014).

To perturb the condensates, we tested 1,6-hexanediol which is known to disrupt hydrophobic interactions among biomolecules (Cho et al., 2018; Sabari et al., 2018). Although we hypothesized that the disruption of condensates may increase chromatin movements by removing physical constraints, 1,6-hexanediol treatment decreased the chromatin motion (**Figure 4A**).

With this result, we speculated that osmotic pressure on the cells caused by 1,6-hexanediol treatment may affect chromatin movements. To test this effect, we exposed the cells to hypertonic buffers composed of polyethylene glycol (PEG) molecules. We observed a drastic decrease in chromatin motions proportional to the concentration of PEG (**Figure 4A**, **Supplementary Figure S2**). Checking multimodal distributions of diffusion constants, as osmotic pressure increases the portion of D_{fixed} becomes dominant (**Figures 4B–E**). Reduced mobility of chromatin is thought to be due to nuclear volume reduction under osmotic pressure.

Effects of Chromatin Architectural Proteins on Chromatin Motions

Regarding our previous observation, we hypothesized that increasing nuclear volume may promote chromatin motion by allowing more space for movements. Rather than changing the volume of the nucleus itself, we decided to induce chromatin packing with chromatin architectural proteins, CCCTC-binding factor (CTCF), and Cohesin, which can indirectly increase the nuclear space for the chromatin mobility.

With advanced 3C-based genome-wide sequencing techniques combined with chromatin immunoprecipitation (ChIP), it has been found that CTCF and Cohesin are enriched at the most (not all) of TAD boundaries, indicating that the chromatin loops are formed by those mechanical units (Dekker and Mirny, 2016; Symmons et al., 2016; Nora et al., 2017; Rowley and Corces, 2018). Recent studies with *in vitro* real-time single-molecule assays have shown that CTCF and Cohesin indeed create chromatin loop structures, through the loop-extrusion mechanism. In detail, the ring-shaped Cohesin entraps and extrudes chromatin until it encounters a convergently oriented chromatin-bound CTCF pair (Sanborn et al., 2015; Fudenberg et al., 2016; Ganji et al., 2018). Based on this mechanism, Cohesin extrudes chromatin fibers as a molecular motor, and CTCF determines the boundaries of the loops.

To test the effects of chromatin architectural proteins on chromatin movements, we overexpressed CTCF and RAD21, a subunit of the Cohesin complex, independently in the cells. As we expected, CTCF did not show a significant change in the mobility of chromatin, meaning that the boundary element CTCF itself does not influence the chromatin packing (**Figure 5A**). On the

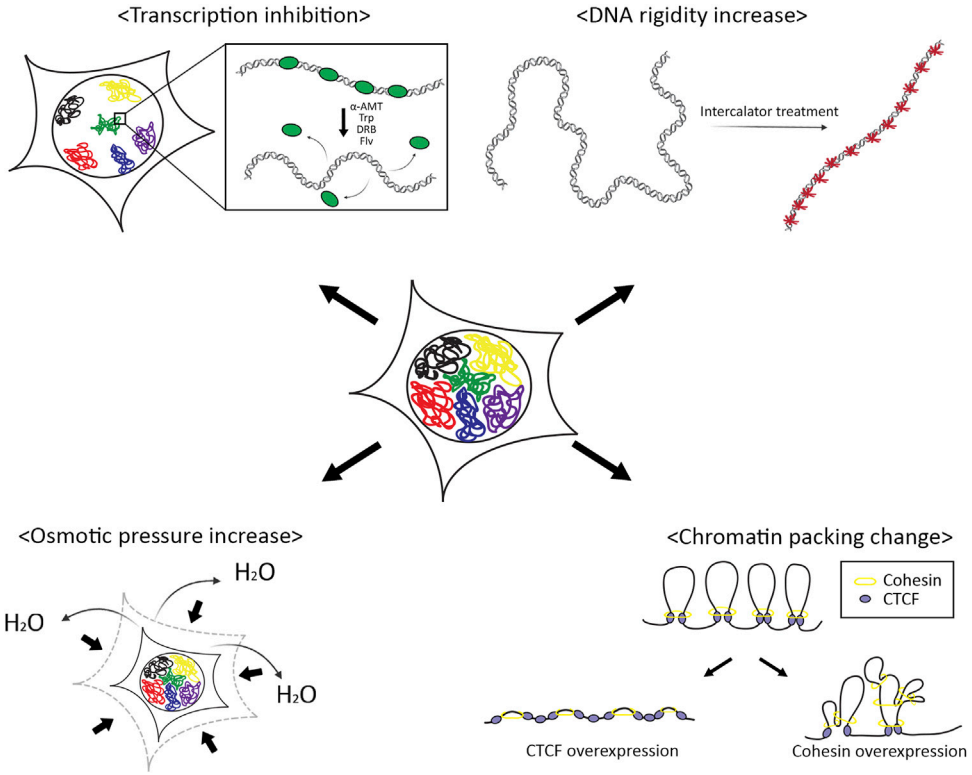

FIGURE 6 | Schematic summary of effects of physical perturbations on chromosomes. The movement of a chromosome is affected by the physical properties of chromatin fibers, rigidity, and volume confinement. Transcription factors associated with chromatin and DNA intercalators make chromatin more rigid. Osmotic pressure and chromatin compaction by chromatin architectural proteins reduce effective nuclear space for chromosome movements.

contrary, the overexpression of RAD21 increased chromatin mobility, suggesting that Cohesin mainly causes chromatin loop formations that lead to chromatin packing. As a result, the effective volume for the chromatin movement is increased as if the nuclear space is widened.

The multimodal distributions of diffusion constants also showed the aspect (**Figures 5A–C**). The portion of D_{fast} has increased for the overexpression of RAD21, indicating that the long-range movement of chromatin becomes more frequent.

We further performed knockdown experiments on CTCF and Rad21. As expected, knockdown of CTCF did not significantly alter chromatin mobility. However, the knockdown of Rad21 still increased chromatin mobility. We speculate this result might be due to that knockdown of Rad21 seems to have a greater effect on reducing rigidity and making chromatin more flexible than the effect of reducing effective volume, similar to the results of transcription inhibitors (**Supplementary Figure S4**).

DISCUSSION

The genetic material, DNA which is wrapped into chromatin fibers, is a physical entity in a finite space, the nucleus. The physical properties of chromatin, therefore, are linked to gene expression regulation (**Figure 6**). We investigated how physical perturbations alter chromatin dynamics in this study.

We tested various chemicals that can inhibit transcription or that can intercalate into the DNA double helical structure inducing increased chromatin stiffness. We observed that transcription inhibitors increased chromatin mobility while DNA intercalators drastically reduced chromatin motions. These opposite responses of the chromatin mobility to different chemicals may indicate the same physical consequence; transcription machinery affected by the transcription inhibitors apply physical constraints by forming chromatin loops and repressing the movements of chromatin. Thus, inhibiting transcription should induce increased flexibility in chromatin structures. On the other hand, DNA intercalators stuck between bases in DNA make the chromatin more rigid.

Upon the treatment of osmotic agents to the cells, we found the declined motions of chromatin. Osmotic pressure with a hypertonic solution to the cell causes an outward flow of water molecules across the nuclear membrane, with shrinking volume to adjust concentrations in and out of the nucleus (Finan and Guilak, 2010). The reduced chromatin mobility could be a result of the volumetric effect or increased viscosity in the nucleus. We further tested whether inducing chromatin packing shows the same result. With the overexpression of chromatin architectural proteins, CTCF and RAD21, we observed increased chromatin mobility with RAD21 overexpression, but not with CTCF. These results are inconsistent with the molecular functions of each protein. During chromatin loop formation, the cohesion complex creates loops

through the loop extrusion mechanism, and CTCF acts as anchors of the loops. Thus, CTCF cannot directly influence the chromatin loop formation while cohesion can promote more chromatin loop formation which results in the compaction of chromatin volume, which gives more spaces for chromatin motions in the nucleus.

Taken together, our experiments perturb the physical properties of chromosomes and showed alterations in the physical environment directly influence the chromosome motions, which is also related to transcriptional activities. Since we measured the motions of chromosomes with telomere regions, which may not fully represent chromosome movements, additional measurements from the movements of whole chromosomes should be required to confirm our conclusions in a further study.

METHODS

Cell Culture

The human cervical cancer cell line HeLa (Korean Cell Line Bank # 10002) was cultured in Dulbecco's modified Eagle medium (DMEM) with high glucose, devoid of phenol red (Gibco, #31053028), supplemented with 10% fetal bovine serum (FBS) (Gibco, #12483020), 1% antibiotic-antimycotic (Gibco, #15240062), 1% GlutaMAX™ supplement (Gibco, #35050061), and 1% sodium pyruvate (Gibco, #11360070). Cells were cultured at 37°C and 5% CO2 in a humidified incubator. Cell lines were periodically tested for *Mycoplasma* contamination using the e-MycoTM *Mycoplasma* PCR Detection kit (iNtRON).

Fluorescence Imaging With Telomere Labeling

For live cell imaging, cells were imaged in DMEM with high glucose, devoid of phenol red, supplemented with 10% FBS and 1% antibiotic-antimycotic. Before imaging, cells were cultured in 35-mm glass-bottom dishes (SPL-confocal dish, #100350) until 80% confluency was reached. For telomere labeling, cells were transfected with 300 ng of SpydCas9-3XmCherry-SgRNA/Telomere-All-in-one vector (Addgene, #85717) and 1,500 ng of SpySgRNA/DTS13-Telomere (Addgene, #85715) using FuGENE® HD Transfection Reagent (Promega, #E2311) in a ratio of 1:5 (Pawluk et al., 2016). Cells were imaged at 37°C and 5% CO2 in a microscope stage-top incubator.

For fixed cell imaging, the culture medium was exchanged with 4% paraformaldehyde (PFA) (Biosensang,#PC2031-100-00) after washing with Dulbecco's phosphate buffered saline (DPBS) (WELGENE, #LB001-02). After 10 min incubation at room temperature, PFA was exchanged with 1x PBS. To completely remove PFA, cells were incubated in DPBS for 5 min, and this process was repeated three times.

Transcription Inhibitor Treatment

Cells were cultured in 35-mm glass-bottom dishes before treatment with transcription inhibitors. For each transcription inhibitor, cells were incubated for 2 h under actinomycin D (Sigma-Aldrich, #A1410), 100 μM 5,6-Dichloro-1-β-D-ribofuranosylbenzimidazole (DRB) (Sigma-Aldrich, #D1916), 5 μM α-amanitin (Sigma-Aldrich, #23109-05-9), 10 μM flavopiridol (Sigma-Aldrich, #F3055), and 125 nM triptolide (Sigma-Aldrich, #T3652) diluted in dimethyl sulfoxide (Sigma-Aldrich, #D8418), respectively, before imaging.

DNA Intercalator Treatment

Cells were cultured in 35-mm glass-bottom dishes before treatment of DNA intercalators. For each DNA intercalator, cells were incubated for 2 h under 2 μM actinomycin D (Sigma-Aldrich, #A1410), for 10 min under 5 μM DRAQ5 (Abcam, #ab108410) and 9 μM Hoechst (Thermo Fisher Scientific, #62249).

Osmotic Agent Treatment

Cells were cultured in 35-mm glass-bottom dishes before treatment with osmotic agents. Cells were treated with 1% (wt/vol) 1,6-hexanediol (Sigma-Aldrich, #240117) for 5 min, with 10%, 30% (wt/vol) Polyethylene glycol (PEG200) (Sigma-Aldrich, #P3015) for 5 min, before imaging on the microscope stage.

Overexpression of Chromatin Architectural Proteins

For expression of chromatin architectural proteins, CTCF or RAD21 (a subunit of cohesion complex), 1 μg of pKS070-pCAGGS-3XFLAG-(human)CTCF-eGFP (Addgene, #156448), and 1 μg of Dendra2-Rad21-C-18 (Addgene, #57737) expression vectors were transfected to the cells for each experiment. We confirmed the expression of each protein in cell nuclei, with GFP signals for CTCF and Dendra2 signals for RAD21, respectively. We imaged and collected data from fluorescence positive cells.

Microscopy With Highly Inclined and Laminated Optical Illumination

Cell imaging was performed with highly inclined and laminated optical (HILO) illumination from a Nikon TIRF microscope based on the Nikon Eclipse Ti microscope body. For detections of telomere loci, mCherry was excited with a built-in 561 nm laser in the microscope. Images were acquired through a 100X objective lens of 1.49 numerical aperture (Nikon, Plan Apochromat TIRF 100x oil-type) with the electron multiplying charge coupled device (EMCCD) (Andor, iXon Ultra 897), and processed using the NIS-Elements software (Nikon). For streaming image acquisition, snapshots were taken every 100 ms for 2 min. Image analysis was performed using ImageJ scripts and custom-built MATLAB codes for mean square displacement calculation.

Single Locus Tracking

Image analysis was performed using ImageJ scripts and custom-built MATLAB codes for mean square displacement calculation. Single locus tracking was performed by an ImageJ plugin-in software, TrackMate. Each fluorescent locus per frame was identified by Laplacian Gaussian fitting with an LoG detector in the TrackMate. Background noise was minimized by the LoG detector which is based on applying an LoG filter on each image and detecting local maxima. 2D trajectories of X-Y coordinates over time for each particle were obtained.

MSD Calculation

For telomere movement analysis, single particle analysis was performed using a custom-built MATLAB code. MSD equation was used to measure the characteristic of diffusion with time-dependent trajectory information of each particle. The mean square displacement (MSD) was obtained through this formula if we know the X-Y coordinates and time interval in 2D for each frame in the trajectory we obtained and the number of total frames. We calculated MSD-values for each individual track using a method previously reported (Qian et al., 1991; Saxton, 1997) where MSD (nΔt) for a given time lag (nΔt) is defined as an average over all points for the given time lag,

$$\mathrm{MSD}(n\Delta t) = \frac{1}{N-n}\sum_{i=1}^{N-n}\left[x(i+n)-x(i)^2\right] + \left[y(i+n)-y(i)\right]^2,$$

where N represents the length of trajectory and Δt the time delay between frames (Weimann et al., 2013).

Plotting MSD-time curve was performed using the custom-built MATLAB code. The MSD of particles tracked for more than 20 s were collected and averaged over time to obtain an ensemble MSD graph. For estimation of a diffusion coefficient (D) and an anomalous diffusion parameter (α), MSD-t plots were fitted by $4Dt^{\alpha}$, for two-dimensional motions.

DATA AVAILABILITY STATEMENT

The original contributions presented in the study are included in the article/**Supplementary Material**; further inquiries can be directed to the corresponding authors.

AUTHOR CONTRIBUTIONS

CJ, W-KC, and JK conceived the project and designed the experiments. HK, JG, HS, and JL performed fluorescence imaging and image data processing. HK and GP analyzed image data. W-KC, GP, HK, and TP drafted the manuscript. CJ, W-KC, and JK edited the manuscript and supervised the project.

FUNDING

This work was supported by the National Research Foundation of Korea (NRF) grants funded by the Korean government (MSIP) (2021R1A2C1095046 to CJ and 2020R1C1C1014599, 2020R1A4A3079755, and 2021H1D3A2A01083165 to W-KC), and the KIST Institutional Program (2E31622 to CJ) and a grant of the Information and Communications Promotion Fund (ICT promotion fund) through the National IT Industry Promotion Agency (NIPA), funded by the Ministry of Science and ICT (MSIT) and funded by the Ministry of Health and Welfare and Ministry of Science and ICT, Republic of Korea (HI20C1234 to CJ), as well as the Suh Kyungbae Foundation (to W-KC).

SUPPLEMENTARY MATERIAL

The Supplementary Material for this article can be found online at: https://www.frontiersin.org/articles/10.3389/fcell.2022.822026/full#supplementary-material

REFERENCES

Almaqwashi, A. A., Andersson, J., Lincoln, P., Rouzina, I., Westerlund, F., and Williams, M. C. (2016a). DNA Intercalation Optimized by Two-step Molecular Lock Mechanism. *Sci. Rep.* 6, 37993. doi:10.1038/srep37993

Almaqwashi, A. A., Paramanathan, T., Rouzina, I., and Williams, M. C. (2016b). Mechanisms of Small Molecule-DNA Interactions Probed by Single-Molecule Force Spectroscopy. *Nucleic Acids Res.* 44, 3971–3988. doi:10.1093/nar/gkw237

Babokhov, M., Hibino, K., Itoh, Y., and Maeshima, K. (2020). Local Chromatin Motion and Transcription. *J. Mol. Biol.* 432, 694–700. doi:10.1016/j.jmb.2019.10.018

Banani, S. F., Lee, H. O., Hyman, A. A., and Rosen, M. K. (2017). Biomolecular Condensates: Organizers of Cellular Biochemistry. *Nat. Rev. Mol. Cell Biol.* 18, 285–298. doi:10.1038/nrm.2017.7

Chang, L.-H., Ghosh, S., and Noordermeer, D. (2020). TADs and Their Borders: Free Movement or Building a Wall? *J. Mol. Biol.* 432, 643–652. doi:10.1016/j.jmb.2019.11.025

Chao, S.-H., and Price, D. H. (2001). Flavopiridol Inactivates P-TEFb and Blocks Most RNA Polymerase II Transcription *In Vivo*. *J. Biol. Chem.* 276, 31793–31799. doi:10.1074/jbc.m102306200

Chen, B., Gilbert, L. A., Cimini, B. A., Schnitzbauer, J., Zhang, W., Li, G.-W., et al. (2013). Dynamic Imaging of Genomic Loci in Living Human Cells by an Optimized CRISPR/Cas System. *Cell* 155, 1479–1491.doi:10.1016/j.cell.2013.12.001

Cho, W. K., Spille, J. H., Hecht, M., Lee, C., Li, C., Grube, V., et al. (2018). Mediator and RNA Polymerase II Clusters Associate in Transcription-dependent Condensates. *Science* 361, 412–415. doi:10.1126/science.aar4199

Dekker, J., and Mirny, L. (2016). The 3D Genome as Moderator of Chromosomal Communication. *Cell* 164, 1110–1121. doi:10.1016/j.cell.2016.02.007

Dixon, J. R., Selvaraj, S., Yue, F., Kim, A., Li, Y., Shen, Y., et al. (2012). Topological Domains in Mammalian Genomes Identified by Analysis of Chromatin Interactions. *Nature* 485, 376–380. doi:10.1038/nature11082

Finan, J. D., and Guilak, F. (2010). The Effects of Osmotic Stress on the Structure and Function of the Cell Nucleus. *J. Cell Biochem.* 109, 460–467. doi:10.1002/jcb.22437

Fudenberg, G., Imakaev, M., Lu, C., Goloborodko, A., Abdennur, N., and Mirny, L. A. (2016). Formation of Chromosomal Domains by Loop Extrusion. *Cell Rep.* 15, 2038–2049. doi:10.1016/j.celrep.2016.04.085

Ganji, M., Shaltiel, I. A., Bisht, S., Kim, E., Kalichava, A., Haering, C. H., et al. (2018). Real-time Imaging of DNA Loop Extrusion by Condensin. *Science* 360, 102–105. doi:10.1126/science.aar7831

Gu, B., Swigut, T., Spencley, A., Bauer, M. R., Chung, M., Meyer, T., et al. (2018). Transcription-coupled Changes in Nuclear Mobility of Mammalian Cis-Regulatory Elements. *Science* 359, 1050–1055. doi:10.1126/science.aao3136

Hilbert, L., Sato, Y., Kuznetsova, K., Bianucci, T., Kimura, H., Julicher, F., et al. (2021). Transcription Organizes Euchromatin via Microphase Separation. *Nat. Commun.* 12, 1360. doi:10.1038/s41467-021-21589-3

Hyman, A. A., Weber, C. A., and Julicher, F. (2014). Liquid-liquid Phase Separation in Biology. *Annu. Rev. Cell Dev. Biol.* 30, 39–58. doi:10.1146/annurev-cellbio-100913-013325

Jacob, S. T., Sajdel, E. M., and Munro, H. N. (1970). Specific Action of Alpha-Amanitin on Mammalian RNA Polymerase Protein. *Nature* 225, 60–62. doi:10.1038/225060b0

Kirk, J. M. (1960). The Mode of Action of Actinomycin D. *Biochim. Biophys. Acta* 42, 167–169. doi:10.1016/0006-3002(60)90769-1

Moyzis, R. K., Buckingham, J. M., Cram, L. S., Dani, M., Deaven, L. L., Jones, M. D., et al. (1988). A Highly Conserved Repetitive DNA Sequence, (TTAGGG)n, Present at the Telomeres of Human Chromosomes. *Proc. Natl. Acad. Sci. U. S. A.* 85, 6622–6626. doi:10.1073/pnas.85.18.6622

Nora, E. P., Goloborodko, A., Valton, A. L., Gibcus, J. H., Uebersohn, A., Abdennur, N., et al. (2017). Targeted Degradation of CTCF Decouples Local Insulation of Chromosome Domains from Genomic Compartmentalization. *Cell* 169, 930–944 e922. doi:10.1016/j.cell.2017.05.004

Nora, E. P., Lajoie, B. R., Schulz, E. G., Giorgetti, L., Okamoto, I., Servant, N., et al. (2012). Spatial Partitioning of the Regulatory Landscape of the X-Inactivation Centre. *Nature* 485, 381–385. doi:10.1038/nature11049

Oudelaar, A. M., and Higgs, D. R. (2021). The Relationship between Genome Structure and Function. *Nat. Rev. Genet.* 22, 154–168. doi:10.1038/s41576-020-00303-x

Pawluk, A., Amrani, N., Zhang, Y., Garcia, B., Hidalgo-Reyes, Y., Lee, J., et al. (2016). Naturally Occurring Off-Switches for CRISPR-Cas9. *Cell* 167, 1829–1838 e1829. doi:10.1016/j.cell.2016.11.017

Peterlin, B. M., and Price, D. H. (2006). Controlling the Elongation Phase of Transcription with P-TEFb. *Mol. Cell* 23, 297–305. doi:10.1016/j.molcel.2006.06.014

Qian, H., Sheetz, M. P., and Elson, E. L. (1991). Single Particle Tracking. Analysis of Diffusion and Flow in Two-Dimensional Systems. *Biophys. J.* 60, 910–921. doi:10.1016/s0006-3495(91)82125-7

Rao, S. S., Huntley, M. H., Durand, N. C., Stamenova, E. K., Bochkov, I. D., Robinson, J. T., et al. (2014). A 3D Map of the Human Genome at Kilobase Resolution Reveals Principles of Chromatin Looping. *Cell* 159, 1665–1680. doi:10.1016/j.cell.2014.11.021

Rowley, M. J., and Corces, V. G. (2018). Organizational Principles of 3D Genome Architecture. *Nat. Rev. Genet.* 19, 789–800. doi:10.1038/s41576-018-0060-8

Sabari, B. R., Dall'Agnese, A., Boija, A., Klein, I. A., Coffey, E. L., Shrinivas, K., et al. (2018). Coactivator Condensation at Super-enhancers Links Phase Separation and Gene Control. *Science* 361. doi:10.1126/science.aar3958

Sabari, B. R., Dall'Agnese, A., and Young, R. A. (2020). Biomolecular Condensates in the Nucleus. *Trends Biochem. Sci.* 45, 961–977. doi:10.1016/j.tibs.2020.06.007

Sanborn, A. L., Rao, S. S., Huang, S. C., Durand, N. C., Huntley, M. H., Jewett, A. I., et al. (2015). Chromatin Extrusion Explains Key Features of Loop and Domain Formation in Wild-type and Engineered Genomes. *Proc. Natl. Acad. Sci. U. S. A.* 112, E6456–E6465. doi:10.1073/pnas.1518552112

Saxton, M. J. (1997). Single-particle Tracking: the Distribution of Diffusion Coefficients. *Biophys. J.* 72, 1744–1753. doi:10.1016/s0006-3495(97)78820-9

Symmons, O., Pan, L., Remeseiro, S., Aktas, T., Klein, F., Huber, W., et al. (2016). The Shh Topological Domain Facilitates the Action of Remote Enhancers by Reducing the Effects of Genomic Distances. *Dev. Cell* 39, 529–543. doi:10.1016/j.devcel.2016.10.015

Titov, D. V., Gilman, B., He, Q. L., Bhat, S., Low, W. K., Dang, Y., et al. (2011). XPB, a Subunit of TFIIH, Is a Target of the Natural Product Triptolide. *Nat. Chem. Biol.* 7, 182–188. doi:10.1038/nchembio.522

Weimann, L., Ganzinger, K. A., McColl, J., Irvine, K. L., Davis, S. J., Gay, N. J., et al. (2013). A Quantitative Comparison of Single-Dye Tracking Analysis Tools Using Monte Carlo Simulations. *PLoS One* 8, e64287. doi:10.1371/journal.pone.0064287

Conflict of Interest: The authors declare that the research was conducted in the absence of any commercial or financial relationships that could be construed as a potential conflict of interest.

Publisher's Note: All claims expressed in this article are solely those of the authors and do not necessarily represent those of their affiliated organizations, or those of the publisher, the editors, and the reviewers. Any product that may be evaluated in this article, or claim that may be made by its manufacturer, is not guaranteed or endorsed by the publisher.

frontiers | Frontiers in Cell and Developmental Biology

ORIGINAL RESEARCH
published: 19 July 2022
doi: 10.3389/fcell.2022.931237

Nuclear Localization Signals for Optimization of Genetically Encoded Tools in Neurons

Maksim M. Karasev[1], *Mikhail Baloban*[2], *Vladislav V. Verkhusha*[1,2] *and Daria M. Shcherbakova*[2]*

[1]Medicum, Faculty of Medicine, University of Helsinki, Helsinki, Finland, [2]Department of Genetics and Gruss-Lipper Biophotonics Center, Albert Einstein College of Medicine, Bronx, NY, United States

Nuclear transport in neurons differs from that in non-neuronal cells. Here we developed a non-opsin optogenetic tool (OT) for the nuclear export of a protein of interest induced by near-infrared (NIR) light. In darkness, nuclear import reverses the OT action. We used this tool for comparative analysis of nuclear transport dynamics mediated by nuclear localization signals (NLSs) with different importin specificities. We found that widely used KPNA2-binding NLSs, such as Myc and SV40, are suboptimal in neurons. We identified uncommon NLSs mediating fast nuclear import and demonstrated that the performance of the OT for nuclear export can be adjusted by varying NLSs. Using these NLSs, we optimized the NIR OT for light-controlled gene expression for lower background and higher contrast in neurons. The selected NLSs binding importins abundant in neurons could improve performance of genetically encoded tools in these cells, including OTs and gene-editing tools.

Keywords: nuclear localization signal, nuclear transport, importins, neurons, optogenetic tools, near-infrared

OPEN ACCESS

Edited by:
Yingxiao Wang,
University of California, San Diego, United States

Reviewed by:
Kai Zhang,
University of Illinois at Urbana-Champaign, United States
Ken Berglund,
Emory University, United States

***Correspondence:**
Daria M. Shcherbakova
daria.shcherbakova@einsteinmed.edu

Specialty section:
This article was submitted to Signaling, a section of the journal Frontiers in Cell and Developmental Biology

Received: *28 April 2022*
Accepted: *24 June 2022*
Published: *19 July 2022*

Citation:
Karasev MM, Baloban M, Verkhusha VV and Shcherbakova DM (2022) Nuclear Localization Signals for Optimization of Genetically Encoded Tools in Neurons. Front. Cell Dev. Biol. 10:931237. doi: 10.3389/fcell.2022.931237

INTRODUCTION

Neurons are highly specialized cells that perform integration of input signals at individual synapses and require communication between distant parts of the cell with its soma containing the nucleus. Therefore, nuclear transport is also specialized. In neurons, importins transport proteins from synapses along axons and dendrites to the nucleus, in addition to active nuclear import in the soma (Lever et al., 2015).

Optogenetic tools (OTs) allow control of cellular processes at a precise time and spatial location defined by instigators. Non-opsin OTs are used for light-induced protein-protein interactions, protein degradation, and activation of signaling cascades, etc. (Ma et al., 2017; Rost et al., 2017; Varady and Distel, 2020). The functionality of some of these tools depends on nuclear transport and, therefore, may vary in different cell types.

Interaction of nuclear localization signals (NLSs) with nuclear transport receptors, karyopherins, is required for active nuclear transport (Cautain et al., 2015; Eibauer et al., 2015). The karyopherin protein family consists of two subfamilies: karyopherin-α (KPNA, importins) and karyopherin-β (KPNB, importins, exportins, and bidirectional transporters) (Cautain et al., 2015). The human genome encodes seven KPNA isoforms, which are classified into clades or families α1, α2, and α3 (Goldfarb et al., 2004; Kelley et al., 2010). KPNA isoforms demonstrate substrate preference (Köhler et al., 1999; Pumroy and Cingolani, 2015; Kimura et al., 2017), however, there are functional redundancies in cargo binding specificity (Ushijima et al.,

2005; Friedrich et al., 2006; Mackmull et al., 2017). The expression of karyopherins varies across different cell and tissue types, and developmental stages (Quan et al., 2008; Pumroy and Cingolani, 2015).

Classical NLSs, such as SV40 large T antigen NLS and Myc NLS, bind KPNA leading to a formation of a complex KPNB1-KPNA-[NLS-cargo], which translocates through the nuclear pore to the nucleus (Cautain et al., 2015). Non-classical NLSs bind KPNB directly without interacting with KPNA (Chook and Süel, 2011). The most studied example of them is the so-called PY-NLS group that is recognized by TNPO1 (Chook and Süel, 2011).

Several factors influence nuclear import: NLS affinity (Efthymiadis et al., 1997; Xiao et al., 1998; Hodel et al., 2006; Timney et al., 2006; Yang et al., 2010), amino acids surrounding NLS (Xiao et al., 1998; Friedrich et al., 2006), protein phosphorylation (Nardozzi et al., 2010), and protein cargo size (Hodel et al., 2006; Böhm et al., 2017). NLS affinity directly correlates with the cargo distribution between the nucleus and the cytoplasm (nucleocytoplasmic ratio) in steady-state, as well as with the rate of nuclear import.

Several non-opsin OTs utilize light control of nuclear localization to regulate the activity of proteins by keeping them inaccessible in the dark and releasing them under illumination (Di Ventura and Kuhlman, 2016). These tools use different light-sensing protein modules. Red-light (660 nm) controlled heterodimeric protein-protein interaction between plant PhyB photoreceptor and its interacting protein PIF were adapted for light-induced nuclear translocation of a protein of interest (Beyer et al., 2015; Juillot et al., 2016; Noda and Ozawa, 2018). The limitations of PhyB-PIF are a requirement to supply exogenous chromophore phycocyanobilin and high light sensitivity to dim ambient light complicating system handling (Pathak et al., 2014).

Several single-component blue-light sensing OTs for nuclear transport were engineered based on the AsLOV2 domain from *Avena sativa* phototropin 1. In these tools, an NLS or a nuclear export signal (NES) was incorporated into the C-terminal Jα helix of AsLOV2 to make them inaccessible in the darkness and "uncaged" under illumination when the Jα helix is undocked and unfolded (Niopek et al., 2014, 2016; Yumerefendi et al., 2015, 2016). Example applications of these OTs include light control of mitosis initiation (Niopek et al., 2014), gene expression (Niopek et al., 2014, 2016; Yumerefendi et al., 2015, 2016), light control of CRM1 binding NES to prevent nuclear export of cargoes (Niopek et al., 2016). *As*LOV2 provides advantages of relatively small size (app. 16 kDa) and usage of flavin chromophores that is ubiquitously present in many cell types. The main limitation of the *As*LOV2-based systems is the requirement for blue light. In addition to poor penetration in tissues (Rumyantsev et al., 2016), blue light is toxic (Marek et al., 2019) and can alter neurons morphology (Diaz Vera et al., 2021) and physiology by activating the expression of immediate-early genes (Tyssowski and Gray, 2019).

Near-infrared (NIR) light above 700 nm is minimally toxic, penetrates deep in tissue (Rumyantsev et al., 2016), and does not influence the behavior of small animals, which cannot see it (Peirson et al., 2018). As a light-sensing module, NIR OTs use bacterial phytochrome photoreceptors incorporating endogenously available chromophore biliverdin (BV). Bacterial phytochrome BphP1 from *Rhodopseudomonas palustris* senses 720–780 nm. In the darkness, BphP1 adopts the Pfr state (inactive) with the absorbance maximum at 760 nm. Upon illumination, it undergoes photoconversion into the Pr state (active) with the absorbance maximum at 680 nm. In the Pr state, it binds PpsR2 (Kaberniuk et al., 2016) or its small engineered derivative QPAS1 (Redchuk et al., 2017). BphP1 was used in several OTs for the regulation of transcription (Kaberniuk et al., 2016; Redchuk et al., 2017, 2018b, 2018a), intracellular protein targeting (Redchuk et al., 2017; 2018b; 2018a, 2020), and cell signaling control (Kaberniuk et al., 2016; Redchuk et al., 2020). Non-invasive control of bacteriophytochome-based OTs was demonstrated in living mice (Kaberniuk et al., 2016; Shao et al., 2017; Fomicheva et al., 2019; Wu et al., 2020; Wang et al., 2021; Yu et al., 2022). The functionality of light-induced BphP1-QPAS1 interaction was also shown in primary neurons (Redchuk et al., 2018b).

In this study, we developed a NIR light-controlled OT for nuclear export of a protein of interest. Using this OT, we identified a difference in nuclear transport dynamics for widely used Myc NLS in primary cortical neurons and non-neuronal cells. Therefore, we further applied this OT to study the nuclear transport dynamics of uncommon NLSs with various importin specificities. We found NLSs that allow fast nuclear import in neurons and showed that the performance of the NIR OT for nuclear export can be adjusted. Using selected NLSs, we optimized a NIR light-activated gene expression system for lower background and higher contrast in neurons.

RESULTS

Development of an OT for NIR Light-Controlled Nuclear Export

As a light sensing module, we used a BphP1-QPAS1 pair interacting under 720–780 nm illumination (**Figure 1A**). We screened NLS and NES combinations in the two protein fusions corresponding to the nuclear component (NC) carrying a cargo protein of interest and the cytoplasmic component (CC) in 293T and HeLa cells. As a model cargo, we used mCherry fused with M13 calmodulin-binding peptide and a fragment of split tobacco etch virus protease. We tested a set of Myc NLS mutants that differed in affinity to importin *a* (Hodel et al., 2001) (**Figure 1B**) in combination with NES signals: strong Super-PKI-2 NES (Güttler et al., 2010) and weaker NES of HIV-1 Rev (Fischer et al., 1995).

Initially, we aimed to develop the CC that would shuttle between the nucleus and the cytoplasm and pull the NC to the cytoplasm upon illumination. We tried both members of the BphP1-QPAS1 optogenetic pair as the NC and the CC. Bulkier BphP1 (80 kDa) fused to cargo as the NC (102 kDa) should not diffuse to the cytoplasm (**Supplementary Figure S1A**). We identified a combination that resulted in partial relocalization of the BphP1-containing NC to the cytoplasm

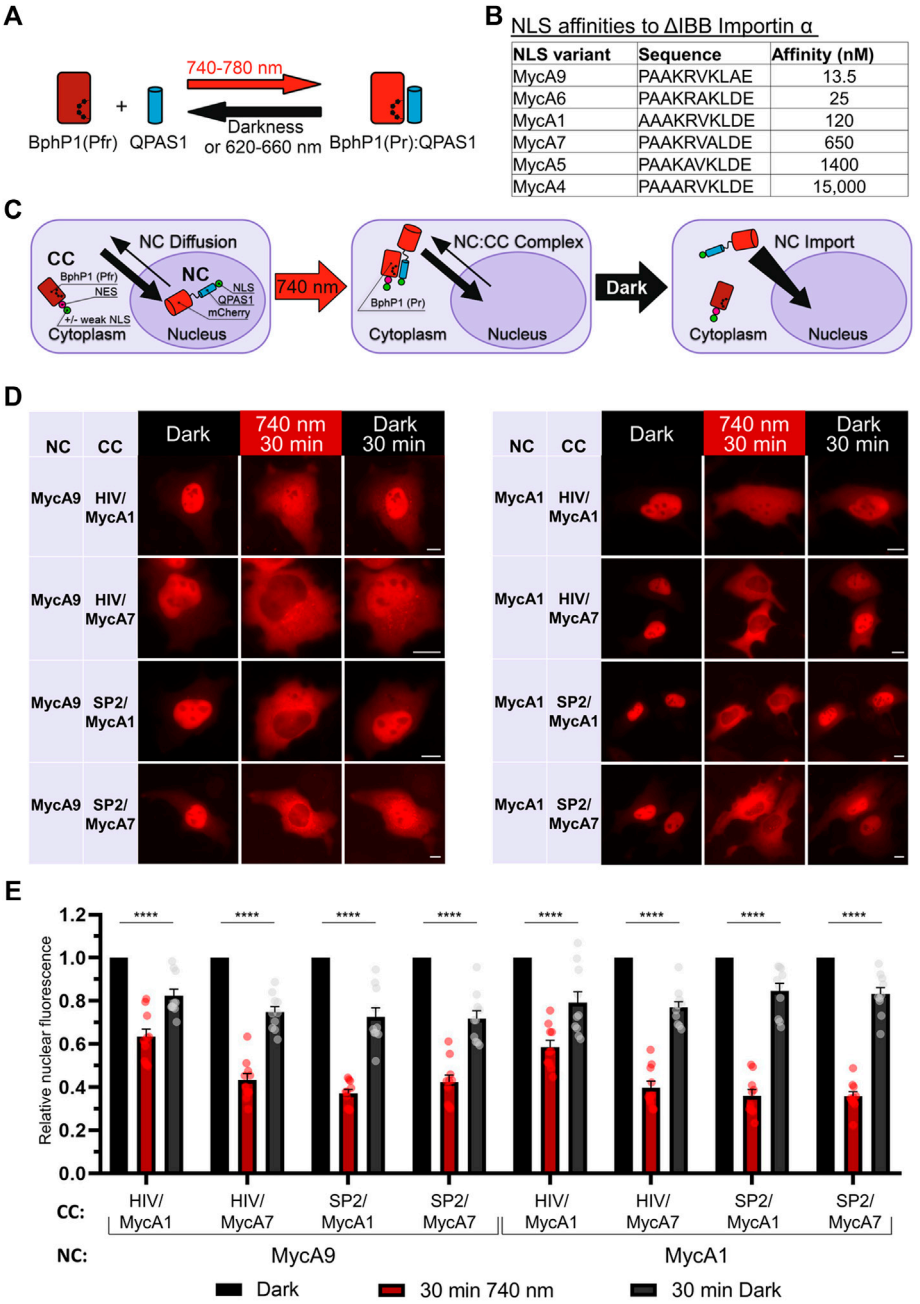

FIGURE 1 | Development of a NIR OT for light-controlled nuclear export. **(A)** Schematic representation of the BphP1-QPAS1 NIR light-induced interaction. **(B)** A selected range of Myc NLS mutants with measured affinities to importin *a* with deleted importin *β*-binding domain (ΔIBB) (Hodel et al., 2001) (*n* = 10). **(C)** Model of interaction for the NIR OT design with the QPAS1-based nuclear component (NC) and the BphP1-based cytoplasmic component (CC). In darkness, the NC is sequestered in the nucleus with its negligible amount diffusing to the cytoplasm. Under illumination, it re-localizes to the cytoplasm through interaction with the CC that contains strong NES. In darkness, the NC:CC complex dissociates, and the NC is imported back to the nucleus. **(D)** Representative images of the mCherry-labeled NC obtained with widefield microscopy in living HeLa cells. Points before illumination, after 30 min of 740 nm light illumination, and after subsequent 30 min in darkness are shown. Scale bar, 10 μm. **(E)** Quantification of relative nuclear fluorescence of the NC for the NC-CC combinations displayed on **(D)**. Mean values for individual cells ± S.E.M. were calculated (*n* = 10). Statistical significance was determined using one-way ANOVA and Tukey's test. ****$p < 0.0001$. SP2—Super-PKI-2 NES; HIV—HIV-1 Rev NES.

under light (**Supplementary Figure S1B**). The working QPAS1-based CC variants contained weaker MycA7 and MycA5 NLSs. Still, this relocalization was inefficient (**Supplementary Figure S1C**). We did not observe any relocalization with the CC variant with no NLS, which indicates that shuttling of the QPAS1-based CC component is critical.

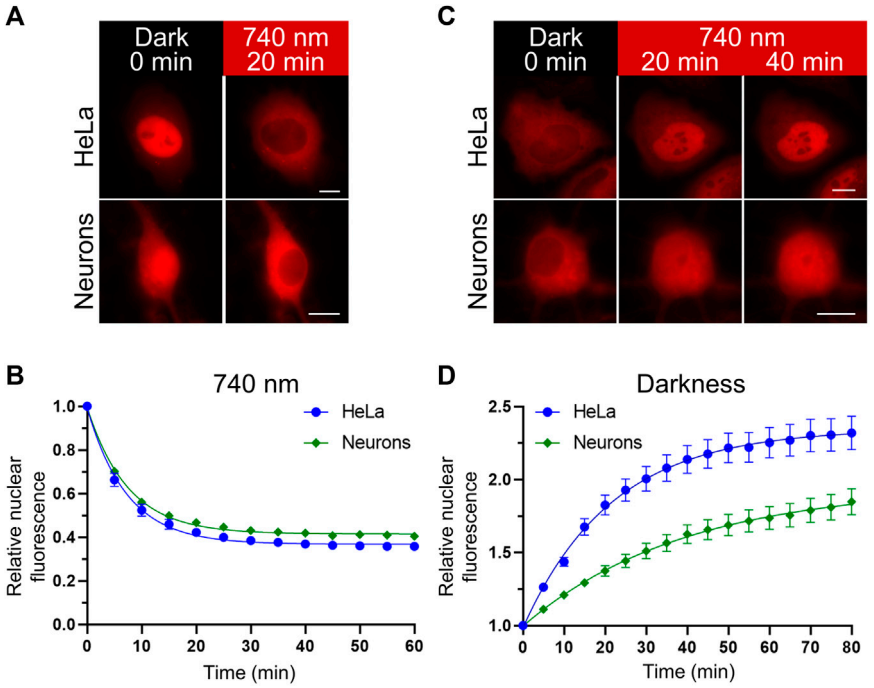

FIGURE 2 | Nuclear transport dynamics in non-neuronal cells and neurons. **(A,C)** Representative images showing relocalization of the mCheery-labeled NC in HeLa and primary rat cortical neurons (at days *in vitro* (DIV) 11) upon NIR (740 nm) light illumination **(A)** and subsequent darkness **(C)** captured with widefield fluorescence microscopy in living cells. Scale bar, 10 μm. **(B,D)** Quantification of the NC relocalization dynamics corresponding to **(A,C)** respectively. Mean values ± S.E.M. were calculated for individual cells (n = 20 each).

Alternatively, we used the BphP1-based CC and the NC containing QPAS1 fused to NLS and the cargo (**Figure 1C**). In this setup, we used strong NES and weak or no NLS on the large BphP1-containing CC (86 kDa) and the strong NLSs on the smaller diffusing NC. We found that the NC size at the border of the diffusion limit (67 kDa) enabled both 1) its sequestration in the nucleus and 2) its diffusion to the cytoplasm. Under illumination, the NC efficiently re-localized to the cytoplasm (**Figures 1D,E**) through interaction with the BphP1-containing CC. The NC variants containing MycA9 and weaker MycA1 NLSs relocalized similarly (**Figure 1E**) in combination with the CC with strong Super-PKI2 NES. We found that removing NLS entirely from the CC did not influence the performance (**Supplementary Figure S2**). This indicates that the diffusion of the NC, not the shuttling of the CC, is the main mechanism behind the light-induced NC relocalization (**Figure 1C**). In darkness, BphP1 released the QPAS1-containing NC that returned to the nucleus. The final OT contained QPAS1 fused with the cargo and a strong MycA9 NLS as the NC and BphP1 fused with a strong Super-PKI2 NES with (or without) attached weak MycA1 NLS as the CC.

Nuclear Transport Dynamics in Neuronal and Non-neuronal Cells

We compared the kinetics of the nuclear transport obtained with the NIR OT in HeLa and primary rat cortical neuronal cultures (**Figure 2**). We detected relocalization of the mCherry-labelled NC in live cells. Upon illumination, the NC was efficiently exported in both cell types. The estimated export half-times ($\tau_{1/2}$) for HeLa and neurons were 5.05 and 5.18 min, respectively (**Figures 2A,B**). Then we compared the kinetics of nuclear import in darkness. We observed a significant difference in the NC nuclear import rates between HeLa and neurons (**Figures 2C,D**). The estimated import half-time for primary neurons was 27.28 min, which is almost twice higher than for HeLa ($\tau_{1/2}$ = 15.05 min). Besides the nuclear import, these measured half-times include the relatively short time needed for QPAS1 release from BphP1 [the BphP1-QPAS1 dissociation was measured as ~4.4 min in darkness (Redchuk et al., 2017)].

Selection of Uncommon NLSs Mediating Fast Nuclear Transport in Neurons

To find a reason for a difference in nuclear import kinetics, we turned to available data on expression levels of importin *a* isoforms in neuronal and non-neuronal cells. Transcriptome analysis of neuronal tissue showed a strikingly low level of transcripts for two importins forming clade *α*2: KPNA2 and KPNA7 (Hodge et al., 2019) in cortical neurons (**Figure 3A**). Lower or absent expression of KPNA2 in mice neural tissue also was shown in an earlier study (Hosokawa et al., 2008). At the same time, the level of KPNA2 in baseline transcription profiling data for HeLa was relatively high (Bekker-Jensen et al., 2017) (**Supplementary Figure S3**).

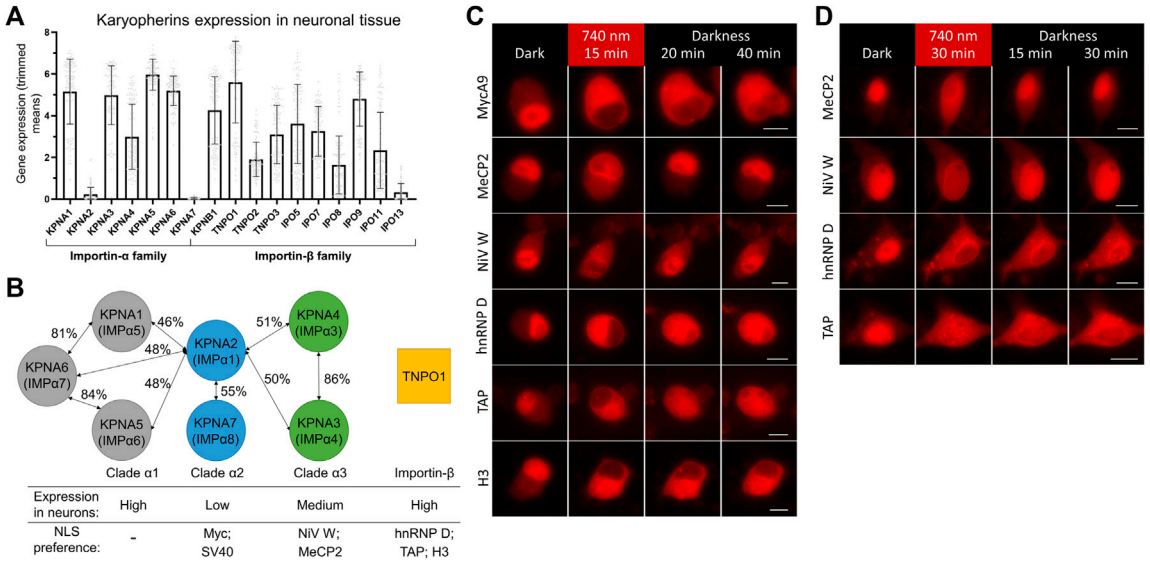

FIGURE 3 | Screening of NLSs with different importin specificities to improve nuclear import dynamics in neurons. **(A)** Neuronal tissue transcriptome profiling for karyopherins built using Human Multiple Cortical Areas SMART-seq dataset (Hodge et al., 2019). Data for neuronal cells are grouped by importin gene. Bars represent mean gene expression values (±SD) for all cortical neuronal sub-types determined by single cell gene expression profiling. **(B)** Schematics of three clades of human importin *a* proteins and TNPO1 transporter from the importin *β* family. Percentages of protein homology between importin *a* isoforms are specified (Goldfarb et al., 2004; Kelley et al., 2010). Relative importin expression levels and selected NLSs specificities are indicated. **(C,D)** Representative fluorescent images of the mCherry-labeled NC in living N2a cells **(C)** and cultured primary neurons at DIV 10 **(D)** expressing the NIR OT for light-controlled nuclear export with different NLSs. Points before illumination and after 15 min of 740 nm light illumination at indicated time points are shown. Scale bar, 10 μm.

It was shown that SV40 and Myc NLSs bind preferentially KPNA2, less strongly KPNA1, and only weakly KPNA4 (Miyamoto et al., 1997; Nadler et al., 1997) and KNPA3 (Nachury et al., 1998). Interestingly, peptide library screening showed that optimal sequences for binding to KPNA2 are very close to SV40 NLS (Yang et al., 2010). KPNA2 preference and its strikingly low expression level in neurons suggest an explanation for a slower import of Myc NLS, and possibly related SV40 NLS, compared to non-neuronal cells.

To find alternative NLSs that mediate fast and efficient nuclear transport, we decided to test NLSs that have importin preferences other than KPNA2. We searched the literature for short high-affinity NLSs, which have been shown to work in fusion with heterologous proteins. We selected five NLSs preferably binding KPNA3, KPNA4, or TNPO1 (**Figure 3B**). First, the NLS of W protein of Nipah virus (NiV W) preferentially binds KPNA4 and KPNA3 with high affinity (K_D is 14.4 nM for KPNA4) (Smith et al., 2018). Second, the NLS identified as a 249–272 region of methyl-CpG binding protein 2 (MeCP2) primarily binds KPNA3 and KPNA4 (Baker et al., 2015). Then, NLSs of heterogeneous nuclear ribonucleoprotein (hnRNP) D and transporter associated with antigen processing (TAP) proteins binding TNPO1 with K_D values of 3.2 and 17 nM, respectively (Imasaki et al., 2007). Finally, the N-terminal tail of histone H3 was shown to bind seven importins with a preference for TNPO1 and IPO5 with K_D values of 77 and 57 nM, respectively (Soniat and Chook, 2016; Soniat et al., 2016).

We tested selected NLSs for their nuclear transport dynamics using the developed OT in live-cell imaging, as described above. For faster turn-around, we first performed screening in neuroblastoma N2a cells, which showed MycA9 import kinetics close to that observed in neurons (**Supplementary Figure S4**). All variants showed nuclear localization of mCherry in darkness and its export to the cytoplasm upon NIR light illumination (**Figure 3C**). This relocalization was slightly less efficient for MeCP2 and NiV W NLSs. While nuclear recovery of the QPAS1-cargo fusions in darkness was inefficient within 40 min for MycA9 NLS (**Figure 3C**), MeCP2 and NiV W showed almost complete re-localization by this time point. hnRNP D and TAP NLS variants showed partial nuclear recovery. The H3 NLS demonstrated almost no recovery, thus, we excluded this variant from further tests.

Next, we tested these constructs in cultured primary cortical neurons (**Figure 3D**). Again, MeCP2 and NiV W NLS variants showed less efficient relocalization to the cytoplasm after illumination, but more complete recovery at 30 min in darkness. The hnRNP D NLS showed complete relocalization to the cytoplasm but demonstrated slower recovery in darkness. Relocalization and recovery for TAP NLS were slower than observed in N2a and we excluded this NLS from further tests.

Characterization of the Selected Uncommon NLSs in Neurons

Since it is known that importin localization may be influenced by neuronal activity (Thompson et al., 2004; Jeffrey et al., 2009) we tested light-mediated export and import of the NC containing MycA9, MeCP2, NiV W, hnRNP D NLSs in silenced (1 μM

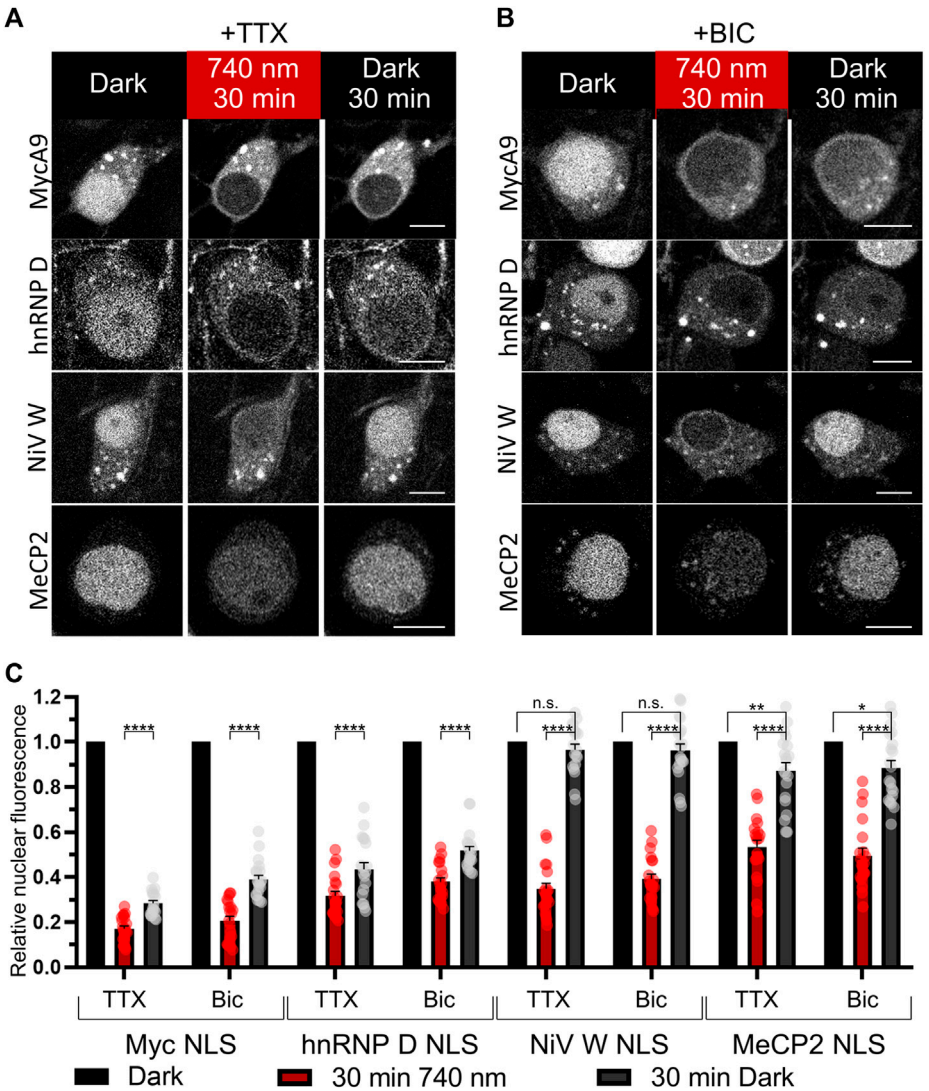

FIGURE 4 | Characterization of selected NLSs with the NIR OT for light-controlled nuclear export in neurons. **(A,B)** The mCherry-labeled NC in living primary cortical neurons expressing CC and different NC variants were imaged with confocal microscopy at DIV 16. Cells were treated with 1 μM tetrodotoxin (TTX) to silence **(A)** or 50 μM bicuculline (BIC) to stimulate neural activity **(B)** and illuminated with NIR light (740 nm) for 30 min followed by 30 min of darkness. Representative images are shown. Scale bar, 10 μm. **(C)** Quantification of relative nuclear fluorescence before illumination, after 30 min of NIR light, and after subsequent 30 min in darkness. Mean values for individual cells ± S.E.M. were calculated ($n = 20$). Statistical significance was determined using one-way ANOVA and Tukey's test. ****$p < 0.0001$, **$p = 0.0043$, *$p = 0.0118$, n. s.—no significance.

tetrodotoxin (TTX)) (**Figures 4A,C**) or stimulated (50 μM bicuculline (BIC)) neurons (**Figures 4B,C**). Only MycA9 NLS showed a low but statistically significant difference demonstrating smaller nuclear fluorescence recovery under TTX treatment (**Supplementary Figure S5A**). This quantitative experiment performed using confocal microscopy also reported relocalization efficiencies of the OTs with selected NLSs (**Figure 4C**). 30 min illumination resulted in the cytoplasmic release of approximately 80% NC for MycA9, 60–70% for NiV W and hnRNP D, and 50% for MeCP2 NLSs. Then 30 min in darkness resulted in the recovery of nuclear fluorescence 30–40% of initial values for MycA9, 40–50% for hnRNP D, 90–100% for NiV W, and 90% for MeCP2 NLSs.

Then we tested NiV W and hnRNP D NLS variants, which demonstrated both efficient light-induced export and relatively fast nuclear recovery, in comparative time-lapse wide-field microscopy imaging as above (**Supplementary Figure S5B,C**). Light-induced nuclear export dynamics were similar between variants ($\tau_{1/2}$ = 3.85, 5.81, 4.65 min for NiV W, hnRNP D, and MycA9 NLSs, respectively). Subsequent nuclear import in darkness demonstrated more than twice faster nuclear import for NiV W NLS ($\tau_{1/2}$ = 10.38 min),

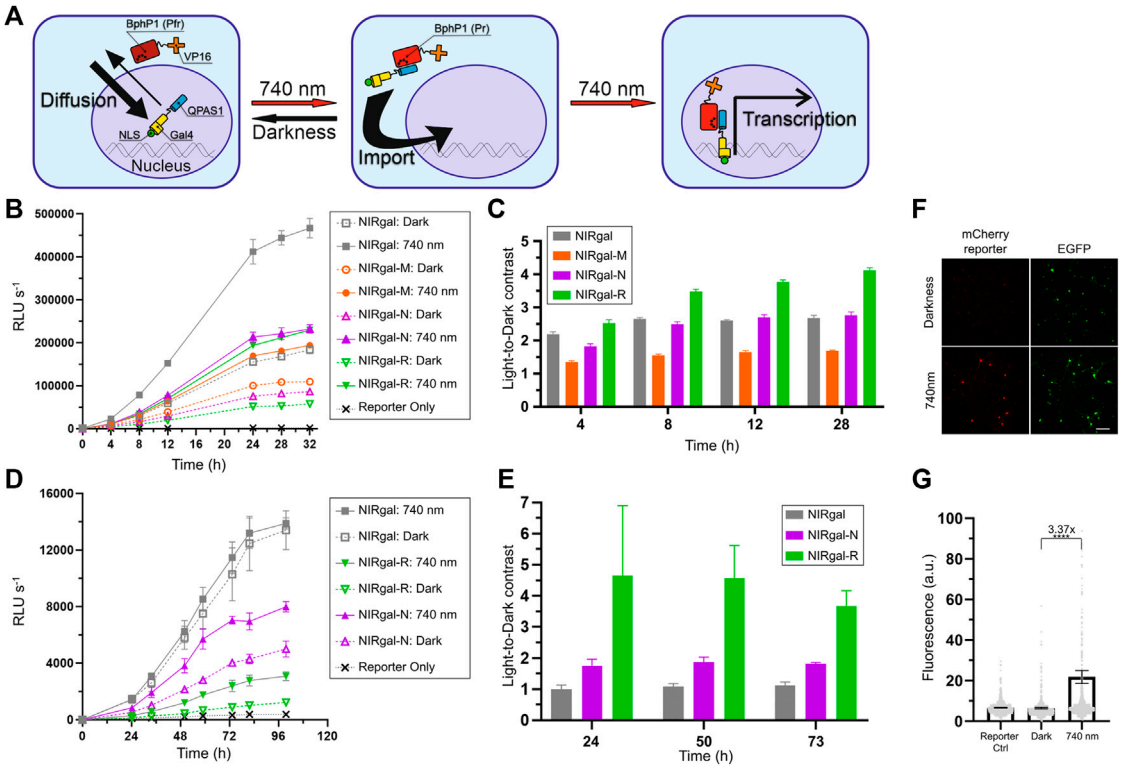

FIGURE 5 | Optimization of NIR OT for light-induced gene expression in neurons. **(A)** Schematics showing how nuclear transport is used in the system. Bulky BphP1-VP16 fusion (97 kDa) is located in the cytoplasm while diffusing smaller QPAS1-Gal4-NLS (39 kDa) is actively imported to the nucleus. Upon illumination, the BphP1 component is pulled to the nucleus through binding to the QPAS1 resulting in the expression of a UAS-controlled reporter gene. **(B–E)** *Gaussia* luciferase reporter expression over time for the system variants containing the selected NLSs in N2a cells **(B,C)** and primary neurons **(D,E)** in response to 740 nm light. Raw signals **(B,D)** corresponding to different illumination time and calculated light-to-dark contrasts **(C,E)** are shown (n = 3; error bars are S.E.M.). RLU, relative light unit. **(F)** Performance of the optimized NIRgal-R system with UAS-mCherry reporter in cultured primary neurons. Cultured cortical neurons were transduced with AAV2 mixture containing NIRgal-R system, UAS-mCherry reporter, and CAG-EGFP as a transduction marker at DIV 6. At DIV 9, neurons were illuminated for 72 h with NIR light (740 nm) or kept in darkness. Fixed cells were imaged with widefield fluorescence microscopy. Scale bar, 100 μm. **(G)** Quantification of the experiment described in **(F)**. mCherry reporter fluorescence is calculated in individual fixed cells identified using combined DAPI and EGFP masks. Mean values for individual cells ± S.E.M are shown (n > 500.). ****p < 0.0001 by Tukey's test.

compared to MycA9 ($\tau_{1/2}$ = 24.99 min). hnRNP D NLS also showed faster dynamics ($\tau_{1/2}$ = 18.50 min) than MycA9.

Thus, by varying NLSs, it is possible to adjust the dynamics and the extent of NIR light-controlled nuclear transport. NiV W NLS provided fast restoration of the initial system state in darkness, while originally tested MycA9 NLS allowed more efficient protein release from the nucleus accompanied by its slower return in darkness.

Additionally, we investigated how decreasing the NC size influences protein distribution. We substituted the linker between the cargo and mCherry with 2A self-cleaving peptide in the NCs with MycA9 and NiV W NLSs and tested their localizations in darkness and under NIR light in N2a cells using immunostaining (**Supplementary Figure S5D,E**). In darkness, the shorter NC with MycA9 (40.9 kDa) was distributed in various ratios between the nucleus and the cytoplasm (**Supplementary Figure S5D**). Under NIR light, it was fully exported to the cytoplasm. In contrast, the smaller NC with NiV W NLS (42.9 kDa) had similar distinct nuclear localization in darkness as the bigger NC (68.9 kDa) and was exported under NIR light (**Supplementary Figure S5E**). Therefore, NLSs influence both transport dynamics and the nucleocytoplasmic ratio, as expected.

Optimization of NIR OT for Light-Induced Gene Expression in Neurons

We reasoned that the performance of NLS-containing OTs in neurons can be improved by selecting NLS with optimal kinetics. We decided to apply selected NLSs to the BphP1-QPAS1-based NIR light-induced Gal4/UAS gene expression system (Redchuk et al., 2018b). This OT consists of two components encoded in a single AAV: BphP1 fused to a VP16 transcriptional activation domain and QPAS1 fused to Gal4 DNA-binding domain and SV40G7 NLS (**Figure 5A**). We named this system as NIRgal. In darkness, the components are mostly separated by the nuclear membrane, since large BphP1-VP16 (97 kDa) does not diffuse to the nucleus and QPAS1-Gal4-NLS (39 kDa), which diffuses to the cytoplasm, is actively

imported. Upon illumination, the components interact and are pulled to the nucleus to drive the expression of a UAS-controlled reporter gene. In contrast to the OT for the nuclear export developed above, the BphP1 component does not contain NES and can be imported to the nucleus in complex with the QPAS1-component. Therefore, NLS fused to QPAS1-GAL4 plays two roles in this OT. First, upon light illumination it is essential to pulling the assembled protein complex into the nucleus where the reporter DNA is located. Second, it is used to spatially separate reactive system components to different cellular compartments, thus limiting their background interaction in darkness. Such approach have been used in similar BphP1-based systems (Kaberniuk et al., 2016; Redchuk et al., 2018a) and photoactivatable split Cre recombinase (Meador et al., 2019). Therefore, the optimal NLS in NIRgal system should provide balance between active nuclear transport needed for strong system response and cytoplasmic availability to bind BphP1-VP16 component. To select such NLS, we performed experimental screening of NLSs with different properties.

We substituted SV40G7 NLS with MeCP2, NiV W, or hnRNP D NLSs in the NIRgal system producing NIRgal-M, NIRgal-N, and NIRgal-R, respectively. First, we tested these variants in N2a cells. We used secreted *Gaussia luciferase* (Gluc) as a reporter and monitored its expression over time using an assay with coelenterazine substrate. NIRgal-R showed the lowest dark background with a relatively high response to light (**Figure 5B**) providing the highest light-to-dark contrast (4.1-fold at 28 h) (**Figure 5C**). NIRgal produced the highest response to illumination accompanied by a high background in darkness too. Then, we tested the systems with the selected NLSs in neurons using the Gluc reporter (**Figures 5D,E**). Again, NIRgal-R demonstrated the highest light-to-dark contrast (4.6-fold at 50 h), compared to the NIRgal and NIRgal-N systems, which showed less than 2-fold maximal contrasts over time. Additionally, we proved the functionality of the NIRgal-R system in cultured primary neurons with mCherry reporter (**Figures 5F,G**).

DISCUSSION

In this work, we provide direct experimental evidence that commonly used NLSs, such as Myc and SV40 preferentially binding KPNA2 importin, promote slower nuclear import in neurons than in non-neuronal cells. We identified uncommon NLSs preferentially binding KPNA3, KPNA4, and TNPO1 transporters, which mediate faster nuclear import, and applied them to the engineering of OTs for use in neurons.

First, we developed the NIR light-controlled OT for the nuclear transport of a protein of interest. Upon 740–780 nm illumination, the protein is exported to the cytoplasm within minutes. In the darkness, it is transported back to the nucleus in time depending on the utilized NLS (no more than 30 min). We used this OT for direct characterization of nuclear import kinetics mediated by NLSs with different transporter specificities.

For widely used Myc NLS, we observed a considerable difference in the kinetics of nuclear import in neuronal and non-neuronal cells (**Figure 2**). It correlated with the difference in expression levels of a respective nuclear transporter. Myc and related SV40 NLSs preferably bind KPNA2, which is depleted in neurons (Hosokawa et al., 2008; Hodge et al., 2019) and abundant in HeLa cells (Bekker-Jensen et al., 2017). Earlier studies reported a correlation between the importin expression and the nucleocytoplasmic ratio in yeast (Timney et al., 2006) and mammalian cell lines (Zannini et al., 2003; Riddick and Macara, 2005, 2007; Hazawa et al., 2020). We directly demonstrated that the nuclear import dynamics is also affected. Overexpression of KPNA2 should result in faster kinetics of nuclear import for KPNA2-dependent Myc and SV40 NLSs (Riddick and Macara, 2005, 2007; Timney et al., 2006). However, upregulation of KPNA2 in neurons was correlated with neuronal apoptosis (Xu et al., 2016) and, therefore, can significantly alter cellular physiology.

We used the developed OT to screen uncommon NLSs preferentially binding more abundant transporters KPNA3, KPNA4, and TNPO1 with high affinity, to identify NLSs that mediate fast and efficient nuclear transport in neurons. We found the NLSs that mediate considerably faster nuclear import than MycA9: NiV W and MeCP2 NLSs binding KPNA3 and KPNA4, and hnRNP D NLS binding TNPO1. Abundant KPNA3 and KPNA4 isoforms play important roles in neuronal cell physiology and their dysregulation was linked to neurodegenerative diseases (Moore et al., 2020; Pasha et al., 2021). KPNA4 regulates chronic pain pathways in peripheral sensory neurons by mediating c-Fos nuclear import (Marvaldi et al., 2020). KPNA3 and KPNA4 were also studied regarding the transport of TAR DNA-binding protein 43 (TDP-43) and the formation of aggregates of this protein in the central nervous system (Pasha et al., 2021), which is a hallmark of many neurodegenerative diseases (Jo et al., 2020).

While this work was performed on primary cortical neurons, we hypothesize that our results and optimized NLSs are applicable to all neuronal subtypes. Indeed, KPNA2 was found downregulated throughout the brain and spinal cord but with a moderate expression level in the olfactory bulb and reticular system (Hosokawa et al., 2008). We explored the Allen Mouse Brain Atlas RNA *in situ* hybridization database (https://mouse.brain-map.org/search/index) (Lein et al., 2007) for the data on importin expression measured in different mouse brain structures (**Supplementary Figure S6**). We found that TNPO1 specific to hnRNP D NLS showed the highest expression level across all brain areas, while KPNA2 and KPNA7 specific to Myc and SV40 NLSs (Miyamoto et al., 1997; Nadler et al., 1997; Oostdyk et al., 2020) were downregulated in most brain areas. KPNA4 specific to NiV W and MeCP2 NLSs demonstrated expression levels higher than KPNA2 in all brain structures.

We found that neuronal activity slightly influenced the efficiency of nuclear transport for MycA9 NLS, in contrast to the other selected NLSs (**Supplementary Figure S5A**). This effect can be explained by the previous observation that nuclear localization of some nuclear receptors including KNPA2 decreases upon silencing of neural activity and increases upon stimulation (Thompson et al., 2004; Jeffrey et al., 2009).

Using uncommon NLSs characterized here in neurons, we adjusted and optimized the performance of NLS-containing OTs in neurons. By changing NLS in the NIR OT for nuclear export, it was possible to regulate the extent of the nuclear export of a protein of interest as well as the dynamics of nuclear import in the darkness that shuts the system down.

By varying NLS in the NIR OT for light-induced gene expression, we developed the system that produced a reliable response to light and low dark background (up to >4-fold light-to-dark contrast) in neurons. hnRNP D NLS attached to the QPAS1-containing NC enabled an optimal balance between spatial separation of QPAS1 and BphP1-containing fusions and their accessibility for interaction.

The optimized NIR OT for gene expression can be activated by the most red-shifted light of 780 nm sensed by natural photoreceptors. It should enable its combinations with OTs and biosensors controlled by different wavelengths of light, such as LOV-based OTs, without crosstalk (Redchuk et al., 2017). Also, it can replace blue light-controlled OTs (Yamada et al., 2018, 2020) to avoid blue light-mediated toxicity (Marek et al., 2019) and off-target activation of immediate-early genes in neurons (Tyssowski and Gray, 2019).

This study suggests that various NLS-containing genetically encoded tools can be optimized for their use in neurons by replacing common NLSs with the NLSs selected in this work. Examples of OT systems that should benefit from NLS optimization include blue light OTs that use NLSs caged on the *As*LOV2 domain (Niopek et al., 2014; Yumerefendi et al., 2015). We observed previously that the blue light-activated *As*LOV2-NLS module of the iRIS tool (Redchuk et al., 2017) showed less efficient nuclear import in N2a cells and primary neurons, compared to non-neuronal cell lines (Redchuk et al., 2018b). iRIS uses LOV2-caged Myc NLS (with P1M substitution) binding KPNA2 depleted in neurons. Also blue light-controlled systems for gene expression that use CRISPR-dCas9 (Nihongaki et al., 2015, 2017; Polstein and Gersbach, 2015; Bubeck et al., 2018) or transcription activator-like effector (TALE) (Konermann et al., 2013) could be optimized in neurons by varying NLSs.

This study should draw more attention to uncommon NLSs and their functionality in neurons. So far, TNPO1-specific M9 NLS of hnRNP A1 was proven to be superior to SV40 for gene delivery in neurons (Ma et al., 2002). Utilizing neuron-specific NLSs instead of common ones should be useful in technologies for neuronal delivery of therapeutic proteins in virus-like particles (Banskota et al., 2022). Beyond OTs, it was shown that the efficiency of all CRISPR-based systems can be improved by increasing their nuclear translocation (Torres-Ruiz et al., 2017; Maggio et al., 2020). We predict that employing NLSs described here will be advantageous for applications of CRISPR-Cas systems in neuroscience (Heidenreich and Zhang, 2016) including recently developed neuron-optimized CRISPR/Cas9 genome editing systems (Fang et al., 2021), CRISPR-based transcriptional activation (Savell et al., 2019) and inhibition (Zheng et al., 2018) systems as well as CRISPR-Cas13 for silencing of neurodegeneration-associated genes in neurons (Powell et al., 2022). To summarize, uncommon neuron-specific NLSs, including NiV W, MeCP2, and hnRNP D characterized here, should become useful building blocks for synthetic biology applications in neurons.

MATERIALS AND METHODS

Constructs and Cloning

All plasmids used in this study are listed in **Supplementary Table S1**. Annotated cDNA and amino acid sequences for optimized constructs are given in **Supplementary Note S1**.

For pAAV vectors designed in this work, we used short woodchuck hepatitis posttranscriptional regulatory element (WPRE3) and bovine growth hormone polyadenylation signal (bGHpA) (Choi et al., 2014). BphP1 and QPAS1 were cloned from Addgene plasmid #102584. All NLS and NES signals (see **Supplementary Table S2**) were cloned using synthesized oligonucleotides. Model cargo containing calmodulin-binding M13 peptide and C-terminal fragment of split tobacco etch virus protease was cloned from Addgene plasmid #92391.

The pAAV-U5-Gluc plasmid was generated by cloning the expression cassette to the pAAV backbone from the reporter vector pU5-Gluc (Wang et al., 2012). Then pAAV-U5-mCherry was obtained by substituting Gluc with mCherry.

DNA fragments for cloning were obtained using PCR amplification with Q5 DNA polymerase (New England Biolabs). Fragments were purified and concentrated using NucleoSpin Gel and PCR Clean-up Kit (Macherey-Nagel). Vector and fragments double-digestion and ligation were done using FastDigest restriction enzymes (Thermo Scientific) and T4 DNA Ligase (Thermo Scientific). Ligated plasmid products were introduced to TOP10 *Escherichia coli* cells using heat-shock transformation. Plasmids were purified using the NucleoSpin Plasmid Mini kit (Macherey-Nagel). Relevant genetic components were confirmed by Sanger sequencing (FIMM Genomics, University of Helsinki, Finland).

Cell Culture and Transfection

Human embryonic kidney 293T cells (CRL-1573, ATCC), human epithelioid cervix carcinoma cells (HeLa; CCL-2, ATCC), mouse neuroblastoma Neuro-2a cells (N2a; CCL-131, ATCC) were cultured in Dulbecco's modified Eagle's medium (DMEM; 41,965-039, Gibco) supplemented with 10% (vol/vol) fetal bovine serum (FBS; 10270106, Gibco) and 1% (vol/vol) Antibiotic-Antimycotic (15240062, Gibco). All cell lines were cultured at 37 C and 5% CO_2.

293T and N2a cells were transfected with Lipofectamine 2000 transfection reagent (11668027, Invitrogen). HeLa cells were transfected using Effectene (301427, Qiagen) or PEI transfection (24765, Polysciences).

For cell lines transfected with BphP1-based constructs, BV (FSIB655-9, CymitQuimica) was supplemented to the culture medium at 25 μM concentration. For primary neurons, we used 5–25 μM BV.

Primary Neuron Culture

Primary rat cortical neuronal cultures were prepared at the Neuronal Cell Culture Unit (University of Helsinki) accordingly to the protocol (Sahu et al., 2019). All animal work was performed following the ethical guidelines of the European Convention and regulations of the Ethics Committee for Animal Research of the University of Helsinki.

Dissociated cortical neurons were plated in 1,050 cells/mm^2 density to 35 mm Cellview glass-bottom dishes (627860, Greiner) for live-cell imaging, 12-well plate plastic coated with poly-L-lysine (0.5 mg/ml solution in 0.1 M borate buffer (Beaudoin et al., 2012), P2636, Sigma–Aldrich) for testing of NIR light-regulated gene expression system with Gluc reporter, and on 12 mm glass coverslips (in 24-well plate) coated with poly-L-lysine (as above) for testing of NIR light-regulated gene expression system with mCherry reporter. Cells were cultured in a complete neuronal media (CNM): neurobasal medium (12348017, Gibco) supplemented with 2% (vol/vol) B-27 Plus Supplement (A3582801, Gibco), 1% (vol/vol) GlutaMAX Supplement (35050061, Gibco), and 1% (vol/vol) penicillin-streptomycin (15140122, Gibco). One-third of culture media was renewed every 3 days, cells were maintained at 37 C and 5% CO_2.

AAV Preparation

AAV particles for delivery of genetic constructs to primary cultured neurons were prepared according to the protocol described in (Challis et al., 2019). All particles have an AAV2 serotype. The pDG plasmid combining pHelper plasmid and AAV2 capsid encoding plasmid was obtained as a gift from the AAV Core Facility of the University of Helsinki. AAV2 bearing CAG-EGFP was purchased from the AAV Core Facility of the University of Helsinki.

Fluorescence Microscopy

Widefield microscopy was performed using an Olympus IX83 inverted epifluorescence microscope equipped with a Xenon arc lamp (Lambda LS, Sutter). An ORCA-Flash4.0 V3 (Hamamatsu) camera was used for image acquisition. Cells were imaged using either a 20 × 0.75 NA air or a 60 × 1.35 NA oil objective lens (UPlanSApo, Olympus). HEK293T, HeLa, and N2a cells were imaged using 35 mm Cellview glass-bottom dishes (627860, Greiner) with a Live Cell Imaging Solution (Invitrogen, A14291DJ) in a humidified 37 C atmospheric chamber (Okolab). All images were captured using SlideBook (Intelligent Imaging Innovations) software.

Confocal imaging was performed with a Leica TCS SP8 microscope equipped with a 63 × 1.2 NA water (HC PL APO CS2) objective lens and several lasers (405, 488, 561, 594, and 633 nm), PMT, and HyD detectors. Images were captured using LAS X (Leica) software.

Cultured primary neurons were imaged in HEPES-based Tyrode's solution (5 mM KCl, app. 120 mM NaCl, 1 mM $MgCl_2$, 1.8 mM $CaCl_2$, 1.04 mM Na_2HPO_4, 26.2 mM $NaHCO_3$, 10.9 mM HEPES, and 10 mM D-glucose) pH 7.4. The osmolarity of Tyrode's solution was adjusted with NaCl to match present neuronal culture media using Micro-Osmometer Model 3,320 (Advanced Instruments).

NIR Light-Induced Export and Nuclear Import Dynamics

For capturing NIR light-induced export, NIR (3 mW/cm^2) illumination was applied using the custom-assembled 740/25 nm LED array (LED Engin). The light intensity was measured by a power meter (PM100D, Thorlabs).

We used the 1:2 NC:CC plasmid or AAV particles ratio for cell lines transfection and primary neurons transduction respectively, if not stated otherwise.

AAV transduction of cultured primary neurons was done at 6 days *in vitro* (DIV). We used a total multiplicity of infection (MOI) of 7.5×10^4 vg/cell. The imaging was done at DIV 10–16.

Z-stacks at multiple fields of view (FOVs) were captured at regular time intervals. Afterward, using Fiji ImageJ (Schindelin et al., 2012) we compiled time-lapse stacks selecting appropriate Z-planes for each time point to counter possible cell or FOV drift and performing stack alignment with Linear Stack Alignment with SIFT plugin. Photobleaching was corrected using a simple ratio method. To measure the dynamics of fluorescent intensity, the region of interest (ROI) for each cell was set on the cell nucleus avoiding nuclear membrane and nuclei for each timepoint. The background fluorescence was subtracted from mean fluorescence values for each cell, and then fluorescent intensity was normalized to the initial value. Graphs plotting and relocalization half-time values calculation with the nonlinear fitting was done using Prism 8 (GraphPad).

Testing NIR Light-Regulated Reporter Expression in Mammalian Cells

NIR light-regulated gene expression system variants have been tested in N2a cells and cultured primary cortical neurons.

N2a cells were transfected using Lipofectamine 2000 (11668027, Invitrogen), with the system-encoded plasmid and Gluc reporter plasmid. All samples were triplicated. 10 μM BV was added to DMEM media supplemented with 10% (vol./vol.) FBS. 12–24 h after transfection the media was renewed. Then half of the samples were left in darkness (in a non-transparent ventilated box) and another half were illuminated. Cells were illuminated directly in a CO_2 incubator with a 740/25 nm LED array (LED Engin) at 1 mW/cm^2 and a 25% duty cycle: 30 s of light and 90 s of darkness. Supernatant samples were collected at selected time points and stored at −20°C.

Cultured primary neurons were transduced at DIV6 with AAV2 mixture encoding the system variant and Gluc or fluorescent protein reporter in 2:1 system:reporter ratio (MOI 0.5×10^5 vg/cell). 25 μM BV was added to the media. At DIV9 the third of the media was renewed, and the experiment proceeded as described above for N2a. Collected supernatant samples containing secreted Gluc reporter were diluted in 5 mM NaCl PBS in 96-well half-area white plates (Costar). Then 5 μM coelenterazine (NanoLight Technology)

was added and bioluminescence signals were immediately measured using Victor X3 multilabel plate reader (PerkinElmer). The light-to-dark contrast was calculated as a ratio of luminescence signals of the illuminated sample to the sample kept in dark [values from the starting point were subtracted from respective samples; background signal generated by reporter alone (Reporter Only control sample) was subtracted from both signals values].

For the system characterization with microscopy, we used UAS-mCherry AAV as a reporter. Additional CAG-EGFP AAV was used as a transduction marker. Neurons were fixed after 3 days of NIR illumination (the same regimen as above) or darkness and imaged using Olympus IX83 microscope with 20 ×0.75 NA air objective lens. To calculate the response, more than ten FOVs of fixed neuron samples were captured in three channels: DAPI (excitation filter: 387/11 nm; emission filter: 480/40 nm), EGFP reporter (ex.f.: 485/20 nm; em.f.: 525/30 nm), and mCherry coexpressed protein (ex.f.: 560/25 nm; em.f.: 607/36 nm). For each sample, captured FOVs were processed in Fiji ImageJ (Schindelin et al., 2012) as follows. For DAPI and EGFP channels, separate masks were created using the AutoThreshold Triangle algorithm, which was then segmented using the Watershed algorithm. For DAPI, the segmented particles were limited by size (120–400 μm^2) and circularity (0.60–1.00) to eliminate debris and artefacts. Then, DAPI and EGFP masks were combined with the "AND create" function in DAPI & EGFP mask selecting nuclei of neurons expressing the EGFP marker (<120 μm^2 particles were excluded). The resulting mask was applied to the mCherry channel to measure the mean mCherry reporter fluorescence signal for each neuron. The resulting individual and mean fluorescence values were plotted using Prism 8 (GraphPad). The background signal in mCherry channel (quantified on the sample without mCherry reporter) was subtracted from values for all samples and the light-to-dark ratio was calculated.

Fixed Samples Preparation and Immunostaining

Cultured primary neurons were fixed with 4% paraformaldehyde (Pierce, 28908) supplemented with 4% of sucrose for 30 min at RT, washed three times with PBS, and mounted using ProLong Glass Antifade Mountant with NucB (P36981, Invitrogen).

For immunostaining of N2a cells (**Supplementary Figures S5D,E**), cells were fixed with 4% paraformaldehyde supplemented with 4% of sucrose for 30 min at RT, washed three times with ice-cold PBS, permeabilized for 5 min with methanol at −20°C, washed twice with ice-cold PBS and blocked with 2% BSA, 22.52 mg/ml glycine PBS for 1 h RT. Then samples were incubated with mouse-anti-HA antibodies (sc-7392; Santa-Cruz) 1:150 in 2% BSA wash buffer (PBS with 0.1% Tween 20) for 1 h RT. After wash, samples were incubated with goat anti-mouse-AlexaFluor488 (A32723; Invitrogen) 1: 1,000 in 2% BSA wash buffer for 1 h RT. Finally, samples were washed three times with the wash buffer and mounted using ProLong Glass Antifade Mountant with NucB (P36981, Invitrogen).

Statistical Analysis

Data acquisition and processing are described above for each experiment. Statistical significance was determined using one-way ANOVA and Tukey's test in Prism 8 (GraphPad), and significance was assigned at $^{****}p < 0.0001$, $^{***}p < 0.001$, $^{**}p < 0.01$, $^{*}p < 0.05$. The number of data points (n) and p values are indicated in the figures or figure legends.

DATA AVAILABILITY STATEMENT

The original contributions presented in the study are included in the article/**Supplementary Materials**, further inquiries can be directed to the corresponding author.

ETHICS STATEMENT

Ethical approval was not required. Primary rat cortical neuronal cultures were purchased from the Neuronal Cell Culture Unit (University of Helsinki). All animal work of the Unit was performed following the ethical guidelines of the European Convention and regulations of the Ethics Committee for Animal Research of the University of Helsinki.

AUTHOR CONTRIBUTIONS

MK performed all experiments and analyzed data with contributions from other authors. MB participated in the early designs of the optogenetic tool for nuclear export. VV and DS directed the project. MK and DS wrote the manuscript with contributions from all authors.

ACKNOWLEDGMENTS

We thank Olena Oliinyk (University of Helsinki) for useful suggestions. We thank the Biomedicum Imaging Unit, the Neuronal Cell Culture Unit, and the AAV Gene Transfer and Cell Therapy core facilities of the University of Helsinki for technical assistance. This work was supported by the grants GM122567 (to VV) and EY030705 (to DS) from the US National Institutes of Health, 322226 from the Academy of Finland (to VV), the Doctoral Programme in Biomedicine of the University of Helsinki (scholarship to MK), and by the grant from Orion Research Foundation (to MK).

SUPPLEMENTARY MATERIAL

The Supplementary Material for this article can be found online at: https://www.frontiersin.org/articles/10.3389/fcell.2022.931237/full#supplementary-material

REFERENCES

Baker, S. A., Lombardi, L. M., and Zoghbi, H. Y. (2015). Karyopherin α 3 and Karyopherin α 4 Proteins Mediate the Nuclear Import of Methyl-CpG Binding Protein 2. *J. Biol. Chem.* 290, 22485–22493. doi:10.1074/jbc.M115.658104

Banskota, S., Raguram, A., Suh, S., Du, S. W., Davis, J. R., Choi, E. H., et al. (2022). Engineered Virus-like Particles for Efficient *In Vivo* Delivery of Therapeutic Proteins. *Cell* 185, 250–265. e16. doi:10.1016/j.cell.2021.12.021

Beaudoin, G. M. J., Lee, S.-H., Singh, D., Yuan, Y., Ng, Y.-G., Reichardt, L. F., et al. (2012). Culturing Pyramidal Neurons from the Early Postnatal Mouse hippocampus and Cortex. *Nat. Protoc.* 7, 1741–1754. doi:10.1038/nprot.2012.099

Bekker-Jensen, D. B., Kelstrup, C. D., Batth, T. S., Larsen, S. C., Haldrup, C., Bramsen, J. B., et al. (2017). An Optimized Shotgun Strategy for the Rapid Generation of Comprehensive Human Proteomes. *Cell Syst.* 4, 587–599. e4. doi:10.1016/j.cels.2017.05.009

Beyer, H. M., Juillot, S., Herbst, K., Samodelov, S. L., Müller, K., Schamel, W. W., et al. (2015). Red Light-Regulated Reversible Nuclear Localization of Proteins in Mammalian Cells and Zebrafish. *ACS Synth. Biol.* 4, 951–958. doi:10.1021/acssynbio.5b00004

Böhm, J., Thavaraja, R., Giehler, S., and Nalaskowski, M. M. (2017). A Set of Enhanced Green Fluorescent Protein Concatemers for Quantitative Determination of Nuclear Localization Signal Strength. *Anal. Biochem.* 533, 48–55. doi:10.1016/j.ab.2017.06.015

Bubeck, F., Hoffmann, M. D., Harteveld, Z., Aschenbrenner, S., Bietz, A., Waldhauer, M. C., et al. (2018). Engineered Anti-CRISPR Proteins for Optogenetic Control of CRISPR-Cas9. *Nat. Methods* 15, 924–927. doi:10.1038/s41592-018-0178-9

Cautain, B., Hill, R., de Pedro, N., and Link, W. (2015). Components and Regulation of Nuclear Transport Processes. *FEBS J.* 282, 445–462. doi:10.1111/febs.13163

Challis, R. C., Ravindra Kumar, S., Chan, K. Y., Challis, C., Beadle, K., Jang, M. J., et al. (2019). Systemic AAV Vectors for Widespread and Targeted Gene Delivery in Rodents. *Nat. Protoc.* 14, 379–414. doi:10.1038/s41596-018-0097-3

Choi, J.-H., Yu, N.-K., Baek, G.-C., Bakes, J., Seo, D., Nam, H. J., et al. (2014). Optimization of AAV Expression Cassettes to Improve Packaging Capacity and Transgene Expression in Neurons. *Mol. Brain* 7, 17. doi:10.1186/1756-6606-7-17

Chook, Y. M., and Süel, K. E. (2011). Nuclear Import by Karyopherin-Bs: Recognition and Inhibition. *Biochimica Biophysica Acta (BBA) - Mol. Cell Res.* 1813, 1593–1606. doi:10.1016/j.bbamcr.2010.10.014

Di Ventura, B., and Kuhlman, B. (2016). Go in! Go Out! Inducible Control of Nuclear Localization. *Curr. Opin. Chem. Biol.* 34, 62–71. doi:10.1016/j.cbpa.2016.06.009

Diaz Vera, D., Soucy, J. R., Lee, A., Koppes, R. A., and Koppes, A. N. (2021). Light Irradiation of Peripheral Nerve Cells: Wavelength Impacts Primary Sensory Neuron Outgrowth *In Vitro*. *J. Photochem. Photobiol. B Biol.* 215, 112105. doi:10.1016/j.jphotobiol.2020.112105

Efthymiadis, A., Shao, H., Hübner, S., and Jans, D. A. (1997). Kinetic Characterization of the Human Retinoblastoma Protein Bipartite Nuclear Localization Sequence (NLS) *In Vivo* Andin Vitro. *J. Biol. Chem.* 272, 22134–22139. doi:10.1074/jbc.272.35.22134

Eibauer, M., Pellanda, M., Turgay, Y., Dubrovsky, A., Wild, A., and Medalia, O. (2015). Structure and Gating of the Nuclear Pore Complex. *Nat. Commun.* 6, 7532. doi:10.1038/ncomms8532

Fang, H., Bygrave, A. M., Roth, R. H., Johnson, R. C., and Huganir, R. L. (2021). An Optimized CRISPR/Cas9 Approach for Precise Genome Editing in Neurons. *eLife* 10, e65202. doi:10.7554/eLife.65202

Fischer, U., Huber, J., Boelens, W. C., Mattajt, L. W., and Lührmann, R. (1995). The HIV-1 Rev Activation Domain Is a Nuclear Export Signal that Accesses an Export Pathway Used by Specific Cellular RNAs. *Cell* 82, 475–483. doi:10.1016/0092-8674(95)90436-0

Fomicheva, A., Zhou, C., Sun, Q.-Q., and Gomelsky, M. (2019). Engineering Adenylate Cyclase Activated by Near-Infrared Window Light for Mammalian Optogenetic Applications. *ACS Synth. Biol.* 8, 1314–1324. doi:10.1021/acssynbio.8b00528

Friedrich, B., Quensel, C., Sommer, T., Hartmann, E., and Köhler, M. (2006). Nuclear Localization Signal and Protein Context Both Mediate Importin α Specificity of Nuclear Import Substrates. *Mol. Cell Biol.* 26, 8697–8709. doi:10.1128/MCB.00708-06

Goldfarb, D. S., Corbett, A. H., Mason, D. A., Harreman, M. T., and Adam, S. A. (2004). Importin α: a Multipurpose Nuclear-Transport Receptor. *Trends Cell Biol.* 14, 505–514. doi:10.1016/j.tcb.2004.07.016

Güttler, T., Madl, T., Neumann, P., Deichsel, D., Corsini, L., Monecke, T., et al. (2010). NES Consensus Redefined by Structures of PKI-type and Rev-type Nuclear Export Signals Bound to CRM1. *Nat. Struct. Mol. Biol.* 17, 1367–1376. doi:10.1038/nsmb.1931

Hazawa, M., Sakai, K., Kobayashi, A., Yoshino, H., Iga, Y., Iwashima, Y., et al. (2020). Disease-specific Alteration of Karyopherin-α Subtype Establishes Feed-Forward Oncogenic Signaling in Head and Neck Squamous Cell Carcinoma. *Oncogene* 39, 2212–2223. doi:10.1038/s41388-019-1137-3

Heidenreich, M., and Zhang, F. (2016). Applications of CRISPR-Cas Systems in Neuroscience. *Nat. Rev. Neurosci.* 17, 36–44. doi:10.1038/nrn.2015.2

Hodel, A. E., Harreman, M. T., Pulliam, K. F., Harben, M. E., Holmes, J. S., Hodel, M. R., et al. (2006). Nuclear Localization Signal Receptor Affinity Correlates with *In Vivo* Localization in *Saccharomyces cerevisiae*. *J. Biol. Chem.* 281, 23545–23556. doi:10.1074/jbc.M601718200

Hodel, M. R., Corbett, A. H., and Hodel, A. E. (2001). Dissection of a Nuclear Localization Signal. *J. Biol. Chem.* 276, 1317–1325. doi:10.1074/jbc.M008522200

Hodge, R. D., Bakken, T. E., Miller, J. A., Smith, K. A., Barkan, E. R., Graybuck, L. T., et al. (2019). Conserved Cell Types with Divergent Features in Human versus Mouse Cortex. *Nature* 573, 61–68. doi:10.1038/s41586-019-1506-7

Hosokawa, K., Nishi, M., Sakamoto, H., Tanaka, Y., and Kawata, M. (2008). Regional Distribution of Importin Subtype mRNA Expression in the Nervous System: Study of Early Postnatal and Adult Mouse. *Neuroscience* 157, 864–877. doi:10.1016/j.neuroscience.2008.09.045

Imasaki, T., Shimizu, T., Hashimoto, H., Hidaka, Y., Kose, S., Imamoto, N., et al. (2007). Structural Basis for Substrate Recognition and Dissociation by Human Transportin 1. *Mol. Cell* 28, 57–67. doi:10.1016/j.molcel.2007.08.006

Jeffrey, R. A., Ch'ng, T. H., O'Dell, T. J., and Martin, K. C. (2009). Activity-Dependent Anchoring of Importin at the Synapse Involves Regulated Binding to the Cytoplasmic Tail of the NR1-1a Subunit of the NMDA Receptor. *J. Neurosci.* 29, 15613–15620. doi:10.1523/JNEUROSCI.3314-09.2009

Jo, M., Lee, S., Jeon, Y.-M., Kim, S., Kwon, Y., and Kim, H.-J. (2020). The Role of TDP-43 Propagation in Neurodegenerative Diseases: Integrating Insights from Clinical and Experimental Studies. *Exp. Mol. Med.* 52, 1652–1662. doi:10.1038/s12276-020-00513-7

Juillot, S., Beyer, H. M., Madl, J., Weber, W., Zurbriggen, M. D., and Römer, W. (2016). Signalling to the Nucleus under the Control of Light and Small Molecules. *Mol. Biosyst.* 12, 345–349. doi:10.1039/C5MB00763A

Kaberniuk, A. A., Shemetov, A. A., and Verkhusha, V. V. (2016). A Bacterial Phytochrome-Based Optogenetic System Controllable with Near-Infrared Light. *Nat. Methods* 13, 591–597. doi:10.1038/nmeth.3864

Kelley, J. B., Talley, A. M., Spencer, A., Gioeli, D., and Paschal, B. M. (2010). Karyopherin α7 (KPNA7), a Divergent Member of the Importin α Family of Nuclear Import Receptors. *BMC Cell Biol.* 11, 63. doi:10.1186/1471-2121-11-63

Kimura, M., Morinaka, Y., Imai, K., Kose, S., Horton, P., and Imamoto, N. (2017). Extensive Cargo Identification Reveals Distinct Biological Roles of the 12 Importin Pathways. *eLife* 6, e21184. doi:10.7554/eLife.21184

Köhler, M., Speck, C., Christiansen, M., Bischoff, F. R., Prehn, S., Haller, H., et al. (1999). Evidence for Distinct Substrate Specificities of Importin Alpha Family Members in Nuclear Protein Import. *Mol. Cell Biol.* 19, 7782–7791. doi:10.1128/mcb.19.11.7782

Konermann, S., Brigham, M. D., Trevino, A. E., Hsu, P. D., Heidenreich, M., Le Cong, L., et al. (2013). Optical Control of Mammalian Endogenous Transcription and Epigenetic States. *Nature* 500, 472–476. doi:10.1038/nature12466

Lein, E. S., Hawrylycz, M. J., Ao, N., Ayres, M., Bensinger, A., Bernard, A., et al. (2007). Genome-wide Atlas of Gene Expression in the Adult Mouse Brain. *Nature* 445, 168–176. doi:10.1038/nature05453

Lever, M. B., Karpova, A., and Kreutz, M. R. (2015). An Importin Code in Neuronal Transport from Synapse-To-Nucleus? *Front. Mol. Neurosci.* 8, 33. doi:10.3389/fnmol.2015.00033

Ma, G., Wen, S., He, L., Huang, Y., Wang, Y., and Zhou, Y. (2017). Optogenetic Toolkit for Precise Control of Calcium Signaling. *Cell Calcium* 64, 36–46. doi:10.1016/j.ceca.2017.01.004

Ma, H., Zhu, J., Maronski, M., Kotzbauer, P. T., Lee, V. M.-Y., Dichter, M. A., et al. (2002). Non-classical Nuclear Localization Signal Peptides for High Efficiency Lipofection of Primary Neurons and Neuronal Cell Lines. *Neuroscience* 112, 1–5. doi:10.1016/s0306-4522(02)00044-1

Mackmull, M. T., Klaus, B., Heinze, I., Chokkalingam, M., Beyer, A., Russell, R. B., et al. (2017). Landscape of Nuclear Transport Receptor Cargo Specificity. *Mol. Syst. Biol.* 13, 962. doi:10.15252/msb.20177608

Maggio, I., Zittersteijn, H. A., Wang, Q., Liu, J., Janssen, J. M., Ojeda, I. T., et al. (2020). Integrating Gene Delivery and Gene-Editing Technologies by Adenoviral Vector Transfer of Optimized CRISPR-Cas9 Components. *Gene Ther.* 27, 209–225. doi:10.1038/s41434-019-0119-y

Marek, V., Potey, A., Réaux-Le-Goazigo, A., Reboussin, E., Charbonnier, A., Villette, T., et al. (2019). Blue Light Exposure *In Vitro* Causes Toxicity to Trigeminal Neurons and Glia through Increased Superoxide and Hydrogen Peroxide Generation. *Free Radic. Biol. Med.* 131, 27–39. doi:10.1016/j.freeradbiomed.2018.11.029

Marvaldi, L., Panayotis, N., Alber, S., Dagan, S. Y., Okladnikov, N., Koppel, I., et al. (2020). Importin α3 Regulates Chronic Pain Pathways in Peripheral Sensory Neurons. *Science* 369, 842–846. doi:10.1126/science.aaz5875

Meador, K., Wysoczynski, C. L., Norris, A. J., Aoto, J., Bruchas, M. R., Tucker, C. L., et al. (2019). Achieving Tight Control of a Photoactivatable Cre Recombinase Gene Switch: New Design Strategies and Functional Characterization in Mammalian Cells and Rodent. *Nucleic Acids Res.* 47, e97. doi:10.1093/nar/gkz585

Miyamoto, Y., Imamoto, N., Sekimoto, T., Tachibana, T., Seki, T., Tada, S., et al. (1997). Differential Modes of Nuclear Localization Signal (NLS) Recognition by Three Distinct Classes of NLS Receptors. *J. Biol. Chem.* 272, 26375–26381. doi:10.1074/jbc.272.42.26375

Moore, S., Rabichow, B. E., and Sattler, R. (2020). The Hitchhiker's Guide to Nucleocytoplasmic Trafficking in Neurodegeneration. *Neurochem. Res.* 45, 1306–1327. doi:10.1007/s11064-020-02989-1

Nachury, M. V., Ryder, U. W., Lamond, A. I., and Weis, K. (1998). Cloning and Characterization of hSRP1γ, a Tissue-specific Nuclear Transport Factor. *Proc. Natl. Acad. Sci. U.S.A.* 95, 582–587. doi:10.1073/pnas.95.2.582

Nadler, S. G., Tritschler, D., Haffar, O. K., Blake, J., Bruce, A. G., and Cleaveland, J. S. (1997). Differential Expression and Sequence-specific Interaction of Karyopherin α with Nuclear Localization Sequences. *J. Biol. Chem.* 272, 4310–4315. doi:10.1074/jbc.272.7.4310

Nardozzi, J. D., Lott, K., and Cingolani, G. (2010). Phosphorylation Meets Nuclear Import: a Review. *Cell Commun. Signal* 8, 32. doi:10.1186/1478-811X-8-32

Nihongaki, Y., Furuhata, Y., Otabe, T., Hasegawa, S., Yoshimoto, K., and Sato, M. (2017). CRISPR-Cas9-based Photoactivatable Transcription Systems to Induce Neuronal Differentiation. *Nat. Methods* 14, 963–966. doi:10.1038/nmeth.4430

Nihongaki, Y., Yamamoto, S., Kawano, F., Suzuki, H., and Sato, M. (2015). CRISPR-Cas9-based Photoactivatable Transcription System. *Chem. Biol.* 22, 169–174. doi:10.1016/j.chembiol.2014.12.011

Niopek, D., Benzinger, D., Roensch, J., Draebing, T., Wehler, P., Eils, R., et al. (2014). Engineering Light-Inducible Nuclear Localization Signals for Precise Spatiotemporal Control of Protein Dynamics in Living Cells. *Nat. Commun.* 5, 4404. doi:10.1038/ncomms5404

Niopek, D., Wehler, P., Roensch, J., Eils, R., and Di Ventura, B. (2016). Optogenetic Control of Nuclear Protein Export. *Nat. Commun.* 7, 10624. doi:10.1038/ncomms10624

Noda, N., and Ozawa, T. (2018). Light-controllable Transcription System by Nucleocytoplasmic Shuttling of a Truncated Phytochrome B. *Photochem Photobiol.* 94, 1071–1076. doi:10.1111/php.12955

Oostdyk, L. T., Wang, Z., Zang, C., Li, H., McConnell, M. J., and Paschal, B. M. (2020). An Epilepsy-Associated Mutation in the Nuclear Import Receptor KPNA7 Reduces Nuclear Localization Signal Binding. *Sci. Rep.* 10, 4844. doi:10.1038/s41598-020-61369-5

Pasha, T., Zatorska, A., Sharipov, D., Rogelj, B., Hortobágyi, T., and Hirth, F. (2021). Karyopherin Abnormalities in Neurodegenerative Proteinopathies. *Brain* 144, 2915–2932. doi:10.1093/brain/awab201

Pathak, G. P., Strickland, D., Vrana, J. D., and Tucker, C. L. (2014). Benchmarking of Optical Dimerizer Systems. *ACS Synth. Biol.* 3, 832–838. doi:10.1021/sb500291r

Peirson, S. N., Brown, L. A., Pothecary, C. A., Benson, L. A., and Fisk, A. S. (2018). Light and the Laboratory Mouse. *J. Neurosci. Methods* 300, 26–36. doi:10.1016/j.jneumeth.2017.04.007

Polstein, L. R., and Gersbach, C. A. (2015). A Light-Inducible CRISPR-Cas9 System for Control of Endogenous Gene Activation. *Nat. Chem. Biol.* 11, 198–200. doi:10.1038/nchembio.1753

Powell, J. E., Lim, C. K. W., Krishnan, R., McCallister, T. X., Saporito-Magriña, C., Zeballos, M. A., et al. (2022). Targeted Gene Silencing in the Nervous System with CRISPR-Cas13. *Sci. Adv.* 8, eabk2485. doi:10.1126/sciadv.abk2485

Pumroy, R. A., and Cingolani, G. (2015). Diversification of Importin-α Isoforms in Cellular Trafficking and Disease States. *Biochem. J.* 466, 13–28. doi:10.1042/BJ20141186

Quan, Y., Ji, Z.-L., Wang, X., Tartakoff, A. M., and Tao, T. (2008). Evolutionary and Transcriptional Analysis of Karyopherin β Superfamily Proteins. *Mol. Cell. Proteomics* 7, 1254–1269. doi:10.1074/mcp.M700511-MCP200

Redchuk, T. A., Kaberniuk, A. A., and Verkhusha, V. V. (2018a). Near-infrared Light-Controlled Systems for Gene Transcription Regulation, Protein Targeting and Spectral Multiplexing. *Nat. Protoc.* 13, 1121–1136. doi:10.1038/nprot.2018.022

Redchuk, T. A., Karasev, M. M., Omelina, E. S., and Verkhusha, V. V. (2018b). Near-Infrared Light-Controlled Gene Expression and Protein Targeting in Neurons and Non-neuronal Cells. *Chembiochem* 19, 1334–1340. doi:10.1002/cbic.201700642

Redchuk, T. A., Karasev, M. M., Verkhusha, P. V., Donnelly, S. K., Hülsemann, M., Virtanen, J., et al. (2020). Optogenetic Regulation of Endogenous Proteins. *Nat. Commun.* 11, 605. doi:10.1038/s41467-020-14460-4

Redchuk, T. A., Omelina, E. S., Chernov, K. G., and Verkhusha, V. V. (2017). Near-infrared Optogenetic Pair for Protein Regulation and Spectral Multiplexing. *Nat. Chem. Biol.* 13, 633–639. doi:10.1038/nchembio.2343

Riddick, G., and Macara, I. G. (2005). A Systems Analysis of Importin-α-β Mediated Nuclear Protein Import. *J. Cell Biol.* 168, 1027–1038. doi:10.1083/jcb.200409024

Riddick, G., and Macara, I. G. (2007). The Adapter Importin-α Provides Flexible Control of Nuclear Import at the Expense of Efficiency. *Mol. Syst. Biol.* 3, 118. doi:10.1038/msb4100160

Rost, B. R., Schneider-Warme, F., Schmitz, D., and Hegemann, P. (2017). Optogenetic Tools for Subcellular Applications in Neuroscience. *Neuron* 96, 572–603. doi:10.1016/j.neuron.2017.09.047

Rumyantsev, K. A., Turoverov, K. K., and Verkhusha, V. V. (2016). Near-infrared Bioluminescent Proteins for Two-Color Multimodal Imaging. *Sci. Rep.* 6, 36588. doi:10.1038/srep36588

Sahu, M. P., Nikkilä, O., Lågas, S., Kolehmainen, S., and Castrén, E. (2019). Culturing Primary Neurons from Rat hippocampus and Cortex. *Neuronal Signal.* 3, NS20180207. doi:10.1042/NS20180207

Savell, K. E., Bach, S. V., Zipperly, M. E., Revanna, J. S., Goska, N. A., Tuscher, J. J., et al. (2019). A Neuron-Optimized CRISPR/dCas9 Activation System for Robust and Specific Gene Regulation. *eNeuro* 6, 495–518. doi:10.1523/ENEURO.0495-18.2019

Schindelin, J., Arganda-Carreras, I., Frise, E., Kaynig, V., Longair, M., Pietzsch, T., et al. (2012). Fiji: an Open-Source Platform for Biological-Image Analysis. *Nat. Methods* 9, 676–682. doi:10.1038/nmeth.2019

Shao, J., Xue, S., Yu, G., Yu, Y., Yang, X., Bai, Y., et al. (2017). Smartphone-controlled Optogenetically Engineered Cells Enable Semiautomatic Glucose Homeostasis in Diabetic Mice. *Sci. Transl. Med.* 9, eaal2298. doi:10.1126/scitranslmed.aal2298

Smith, K. M., Tsimbalyuk, S., Edwards, M. R., Cross, E. M., Batra, J., Soares da Costa, T. P., et al. (2018). Structural Basis for Importin Alpha 3 Specificity of W Proteins in Hendra and Nipah Viruses. *Nat. Commun.* 9, 1–13. doi:10.1038/s41467-018-05928-5

Soniat, M., Cağatay, T., and Chook, Y. M. (2016). Recognition Elements in the Histone H3 and H4 Tails for Seven Different Importins. *J. Biol. Chem.* 291, 21171–21183. doi:10.1074/jbc.M116.730218

Soniat, M., and Chook, Y. M. (2016). Karyopherin-β2 Recognition of a PY-NLS Variant that Lacks the Proline-Tyrosine Motif. *Structure* 24, 1802–1809. doi:10.1016/j.str.2016.07.018

Thompson, K., Otis, K., Chen, D., Zhao, Y., Odell, T., and Martin, K. (2004). Synapse to Nucleus Signaling during Long-Term Synaptic Plasticitya Role for the Classical Active Nuclear Import Pathway. *Neuron* 44, 997–1009. doi:10.1016/j.neuron.2004.11.02510.1016/s0896-6273(04)00761-5

Timney, B. L., Tetenbaum-Novatt, J., Agate, D. S., Williams, R., Zhang, W., Chait, B. T., et al. (2006). Simple Kinetic Relationships and Nonspecific Competition Govern Nuclear Import Rates *In Vivo*. *J. Cell Biol.* 175, 579–593. doi:10.1083/jcb.200608141

Torres-Ruiz, R., Martinez-Lage, M., Martin, M. C., Garcia, A., Bueno, C., Castaño, J., et al. (2017). Efficient Recreation of T(11;22) EWSR1-FLI1 + in Human Stem Cells Using CRISPR/Cas9. *Stem Cell Rep.* 8, 1408–1420. doi:10.1016/j.stemcr.2017.04.014

Tyssowski, K. M., and Gray, J. M. (2019). Blue Light Increases Neuronal Activity-Regulated Gene Expression in the Absence of Optogenetic Proteins. *eNeuro* 6, 85–95. doi:10.1523/ENEURO.0085-19.2019

Ushijima, R., Sakaguchi, N., Kano, A., Maruyama, A., Miyamoto, Y., Sekimoto, T., et al. (2005). Extracellular Signal-dependent Nuclear Import of STAT3 Is Mediated by Various Importin αs. *Biochem. Biophysical Res. Commun.* 330, 880–886. doi:10.1016/j.bbrc.2005.03.063

Varady, A., and Distel, M. (2020). Non-neuromodulatory Optogenetic Tools in Zebrafish. *Front. Cell Dev. Biol.* 8, 418. doi:10.3389/fcell.2020.00418

Wang, X., Chen, X., and Yang, Y. (2012). Spatiotemporal Control of Gene Expression by a Light-Switchable Transgene System. *Nat. Methods* 9, 266–269. doi:10.1038/nmeth.1892

Wang, X., Dong, K., Kong, D., Zhou, Y., Yin, J., Cai, F., et al. (2021). A Far-Red Light-Inducible CRISPR-Cas12a Platform for Remote-Controlled Genome Editing and Gene Activation. *Sci. Adv.* 7, eabh2358. doi:10.1126/sciadv.abh2358

Wu, J., Wang, M., Yang, X., Yi, C., Jiang, J., Yu, Y., et al. (2020). A Non-invasive Far-Red Light-Induced Split-Cre Recombinase System for Controllable Genome Engineering in Mice. *Nat. Commun.* 11, 3708. doi:10.1038/s41467-020-17530-9

Xiao, C.-Y., Jans, P., and Jans, D. A. (1998). Negative Charge at the Protein Kinase CK2 Site Enhances Recognition of the SV40 Large T-Antigen NLS by Importin: Effect of Conformation. *FEBS Lett.* 440, 297–301. doi:10.1016/s0014-5793(98)01478-1

Xu, Z., Chen, J., Shi, J., Zhao, J., Wang, J., Ji, Y., et al. (2016). Upregulated Expression of Karyopherin α2 Is Involved in Neuronal Apoptosis Following Intracerebral Hemorrhage in Adult Rats. *Cell Mol. Neurobiol.* 36, 755–765. doi:10.1007/s10571-015-0258-7

Yamada, M., Nagasaki, S. C., Suzuki, Y., Hirano, Y., and Imayoshi, I. (2020). Optimization of Light-Inducible Gal4/UAS Gene Expression System in Mammalian Cells. *iScience* 23, 101506. doi:10.1016/j.isci.2020.101506

Yamada, M., Suzuki, Y., Nagasaki, S. C., Okuno, H., and Imayoshi, I. (2018). Light Control of the Tet Gene Expression System in Mammalian Cells. *Cell Rep.* 25, 487–500. e6. doi:10.1016/j.celrep.2018.09.026

Yang, S. N. Y., Takeda, A. A. S., Fontes, M. R. M., Harris, J. M., Jans, D. A., and Kobe, B. (2010). Probing the Specificity of Binding to the Major Nuclear Localization Sequence-Binding Site of Importin-α Using Oriented Peptide Library Screening. *J. Biol. Chem.* 285, 19935–19946. doi:10.1074/jbc.M109.079574

Yu, G., Zhang, M., Gao, L., Zhou, Y., Qiao, L., Yin, J., et al. (2022). Far-red Light-Activated Human Islet-like Designer Cells Enable Sustained Fine-Tuned Secretion of Insulin for Glucose Control. *Mol. Ther.* 30, 341–354. doi:10.1016/j.ymthe.2021.09.004

Yumerefendi, H., Dickinson, D. J., Wang, H., Zimmerman, S. P., Bear, J. E., Goldstein, B., et al. (2015). Control of Protein Activity and Cell Fate Specification via Light-Mediated Nuclear Translocation. *PLOS ONE* 10, e0128443. doi:10.1371/journal.pone.0128443

Yumerefendi, H., Lerner, A. M., Zimmerman, S. P., Hahn, K., Bear, J. E., Strahl, B. D., et al. (2016). Light-induced Nuclear Export Reveals Rapid Dynamics of Epigenetic Modifications. *Nat. Chem. Biol.* 12, 399–401. doi:10.1038/nchembio.2068

Zannini, L., Lecis, D., Lisanti, S., Benetti, R., Buscemi, G., Schneider, C., et al. (2003). Karyopherin-α2 Protein Interacts with Chk2 and Contributes to its Nuclear Import. *J. Biol. Chem.* 278, 42346–42351. doi:10.1074/jbc.M303304200

Zheng, Y., Shen, W., Zhang, J., Yang, B., Liu, Y.-N., Qi, H., et al. (2018). CRISPR Interference-Based Specific and Efficient Gene Inactivation in the Brain. *Nat. Neurosci.* 21, 447–454. doi:10.1038/s41593-018-0077-5

Conflict of Interest: The authors declare that the research was conducted in the absence of any commercial or financial relationships that could be construed as a potential conflict of interest.

Publisher's Note: All claims expressed in this article are solely those of the authors and do not necessarily represent those of their affiliated organizations, or those of the publisher, the editors and the reviewers. Any product that may be evaluated in this article, or claim that may be made by its manufacturer, is not guaranteed or endorsed by the publisher.

frontiers | Frontiers in Cell and Developmental Biology

TYPE Review
PUBLISHED 29 September 2022
DOI 10.3389/fcell.2022.1007893

OPEN ACCESS

EDITED BY
Achilleas D. Theocharis,
University of Patras, Greece

REVIEWED BY
Vsevolod V. Gurevich,
Vanderbilt University, United States
Neil J. Grimsey,
University of Georgia, United States

*CORRESPONDENCE
Jihye Seong,
jseong@kist.re.kr

SPECIALTY SECTION
This article was submitted to Signaling, a section of the journal Frontiers in Cell and Developmental Biology

RECEIVED 31 July 2022
ACCEPTED 09 September 2022
PUBLISHED 29 September 2022

CITATION
Kim H, Baek I-Y and Seong J (2022), Genetically encoded fluorescent biosensors for GPCR research. *Front. Cell Dev. Biol.* 10:1007893. doi: 10.3389/fcell.2022.1007893

Genetically encoded fluorescent biosensors for GPCR research

Hyunbin Kim[1,2], In-Yeop Baek[1,3] and Jihye Seong[1,2,3]*

[1]Brain Science Institute, Korea Institute of Science and Technology (KIST), Seoul, South Korea, [2]Division of Bio-Medical Science and Technology, KIST School, Korea University of Science and Technology, Seoul, South Korea, [3]Department of Converging Science and Technology, Kyung Hee University, Seoul, South Korea

G protein-coupled receptors (GPCRs) regulate a wide range of physiological and pathophysiological cellular processes, thus it is important to understand how GPCRs are activated and function in various cellular contexts. In particular, the activation process of GPCRs is dynamically regulated upon various extracellular stimuli, and emerging evidence suggests the subcellular functions of GPCRs at endosomes and other organelles. Therefore, precise monitoring of the GPCR activation process with high spatiotemporal resolution is required to investigate the underlying molecular mechanisms of GPCR functions. In this review, we will introduce genetically encoded fluorescent biosensors that can precisely monitor the real-time GPCR activation process in live cells. The process includes the binding of extracellular GPCR ligands, conformational change of GPCR, recruitment of G proteins or β-arrestin, GPCR internalization and trafficking, and the GPCR-related downstream signaling events. We will introduce fluorescent GPCR biosensors based on a variety of strategies such as fluorescent resonance energy transfer (FRET), bioluminescence resonance energy transfer (BRET), circular permuted fluorescent protein (cpFP), and nanobody. We will discuss the pros and cons of these GPCR biosensors as well as their applications in GPCR research.

KEYWORDS

GPCR, fluorescent protein, genetically encoded fluorescent biosensor, FRET, circular permutation, BRET, nanobody

Introduction

G protein-coupled receptor (GPCR) is the biggest receptor family involved in the regulation of diverse cellular processes (Pierce et al., 2002; Lefkowitz, 2013). About 800 members of the GPCR family recognize a variety of ligands, including hormones, lipids, and neurotransmitters, then transfer this diverse information to the cells. GPCRs also sense other external stimuli, such as light, odors, and mechanical signals, and convert them into biochemical signals in the cells. As expected from their diverse functions (Lagerstrom and Schioth, 2008; Wu et al., 2019), GPCRs are major therapeutic targets of more than 30% of FDA-approved drugs (Insel et al., 2019). Thus, it is important to understand how GPCRs are activated and function in various cellular contexts.

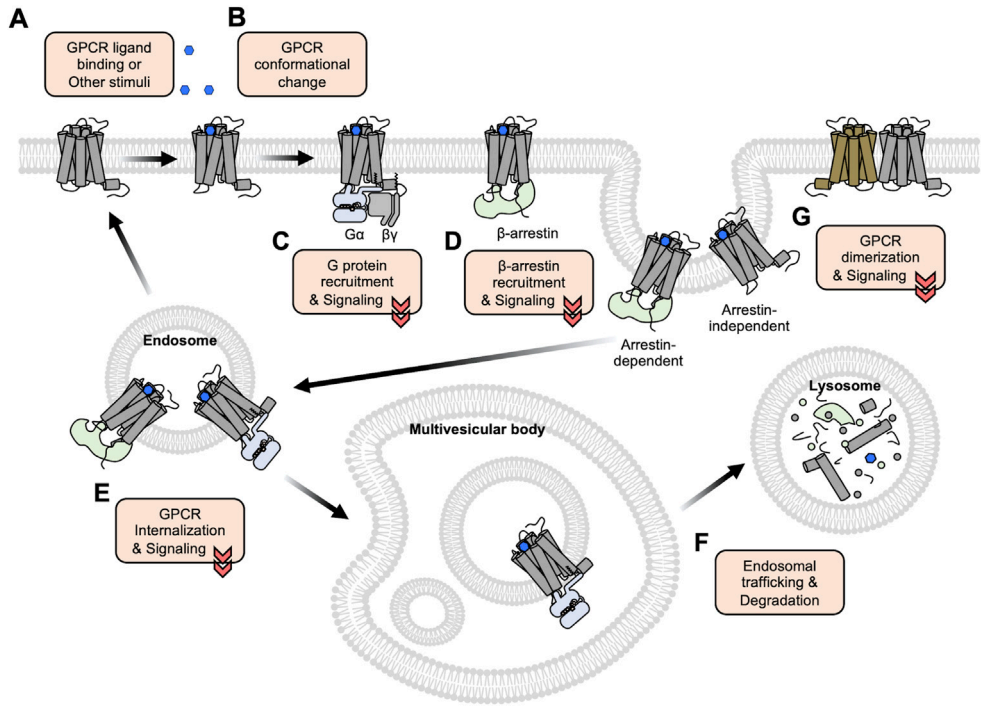

FIGURE 1
An overview of GPCR activation, trafficking, and degradation. **(A)** GPCRs bind to the extracellular ligands or other stimuli at the plasma membrane. **(B)** The ligand-bound GPCRs change their conformations, in particular between TM5 and TM6. **(C–D)** The conformational changes of the GPCRs induce the recruitment of G proteins **(C)** or β-arrestin **(D)** to initiate the downstream signaling pathways. **(E)** The recruited β-arrestin promotes the internalization of GPCRs via the clathrin-mediated endocytosis pathway. Some GPCRs can maintain their activity and function at the internalized endosomes or subcellular organelles. **(F)** Following the endosomal trafficking pathways, the GPCRs can finally be degraded in the lysosome. **(G)** Some GPCRs form dimers or oligomers. Functional crosstalk between these GPCRs may influence the ligand binding affinity, downstream signaling pathways, and trafficking patterns.

GPCRs are composed of seven transmembrane (TM) domains connected by three extracellular loops (ECLs) and three intracellular loops (ICLs) with an extracellular N-terminus and an intracellular C-terminus (Vassilatis et al., 2003). When a ligand binds to the corresponding GPCR from the extracellular side (Figure 1A), the receptor changes its conformation (Figure 1B), facilitating the interactions with G proteins or β-arrestin at the intracellular side of the plasma membrane (Figure 1C,D) which further mediates the downstream signaling pathways. It has been traditionally believed that GPCRs function at the plasma membrane and lose their activity after internalization, but recent studies show that some GPCRs can keep their activity at the internalized endosomes or subcellular organelles (Eichel and von Zastrow, 2018; Mohammad Nezhady et al., 2020) (Figure 1E). In addition, class C GPCRs function as obligatory dimers and emerging evidence indicates that some of class A GPCRs can be also dimerized or oligomerized, which can affect the ligand binding affinity, downstream signaling pathways, and trafficking patterns (Pin et al., 2007; Lohse, 2010) (Figure 1G). Therefore, it is crucial to investigate the molecular mechanisms of GPCR activation and function at the subcellular levels for the correct understanding of the complex physiology of GPCRs and the pathophysiology of related diseases.

To elucidate the molecular mechanisms of GPCR activation and function with high spatiotemporal resolution, a variety of strategies of GPCR biosensors based on fluorescent proteins (FPs) are developed, which allow the real-time monitoring of the GPCR activation in live cells (Alvarez-Curto et al., 2010; Lohse et al., 2012; Clister et al., 2015; Haider et al., 2019). First, the GPCR biosensors based on fluorescent resonance energy transfer (FRET) are designed to detect extracellular GPCR ligands (Okumoto et al., 2005; Hires et al., 2008; Zhang et al., 2018) (Figure 2A) and to monitor the conformational change of GPCRs upon the binding of the ligands (Stumpf and Hoffmann, 2016; Kauk and Hoffmann, 2018) (Figure 2B, left). The FRET technology is also utilized to detect the interaction between GPCRs and

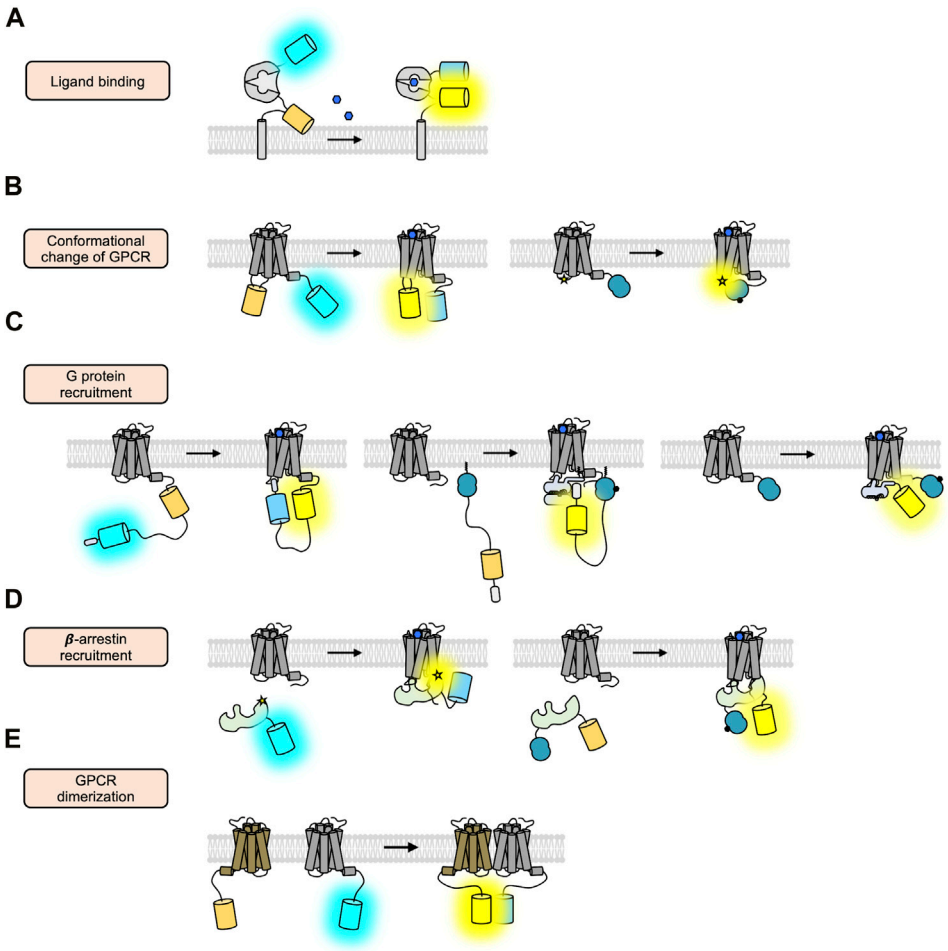

FIGURE 2
FRET/BRET-based GPCR biosensors. **(A)** Schematic design of the ligand-sensing biosensors based on FRET (Tsien, 2006). The FRET signal between cyan and yellow FP inserted in the N- and C-terminus of the ligand-sensing domain is increased upon ligand binding. **(B)** Schematic design of the FRET/BRET-based biosensors detecting the conformational change of GPCRs (Griffin et al., 1998; Vilardaga et al., 2005). In the right panel, a blue circle represents a luciferase and a star displays FlAsH. **(C)** Schematic design of the FRET/BRET-based biosensors detecting the recruitment of G proteins (Malik et al., 2013; Wan et al., 2018; Maziarz et al., 2020). **(D)** Schematic design of the FRET/BRET-based biosensors detecting the recruitment of β-arrestin (Charest et al., 2005; Nuber et al., 2016). **(E)** Schematic design of the FRET-based biosensors detecting the dimerization of GPCRs (Lukasiewicz et al., 2010).

their downstream G proteins (Hein et al., 2005) (Figure 2C, left) or β-arrestin (Krasel et al., 2005) (Figure 2D, left), as well as GPCR oligomerization (Pfleger and Eidne, 2005) (Figure 2E). Similarly, bioluminescence resonance energy transfer (BRET) is also applied to monitor the recruitment of G proteins (Salahpour et al., 2012) (Figure 2C, middle and right) or β-arrestin to the activated GPCRs (Salahpour et al., 2012; Zhou et al., 2021) (Figure 2D, right, Table 1). More recently, a novel strategy of biosensors utilizing nanobodies has been developed to detect the active GPCR conformation or the recruitment of β-arrestin (Shukla et al., 2013; De Groof et al., 2019) (Figure 3B,C, right). In addition, the circular permuted FP-based GPCR biosensors are developed to detect the extracellular GPCR ligands (Marvin et al., 2013; Marvin et al., 2018; Dana et al., 2019; Marvin et al., 2019; Borden et al., 2020; Aggarwal et al., 2022), the conformational change of GPCR upon ligand binding (Labouesse and Patriarchi, 2021), or the recruitment of β-arrestin (Hoare et al., 2020) (Figure 3A–C, left).

In this review, we present genetically encoded fluorescent biosensors that can reveal different stages of the GPCR activation with high spatiotemporal resolution. These stages include 1) binding extracellular ligand to GPCR, 2) conformational change of GPCRs, 3) recruitment with G proteins or β-arrestin, 4) GPCR internalization and trafficking, and 5) GPCR-related downstream signaling

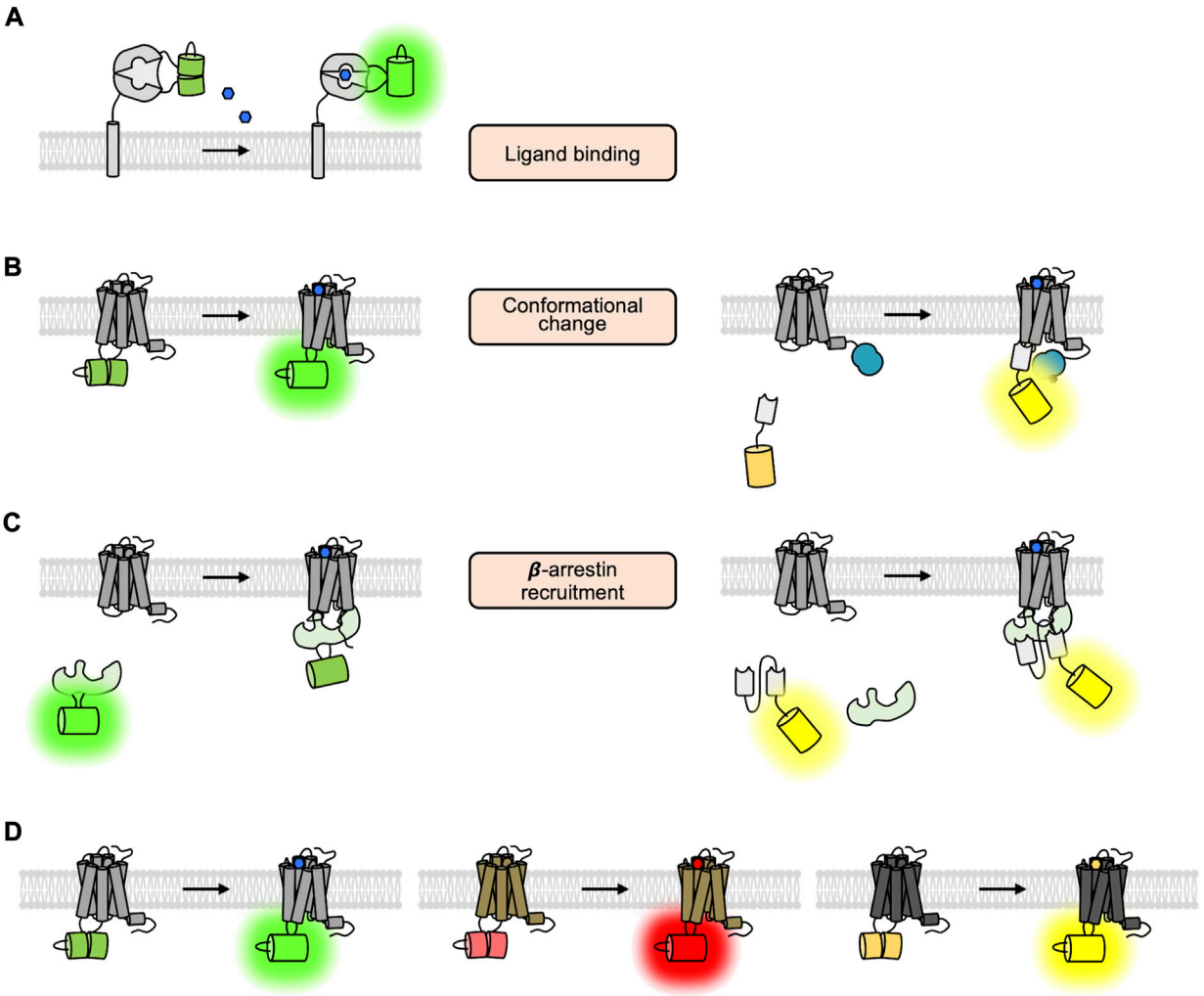

FIGURE 3
The GPCR biosensors utilizing cpFP and nanobody. **(A)** Schematic design of the ligand-sensing biosensors based on cpFP (Marvin et al., 2013). The fluorescent signal of cpFP inserted in the ligand-sensing domain is increased upon ligand binding. **(B)** Schematic design of fluorescent biosensors detecting the conformational change of GPCRs (Patriarchi et al., 2018; Sun et al., 2018). In the left panel, the fluorescent signal of the cpFP inserted in the ICL3 region of the GPCR is increased upon the conformational change of the GPCR. In the right panel, the YFP-tagged nanobody can specifically bind to the GPCR of active conformation. As a luciferase is fused to the GPCR, thus the BRET signal between the YFP and the luciferase is increased. **(C)** Schematic design of the cpFP- and nanobody-based biosensors detecting the recruitment of G proteins (Hoare et al., 2020). **(D)** Different color variants of cpFP-based GPCR biosensors (Patriarchi et al., 2020; Sun et al., 2020; Labouesse and Patriarchi, 2021).

events. We will also cover the fluorescent biosensors to monitor the GPCR dimerization and oligomerization. The pros and cons of these GPCR biosensors will be discussed as well as our perspective on this research area.

Binding extracellular ligand to GPCR

The first step of the GPCR activation is binding to its extracellular ligand (Figure 1A). The GPCR activation is initiated by the increased ligand concentrations in the extracellular space, thus the fluorescent biosensors detecting extracellular GPCR ligands have been designed whose response can indicate the initiation of the GPCR activation.

First, the FRET-based biosensors to detect extracellular GPCR ligands are composed of a ligand-binding protein interspersed with a FRET pair of FPs. They are presented outside of the plasma membrane, thus can change the FRET signals upon binding to the ligands (Figure 2A). We can monitor the increased ligand concentrations in live cells by detecting the FRET changes of the biosensors, which in turn will initiate the activation of GPCRs and intracellular signaling pathways. For example, the Tsien group developed the glutamate-sensing fluorescent reporter

(GluSnFR) (Tsien, 2006) that is composed of a glutamate periplasmic binding protein, GltI, between cyan and yellow FPs in a pDisplay vector containing the TM domain of platelet-derived growth factor receptor (PDGFR). It has been shown that the improved version of GluSnFR, SuperGluSnFR, can report the level of glutamate during synaptic release, spillover, and reuptake in cultured hippocampal neurons (Hires et al., 2008). Similar design strategy can be applied to develop the fluorescent sensors for other ligands (Zhang et al., 2018).

The second design of the ligand-sensing fluorescent biosensors is composed of a circular permutated FP (cpFP) (Baird et al., 1999) inserted in a specific ligand-binding domain and located at the outside plasma membrane (Figure 3A). Upon binding of the ligand, the conformation of the ligand-binding domain is changed, which then stabilizes the chromophore of the cpFP, increasing its fluorescence intensity (Kostyuk et al., 2019). Thus, we can detect the increased concentration of the GPCR ligand by measuring the intensity of fluorescence of the biosensor and expect the subsequent activation of the GPCRs. Compared to the FRET-based biosensors utilizing two FPs (donor and acceptor), the cpFP-based biosensors based on a single FP are smaller in size, and the fold-change in fluorescence signals (ΔF/F) is generally larger (~250%) than the one of FRET-based biosensors (~44%) (Kostyuk et al., 2019).

The representative example of the cp-based ligand-sensing fluorescent biosensor is iGluSnFR, which is composed of the glutamate binding domain GltI, an inserted cpEGFP, and the TM domain from PDGFR (Marvin et al., 2013). In addition to the cpEGFP-based green iGluSnFR, a red-colored R-iGluSnFR1 was developed, expanding the color palette of the glutamate biosensor (Wu et al., 2018). The second generation of iGluSnFR was generated by replacing EGFP with superfolder GFP (sfGFP), which shows the improved fluorescent signal change and a higher expression level (Marvin et al., 2018). Furthermore, different colors of SF-iGluSnFR are developed: SF-Azurite-iGluSnFR (blue), SF-iGluSnFR (green), and SF-Venus-iGluSnFR (yellow) (Marvin et al., 2018).

The third generation iGluSnFR3 was recently developed with further improved signal-to-noise ratios (ΔF/F = ~5,400 ± 260%) (Aggarwal et al., 2022). Different membrane-targeting strategies, in addition to the PDGFR TM domain, were applied, such as glycosylphosphatidylinositol (GPI) anchor and the cytosolic C-terminal domain of Stargazin thus iGluSnFR3 shows the better membrane trafficking and localization (Aggarwal et al., 2022). The ligand-sensing biosensors for other GPCR ligands have also been developed, for example, γ-aminobutyric acid (GABA), nicotine, and acetylcholine biosensors (Marvin et al., 2013; McManus et al., 2019; Borden et al., 2020). These GPCR biosensors enabled the real-time monitoring of the ligand release in cultured cells as well as *in vivo* (Sabatini and Tian, 2020).

Conformational change of GPCR

Ligand-induced GPCR activation

Upon binding to the ligands, GPCRs undergo conformational changes (Figure 1B), which can stabilize the interaction with heterotrimeric G proteins (Kobilka, 2007; Manglik and Kruse, 2017; Weis and Kobilka, 2018). The biosensors detecting GPCR ligands, explained above, inform the changes in the levels of extracellular GPCR ligands but cannot fully confirm the activation of GPCRs. Furthermore, the same ligand can activate different GPCR subtypes, which sometimes mediate opposite cellular outcomes (Wheatley et al., 2012; Wacker et al., 2017). For example, dopamine can bind to all five subtypes of dopamine receptors (DRD1 to DRD5), but the activated DRD subtypes induce different signaling pathways depending on the recruited G proteins. For example, the activated DRD1 activates adenylyl cyclase (AC) increasing cAMP in contrast the DRD2 activation inhibits AC decreasing cAMP (Neve et al., 2004; Undieh, 2010). Therefore, the fluorescent biosensors that detect the conformational changes of individual GPCRs, such as DRD1 and DRD2 biosensors, would be useful in understanding the dopamine-related signaling pathways through the different subtypes of DRD.

Crystal structures of GPCRs have revealed that the largest conformational change occurs between TM5 and TM6 during GPCR activation (Kobilka, 2007; Manglik and Kruse, 2017; Weis and Kobilka, 2018). These structural features are applied to design the FRET-based sensors that are fused to a donor FP in the C-terminus and an acceptor FP in the intracellular loop 3 (ICL3) between TM5 and TM6 of GPCRs (Figure 2B, left), for example, α2A adrenergic receptor (α2AAR) (Vilardaga et al., 2005), β1 adrenergic receptor (β1AR) (Rochais et al., 2007), β2 adrenergic receptor (β2AR) (Reiner et al., 2010), parathyroid hormone 1 receptor (PTH1R) (Vilardaga et al., 2003), and B2-bradykinin receptor (B2R) (Chachisvilis et al., 2006). Upon the binding to the ligands, the structural change between TM5 and TM6 of the biosensor induces the rearrangement of the acceptor FP inserted in the ICL3, causing the FRET changes. Thus, these FRET biosensors can report the conformational change of GPCRs upon activation in live cells.

Similarly, the FRET biosensors detecting the GPCR conformational change were developed based on donor FP and fluorescein arsenical hairpin binder (FlAsH) (Griffin et al., 1998). In this design, the sequence for the attachment of the FlAsH (i.e., CCPGCC) is encoded in the ICL3, and the donor FP (e.g., CFP) is fused to the C-terminus of GPCRs, for example, muscarinic acetylcholine receptor (mAChR) (Maier-Peuschel et al., 2010), α2AAR (Nikolaev et al., 2006), β2AR (Nakanishi et al., 2006), and A_{2A} adenosine receptors (A2AR) (Hoffmann et al., 2005). Thus, the FRET changes between CFP and FlAsH can report the ligand-induced conformational

changes of these GPCRs in live cells. Because the chemical coupling reaction between FlAsH and the encoded motif sequence is required, this design is not completely genetically encodable (Hoffmann et al., 2010). On the other hand, the size of the fluorescent dye FlAsH is smaller than FPs (Griffin et al., 1998), thus this design of biosensor may mimic the natural structural states of the GPCR activation with less steric hindrance (Hoffmann et al., 2005). The donor FP in the C-terminus of the biosensor can be replaced with Renilla luciferase (RLuc) (Hastings, 1996) to generate the BRET-based biosensor, and the BRET changes between RLuc and the FlAsH can report the conformational change of GPCRs upon activation (Szalai et al., 2012; Zhang et al., 2013) (Figure 2B, right).

More recently, the cpFP-based biosensors detecting the conformational change between TM5 and TM6 of GPCRs have been developed (Figure 3B, left). The representative examples of this strategy are dLight and GRAB-DA, which are DRD biosensors developed by Tian and Li groups, respectively (Patriarchi et al., 2018; Sun et al., 2018). These DRD biosensors were constructed by inserting cpGFP into the ICL3 region of DRDs, and the conformational change of DRD can increase the fluorescent intensity of the inserted cpFP in the biosensor. From the optimization process in the linker sequences between GPCR and the inserted cpGFP, the dynamic range of these sensors was dramatically increased ($\Delta F/F_{dLight1.1}$ = 230% and $\Delta F/F_{GRAB\text{-}DA1m}$ = 190%). As dLight and GRAB-DA can sensitively detect the dopamine-induced activation of DRDs, these DRD biosensors have been successfully applied to measure dopamine signals in various brain regions of mice (Kunishima et al., 2000; Patriarchi et al., 2018; Augustine et al., 2019; Lutas et al., 2019; Mohebi et al., 2019; Qian et al., 2019; Lefevre et al., 2020; Unger et al., 2020) as well as fly and zebrafish (Sun et al., 2018). We further developed a red-colored DRD1 sensor (R-DRD1) and a green-colored DRD2 sensor (G-DRD2), which can distinguish the activation of different DRD subtypes, i.e., DRD1 and DRD2, in the same cells (Kim et al., 2022) (Figure 3D). The cpFP-based biosensors that detect the conformational change of other GPCRs have also been developed (Feng et al., 2019; Jing et al., 2020; Patriarchi et al., 2020; Sun et al., 2020; Unger et al., 2020; Wan et al., 2021).

Another strategy to report the conformational change of GPCRs is based on nanobody (Nb) (Figure 3B, right). Nanobody is a recombinant single variable domain of a heavy chain fragment that was first isolated from the Camelidae family (Hamers-Casterman et al., 1993). While maintaining the ability for antigen binding, nanobody has useful biochemical properties such as tiny size, excellent solubility, and high stability (Muyldermans, 2013). The representative example of the Nb-based GPCR sensor is Nb80-GFP developed by the Zastrow group, which specifically binds to the active conformation of the β2AR (Rasmussen et al., 2011a). Nb80-GFP can visualize the β2AR activation by green fluorescent signals in live cells, which are displayed at the plasma membrane right after the treatment of an agonist for β2AR. Nb80-GFP further revealed the prolonged GFP signals at the internalized endosomes, providing direct evidence that β2ARs can keep their active conformation in endosomes after being internalized from the plasma membrane.

Another Nb-based GPCR sensor, Nb33-GFP, that specifically binds to the activated mu and delta opioid receptor (MOR and DOR), revealed a spatiotemporal landscape of OR activation in a ligand-dependent manner; peptide agonists activate ORs at the plasma membrane and internalized endosomes, in contrast, non-peptide drugs can activate a Golgi-localized internal OR pool (Stoeber et al., 2018). In addition to its specificity to GPCRs, these Nb-based biosensors can report the activation status of endogenous GPCRs without overexpression of exogenous GPCRs. On the other hand, the Nb-based biosensors may not be able to bind to the GPCRs surrounded by clathrin coats during the early stage of the internalization process (Irannejad et al., 2013), thus cannot report the status of GPCRs in this stage. Furthermore, Nb-based biosensors are designed to measure the activation state of specific GPCRs, thus these tools are not appropriate for research on multiple GPCRs.

Mechanical stimulation-mediated GPCR activation

In addition to diverse GPCR ligands, some GPCRs respond to mechanical stimulation to mediate various physiological processes. For example, in the vascular endothelial cells of small-diameter arteries, fluid shear stress was identified as a mechanical stimulation through mechanosensitive G protein-coupled receptor 68 (GPR68), which is involved in the local regulation of vascular resistance (Xu et al., 2018). However, the precise mechanism by which mechanosensitive GPCRs transduce mechanical stimuli into intracellular responses remains unclear. Thus, the investigation of the conformational dynamics of mechanosensitive GPCRs upon mechanical stimulus is important to understand their roles in physiology and pathophysiology.

The FRET technique was applied to visualize the conformational changes of mechanosensitive GPCRs upon mechanical stimulations such as fluid shear stress and hypotonic membrane stretch. For example, B2R (Chachisvilis et al., 2006) and PTH1R (Zhang et al., 2009) were demonstrated to be mechanosensitive by intra-molecular FRET biosensors that are constructed by inserting YFP into the ICL3 and fusing CFP to the C terminus (Figure 2B, left). In addition, the series of FlAsH-based FRET sensors, which are encoded with the FlAsH motif in different regions of GPCRs, revealed the mechanical force-mediated elongation of the helix 8 (H8) domain of GPCRs

might be essential for the mechanosensitive response (Erdogmus et al., 2019).

In addition, the cpFP-based biosensor iGlow was developed to detect the mechanical stimulation-induced conformational change of a GPR68 (Ozkan et al., 2021). (Figure 3B, left). It was generated by inserting cpGFP into the ICL3 of GPR68, thus increasing its fluorescent intensity in response to fluid shear stress. The dynamic range of iGlow is from 25% to a maximum of 75% under a single fluid shear stress pulse between 10.4 and 20.8 dyne/cm^2. Further investigation using this strategy of biosensors will provide more information on the mechanosensitive GPCRs.

G protein coupling to GPCR

The next step of the GPCR signaling pathway after the conformational change of the receptor is the coupling of heterotrimeric G proteins to the GPCR (Figure 1C). The recruited G proteins to the GPCRs then initiate the downstream signaling events, thus fluorescent biosensors for detecting the recruitment of G proteins are developed utilizing the following strategies.

The first strategy is to directly visualize the translocation of the FP-tagged G alpha protein to GPCR to the plasma membrane (Hynes et al., 2004). In addition, the inter-FRET signals between the G alpha protein tagged with a donor FP, and the GPCR fused to an acceptor FP can be measured to quantify the levels of G protein coupling to the GPCR (Hein et al., 2005). Similarly, the donor FP can be replaced with luciferase, and thus the inter-BRET signals can report the coupling between the G protein and activated GPCR (Gales et al., 2005). However, these approaches include the overexpression of G proteins (Azzi et al., 2001; Janssen et al., 2002), and require the expression of the heterotrimeric form of G proteins (G alpha, beta, and gamma) for the correct localization at the plasma membrane (Rasmussen et al., 2011b; Rosenbaum et al., 2011) may influence higher basal levels of the G protein-related downstream pathways.

Mini-G is the engineered G alpha protein that contains only essential sequences for the coupling to the GPCR (Oldham et al., 2006; Carpenter and Tate, 2016). To construct the mini-Gs, three regions of Gs, i.e., GαAH, switch III, and half of the N-terminal helix, were deleted and several mutations were applied to the residues in the nucleotide-binding pocket, switch II, and the α5 helix (Carpenter and Tate, 2016). Different versions of mini-G, i.e., mini-Gs, mini-Gi, mini-Gq, and mini-G12, have been further developed to detect the coupling of different G proteins (i.e., G alpha s, i, q, 12) to the relevant GPCRs (Nehme et al., 2017). Mini-G can be fused to FP for the direct monitoring of the translocation to the plasma membrane in response to ligands for the target GPCRs; in addition, mini-G and the target GPCR are fused to FPs or luciferases, and the interaction between specific G proteins and target GPCRs can be measured by FRET or BRET signals (Wan et al., 2018; Manchanda et al., 2021) (Figure 2C). The overexpression of these biosensors, however, may perturb endogenous G protein downstream signaling pathways, thus they can be optimally used to monitor and measure the step of the G protein recruitment.

The second sensing strategy to detect the G protein coupling to the receptor is the intra-molecular FRET-based GPCR sensor which is composed of GPCR, FRET pair FPs between ER/K linker (Sivaramakrishnan and Spudich, 2011), and short C-terminal sequences from the alpha helix 5 of G alpha protein (Figure 2C, left). During the coupling of the G alpha protein to the activated GPCR, the selection of G alpha protein, e.g., G alpha s, i/o, q, 12/13, is dependent on the direct interaction between the GPCR and the C-terminus sequences of the G alpha protein (Semack et al., 2016; Tsai et al., 2019). Thus, the alpha helix 5 sequences of each G protein are crucial to determine the binding specificity to relevant GPCRs (Flock et al., 2017; Inoue et al., 2019a).

For example, β2AR-Gs FRET biosensor was developed which contains β2AR, cyan and yellow FPs, and the C-terminal 27 residues from the alpha helix 5 of Gs (Malik et al., 2013). The ER/K linker, which is a subset of single alpha-helical domains that contains 73 amino acids (Sivaramakrishnan and Spudich, 2011), enables the efficient separation between the donor and acceptor FPs to keep the low FRET level in the default state. When the activated β2AR in the biosensor undergoes the conformational change, the C-terminal sequences derived from Gs can directly bind to the β2AR in the biosensor. This increases the proximity between the donor and acceptor FPs in the β2AR-Gs biosensor, thus the increased FRET level can report the G protein coupling to the activated GPCR in live cells.

Utilizing these FRET-based biosensors, the structural basis of selective interactions between GPCR and the C-terminus of G alpha protein was further investigated (Semack et al., 2016). In particular, the FRET-based β2AR-Gs biosensor and vasopressin receptor 1A (V1AR)-Gq biosensor were constructed. The FRET measurement discovered three hot spot residues in the C-terminus of G alpha protein that are critical for determining the coupling specificity of G protein. Additional mutation experiments in these residues further revealed that electrostatic interaction is important for the β2AR-Gs complex, whereas the V1AR-Gq interface is predominantly hydrophobic (Semack et al., 2016), suggesting different coupling mechanisms of Gs and Gq to relevant GPCRs. In addition, another study utilizing these biosensors revealed that non-cognate G alpha proteins could modulate the ligand-binding affinity of the GPCR through allosteric interaction or different binding modes to the receptor (Gupte et al., 2017).

Finally, the third strategy is the BRET-based detection of endogenous interaction between G proteins to GPCRs via the specific detector module that binds to the activated G proteins (Figure 2C, middle). This BRET-based biosensor with ER/K linker and YFP (BERKY biosensor) is composed of membrane

anchoring sequence, NanoLuc, ER/K linker, YFP, and KB-1753 that is a synthetic peptide specifically binding to Gαi-GTP (Maziarz et al., 2020). In the default state, the ER/K linker in the Gαi-BERKY biosensor efficiently separates the donor and acceptor of BRET, minimizing the basal BRET level. When endogenous GPCRs are activated and coupled to Gαi-GTP, the KB-1753 in the Gαi-BERKY biosensor binds to the endogenous Gαi-GTP proteins coupled to GPCR. This allows the ER/K linker to bring the donor and acceptor proximal to each other, resulting in an increased BRET signal. In addition, the BERKY sensors for Gαq-GTP, Gα13-GTP, free Gβγ and Rho-GTP were further developed by replacing the G protein-specific module (Maziarz et al., 2020). Thus, the endogenous GPCR-G protein coupling event can be monitored by the BERKY biosensor in live cells.

Recruitment of β-arrestin to GPCR

After the activation of the G protein-mediated signaling pathway, the C-terminus sequences of the GPCR can be phosphorylated by G protein-coupled receptor kinases (GRKs) which in turn can recruit β-arrestins (Figure 1D). This prevents the G protein-mediated signal transduction by sterically hindering G protein coupling (Lefkowitz and Shenoy, 2005). Although some GPCRs can be internalized through arrestin-independent mechanisms (Moo et al., 2021), it is known that the β-arrestin facilitates the internalization of GPCR via interaction with clathrin and adaptor protein 2 (AP2). (Goodman et al., 1996; Laporte et al., 1999). In addition to this classical role of β-arrestin for GPCR internalization, emerging evidence suggests that β-arrestin can mediate signaling cascades via G protein-independent pathways (Lefkowitz and Shenoy, 2005) (Figure 1D). For example, β-arrestin can serve as a scaffolding protein for mitogen-activated protein kinases (MAPKs) cascades, which regulate various cellular functions, including proliferation, transcriptional regulation, and apoptosis (DeWire et al., 2007).

For such a different function, β-arrestin may adopt multiple conformations and be modulated at various levels (Shukla et al., 2008). Different β-arrestin conformations include 1) "tail" conformation, with β-arrestin coupled to the phosphorylated C-terminal tail of GPCR, and 2) "core" conformation, where β-arrestin interacts with the receptor TM core region through its finger-loop region (Shukla et al., 2014). Because GPCRs may exist in multiple conformational states, the ligands which can selectively stabilize different conformational states of the GPCRs can recruit distinct effector proteins, initiating G protein- or β-arrestin-mediated signaling pathways (Kobilka and Deupi, 2007). This functional selectivity, also called biased agonism, allows the selective targeting of beneficial pathways while avoiding potentially detrimental ones (Wootten et al., 2018). Considering the critical roles of β-arrestin in various cellular events, it is necessary to develop fluorescent biosensors for monitoring the formation of the GPCR-β-arrestin complex or visualizing the active conformation of β-arrestin in live cells.

First, intra-molecular BRET-based biosensors were constructed to probe conformational change of β-arrestin by fusing RLuc and YFP to the N- and C-terminus of β-arrestin respectively (Charest et al., 2005) (Figure 2D, right). In addition, GFP was fused to the C-terminus of GPCR to assess whether RLuc-β-arrestin-YFP is recruited to the agonist-activated GPCR, and the intermolecular BRET signals between RLuc and GFP reflect the recruitment of RLuc-β-arrestin-YFP to the GPCR. In a similar way, another intra-molecular BRET biosensor was developed with NanoLuc and CyOFP1 as a donor and an acceptor, respectively. Nanoluc has a smaller size (19 kDa) compared to RLuc (36 kDa) with an improved brightness (~150-fold) (Hall et al., 2012), and CyOFP1 is a cyan-excitable orange FP (Oishi et al., 2020). This β-arrestin biosensor allows the detection of different conformations of β-arrestin associated with GPCR, i.e., tail and core conformations.

In addition, the FlAsH-based intra-molecular FRET/BRET biosensors were developed to predict more precisely the conformational changes of β-arrestin during activation, e.g. a BRET-based biosensor based on FlAsH-RLuc pair (Lee et al., 2016) and a FRET-based biosensor with FlAsH-CFP pair (Nuber et al., 2016) (Figure 2D, left). These biosensors were generated as a series of different biosensors in which the FlAsH motif was encoded at different regions of β-arrestin. First, the BRET-based β-arrestin biosensors with six different FlAsH sites were examined with various GPCRs. The results revealed the conserved features of BRET signals between GPCRs for controlling the ERK1/2 phosphorylation, indicating a distinctive β-arrestin conformational signature for the β-arrestin-dependent downstream signaling events. In addition, the FRET-based β-arrestin biosensors with eight different FlAsH sites were used to investigate the kinetics in the conformational changes of β-arrestin during the coupling and uncoupling between β-arrestin and GPCRs.

Finally, the single FP-based β-arrestin biosensor was engineered by inserting the entire β-arrestin into the critical seventh stave of the β-sheet directly adjacent to the chromophore of mNeonGreen (Hoare et al., 2020) (Figure 3C, left). Interestingly, mNeonGreen in this biosensor is not circularly permuted, thus it has a high quantum yield allowing the biosensor to read sufficient signals with a brief excitation time and thereby minimizing photobleaching (Shaner et al., 2013). When β-arrestin binds to the phosphorylated GPCR, the conformational rearrangement in the biosensor changes the chromophore environment, resulting in a decrease in fluorescence intensity. Due to its high temporal resolution and minimal photobleaching, the biosensor can be used to measure

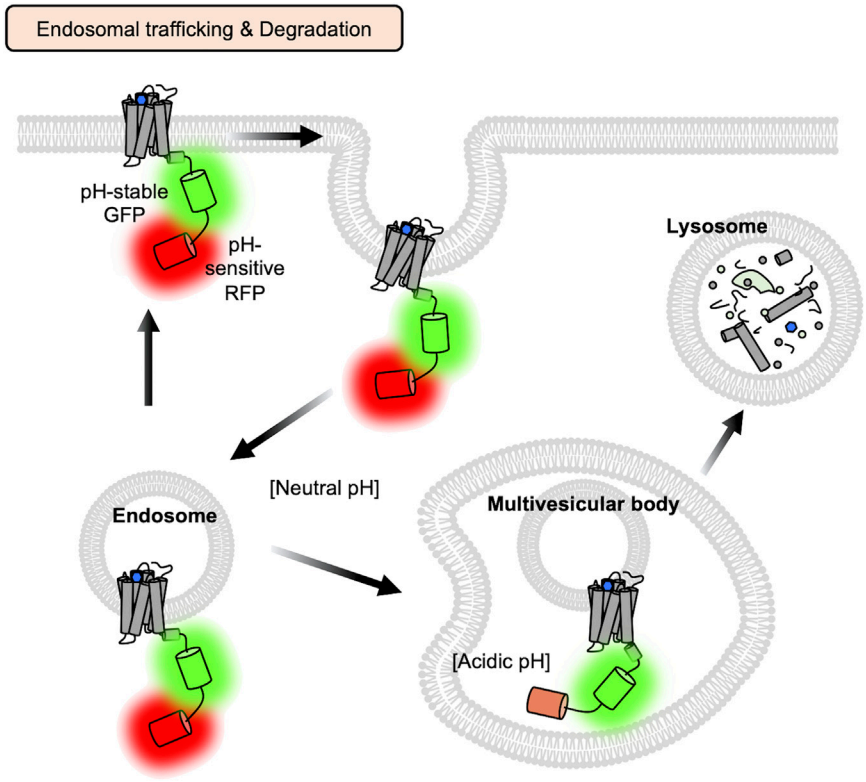

FIGURE 4
Monitoring endosomal trafficking and degradation process of GPCRs with the GPCR-pH sensor. To confirm that GPCRs encounter the more acidic environment during the endosomal trafficking and degradation process (Marchese et al., 2008; Kim et al., 2021a), a GPCR-pH sensor is designed, which is composed of β2AR, a pH-sensitive FP (Bizzarri et al., 2009; Shen et al., 2014) and a pH-stable reference FP, which can confirm that GPCRs encounter acidic environment during endosomal trafficking pathways. Acidification in the endosomes and lysosomes decreases the fluorescent intensity of the pH-sensitive RFP, but not the reference FP, thus the acidic state of GPCRs can be predicted by the intensity ratios of pH sensitive-FP (red) and reference FP (green).

the dynamic kinetics of the arrestin-dependent signaling pathway.

GPCR signaling at internalized endosomes and other organelles

Previous studies focus on GPCR activity at or near the plasma membrane, where the GPCRs are known to mainly function in response to extracellular stimuli. Likewise, it has been believed that GPCRs transmit these signals only at the plasma membrane and are desensitized after internalization (Ferguson, 2001). However, emerging evidence suggests that some GPCRs can maintain their activity at endosomes or subcellular organelles even after internalization (Eichel and von Zastrow, 2018) (Figure 1E). For example, the internalized β2AR can continue its function at endosomes, which is crucial for altering the expression patterns of cAMP-dependent transcriptional factors (Tsvetanova and von Zastrow, 2014). Therefore, it is important to develop fluorescent biosensors which can monitor the real-time activity of GPCRs at subcellular organelles in live cells.

The sustained GPCR activity at the internalized endosomes was visualized by Nb-based fluorescent biosensors. As mentioned in the previous section, the Zastrow group showed that β2ARs could keep their active conformation at the internalized endosomes utilizing Nb80-GFP (Irannejad et al., 2013). It was also revealed, using a nanobody-based biosensor Nb80-FP, that the β1AR-induced G protein signaling occurs in the Golgi, suggesting novel pharmacological approaches for the treatment of heart failure (Nash et al., 2019). In addition, Nb37-FP showed that the internalized Thyroid stimulating hormone (TSH) receptor maintains its function in the Golgi and Trans-Golgi network (TGN) (Godbole et al., 2017). This sustained activity of TSH produces cAMP near the nucleus, which can efficiently induce the phosphorylation of cAMP response element-binding protein (CREB) (Godbole et al., 2017). The Nb-based OR sensor Nb33-GFP also discovered

the Golgi-localized internal OR pool which can be activated by non-peptide drugs, while peptide agonists activate ORs conventionally at the plasma membrane and internalized endosomes (Stoeber et al., 2018). These studies using the nanobody-based fluorescent biosensors provide strong evidence that GPCRs maintain their functions at internalized endosomes and other organelles.

For the real-time monitoring of GPCR activation kinetics during endosomal trafficking and degradation pathways (Figure 1F), we conducted long-term live-cell imaging of the FRET-based β2AR biosensor, which contains β2AR, a FRET pair FPs, and the C-terminal sequences from Gs (Kim et al., 2021a) (Figure 2C, left). As sensitive and reversible FRET signals can report the real-time status of β2AR activity during the entire process of the endosomal trafficking pathway, we can confirm that the internalized β2AR is active at the endosomes for several hours before it is degraded (Kim et al., 2021a). We further calculated the kinetic factors of β2AR activation during endosomal trafficking and degradation pathways, which would be useful for assessing the functional kinetics of particular drugs on target GPCRs. We also designed a GPCR-pH sensor which is composed of β2AR, a pH-sensitive FP (Bizzarri et al., 2009; Shen et al., 2014) and a pH-stable reference FP, which can confirm that GPCRs encounter an acidic environment during endosomal trafficking pathways (Marchese et al., 2008; Kim et al., 2021a) (Figure 4).

Dimerization or oligomerization of GPCR

Emerging evidence suggests that some GPCRs can be dimerized or oligomerized (Hebert and Bouvier, 1998; Fuxe et al., 2010; Ferre et al., 2014) (Figure 1G). Functional crosstalk between these GPCRs may influence the ligand binding affinity, downstream signaling pathways, and trafficking patterns (Jordan and Devi, 1999; Casado et al., 2007; Fiorentini et al., 2008; Milligan, 2010; Gonzalez-Maeso, 2011; Gomes et al., 2016), and some GPCR oligomerization populations may be related to disease states (Ferre et al., 1991; Jordan et al., 2003; Gonzalez-Maeso et al., 2008). However, previous GPCR studies assumed that each GPCR generally exists as a monomer. Therefore, it is important to monitor the status of dimerization or oligomerization of GPCRs and to detect functional crosstalk between the GPCR dimers or oligomers.

First, FRET or BRET techniques can be applied to identify the GPCR dimers or oligomers. For example, the physical interaction between DRD2 and serotonin receptor 2A (5HT2A) was demonstrated by analyzing inter-FRET signals between 5HT2A-CFP and DRD2-YFP (Lukasiewicz et al., 2010) (Figure 2E). In addition, the functional crosstalk between 5HT2A and DRD2 was first revealed through analysis of the inter-BRET signal between DRD2-RLuc and 5HT2A-GFP upon stimulation of selective agonist or antagonist of each receptor (Borroto-Escuela et al., 2010). As FRET and BRET can occur when the donor and the acceptor are proximal within 10 nm, it is generally believed that the attached molecules may interact closely each other (Padilla-Parra and Tramier, 2012). Nevertheless, other biochemical methods such as co-immunoprecipitation and PLA assay would be helpful to confirm the formation of the GPCR complexes (Faron-Gorecka et al., 2019).

Studies on homodimers were also conducted using FRET technology. For example, metabotropic glutamate receptor 1 (mGluR1) is known to form a homodimer when activated (Kunishima et al., 2000). However, the molecular sequence of homodimerization and the conformational change was not clear, thus inter-FRET and intra-FRET mGluR1 biosensors were constructed (Hlavackova et al., 2012). For the monitoring of the homodimerization process of mGluR1, subunits of inter-molecular FRET biosensors were constructed by fusing CFP or YFP to ICL2 of mGluR1. On the other hand, intra-molecular FRET sensor was developed by fusing YFP to ICL2 and CFP to the C-terminus for measuring conformational changes of mGluR1. The results utilizing these FRET sensors revealed that, upon ligand binding, the homodimerization of mGluR1 through the Venus flytrap (VFT) domain occurs first, and then the conformational changes in the ICL of mGluR1 follow next to induce the G protein-mediated signaling pathways. Thus, FRET-based biosensors are useful to elucidate the molecular mechanism of the GPCR activation process.

Functional crosstalk between GPCR heterodimers can also be investigated by cpFP-based biosensors. For example, we developed the cpFP-based red DRD1 biosensor and green DRD2 biosensor, R-DRD1 and G-DRD2, which selectively increase red or green fluorescence upon the activation of DRD1 or DRD2, respectively (Kim et al., 2022). The R-DRD1 biosensor was co-expressed with DRD2 to form the DRD1-DRD2 heterodimer (Hasbi et al., 2009; Urizar et al., 2011; Chun et al., 2013), then the activation status of DRD1 in the heterodimer was closely monitored in live cells. Also, G-DRD2 co-expressed with DRD1 can report the activation status of DRD2 in the heterodimer. The results of this study demonstrated that DRD1 in the DRD1-DRD2 heterodimer is selectively inhibited in response to high levels of dopamine, whereas DRD2 is inhibited only upon low levels of dopamine, suggesting differential functional crosstalk in the DRD1-DRD2 heterodimer under different physiological conditions (Kim et al., 2022). These methods utilizing fluorescent GPCR biosensors can be further applied to investigate functional crosstalk in other GPCR dimers and oligomers, promising a deeper understanding of the molecular mechanism of GPCR activation and function.

TABLE 1 Examples of currently available FRET and BRET biosensors for GPCR studies.

Detection step	Target GPCR	Ligand used	Detection method	FRET or BRET pair	Cell lines tested	Notes	Reference
Ligand binding	GltI (mGluR)	Glutamate	FRET	ECFP-Venus	HEK293, HeLa		Hires et al., 2008 Tsien, 2006
Conformational change of GPCR	α2AAR	Noradrenaline, Norepinephrine	FRET	CFP-YFP, CFP-FlAsH	HEK293		Vilardaga et al., 2005 Nikolaev et al., 2006
	β1AR	Norepinephrine, Isoproterenol	FRET	Cerulean-YFP, Cerulean-FlAsH	HEK293		Rochais et al., 2007
	β2AR	Isoproterenol	FRET	CFP-YFP, CFP-FlAsH	HEK293		Reiner et al., 2010 Nakanishi et al., 2006
	A2AR	Adenosine	FRET	CFP-YFP, CFP-FlAsH	HEK293, COS-1		Hoffmann et al., 2005
	B1R	Carboxypeptidase M	FRET	CFP-FlAsH	HEK293		Zhang et al., 2013
	B2R	Bradykinin, Mechanical force	FRET	CFP-YFP	HEK293, BAEC		Chachisvilis et al., 2006
	H1R	Histamine, Mechanical force	FRET	Cerulean-FlAsH	HEK293		Erdogmus et al., 2019
	mAChR	Carbachol	FRET	CFP-FlAsH	HEK-TsA201		Maier-Peuschel et al., 2010
	PTH1R	PTH, Mechanical force	FRET	CFP-YFP, Cerulean-Citrine	HEK293, NC3T3-E1		Vilardaga et al., 2003, Zhang et al., 2009
	AT1R	Angiotensin II	BRET	RLuc-YFP	CHO		Szalai et al., 2012
	B1R	Carboxypeptidase M	BRET	RLuc-FlAsH	HEK293		Zhang et al., 2013
G protein recruitment	β2AR	Isoproterenol	FRET	mCerulean-mCitrine	HEK293		Malik et al., 2013
	V1AR	AVP	FRET	mCerulean-mCitrine	HEK293		Gupte et al., 2017
	A1AR	Adenosine	FRET	Cerulean-Venus	HEK293	Mini-G	Wan et al., 2018
	α2AAR	Brimonidine	BRET	NLuc-YFP	HEK293T	BERKY	Maziarz et al., 2020
	β2AR	Isoproterenol	BRET	RLuc-GFP	HEK293T		Gales et al., 2005
	β2AR	Isoproterenol	BRET	RLuc8-Venus	HEK293	Mini-G	Wan et al., 2018
	GLP-1R	GLP-1	BRET	NLuc-Venus	HEK293	Mini-G	Manchanda et al., 2021
β-arrestin recruitment	β2AR	Isoproterenol	FRET	CFP-FlAsH	HEK293		Nuber et al., 2016
	β2AR, V2R	Isoproterenol, AVP	BRET	RLuc-YFP	HEK293, COS		Charest et al., 2005
	β2AR, AT1R	Isoproterenol, Angiotensin II	BRET	NLuc-CyOFP1	HEK293T		Oishi et al., 2020
	PTH1R	PTH	BRET	RLuc-FlAsH	HEK293		Lee et al., 2016
GPCR dimerization	5HT2A/DRD2	DOI, Quinpirole	FRET	ECFP-EYFP	HEK293		Lukasiewicz et al., 2010
	mGluR1	Quisqualate	FRET	CFP-YFP	HEK293, COS-7		Hlavackova et al., 2012
	5HT2A/DRD2	5-HT, Quinpirole	BRET	RLuc-GFP2	HEK293T		Borroto-Escuela et al., 2010

GltI, Glutamate/aspartate import solute-binding protein; α2AAR, α2A adrenergic receptor; β1AR, β1 adrenergic receptor; β2AR, β2 adrenergic receptor; A2AR, A2A adenosine receptors; B1R, B1-bradykinin receptor; B2R, B2-bradykinin receptor; H1R, Histamine H1 receptor; mAChR, Muscarinic acetylcholine receptor; PTH1R, Parathyroid hormone 1 receptor; AT1R, Angiotensin II type 1 receptor; V1AR, Vasopressin receptor 1A; A1AR, A1A adenosine receptors; GLP-1R, Glucagon like peptide-1 receptor; V2R, Vasopressin receptor 2; 5HT2A, Serotonin receptor 2A; DRD2, Dopamine receptor 2; mGluR1, Metabotropic glutamate receptor 1; PTH, Parathyroid hormone; AVP, Arginine Vasopressin; GLP-1, Glucagon like peptide-1; DOI, 2,5-Dimethoxy-4-iodoamphetamine.

GPCR downstream signaling

We have discussed a variety of fluorescent sensors to monitor the different status of the GPCR activation process, for example, the binding of an extracellular ligand to GPCR, conformational change of GPCRs, recruitment with G proteins or β-arrestin, GPCR internalization and trafficking, and GPCR dimerization and oligomerization (Figure 1). The final step of GPCR activation initiates the intracellular signaling events specific to the recruited G proteins.

First, the activation of GPCR coupled to Gs protein induces the production of cAMP through the activation of adenylyl cyclase (AC), while the activated GPCR coupled to Gi protein inhibits AC, thus reducing the level of cAMP (Sunahara and

Taussig, 2002; Moreira, 2014). The cAMP level plays an important role in controlling protein kinase A (PKA) activity, which is crucial for CREB-mediated transcription (Delghandi et al., 2005). Therefore, it is useful to apply fluorescent sensors detecting cAMP level or PKA activation for monitoring the downstream functions of GPCRs coupled to Gs and Gi protein. An excellent review of these biosensors is available for further reading (Massengill et al., 2021).

Second, the activation of GPCRs coupled to Gq protein increases intracellular Ca^{2+} levels through the phospholipase C (PLC) signaling pathway (Smrcka et al., 1991; Taylor et al., 1991; Moreira, 2014). Because Ca^{2+} is an important second messenger for a wide variety of cellular processes, there are continuous efforts to develop efficient and sensitive Ca^{2+} sensors. The first FRET-based Ca^{2+} sensors were developed by the Tsien group, which can measure the FRET changes between a donor and an acceptor FP induced by the interaction of Ca^{2+}-bound M13 and calmodulin (Miyawaki et al., 1997). This interaction was also applied to design the first cpFP-based Ca^{2+} sensors GCaMP (Nakai et al., 2001), which has been continuously improved for better sensitivity, brightness, stability, signal-to-noise ratio (Chen et al., 2013; Dana et al., 2019), and different colors (Zhao et al., 2011; Inoue et al., 2019b; Qian et al., 2019). Excellent reviews for the Ca^{2+} sensors are available (Kerruth et al., 2019; Li and Saha, 2021; Lohr et al., 2021).

Finally, the activation of $G_{12/13}$-coupled GPCRs can induce the activation of Rho GTPases (Dhanasekaran and Dermott, 1996; Kozasa et al., 1998). Genetically encoded fluorescent sensors have been developed to monitor the activation of Rho GTPases in live cells based on FRET and dimerization-dependent FP (ddFP) (Kim et al., 2019). More information on the Rho biosensors is available in the previous review (Kim et al., 2021b). These biosensors detecting the GPCR downstream signaling can report the real-time functional outputs of GPCR activation, thus can be applied sequentially or together with other GPCR biosensors discussed in the previous sections.

Conclusion

Upon the binding of extracellular ligands, GPCRs change their conformations to recruit G proteins and/or β-arrestin and mediate downstream signaling events. Then the GPCRs can be internalized and follow endosomal trafficking pathways for recycling or degradation (Figure 1). In this review, we discussed various strategies of genetically encoded fluorescent biosensors that can monitor these stages of GPCR activation with high spatiotemporal resolution. For example, the FRET/BRET-based GPCR biosensors have been designed to monitor different steps of GPCR activation (Figure 2). We discussed the circular permuted FP-based GPCR biosensors, which generally show higher dynamic ranges compared to the FRET/BRET-based biosensors (Figure 3). We also introduced nanobody-based GPCR biosensors (Figure 3) and the GPCR-pH sensor utilizing pH-sensitive FPs (Figure 4). These genetically encoded fluorescent biosensors can be applied to a wide range of GPCR-related research, therefore researchers need to choose the most appropriate GPCR biosensors for their research.

First, the GPCR biosensors are used to elucidate precise molecular mechanisms of GPCR activation and function. For example, the FRET-based biosensors that detect the conformational change of GPCRs provided important information regarding the structural rearrangement of GPCRs during activation (Erdogmus et al., 2019). The sustained GPCR activity at the internalized endosomes (Rasmussen et al., 2011a) as well as other organelles (Godbole et al., 2017; Stoeber et al., 2018) were revealed by Nb-based GPCR biosensors. The fluorescent biosensors that detect the coupling of G protein to GPCRs discovered the structural basis of selective interactions between GPCR and different G proteins (Semack et al., 2016). The dimerization of GPCRs can be identified by FRET-based biosensors (Hlavackova et al., 2012), and functional crosstalk between GPCR dimers can be assessed by cpFP-based GPCR biosensors (Kim et al., 2022). We expect that the development of novel GPCR biosensors and their applications with advanced imaging techniques will promise further exciting discoveries on the molecular mechanisms of GPCR activation and function.

Second, the GPCR biosensors can be used to sensitively monitor the activation of GPCRs in live cells and *in vivo*. Genetically encoded fluorescent biosensors are particularly useful in neuroscience due to their ability to visualize the spatiotemporal activity of neurotransmitter receptors, which are also GPCRs, in complex brain networks. For example, the cpFP-based biosensors were successfully used to detect the release of neurotransmitters such as glutamate (Hires et al., 2008) and GABA (Marvin et al., 2019). Moreover, the real-time activity of neurotransmitter receptors, for example, dopamine receptors (Patriarchi et al., 2018; Sun et al., 2018), was monitored in the mouse brain with the cpFP-based GPCR biosensors. For the understanding of complex brain functions, further efforts will be required to develop improved fluorescent biosensors with enhanced fluorescent response and higher expression levels. In addition to genetically encoded GPCR biosensors, the optogenetic technology which can spatiotemporally control the activity of GPCR, such as OptoXRs (Airan et al., 2009; Tichy et al., 2019), will be further useful to investigate the function of neurotransmission in the brain.

Finally, the GPCR biosensors can be applied for the screening of the drug candidates targeting GPCRs. As GPCRs are major therapeutic targets of more than 30% of FDA-approved drugs (Insel et al., 2019), the genetically encoded GPCR biosensors can be a useful platform for drug screening (Unger et al., 2020). The efficient agonists can be screened and selected by quantifying the fluorescent signals of GPCR biosensors in live cells. For the selected candidates, the functional kinetics of the agonist-induced GPCR activation can be accessed by the GPCR

biosensors (Kim et al., 2021a). Furthermore, the biased agonism can be tested and characterized by the β-arrestin biosensors (Shukla et al., 2008; Hoare et al., 2020). Therefore, the genetically encoded GPCR biosensors are powerful tools to screen and evaluate the drug candidates targeting GPCRs.

Author contributions

HK, I-YB, and JS wrote the manuscript. All authors contributed to the article and approved the submitted version.

Funding

This work was supported by National Research Foundation of Korea grant 2021R1A2C1093429, KIST Institutional grant 2E31523, and Samsung Research Funding and Incubation Center of Samsung Electronics under Project Number SRFC-TC2003-02 (JS), and UST Young Scientist Research Program 2021 through the Korea University of Science and Technology No. 2021YS21 (HK).

Conflict of interest

The authors declare that the research was conducted in the absence of any commercial or financial relationships that could be construed as a potential conflict of interest.

Publisher's note

All claims expressed in this article are solely those of the authors and do not necessarily represent those of their affiliated organizations, or those of the publisher, the editors and the reviewers. Any product that may be evaluated in this article, or claim that may be made by its manufacturer, is not guaranteed or endorsed by the publisher.

References

Aggarwal, A., Liu, R., Chen, Y., Ralowicz, A. J., Bergerson, S. J., Tomaska, F., et al. (2022). Glutamate indicators with improved activation kinetics and localization for imaging synaptic transmission. *bioRxiv*, 2022. doi:10.1101/2022.02.13.480251

Airan, R. D., Thompson, K. R., Fenno, L. E., Bernstein, H., and Deisseroth, K. (2009). Temporally precise *in vivo* control of intracellular signalling. *Nature* 458 (7241), 1025–1029. doi:10.1038/nature07926

Alvarez-Curto, E., Pediani, J. D., and Milligan, G. (2010). Applications of fluorescence and bioluminescence resonance energy transfer to drug discovery at G protein coupled receptors. *Anal. Bioanal. Chem.* 398 (1), 167–180. doi:10.1007/s00216-010-3823-4

Augustine, V., Ebisu, H., Zhao, Y., Lee, S., Ho, B., Mizuno, G. O., et al. (2019). Temporally and spatially distinct thirst satiation signals. *Neuron* 103 (2), 242–249. doi:10.1016/j.neuron.2019.04.039

Azzi, M., Pineyro, G., Pontier, S., Parent, S., Ansanay, H., and Bouvier, M. (2001). Allosteric effects of G protein overexpression on the binding of beta-adrenergic ligands with distinct inverse efficacies. *Mol. Pharmacol.* 60 (5), 999–1007. doi:10.1124/mol.60.5.999

Baird, G. S., Zacharias, D. A., and Tsien, R. Y. (1999). Circular permutation and receptor insertion within green fluorescent proteins. *Proc. Natl. Acad. Sci. U. S. A.* 96 (20), 11241–11246. doi:10.1073/pnas.96.20.11241

Bizzarri, R., Serresi, M., Luin, S., and Beltram, F. (2009). Green fluorescent protein based pH indicators for *in vivo* use: A review. *Anal. Bioanal. Chem.* 393 (4), 1107–1122. doi:10.1007/s00216-008-2515-9

Borden, P. M., Zhang, P., Shivange, A. V., Marvin, J. S., Cichon, J., Dan, C., et al. (2020). A fast genetically encoded fluorescent sensor for faithful *in vivo* acetylcholine detection in mice, fish, worms and flies. *bioRxiv*. doi:10.1101/2020.02.07.939504

Borroto-Escuela, D. O., Romero-Fernandez, W., Tarakanov, A. O., Marcellino, D., Ciruela, F., Agnati, L. F., et al. (2010). Dopamine D2 and 5-hydroxytryptamine 5-HT(2A) receptors assemble into functionally interacting heteromers. *Biochem. Biophys. Res. Commun.* 401 (4), 605–610. doi:10.1016/j.bbrc.2010.09.110

Carpenter, B., and Tate, C. G. (2016). Engineering a minimal G protein to facilitate crystallisation of G protein-coupled receptors in their active conformation. *Protein Eng. Des. Sel.* 29 (12), 583–594. doi:10.1093/protein/gzw049

Casado, V., Cortes, A., Ciruela, F., Mallol, J., Ferre, S., Lluis, C., et al. (2007). Old and new ways to calculate the affinity of agonists and antagonists interacting with G-protein-coupled monomeric and dimeric receptors: The receptor-dimer cooperativity index. *Pharmacol. Ther.* 116 (3), 343–354. doi:10.1016/j.pharmthera.2007.05.010

Chachisvilis, M., Zhang, Y. L., and Frangos, J. A. (2006). G protein-coupled receptors sense fluid shear stress in endothelial cells. *Proc. Natl. Acad. Sci. U. S. A.* 103 (42), 15463–15468. doi:10.1073/pnas.0607224103

Charest, P. G., Terrillon, S., and Bouvier, M. (2005). Monitoring agonist-promoted conformational changes of beta-arrestin in living cells by intramolecular BRET. *EMBO Rep.* 6 (4), 334–340. doi:10.1038/sj.embor.7400373

Chen, T. W., Wardill, T. J., Sun, Y., Pulver, S. R., Renninger, S. L., Baohan, A., et al. (2013). Ultrasensitive fluorescent proteins for imaging neuronal activity. *Nature* 499 (7458), 295–300. doi:10.1038/nature12354

Chun, L. S., Free, R. B., Doyle, T. B., Huang, X. P., Rankin, M. L., and Sibley, D. R. (2013). D1-D2 dopamine receptor synergy promotes calcium signaling via multiple mechanisms. *Mol. Pharmacol.* 84 (2), 190–200. doi:10.1124/mol.113.085175

Clister, T., Mehta, S., and Zhang, J. (2015). Single-cell analysis of G-protein signal transduction. *J. Biol. Chem.* 290 (11), 6681–6688. doi:10.1074/jbc.R114.616391

Dana, H., Sun, Y., Mohar, B., Hulse, B. K., Kerlin, A. M., Hasseman, J. P., et al. (2019). High-performance calcium sensors for imaging activity in neuronal populations and microcompartments. *Nat. Methods* 16 (7), 649–657. doi:10.1038/s41592-019-0435-6

De Groof, T. W. M., Bobkov, V., Heukers, R., and Smit, M. J. (2019). Nanobodies: New avenues for imaging, stabilizing and modulating GPCRs. *Mol. Cell. Endocrinol.* 484, 15–24. doi:10.1016/j.mce.2019.01.021

Delghandi, M. P., Johannessen, M., and Moens, U. (2005). The cAMP signalling pathway activates CREB through PKA, p38 and MSK1 in NIH 3T3 cells. *Cell. Signal.* 17 (11), 1343–1351. doi:10.1016/j.cellsig.2005.02.003

DeWire, S. M., Ahn, S., Lefkowitz, R. J., and Shenoy, S. K. (2007). Beta-arrestins and cell signaling. *Annu. Rev. Physiol.* 69, 483–510. doi:10.1146/annurev.physiol.69.022405.154749

Dhanasekaran, N., and Dermott, J. M. (1996). Signaling by the G12 class of G proteins. *Cell. Signal.* 8 (4), 235–245. doi:10.1016/0898-6568(96)00048-4

Eichel, K., and von Zastrow, M. (2018). Subcellular organization of GPCR signaling. *Trends Pharmacol. Sci.* 39 (2), 200–208. doi:10.1016/j.tips.2017.11.009

Erdogmus, S., Storch, U., Danner, L., Becker, J., Winter, M., Ziegler, N., et al. (2019). Helix 8 is the essential structural motif of mechanosensitive GPCRs. *Nat. Commun.* 10 (1), 5784. doi:10.1038/s41467-019-13722-0

Faron-Gorecka, A., Szlachta, M., Kolasa, M., Solich, J., Gorecki, A., Kusmider, M., et al. (2019). Understanding GPCR dimerization. *Methods Cell Biol.* 149, 155–178. doi:10.1016/bs.mcb.2018.08.005

Feng, J., Zhang, C., Lischinsky, J. E., Jing, M., Zhou, J., Wang, H., et al. (2019). A genetically encoded fluorescent sensor for rapid and specific *in vivo* detection of norepinephrine. *Neuron* 102 (4), 745–761. doi:10.1016/j.neuron.2019.02.037

Ferguson, S. S. (2001). Evolving concepts in G protein-coupled receptor endocytosis: The role in receptor desensitization and signaling. *Pharmacol. Rev.* 53 (1), 1–24.

Ferre, S., Casado, V., Devi, L. A., Filizola, M., Jockers, R., Lohse, M. J., et al. (2014). G protein-coupled receptor oligomerization revisited: Functional and pharmacological perspectives. *Pharmacol. Rev.* 66 (2), 413–434. doi:10.1124/pr.113.008052

Ferre, S., von Euler, G., Johansson, B., Fredholm, B. B., and Fuxe, K. (1991). Stimulation of high-affinity adenosine A2 receptors decreases the affinity of dopamine D2 receptors in rat striatal membranes. *Proc. Natl. Acad. Sci. U. S. A.* 88 (16), 7238–7241. doi:10.1073/pnas.88.16.7238

Fiorentini, C., Busi, C., Gorruso, E., Gotti, C., Spano, P., and Missale, C. (2008). Reciprocal regulation of dopamine D1 and D3 receptor function and trafficking by heterodimerization. *Mol. Pharmacol.* 74 (1), 59–69. doi:10.1124/mol.107.043885

Flock, T., Hauser, A. S., Lund, N., Gloriam, D. E., Balaji, S., and Babu, M. M. (2017). Selectivity determinants of GPCR-G-protein binding. *Nature* 545 (7654), 317–322. doi:10.1038/nature22070

Fuxe, K., Marcellino, D., Leo, G., and Agnati, L. F. (2010). Molecular integration via allosteric interactions in receptor heteromers. A working hypothesis. *Curr. Opin. Pharmacol.* 10 (1), 14–22. doi:10.1016/j.coph.2009.10.010

Gales, C., Rebois, R. V., Hogue, M., Trieu, P., Breit, A., Hebert, T. E., et al. (2005). Real-time monitoring of receptor and G-protein interactions in living cells. *Nat. Methods* 2 (3), 177–184. doi:10.1038/nmeth743

Godbole, A., Lyga, S., Lohse, M. J., and Calebiro, D. (2017). Internalized TSH receptors en route to the TGN induce local Gs-protein signaling and gene transcription. *Nat. Commun.* 8 (1), 443. doi:10.1038/s41467-017-00357-2

Gomes, I., Ayoub, M. A., Fujita, W., Jaeger, W. C., Pfleger, K. D., and Devi, L. A. G. (2016). G protein-coupled receptor heteromers. *Annu. Rev. Pharmacol. Toxicol.* 56, 403–425. doi:10.1146/annurev-pharmtox-011613-135952

Gonzalez-Maeso, J., Ang, R. L., Yuen, T., Chan, P., Weisstaub, N. V., Lopez-Gimenez, J. F., et al. (2008). Identification of a serotonin/glutamate receptor complex implicated in psychosis. *Nature* 452 (7183), 93–97. doi:10.1038/nature06612

Gonzalez-Maeso, J. (2011). GPCR oligomers in pharmacology and signaling. *Mol. Brain* 4 (1), 20. doi:10.1186/1756-6606-4-20

Goodman, O. B., Jr., Krupnick, J. G., Santini, F., Gurevich, V. V., Penn, R. B., Gagnon, A. W., et al. (1996). Beta-arrestin acts as a clathrin adaptor in endocytosis of the beta2-adrenergic receptor. *Nature* 383 (6599), 447–450. doi:10.1038/383447a0

Griffin, B. A., Adams, S. R., and Tsien, R. Y. (1998). Specific covalent labeling of recombinant protein molecules inside live cells. *Science* 281 (5374), 269–272. doi:10.1126/science.281.5374.269

Gupte, T. M., Malik, R. U., Sommese, R. F., Ritt, M., and Sivaramakrishnan, S. (2017). Priming GPCR signaling through the synergistic effect of two G proteins. *Proc. Natl. Acad. Sci. U. S. A.* 114 (14), 3756–3761. doi:10.1073/pnas.1617232114

Haider, R. S., Godbole, A., and Hoffmann, C. (2019). To sense or not to sense-new insights from GPCR-based and arrestin-based biosensors. *Curr. Opin. Cell Biol.* 57, 16–24. doi:10.1016/j.ceb.2018.10.005

Hall, M. P., Unch, J., Binkowski, B. F., Valley, M. P., Butler, B. L., Wood, M. G., et al. (2012). Engineered luciferase reporter from a deep sea shrimp utilizing a novel imidazopyrazinone substrate. *ACS Chem. Biol.* 7 (11), 1848–1857. doi:10.1021/cb3002478

Hamers-Casterman, C., Atarhouch, T., Muyldermans, S., Robinson, G., Hamers, C., Songa, E. B., et al. (1993). Naturally occurring antibodies devoid of light chains. *Nature* 363 (6428), 446–448. doi:10.1038/363446a0

Hasbi, A., Fan, T., Alijaniaram, M., Nguyen, T., Perreault, M. L., O'Dowd, B. F., et al. (2009). Calcium signaling cascade links dopamine D1-D2 receptor heteromer to striatal BDNF production and neuronal growth. *Proc. Natl. Acad. Sci. U. S. A.* 106 (50), 21377–21382. doi:10.1073/pnas.0903676106

Hastings, J. W. (1996). Chemistries and colors of bioluminescent reactions: A review. *Gene* 173, 5–11. doi:10.1016/0378-1119(95)00676-1

Hebert, T. E., and Bouvier, M. (1998). Structural and functional aspects of G protein-coupled receptor oligomerization. *Biochem. Cell Biol.* 76 (1), 1–11. doi:10.1139/bcb-76-1-1

Hein, P., Frank, M., Hoffmann, C., Lohse, M. J., and Bunemann, M. (2005). Dynamics of receptor/G protein coupling in living cells. *EMBO J.* 24 (23), 4106–4114. doi:10.1038/sj.emboj.7600870

Hires, S. A., Zhu, Y., and Tsien, R. Y. (2008). Optical measurement of synaptic glutamate spillover and reuptake by linker optimized glutamate-sensitive fluorescent reporters. *Proc. Natl. Acad. Sci. U. S. A.* 105 (11), 4411–4416. doi:10.1073/pnas.0712008105

Hlavackova, V., Zabel, U., Frankova, D., Batz, J., Hoffmann, C., Prezeau, L., et al. (2012). Sequential inter- and intrasubunit rearrangements during activation of dimeric metabotropic glutamate receptor 1. *Sci. Signal.* 5 (237), ra59. doi:10.1126/scisignal.2002720

Hoare, S. R. J., Tewson, P. H., Quinn, A. M., and Hughes, T. E. (2020). A kinetic method for measuring agonist efficacy and ligand bias using high resolution biosensors and a kinetic data analysis framework. *Sci. Rep.* 10 (1), 1766. doi:10.1038/s41598-020-58421-9

Hoffmann, C., Gaietta, G., Bunemann, M., Adams, S. R., Oberdorff-Maass, S., Behr, B., et al. (2005). A FlAsH-based FRET approach to determine G protein-coupled receptor activation in living cells. *Nat. Methods* 2 (3), 171–176. doi:10.1038/nmeth742

Hoffmann, C., Gaietta, G., Zurn, A., Adams, S. R., Terrillon, S., Ellisman, M. H., et al. (2010). Fluorescent labeling of tetracysteine-tagged proteins in intact cells. *Nat. Protoc.* 5 (10), 1666–1677. doi:10.1038/nprot.2010.129

Hynes, T. R., Mervine, S. M., Yost, E. A., Sabo, J. L., and Berlot, C. H. (2004). Live cell imaging of Gs and the beta2-adrenergic receptor demonstrates that both alphas and beta1gamma7 internalize upon stimulation and exhibit similar trafficking patterns that differ from that of the beta2-adrenergic receptor. *J. Biol. Chem.* 279 (42), 44101–44112. doi:10.1074/jbc.M405151200

Inoue, A., Raimondi, F., Kadji, F. M. N., Singh, G., Kishi, T., Uwamizu, A., et al. (2019). Illuminating G-protein-coupling selectivity of GPCRs. *Cell* 177 (7), 1933–1947. doi:10.1016/j.cell.2019.04.044

Inoue, M., Takeuchi, A., Manita, S., Horigane, S. I., Sakamoto, M., Kawakami, R., et al. (2019). Rational engineering of XCaMPs, a multicolor GECI suite for *in vivo* imaging of complex brain circuit dynamics. *Cell* 177 (5), 1346–1360. doi:10.1016/j.cell.2019.04.007

Insel, P. A., Sriram, K., Gorr, M. W., Wiley, S. Z., Michkov, A., Salmeron, C., et al. (2019). GPCRomics: An approach to discover GPCR drug targets. *Trends Pharmacol. Sci.* 40 (6), 378–387. doi:10.1016/j.tips.2019.04.001

Irannejad, R., Tomshine, J. C., Tomshine, J. R., Chevalier, M., Mahoney, J. P., Steyaert, J., et al. (2013). Conformational biosensors reveal GPCR signalling from endosomes. *Nature* 495 (7442), 534–538. doi:10.1038/nature12000

Janssen, P. M., Schillinger, W., Donahue, J. K., Zeitz, O., Emami, S., Lehnart, S. E., et al. (2002). Intracellular beta-blockade: Overexpression of galpha(i2) depresses the beta-adrenergic response in intact myocardium. *Cardiovasc. Res.* 55 (2), 300–308. doi:10.1016/s0008-6363(02)00406-6

Jing, M., Li, Y., Zeng, J., Huang, P., Skirzewski, M., Kljakic, O., et al. (2020). An optimized acetylcholine sensor for monitoring *in vivo* cholinergic activity. *Nat. Methods* 17 (11), 1139–1146. doi:10.1038/s41592-020-0953-2

Jordan, B. A., and Devi, L. A. (1999). G-protein-coupled receptor heterodimerization modulates receptor function. *Nature* 399 (6737), 697–700. doi:10.1038/21441

Jordan, B. A., Gomes, I., Rios, C., Filipovska, J., and Devi, L. A. (2003). Functional interactions between mu opioid and alpha 2A-adrenergic receptors. *Mol. Pharmacol.* 64 (6), 1317–1324. doi:10.1124/mol.64.6.1317

Kauk, M., and Hoffmann, C. (2018). Intramolecular and intermolecular FRET sensors for GPCRs - monitoring conformational changes and beyond. *Trends Pharmacol. Sci.* 39 (2), 123–135. doi:10.1016/j.tips.2017.10.011

Kerruth, S., Coates, C., Durst, C. D., Oertner, T. G., and Torok, K. (2019). The kinetic mechanisms of fast-decay red-fluorescent genetically encoded calcium indicators. *J. Biol. Chem.* 294 (11), 3934–3946. doi:10.1074/jbc.RA118.004543

Kim, H., Ju, J., Lee, H. N., Chun, H., and Seong, J. (2021). Genetically encoded biosensors based on fluorescent proteins. *Sensors (Basel).* 21 (3), 795. doi:10.3390/s21030795

Kim, H., Lee, H. N., Choi, J., and Seong, J. (2021). Spatiotemporal characterization of GPCR activity and function during endosomal trafficking pathway. *Anal. Chem.* 93 (4), 2010–2017. doi:10.1021/acs.analchem.0c03323

Kim, H., Nam, M. H., Jeong, S., Lee, H., Oh, S. J., Kim, J., et al. (2022). Visualization of differential GPCR crosstalk in DRD1-DRD2 heterodimer upon different dopamine levels. *Prog. Neurobiol.* 213, 102266. doi:10.1016/j.pneurobio.2022.102266

Kim, J., Lee, S., Jung, K., Oh, W. C., Kim, N., Son, S., et al. (2019). Intensiometric biosensors visualize the activity of multiple small GTPases *in vivo*. *Nat. Commun.* 10 (1), 211. doi:10.1038/s41467-018-08217-3

Kobilka, B. K., and Deupi, X. (2007). Conformational complexity of G-protein-coupled receptors. *Trends Pharmacol. Sci.* 28 (8), 397–406. doi:10.1016/j.tips.2007.06.003

Kobilka, B. K. (2007). G protein coupled receptor structure and activation. *Biochim. Biophys. Acta* 1768 (4), 794–807. doi:10.1016/j.bbamem.2006.10.021

Kostyuk, A. I., Demidovich, A. D., Kotova, D. A., Belousov, V. V., and Bilan, D. S. (2019). Circularly permuted fluorescent protein-based indicators: History, principles, and classification. *Int. J. Mol. Sci.* 20 (17), E4200. doi:10.3390/ijms20174200

Kozasa, T., Jiang, X., Hart, M. J., Sternweis, P. M., Singer, W. D., Gilman, A. G., et al. (1998). p115 RhoGEF, a GTPase activating protein for Galpha12 and Galpha13. *Science* 280 (5372), 2109–2111. doi:10.1126/science.280.5372.2109

Krasel, C., Bunemann, M., Lorenz, K., and Lohse, M. J. (2005). Beta-arrestin binding to the beta2-adrenergic receptor requires both receptor phosphorylation and receptor activation. *J. Biol. Chem.* 280 (10), 9528–9535. doi:10.1074/jbc.M413078200

Kunishima, N., Shimada, Y., Tsuji, Y., Sato, T., Yamamoto, M., Kumasaka, T., et al. (2000). Structural basis of glutamate recognition by a dimeric metabotropic glutamate receptor. *Nature* 407 (6807), 971–977. doi:10.1038/35039564

Labouesse, M. A., and Patriarchi, T. (2021). A versatile GPCR toolkit to track *in vivo* neuromodulation: Not a one-size-fits-all sensor. *Neuropsychopharmacology* 46 (12), 2043–2047. doi:10.1038/s41386-021-00982-y

Lagerstrom, M. C., and Schioth, H. B. (2008). Structural diversity of G protein-coupled receptors and significance for drug discovery. *Nat. Rev. Drug Discov.* 7 (4), 339–357. doi:10.1038/nrd2518

Laporte, S. A., Oakley, R. H., Zhang, J., Holt, J. A., Ferguson, S. S., Caron, M. G., et al. (1999). The beta2-adrenergic receptor/betaarrestin complex recruits the clathrin adaptor AP-2 during endocytosis. *Proc. Natl. Acad. Sci. U. S. A.* 96 (7), 3712–3717. doi:10.1073/pnas.96.7.3712

Lee, M. H., Appleton, K. M., Strungs, E. G., Kwon, J. Y., Morinelli, T. A., Peterson, Y. K., et al. (2016). The conformational signature of beta-arrestin2 predicts its trafficking and signalling functions. *Nature* 531 (7596), 665–668. doi:10.1038/nature17154

Lefevre, E. M., Pisansky, M. T., Toddes, C., Baruffaldi, F., Pravetoni, M., Tian, L., et al. (2020). Interruption of continuous opioid exposure exacerbates drug-evoked adaptations in the mesolimbic dopamine system. *Neuropsychopharmacology* 45 (11), 1781–1792. doi:10.1038/s41386-020-0643-x

Lefkowitz, R. J. (2013). A brief history of G-protein coupled receptors (Nobel Lecture). *Angew. Chem. Int. Ed. Engl.* 52 (25), 6366–6378. doi:10.1002/anie.201301924

Lefkowitz, R. J., and Shenoy, S. K. (2005). Transduction of receptor signals by beta-arrestins. *Science* 308 (5721), 512–517. doi:10.1126/science.1109237

Li, E. S., and Saha, M. S. (2021). Optimizing calcium detection methods in animal systems: A sandbox for synthetic biology. *Biomolecules* 11 (3), 343. doi:10.3390/biom11030343

Lohr, C., Beiersdorfer, A., Fischer, T., Hirnet, D., Rotermund, N., Sauer, J., et al. (2021). Using genetically encoded calcium indicators to study astrocyte physiology: A field guide. *Front. Cell. Neurosci.* 15, 690147. doi:10.3389/fncel.2021.690147

Lohse, M. J. (2010). Dimerization in GPCR mobility and signaling. *Curr. Opin. Pharmacol.* 10 (1), 53–58. doi:10.1016/j.coph.2009.10.007

Lohse, M. J., Nuber, S., and Hoffmann, C. (2012). Fluorescence/bioluminescence resonance energy transfer techniques to study G-protein-coupled receptor activation and signaling. *Pharmacol. Rev.* 64 (2), 299–336. doi:10.1124/pr.110.004309

Lukasiewicz, S., Polit, A., Kedracka-Krok, S., Wedzony, K., Mackowiak, M., and Dziedzicka-Wasylewska, M. (2010). Hetero-dimerization of serotonin 5-HT(2A) and dopamine D(2) receptors. *Biochim. Biophys. Acta* 1803 (12), 1347–1358. doi:10.1016/j.bbamcr.2010.08.010

Lutas, A., Kucukdereli, H., Alturkistani, O., Carty, C., Sugden, A. U., Fernando, K., et al. (2019). State-specific gating of salient cues by midbrain dopaminergic input to basal amygdala. *Nat. Neurosci.* 22 (11), 1820–1833. doi:10.1038/s41593-019-0506-0

Maier-Peuschel, M., Frolich, N., Dees, C., Hommers, L. G., Hoffmann, C., Nikolaev, V. O., et al. (2010). A fluorescence resonance energy transfer-based M2 muscarinic receptor sensor reveals rapid kinetics of allosteric modulation. *J. Biol. Chem.* 285 (12), 8793–8800. doi:10.1074/jbc.M109.098517

Malik, R. U., Ritt, M., DeVree, B. T., Neubig, R. R., Sunahara, R. K., and Sivaramakrishnan, S. (2013). Detection of G protein-selective G protein-coupled receptor (GPCR) conformations in live cells. *J. Biol. Chem.* 288 (24), 17167–17178. doi:10.1074/jbc.M113.464065

Manchanda, Y., Ramchunder, Z., Shchepinova, M. M., Rutter, G. A., Inoue, A., Tate, E. W., et al. (2021). Expression of mini-G proteins specifically halt cognate GPCR trafficking and intracellular signalling. *bioRxiv*, 2021. doi:10.1101/2021.11.24.469908

Manglik, A., and Kruse, A. C. (2017). Structural basis for G protein-coupled receptor activation. *Biochemistry* 56 (42), 5628–5634. doi:10.1021/acs.biochem.7b00747

Marchese, A., Paing, M. M., Temple, B. R., and Trejo, J. (2008). G protein-coupled receptor sorting to endosomes and lysosomes. *Annu. Rev. Pharmacol. Toxicol.* 48, 601–629. doi:10.1146/annurev.pharmtox.48.113006.094646

Marvin, J. S., Borghuis, B. G., Tian, L., Cichon, J., Harnett, M. T., Akerboom, J., et al. (2013). An optimized fluorescent probe for visualizing glutamate neurotransmission. *Nat. Methods* 10 (2), 162–170. doi:10.1038/nmeth.2333

Marvin, J. S., Scholl, B., Wilson, D. E., Podgorski, K., Kazemipour, A., Muller, J. A., et al. (2018). Stability, affinity, and chromatic variants of the glutamate sensor iGluSnFR. *Nat. Methods* 15 (11), 936–939. doi:10.1038/s41592-018-0171-3

Marvin, J. S., Shimoda, Y., Magloire, V., Leite, M., Kawashima, T., Jensen, T. P., et al. (2019). A genetically encoded fluorescent sensor for *in vivo* imaging of GABA. *Nat. Methods* 16 (8), 763–770. doi:10.1038/s41592-019-0471-2

Massengill, C. I., Day-Cooney, J., Mao, T., and Zhong, H. (2021). Genetically encoded sensors towards imaging cAMP and PKA activity *in vivo*. *J. Neurosci. Methods* 362, 109298. doi:10.1016/j.jneumeth.2021.109298

Maziarz, M., Park, J. C., Leyme, A., Marivin, A., Garcia-Lopez, A., Patel, P. P., et al. (2020). Revealing the activity of trimeric G-proteins in live cells with a versatile biosensor design. *Cell* 182 (3), 770–785. e16. doi:10.1016/j.cell.2020.06.020

McManus, O. B., Werley, C. A., and Dempsey, G. T. (2019). Inhale, exhale: Probing the inside-out mechanism of nicotine addiction using novel fluorescent sensors. *J. Gen. Physiol.* 151 (6), 714–717. doi:10.1085/jgp.201912325

Milligan, G. (2010). The role of dimerisation in the cellular trafficking of G-protein-coupled receptors. *Curr. Opin. Pharmacol.* 10 (1), 23–29. doi:10.1016/j.coph.2009.09.010

Miyawaki, A., Llopis, J., Heim, R., McCaffery, J. M., Adams, J. A., Ikura, M., et al. (1997). Fluorescent indicators for Ca2+ based on green fluorescent proteins and calmodulin. *Nature* 388 (6645), 882–887. doi:10.1038/42264

Mohammad Nezhady, M. A., Rivera, J. C., and Chemtob, S. (2020). Location bias as emerging paradigm in GPCR biology and drug discovery. *iScience* 23 (10), 101643. doi:10.1016/j.isci.2020.101643

Mohebi, A., Pettibone, J. R., Hamid, A. A., Wong, J. T., Vinson, L. T., Patriarchi, T., et al. (2019). Publisher Correction: Dissociable dopamine dynamics for learning and motivation. *Nature* 571 (7763), E3. doi:10.1038/s41586-019-1353-6

Moo, E. V., van Senten, J. R., Brauner-Osborne, H., and Moller, T. C. (2021). Arrestin-dependent and -independent internalization of G protein-coupled receptors: Methods, mechanisms, and implications on cell signaling. *Mol. Pharmacol.* 99 (4), 242–255. doi:10.1124/molpharm.120.000192

Moreira, I. S. (2014). Structural features of the G-protein/GPCR interactions. *Biochim. Biophys. Acta* 1840 (1), 16–33. doi:10.1016/j.bbagen.2013.08.027

Muyldermans, S. (2013). Nanobodies: Natural single-domain antibodies. *Annu. Rev. Biochem.* 82, 775–797. doi:10.1146/annurev-biochem-063011-092449

Nakai, J., Ohkura, M., and Imoto, K. (2001). A high signal-to-noise Ca(2+) probe composed of a single green fluorescent protein. *Nat. Biotechnol.* 19 (2), 137–141. doi:10.1038/84397

Nakanishi, J., Takarada, T., Yunoki, S., Kikuchi, Y., and Maeda, M. (2006). FRET-based monitoring of conformational change of the beta2 adrenergic receptor in living cells. *Biochem. Biophys. Res. Commun.* 343 (4), 1191–1196. doi:10.1016/j.bbrc.2006.03.064

Nash, C. A., Wei, W., Irannejad, R., and Smrcka, A. V. (2019). Golgi localized β1-adrenergic receptors stimulate Golgi PI4P hydrolysis by PLCε to regulate cardiac hypertrophy. *Elife* 8, e48167. doi:10.7554/eLife.48167

Nehme, R., Carpenter, B., Singhal, A., Strege, A., Edwards, P. C., White, C. F., et al. (2017). Mini-G proteins: Novel tools for studying GPCRs in their active conformation. *PLoS One* 12 (4), e0175642. doi:10.1371/journal.pone.0175642

Neve, K. A., Seamans, J. K., and Trantham-Davidson, H. (2004). Dopamine receptor signaling. *J. Recept. Signal Transduct. Res.* 24 (3), 165–205. doi:10.1081/rrs-200029981

Nikolaev, V. O., Hoffmann, C., Bunemann, M., Lohse, M. J., and Vilardaga, J. P. (2006). Molecular basis of partial agonism at the neurotransmitter alpha2A-adrenergic receptor and Gi-protein heterotrimer. *J. Biol. Chem.* 281 (34), 24506–24511. doi:10.1074/jbc.M603266200

Nuber, S., Zabel, U., Lorenz, K., Nuber, A., Milligan, G., Tobin, A. B., et al. (2016). β-Arrestin biosensors reveal a rapid, receptor-dependent activation/deactivation cycle. *Nature* 531 (7596), 661–664. doi:10.1038/nature17198

Oishi, A., Dam, J., and Jockers, R. (2020). β-Arrestin-2 BRET biosensors detect different β-arrestin-2 conformations in interaction with GPCRs. *ACS Sens.* 5 (1), 57–64. doi:10.1021/acssensors.9b01414

Okumoto, S., Looger, L. L., Micheva, K. D., Reimer, R. J., Smith, S. J., and Frommer, W. B. (2005). Detection of glutamate release from neurons by genetically encoded surface-displayed FRET nanosensors. *Proc. Natl. Acad. Sci. U. S. A.* 102 (24), 8740–8745. doi:10.1073/pnas.0503274102

Oldham, W. M., Van Eps, N., Preininger, A. M., Hubbell, W. L., and Hamm, H. E. (2006). Mechanism of the receptor-catalyzed activation of heterotrimeric G proteins. *Nat. Struct. Mol. Biol.* 13 (9), 772–777. doi:10.1038/nsmb1129

Ozkan, A. D., Gettas, T., Sogata, A., Phaychanpheng, W., Zhou, M., and Lacroix, J. J. (2021). Mechanical and chemical activation of GPR68 probed with a genetically encoded fluorescent reporter. *J. Cell Sci.* 134 (16), jcs255455. doi:10.1242/jcs.255455

Padilla-Parra, S., and Tramier, M. (2012). FRET microscopy in the living cell: Different approaches, strengths and weaknesses. *Bioessays* 34 (5), 369–376. doi:10.1002/bies.201100086

Patriarchi, T., Cho, J. R., Merten, K., Howe, M. W., Marley, A., Xiong, W. H., et al. (2018). Ultrafast neuronal imaging of dopamine dynamics with designed genetically encoded sensors. *Science* 360 (6396), eaat4422. doi:10.1126/science.aat4422

Patriarchi, T., Mohebi, A., Sun, J., Marley, A., Liang, R., Dong, C., et al. (2020). An expanded palette of dopamine sensors for multiplex imaging *in vivo*. *Nat. Methods* 17 (11), 1147–1155. doi:10.1038/s41592-020-0936-3

Pfleger, K. D., and Eidne, K. A. (2005). Monitoring the formation of dynamic G-protein-coupled receptor-protein complexes in living cells. *Biochem. J.* 385, 625–637. doi:10.1042/BJ20041361

Pierce, K. L., Premont, R. T., and Lefkowitz, R. J. (2002). Seven-transmembrane receptors. *Nat. Rev. Mol. Cell Biol.* 3 (9), 639–650. doi:10.1038/nrm908

Pin, J. P., Neubig, R., Bouvier, M., Devi, L., Filizola, M., Javitch, J. A., et al. (2007). International Union of Basic and Clinical Pharmacology. LXVII. Recommendations for the recognition and nomenclature of G protein-coupled receptor heteromultimers. *Pharmacol. Rev.* 59 (1), 5–13. doi:10.1124/pr.59.1.5

Qian, Y., Piatkevich, K. D., Mc Larney, B., Abdelfattah, A. S., Mehta, S., Murdock, M. H., et al. (2019). A genetically encoded near-infrared fluorescent calcium ion indicator. *Nat. Methods* 16 (2), 171–174. doi:10.1038/s41592-018-0294-6

Rasmussen, S. G., Choi, H. J., Fung, J. J., Pardon, E., Casarosa, P., Chae, P. S., et al. (2011). Structure of a nanobody-stabilized active state of the β(2) adrenoceptor. *Nature* 469 (7329), 175–180. doi:10.1038/nature09648

Rasmussen, S. G., DeVree, B. T., Zou, Y., Kruse, A. C., Chung, K. Y., Kobilka, T. S., et al. (2011). Crystal structure of the β2 adrenergic receptor-Gs protein complex. *Nature* 477 (7366), 549–555. doi:10.1038/nature10361

Reiner, S., Ambrosio, M., Hoffmann, C., and Lohse, M. J. (2010). Differential signaling of the endogenous agonists at the beta2-adrenergic receptor. *J. Biol. Chem.* 285 (46), 36188–36198. doi:10.1074/jbc.M110.175604

Rochais, F., Vilardaga, J. P., Nikolaev, V. O., Bunemann, M., Lohse, M. J., and Engelhardt, S. (2007). Real-time optical recording of beta1-adrenergic receptor activation reveals supersensitivity of the Arg389 variant to carvedilol. *J. Clin. Invest.* 117 (1), 229–235. doi:10.1172/JCI30012

Rosenbaum, D. M., Zhang, C., Lyons, J. A., Holl, R., Aragao, D., Arlow, D. H., et al. (2011). Structure and function of an irreversible agonist-β(2) adrenoceptor complex. *Nature* 469 (7329), 236–240. doi:10.1038/nature09665

Sabatini, B. L., and Tian, L. (2020). Imaging neurotransmitter and neuromodulator dynamics *in vivo* with genetically encoded indicators. *Neuron* 108 (1), 17–32. doi:10.1016/j.neuron.2020.09.036

Salahpour, A., Espinoza, S., Masri, B., Lam, V., Barak, L. S., and Gainetdinov, R. R. (2012). BRET biosensors to study GPCR biology, pharmacology, and signal transduction. *Front. Endocrinol.* 3, 105. doi:10.3389/fendo.2012.00105

Semack, A., Sandhu, M., Malik, R. U., Vaidehi, N., and Sivaramakrishnan, S. (2016). Structural elements in the gαs and Gαq C termini that mediate selective G protein-coupled receptor (GPCR) signaling. *J. Biol. Chem.* 291 (34), 17929–17940. doi:10.1074/jbc.M116.735720

Shaner, N. C., Lambert, G. G., Chammas, A., Ni, Y., Cranfill, P. J., Baird, M. A., et al. (2013). A bright monomeric green fluorescent protein derived from *Branchiostoma lanceolatum*. *Nat. Methods* 10 (5), 407–409. doi:10.1038/nmeth.2413

Shen, Y., Rosendale, M., Campbell, R. E., and Perrais, D. (2014). pHuji, a pH-sensitive red fluorescent protein for imaging of exo- and endocytosis. *J. Cell Biol.* 207 (3), 419–432. doi:10.1083/jcb.201404107

Shukla, A. K., Manglik, A., Kruse, A. C., Xiao, K., Reis, R. I., Tseng, W. C., et al. (2013). Structure of active beta-arrestin-1 bound to a G-protein-coupled receptor phosphopeptide. *Nature* 497 (7447), 137–141. doi:10.1038/nature12120

Shukla, A. K., Violin, J. D., Whalen, E. J., Gesty-Palmer, D., Shenoy, S. K., and Lefkowitz, R. J. (2008). Distinct conformational changes in beta-arrestin report biased agonism at seven-transmembrane receptors. *Proc. Natl. Acad. Sci. U. S. A.* 105 (29), 9988–9993. doi:10.1073/pnas.0804246105

Shukla, A. K., Westfield, G. H., Xiao, K., Reis, R. I., Huang, L. Y., Tripathi-Shukla, P., et al. (2014). Visualization of arrestin recruitment by a G-protein-coupled receptor. *Nature* 512 (7513), 218–222. doi:10.1038/nature13430

Sivaramakrishnan, S., and Spudich, J. A. (2011). Systematic control of protein interaction using a modular ER/K alpha-helix linker. *Proc. Natl. Acad. Sci. U. S. A.* 108 (51), 20467–20472. doi:10.1073/pnas.1116066108

Smrcka, A. V., Hepler, J. R., Brown, K. O., and Sternweis, P. C. (1991). Regulation of polyphosphoinositide-specific phospholipase C activity by purified Gq. *Science* 251 (4995), 804–807. doi:10.1126/science.1846707

Stoeber, M., Jullie, D., Lobingier, B. T., Laeremans, T., Steyaert, J., Schiller, P. W., et al. (2018). A genetically encoded biosensor reveals location bias of opioid drug action. *Neuron* 98 (5), 963–976. doi:10.1016/j.neuron.2018.04.021

Stumpf, A. D., and Hoffmann, C. (2016). Optical probes based on G protein-coupled receptors - added work or added value? *Br. J. Pharmacol.* 173 (2), 255–266. doi:10.1111/bph.13382

Sun, F., Zeng, J., Jing, M., Zhou, J., Feng, J., Owen, S. F., et al. (2018). A genetically encoded fluorescent sensor enables rapid and specific detection of dopamine in flies, fish, and mice. *Cell* 174 (2), 481–496. doi:10.1016/j.cell.2018.06.042

Sun, F., Zhou, J., Dai, B., Qian, T., Zeng, J., Li, X., et al. (2020). Next-generation GRAB sensors for monitoring dopaminergic activity *in vivo*. *Nat. Methods* 17 (11), 1156–1166. doi:10.1038/s41592-020-00981-9

Sunahara, R. K., and Taussig, R. (2002). Isoforms of mammalian adenylyl cyclase: Multiplicities of signaling. *Mol. Interv.* 2 (3), 168–184. doi:10.1124/mi.2.3.168

Szalai, B., Barkai, L., Turu, G., Szidonya, L., Varnai, P., and Hunyady, L. (2012). Allosteric interactions within the AT_1 angiotensin receptor homodimer: Role of the conserved DRY motif. *Biochem. Pharmacol.* 84 (4), 477–485. doi:10.1016/j.bcp.2012.04.014

Taylor, S. J., Chae, H. Z., Rhee, S. G., and Exton, J. H. (1991). Activation of the beta 1 isozyme of phospholipase C by alpha subunits of the Gq class of G proteins. *Nature* 350 (6318), 516–518. doi:10.1038/350516a0

Tichy, A. M., Gerrard, E. J., Sexton, P. M., and Janovjak, H. (2019). Light-activated chimeric GPCRs: Limitations and opportunities. *Curr. Opin. Struct. Biol.* 57, 196–203. doi:10.1016/j.sbi.2019.05.006

Tsai, C. J., Marino, J., Adaixo, R., Pamula, F., Muehle, J., Maeda, S., et al. (2019). Cryo-EM structure of the rhodopsin-Gαi-βγ complex reveals binding of the rhodopsin C-terminal tail to the gβ subunit. *Elife* 8, e46041. doi:10.7554/eLife.46041

Tsien, R. Y. (2006). Breeding and building molecules to spy on cells and tumors. *Keio J. Med.* 55 (4), 127–140. doi:10.2302/kjm.55.127

Tsvetanova, N. G., and von Zastrow, M. (2014). Spatial encoding of cyclic AMP signaling specificity by GPCR endocytosis. *Nat. Chem. Biol.* 10 (12), 1061–1065. doi:10.1038/nchembio.1665

Undieh, A. S. (2010). Pharmacology of signaling induced by dopamine D(1)-like receptor activation. *Pharmacol. Ther.* 128 (1), 37–60. doi:10.1016/j.pharmthera.2010.05.003

Unger, E. K., Keller, J. P., Altermatt, M., Liang, R., Matsui, A., Dong, C., et al. (2020). Directed evolution of a selective and sensitive serotonin sensor via machine learning. *Cell* 183 (7), 1986–2002 e26. doi:10.1016/j.cell.2020.11.040

Urizar, E., Yano, H., Kolster, R., Gales, C., Lambert, N., and Javitch, J. A. (2011). CODA-RET reveals functional selectivity as a result of GPCR heteromerization. *Nat. Chem. Biol.* 7 (9), 624–630. doi:10.1038/nchembio.623

Vassilatis, D. K., Hohmann, J. G., Zeng, H., Li, F., Ranchalis, J. E., Mortrud, M. T., et al. (2003). The G protein-coupled receptor repertoires of human and mouse. *Proc. Natl. Acad. Sci. U. S. A.* 100 (8), 4903–4908. doi:10.1073/pnas.0230374100

Vilardaga, J. P., Bunemann, M., Krasel, C., Castro, M., and Lohse, M. J. (2003). Measurement of the millisecond activation switch of G protein-coupled receptors in living cells. *Nat. Biotechnol.* 21 (7), 807–812. doi:10.1038/nbt838

Vilardaga, J. P., Steinmeyer, R., Harms, G. S., and Lohse, M. J. (2005). Molecular basis of inverse agonism in a G protein-coupled receptor. *Nat. Chem. Biol.* 1 (1), 25–28. doi:10.1038/nchembio705

Wacker, D., Stevens, R. C., and Roth, B. L. (2017). How ligands illuminate GPCR molecular pharmacology. *Cell* 170 (3), 414–427. doi:10.1016/j.cell.2017.07.009

Wan, J., Peng, W., Li, X., Qian, T., Song, K., Zeng, J., et al. (2021). A genetically encoded sensor for measuring serotonin dynamics. *Nat. Neurosci.* 24 (5), 746–752. doi:10.1038/s41593-021-00823-7

Wan, Q., Okashah, N., Inoue, A., Nehme, R., Carpenter, B., Tate, C. G., et al. (2018). Mini G protein probes for active G protein-coupled receptors (GPCRs) in live cells. *J. Biol. Chem.* 293 (19), 7466–7473. doi:10.1074/jbc.RA118.001975

Weis, W. I., and Kobilka, B. K. (2018). The molecular basis of G protein-coupled receptor activation. *Annu. Rev. Biochem.* 87, 897–919. doi:10.1146/annurev-biochem-060614-033910

Wheatley, M., Wootten, D., Conner, M. T., Simms, J., Kendrick, R., Logan, R. T., et al. (2012). Lifting the lid on GPCRs: The role of extracellular loops. *Br. J. Pharmacol.* 165 (6), 1688–1703. doi:10.1111/j.1476-5381.2011.01629.x

Wootten, D., Christopoulos, A., Marti-Solano, M., Babu, M. M., and Sexton, P. M. (2018). Mechanisms of signalling and biased agonism in G protein-coupled receptors. *Nat. Rev. Mol. Cell Biol.* 19 (10), 638–653. doi:10.1038/s41580-018-0049-3

Wu, J., Abdelfattah, A. S., Zhou, H., Ruangkittisakul, A., Qian, Y., Ballanyi, K., et al. (2018). Genetically encoded glutamate indicators with altered color and topology. *ACS Chem. Biol.* 13 (7), 1832–1837. doi:10.1021/acschembio.7b01085

Wu, V., Yeerna, H., Nohata, N., Chiou, J., Harismendy, O., Raimondi, F., et al. (2019). Illuminating the Onco-GPCRome: Novel G protein-coupled receptor-driven oncocrine networks and targets for cancer immunotherapy. *J. Biol. Chem.* 294 (29), 11062–11086. doi:10.1074/jbc.REV119.005601

Xu, J., Mathur, J., Vessieres, E., Hammack, S., Nonomura, K., Favre, J., et al. (2018). GPR68 senses flow and is essential for vascular physiology. *Cell* 173 (3), 762–775. e16. doi:10.1016/j.cell.2018.03.076

Zhang, W. H., Herde, M. K., Mitchell, J. A., Whitfield, J. H., Wulff, A. B., Vongsouthi, V., et al. (2018). Monitoring hippocampal glycine with the computationally designed optical sensor GlyFS. *Nat. Chem. Biol.* 14 (9), 861–869. doi:10.1038/s41589-018-0108-2

Zhang, X., Tan, F., and Skidgel, R. A. (2013). Carboxypeptidase M is a positive allosteric modulator of the kinin B1 receptor. *J. Biol. Chem.* 288 (46), 33226–33240. doi:10.1074/jbc.M113.520791

Zhang, Y. L., Frangos, J. A., and Chachisvilis, M. (2009). Mechanical stimulus alters conformation of type 1 parathyroid hormone receptor in bone cells. *Am. J. Physiol. Cell Physiol.* 296 (6), C1391–C1399. doi:10.1152/ajpcell.00549.2008

Zhao, Y., Araki, S., Wu, J., Teramoto, T., Chang, Y. F., Nakano, M., et al. (2011). An expanded palette of genetically encoded Ca^{2+} indicators. *Science* 333 (6051), 1888–1891. doi:10.1126/science.1208592

Zhou, Y., Meng, J., Xu, C., and Liu, J. (2021). Multiple GPCR functional assays based on resonance energy transfer sensors. *Front. Cell Dev. Biol.* 9, 611443. doi:10.3389/fcell.2021.611443

Advantages of publishing in Frontiers

OPEN ACCESS
Articles are free to read for greatest visibility and readership

FAST PUBLICATION
Around 90 days from submission to decision

HIGH QUALITY PEER-REVIEW
Rigorous, collaborative, and constructive peer-review

TRANSPARENT PEER-REVIEW
Editors and reviewers acknowledged by name on published articles

Frontiers
Avenue du Tribunal-Fédéral 34
1005 Lausanne | Switzerland

Visit us: www.frontiersin.org
Contact us: frontiersin.org/about/contact

REPRODUCIBILITY OF RESEARCH
Support open data and methods to enhance research reproducibility

DIGITAL PUBLISHING
Articles designed for optimal readership across devices

FOLLOW US
@frontiersin

IMPACT METRICS
Advanced article metrics track visibility across digital media

EXTENSIVE PROMOTION
Marketing and promotion of impactful research

LOOP RESEARCH NETWORK
Our network increases your article's readership